technische universität
dortmund

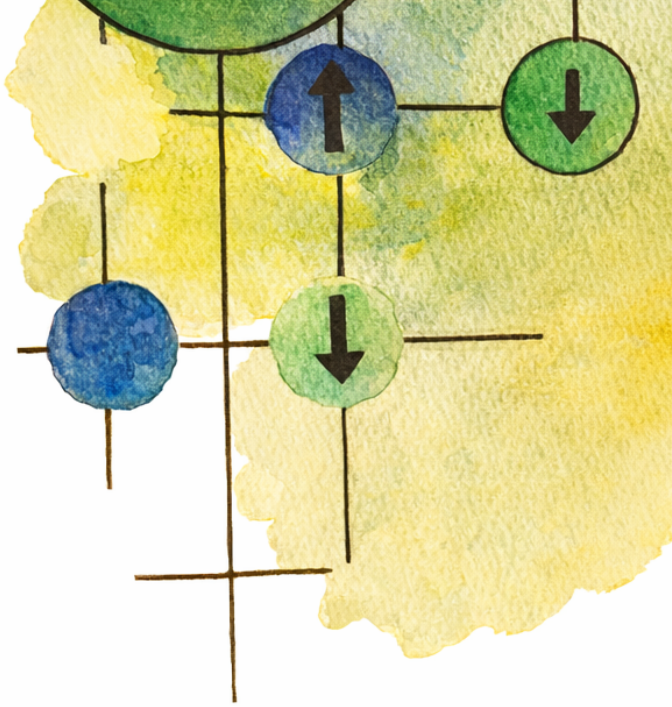

Spin wave excitations and their interactions in two-dimensional antiferromagnets

Dissertation to obtain the academic degree
Doctor rerum naturalium

2026

Dag-Björn Hering
born in Castrop-Rauxel

Uhrig Group — Condensed Matter Theory
Department of Physics
TU Dortmund University

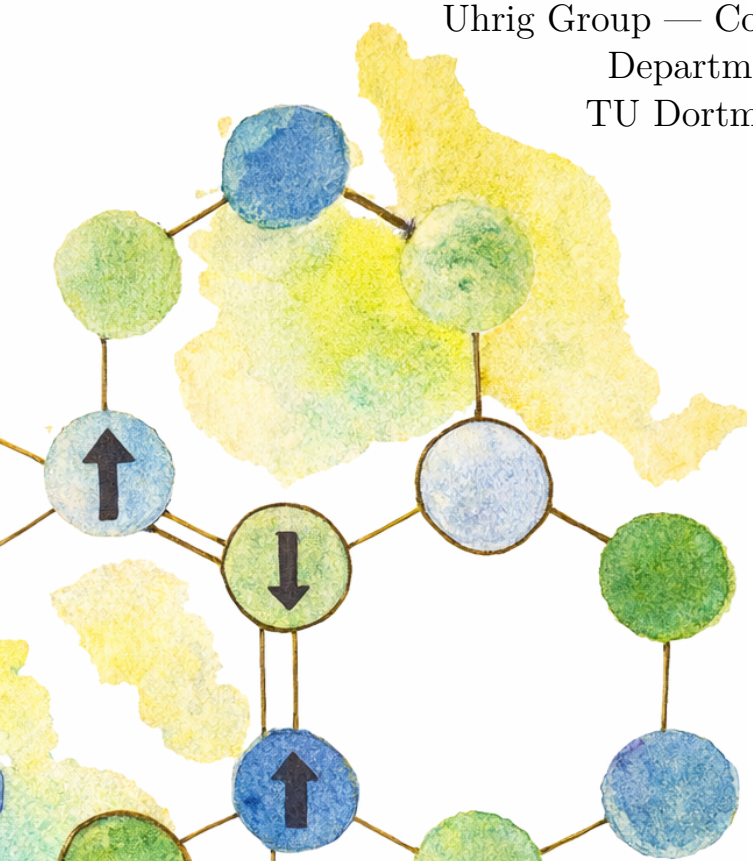

Submission date:	27 February 2026
Date of the thesis defense:	6 May 2026
First corrector:	Prof. Dr. Götz S. Uhrig
Second corrector:	Prof. Dr. Kai P. Schmidt

Thanks to my sister Lara Lange for creating the cover image!

Abstract

This thesis investigates two-dimensional quantum antiferromagnets, with a focus on the spin-$\frac{1}{2}$ antiferromagnetic easy-axis XXZ model on a square and a honeycomb lattice. Describing the excitations and interactions of magnons in these models is of substantial interest, as magnons are the fundamental quasiparticles and can thus explain experimental observations. Already for the paradigmatic antiferromagnetic spin-$\frac{1}{2}$ Heisenberg model on the square lattice, high-energy features of the magnon dispersion are understood via strong magnon-magnon interactions. Besides that, interesting high-energy features were recently observed in the honeycomb lattice, including a possible decay of the single-magnon mode. The goal of this thesis is to obtain effective descriptions of the aforementioned systems that capture the relevant features of the magnon excitations and their interactions.

To study these features, this thesis employs continuous similarity transformations (CSTs), which enables a systematic derivation of an effective quasiparticle picture via so-called flow equations. The approach enables decoupling different magnon sectors and thus for investigating ground-state properties, single-magnon excitations, and multi-magnon bound states. The magnon description is derived from the non-Hermitian Dyson-Maleev representation, which describes fluctuations around a long-range magnetically ordered ground state. The flow equations are set up in momentum space, truncated by the scaling dimension, retaining only operators up to scaling dimension of two, and solved numerically.

For the square lattice, a magnon-conserving effective Hamiltonian is obtained across the full anisotropy range by interpolating between the Ising limit and the Heisenberg limit. The ground-state energy, staggered magnetization, dispersion, and critical exponents are in excellent agreement with the literature, supporting the validity of CST also for gapped phases. Two-magnon excitations in the $S^z = 0$ subspace comprise four bound states, which are tracked across the anisotropy range. Their successive decay into the two-magnon continuum is determined by using the inverse participation ratio.

For the honeycomb lattice, the magnon-conserving CST is reliable only up to $\lambda \lesssim 0.57$; an adapted CST scheme that decouples only the ground state while preserving couplings between different higher-magnon sectors yields effective descriptions for all λ and confirms stable long-range order. The low-energy properties determined in this way match the literature values. However, in the Heisenberg limit, the adapted approach fails to capture high-energy features, such as the experimentally observed decay into the multi-particle continuum at corners of the Brillouin zone. A termination of the magnon-conserving flow equations at a finite flow parameter before the divergence reveals a single-magnon decay at high energies, which is connected to a crossing of a two-magnon bound state with the single-magnon mode. The observed energy dip qualitatively agrees with Quantum Monte Carlo results, but magnon–magnon interactions are overestimated, hindering a fully quantitative characterization of the single-magnon dispersion. Analyzing multi-magnon bound states over the anisotropy range unveils that the crossing of a three-magnon bound state with the single-magnon mode accounts for the breakdown of the magnon-conserving CST at higher λ.

This work demonstrates that CST with scaling-dimension truncation provides a powerful framework for studying two-dimensional quantum magnets, capturing low-energy properties and bound states. Nevertheless, challenges remain in accurately describing high-energy features arising from a persistent overlap of magnon sectors due to strong binding effects.

Kurzfassung

Diese Arbeit untersucht zweidimensionale Quantenantiferromagneten mit Fokus auf dem Spin-$\frac{1}{2}$ Easy-Axis-XXZ-Modell auf Quadrat- und Honigwabengittern. Innerhalb dieser Modelle sind die korrekte Beschreibung der Magnon-Anregungen und ihre Wechselwirkungen zentral für das Verständnis dieser Systeme. Bereits für das paradigmatische antiferromagnetische Spin-$\frac{1}{2}$ Heisenberg-Modell auf dem quadratischen Gitter konnten die Hochenergieeigenschaften der Magnondispersion durch starke Magnon-Magnon-Wechselwirkungen verstanden werden. Auch für das Honigwabengitter wurden jüngst interessante Hochenergieeigenschaften beobachtet, etwa ein möglicher Zerfall der Ein-Magnon-Mode. Das Ziel dieser Arbeit ist es, effektive Beschreibungen des Spin-$\frac{1}{2}$ antiferromagnetischen Easy-Axis-XXZ-Modells für beide Gitter zu erhalten, die die relevanten Eigenschaften der Magnon-Anregungen und ihrer Wechselwirkungen erfassen.

Zur Untersuchung dieser Eigenschaften werden kontinuierliche Ähnlichkeitstransformationen (continuous similarity transformations (CSTs)) angewendet, welche über Flussgleichungen ein effektives Quasiteilchenbild ableiten. So können verschiedene Magnon-Sektoren entkoppelt und Eigenschaften des Grundzustandes, sowie Ein- und Multi-Magnon-Anregungen analysiert werden. Das zugrunde liegende Magnonbild basiert auf der nicht-hermitischen Dyson-Maleev-Darstellung, die Fluktuationen um einen langreichweitig geordneten Zustand beschreibt. Die im Impulsraum formulierten Flussgleichungen werden durch die Skalierungsdimension bis zu einer Skalierungsdimension von zwei begrenzt und numerisch gelöst.

Für das quadratische Gitter ergibt sich über den gesamten Anisotropiebereich ein magnonerhaltender effektiver Hamiltonian, der zwischen dem Ising- und dem Heisenberg-Limes interpoliert. Grundzustandsenergie, Untergittermagnetisierung, Dispersion und kritische Exponenten stimmen hervorragend mit der Literatur überein und bestätigen die Anwendbarkeit der CST auch für Phasen mit Energielücke. Im Zwei-Magnon-Unterraum mit $S^z = 0$ treten vier gebundene Zwei-Magnon-Zustände auf, deren suksessiver Zerfall in das Kontinuum durch das inverse Partizipationsverhältnis bestimmt wird.

Für das Honigwabengitter konvergiert die Magnon-erhaltende CST nur bis zu $\lambda \lesssim 0.57$. Eine modifizierte CST, die lediglich den Grundzustand entkoppelt und Kopplungen zwischen höheren Magnon-Sektoren beibehält, ermöglicht effektive Beschreibungen für alle λ und bestätigt eine stabile langreichweitige Ordnung. Während die Niedrigenergieeigenschaften mit den Literaturwerten übereinstimmen, kann der angepasste Ansatz im Heisenberg-Limit keine Hochenergiephänomene wie den experimentell beobachteten Zerfall der Ein-Magnon-Mode erfassen. Eine Terminierung der magnonerhaltenden CST vor der Divergenz zeigt hingegen einen Zerfall der Ein-Magnon-Mode bei hohen Energien infolge einer Überschneidung eines Zwei-Magnon-Bindungszustands mit der Ein-Magnon-Mode. Die beobachtete Energierenormalisierung stimmt qualitativ mit Quanten-Monte-Carlo-Ergebnissen überein, jedoch wird die Ausdehnung der Magnon-Magnon-Wechselwirkungseffekte überschätzt, wodurch eine quantitative Bestimmung der Ein-Magnon-Mode verhindert wird. Die Analyse gebundener Mehrmagnon-Zustände über den gesamten Anisotropiebereich zeigt, dass die Überschneidung eines Drei-Magnon-Bindungszustands mit der Ein-Magnon-Mode für den Zusammenbruch der magnonerhaltenden CST bei höheren λ verantwortlich ist.

Diese Arbeit zeigt, dass die CST mit Skalierungsdimensions eine leistungsstarke Methode für die Untersuchung zweidimensionaler Quantenmagnete bietet, die Niedrigenergieeigenschaften und gebundene Zustände erfasst. Herausforderungen bleiben jedoch noch bestehen bei der genauen Beschreibung von Hochenergieeigenschaften, die aus einer anhaltenden Überlappung von Magnon-Sektoren aufgrund starker Bindungseffekte resultieren.

Contents

List of publications

Related to this work:

- Matthias R. Walther, Dag-Björn Hering, Götz S. Uhrig, and Kai P. Schmidt. "Continuous Similarity Transformation for Critical Phenomena: Easy-axis Antiferromagnetic XXZ Model." *Physical Review Research* **5**,1, Feb. 21, 2023, page 013132.
  DOI: 10.1103/PhysRevResearch.5.013132
- Nils Caci, Dag-Björn Hering, Matthias R. Walther, Kai P. Schmidt, Stefan Wessel, and Götz S. Uhrig. "Quantitative Description of Long-Range Order in the spin$-\frac{1}{2}$ XXZ Antiferromagnet on the Square Lattice." *Physical Review B* **110**,5, Aug. 6, 2024, page 054411.
  DOI: 10.1103/PhysRevB.110.054411
- Dag-Björn Hering, Matthias R. Walther, Kai P. Schmidt, and Götz S. Uhrig. "Quantum Melting of Long-Range Ordered Quantum Antiferromagnets Investigated by Momentum-Space Continuous Similarity Transformations." *Physical Review B* **110**,8, Aug. 7, 2024, page 085115.
  DOI: 10.1103/PhysRevB.110.085115
- Raymond Wiedmann, Dag-Björn Hering, Vanessa Sulaiman, Matthias R. Walther, Kai P. Schmidt, and Götz S. Uhrig. *Quantum Effects in the Magnon Spectrum of 2D Altermagnets via Continuous Similarity Transformations*. Nov. 5, 2025.
  DOI: 10.48550/arXiv.2511.03528. ARXIV: 2511.03528. Preprint
- Calvin Krämer, Dag-Björn Hering, Vanessa Sulaiman, Matthias R. Walther, Götz S. Uhrig, and Kai Phillip Schmidt. *Quantum Decay of Magnons in the Unfrustrated Honeycomb Heisenberg Model*. Dec. 22, 2025.
  DOI: 10.48550/arXiv.2512.19162. ARXIV: 2512.19162. Preprint

Dataset related to this work:

- Dag-Björn Hering. *Spin Wave Excitations and Their Interactions in Two-Dimensional Antiferromagnets*. Version V1. TUDOdata, 2026.
  DOI: 10.17877/TUDODATA-2026-MP10K2XT

Not related to this work:

- Timo Gräßer, Philip Bleicker, Dag-Björn Hering, Mohsen Yarmohammadi, and Götz S. Uhrig. "Dynamic Mean-Field Theory for Dense Spin Systems at Infinite Temperature." *Physical Review Research* **3**,4, Dec. 10, 2021, page 043168. ISSN: 2643-1564.
  DOI: 10.1103/PhysRevResearch.3.043168
- Philip Bleicker, Dag-Björn Hering, and Götz S. Uhrig. "Charge Dynamics in Magnetically Disordered Mott Insulators." *Physical Review B* **105**,8, Feb. 14, 2022, page 085121.
  DOI: 10.1103/PhysRevB.105.085121

List of Acronyms

$0n$ **generator** particle-block-separating generator with $k = 0$

afHM antiferromagnetic Heisenberg model

BZ Brillouin zone

CCM coupled cluster method

CST continuous similarity transformation

CUT continuous unitary transformation

deepCUT directly evaluated enhanced perturbative CUT

DM Dyson-Maleev representation

DMRG density matrix renormalization group

epCUT enhanced perturbative CUT

fHM ferromagnetic Heisenberg model

gCUT graph-theory based CUT

gpc generator generalized particle-conserving generator

HP Holstein-Primakoff representation

INS inelastic neutron scattering

IPR inverse partition ratio

L-SWT linear spin-wave theory

MBZ magnetic Brillouin zone

MF-SWT mean-field spin-wave theory

NL-SWT nonlinear spin-wave theory

NN nearest neighbor

pbs generator particle-block-separating generator

pCUT perturbative CUT

pc generator particle-conserving generator

QMC quantum Monte Carlo

RIXS resonant inelastic x-ray scattering

ROD residual-off-diagonality

scMF-SWT self-consistent mean-field spin-wave theory

scNL-SWT self-consistent nonlinear spin-wave theory

sCUT self-similar CUT

SE series expansion

SWT spin-wave theory

1 | Motivation and Overview

Collective behaviors are found throughout the natural sciences, where simple interactions among elementary constituents give rise to rich, often unexpected phenomena at macroscopic scales. In fact, they are not even limited to natural sciences alone but can also be observed in social systems, economics, and other complex systems. Such unexpected observations are called emergent phenomena, and they cannot be easily inferred from the properties of individual components alone; instead, the whole system must be considered [Lau99]. This seems to contradict the traditional yet highly successful reductionist approach in physics, which aims to understand complex systems by breaking them down into their simplest parts and studying their interactions. Anderson famously summarized this apparent contradiction with his quote "More is Different" [And72]. For example, in biology, swarm intelligence emerges from simple rules followed by individual organisms, leading to complex group behaviors such as flocking in birds or schooling in fish [Wan+25]. Nevertheless, drawing conclusions about swarm behavior from observing a single bird or fish alone would not reveal the underlying principles of these collective behaviors. Similarly, in physics, the building blocks of ordinary matter and the interaction between them are fully covered by the standard model [Eck19]. Considering many of these microscopic building blocks together, unexpected emergent phenomena can arise that cannot be easily predicted from the properties of individual particles alone. The field of condensed matter physics offers a particularly fertile ground for such unexpected emergent phenomena. A typical condensed matter system consists of an enormous number of interacting particles ($N \approx \mathcal{O}(10^{23})$) [AS23], where collective quantum mechanical interactions among electrons or atoms lead to macroscopic quantum states with unique properties [KM17]. Famous examples include superconductivity [BCS57; Che+24] and superfluidity [Str+18]. Therefore, particularly in condensed matter physics, it is essential to balance the reductionist approach with considerations of emergent behavior to effectively understand and model complex many-body systems.

The Concept of Quasiparticles

To understand such emergent phenomena, the interplay between theoretical methods and experimental observations is crucial. Theoretical methods provide a solid foundation for understanding and even predicting novel phenomena, while experiments either confirm theoretical predictions or reveal new phenomena that require new theoretical methods to be understood. This thesis is of a theoretical nature. In the theoretical description of emergent phenomena in condensed matter physics, the concept of quasiparticles plays a central role. It replaces describing the behavior of each particle individually and instead focuses on collective modes as elementary excitations that behave like particles. The crucial difference to physical particles is that quasiparticles are not elementary. They are excitations in the first place and consequently cease to exist outside the medium they emerge from [AS23; Fal15], hence the prefix "quasi". In condensed matter physics, there exist a plethora of different types of quasiparticles, such as phonons (quantized lattice oscillations), excitons (bonded electron-hole pairs), plasmons (quantized oscillations in a plasma), and magnons (collective spin excitations), to name a few [Ven+16]. Quasiparticles even interact with other particles or quasiparticles, as ordinary particles would do. Studying these interactions often reveals new emergent phenomena, possibly described by new quasiparticles. In superconductivity, for instance, the electron-phonon interactions give rise to Cooper pairs, which

are the elementary excitations of the superconducting state [BCS57]. Another example is the interaction between photons and excitons, which leads to the formation of polaritons [Hop58; SK16]. Correctly capturing the essential low-energy excitations and their interactions is key to obtaining theoretical descriptions and predictions. Thus, the introduction of quasiparticles in condensed matter physics is a powerful concept to break down complex many-body systems into simpler, more effective descriptions. It also reflects the balance required within the reductionist approach necessary to understand emergent phenomena, as it focuses on the relevant collective excitations rather than the individual particles themselves.

Quantum Magnetism and Magnons

The focus of this work lies on the description of quasiparticles called magnons, which describe collective spin excitations in magnetic materials. Magnetic materials and magnetism itself have a long history in applications by humankind, dating back to ancient times with the discovery of naturally occurring magnets like lodestone [Mat81]. It completely revolutionized navigation and trade by enabling compasses for orientation in the Earth's magnetic field. Only with the discovery of electromagnetism in the 19th century, magnetism again completely changed the fate of humankind, enabling countless technological applications, such as the generator and the electric motor [Rez20]. The understanding of the microscopic origin of magnetism itself did not take as long as the two revolutions mentioned before. With the advent of quantum mechanics in the early 20th century, it was understood that magnetism arises from the intrinsic angular momentum of elementary particles, called spin. The concept of spin was formally derived from the Dirac equation [Dir28], which merged quantum mechanics with special relativity. In conjunction with the Schrödinger equation [Sch26], it enabled explanations of different phases of magnetic materials, such as ferromagnetism, in which all spins in the material align parallel to each other, leading to a strong overall magnetic moment, and antiferromagnetism, in which neighboring spins align antiparallel, leading to a net zero magnetic moment [Née32]. With this understanding, theoretical models to describe magnetic interactions were developed, such as the Heisenberg model [Hei28]. Based on the Heisenberg model, the idea of collective excitations in magnetically ordered materials, known as spin waves or magnons, started to emerge [Blo30; HP40; Dys56a]. In recent years, the interest in collective excitations in quantum magnetism has increased due to the emerging field of spintronics [Sta+14; San+17; Ved+20]. As the name suggests, in spintronics, the spin is the decisive degree of freedom rather than the charge of the electron as in traditional electronics. One subfield of spintronics is magnonics, where magnons are used to store, process, or transport information [Chu+15; Rez20]. Magnonics has gained increasing attention in the past few years due to promising features such as lower energy consumption, thanks to the absence of Joule heating otherwise caused by charge currents, as well as integrability and compatibility with existing semiconductor technology. Additionally, magnonics also has a huge potential for high-speed operation due to its wide frequency range from GHz to THz combined with unprecedented miniaturization of circuits [Bar+21; Fle+24].

A special interest of magnonics lies in antiferromagnetic materials. Contrary to the quote of Louis Néel in his 1970 Nobel lecture that "They are extremely interesting from the theoretical standpoint but do not appear to have any practical applications." [Née71], antiferromagnetic materials actually offer several advantages compared to ferromagnetic materials for applications in magnonics. The absence of a net magnetization makes them robust against external magnetic-field perturbations. It allows, if used for data storage, a higher density of stored information since neighboring bits do not interact via stray fields [BKU23]. Additionally, antiferromagnetic materials exhibit ultrafast spin dynamics in the THz regime compared to GHz in ferromagnets, and they are abundant in nature [Jun+16; Bal+18].

Two-Dimensional Antiferromagnetic Quantum Spin Systems

Two-dimensional antiferromagnetic quantum spin systems have been studied for a few decades by now. This research is particularly motivated by the long-standing problem of high-temperature superconductivity in cuprate materials, where the undoped parent compounds are well described by the paradigmatic two-dimensional spin-$\frac{1}{2}$ antiferromagnetic Heisenberg model (afHM) on a square lattice [Man91]. Nevertheless, these systems are also interesting from a more general point of view, as two-dimensional quantum antiferromagnets exhibit a wide variety of emergent quantum phenomena due to the interplay of low dimensionality, strong quantum fluctuations, and competing interactions [Wei+20; Ved+20]. In nature, realizations of two-dimensional quantum antiferromagnets are found in layered antiferromagnetic materials, in which each layer is weakly coupled to its neighbors. These weak couplings enable the experimental study of effective two-dimensional systems. Additionally, advances in materials science, starting with the fabrication of graphene [Nov+04], even opened the possibility of creating artificial, effective two-dimensional magnetic materials by stacking different two-dimensional materials on top of each other, held together by van der Waals forces. These so-called van der Waals materials enable precise tuning of material properties [Nov+16; BMP18]. Moreover, ultracold atoms in optical lattices provide a versatile platform for simulating two-dimensional quantum antiferromagnets, offering high tunability and control [BDN12; GB17]. Altogether, experiments with these tunable artificial materials provide a perfect test bed for various theoretical approaches for effectively describing two-dimensional antiferromagnetic quantum spin systems.

An excellent example of a productive interplay between experiment and theory concerns an observed high-energy feature in the magnon dispersion of the paradigmatic microscopic two-dimensional spin-$\frac{1}{2}$ afHM on the square lattice. Here, experimental measurements and numerical simulations revealed a discrepancy from the predictions of conventional spin wave theory [Chr+04; SS01; ZOH05]. This discrepancy led to an intense debate about the correct theoretical description of this high-energy feature, where even other quasiparticles such as spinons rather than magnons were considered as an explanation [Chr+07; Syr10; UM13; Dal+15]. However, in studies preceding this thesis, the discrepancy could be traced back to strong magnon-magnon interactions, which are inadequately captured by conventional spin-wave theory. By establishing an effective magnon description accounting for strong magnon-magnon interactions, perfect agreement with experiments was achieved [PUS15; Pow17; PSU18]. Such an effective model, which correctly captures the strong magnon-magnon interactions, can be derived using the method of continuous similarity transformation (CST).

Flow Equation Approach – Continuous Similarity Transformation

The CST approach provides a powerful, systematic framework for deriving effective quasiparticle descriptions of complex many-body systems. It originates from the idea of the continuous unitary transformation (CUT) approach, also known as the flow equation approach, first introduced independently by Wegner [Weg94] and by Głazek and Wilson [GW93]. The key concept of CUT embodies the same principle of energy-scale separation as other renormalization group approaches. However, instead of reducing the degrees of freedom step by step, the flow equation approach aims to retain the full Hilbert space while transforming the Hamiltonian into a more diagonal form, i.e., eliminating first off-diagonal matrix elements between states which differ strongly in energy and then progressing to smaller and smaller energy differences [Weg06]. Combined with the quasiparticle concept, the flow equation approach provides a systematic way to derive effective quasiparticle-conserving Hamiltonians, rendering the subsequent calculation of physical quantities much easier [KSU03b]. The CST approach was developed as an extension of the CUT approach

for non-Hermitian Hamiltonians. In the case of the afHM, it is applied in the momentum space to particularly capture gapless systems [PUS15; Pow17; PSU18]. It is precisely the ability to capture processes at different energy scales that makes the flow equation approach such a powerful tool for explaining emergent phenomena in many-body systems. For the spin-$\frac{1}{2}$ afHM on a square lattice, this attribute enabled the accurate description of strong magnon-magnon interactions at high energies without losing the ability to describe the low-energy magnon excitations correctly. However, the approach encounters limitations as well. Particularly, when dealing with systems where the separation of energy scales is not well-defined and energetic overlap persists, the effectiveness of the flow equation approach may be compromised. In Fig. 1.1 a metaphorical illustration of the effect of the flow equation approach is shown, which will be discussed in detail at the beginning of Chapter 3.

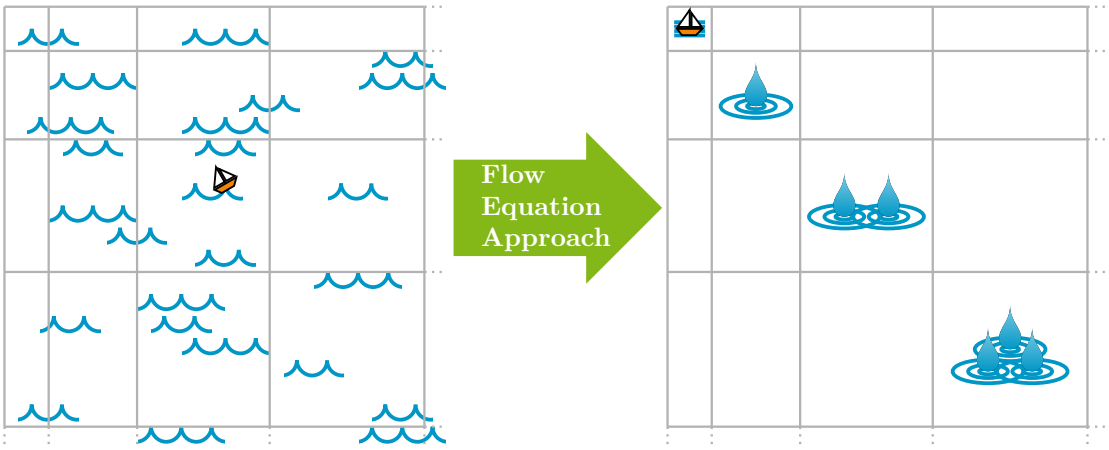

Figure 1.1: Metaphorical depiction illustrating the effect of the flow equation approach on the Hamiltonian of a many-body system. On the left-hand side of the image, a rough sea is shown symbolizing the inherent complexity of many-body problems, which is explored by a sailing boat. On the right-hand side, the sea is shown after applying the flow equation approach. A green arrow represents the transformation induced by the flow equation approach. The right-hand side is characterized by the classification of the sea into distinct regions after the flow equation approach. These regions are defined by the number of drops (quasiparticles), allowing a systematic and controlled exploration of the sea of the many-body problem by the sailing boat.

Aim and Structure of This Thesis

This thesis aims to further investigate the description of magnon excitations and interactions in two-dimensional quantum antiferromagnets through the CST method. A comprehensive theoretical description of magnons is key for future applications in magnonics and spintronics. Up to this point, the CST method has been successfully applied only to the afHM on a square lattice [PUS15; Pow17; PSU18]. This thesis builds on a series of studies conducted with the CST. It started with Refs. [Wal+23; Cac+24], which considered the spin-$\frac{1}{2}$ easy-axis model on a square lattice, leading to a gap in the magnon spectrum. The studies extended to models that exhibit a quantum phase

transition, i.e., the J_1-J_2 model and the Heisenberg bilayer [Her+24]. These prior studies already contributed to the doctoral thesis [Wal24]. Subsequently, studies were commenced on altermagnetic systems [Wie+25] and different lattice geometries such as the honeycomb lattice [Krä+25]

Of all the studies mentioned, this thesis focuses on two specific aspects. First, this work considers the spin-$\frac{1}{2}$ easy-axis XXZ model on the square lattice, which, due to its anisotropy, leads to a gap in the magnon spectrum. Thereby, a specific research question addressed is whether the CST method can also be successfully applied to this extended case. It should be noted that there is an inevitable overlap with the work presented in Ref. [Wal24], which also considers the same model. Additionally, recent experiments [Sal+21; Sal+23] revealed intriguing high-energy features in the magnon spectrum of the spin-$\frac{1}{2}$ afHM on a honeycomb lattice. Therefore, another goal of this thesis is to apply the CST method to the honeycomb lattice and investigate whether it can accurately capture the observed high-energy features. This lattice is also studied with respect to the spin-$\frac{1}{2}$ easy-axis XXZ model. In Fig. 1.2 both studied lattices are shown in their Néel configurations.

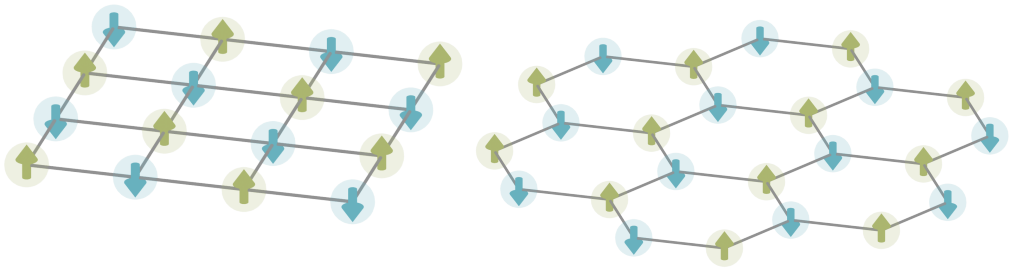

Figure 1.2: Both lattice configurations for the XXZ model are studied in this thesis. On the left-hand side, a schematic of the square lattice is shown, and on the right-hand side, a schematic of the honeycomb lattice is depicted. The blue and green arrows represent the two spin orientations of the two sublattices in the classical Néel state.

The thesis is structured as follows: In Chapter 2, the theoretical foundation of spin-wave theory is introduced, which serves as the starting point for the CST method. In Chapter 3 the CST method is presented in detail, giving an overview of the general flow equation approach and subsequently focusing on the implementation of the CST. Details on implementing the CST method, including setting up the flow equations and incorporating symmetries to reduce computational effort, are presented in Chapter 4. Furthermore, challenges with respect to the non-Hermitian nature of the CST are addressed. Chapter 5 presents the main results of this thesis, namely, the extension of the CST method to the anisotropic spin-$\frac{1}{2}$ easy-axis XXZ model on a square lattice. Thereby, properties of different particle sectors are discussed and compared to results from other theoretical methods. In Chapter 6, the same model is adapted to the honeycomb lattice. Necessary modifications to the CST method for the honeycomb lattice are discussed, and the results are compared to other theoretical methods. Here, a specific focus is on the afHM on the honeycomb lattice, given its relevance to recent experiments and numerical studies that indicate magnon decay at higher momenta. Finally, conclusions are given in Chapter 7 containing a summary of the main findings and an outlook on future research directions.

2 | Spin-Wave Theory

This chapter establishes the theoretical foundation for describing spin excitations in the various spin models discussed in this thesis. It introduces the concept of spin-wave theory (SWT), which addresses the low-energy physics of magnetically ordered systems, resulting in a description of the elementary excitations within these systems. The key idea is to express spin operators in terms of bosonic operators. However, the exact representation of the spin operators in terms of bosonic operators is not unique, leading to various SWT formulations. In this thesis, the Dyson-Maleev representation (DM) representation is employed to describe the spin operators. Although the bosonic representation is chosen, distinct variants of SWT exist. This chapter provides a detailed overview of the SWT variants employed in this work, namely linear spin-wave theory (L-SWT), mean-field spin-wave theory (MF-SWT), and self-consistent mean-field spin-wave theory (scMF-SWT) as well as nonlinear spin-wave theory (NL-SWT) and self-consistent nonlinear spin-wave theory (scNL-SWT). Furthermore, the nonlinear manifestations serve as the starting point for the subsequent continuous similarity transformation.

The chapter is structured as follows. Initially, the concept of SWT is introduced, followed by an in-depth discussion of some bosonic spin representations, all presented in the example of the ferromagnetic Heisenberg spin-$\frac{1}{2}$ model on a square lattice. Subsequently, the SWT variants based on the DM are formulated for the antiferromagnetic easy-axis XXZ model on a square lattice. Each step of their derivation is explained in detail, and the difference between the individual SWT variants is highlighted.

Most of the chapter content has been discussed extensively in the literature, but to be self-contained, all relevant steps are described here nonetheless. The chapter follows the structure of renowned textbooks [Mat81; Aue94; Pir21] and reviews [Man91] regarding this topic.

2.1 General Spin-Wave Theory

The SWT was first developed by Bloch in 1930 [Blo30] to analyze the ferromagnetic Heisenberg model (fHM) proposed by Heisenberg in 1928 [Hei28], which aimed to provide a theoretical model for the emergence of ferromagnetism in solids. Generally, a Heisenberg Hamiltonian has the form

$$\hat{\mathcal{H}} = \sum_{\langle i,j \rangle} J_{ij} \hat{\boldsymbol{S}}_i \cdot \hat{\boldsymbol{S}}_j \tag{2.1}$$

with $\langle i, j \rangle$ denoting a sum over all spins on nearest-neighbor sites $\hat{\boldsymbol{S}}$ which couple with an interaction strength J_{ij} to each other. The notation $\langle i, j \rangle$ also implies that each bond connecting two spins is only counted once. The interaction strength J_{ij} can be either ferromagnetic ($J_{ij} < 0$), where the coupling favors a parallel alignment, or antiferromagnetic ($J_{ij} > 0$), where the coupling favors an antiparallel alignment. Initially, the Heisenberg model was derived from quantum mechanical exchange interactions, leading to ferromagnetic interaction between localized spins. Nevertheless, other mechanisms can yield an effective Heisenberg model. In the case of an antiferromagnetic interaction, an effective Heisenberg model can be derived from the Hubbard model [Gut63; Hub63], describing strongly correlated electrons on a lattice. At half-filling and in the limit $U \gg t$,

where U describes the Coulomb repulsion and t the hopping amplitude between lattice sites, the Hubbard model can be mapped onto an antiferromagnetic Heisenberg model (afHM) with $J_{ij} = \frac{4t^2}{U}$ [Tak77].

The fundamental idea underlying the SWT used in this thesis is to map small fluctuations around the ground state of the Heisenberg Hamiltonian to bosonic excitations instead of using the spin operators. For an adequate description of the system, it is essential to capture its quantum mechanical nature. To this end, the following section revisits the fundamentals of general angular momentum in quantum mechanics.

2.2 Angular Momentum

The spin-vector operators $\hat{\boldsymbol{S}}_i$ in Eq. (2.1) comprise the three components $\hat{S}^x$, $\hat{S}^y$ and $\hat{S}^z$ which obey the commutation relations

$$\left[\hat{\boldsymbol{S}}^2, \hat{S}^a\right] = 0 \ , \qquad \left[\hat{S}^a, \hat{S}^b\right] = \mathrm{i}\sum_c \epsilon_{abc}\hat{S}^c \quad \text{with} \quad \{a,b,c\} \in \{x,y,z\} \ , \tag{2.2}$$

where ϵ_{abc} is the Levi-Civita symbol. Here and throughout the thesis $\hbar$ is set to one. A possible set of commuting operators is $\{\hat{\boldsymbol{S}}^2, \hat{S}^a\}$, defining a possible basis for a single spin state. The corresponding basis is expressed as $|S, m_a\rangle$, where S is the spin quantum number, which allows for positiv half-integer or integer values and m_a is the spin projection quantum number along the a-axis with $2S+1$ possible values in the range $m_a \in \{S, -(S-1), \dots, S-1, S\}$. The eigenvalues of the basis-defining operators are

$$\hat{\boldsymbol{S}}^2 |S, m_a\rangle = S(S+1)\,|S, m_a\rangle \ , \qquad \hat{S}^a |S, m_a\rangle = m_a\,|S, m_a\rangle \ . \tag{2.3}$$

In this thesis, the z-direction ($a = z$) is chosen as the quantization axis. As a consequence, it is convenient to combine the operators $\hat{S}^x$ and $\hat{S}^y$ into the spin-raising and spin-lowering ladder operators

$$\hat{S}^+ = \hat{S}^x + \mathrm{i}\hat{S}^y \ , \qquad \hat{S}^- = \hat{S}^x - \mathrm{i}\hat{S}^y \ . \tag{2.4}$$

The action of these ladder operators on the previously defined basis states yields

$$\hat{S}^+ |S, m_z\rangle = \sqrt{S(S+1) - m_z(m_z+1)}\,|S, m_z+1\rangle \ , \tag{2.5a}$$

$$\hat{S}^- |S, m_z\rangle = \sqrt{S(S+1) - m_z(m_z-1)}\,|S, m_z-1\rangle \ . \tag{2.5b}$$

Raising $|m_z|$ to values larger than S is not possible, as the prefactors are zero in case of $\hat{S}^- |S, -S\rangle$ or $\hat{S}^+ |S, S\rangle$. This is important, since the physical Hilbert space of the basis is limited to the range of $m_z \in \{-S, \dots, S\}$ as discussed above. The commutation relations of the ladder operators are

$$\left[\hat{S}^+, \hat{S}^-\right] = 2\hat{S}^z \quad \text{and} \quad \left[\hat{S}^z, \hat{S}^\pm\right] = \pm\hat{S}^\pm \ . \tag{2.6}$$

Up to this point, only a single spin has been considered; however, a solid-state system inherently is a many-particle problem. Already, coupling two spins, they form new states, with the superpositions described by the Clebsch-Gordan coefficients. In the context of the discussed Heisenberg model in Eq. (2.1), spins with nearest-neighbors coupling give rise to a large number of states, as for a spin system of N spin-S the Hilbert space grows exponentially with $(2S+1)^N$, so that a general solution is no longer analytically accessible. Therefore, extracting relevant physical properties from a large system is a non-trivial task and requires sophisticated approximation methods. The aforementioned SWT in its diverse manifestations achieves this to varying degrees of success depending on the physical subject of interest. First, practical examples are studied.

2.3 Holstein-Primakoff Representation

The first representation presented here and commonly used in literature is the Holstein-Primakoff representation (HP), which Holstein and Primakoff developed in 1940 [HP40]. They introduced bosonic operators to describe the action of the spin operators discussed in Section 2.2 according to

$$\hat{S}_l^+ = \sqrt{2S - \hat{a}_l^\dagger \hat{a}_l}\, \hat{a}_l \ , \qquad \hat{S}_l^- = \hat{a}_l^\dagger \sqrt{2S - \hat{a}_l^\dagger \hat{a}_l} \ , \qquad \hat{S}_l^z = S - \hat{a}_l^\dagger \hat{a}_l \ . \tag{2.7}$$

The operator $\hat{a}_l^\dagger$ creates and $\hat{a}_l$ annihilates a spin excitations at site l. Effectively, the spins are viewed as coupled harmonic oscillators with the operators having the usual effect on a given state, with

$$\hat{a}_l \left|n_l\right\rangle = \sqrt{n_l}\left|n_l - 1\right\rangle \ , \quad \hat{a}_l^\dagger \left|n_l\right\rangle = \sqrt{n_l + 1}\left|n_l + 1\right\rangle \ , \quad \hat{a}_l^\dagger \hat{a}_l \left|n_l\right\rangle = \hat{n}_l \left|n_l\right\rangle = n_l \left|n_l\right\rangle \ . \tag{2.8}$$

With the definition of Eq. (2.7), the ground state $|0\rangle$ of a single harmonic oscillator is then connected to a maximal alignment of the spin

$$|0\rangle \mathrel{\widehat{=}} |S, m_z = S\rangle \ . \tag{2.9}$$

The occupation number n of the harmonic oscillator is consequently connected to the magnetic quantum number m_z via

$$n = S - m_z \ . \tag{2.10}$$

Through this connection, it is possible to derive the HP by comparing the effect of Eqs. (2.3) and (2.5) with Eq. (2.8). The commutation rules of Eq. (2.6) are still satisfied in the bosonic representation. Additionally, the commutator of two single-boson operators on site i and j is given by

$$\left[\hat{a}_i, \hat{a}_j^\dagger\right] = \delta_{ij} \ , \tag{2.11}$$

which eliminates the otherwise tedious work with the commutators of the spin operators. Note that the mapping can also be defined with the roles of $\hat{S}^+$ and $\hat{S}^-$ reversed, which is often used in the context of antiferromagnetic systems.

Nevertheless, there are some caveats regarding this representation. The first apparent issue with this mapping concerns the size of the different Hilbert spaces. For spin operators, the local Hilbert space with $2S + 1$ states is finite, whereas for bosons, it is infinite for a single site. To overcome this difference, the condition

$$\hat{S}_i^- \left|n = 2S\right\rangle \stackrel{!}{=} 0 \ , \tag{2.12}$$

must be fulfilled, separating the physical Hilbert space with $0 \leq n \leq 2S$ from the unphysical one with $n > 2S$. Figure 2.1 shows a schematic representation of a single site for both the spin representation and the bosonic representation.

Equation (2.7) fulfills this condition; in practice, however, square root functions containing operators need to be represented by a truncated power series. In the case of the HP, the square-root expansion reads

$$\sqrt{2S - \hat{a}_l^\dagger \hat{a}_l} = \sqrt{2S}\sqrt{1 - \frac{\hat{a}_l^\dagger \hat{a}_l}{2S}} = \sqrt{2S}\left(1 - \frac{\hat{a}_l^\dagger \hat{a}_l}{4S} - \frac{(\hat{a}_l^\dagger \hat{a}_l)^2}{32S^2} - \ldots\right) \ . \tag{2.13}$$

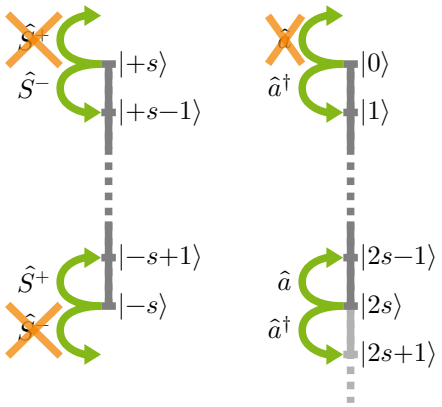

Figure 2.1: Schematic explanation of the basic states and the transitions at a single site. The left figure shows the situation in spin representation. The right figure shows the situation for the HP, i.e., in a bosonic language. In the bosonic case, the physical space (dark grey) and unphysical space (light grey) are connected via the bosonic creation and annihilation operators. However, the overlap between these two spaces is prevented by a suitable prefactor.

Truncating the series at any order renders the condition of Eq. (2.12) invalid and thus the decoupling of the physical and unphysical Hilbert space. Furthermore, the commutation relations are only fulfilled up to the corresponding order in $\frac{1}{S}$. The truncation can still be justified if the ground-state expectation value $\langle \hat{a}^\dagger \hat{a} \rangle$ is small compared to $2S (\langle \hat{a}^\dagger \hat{a} \rangle \ll 2S)$ [Man91]. This assumption should be explicitly verified for consistency.

Example — Two Dimensional Ferromagnetic Heisenberg Model with HP

In this example, the HP is applied to the spin-$\frac{1}{2}$ fHM on a square lattice. The Hamiltonian for this model is given by

$$\hat{\mathcal{H}} = -J \sum_{\langle i,j \rangle} \hat{\boldsymbol{S}}_i \cdot \hat{\boldsymbol{S}}_j = -\frac{J}{2} \sum_{i=1}^{N} \sum_{\boldsymbol{d} \in \mathfrak{D}} \left[\hat{S}_i^z \hat{S}_{i+\boldsymbol{d}}^z + \frac{1}{2} \left(\hat{S}_i^- \hat{S}_{i+\boldsymbol{d}}^+ + \hat{S}_i^+ \hat{S}_{i+\boldsymbol{d}}^- \right) \right] \tag{2.14}$$

where the interaction strength J is isotropic with $J > 0$. The sum over the nearest neighbors (NNs) $\langle i, j \rangle$ can be replaced by a sum over all lattice sites N in combination with a sum over a set of lattice vectors $\mathfrak{D} = \{\boldsymbol{a}_1, -\boldsymbol{a}_1, \boldsymbol{a}_2, -\boldsymbol{a}_2\}$. A prefactor of $\frac{1}{2}$ is introduced to compensate for the double counting of bonds. The primitive translation vectors are $\boldsymbol{a}_1 = (0, a)^T$ and $\boldsymbol{a}_1 = (a, 0)^T$ where a is the lattice constant. The ground state of the spin-$\frac{1}{2}$ fHM on a square lattice is exactly understood and is known to break SU(2) symmetry [Lan66]. In fact, all spins in the symmetry-breaking ground state point in the same direction, resulting in a non-zero magnetization. The direction, on the other hand, is arbitrary, and the ground state is therefore highly degenerate, precisely with a factor of $2SN + 1$. The coordinate system is usually defined such that the z-axis is aligned with the magnetization. Figure 2.2 shows a sketch of the ground state with the aforementioned vectors and the primitive unit cell marked with an orange box.

Two renowned theorems are associated with this symmetry breaking. First, the Goldstone theorem [Gol61; GSW62] states that within a system characterized by short-range interaction, the breaking of a continuous symmetry gives rise to gapless bosonic excitations called Goldstone bosons. Here, the breaking of the SU(2) symmetry is responsible for the emergence of gapless

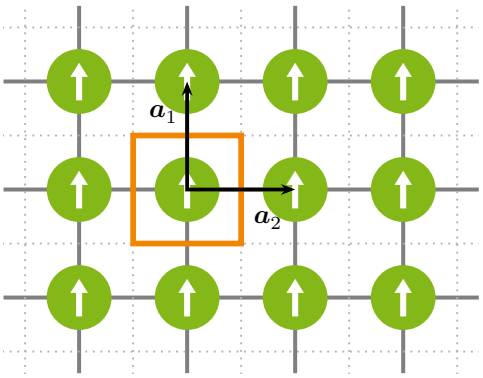

Figure 2.2: Sketch of a square lattice with ferromagnetic alignment of spins. The primitive unit cell is marked as an orange square, and the corresponding lattice vectors $\boldsymbol{a}_1$ and $\boldsymbol{a}_2$ are depicted.

Goldstone bosons called magnons. Consequently, the bosonic nature of these excitations is another motivation for the bosonic representation of the spin operators.

Second, the Mermin-Wagner theorem [MW66] states that a spontaneously symmetry-broken phase cannot exist at finite temperature with a continuous symmetry and short-range interactions for systems with dimension $d \leq 2$. In such systems, thermal fluctuations forbid the existence of such an ordered ground state. In this thesis, specifically systems with dimension $d = 2$ are considered, but all calculations are carried out for $T = 0$ so that the implications of the Mermin-Wagner theorem are ultimately avoided. Regarding two-dimensional materials at finite temperatures in reality, the Mermin-Wagner theorem implies that no long-range magnetic order can exist. However, in practice, magnetic anisotropies or interlayer couplings are present, which break the continuous symmetry and can thus stabilize magnetic order even in two-dimensional systems at finite temperatures.

Having discussed the two apparent main theorems, the HP is applied to obtain the SWT result. This is done by inserting the representation of Eq. (2.7) to the Hamiltonian of Eq. (2.14) resulting in

$$\hat{\mathcal{H}} = -\frac{J}{2}\sum_{i}^{N}\sum_{\boldsymbol{d}\in\mathfrak{D}}\left[\hat{S}_i^z\hat{S}_{i+\boldsymbol{d}}^z + \frac{1}{2}\left(\hat{S}_i^-\hat{S}_{i+\boldsymbol{d}}^+ + \hat{S}_i^+\hat{S}_{i+\boldsymbol{d}}^-\right)\right] \tag{2.15a}$$

$$\begin{aligned} = -\frac{J}{2}\sum_{i}^{N}\sum_{\boldsymbol{d}\in\mathfrak{D}}\Bigg[&(S-\hat{a}_i^\dagger\hat{a}_i)(S-\hat{a}_{i+\boldsymbol{d}}^\dagger\hat{a}_{i+\boldsymbol{d}}) \\ &+ S\hat{a}_i^\dagger\sqrt{1-\frac{\hat{a}_i^\dagger\hat{a}_i}{2S}}\sqrt{1-\frac{\hat{a}_{i+\boldsymbol{d}}^\dagger\hat{a}_{i+\boldsymbol{d}}}{2S}}\hat{a}_{i+\boldsymbol{d}} \\ &+ S\sqrt{1-\frac{\hat{a}_i^\dagger\hat{a}_i}{2S}}\hat{a}_i\hat{a}_{i+\boldsymbol{d}}^\dagger\sqrt{1-\frac{\hat{a}_{i+\boldsymbol{d}}^\dagger\hat{a}_{i+\boldsymbol{d}}}{2S}}\Bigg] . \end{aligned} \tag{2.15b}$$

The next step is to use the series expansion of Eq. (2.13) and categorize the terms in the form of

powers of $\frac{1}{S}$, yielding

$$\hat{\mathcal{H}} = -\frac{JNS^2Z}{2} + \frac{J}{2}\sum_{i}^{N}\sum_{\boldsymbol{d}\in\mathfrak{D}}\Big[S\left(\hat{a}_i^\dagger\hat{a}_i + \hat{a}_{i+\boldsymbol{d}}^\dagger\hat{a}_{i+\boldsymbol{d}} - \hat{a}_i^\dagger\hat{a}_{i+\boldsymbol{d}} - \hat{a}_i\hat{a}_{i+\boldsymbol{d}}^\dagger\right) \tag{2.16a}$$

$$+ \hat{a}_i^\dagger\hat{a}_i\hat{a}_{i+\boldsymbol{d}}^\dagger\hat{a}_{i+\boldsymbol{d}} - \frac{1}{4}\hat{a}_i^\dagger\hat{a}_{i+\boldsymbol{d}}^\dagger\hat{a}_{i+\boldsymbol{d}}^\dagger\hat{a}_{i+\boldsymbol{d}} - \frac{1}{4}\hat{a}_i^\dagger\hat{a}_i\hat{a}_i\hat{a}_{i+\boldsymbol{d}}^\dagger$$
$$-\frac{1}{4}\hat{a}_i^\dagger\hat{a}_i^\dagger\hat{a}_i\hat{a}_{i+\boldsymbol{d}}^\dagger - \frac{1}{4}\hat{a}_i^\dagger\hat{a}_{i+\boldsymbol{d}}^\dagger\hat{a}_{i+\boldsymbol{d}}\hat{a}_{i+\boldsymbol{d}} + \mathcal{O}\left(\frac{1}{S}\right)\Big] \ , \tag{2.16b}$$

where Z is the number of nearest neighbors arising from $\sum_{\boldsymbol{d}\in\mathfrak{D}} 1 = Z = 4$. Explicitly at $T = 0$ the condition $\langle\hat{a}^\dagger\hat{a}\rangle \ll 2S$ is fulfilled even for $S = \frac{1}{2}$. This can be verified *a posteriori* by simply calculating the expectation value. Hence, it is a good approximation to keep only terms of the zeroth order of the expansion in Eq. (2.13), which are terms with S and S^2, and omit the rest. As a consequence, the Hamiltonian boils down to Eq. (2.16a) with terms of Eq. (2.16b) being neglected. Neglecting terms beyond quadratic operators such as Eq. (2.16b) corresponds to a L-SWT. A Fourier transformation can straightforwardly diagonalize this remaining part according to

$$\hat{a}_{\boldsymbol{k}} = \frac{1}{\sqrt{N}}\sum_{i}^{N}\hat{a}_i\mathrm{e}^{-\mathrm{i}\boldsymbol{k}\boldsymbol{r}_i} \ , \qquad\qquad \hat{a}_i = \frac{1}{\sqrt{N}}\sum_{\boldsymbol{k}\in\mathrm{BZ}}\hat{a}_{\boldsymbol{k}}\mathrm{e}^{\mathrm{i}\boldsymbol{k}\boldsymbol{r}_i} \ , \tag{2.17}$$

where $\boldsymbol{k}$ is a reciprocal lattice vector taken from the first Brillouin zone (BZ). The basis vectors $\boldsymbol{b}_1$ and $\boldsymbol{b}_2$ of the reciprocal lattice are determined via the relation

$$\boldsymbol{a}_i\boldsymbol{b}_j = 2\pi\delta_{ij} \ . \tag{2.18}$$

For the square lattice, this implies

$$\boldsymbol{b}_1 = \frac{2\pi}{a}\begin{pmatrix}1\\0\end{pmatrix} \quad \text{and} \quad \boldsymbol{b}_2 = \frac{2\pi}{a}\begin{pmatrix}0\\1\end{pmatrix} \ . \tag{2.19}$$

Expressed by the ladder operators in momentum space, the Hamiltonian takes the diagonal form,

$$\hat{\mathcal{H}} = -\frac{JNS^2Z}{2} + \sum_{\boldsymbol{k}\in\mathrm{BZ}}\omega_{\boldsymbol{k}}\hat{a}_{\boldsymbol{k}}^\dagger\hat{a}_{\boldsymbol{k}} \ , \tag{2.20}$$

where the dispersion of a single magnon reads

$$\omega_{\boldsymbol{k}} \coloneqq JSZ(1-\gamma_{\boldsymbol{k}}) \quad \text{with} \quad \gamma_k \coloneqq \frac{1}{Z}\sum_{\boldsymbol{d}\in\mathfrak{D}}\mathrm{e}^{-\mathrm{i}\boldsymbol{k}\delta} = \frac{2}{Z}\left(\cos\left(k_x\right) + \cos\left(k_y\right)\right) \ . \tag{2.21}$$

In fact, this dispersion is the exact solution for the fHM on a square lattice. Figure 2.3 shows the dispersion for a specific path through the BZ. Undoubtedly, the effect of the Goldstone theorem is evident in Fig. 2.3 due to the gapless energy spectrum, which closes quadratically at $\boldsymbol{k} = (0, 0)$.

In summary, based on the HP, it is possible to express the spin Hamiltonian exactly by bosonic excitations. In this representation, a square root of operators occurs, which needs to be expanded and truncated. In the presented L-SWT, only quadratic terms, corresponding to the zeroth order in the $\frac{1}{S}$ expansion, are considered, yielding a gapless spectrum agreement with the Goldstone theorem. The truncation of the square root expansion is clearly a disadvantage, as it is only valid if the prerequisite $\langle\hat{a}^\dagger\hat{a}\rangle \ll 2S$ is fulfilled. The next section presents a spin representation that avoids this drawback.

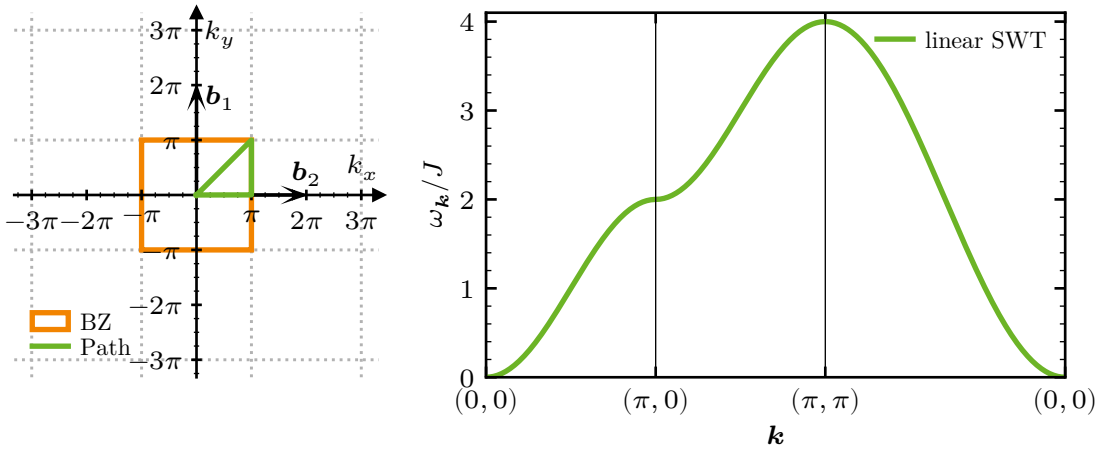

Figure 2.3: On the left-hand side, the reciprocal lattice for the spin-$\frac{1}{2}$ fHM on a square lattice is shown. The lattice constant a is set to unity. The orange rectangle represents the edge of the first BZ and the reciprocal lattice vectors $\boldsymbol{b}_{1,2}$ are indicated by black arrows. The green triangle represents a specific path through the BZ. The dispersion $\omega_{\boldsymbol{k}}$ associated with this path is shown on the right-hand side.

2.4 Dyson-Maleev Representation

This section presents the DM, which forms another possibility to express the spin operator by bosonic excitations in addition to the previously discussed HP. The generalized bosonic representation [Faz99]

$$\hat{S}_l^+ = \sqrt{2S}\left(1-\frac{\hat{a}_l^\dagger \hat{a}_l}{2S}\right)^{\alpha}\hat{a}_l\,, \qquad \hat{S}_l^- = \sqrt{2S}\hat{a}_l^\dagger\left(1-\frac{\hat{a}_l^\dagger \hat{a}_l}{2S}\right)^{1-\alpha}, \qquad \hat{S}_l^z = S-\hat{a}_l^\dagger\hat{a}_l \tag{2.22}$$

fulfills the important commutation relations in Eq. (2.6). For $\alpha = \frac{1}{2}$ the HP is obtained and the occurring square root is handled as discussed in Section 2.3. There are two limiting cases $\alpha = 0$ and $\alpha = 1$ where the representation takes the following form

$$\hat{S}_l^+ = \sqrt{2S}\left(1-\frac{\hat{a}_l^\dagger \hat{a}_l}{2S}\right)\hat{a}_l\,, \qquad \hat{S}_l^- = \sqrt{2S}\hat{a}_l^\dagger\,, \qquad \hat{S}_l^z = S-\hat{a}_l^\dagger\hat{a}_l \tag{2.23a}$$

for $\alpha = 1$ and for $\alpha = 0$

$$\hat{S}_l^+ = \sqrt{2S}\hat{a}_l\,, \qquad \hat{S}_l^- = \sqrt{2S}\hat{a}_l^\dagger\left(1-\frac{\hat{a}_l^\dagger \hat{a}_l}{2S}\right), \qquad \hat{S}_l^z = S-\hat{a}_l^\dagger\hat{a}_l\,. \tag{2.23b}$$

Both cases are essentially equivalent and known as the DM, first introduced by Dyson [Dys56a; Dys56b] and further developed by Maleev [Mal58a; Mal58b]. A crucial advantage of the DM is the absence of fractional powers, eliminating the need for an expansion. This has several implications. First and foremost, the representation is non-Hermitian, i.e., $\left(\hat{S}^+\right)^\dagger \neq \hat{S}^-$. Second, while the HP ensures that the physical and non-physical parts of the bosonic Hilbert space are disconnected via Eq. (2.12), this separation is not apparent for the DM. Of course, using the low-order series

expansion in the HP also violates this decoupling. Therefore, as long as only L-SWT is considered, i.e., take only terms up to a quadratic level into account, HP and DM lead to the same results as shown in the following section.

Example — Two Dimensional Ferromagnetic Heisenberg Model with DM

Once again, the two dimensional spin-$\frac{1}{2}$ fHM is considered and the DM from Eq. (2.23a) is inserted yielding

$$\hat{\mathcal{H}} = -\frac{J}{2}\sum_{i=0}^{N}\sum_{\boldsymbol{d}\in\mathfrak{D}}\left[\hat{S}_i^z\hat{S}_{i+\boldsymbol{d}}^z + \frac{1}{2}\left(\hat{S}_i^-\hat{S}_{i+\boldsymbol{d}}^+ + \hat{S}_i^+\hat{S}_{i+\boldsymbol{d}}^-\right)\right] \tag{2.24a}$$

$$\begin{aligned} &= -\frac{J}{2}\sum_{i=0}^{N}\sum_{\boldsymbol{d}\in\mathfrak{D}}\Bigg[(S-\hat{a}_i^\dagger\hat{a}_i)(S-\hat{a}_{i+\boldsymbol{d}}^\dagger\hat{a}_{i+\boldsymbol{d}}) \\ &\qquad + S\hat{a}_i^\dagger\left(1-\frac{\hat{a}_{i+\boldsymbol{d}}^\dagger\hat{a}_{i+\boldsymbol{d}}}{2S}\right)\hat{a}_{i+\boldsymbol{d}} \\ &\qquad + S\left(1-\frac{\hat{a}_i^\dagger\hat{a}_i}{2S}\right)\hat{a}_i\hat{a}_{i+\boldsymbol{d}}^\dagger\Bigg] \ . \end{aligned} \tag{2.24b}$$

This simplifies to

$$\hat{\mathcal{H}} = -\frac{JNS^2Z}{2} - \frac{J}{2}\sum_{i}^{N}\sum_{\boldsymbol{d}\in\mathfrak{D}}\Big[S\left(\hat{a}_i^\dagger\hat{a}_i + \hat{a}_{i+\boldsymbol{d}}^\dagger\hat{a}_{i+\boldsymbol{d}} - \hat{a}_i^\dagger\hat{a}_{i+\boldsymbol{d}} - \hat{a}_i\hat{a}_{i+\boldsymbol{d}}^\dagger\right) \tag{2.25a}$$

$$+ \hat{a}_i^\dagger\hat{a}_i\hat{a}_{i+\boldsymbol{d}}^\dagger\hat{a}_{i+\boldsymbol{d}} - \frac{1}{2}\hat{a}_i^\dagger\hat{a}_{i+\boldsymbol{d}}^\dagger\hat{a}_{i+\boldsymbol{d}}\hat{a}_{i+\boldsymbol{d}} - \frac{1}{2}\hat{a}_i^\dagger\hat{a}_i\hat{a}_i\hat{a}_{i+\boldsymbol{d}}^\dagger\Big] \ . \tag{2.25b}$$

As previously mentioned, the linear part in S in Eq. (2.25a) is identical to the one in Eq. (2.16a). Applying the Fourier transformation used in Section 2.3 yields the same single-particle dispersion as in Eq. (2.21). Thus, the L-SWT remains consistent across both representations. However, for the higher-order terms of Eq. (2.25b) and Eq. (2.16b), this equality no longer holds.

An essential advantage of the DM is that it is already exact when incorporating the quartic terms. Of course, this happens at the expense of losing Hermiticity. Moreover, considering only a single spin operator, a coupling to the non-physical bosonic Hilbert space arises, see Eq. (2.23). Nevertheless, this problem is circumvented as the spin operators occur in pairs in the Hamiltonian, see Eq. (2.25).

2.5 Spin-Wave Theory for Two-Dimensional Antiferromagnets

In this section the spin-$\frac{1}{2}$ antiferromagnetic easy-axis XXZ model on a square lattice is discussed in the context of SWT. The model includes, as its limiting case, the afHM and the Ising model. Compared to the ferromagnetic case, the antiferromagnetic case is more challenging. It is necessary to carry out the DM in a modified way, considering the antiferromagnetic properties. The first step in applying a SWT is to determine the ordered phase from which the small fluctuations deviate.

Compared to the ground state of the ferromagnetic case, where every spin is aligned in the same direction for any lattice, the existence of an ordered phase for an antiferromagnetic interaction

is not so clear. For an antiferromagnetic interaction with $J > 0$, two neighboring spins favor an antiparallel alignment. To satisfy such alignment for an entire lattice, a bipartite lattice is required, i.e., a lattice where a separation into two sublattices Γ_A and Γ_B is possible, such that each site on sublattice Γ_A is only connected to sites on sublattice Γ_B and vice versa. In a non-bipartite lattice, such alignment is not possible because interactions within the sublattices lead to geometrical frustration. Figuratively speaking, if the lattice possesses loops with an odd number of sites, it is impossible to arrange the spins such that all neighboring spins are antiparallel aligned. Consequently, such configurations counteract this specific type of long-range order. Examples of non-bipartite lattices include the triangular and Kagome lattice. The square lattice, on the other hand, is bipartite, as it allows a separation into two sublattices Γ_A and Γ_B, as shown with the green and blue sites in Fig. 2.4. Nevertheless, finding the exact ground state is notoriously difficult. The problem is easy to identify by looking at the Hamiltonian of the isotropic afHM and introducing an anisotropy λ in the xy plane. This Hamiltonian describes a so-called XXZ model and reads

$$\hat{\mathcal{H}} = J \sum_{\langle i,j \rangle} \hat{S}_i^z \hat{S}_j^z + \lambda \left(\hat{S}_i^x \hat{S}_j^x + \hat{S}_i^y \hat{S}_j^y \right) = J \sum_{\langle i,j \rangle} \hat{S}_i^z \hat{S}_j^z + \frac{\lambda}{2} \left(\hat{S}_i^- \hat{S}_j^+ + \hat{S}_i^+ \hat{S}_j^- \right) \quad . \tag{2.26}$$

Depending on the parameter range of λ, it corresponds to either an easy-axis XXZ model for ($\lambda < 1$), or easy-plane XXZ model for ($\lambda > 1$). This work focuses exclusively on the easy-axis regime. Within this regime, the system continuously interpolates between the Ising limit at ($\lambda = 0$) and the isotropic Heisenberg limit at ($\lambda = 1$). In the Ising limit, the ground state is exactly known to be the classical Néel state, in which the lattice can be partitioned into two sublattices with antiparallel spin alignment, either $\Gamma_A : \uparrow ; \Gamma_B : \downarrow$ or vice versa. Consequently, the ground state exhibits a twofold degeneracy.

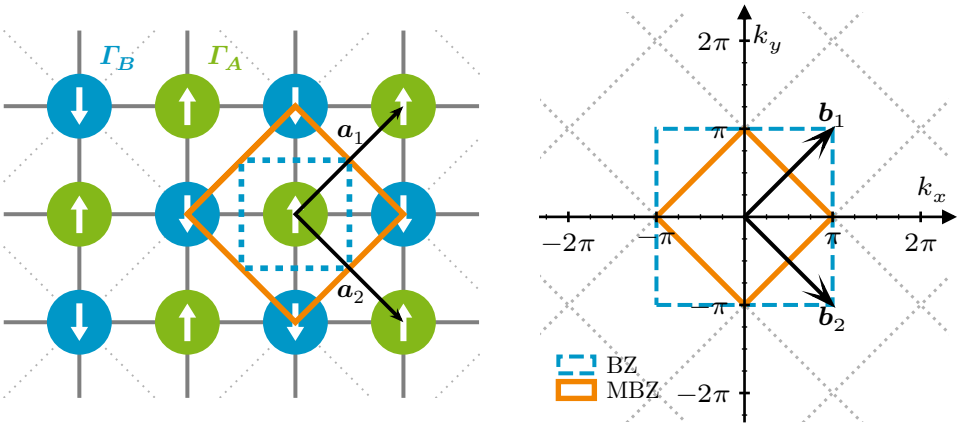

Figure 2.4: The left-hand side shows a sketch of spins on the square lattice with lattice constant a and an antiferromagnetic alignment of spins. The dashed blue lines mark the primitive unit cell, and the orange lines mark the magnetic unit cell. Lattice vectors $\boldsymbol{a}_1$ and $\boldsymbol{a}_2$ correspond to the magnetic unit cell. The right-hand side shows the reciprocal space; the first BZ is marked with dashed blue lines and the first magnetic Brillouin zone (MBZ) is marked with orange lines. The reciprocal lattice vectors associated with the magnetic Brillouin zone (MBZ) are shown, with the lattice constant set to unity.

For finite λ, the classical Néel state still corresponds to a relatively low energy, but does not correspond to the true ground state. This becomes evident when considering the action of the so-called exchange or flip-flop terms ($\hat{S}_i^{\pm} \hat{S}_j^{\mp}$), which appear in Eq. (2.26) for finite λ. While in

the ferromagnetic case the action of these terms on the ground state is simply zero applied to the ground state, they have a non-vanishing contribution and change the state if applied to the classical Néel state. As a consequence, the classical Néel state is no longer an eigenstate of the Hamiltonian. Therefore, the question of whether the ground state of the afHM still exhibits long-range order, thus breaking the continuous symmetry and giving rise to massless Goldstone bosons, cannot be answered straightforwardly. Nevertheless, based on the *a priori* assumption that the ground state is adiabatically connected to the Néel state by a continuous change of the parameter λ, SWT calculations can be performed as has been done by Anderson [And51], Kubo [Kub52] or Oguchi [Ogu60]. These predict a ground state with long-range order, but its staggered magnetization is reduced by about 40 % with respect to the Néel state due to quantum fluctuations [Man91]. Later, it was confirmed by numerical studies [LM89] that the assumption of a long-range ordered ground state is correct. Although, so far, a rigorous proof for long-range order on the square lattice was only possible for $S \geq 1$ [KLS88].

Nevertheless, it is reasonable to start with the classical Néel state as a reference state for the derivation of a SWT and then later verify whether the long-range order still exists. As a consequence, it is necessary to distinguish between the primitive unit cell and the primitive magnetic unit cell, since the Néel state requires a two-atom basis. For the bipartite square lattice the primitive magnetic unit cell is a diamond as marked in orange in the left of Fig. 2.4 containing effectively one lattice site of each sublattice Γ_A and Γ_B with the primitive translation vectors being $\boldsymbol{a}_1 = (a, a)^T$ and $\boldsymbol{a}_1 = (a, -a)^T$. It is twice the size of the primitive unit cell of the ferromagnet, shown as a blue-dashed square. Thus the Néel order inflates the unit cell in real space and deflates the reciprocal unit cell as shown in Fig. 2.4 on the right-hand side, with the reciprocal lattice vectors being $\boldsymbol{b}_1 = (\frac{2\pi}{a}, \frac{2\pi}{a})^T$ and $\boldsymbol{b}_2 = (\frac{2\pi}{a}, -\frac{2\pi}{a})^T$. Hence, the BZ is smaller than that of the ferromagnetic order. Of course, in the crystal, the atoms still have the same periodicity as in the ferromagnetic case. Only the assumed magnetic order leads to this distinction and a change of the discrete translation symmetry. Therefore, the BZ of the magnetic order is referred to as the magnetic Brillouin zone (MBZ).

Starting from Γ_A, the set of nearest neighbors $\mathfrak{D}$ is still the same as in the ferromagnetic case, but with the new primitive translation vectors, is given by

$$\mathfrak{D} = \left\{ \frac{-\boldsymbol{a}_1 - \boldsymbol{a}_2}{2}, \frac{\boldsymbol{a}_1 - \boldsymbol{a}_2}{2}, \frac{-\boldsymbol{a}_1 + \boldsymbol{a}_2}{2}, \frac{\boldsymbol{a}_1 + \boldsymbol{a}_2}{2} \right\} . \tag{2.27}$$

With these vectors Eq. (2.26) can be rewritten as

$$\hat{\mathcal{H}} = J \sum_{\boldsymbol{r}_i \in \Gamma_A}^{N_A} \sum_{\boldsymbol{d} \in \mathfrak{D}} \left[\hat{S}_i^z \hat{S}_{i+\boldsymbol{d}}^z + \frac{\lambda}{2} \left(\hat{S}_i^- \hat{S}_{i+\boldsymbol{d}}^+ + \hat{S}_i^+ \hat{S}_{i+\boldsymbol{d}}^- \right) \right] \tag{2.28}$$

where the sum only runs over all sites N_A of sublattice Γ_A with $N_A = \frac{N}{2}$ and N is the total number of all sites in Γ_A and Γ_B combined. The sum over Γ_A counts each interacting once, unlike in Eq. (2.14) where an additional factor of $\frac{1}{2}$ is introduced to compensate for double counting. The next step is to introduce the DM, which is suited to describe the antiferromagnetic alignment.

2.5.1 Dyson-Maleev Representation — Adaptations

For the sublattice Γ_A, where all spins point upwards, the representation of the ferromagnetic case can be adopted. The situation for the sublattice Γ_B differs. Here, all spins point downwards, making the representation inappropriate. There are various ways to solve this issue. One way is to introduce a sublattice rotation, rotating each spin on the sublattice Γ_B around $\hat{S}^x$ by 180° [Dus+10].

Another way is to introduce a new boson flavor $\hat{b}$ to describe fluctuations around the spin-down direction. In this thesis, the latter approach is used. The first step is to adapt the DM for the spin-down case. The $\hat{b}$ bosons represent deviation around the $-S$ direction and thus the following modifications are necessary. The $\hat{S}^z$ representation gains an additional minus for the sublattice Γ_B and, in addition, the action of $\hat{S}^+$ and $\hat{S}^-$ are interchanged compared to the spin-up case. Thus, $\hat{S}^+$ corresponds to a creation and $\hat{S}^-$ to an annihilation of a $\hat{b}$ boson. Instead of simply swapping the operators and renaming $\hat{a} \to \hat{b}$, it is strategically preferable to change the representation used beforehand. Consequently, instead of using Eq. (2.23a) with $\alpha = 1$, it is recommended to use Eq. (2.23b) with $\alpha = 0$ on the sublattice Γ_B, which leads to the following representations

$$\hat{S}^+_{A,i} = \sqrt{2S}\left(1 - \frac{\hat{a}_i^\dagger \hat{a}_i}{2S}\right)\hat{a}_i \,, \qquad \hat{S}^-_{A,i} = \sqrt{2S}\hat{a}_i^\dagger \,, \qquad \hat{S}^z_{A,i} = S - \hat{a}_i^\dagger \hat{a}_i \,, \tag{2.29a}$$

$$\hat{S}^+_{B,j} = \sqrt{2S}\hat{b}_j^\dagger\left(1 - \frac{\hat{b}_j^\dagger \hat{b}_j}{2S}\right) \,, \qquad \hat{S}^-_{B,j} = \sqrt{2S}\hat{b}_j \,, \qquad \hat{S}^z_{B,j} = -S + \hat{b}_j^\dagger \hat{b}_j \,. \tag{2.29b}$$

The question remains as to why this presentation is preferable. It can be answered by examining the initial Hamiltonian in Eq. (2.28), denoting the sublattices explicitly,

$$\hat{\mathcal{H}} = J \sum_{\boldsymbol{r}_i \in \Gamma_A}^{N_A} \sum_{\boldsymbol{d} \in \mathfrak{D}} \left[\hat{S}^z_{A,i}\hat{S}^z_{B,i+\boldsymbol{d}} + \frac{\lambda}{2}\left(\hat{S}^-_{A,i}\hat{S}^+_{B,i+\boldsymbol{d}} + \hat{S}^+_{A,i}\hat{S}^-_{B,i+\boldsymbol{d}}\right)\right] \,. \tag{2.30}$$

With this choice, only quartic boson terms appear after inserting Eq. (2.29) into the Hamiltonian. For the other choice, i.e., $\alpha = 1$ for sublattice Γ_B, additional hexatic terms appear, making the calculations more complicated. Another important advantage of the representation in Eq. (2.29) concerns the separation of physical and non-physical subspaces. As a reminder, the physical subspace is defined by the condition that the number of bosons on each site may not exceed the number of available spin states, i.e., $n_{\hat{a}}, n_{\hat{b}} \leq 2S$. One previously discussed disadvantage of the DM is the lack of complete separation of these spaces. However, since Eq. (2.29a) prevents bosons from entering the physical subspace and Eq. (2.29b) prevents bosons from leaving the physical subspace, the combinations in the terms $\hat{S}^-_{A,i}\hat{S}^+_{B,j}$ and $\hat{S}^+_{A,i}\hat{S}^-_{B,j}$ have no such disadvantage. After inserting the advantageous representation of Eq. (2.29) in Eq. (2.30), the Hamiltonian takes the form

$$\begin{aligned}\hat{\mathcal{H}} =& J \sum_{\boldsymbol{r}_i \in \Gamma_A}^{N_A} \sum_{\boldsymbol{d} \in \mathfrak{D}} \Bigg[\left(S - \hat{a}_i^\dagger \hat{a}_i\right)\left(-S + \hat{b}_{i+\boldsymbol{d}}^\dagger \hat{b}_{i+\boldsymbol{d}}\right) \\ &+ \frac{\lambda}{2}\left(2S\hat{a}_i^\dagger \hat{b}_{i+\boldsymbol{d}}^\dagger\left(1 - \frac{\hat{b}_{i+\boldsymbol{d}}^\dagger \hat{b}_{i+\boldsymbol{d}}}{2S}\right) + 2S\left(1 - \frac{\hat{a}_i^\dagger \hat{a}_i}{2S}\right)\hat{a}_i \hat{b}_{i+\boldsymbol{d}}\right)\Bigg] \qquad (2.31) \\ =& -JN_A S^2 Z + J \sum_{\boldsymbol{r}_i \in \Gamma_A}^{N_A} \sum_{\boldsymbol{d} \in \mathfrak{D}} \Big[S\hat{a}_i^\dagger \hat{a}_i + S\hat{b}_{i+\boldsymbol{d}}^\dagger \hat{b}_{i+\boldsymbol{d}} + \underline{\lambda S\hat{a}_i^\dagger \hat{b}_{i+\boldsymbol{d}}^\dagger + \lambda S\hat{a}_i \hat{b}_{i+\boldsymbol{d}}} \\ &- \hat{a}_i^\dagger \hat{a}_i \hat{b}_{i+\boldsymbol{d}}^\dagger \hat{b}_{i+\boldsymbol{d}} - \frac{\lambda}{2}\hat{a}_i^\dagger \hat{b}_{i+\boldsymbol{d}}^\dagger \hat{b}_{i+\boldsymbol{d}}^\dagger \hat{b}_{i+\boldsymbol{d}} - \frac{\lambda}{2}\hat{a}_i^\dagger \hat{a}_i \hat{a}_i \hat{b}_{i+\boldsymbol{d}} \Big] \,, \qquad (2.32)\end{aligned}$$

with $Z = 4$ being the number of nearest neighbors and N_A being the number of sites in the sublattice Γ_A. The result is certainly different and more complex compared to the ferromagnetic case. First, there are now two different types of bosons, $\hat{a}_i$ and $\hat{b}_j$, representing each a deviation from the classical Néel state. Second, there are quadratic operator terms that consist only of pairs of creation or pairs of annihilation operators. These terms are underlined in Eq. (2.32). Due to

their presence, a simple Fourier transformation is no longer sufficient to calculate the single-particle dispersion in L-SWT as in the ferromagnetic case. Instead, an additional Bogoliubov transformation is necessary after the Fourier transformation, which is discussed in detail in Section 2.5.3. First, however, the focus lies on the subtleties of the Fourier transformation encountered when dealing with a non-Bravais lattice.

2.5.2 Fourier Transformation

Considering the ferromagnet on a square lattice, the primitive unit cell of the Bravais lattice consists of a single atomic basis. All lattice sides can be reached by discrete translations given by the unit vectors $\boldsymbol{a}_1$ and $\boldsymbol{a}_2$ with the length of the lattice constant a. Contrary, any antiferromagnet that assumes a Néel ordering needs a basis of at least two atoms in its primitive unit cell to describe the magnetic order. For the square lattice, a two-atomic basis is required as shown in the left-hand side of Fig. 2.4, which leads to implications for the Fourier transformation of the Hamiltonian. To be precise, for two atoms per unit cell, there exist various gauge options for the Fourier transformation [BM09; DDM15]. Of course, the physical properties of the system do not depend on the gauge. However, different gauges offer distinct advantages that can be exploited, or they can be used to confirm results obtained with another gauge. In the following, the two gauges used in this work are introduced. The key difference between the two gauges lies in the phase factors acquired by the bosonic operators during the Fourier transformation.

Bloch gauge: In this gauge, the Fourier transformations of $\hat{a}_i$ and $\hat{b}_i$ are equivalent, and the back and forth transformations read

$$\hat{a}_i = \frac{1}{\sqrt{N_\mathfrak{T}}} \sum_{\boldsymbol{k}\in\mathrm{MBZ}} \mathrm{e}^{\mathrm{i}\boldsymbol{k}\boldsymbol{r}_i} \hat{a}_{\boldsymbol{k}} \qquad \hat{a}_{\boldsymbol{k}} = \frac{1}{\sqrt{N_\mathfrak{T}}} \sum_{\boldsymbol{r}_i\in\mathfrak{T}} \mathrm{e}^{-\mathrm{i}\boldsymbol{k}\boldsymbol{r}_i} \hat{a}_i \tag{2.33a}$$

$$\hat{b}_i = \frac{1}{\sqrt{N_\mathfrak{T}}} \sum_{\boldsymbol{k}\in\mathrm{MBZ}} \mathrm{e}^{\mathrm{i}\boldsymbol{k}\boldsymbol{r}_i} \hat{b}_{\boldsymbol{k}} \qquad \hat{b}_{\boldsymbol{k}} = \frac{1}{\sqrt{N_\mathfrak{T}}} \sum_{\boldsymbol{r}_i\in\mathfrak{T}} \mathrm{e}^{-\mathrm{i}\boldsymbol{k}\boldsymbol{r}_i} \hat{b}_i \tag{2.33b}$$

with $N_\mathfrak{T}$ being the number of magnetic unit cells, so that $N_\mathfrak{T} = N_A = N_B = \frac{N}{2}$ holds. On the left-hand side, the sum runs over the MBZ, which is only half of the BZ as discussed before. On the right-hand side, the sum runs over all Bravais lattice points $\mathfrak{T} \coloneqq \{n_1\boldsymbol{a}_1 + n_2\boldsymbol{a}_2 | n_1, n_2 \in \mathbb{Z}\}$, such that $\boldsymbol{r}_i$ is placed in the center of unit cell i. Consequently, both $\hat{a}_i$ and $\hat{b}_i$ acquire a phase only depending on $\boldsymbol{r}_i$. Figuratively speaking, first a combination of the atomic wave function is constructed within the unit cell and then a phase factor is attached to each cell to construct a Bloch As a result, any nearest-neighbor interaction term on the square lattice can be rewritten as

$$\sum_{\langle i,j\rangle} \hat{a}_i \hat{b}_j = \sum_{\boldsymbol{r}_i\in\mathfrak{T},\boldsymbol{d}\in\mathfrak{D}} \hat{a}_i \hat{b}_{i+\boldsymbol{d}} \ , \tag{2.34}$$

where $\boldsymbol{d}$ represents the distance to a unit cell of the spin on sublattice B. It is important to note that this distance is different from the distance in real space. So only the distance $\boldsymbol{d} = \boldsymbol{r}_i - \boldsymbol{r}_j$ between two unit cells i and j matters and not the actual positions. This results in a different set $\mathfrak{D} \coloneqq \{0, \boldsymbol{a}_1, \boldsymbol{a}_2, \boldsymbol{a}_1 + \boldsymbol{a}_2\}$ which is also depicted in Fig. 2.5 where the reference unit cell i in this gauge is marked by an orange diamond around it. There is an interaction bond within a unit cell, and three other interaction bonds connecting to other unit cells, where the corresponding three unit cells are marked with transparent orange diamonds. In the example interaction of Eq. (2.34),

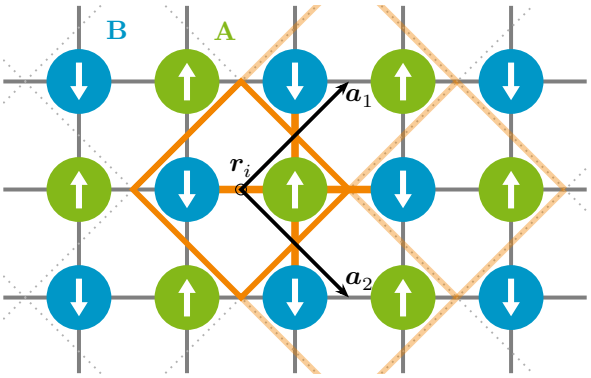

Figure 2.5: Sketch of spins on a square lattice with lattice constant a and an antiferromagnetic coupling. The magnetic unit cell is marked in orange and chosen so that each lattice site can be clearly assigned to a single cell. Neighboring cells that interact with the spin-up site are marked with a transparent orange diamond and the corresponding interaction bonds are highlighted in orange. The lattice vectors $\boldsymbol{a}_1$ and $\boldsymbol{a}_2$ correspond to the magnetic unit cell.

after the Fourier transformation is carried out, the following term results

$$\begin{aligned}\sum_{\boldsymbol{r}_i\in\mathfrak{T},\boldsymbol{d}\in\mathfrak{D}} \hat{a}_i\hat{b}_{i+\boldsymbol{d}} =& \frac{1}{N_\mathfrak{T}} \sum_{\boldsymbol{k}_1,\boldsymbol{k}_2\in\mathrm{MBZ}} \overbrace{\sum_{\boldsymbol{r}_i\in\mathfrak{T}} \mathrm{e}^{-\mathrm{i}(-\boldsymbol{k}_1-\boldsymbol{k}_2)\boldsymbol{r}_i}}^{N_\mathfrak{T}\delta_{\boldsymbol{G}}(-\boldsymbol{k}_1-\boldsymbol{k}_2)} \overbrace{\sum_{\boldsymbol{d}\in\mathfrak{D}} \mathrm{e}^{\mathrm{i}\boldsymbol{k}_2\boldsymbol{d}}}^{Z\gamma_\mathrm{B}(-\boldsymbol{k}_2)} \hat{a}_{\boldsymbol{k}_1}\hat{b}_{\boldsymbol{k}_2} \\ =& Z \sum_{\boldsymbol{k}_1,\boldsymbol{k}_2\in\mathrm{MBZ}} \delta_{\boldsymbol{G}}\left(-\boldsymbol{k}_1-\boldsymbol{k}_2\right)\gamma_\mathrm{B}(-\boldsymbol{k}_2)\hat{a}_{\boldsymbol{k}_1}\hat{b}_{\boldsymbol{k}_2}\end{aligned} \tag{2.35}$$

with

$$\gamma_\mathrm{B}(\boldsymbol{k}) = \frac{1}{Z}\sum_{\boldsymbol{d}\in\mathfrak{D}} \mathrm{e}^{-\mathrm{i}\boldsymbol{k}\boldsymbol{d}} = \frac{1}{Z}\left(1+\mathrm{e}^{-\mathrm{i}\boldsymbol{k}\boldsymbol{a}_1}+\mathrm{e}^{-\mathrm{i}\boldsymbol{k}\boldsymbol{a}_2}+\mathrm{e}^{-\mathrm{i}\boldsymbol{k}(\boldsymbol{a}_1+\boldsymbol{a}_2)}\right) , \tag{2.36}$$

and the coordination number of the square lattice $Z = 4$. Further, the δ-function in the reciprocal space is used with

$$\delta_{\boldsymbol{G}}\left(\boldsymbol{k}\right) = \frac{1}{N_\mathfrak{T}}\sum_{\boldsymbol{r}_i\in\mathfrak{T}} \mathrm{e}^{-\mathrm{i}\boldsymbol{k}\boldsymbol{r}_i} = \delta\left(\boldsymbol{k}-\boldsymbol{G}\right) , \tag{2.37}$$

where $\boldsymbol{G}$ is any reciprocal lattice vector with $\boldsymbol{G} = g_1\boldsymbol{b}_1 + g_2\boldsymbol{b}_2$ and $g_i \in \mathbb{Z}$. Subsequently, in Eq. (2.35) the evaluation of the δ-function results in

$$\sum_{\boldsymbol{r}_i\in\mathfrak{T},\boldsymbol{d}\in\mathfrak{D}} \hat{a}_i\hat{b}_{i+\boldsymbol{d}} = Z\sum_{\boldsymbol{k}\in\mathrm{MBZ}} \gamma_\mathrm{B}(\boldsymbol{k}+\boldsymbol{G})\hat{a}_{\boldsymbol{k}}\hat{b}_{-\boldsymbol{k}-\boldsymbol{G}} \tag{2.38}$$

The important property of the Bloch gauge is that any momentum $\boldsymbol{k}$ can be shifted by a reciprocal lattice vector $\boldsymbol{G}$ without changing the prefactor

$$\begin{aligned}\gamma_\mathrm{B}(\boldsymbol{k}+\boldsymbol{G}) =& \frac{1}{4}\left(1+\mathrm{e}^{-\mathrm{i}(\boldsymbol{k}+\boldsymbol{G})\boldsymbol{a}_1}+\mathrm{e}^{-\mathrm{i}(\boldsymbol{k}+\boldsymbol{G})\boldsymbol{a}_2}+\mathrm{e}^{-\mathrm{i}(\boldsymbol{k}+\boldsymbol{G})(\boldsymbol{a}_1+\boldsymbol{a}_2)}\right) \\ =& \frac{1}{4}\left(1+\mathrm{e}^{-\mathrm{i}\boldsymbol{k}\boldsymbol{a}_1}\mathrm{e}^{\mathrm{i}2\pi g_1}+\mathrm{e}^{-\mathrm{i}\boldsymbol{k}\boldsymbol{a}_2}\mathrm{e}^{\mathrm{i}2\pi g_2}+\mathrm{e}^{-\mathrm{i}\boldsymbol{k}(\boldsymbol{a}_1+\boldsymbol{a}_2)}\mathrm{e}^{-\mathrm{i}2\pi(g_1+g_2)}\right) \\ =& \gamma_\mathrm{B}(\boldsymbol{k}) ,\end{aligned} \tag{2.39}$$

where the relation $\boldsymbol{a}_i\boldsymbol{b}_j = 2\pi\delta_{ij}$ has been used. Hence the name Bloch gauge, since, as in the Bloch theorem, a shift of the momentum by a reciprocal lattice vector $\boldsymbol{G}$ has no impact. As a result, it

is reasonable to neglect any shifts by $\boldsymbol{G}$ in the Fourier representation of the Hamiltonian in the Bloch gauge, resulting in

$$\hat{\mathcal{H}} = -JN_{\mathfrak{T}}S^2Z + JSZ\sum_{\boldsymbol{k}}\left[\hat{a}^\dagger_{\boldsymbol{k}}\hat{a}_{\boldsymbol{k}} + \hat{b}^\dagger_{\boldsymbol{k}}\hat{b}_{\boldsymbol{k}} + \lambda\gamma_{\mathrm{B}}(\boldsymbol{k})\hat{a}_{\boldsymbol{k}}\hat{b}_{-\boldsymbol{k}} + \lambda\gamma^*_{\mathrm{B}}(\boldsymbol{k})\hat{a}^\dagger_{\boldsymbol{k}}\hat{b}^\dagger_{-\boldsymbol{k}}\right] \tag{2.40a}$$

$$\begin{aligned} -\frac{JZ}{N_{\mathfrak{T}}}\sum_{\substack{\boldsymbol{k}_1,\boldsymbol{k}_2,\\ \boldsymbol{k}_3,\boldsymbol{k}_4}}\Bigg[& \gamma_{\mathrm{B}}(\boldsymbol{k}_3-\boldsymbol{k}_4)\delta_{\boldsymbol{G}}\left(\boldsymbol{k}_1-\boldsymbol{k}_2+\boldsymbol{k}_3-\boldsymbol{k}_4\right)\hat{a}^\dagger_{\boldsymbol{k}_1}\hat{a}_{\boldsymbol{k}_2}\hat{b}^\dagger_{\boldsymbol{k}_3}\hat{b}_{\boldsymbol{k}_4} \\ & +\frac{\lambda}{2}\gamma_{\mathrm{B}}(\boldsymbol{k}_2+\boldsymbol{k}_3-\boldsymbol{k}_4)\delta_{\boldsymbol{G}}\left(\boldsymbol{k}_1+\boldsymbol{k}_2+\boldsymbol{k}_3-\boldsymbol{k}_4\right)\hat{a}^\dagger_{\boldsymbol{k}_1}\hat{b}^\dagger_{\boldsymbol{k}_2}\hat{b}^\dagger_{\boldsymbol{k}_3}\hat{b}_{\boldsymbol{k}_4} \\ & +\frac{\lambda}{2}\gamma_{\mathrm{B}}(-\boldsymbol{k}_4)\delta_{\boldsymbol{G}}\left(\boldsymbol{k}_1-\boldsymbol{k}_2-\boldsymbol{k}_3-\boldsymbol{k}_4\right)\hat{a}^\dagger_{\boldsymbol{k}_1}\hat{a}_{\boldsymbol{k}_2}\hat{a}_{\boldsymbol{k}_3}\hat{b}_{\boldsymbol{k}_4}\Bigg] , \end{aligned} \tag{2.40b}$$

where all sums of momenta run over the first MBZ. The Hamiltonian in Eq. (2.40) consists of a quadratic part (2.40a) and a quartic part (2.40b), where all coefficients depend on $\gamma_{\mathrm{B}}(\boldsymbol{k})$ in various forms. Later, it becomes evident that specific symmetries of an operator coefficient are contained in $\gamma_{\mathrm{B}}(\boldsymbol{k})$. Therefore, it makes sense to discuss the symmetries of $\gamma_{\mathrm{B}}(\boldsymbol{k})$ in the Bloch gauge.

Figure 2.6 shows the real and the imaginary part of $\gamma_{\mathrm{B}}(\boldsymbol{k})$ for the first MBZ and the adjacent zones. The $\boldsymbol{G}$ periodicity of Eq. (2.39) is clearly recognizable. Moreover, the point-group symmetries

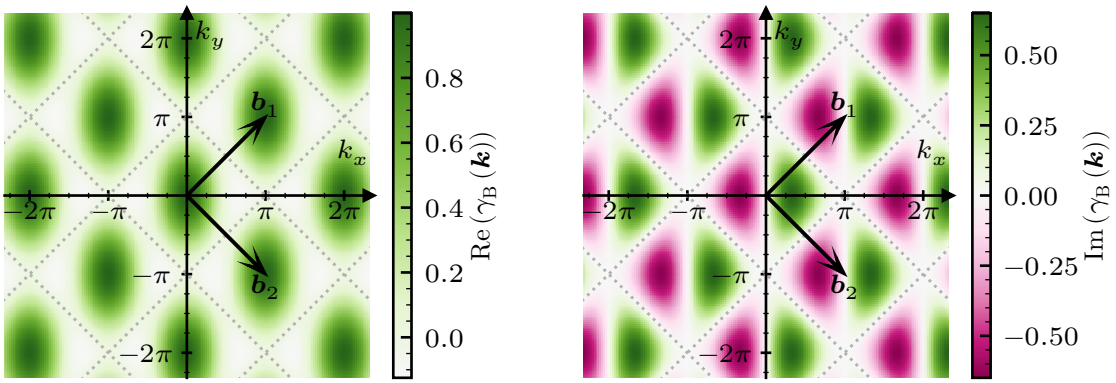

Figure 2.6: The figure depicts $\gamma_{\mathrm{B}}(\boldsymbol{k})$ in the Bloch gauge on the square lattice. The real part of $\gamma_{\mathrm{B}}(\boldsymbol{k})$ is shown on the left-hand side, and the imaginary part of $\gamma_{\mathrm{B}}(\boldsymbol{k})$ is shown on the right-hand side. In both cases, grey dashed lines mark the first MBZ and its extensions.

of $\gamma_{\mathrm{B}}(\boldsymbol{k})$ can be seen from Fig. 2.6. It is reasonable to express the symmetries according to components of the reciprocal lattice vectors $\boldsymbol{b}_1$ and $\boldsymbol{b}_2$ with

$$\boldsymbol{k}(m_1, m_2) = m_1\boldsymbol{b}_1 + m_2\boldsymbol{b}_2 \ . \tag{2.41}$$

With this representation, the point-group symmetries for the Bloch gauge are

$$\gamma_{\mathrm{B}}(\boldsymbol{k}(m_1,m_2)) = \gamma_{\mathrm{B}}(\boldsymbol{k}(m_2,m_1)) = \gamma^*_{\mathrm{B}}(\boldsymbol{k}(-m_1,-m_2)) = \gamma^*_{\mathrm{B}}(\boldsymbol{k}(-m_2,-m_1)) \ . \tag{2.42}$$

Of course, the symmetries can also be identified from Eq. (2.36). Compared to the bare square lattice, which has a D_4 point-group symmetry including 8 symmetry operations, the Bloch gauge in the Fourier transformation leads to a loss of intrinsic system symmetries. This results in only some symmetries remaining intact and necessitates complex conjugations, reducing the effective symmetry operations from 8 to 4.

All in all, the Bloch gauge has both advantages and disadvantages. The first and the most relevant advantage is the periodicity with respect to a reciprocal lattice vector $\boldsymbol{G}$, stemming from the

fact that all operators depend on $\gamma_{\mathrm{B}}(\boldsymbol{k})$, which fulfills $\gamma_{\mathrm{B}}(\boldsymbol{k}) = \gamma_{\mathrm{B}}(\boldsymbol{k}+\boldsymbol{G})$. At first glance, this advantage may not seem significant. However, throughout the thesis, there are cases where this feature proves useful, particularly in connection with so-called Umklapp processes, i.e., when a wave vector $\boldsymbol{k}$ is folded back into the first MBZ. Contrary, the Bloch gauge also has drawbacks. The first drawback is the loss of the full point-group symmetries of the initial lattice. Symmetries can be useful to reduce the number of arithmetic operations. Thus, their absence can result in significantly higher computational effort. The extent of this effect for the Bloch gauge depends on the symmetry of the initial system. Another issue with the Bloch gauge is that it forces the coefficients to have an imaginary part, which roughly doubles the computational effort.

Symmetric Gauge: The breaking of the point-group symmetry of the square lattice in the case of the Bloch gauge motivates the symmetric gauge. Here, the Fourier transformation for each boson $\hat{a}_i$ and $\hat{b}_j$ is carried out separately on its corresponding sub-lattice, resulting in

$$\hat{a}_i = \frac{1}{\sqrt{N_A}} \sum_{\boldsymbol{k}\in\mathrm{MBZ}} \mathrm{e}^{\mathrm{i}\boldsymbol{k}\boldsymbol{r}_i}\hat{a}_{\boldsymbol{k}} \;, \qquad \hat{a}_{\boldsymbol{k}} = \frac{1}{\sqrt{N_A}} \sum_{\boldsymbol{r}_i\in\Gamma_A} \mathrm{e}^{-\mathrm{i}\boldsymbol{k}\boldsymbol{r}_i}\hat{a}_i \;, \tag{2.43a}$$

$$\hat{b}_j = \frac{1}{\sqrt{N_B}} \sum_{\boldsymbol{k}\in\mathrm{MBZ}} \mathrm{e}^{\mathrm{i}\boldsymbol{k}\boldsymbol{r}_j}\hat{b}_{\boldsymbol{k}} \;, \qquad \hat{b}_{\boldsymbol{k}} = \frac{1}{\sqrt{N_B}} \sum_{\boldsymbol{r}_j\in\Gamma_B} \mathrm{e}^{-\mathrm{i}\boldsymbol{k}\boldsymbol{r}_j}\hat{b}_j \;. \tag{2.43b}$$

With $N_A = N_B = \frac{N}{2}$ being the number of sites in each sub-lattice Γ_A and Γ_B. Therefore, it is reasonable to shift the center of the unit cells either to the Γ_A or Γ_B lattice. Here, the sub-lattice Γ_A is chosen as in Fig. 2.4. As a consequence, for the simple case of the nearest-neighbor example interaction, which has already been discussed for the Bloch gauge, results in

$$\sum_{\langle i,j\rangle} \hat{a}_i\hat{b}_j = \sum_{\boldsymbol{r}_i\in\Gamma_A,\boldsymbol{d}\in\mathfrak{D}} \hat{a}_i\hat{b}_{i+\boldsymbol{d}} \tag{2.44}$$

with now $\mathfrak{D} = \left\{\frac{-\boldsymbol{a}_1-\boldsymbol{a}_2}{2}, \frac{\boldsymbol{a}_1-\boldsymbol{a}_2}{2}, \frac{-\boldsymbol{a}_1+\boldsymbol{a}_2}{2}, \frac{\boldsymbol{a}_1+\boldsymbol{a}_2}{2}\right\}$. The next step is to carry out the Fourier transformation of Eq. (2.43), yielding

$$\begin{aligned}\sum_{\boldsymbol{r}_i\in\Gamma_A,\boldsymbol{d}\in\mathfrak{D}} \hat{a}_i\hat{b}_{i+\boldsymbol{d}} =& \frac{1}{N_A} \sum_{\boldsymbol{k}_1,\boldsymbol{k}_2\in\mathrm{MBZ}} \overbrace{\sum_{\boldsymbol{r}_i\in\Gamma_A} \mathrm{e}^{-\mathrm{i}(-\boldsymbol{k}_1-\boldsymbol{k}_2)\boldsymbol{r}_i}}^{N_A\delta_{\boldsymbol{G}}(-\boldsymbol{k}_1-\boldsymbol{k}_2)} \overbrace{\sum_{\boldsymbol{d}\in\mathfrak{D}} \mathrm{e}^{\mathrm{i}\boldsymbol{k}_2\boldsymbol{d}}}^{Z\gamma_{\mathrm{S}}(-\boldsymbol{k}_2)} \hat{a}_{\boldsymbol{k}_1}\hat{b}_{\boldsymbol{k}_2} \\ =& Z \sum_{\boldsymbol{k}_1,\boldsymbol{k}_2\in\mathrm{MBZ}} \delta_{\boldsymbol{G}}\left(-\boldsymbol{k}_1-\boldsymbol{k}_2\right)\gamma_{\mathrm{S}}(-\boldsymbol{k}_2)\hat{a}_{\boldsymbol{k}_1}\hat{b}_{\boldsymbol{k}_2}\end{aligned} \tag{2.45}$$

which is almost the same as before, but with a subtle difference in $\gamma_{\mathrm{S}}(\boldsymbol{k})$, which now reads

$$\begin{aligned}\gamma_{\mathrm{S}}(\boldsymbol{k}) &= \frac{1}{Z}\sum_{\boldsymbol{d}\in\mathfrak{D}} \mathrm{e}^{-\mathrm{i}\boldsymbol{k}\boldsymbol{d}} = \frac{1}{Z}\left(\mathrm{e}^{-\frac{\mathrm{i}}{2}\boldsymbol{k}(\boldsymbol{a}_1+\boldsymbol{a}_2)} + \mathrm{e}^{\frac{\mathrm{i}}{2}\boldsymbol{k}(\boldsymbol{a}_1-\boldsymbol{a}_2)} + \mathrm{e}^{-\frac{\mathrm{i}}{2}\boldsymbol{k}(\boldsymbol{a}_1-\boldsymbol{a}_2)} + \mathrm{e}^{\frac{\mathrm{i}}{2}\boldsymbol{k}(\boldsymbol{a}_1+\boldsymbol{a}_2)}\right) \\ &= \frac{1}{Z}\underbrace{\left(\mathrm{e}^{\frac{\mathrm{i}}{2}\boldsymbol{k}\boldsymbol{a}_1} + \mathrm{e}^{-\frac{\mathrm{i}}{2}\boldsymbol{k}\boldsymbol{a}_1}\right)}_{2\cos\left(\frac{1}{2}\boldsymbol{k}\boldsymbol{a}_1\right)} \underbrace{\left(\mathrm{e}^{\frac{\mathrm{i}}{2}\boldsymbol{k}\boldsymbol{a}_2} + \mathrm{e}^{-\frac{\mathrm{i}}{2}\boldsymbol{k}\boldsymbol{a}_2}\right)}_{2\cos\left(\frac{1}{2}\boldsymbol{k}\boldsymbol{a}_2\right)} \\ &= \frac{4}{Z}\cos\left(\frac{1}{2}\boldsymbol{k}\boldsymbol{a}_1\right)\cos\left(\frac{1}{2}\boldsymbol{k}\boldsymbol{a}_2\right) \;.\end{aligned} \tag{2.46}$$

It is immediately apparent that $\gamma_{\mathrm{S}}(\boldsymbol{k})$ is no longer imaginary in this gauge. Furthermore, if the momentum $\boldsymbol{k}$ is represented via its reciprocal lattice vectors as in Eq. (2.41), it yields

$$\gamma_{\mathrm{S}}(\boldsymbol{k}) = \gamma_{\mathrm{S}}(\boldsymbol{k}(m_1,m_2)) = \frac{4}{Z}\cos(\pi m_1)\cos(\pi m_2) \tag{2.47}$$

where, again, the relation $\boldsymbol{a}_i\boldsymbol{b}_j = 2\pi\delta_{ij}$ is used to simplify the expression. Due to the simple form with only two cosine terms, the symmetries under which $\gamma_\mathrm{S}(\boldsymbol{k}(m_1, m_2))$ remain the same are straightforward to identify. They are

$$\begin{aligned}\gamma_\mathrm{S}(\boldsymbol{k}(m_1,m_2)) = \gamma_\mathrm{S}(\boldsymbol{k}(-m_1,m_2)) = \gamma_\mathrm{S}(\boldsymbol{k}(m_1,-m_2)) = \gamma_\mathrm{S}(\boldsymbol{k}(-m_1,-m_2))\\ =\gamma_\mathrm{S}(\boldsymbol{k}(m_2,m_1)) = \gamma_\mathrm{S}(\boldsymbol{k}(-m_2,m_1)) = \gamma_\mathrm{S}(\boldsymbol{k}(m_2,-m_1)) = \gamma_\mathrm{S}(\boldsymbol{k}(-m_2,-m_1))\ ,\end{aligned} \tag{2.48}$$

which preserves the D_4 point-group symmetries with 8 symmetry operations, held by the square lattice. So unlike the Bloch gauge, the symmetric gauge conserves the full point-group symmetry of the lattice, hence the name symmetric gauge. The symmetries can also be identified in Fig. 2.7, where $\gamma_\mathrm{S}(\boldsymbol{k})$ is visualized for the first MBZ and adjacent zones.

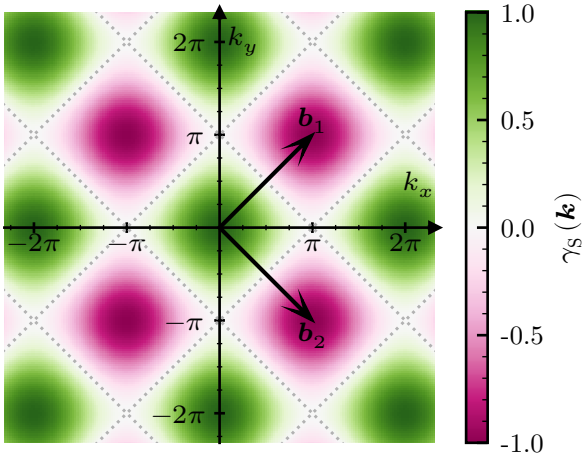

Figure 2.7: The figure depicts $\gamma_\mathrm{S}(\boldsymbol{k})$ in the symmetric gauge on the square lattice. Since $\gamma_\mathrm{S}(\boldsymbol{k})$ is real, one panel is sufficient. Grey dashed lines mark the first MBZ and its extensions.

What is striking about Fig. 2.7 is that the MBZ does not retain the same value for γ_S when it is shifted by a reciprocal lattice vector $\boldsymbol{G}$, contrary to the Bloch gauge. More precisely, if a shift by $\boldsymbol{G}$ is applied to $\boldsymbol{k}$, $\gamma_\mathrm{S}(\boldsymbol{k})$ results in

$$\gamma_\mathrm{S}(\boldsymbol{k}+\boldsymbol{G}) = \frac{4}{Z}\cos\left(\frac{1}{2}(\boldsymbol{k}+\boldsymbol{G})\boldsymbol{a}_1\right)\cos\left(\frac{1}{2}(\boldsymbol{k}+\boldsymbol{G})\boldsymbol{a}_2\right) \tag{2.49a}$$

$$= \frac{4}{Z}\cos\left(\frac{1}{2}\boldsymbol{k}\boldsymbol{a}_1\right)\cos\left(\frac{1}{2}\boldsymbol{G}\boldsymbol{a}_1\right)\cos\left(\frac{1}{2}\boldsymbol{k}\boldsymbol{a}_2\right)\cos\left(\frac{1}{2}\boldsymbol{G}\boldsymbol{a}_2\right) \tag{2.49b}$$

$$= \gamma_\mathrm{S}(\boldsymbol{G})\gamma_\mathrm{S}(\boldsymbol{k}) \tag{2.49c}$$

$$= \cos(\pi g_1)\cos(\pi g_2)\,\gamma_\mathrm{S}(\boldsymbol{k}) \tag{2.49d}$$

$$= (-1)^{g_1+g_2}\gamma_\mathrm{S}(\boldsymbol{k})\ . \tag{2.49e}$$

To obtain this relation, $\boldsymbol{G} = g_1\boldsymbol{b}_1 + g_2\boldsymbol{b}_2$ with $g_i \in \mathbb{Z}$ and the relation $\boldsymbol{a}_i\boldsymbol{b}_j = 2\pi\delta_{ij}$ are used. Hence, in the symmetric gauge for the square lattice, shifting the momentum $\boldsymbol{k}$ via a reciprocal lattice vector $\boldsymbol{G}$ can result in an additional minus sign, depending on whether the sum of $g_1 + g_2$ is even or odd. This is also the case for shifting the momentum of any $\hat{b}_{\boldsymbol{k}}$ by $\boldsymbol{G}$, which becomes clear upon looking at the definition of the Fourier transformation in Eq. (2.43). Starting with

$$\hat{b}_{\boldsymbol{k}+\boldsymbol{G}} = \frac{1}{\sqrt{N_B}}\sum_{\boldsymbol{r}_j\in\Gamma_B} \mathrm{e}^{-\mathrm{i}(\boldsymbol{k}+\boldsymbol{G})\boldsymbol{r}_j}\hat{b}_j \tag{2.50a}$$

and changing the sum over the sub-lattice $\Gamma_B \to \Gamma_A$ with $N_A = N_B$

$$= \frac{1}{\sqrt{N_A}} \sum_{\boldsymbol{r}_i \in \Gamma_A} \mathrm{e}^{-\mathrm{i}(\boldsymbol{k}+\boldsymbol{G})(\boldsymbol{r}_i - \boldsymbol{d}_0)} \hat{b}_i \tag{2.50b}$$

where $\boldsymbol{d}_0$ is only a single element of $\mathfrak{D}$ here $\boldsymbol{d}_0 = \frac{\boldsymbol{a}_1+\boldsymbol{a}_2}{2}$ to reach all Γ_B sites, the result is

$$= \mathrm{e}^{\mathrm{i}\pi(g_1+g_2)} \hat{b}_{\boldsymbol{k}} = (-1)^{g_1+g_2} \hat{b}_{\boldsymbol{k}} \ . \tag{2.50c}$$

Accordingly, a shift by a reciprocal lattice vector $\boldsymbol{G}$ is not as trivial as in the Bloch gauge, and it is essential to keep track of the correct signs in both prefactors and operators in this gauge. Note that the prefactor of a shift with $\boldsymbol{G}$ stems from the $\gamma_{\mathrm{S}}(\boldsymbol{k})$ function. Since $\gamma_{\mathrm{S}}(\boldsymbol{k})$ depends on the underlying lattice, it changes when the lattice is modified, resulting in a different prefactor that may not be as simple as in the case of the square lattice.

The prefactor will receive more attention in the context of the application of flow equations in Section 4.3.2, particularly when using symmetries both to reduce computational effort and to enhance numerical stability during numerical calculations. When the symmetric gauge is applied to the full Hamiltonian, it yields almost the same result as the Bloch gauge

$$\hat{\mathcal{H}} = -JN_A S^2 Z + JSZ \sum_{\boldsymbol{k}} \left[\hat{a}^\dagger_{\boldsymbol{k}} \hat{a}_{\boldsymbol{k}} + \hat{b}^\dagger_{\boldsymbol{k}} \hat{b}_{\boldsymbol{k}} + \lambda \gamma_{\mathrm{S}}(\boldsymbol{k}) \hat{a}_{\boldsymbol{k}} \hat{b}_{-\boldsymbol{k}} + \lambda \gamma_{\mathrm{S}}(\boldsymbol{k}) \hat{a}^\dagger_{\boldsymbol{k}} \hat{b}^\dagger_{-\boldsymbol{k}} \right] \tag{2.51a}$$

$$\begin{aligned} -\frac{JZ}{N_A} \sum_{\substack{\boldsymbol{k}_1,\boldsymbol{k}_2,\\ \boldsymbol{k}_3,\boldsymbol{k}_4}} \Bigg[& \gamma_{\mathrm{S}}(\boldsymbol{k}_3 - \boldsymbol{k}_4) \delta_{\boldsymbol{G}} (\boldsymbol{k}_1 - \boldsymbol{k}_2 + \boldsymbol{k}_3 - \boldsymbol{k}_4) \hat{a}^\dagger_{\boldsymbol{k}_1} \hat{a}_{\boldsymbol{k}_2} \hat{b}^\dagger_{\boldsymbol{k}_3} \hat{b}_{\boldsymbol{k}_4} \\ & + \frac{\lambda}{2} \gamma_{\mathrm{S}}(\boldsymbol{k}_2 + \boldsymbol{k}_3 - \boldsymbol{k}_4) \delta_{\boldsymbol{G}} (\boldsymbol{k}_1 + \boldsymbol{k}_2 + \boldsymbol{k}_3 - \boldsymbol{k}_4) \hat{a}^\dagger_{\boldsymbol{k}_1} \hat{b}^\dagger_{\boldsymbol{k}_2} \hat{b}^\dagger_{\boldsymbol{k}_3} \hat{b}_{\boldsymbol{k}_4} \\ & + \frac{\lambda}{2} \gamma_{\mathrm{S}}(-\boldsymbol{k}_4) \delta_{\boldsymbol{G}} (\boldsymbol{k}_1 - \boldsymbol{k}_2 - \boldsymbol{k}_3 - \boldsymbol{k}_4) \hat{a}^\dagger_{\boldsymbol{k}_1} \hat{a}_{\boldsymbol{k}_2} \hat{a}_{\boldsymbol{k}_3} \hat{b}_{\boldsymbol{k}_4} \Bigg] \end{aligned} \tag{2.51b}$$

Since $N_{\mathfrak{T}} = N_A$, the only differences are that $\gamma_{\mathrm{B}}(\boldsymbol{k})$ is replaced by $\gamma_{\mathrm{S}}(\boldsymbol{k})$ and that no complex conjugations are necessary. Effectively, the difference between the symmetric gauge and Bloch gauge is simply that all $\hat{b}_{\boldsymbol{k}}$ operators gain an additional phase $\mathrm{e}^{\mathrm{i}\boldsymbol{k}\boldsymbol{d}_0}$ with $\boldsymbol{d}_0 = \frac{\boldsymbol{a}_1+\boldsymbol{a}_2}{2}$ in the symmetric gauge. This is also apparent when considering both functions $\gamma_{\mathrm{S}}(\boldsymbol{k})$ and $\gamma_{\mathrm{B}}(\boldsymbol{k})$ where

$$\begin{aligned} \gamma_{\mathrm{S}}(\boldsymbol{k}) =& \frac{1}{Z} \left(\mathrm{e}^{-\frac{\mathrm{i}}{2}\boldsymbol{k}(\boldsymbol{a}_1+\boldsymbol{a_2})} + \mathrm{e}^{\frac{\mathrm{i}}{2}\boldsymbol{k}(\boldsymbol{a}_1-\boldsymbol{a_2})} + \mathrm{e}^{-\frac{\mathrm{i}}{2}\boldsymbol{k}(\boldsymbol{a}_1-\boldsymbol{a_2})} + \mathrm{e}^{\frac{\mathrm{i}}{2}\boldsymbol{k}(\boldsymbol{a}_1+\boldsymbol{a}_2)} \right) \\ =& \frac{1}{Z} \left(1 + \mathrm{e}^{-\mathrm{i}\boldsymbol{k}\boldsymbol{a}_1} + \mathrm{e}^{-\mathrm{i}\boldsymbol{k}\boldsymbol{a}_2} + \mathrm{e}^{-\mathrm{i}\boldsymbol{k}(\boldsymbol{a}_1+\boldsymbol{a}_2)} \right) \mathrm{e}^{\frac{\mathrm{i}}{2}\boldsymbol{k}(\boldsymbol{a}_1+\boldsymbol{a}_2)} \\ =& \gamma_B(\boldsymbol{k}) \mathrm{e}^{\mathrm{i}\boldsymbol{k}\boldsymbol{d}} \end{aligned} \tag{2.52}$$

holds.

To summarize, for assuming an antiferromagnetic order on the square lattice, there are different choices of Fourier transformations called gauges: The Bloch gauge, which remains unaffected by adding a reciprocal lattice vector but necessitates calculations with complex numbers and does not retain the full point-group symmetry of the system, and the symmetric gauge, which preserves the full point-group symmetry of the system, but a shift by a reciprocal lattice vector can lead to a change in sign. In the case of the antiferromagnetic spin-$\frac{1}{2}$ easy-axis XXZ model on a square lattice, the advantages of the symmetric gauge outweigh the disadvantages, rendering it superior to the Bloch gauge. However, while the symmetric gauge may be superior in this case, for other models or underlying lattices, this has to be reconsidered. Nevertheless, the consideration and check of two different gauges makes it feasible to eliminate possible errors in the results, as the

physical observables behave independently of the gauge. Therefore, the result of the Bloch gauge in Eq. (2.40) is considered further since it represents the more general result that takes also complex prefactors into account.

2.5.3 Bogoliubov Transformation

The final result in the Bloch gauge for the antiferromagnetic spin-$\frac{1}{2}$ easy-axis XXZ model on a square lattice, considering only quadratic operator terms, i.e., Eq. (2.40a), can be rewritten in a general form

$$\widehat{\mathcal{H}} = E_0 + \sum_{\boldsymbol{k}} \left[g_{\boldsymbol{k}} \hat{a}_{\boldsymbol{k}}^\dagger \hat{a}_{\boldsymbol{k}} + f_{-\boldsymbol{k}} \hat{b}_{-\boldsymbol{k}} \hat{b}_{-\boldsymbol{k}}^\dagger + h_{\boldsymbol{k}} \hat{a}_{\boldsymbol{k}} \hat{b}_{-\boldsymbol{k}} + h_{\boldsymbol{k}}^* \hat{a}_{\boldsymbol{k}}^\dagger \hat{b}_{-\boldsymbol{k}}^\dagger \right] , \tag{2.53}$$

where the order of $\hat{b}_{\boldsymbol{k}}^\dagger \hat{b}_{\boldsymbol{k}}$ was changed with the help of the commutator $\hat{b}_{\boldsymbol{k}}^\dagger \hat{b}_{\boldsymbol{k}} = \hat{b}_{\boldsymbol{k}} \hat{b}_{\boldsymbol{k}}^\dagger - 1$. The additional term of $-\sum_{\boldsymbol{k}} f_{\boldsymbol{k}}$ arising from the commutator is absorbed into E_0. Furthermore, in $\hat{b}_{\boldsymbol{k}} \hat{b}_{\boldsymbol{k}}^\dagger$ the momentum is shifted $\boldsymbol{k} \to -\boldsymbol{k}$ to match with the index of $\hat{b}^{(\dagger)}$ in off-diagonal parts $\hat{a}_{\boldsymbol{k}}^{(\dagger)} \hat{b}_{-\boldsymbol{k}}^{(\dagger)}$. This allows the Hamiltonian to be rewritten in a compact matrix form

$$\widehat{\mathcal{H}} = E_0 + \sum_{\boldsymbol{k}} \boldsymbol{\Psi}_{\boldsymbol{k}}^\dagger \underline{\boldsymbol{M}}_{\boldsymbol{k}} \boldsymbol{\Psi}_{\boldsymbol{k}} , \quad \text{with} \quad \underline{\boldsymbol{M}}_{\boldsymbol{k}} = \begin{pmatrix} g_{\boldsymbol{k}} & h_{\boldsymbol{k}}^* \\ h_{\boldsymbol{k}} & f_{-\boldsymbol{k}} \end{pmatrix} \quad \text{and} \quad \boldsymbol{\Psi}_{\boldsymbol{k}} = \begin{pmatrix} \hat{a}_{\boldsymbol{k}} \\ \hat{b}_{-\boldsymbol{k}}^\dagger \end{pmatrix} . \tag{2.54}$$

In comparison to the ferromagnetic case, $h_{\boldsymbol{k}}$ is not zero, so that off-diagonal terms are present. Therefore, the solution for the L-SWT cannot be directly inferred from $g_{\boldsymbol{k}}$ and $f_{-\boldsymbol{k}}$. Although in the discussed Hamiltonian, $g_{\boldsymbol{k}}$ and $f_{-\boldsymbol{k}}$ are identical, they are continued to be treated as distinct functions to preserve generality. To diagonalize the Hamiltonian, a general Bogoliubov-Valatin transformation, also abbreviated as Bogoliubov transformation, is applied. This linear transformation finds application in many areas; notably, it was first used in the field of superfluidity [Bog47] and superconductivity [Val58; Bog58]. The goal of this transformation is to express the operators $\hat{a}_{\boldsymbol{k}}^{(\dagger)}$ and $\hat{b}_{-\boldsymbol{k}}^{(\dagger)}$ as superpositions of new bosonic operators $\hat{\alpha}_{\boldsymbol{k}}^{(\dagger)}$ and $\hat{\beta}_{-\boldsymbol{k}}^{(\dagger)}$. The new operators must satisfy certain constraints. First, they must still obey the general bosonic commutation relations. Furthermore, the action of each operator with respect to total S_{tot}^z must be preserved. Specifically, $\hat{\alpha}^\dagger$ decreases the total S_{tot}^z, analogous to $\hat{a}^\dagger$, whereas $\hat{\alpha}$ increases it in correspondence with $\hat{a}$. Likewise, $\hat{\beta}^\dagger$ increases the total S_{tot}^z, analogous to $\hat{b}^\dagger$, while $\hat{\beta}$ reduces it similarly to $\hat{b}$. Thus, a valid transformation can be expressed as

$$\hat{a}_{\boldsymbol{k}} = \; l(\boldsymbol{k}) \hat{\alpha}_{\boldsymbol{k}} + m^*(\boldsymbol{k}) \hat{\beta}_{-\boldsymbol{k}}^\dagger \tag{2.55a}$$

$$\hat{b}_{-\boldsymbol{k}}^\dagger = m(\boldsymbol{k}) \hat{\alpha}_{\boldsymbol{k}} + \; l^*(\boldsymbol{k}) \hat{\beta}_{-\boldsymbol{k}}^\dagger \tag{2.55b}$$

This corresponds to a linear transformation represented in matrix notation as

$$\boldsymbol{\Psi}_{\boldsymbol{k}} = \underline{\boldsymbol{T}} \boldsymbol{\Phi}_{\boldsymbol{k}} , \quad \text{where} \quad \underline{\boldsymbol{T}} = \begin{pmatrix} l(\boldsymbol{k}) & m^*(\boldsymbol{k}) \\ m(\boldsymbol{k}) & l^*(\boldsymbol{k}) \end{pmatrix} \quad \text{and} \quad \boldsymbol{\Phi}_{\boldsymbol{k}} = \begin{pmatrix} \hat{\alpha}_{\boldsymbol{k}} \\ \hat{\beta}_{-\boldsymbol{k}}^\dagger \end{pmatrix} . \tag{2.56}$$

As a result, the Hamiltonian can be expressed as

$$\widehat{\mathcal{H}} = \sum_{\boldsymbol{k}} \boldsymbol{\Phi}_{\boldsymbol{k}}^\dagger \underline{\boldsymbol{T}}^\dagger \underline{\boldsymbol{M}}_{\boldsymbol{k}} \underline{\boldsymbol{T}} \boldsymbol{\Phi}_{\boldsymbol{k}} . \tag{2.57}$$

Naively, one might think that it is enough to diagonalize the matrix $\underline{\boldsymbol{T}}^\dagger \underline{\boldsymbol{M}}_{\boldsymbol{k}} \underline{\boldsymbol{T}}$ and thereby determine the functions $l(\boldsymbol{k})$ and $m(\boldsymbol{k})$ that diagonalize the Hamiltonian. However, a naive diagonalization of the Hamiltonian is not sufficient to determine the eigenvalues associated with the matrix $\underline{\boldsymbol{T}}^\dagger \underline{\boldsymbol{M}}_{\boldsymbol{k}} \underline{\boldsymbol{T}}$,

because such a solution does not necessarily satisfy the general bosonic commutation relations. To ensure compliance with the relations

$$\left[\Psi_{i,\boldsymbol{k}}, \Psi_{j,\boldsymbol{k}}^{\dagger}\right] = \left[\Phi_{i,\boldsymbol{k}}, \Phi_{j,\boldsymbol{k}}^{\dagger}\right] = \eta_{ij} \quad \text{with} \quad \underline{\boldsymbol{\eta}} = \begin{pmatrix} 1 & 0 \\ 0 & -1 \end{pmatrix} , \tag{2.58}$$

the transformation matrix $\underline{\boldsymbol{T}}$ must be paraunitary [Col78], i.e., it must satisfy the condition

$$\underline{\boldsymbol{T}}\underline{\boldsymbol{\eta}}\underline{\boldsymbol{T}}^{\dagger} = \underline{\boldsymbol{\eta}} . \tag{2.59}$$

By calculating the diagonal form of the effective matrix

$$\underline{\boldsymbol{K}}_{\boldsymbol{k}} = \underline{\boldsymbol{\eta}}\underline{\boldsymbol{M}}_{\boldsymbol{k}} , \tag{2.60}$$

the transformation matrix $\underline{\boldsymbol{T}}$ is determined that also satisfies the paraunitary condition Eq. (2.59). A detailed step-by-step procedure for calculating this diagonalization is omitted here but can be found in the appendix of [Wal24]. For the Hamiltonian described in Eq. (2.53), the eigenvalues of $\underline{\boldsymbol{M}}_{\boldsymbol{k}}$ are given by

$$\omega_{\alpha}(\boldsymbol{k}) = \Delta_{\boldsymbol{k}} + \sqrt{R_{\boldsymbol{k}}^2 - |h_{\boldsymbol{k}}|^2} , \qquad \omega_{\beta}(-\boldsymbol{k}) = -\Delta_{\boldsymbol{k}} + \sqrt{R_{\boldsymbol{k}}^2 - |h_{\boldsymbol{k}}|^2} \tag{2.61}$$

with

$$R_{\boldsymbol{k}} = \frac{g_{\boldsymbol{k}} + f_{-\boldsymbol{k}}}{2} , \qquad \Delta_{\boldsymbol{k}} = \frac{g_{\boldsymbol{k}} - f_{-\boldsymbol{k}}}{2} . \tag{2.62}$$

The elements of the transformation matrix $\underline{\boldsymbol{T}}$ read

$$l(\boldsymbol{k}) = -\frac{\mu_{\boldsymbol{k}}}{\sqrt{|\mu_{\boldsymbol{k}}|^2 - |h_{\boldsymbol{k}}|^2}} \quad \text{and} \quad m(\boldsymbol{k}) = \frac{h_{\boldsymbol{k}}}{\sqrt{|\mu_{\boldsymbol{k}}|^2 - |h_{\boldsymbol{k}}|^2}} \quad \text{and} \quad \mu_{\boldsymbol{k}} = \omega_{\alpha}(\boldsymbol{k}) + f_{-\boldsymbol{k}} . \tag{2.63}$$

Eventually, the diagonalized Hamiltonian reads

$$\hat{\mathcal{H}} = E_0 + \sum_{\boldsymbol{k}} \left[\omega_{\alpha}(\boldsymbol{k})\hat{\alpha}_{\boldsymbol{k}}^{\dagger}\hat{\alpha}_{\boldsymbol{k}} + \omega_{\beta}(-\boldsymbol{k})\hat{\beta}_{-\boldsymbol{k}}\hat{\beta}_{-\boldsymbol{k}}^{\dagger}\right] . \tag{2.64}$$

With the general procedure regarding a Bogoliubov transformation outlined, it is possible to diagonalize Eq. (2.40a). The result is the L-SWT single-particle dispersion. To this end, the Hamiltonian is transformed into the same form as in Eq. (2.53), which yields

$$\begin{aligned} \hat{\mathcal{H}} =& - JN_{\mathfrak{T}}S^2Z - JN_{\mathfrak{T}}SZ \\ &+ JSZ\sum_{\boldsymbol{k}} \left[\hat{a}_{\boldsymbol{k}}^{\dagger}\hat{a}_{\boldsymbol{k}} + \hat{b}_{-\boldsymbol{k}}\hat{b}_{-\boldsymbol{k}}^{\dagger} + \lambda\gamma_{\mathrm{B}}(\boldsymbol{k})\hat{a}_{\boldsymbol{k}}\hat{b}_{-\boldsymbol{k}} + \lambda\gamma_{\mathrm{B}}^{*}(\boldsymbol{k})\hat{a}_{\boldsymbol{k}}^{\dagger}\hat{b}_{-\boldsymbol{k}}^{\dagger}\right] . \end{aligned} \tag{2.65}$$

Consequently, the coefficients are

$$g_{\boldsymbol{k}} = f_{-\boldsymbol{k}} = JSZ \quad \text{and} \quad h_{\boldsymbol{k}} = JSZ\lambda\gamma_{\mathrm{B}}(\boldsymbol{k}) . \tag{2.66}$$

Since $|\gamma_{\mathrm{B}}(\boldsymbol{k})|^2 = |\gamma_{\mathrm{B}}(-\boldsymbol{k})|^2$ and $g_{\boldsymbol{k}} = f_{-\boldsymbol{k}}$, a degenerate dispersion

$$\omega_{\boldsymbol{k}} = \omega_{\alpha,\beta}(\boldsymbol{k}) = JSZ\sqrt{1 - \lambda^2|\gamma_{\mathrm{B}}(\boldsymbol{k})|^2} \tag{2.67}$$

is obtained for both $\hat{\alpha}$ and $\hat{\beta}$. Here it becomes evident that the different gauges do not influence the physical observables, since the magnon dispersion is independent of the choice of gauge as the different phases in $\gamma(\boldsymbol{k})$ annul in the absolute square. Finally, the resulting diagonal Hamiltonian in L-SWT for the antiferromagnetic spin-$\frac{1}{2}$ easy-axis XXZ model on a square lattice is given by

$$\hat{\mathcal{H}} = -JN_{\mathfrak{T}}S^2Z - JN_{\mathfrak{T}}SZ + \sum_{\boldsymbol{k}} \omega_{\boldsymbol{k}} + \sum_{\boldsymbol{k}} \omega_{\boldsymbol{k}} \left[\hat{\alpha}^\dagger_{\boldsymbol{k}}\hat{\alpha}_{\boldsymbol{k}} + \hat{\beta}^\dagger_{\boldsymbol{k}}\hat{\beta}_{\boldsymbol{k}}\right] . \tag{2.68}$$

Figure 2.8 illustrates the magnon dispersion for a given path through the MBZ obtained from the L-SWT for different anisotropy parameters λ. Expectedly, for the isotropic limit $\lambda = 1$, i.e., the afHM, the dispersion features massless Goldstone bosons. The dispersion closes linearly at $\boldsymbol{k} = (0, 0)$ in contrast to the ferromagnetic case. In the anisotropic case $\lambda < 1$, the symmetry of the Hamiltonian is no longer continuous but a discrete $\mathbb{Z}_2$ symmetry. As the Goldstone theorem does not apply to discrete symmetries, the dispersion becomes gapped. For the Ising limit $\lambda = 0$, the excitations are immobile. Consequently, the dispersion is constant and shows no $\boldsymbol{k}$ dependence. For increasing λ, the gap starts to close. Nevertheless the dispersion features a plateau for all values of λ which ranges from $\boldsymbol{k} = (\pi, 0)^T$ to $\boldsymbol{k} = (\frac{\pi}{2}, \frac{\pi}{2})^T$ with the constant value of $\omega_{\boldsymbol{k}} = 2J$.

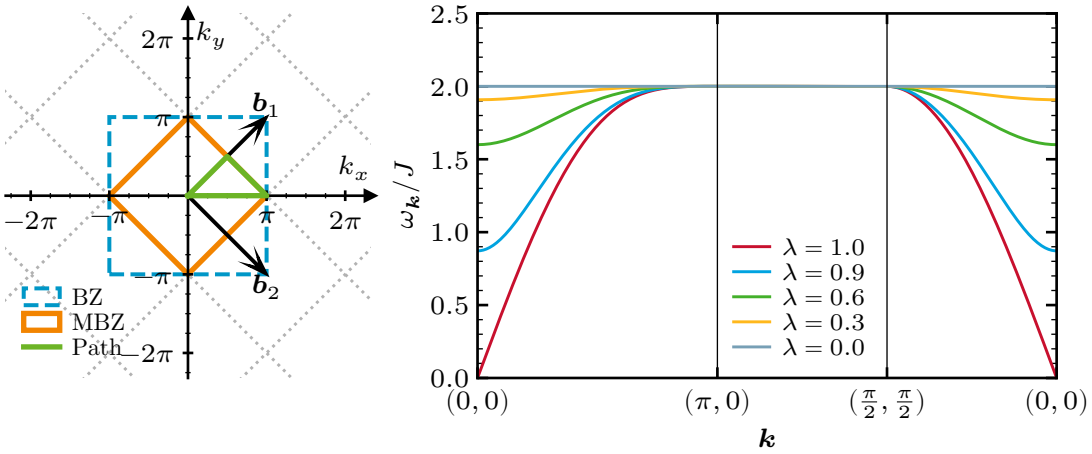

Figure 2.8: The left panel depicts the reciprocal lattice for the antiferromagnetic spin-$\frac{1}{2}$ easy-axis XXZ model on a square lattice. The dashed blue square marks the first BZ, the orange rhombus marks the first MBZ, and the reciprocal lattice vectors $\boldsymbol{b}_{1,2}$ belonging to the MBZ are also depicted. The green line represents the path through the MBZ for which the associated dispersion $\omega_{\boldsymbol{k}}$ for various anisotropy parameter λ is shown in the right panel. The lattice constant a is set to unity.

Furthermore, from Eq. (2.68), it becomes apparent that the ground state energy corresponding to the classical Néel state $E_0 = -JN_{\mathfrak{T}}S^2Z$ is shifted by $-JN_{\mathfrak{T}}SZ + \sum_{\boldsymbol{k}} \omega_{\boldsymbol{k}}$, which accounts for quantum fluctuations of the magnons. Additionally, it is possible to calculate the expectation value of the density of the originally defined operators $\hat{a}_{\boldsymbol{k}}$ and $\hat{b}_{\boldsymbol{k}}$ in the ground state. This is achieved by averaging, applying a Fourier transformation, and utilizing the Bogoliubov transformation. For the isotropic case $\lambda = 1$ this results in

$$\begin{aligned} \langle \hat{a}^\dagger_i \hat{a}_i \rangle_0 &= \frac{1}{N_{\mathfrak{T}}} \sum_{\boldsymbol{r}_i \in \Gamma_{\mathfrak{T}}} \langle \hat{a}^\dagger_i \hat{a}_i \rangle_0 = \frac{1}{N_{\mathfrak{T}}} \sum_{\boldsymbol{k}} \langle \hat{a}^\dagger_{\boldsymbol{k}} \hat{a}_{\boldsymbol{k}} \rangle_0 \\ &= \frac{1}{N_{\mathfrak{T}}} \sum_{\boldsymbol{k}} |m(\boldsymbol{k})|^2 \langle \hat{\beta}_{-\boldsymbol{k}} \hat{\beta}^\dagger_{-\boldsymbol{k}} \rangle_0 = \frac{1}{N_{\mathfrak{T}}} \sum_{\boldsymbol{k}} |m(\boldsymbol{k})|^2 \approx 0.19 . \end{aligned} \tag{2.69}$$

The same result applies to $\langle \hat{b}^\dagger_i \hat{b}_i \rangle_0$, thus approximately 40 % of the spins in the classical Néel state are flipped due to quantum fluctuations in the afHM, as aforementioned.

In summary, the Bogoliubov transformation enables the diagonalization of the quadratic part of a Hamiltonian by superposing the original operators and thus creates new bosonic operators. In

the Heisenberg limit $\lambda = 1$, this transformation yields a degenerate magnon dispersion relation featuring massless Goldstone bosons and introduces a quantum correction to the classical Néel state. However, all calculations up to this point neglected operator terms beyond quadratic order. In the next section, a method is presented to partially incorporate these higher-order terms, at least their single-particle contribution. This provides more accurate results for the dispersion relation and ground-state energy of the system.

2.5.4 Nonlinear Spin-Wave Theory

The L-SWT provides a decent starting point for the analysis of the antiferromagnetic spin-$\frac{1}{2}$ easy-axis XXZ model on a square lattice. However, since the Bogoliubov transformation diagonalizes only the quadratic part of the Hamiltonian, the L-SWT is insufficient to describe the system fully. The next step toward a more accurate SWT involves incorporating single-particle contributions from higher-order operators in Eq. (2.40b) but still neglecting their true higher-order contributions. This approach is referred to as mean-field spin-wave theory (MF-SWT). One straightforward approach to achieve a MF-SWT is to insert the result of the Bogoliubov transformation also in the quartic terms. When this approach is applied, the first term of Eq. (2.40b) for example reads

$$\begin{aligned}\hat{a}^\dagger_{\boldsymbol{k}_1}\hat{a}_{\boldsymbol{k}_2}\hat{b}^\dagger_{\boldsymbol{k}_3}\hat{b}_{\boldsymbol{k}_4} = &\left(l^*(\boldsymbol{k}_1)\hat{\alpha}^\dagger_{\boldsymbol{k}_1} + m(\boldsymbol{k}_1)\hat{\beta}_{-\boldsymbol{k}_1}\right)\left(l(\boldsymbol{k}_2)\hat{\alpha}_{\boldsymbol{k}_2} + m^*(\boldsymbol{k}_2)\hat{\beta}^\dagger_{-\boldsymbol{k}_2}\right)\\ &\left(m(-\boldsymbol{k}_3)\hat{\alpha}_{-\boldsymbol{k}_3} + l^*(-\boldsymbol{k}_3)\hat{\beta}^\dagger_{\boldsymbol{k}_3}\right)\left(m^*(-\boldsymbol{k}_4)\hat{\alpha}^\dagger_{-\boldsymbol{k}_4} + l(-\boldsymbol{k}_4)\hat{\beta}_{\boldsymbol{k}_4}\right)\ .\end{aligned} \tag{2.70}$$

This transformation produces a total of 16 terms. After normal-ordering, i.e., placing all creation operators left to annihilation operators, even more terms are generated due to the non-commutativity of operators of the same flavor. These additional terms contribute to the ground-state energy and to the quadratic part of the Hamiltonian. Notably, these additional terms may also contain off-diagonal quadratic parts, which were initially rotated to zero with the Bogoliubov transformation in the L-SWT. Consequently, this approach to obtain a MF-SWT Hamiltonian is impractical as it is cumbersome to normal-order all quartic operators and generally does not lead to a Hamiltonian that is diagonal on a quadratic level.

Instead, a general normal-ordering is applied to the Hamiltonian, which is a common technique in many-body physics [Nol15]. The foundation of this method involves introducing a generalized definition of the normal-ordering of operators, which is expressed as

$$\hat{A} = :\hat{A}: + \langle\hat{A}\rangle_0 \tag{2.71}$$

where $:\ldots:$ denotes the normal-ordering and $\langle\ldots\rangle_0$ represents the vacuum expectation value, respectively. For a general quadratic operator term, this expression becomes

$$\hat{a}_i^{(\dagger)}\hat{b}_j^{(\dagger)} = :\hat{a}_i^{(\dagger)}\hat{b}_j^{(\dagger)}: + \langle\hat{a}_i^{(\dagger)}\hat{b}_j^{(\dagger)}\rangle_0\ . \tag{2.72}$$

The key distinction between this generalized normal-ordering and standard normal-ordering based on commutators lies in the fact that the reference vacuum $\langle\ \rangle_0$ does not necessarily correspond to the vacuum state of the bosons at hand. If the boson operators do not correspond to the chosen reference vacuum, $:\ldots:$ and $\langle\ldots\rangle_0$ cannot be evaluated directly. Instead, these terms are temporarily retained and evaluated at a later stage. Thus, under this definition of normal-order, an operator can be decomposed into true fluctuations $:\ldots:$ and energy renormalizations $\langle\ldots\rangle_0$ around a renormalized vacuum $\langle\ \rangle_0$. To clarify the distinction between retaining or changing the reference vacuum, two simple examples are given below.

The operator term

$$\hat{a}_i\hat{a}_j^\dagger = :\hat{a}_i\hat{a}_j^\dagger: + \langle \hat{a}_i\hat{a}_j^\dagger \rangle_0 \tag{2.73}$$

can be explicitly evaluated when $\langle\ \rangle_0$ corresponds to the reference vacuum state of $\hat{a}^{(\dagger)}$, yielding

$$\hat{a}_i\hat{a}_j^\dagger = :\hat{a}_i\hat{a}_j^\dagger: + \langle \hat{a}_i\hat{a}_j^\dagger \rangle_0 = \hat{a}_i^\dagger\hat{a}_j + \delta_{ij} \ . \tag{2.74}$$

As expected, this result matches the standard commutator relation for bosonic operators. Similarly, an already normal-ordered term yields

$$\hat{a}_i^\dagger\hat{a}_j = :\hat{a}_i^\dagger\hat{a}_j: + \langle \hat{a}_i^\dagger\hat{a}_j \rangle_0 = \hat{a}_i^\dagger\hat{a}_j \ . \tag{2.75}$$

If $\langle\ \rangle_0$ does not correspond to the reference vacuum of $\hat{a}^{(\dagger)}$, both equalities $=$ cannot be utilized. In such cases, terms remain in their respective form of $:\ldots:$ and $\langle \ldots \rangle_0$ until the appropriate boson representation is determined.

In this context, the renormalized reference vacuum corresponds to the Bogoliubov bosons. Therefore, only after performing a Bogoliubov transformation, both $:\ldots:$ and $\langle \ldots \rangle_0$ can be explicitly evaluated. Until now, only the behavior of quadratic operator terms under normal-ordering has been discussed. For higher order terms, Wick's theorem [Wic50; Nol15] is employed. For a general bosonic quartic operator term, the normal-ordering reads

$$\hat{a}_i^{(\dagger)}\hat{b}_j^{(\dagger)}\hat{c}_k^{(\dagger)}\hat{d}_l^{(\dagger)} = :\hat{a}_i^{(\dagger)}\hat{b}_j^{(\dagger)}\hat{c}_k^{(\dagger)}\hat{d}_l^{(\dagger)}: \tag{2.76a}$$

$$\begin{aligned} &+ :\hat{a}_i^{(\dagger)}\hat{b}_j^{(\dagger)}:\langle \hat{c}_k^{(\dagger)}\hat{d}_l^{(\dagger)} \rangle_0 + :\hat{a}_i^{(\dagger)}\hat{c}_k^{(\dagger)}:\langle \hat{b}_j^{(\dagger)}\hat{d}_l^{(\dagger)} \rangle_0 + :\hat{a}_i^{(\dagger)}\hat{d}_l^{(\dagger)}:\langle \hat{b}_j^{(\dagger)}\hat{c}_k^{(\dagger)} \rangle_0 \\ &+ :\hat{b}_j^{(\dagger)}\hat{c}_k^{(\dagger)}:\langle \hat{a}_i^{(\dagger)}\hat{d}_l^{(\dagger)} \rangle_0 + :\hat{b}_j^{(\dagger)}\hat{d}_l^{(\dagger)}:\langle \hat{a}_i^{(\dagger)}\hat{c}_k^{(\dagger)} \rangle_0 + :\hat{c}_k^{(\dagger)}\hat{d}_l^{(\dagger)}:\langle \hat{a}_i^{(\dagger)}\hat{b}_j^{(\dagger)} \rangle_0 \end{aligned} \tag{2.76b}$$

$$+\langle \hat{a}_i^{(\dagger)}\hat{b}_j^{(\dagger)} \rangle_0 \langle \hat{c}_k^{(\dagger)}\hat{d}_l^{(\dagger)} \rangle_0 + \langle \hat{a}_i^{(\dagger)}\hat{c}_k^{(\dagger)} \rangle_0 \langle \hat{b}_j^{(\dagger)}\hat{d}_l^{(\dagger)} \rangle_0 + \langle \hat{a}_i^{(\dagger)}\hat{d}_l^{(\dagger)} \rangle_0 \langle \hat{b}_j^{(\dagger)}\hat{c}_k^{(\dagger)} \rangle_0 \ . \tag{2.76c}$$

Once again, the normal-order yields the fluctuations around the renormalized reference vacuum state. The fluctuations consist both of a true quartic term in Eq. (2.76a) and a summation over various quadratic terms in Eq. (2.76b). The remaining terms in Eq. (2.76c) are expectation values contributing solely to the energy offset.

It is important to emphasize that the generalized normal-ordering is already applied to the real-space representation of the Hamiltonian prior to performing both the Fourier and Bogoliubov transformation, i.e., on the Hamiltonian of Eq. (2.32). The generalized normal-ordering of all terms in the Hamiltonian is performed analogously to Eqs. (2.72) and (2.76). First, the quadratic terms are considered

$$\begin{aligned} \hat{a}_i^\dagger\hat{a}_i &= :\hat{a}_i^\dagger\hat{a}_i: + \langle \hat{a}_i^\dagger\hat{a}_i \rangle_0 \ , & \hat{a}_i\hat{b}_{i+d} &= :\hat{a}_i\hat{b}_{i+d}: + \langle \hat{a}_i\hat{b}_{i+d} \rangle_0 \ , \\ \hat{b}_{i+d}^\dagger\hat{b}_{i+d} &= :\hat{b}_{i+d}^\dagger\hat{b}_{i+d}: + \langle \hat{b}_{i+d}^\dagger\hat{b}_{i+d} \rangle_0 \ , & \hat{a}_i^\dagger\hat{b}_{i+d}^\dagger &= :\hat{a}_i^\dagger\hat{b}_{i+d}^\dagger: + \langle \hat{a}_i^\dagger\hat{b}_{i+d}^\dagger \rangle_0 \ , \end{aligned} \tag{2.77}$$

which gives rise to four different expectation values. At this stage, computing these expectation values is not advantageous. However, they can be evaluated on the level of an unspecified Bogoliubov transformation as shown in Eq. (2.55) using a similar approach as in Eq. (2.69). This reduces the parameter to two constants. Alternatively, an equivalent reduction can be achieved by invoking the $\mathcal{PT}$-symmetry of the Hamiltonian. The two introduced constants, also referred to as

mean-field parameters, are

$$\begin{aligned} n_{\mathrm{mf}} :=& \langle \hat{b}_{i+d}^\dagger \hat{b}_{i+d} \rangle_0 = \langle \hat{a}_i^\dagger \hat{a}_i \rangle_0 = \frac{1}{N_{\mathfrak{T}}} \sum_{\boldsymbol{k}} \langle \hat{a}_{\boldsymbol{k}}^\dagger \hat{a}_{\boldsymbol{k}} \rangle_0 \\ =& \frac{1}{N_{\mathfrak{T}}} \sum_{\boldsymbol{k}} \langle \left(l^*(\boldsymbol{k}) \hat{\alpha}_{\boldsymbol{k}}^\dagger + m(\boldsymbol{k}) \hat{\beta}_{-\boldsymbol{k}} \right) \left(l(\boldsymbol{k}) \hat{\alpha}_{\boldsymbol{k}} + m^*(\boldsymbol{k}) \hat{\beta}_{-\boldsymbol{k}}^\dagger \right) \rangle_0 \\ =& \frac{1}{N_{\mathfrak{T}}} \sum_{\boldsymbol{k}} |m(\boldsymbol{k})|^2 \ , \end{aligned} \tag{2.78a}$$

$$\begin{aligned} \Delta_{\mathrm{mf}} :=& \langle \hat{a}_i^\dagger \hat{b}_{i+d}^\dagger \rangle_0 = \langle \hat{a}_i \hat{b}_{i+d} \rangle_0 = \frac{1}{N_{\mathfrak{T}}} \sum_{\boldsymbol{k}} \gamma_{\mathrm{B}}(\boldsymbol{k}) \langle \hat{a}_{\boldsymbol{k}} \hat{b}_{-\boldsymbol{k}} \rangle_0 \\ =& \frac{1}{N_{\mathfrak{T}}} \sum_{\boldsymbol{k}} \gamma_{\mathrm{B}}(\boldsymbol{k}) \langle \left(l(\boldsymbol{k}) \hat{\alpha}_{\boldsymbol{k}} + m^*(\boldsymbol{k}) \hat{\beta}_{-\boldsymbol{k}}^\dagger \right) \left(m^*(\boldsymbol{k}) \hat{\alpha}_{\boldsymbol{k}}^\dagger + l(\boldsymbol{k}) \hat{\beta}_{-\boldsymbol{k}} \right) \rangle_0 \\ =& \frac{1}{N_{\mathfrak{T}}} \sum_{\boldsymbol{k}} \gamma_{\mathrm{B}}(\boldsymbol{k}) l(\boldsymbol{k}) m^*(\boldsymbol{k}) \ . \end{aligned} \tag{2.78b}$$

Here, the Bloch gauge for the Fourier transformation is used, which is indicated by $\gamma_{\mathrm{B}}(\boldsymbol{k})$. It is crucial to avoid mixing different gauges when evaluating expectation values since both $l(\boldsymbol{k})$ and $m(\boldsymbol{k})$ also implicitly depend on the specific gauge. However, here the subscripts for l and m are omitted for better readability.

In the next step, the three quartic terms of the Hamiltonian in Eq. (2.32) are treated utilizing the general form of the normal-ordering in Eq. (2.76). For the first term, the result is

$$\hat{a}_i^\dagger \hat{a}_i \hat{b}_{i+d}^\dagger \hat{b}_{i+d} = :\hat{a}_i^\dagger \hat{a}_i \hat{b}_{i+d}^\dagger \hat{b}_{i+d}: \tag{2.79a}$$

$$+ :\hat{a}_i^\dagger \hat{a}_i: \langle \hat{b}_{i+d}^\dagger \hat{b}_{i+d} \rangle_0 + :\hat{a}_i^\dagger \hat{b}_{i+d}^\dagger: \langle \hat{a}_i \hat{b}_{i+d} \rangle_0 + :\hat{a}_i^\dagger \hat{b}_{i+d}: \langle \hat{a}_i \hat{b}_{i+d}^\dagger \rangle_0 \tag{2.79b}$$

$$+ :\hat{a}_i \hat{b}_{i+d}^\dagger: \langle \hat{a}_i^\dagger \hat{b}_{i+d} \rangle_0 + :\hat{a}_i \hat{b}_{i+d}: \langle \hat{a}_i^\dagger \hat{b}_{i+d}^\dagger \rangle_0 + :\hat{b}_{i+d}^\dagger \hat{b}_{i+d}: \langle \hat{a}_i^\dagger \hat{a}_i \rangle_0 \tag{2.79c}$$

$$+ \langle \hat{a}_i^\dagger \hat{a}_i \rangle_0 \langle \hat{b}_{i+d}^\dagger \hat{b}_{i+d} \rangle_0 + \langle \hat{a}_i^\dagger \hat{b}_{i+d}^\dagger \rangle_0 \langle \hat{a}_i \hat{b}_{i+d} \rangle_0 + \langle \hat{a}_i^\dagger \hat{b}_{i+d} \rangle_0 \langle \hat{a}_i \hat{b}_{i+d}^\dagger \rangle_0 \tag{2.79d}$$

$$= :\hat{a}_i^\dagger \hat{a}_i \hat{b}_{i+d}^\dagger \hat{b}_{i+d}: + n_{\mathrm{mf}} (:\hat{a}_i^\dagger \hat{a}_i: + :\hat{b}_{i+d}^\dagger \hat{b}_{i+d}:) \tag{2.79e}$$

$$+ \Delta_{\mathrm{mf}} (:\hat{a}_i \hat{b}_{i+d}: + :\hat{a}_i^\dagger \hat{b}_{i+d}^\dagger:) + n_{\mathrm{mf}}^2 + \Delta_{\mathrm{mf}}^2 \ . \tag{2.79f}$$

In the second step, all known expectation values are replaced by the constants n_{mf} and Δ_{mf}. Additionally, any expectation values that yield zero, e.g.,

$$\langle \hat{a}_i \hat{b}_{i+d}^\dagger \rangle_0 = \langle \hat{a}_i^\dagger \hat{b}_{i+d} \rangle_0 = 0 \tag{2.80}$$

are omitted. These can be identified by rewriting them in terms of the Bogoliubov bosons or also by recognizing that any expectation values violating conservation of the total spin S_{tot}^z must vanish. Since the Hamiltonian commutes with $\hat{S}_{\mathrm{tot}}^z$, it follows that contributions from different S_{tot}^z-subspaces cannot appear in the ground state. Similarly, the other two quartic terms are normal-ordered, resulting in

$$\begin{aligned} \hat{a}_i^\dagger \hat{b}_{i+d}^\dagger \hat{b}_{i+d}^\dagger \hat{b}_{i+d} =& :\hat{a}_i^\dagger \hat{b}_{i+d}^\dagger \hat{b}_{i+d}^\dagger \hat{b}_{i+d}: \\ &+ 2 n_{\mathrm{mf}} :\hat{a}_i^\dagger \hat{b}_{i+d}^\dagger: + 2 \Delta_{\mathrm{mf}} :\hat{b}_{i+d}^\dagger \hat{b}_{i+d}: + 2 n_{\mathrm{mf}} \Delta_{\mathrm{mf}} \ , \end{aligned} \tag{2.81}$$

$$\begin{aligned} \hat{a}_i^\dagger \hat{a}_i \hat{a}_i \hat{b}_{i+d} =& :\hat{a}_i^\dagger \hat{a}_i \hat{a}_i \hat{b}_{i+d}: \\ &+ 2 \Delta_{\mathrm{mf}} :\hat{a}_i^\dagger \hat{a}_i: + 2 n_{\mathrm{mf}} :\hat{a}_i \hat{b}_{i+d}: + 2 n_{\mathrm{mf}} \Delta_{\mathrm{mf}} \ . \end{aligned} \tag{2.82}$$

In addition to the expectation values in Eq. (2.80), terms such as

$$\langle \hat{a}_i^\dagger \hat{a}_i^\dagger \rangle_0 = \langle \hat{b}_{i+d}^\dagger \hat{b}_{i+d}^\dagger \rangle_0 = 0 \tag{2.83}$$

appear and are omitted as they yield zero for the same reason discussed above. The normal-ordered NL-SWT Hamiltonian for the antiferromagnetic spin-$\frac{1}{2}$ easy-axis XXZ model on a square lattice reads

$$\begin{aligned}\mathcal{H}_{\mathrm{mf}} =& -JN_{\mathfrak{T}}Z\left(S^2+n_{\mathrm{mf}}^2+\Delta_{\mathrm{mf}}^2-2Sn_{\mathrm{mf}}-2\lambda S\Delta_{\mathrm{mf}}+2\lambda n_{\mathrm{mf}}\Delta_{\mathrm{mf}}\right)\\ &+J\sum_{\boldsymbol{r}_i\in\mathfrak{T}}\sum_{\boldsymbol{d}\in\mathfrak{D}}\Big[(S-n_{\mathrm{mf}}-\lambda\Delta_{\mathrm{mf}})\left(:\hat{a}_i^\dagger\hat{a}_i:+:\hat{b}_{i+\boldsymbol{d}}^\dagger\hat{b}_{i+\boldsymbol{d}}:\right)\\ &+(\lambda S-\lambda n_{\mathrm{mf}}-\Delta_{\mathrm{mf}})\left(:\hat{a}_i\hat{b}_{\boldsymbol{d}+i}:+:\hat{a}_i^\dagger\hat{b}_{\boldsymbol{d}+i}^\dagger:\right)\\ &-:\hat{a}_i^\dagger\hat{a}_i\hat{b}_{i+\boldsymbol{d}}^\dagger\hat{b}_{i+\boldsymbol{d}}:-\frac{\lambda}{2}:\hat{a}_i^\dagger\hat{a}_i\hat{a}_i\hat{b}_{i+\boldsymbol{d}}:-\frac{\lambda}{2}:\hat{a}_i^\dagger\hat{b}_{i+\boldsymbol{d}}^\dagger\hat{b}_{i+\boldsymbol{d}}^\dagger\hat{b}_{i+\boldsymbol{d}}:\Big]\ .\end{aligned}\tag{2.84}$$

Compared to the initial non-normal-ordered Hamilton in Eq. (2.32), the ground-state energy $E_0=-JN_{\mathfrak{T}}ZS^2$ is now modified by the mean-field parameters and reads

$$E_{0,\mathrm{mf}}=E_0-JN_{\mathfrak{T}}Z\left(n_{\mathrm{mf}}^2+\Delta_{\mathrm{mf}}^2-2Sn_{\mathrm{mf}}-2\lambda S\Delta_{\mathrm{mf}}+2\lambda n_{\mathrm{mf}}\Delta_{\mathrm{mf}}\right)\ .\tag{2.85}$$

Furthermore, the prefactors of the quadirlinear terms are also modified, resulting in $(S-n_{\mathrm{mf}}-\lambda\Delta_{\mathrm{mf}})$ and $(S-\lambda n_{\mathrm{mf}}-\Delta_{\mathrm{mf}})$. Finally, all operators are now marked as normal-ordered, denoted by $:\ldots:$.

In the next step, the Fourier transformation is applied to the normal-ordered Hamiltonian in Eq. (2.84). The procedure follows the same steps as those outlined in Section 2.5.2. Again, the Bloch gauge is used. The resulting Hamiltonian reads

$$\begin{aligned}\mathcal{H}_{\mathrm{mf}} =& E_{0,\mathrm{mf}}+JZ\sum_{\boldsymbol{k}}\Big[(S-n_{\mathrm{mf}}-\lambda\Delta_{\mathrm{mf}})\left(:\hat{a}_{\boldsymbol{k}}^\dagger\hat{a}_{\boldsymbol{k}}:+:\hat{b}_{\boldsymbol{k}}^\dagger\hat{b}_{\boldsymbol{k}}:\right)\\ &+(\lambda S-\lambda n_{\mathrm{mf}}-\Delta_{\mathrm{mf}})\left(\gamma_{\mathrm{B}}(\boldsymbol{k})\,:\hat{a}_{\boldsymbol{k}}\hat{b}_{-\boldsymbol{k}}:+\gamma_{\mathrm{B}}^*(\boldsymbol{k})\,:\hat{a}_{\boldsymbol{k}}^\dagger\hat{b}_{-\boldsymbol{k}}^\dagger:\right)\Big]\end{aligned}\tag{2.86a}$$

$$\begin{aligned}&-\frac{JZ}{N_{\mathfrak{T}}}\sum_{\substack{\boldsymbol{k}_1,\boldsymbol{k}_2,\\ \boldsymbol{k}_3,\boldsymbol{k}_4}}\Big[\gamma_{\mathrm{B}}(\boldsymbol{k}_3-\boldsymbol{k}_4)\delta_{\boldsymbol{G}}\left(\boldsymbol{k}_1-\boldsymbol{k}_2+\boldsymbol{k}_3-\boldsymbol{k}_4\right):\hat{a}_{\boldsymbol{k}_1}^\dagger\hat{a}_{\boldsymbol{k}_2}\hat{b}_{\boldsymbol{k}_3}^\dagger\hat{b}_{\boldsymbol{k}_4}:\\ &+\frac{\lambda}{2}\gamma_{\mathrm{B}}(\boldsymbol{k}_2+\boldsymbol{k}_3-\boldsymbol{k}_4)\delta_{\boldsymbol{G}}\left(\boldsymbol{k}_1+\boldsymbol{k}_2+\boldsymbol{k}_3-\boldsymbol{k}_4\right):\hat{a}_{\boldsymbol{k}_1}^\dagger\hat{b}_{\boldsymbol{k}_2}^\dagger\hat{b}_{\boldsymbol{k}_3}^\dagger\hat{b}_{\boldsymbol{k}_4}:\\ &+\frac{\lambda}{2}\gamma_{\mathrm{B}}(-\boldsymbol{k}_4)\delta_{\boldsymbol{G}}\left(\boldsymbol{k}_1-\boldsymbol{k}_2-\boldsymbol{k}_3-\boldsymbol{k}_4\right):\hat{a}_{\boldsymbol{k}_1}^\dagger\hat{a}_{\boldsymbol{k}_2}\hat{a}_{\boldsymbol{k}_3}\hat{b}_{\boldsymbol{k}_4}:\Big]\ .\end{aligned}\tag{2.86b}$$

The quadratic part of the normal-ordered Hamiltonian, see Eq. (2.86a), is nearly in the form suitable for diagonalization via a Bogoliubov transformation. To transform it into the form similar to Eq. (2.53), the term $:\hat{b}_{\boldsymbol{k}}^\dagger\hat{b}_{\boldsymbol{k}}:$ is rewritten to $:\hat{b}_{-\boldsymbol{k}}\hat{b}_{-\boldsymbol{k}}^\dagger:$, using the substitution $\boldsymbol{k}\to-\boldsymbol{k}$. In this context, the double dots $:\ldots:$ around the operators ensure that no additional terms arise from the commutation, as these have already been accounted for within the generalized normal-ordering. Consequently, the functions determining the solution of the Bogoliubov transformation can be extracted from Eq. (2.86)

$$f_{\boldsymbol{k}}=g_{\boldsymbol{k}}=JZ\left(S-n_{\mathrm{mf}}-\lambda\Delta_{\mathrm{mf}}\right)\ ,\tag{2.87a}$$

$$h_{\boldsymbol{k}}=JZ\left(S-\lambda n_{\mathrm{mf}}-\Delta_{\mathrm{mf}}\right)\gamma_{\mathrm{B}}(\boldsymbol{k})\ .\tag{2.87b}$$

The resulting MF-SWT single-particle dispersion for both $\hat{\alpha}_{\boldsymbol{k}}$ and $\hat{\beta}_{\boldsymbol{k}}$ is given by

$$\begin{aligned}\omega_{\boldsymbol{k}}=\omega_{\alpha,\beta}(\boldsymbol{k})&=JZ\sqrt{\left(S-n_{\mathrm{mf}}-\lambda\Delta_{\mathrm{mf}}\right)^2-\left(S-\lambda n_{\mathrm{mf}}-\Delta_{\mathrm{mf}}\right)^2\left|\gamma_{\mathrm{B}}(\boldsymbol{k})\right|^2}\\ &=JZ\left(S-n_{\mathrm{mf}}-\lambda\Delta_{\mathrm{mf}}\right)\sqrt{1-\left|\frac{S-\lambda n_{\mathrm{mf}}-\Delta_{\mathrm{mf}}}{S-n_{\mathrm{mf}}-\lambda\Delta_{\mathrm{mf}}}\gamma_{\mathrm{B}}(\boldsymbol{k})\right|^2}\ .\end{aligned}\tag{2.88}$$

It is once again degenerate as $f_{\boldsymbol{k}}$ and $g_{\boldsymbol{k}}$ are still equal, due to the $\mathcal{PT}$-symmetry of the Hamiltonian. Considering only the diagonalized quadratic part of the Hamiltonian seems like the same approximation as for the L-SWT, i.e., neglecting the quartic terms. However, the mean-field parameters n_{mf} and Δ_{mf} are now incorporated into the dispersion relation, leading to its renormalization. Therefore, unlike in L-SWT, the MF-SWT dispersion effectively incorporates single-particle contributions of the quartic terms.

At this point, the MF-SWT dispersion $\omega_{\boldsymbol{k}}$ still depends on the unknown mean-field parameters n_{mf} and Δ_{mf}. However, the mean-field parameters n_{mf} and Δ_{mf} themselves depend on the functions $l(\boldsymbol{k})$ and $m(\boldsymbol{k})$ of the Bogoliubov transformation, see Eq. (2.78), but also influence them, see Eqs. (2.63) and (2.87). Consequently, the calculation of the mean-field parameters resembles a "cat chasing its own tail", which is also referred to as a self-consistent problem. Therefore, the equations for the mean-field parameters, including their hidden dependencies, can be expressed as

$$n_{\mathrm{mf}}(n_{\mathrm{mf}}, \Delta_{\mathrm{mf}}) = \frac{1}{N_{\mathfrak{T}}} \sum_{\boldsymbol{k}} |m(\boldsymbol{k}, n_{\mathrm{mf}}, \Delta_{\mathrm{mf}})|^2 \ , \tag{2.89a}$$

$$\Delta_{\mathrm{mf}}(n_{\mathrm{mf}}, \Delta_{\mathrm{mf}}) = \frac{1}{N_{\mathfrak{T}}} \sum_{\boldsymbol{k}} \gamma_{\mathrm{B}}(\boldsymbol{k}) l(\boldsymbol{k}, n_{\mathrm{mf}}, \Delta_{\mathrm{mf}}) m^*(\boldsymbol{k}, n_{\mathrm{mf}}, \Delta_{\mathrm{mf}}) \ . \tag{2.89b}$$

Here, the goal is to find a fixed point in the two-dimensional space of the mean-field parameters $(n_{\mathrm{mf}}, \Delta_{\mathrm{mf}})$ that does not change the parameters when inserted on the right-hand side of Eq. (2.89). If this condition is met, the self-consistent problem is solved and the quadratic part of the Hamiltonian is truly diagonalized. The dispersion of this Hamiltonian is then referred to as the scMF-SWT dispersion. To solve this self-consistent problem in practice, the mean-field parameters are iteratively calculated by first solving the Bogoliubov transformation with initial mean-field parameters, then determining the new mean-field parameters and repeating this loop until a fixed point in the mean-field parameters is reached. Alternatively, the self-consistent problem can also be formulated as a two-dimensional root-finding problem. Within this work, the former approach is applied. In this calculation, the sums in Eq. (2.78) are evaluated in the thermodynamic limit and the initial values are $n_{\mathrm{mf}} = \Delta_{\mathrm{mf}} = 0$. Table 2.1 presents the calculated mean-field parameters n_{mf} and Δ_{mf} for various values of the anisotropy parameter λ. With these mean-field

Table 2.1: Self-consistent mean-field parameters n_{mf} and Δ_{mf} for varying values of the anisotropy parameter λ in the antiferromagnetic spin-$\frac{1}{2}$ easy-axis XXZ model on a square lattice. The integrations are performed numerically with a Gauss-Kronrod quadrature with 600 points in each dimension.

λ	0.0	0.3	0.6	0.9	1.0
n_{mf}	0.0	0.010 321	0.045 917	0.131 103	0.196 602
Δ_{mf}	0.0	−0.051 390	−0.112 802	−0.209 489	−0.275 576

parameters determined, it is possible to calculate the scMF-SWT dispersion relation for different λ. The results are displayed in Fig. 2.9 alongside the results of the L-SWT for comparison. The scMF-SWT dispersion is renormalized by the mean-field parameters relative to the L-SWT. This renormalization manifests itself as a shift of the dispersion minimum towards lower values and a shift of the dispersion maximum towards higher values. Nevertheless, the overall shape of the dispersion remains unchanged. This behavior is plausible because the additional mean-field parameters act as a constant correction without any momentum dependencies. As a result, the overall shape continues to depend solely on $|\gamma_{\mathrm{B}}(\boldsymbol{k})|^2$. Accordingly, the plateau in the dispersion between $\boldsymbol{k} = (\pi, 0)^T$ to $\boldsymbol{k} = (\frac{\pi}{2}, \frac{\pi}{2})^T$ is still present. Compared to L-SWT, the value of the plateau

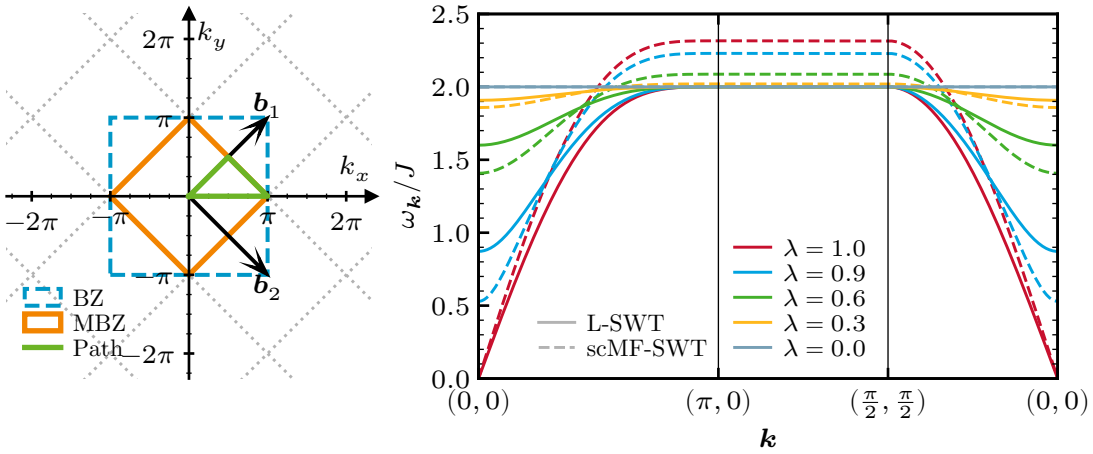

Figure 2.9: On the left-hand side, the reciprocal lattice is shown for the antiferromagnetic spin-$\frac{1}{2}$ easy-axis XXZ model on a square lattice. The dashed blue rectangle marks the first BZ, the orange rhombus marks the first MBZ, and the reciprocal lattice vectors $\boldsymbol{b}_{1,2}$ connected to the MBZ are colored in grey. The green line represents the path through the MBZ for which momentum $\boldsymbol{k}$ and the associated dispersion $\omega_{\boldsymbol{k}}$ for different anisotropy parameter λ is shown on the right-hand side. Both the dispersion of linear spin-wave theory (L-SWT) and self-consistent mean-field spin-wave theory (scMF-SWT) are displayed. The lattice constant a is set to unity.

in the scMF-SWT solution now depends on the anisotropy parameter λ and increases for increasing λ. It should be noted that to obtain the scMF-SWT solution for $\lambda = 1$, the self-consistent iteration already converged after a single step since the terms $S - \lambda n_{\mathrm{mf}} - \Delta_{\mathrm{mf}}$ and $S - n_{\mathrm{mf}} - \lambda\Delta_{\mathrm{mf}}$ cancel each other in the Bogoliubov transformation.

So far, only the quadratic part of the scNL-SWT Hamiltonian in the form of the scMF-SWT has been considered. Thus, an additional step is to examine the operators again from the beginning of Eq. (2.70), which are now normal-ordered in the Hamiltonian of Eq. (2.86b). Once again, applying the Bogoliubov transformation results in

$$
\begin{aligned}
:\hat{a}^\dagger_{\boldsymbol{k}_1}\hat{a}_{\boldsymbol{k}_2}\hat{b}^\dagger_{\boldsymbol{k}_3}\hat{b}_{\boldsymbol{k}_4}: &= :\left(l^*(\boldsymbol{k}_1)\hat{\alpha}^\dagger_{\boldsymbol{k}_1} + m(\boldsymbol{k}_1)\hat{\beta}_{-\boldsymbol{k}_1}\right)\left(l(\boldsymbol{k}_2)\hat{\alpha}_{\boldsymbol{k}_2} + m^*(\boldsymbol{k}_2)\hat{\beta}^\dagger_{-\boldsymbol{k}_2}\right) && \text{(2.90a)}\\
&\quad \left(m(-\boldsymbol{k}_3)\hat{\alpha}_{-\boldsymbol{k}_3} + l^*(-\boldsymbol{k}_3)\hat{\beta}^\dagger_{\boldsymbol{k}_3}\right)\left(m^*(-\boldsymbol{k}_4)\hat{\alpha}^\dagger_{-\boldsymbol{k}_4} + l(-\boldsymbol{k}_4)\hat{\beta}_{\boldsymbol{k}_4}\right):\\
&= \; l^*(\boldsymbol{k}_1)l(\boldsymbol{k}_2)m(-\boldsymbol{k}_3)m^*(-\boldsymbol{k}_4)\; :\hat{\alpha}^\dagger_{\boldsymbol{k}_1}\hat{\alpha}_{\boldsymbol{k}_2}\hat{\alpha}_{-\boldsymbol{k}_3}\hat{\alpha}^\dagger_{-\boldsymbol{k}_4}: && \text{(2.90b)}\\
&\quad + \cdots + \quad m(\boldsymbol{k}_1)m^*(\boldsymbol{k}_2)l^*(-\boldsymbol{k}_3)l(-\boldsymbol{k}_4)\; :\hat{\beta}_{-\boldsymbol{k}_1}\hat{\beta}^\dagger_{-\boldsymbol{k}_2}\hat{\beta}^\dagger_{\boldsymbol{k}_3}\hat{\beta}_{\boldsymbol{k}_4}:\\
&= \; l^*(\boldsymbol{k}_1)l(\boldsymbol{k}_2)m(-\boldsymbol{k}_3)m^*(-\boldsymbol{k}_4)\hat{\alpha}^\dagger_{\boldsymbol{k}_1}\hat{\alpha}^\dagger_{-\boldsymbol{k}_4}\hat{\alpha}_{\boldsymbol{k}_2}\hat{\alpha}_{-\boldsymbol{k}_3} && \text{(2.90c)}\\
&\quad + \cdots + \quad m(\boldsymbol{k}_1)m^*(\boldsymbol{k}_2)l^*(-\boldsymbol{k}_3)l(-\boldsymbol{k}_4)\hat{\beta}^\dagger_{-\boldsymbol{k}_2}\hat{\beta}^\dagger_{\boldsymbol{k}_3}\hat{\beta}_{-\boldsymbol{k}_1}\hat{\beta}_{\boldsymbol{k}_4}\;.
\end{aligned}
$$

The crucial difference compared to the non-generalized normal-ordering is that, to normal-order the terms, the commutator is not necessary. Instead, $:\ldots:$ around operators is removed, and creation operators are simply placed left to annihilation operators. As a result, after assessing the general normal-ordering, only 16 quartic terms remain. In contrast, the normal-ordering by commutation may additionally yield quadratic or constant contributions, but here they are already considered in n_{mf} and Δ_{mf}.

Furthermore, with the self-consistent approaches, the Bogoliubov transformation is determined such that all quadratic off-diagonal terms vanish in the complete scNL-SWT Hamiltonian. This

cancellation of quadratic off-diagonal contributions does not necessarily occur when normal-ordering is carried out using commutator relations. Nevertheless, within the framework of generalized normal-ordering, it is possible to reproduce the case corresponding to normal-ordering based on commutators, which is referred to as NL-SWT. In this scenario, the mean-field parameters, n_{mf} and Δ_{mf}, are evaluated only once and not determined iteratively. Accordingly, the solution of the Bogoliubov transformation remains fixed and is not modified to incorporate additional contributions stemming from these mean-field parameters. Therefore, the resulting Bogoliubov transformation coincides with that employed in L-SWT. However, the evaluated mean-field parameters lead to renormalizations of the ground-state energy and the single-particle dispersion. In addition, they give rise to finite quadratic off-diagonal terms for $\lambda \neq 1$, in contrast to the L-SWT and scNL-SWT. Consequently, the NL-SWT Hamiltonian is not diagonal on a quadratic level compared to the scNL-SWT Hamiltonian.

To analyze the complete set of quartic terms in the NL-SWT(scNL-SWT) Hamiltonian after the Bogoliubov transformation, a useful approach is to determine all possible terms that satisfy the constraint of S^z_{tot} conservation. The first step involves examining the terms present in the quadratic Hamiltonian. All normal-ordered quadratic terms can be expressed as combinations of single spin-lowering $(\hat{\alpha}^\dagger, \hat{\beta})$ and spin-raising $(\hat{\alpha}, \hat{\beta}^\dagger)$ operators. These can be represented as a normal-ordered outer product of these two vectors, forming a matrix

$$\{\hat{\underline{\boldsymbol{O}}}_2\} \widehat{=} :\begin{pmatrix} \hat{\alpha}^\dagger \\ \hat{\beta} \end{pmatrix} \otimes \begin{pmatrix} \hat{\alpha} & \hat{\beta}^\dagger \end{pmatrix}: = \begin{pmatrix} :\hat{\alpha}^\dagger\hat{\alpha}: & :\hat{\alpha}^\dagger\hat{\beta}^\dagger: \\ :\hat{\alpha}\hat{\beta}: & :\hat{\beta}^\dagger\hat{\beta}: \end{pmatrix} \tag{2.91}$$

containing all possible normal-ordered quadratic terms. This concept can be extended to obtain all quartic operator terms. The process begins by identifying the vector that lowers the spin "$n = 2$" times and the vector that raises the spin "$n = 2$" times. As before, the normal-ordered outer product of these two vectors results in a matrix

$$\begin{aligned} \{\hat{\underline{\boldsymbol{O}}}_4\} &\widehat{=} :\begin{pmatrix} \hat{\alpha}^\dagger\hat{\alpha}^\dagger \\ \hat{\alpha}^\dagger\hat{\beta} \\ \hat{\beta}\hat{\beta} \end{pmatrix} \otimes \begin{pmatrix} \hat{\alpha}\hat{\alpha} & \hat{\alpha}\hat{\beta}^\dagger & \hat{\beta}^\dagger\hat{\beta}^\dagger \end{pmatrix}: \\ &\widehat{=} \begin{pmatrix} :\hat{\alpha}^\dagger\hat{\alpha}^\dagger\hat{\alpha}\hat{\alpha}: & :\hat{\alpha}^\dagger\hat{\alpha}^\dagger\hat{\alpha}\hat{\beta}^\dagger: & :\hat{\alpha}^\dagger\hat{\alpha}^\dagger\hat{\beta}^\dagger\hat{\beta}^\dagger: \\ :\hat{\alpha}^\dagger\hat{\alpha}\hat{\alpha}\hat{\beta}: & :\hat{\alpha}^\dagger\hat{\alpha}\hat{\beta}^\dagger\hat{\beta}: & :\hat{\alpha}^\dagger\hat{\beta}^\dagger\hat{\beta}^\dagger\hat{\beta}: \\ :\hat{\alpha}\hat{\alpha}\hat{\beta}\hat{\beta}: & :\hat{\alpha}\hat{\beta}^\dagger\hat{\beta}\hat{\beta}: & :\hat{\beta}^\dagger\hat{\beta}^\dagger\hat{\beta}\hat{\beta}: \end{pmatrix} \end{aligned} \tag{2.92}$$

in which all nine possible normal-ordered quartic terms are contained. Thus, the Hamiltonian of the NL-SWT(scNL-SWT), after applying the Bogoliubov transformation, may be written as

$$\hat{\mathcal{H}} = C^0 \tag{2.93a}$$

$$+ \sum_{\boldsymbol{k}_1,\boldsymbol{k}_2} \Big[C^{\hat{\alpha}^\dagger\hat{\alpha}}_{\boldsymbol{k}_1,\boldsymbol{k}_2} \hat{\alpha}^\dagger_{\boldsymbol{k}_1}\hat{\alpha}_{\boldsymbol{k}_2} + C^{\hat{\beta}^\dagger\hat{\beta}}_{\boldsymbol{k}_1,\boldsymbol{k}_2} \hat{\beta}^\dagger_{\boldsymbol{k}_1}\hat{\beta}_{\boldsymbol{k}_2} + C^{\hat{\alpha}^\dagger\hat{\beta}^\dagger}_{\boldsymbol{k}_1,\boldsymbol{k}_2} \hat{\alpha}^\dagger_{\boldsymbol{k}_1}\hat{\beta}^\dagger_{\boldsymbol{k}_2} + C^{\hat{\alpha}\hat{\beta}}_{\boldsymbol{k}_1,\boldsymbol{k}_2} \hat{\alpha}_{\boldsymbol{k}_1}\hat{\beta}_{\boldsymbol{k}_2} \Big] \tag{2.93b}$$

$$\begin{aligned} + \sum_{\boldsymbol{k}_1,\boldsymbol{k}_2,\boldsymbol{k}_3,\boldsymbol{k}_4} \Big[& C^{\hat{\alpha}^\dagger\hat{\alpha}^\dagger\hat{\beta}^\dagger\hat{\beta}^\dagger}_{\boldsymbol{k}_1,\boldsymbol{k}_2,\boldsymbol{k}_3,\boldsymbol{k}_4} \hat{\alpha}^\dagger_{\boldsymbol{k}_1}\hat{\alpha}^\dagger_{\boldsymbol{k}_2}\hat{\beta}^\dagger_{\boldsymbol{k}_3}\hat{\beta}^\dagger_{\boldsymbol{k}_4} + C^{\hat{\alpha}\hat{\alpha}\hat{\beta}\hat{\beta}}_{\boldsymbol{k}_1,\boldsymbol{k}_2,\boldsymbol{k}_3,\boldsymbol{k}_4} \hat{\alpha}_{\boldsymbol{k}_1}\hat{\alpha}_{\boldsymbol{k}_2}\hat{\beta}_{\boldsymbol{k}_3}\hat{\beta}_{\boldsymbol{k}_4} \\ & + C^{\hat{\alpha}^\dagger\hat{\alpha}^\dagger\hat{\alpha}\hat{\beta}^\dagger}_{\boldsymbol{k}_1,\boldsymbol{k}_2,\boldsymbol{k}_3,\boldsymbol{k}_4} \hat{\alpha}^\dagger_{\boldsymbol{k}_1}\hat{\alpha}^\dagger_{\boldsymbol{k}_2}\hat{\alpha}_{\boldsymbol{k}_3}\hat{\beta}^\dagger_{\boldsymbol{k}_4} + C^{\hat{\alpha}\hat{\beta}^\dagger\hat{\beta}\hat{\beta}}_{\boldsymbol{k}_1,\boldsymbol{k}_2,\boldsymbol{k}_3,\boldsymbol{k}_4} \hat{\alpha}_{\boldsymbol{k}_1}\hat{\beta}^\dagger_{\boldsymbol{k}_2}\hat{\beta}_{\boldsymbol{k}_3}\hat{\beta}_{\boldsymbol{k}_4} \\ & + C^{\hat{\alpha}^\dagger\hat{\beta}^\dagger\hat{\beta}^\dagger\hat{\beta}}_{\boldsymbol{k}_1,\boldsymbol{k}_2,\boldsymbol{k}_3,\boldsymbol{k}_4} \hat{\alpha}^\dagger_{\boldsymbol{k}_1}\hat{\beta}^\dagger_{\boldsymbol{k}_2}\hat{\beta}^\dagger_{\boldsymbol{k}_3}\hat{\beta}_{\boldsymbol{k}_4} + C^{\hat{\alpha}^\dagger\hat{\alpha}\hat{\alpha}\hat{\beta}}_{\boldsymbol{k}_1,\boldsymbol{k}_2,\boldsymbol{k}_3,\boldsymbol{k}_4} \hat{\alpha}^\dagger_{\boldsymbol{k}_1}\hat{\alpha}_{\boldsymbol{k}_2}\hat{\alpha}_{\boldsymbol{k}_3}\hat{\beta}_{\boldsymbol{k}_4} \\ & + C^{\hat{\alpha}^\dagger\hat{\alpha}^\dagger\hat{\alpha}\hat{\alpha}}_{\boldsymbol{k}_1,\boldsymbol{k}_2,\boldsymbol{k}_3,\boldsymbol{k}_4} \hat{\alpha}^\dagger_{\boldsymbol{k}_1}\hat{\alpha}^\dagger_{\boldsymbol{k}_2}\hat{\alpha}_{\boldsymbol{k}_3}\hat{\alpha}_{\boldsymbol{k}_4} + C^{\hat{\beta}^\dagger\hat{\beta}^\dagger\hat{\beta}\hat{\beta}}_{\boldsymbol{k}_1,\boldsymbol{k}_2,\boldsymbol{k}_3,\boldsymbol{k}_4} \hat{\beta}^\dagger_{\boldsymbol{k}_1}\hat{\beta}^\dagger_{\boldsymbol{k}_2}\hat{\beta}_{\boldsymbol{k}_3}\hat{\beta}_{\boldsymbol{k}_4} \\ & + C^{\hat{\alpha}^\dagger\hat{\alpha}\hat{\beta}^\dagger\hat{\beta}}_{\boldsymbol{k}_1,\boldsymbol{k}_2,\boldsymbol{k}_3,\boldsymbol{k}_4} \hat{\alpha}^\dagger_{\boldsymbol{k}_1}\hat{\alpha}_{\boldsymbol{k}_2}\hat{\beta}^\dagger_{\boldsymbol{k}_3}\hat{\beta}_{\boldsymbol{k}_4} \Big] \end{aligned} \tag{2.93c}$$

with the coefficient functions C_i. The coefficient functions allow the Hamiltonian to be expressed in a clearer and more compact form. To this end, it is necessary to rewrite the resulting terms from the Bogoliubov transformation into a generic form.

First, as already shown in (2.93), all $\hat{\alpha}^{(\dagger)}$ bosons are positioned to the left of the $\hat{\beta}^{(\dagger)}$ bosons, and within each bosonic flavor, the operators are normal-ordered.

Second, their momentum indices are incremented sequentially according to this arrangement. In the case of the given example of $:\hat{a}^\dagger_{\boldsymbol{k}_1}\hat{a}_{\boldsymbol{k}_2}\hat{b}^\dagger_{\boldsymbol{k}_3}\hat{b}_{\boldsymbol{k}_4}:$, the momentum indices in the terms of Eq. (2.90c)

$$\begin{aligned} & l^*(\boldsymbol{k}_1)l(\boldsymbol{k}_2)m(-\boldsymbol{k}_3)m^*(-\boldsymbol{k}_4)\hat{\alpha}^\dagger_{\boldsymbol{k}_1}\hat{\alpha}^\dagger_{-\boldsymbol{k}_4}\hat{\alpha}_{\boldsymbol{k}_2}\hat{\alpha}_{-\boldsymbol{k}_3} \\ +\cdots+ \quad & m(\boldsymbol{k}_1)m^*(\boldsymbol{k}_2)l^*(-\boldsymbol{k}_3)l(-\boldsymbol{k}_4)\hat{\beta}^\dagger_{-\boldsymbol{k}_2}\hat{\beta}^\dagger_{\boldsymbol{k}_3}\hat{\beta}_{-\boldsymbol{k}_1}\hat{\beta}_{\boldsymbol{k}_4} \end{aligned} \tag{2.94}$$

are substituted to

$$\begin{aligned} = \quad & l^*(\boldsymbol{k}_1)l(\boldsymbol{k}_3)m(\boldsymbol{k}_4)m^*(\boldsymbol{k}_2)\hat{\alpha}^\dagger_{\boldsymbol{k}_1}\hat{\alpha}^\dagger_{\boldsymbol{k}_2}\hat{\alpha}_{\boldsymbol{k}_3}\hat{\alpha}_{\boldsymbol{k}_4} \\ +\cdots+ \quad & m(-\boldsymbol{k}_3)m^*(-\boldsymbol{k}_1)l^*(-\boldsymbol{k}_2)l(-\boldsymbol{k}_4)\hat{\beta}^\dagger_{\boldsymbol{k}_1}\hat{\beta}^\dagger_{\boldsymbol{k}_2}\hat{\beta}_{\boldsymbol{k}_3}\hat{\beta}_{\boldsymbol{k}_4} \end{aligned} \tag{2.95}$$

to comply with the defined order of Eq. (2.93).

Third, the coefficient function itself must exhibit the same symmetries regarding the permutations of momentum indices. For example, the operator $\hat{\alpha}^\dagger_{\boldsymbol{k}_1}\hat{\alpha}^\dagger_{\boldsymbol{k}_2}\hat{\alpha}_{\boldsymbol{k}_3}\hat{\alpha}_{\boldsymbol{k}_4}$ has four different permutations of its momentum indices, which are

$$\hat{\alpha}^\dagger_{\boldsymbol{k}_1}\hat{\alpha}^\dagger_{\boldsymbol{k}_2}\hat{\alpha}_{\boldsymbol{k}_3}\hat{\alpha}_{\boldsymbol{k}_4}, \quad \hat{\alpha}^\dagger_{\boldsymbol{k}_1}\hat{\alpha}^\dagger_{\boldsymbol{k}_2}\hat{\alpha}_{\boldsymbol{k}_4}\hat{\alpha}_{\boldsymbol{k}_3}, \quad \hat{\alpha}^\dagger_{\boldsymbol{k}_2}\hat{\alpha}^\dagger_{\boldsymbol{k}_1}\hat{\alpha}_{\boldsymbol{k}_3}\hat{\alpha}_{\boldsymbol{k}_4}, \quad \hat{\alpha}^\dagger_{\boldsymbol{k}_2}\hat{\alpha}^\dagger_{\boldsymbol{k}_1}\hat{\alpha}_{\boldsymbol{k}_4}\hat{\alpha}_{\boldsymbol{k}_3}\ . \tag{2.96}$$

To ensure that all the coefficient functions C_i fulfill the symmetries of the assigned operators, a superposition with all permutations of the resulting coefficient after the Bogoliubov transformation, here marked as $\tilde{C}_i$, is used as a coefficient. For example, this results in

$$\begin{aligned} C^{\hat{\alpha}^\dagger\hat{\alpha}^\dagger\hat{\alpha}\hat{\alpha}}_{\boldsymbol{k}_1,\boldsymbol{k}_2,\boldsymbol{k}_3,\boldsymbol{k}_4} = \frac{1}{4}\Big(& \tilde{C}^{\hat{\alpha}^\dagger\hat{\alpha}^\dagger\hat{\alpha}\hat{\alpha}}_{\boldsymbol{k}_1,\boldsymbol{k}_2,\boldsymbol{k}_3,\boldsymbol{k}_4} + \tilde{C}^{\hat{\alpha}^\dagger\hat{\alpha}^\dagger\hat{\alpha}\hat{\alpha}}_{\boldsymbol{k}_1,\boldsymbol{k}_2,\boldsymbol{k}_4,\boldsymbol{k}_3} \\ & + \tilde{C}^{\hat{\alpha}^\dagger\hat{\alpha}^\dagger\hat{\alpha}\hat{\alpha}}_{\boldsymbol{k}_2,\boldsymbol{k}_1,\boldsymbol{k}_3,\boldsymbol{k}_4} + \tilde{C}^{\hat{\alpha}^\dagger\hat{\alpha}^\dagger\hat{\alpha}\hat{\alpha}}_{\boldsymbol{k}_2,\boldsymbol{k}_1,\boldsymbol{k}_4,\boldsymbol{k}_3}\Big)\ . \end{aligned} \tag{2.97}$$

With the above conventions, the Hamiltonian of Eq. (2.93) is now in a uniquely defined form. The coefficient functions with all the dependencies on the mean-field parameters and Bogoliubov functions, $m(\boldsymbol{k})$ and $l(\boldsymbol{k})$, can be found in the Appendix A.1.

Up to this point, many different transformations have been applied to the initial Hamiltonian of the easy-axis spin-$\frac{1}{2}$ XXZ model in Eq. (2.26) from the beginning of Section 2.5. With all transformations executed one after the other, the Hamiltonian of Eq. (2.93) emerges. To gain a better overview of the consecutive transformations, Fig. 2.10 provides a comprehensive visualization of all transformations, including their main features. It is important to emphasize that no approximations have been made up to this point, as each transformation is performed on an analytical level without any truncation. Only the evaluation of the mean-field parameters is done numerically. However, it is done in the thermodynamic limit without introducing any finite-size effect. Therefore, the numerical error is negligible either in the scNL-SWT or in the NL-SWT. Furthermore, besides the initial spin Hamiltonian, the same transformations can be applied to all sorts of spin operators, which are needed to calculate physical observables. Therefore, Fig. 2.10 also implies the transformation of observables. In Appendix A.2, a comprehensive overview is given, of how the transformations are applied to an observable instead of the Hamiltonian.

In addition, the figure shows another transformation that has not yet been addressed, which is applied to the final Hamiltonian or observable. This last transformation is the CST. Why is this transformation necessary? Even if the scNL-SWT Hamiltonian of Eq. (2.93) is diagonal on the quadratic level, due to the self-consistent solution of the Bogoliubov transformation, there are still quartic terms coupling single particle states to higher particle spaces. Terms such as $\hat{\alpha}^\dagger_{\boldsymbol{k}_1}\hat{\alpha}^\dagger_{\boldsymbol{k}_2}\hat{\alpha}_{\boldsymbol{k}_3}\hat{\beta}^\dagger_{\boldsymbol{k}_4}$ describe a scattering process, where a single magnon decays into three magnons, or $\hat{\alpha}^\dagger_{\boldsymbol{k}_1}\hat{\alpha}^\dagger_{\boldsymbol{k}_2}\hat{\beta}^\dagger_{\boldsymbol{k}_3}\hat{\beta}^\dagger_{\boldsymbol{k}_4}$, where four magnons are created out of the vacuum. All those terms are neglected in the single-particle dispersion of the scMF-SWT. The CST is a powerful tool to incorporate these terms in a sophisticated manner. The next chapter gives a broad overview of this method.

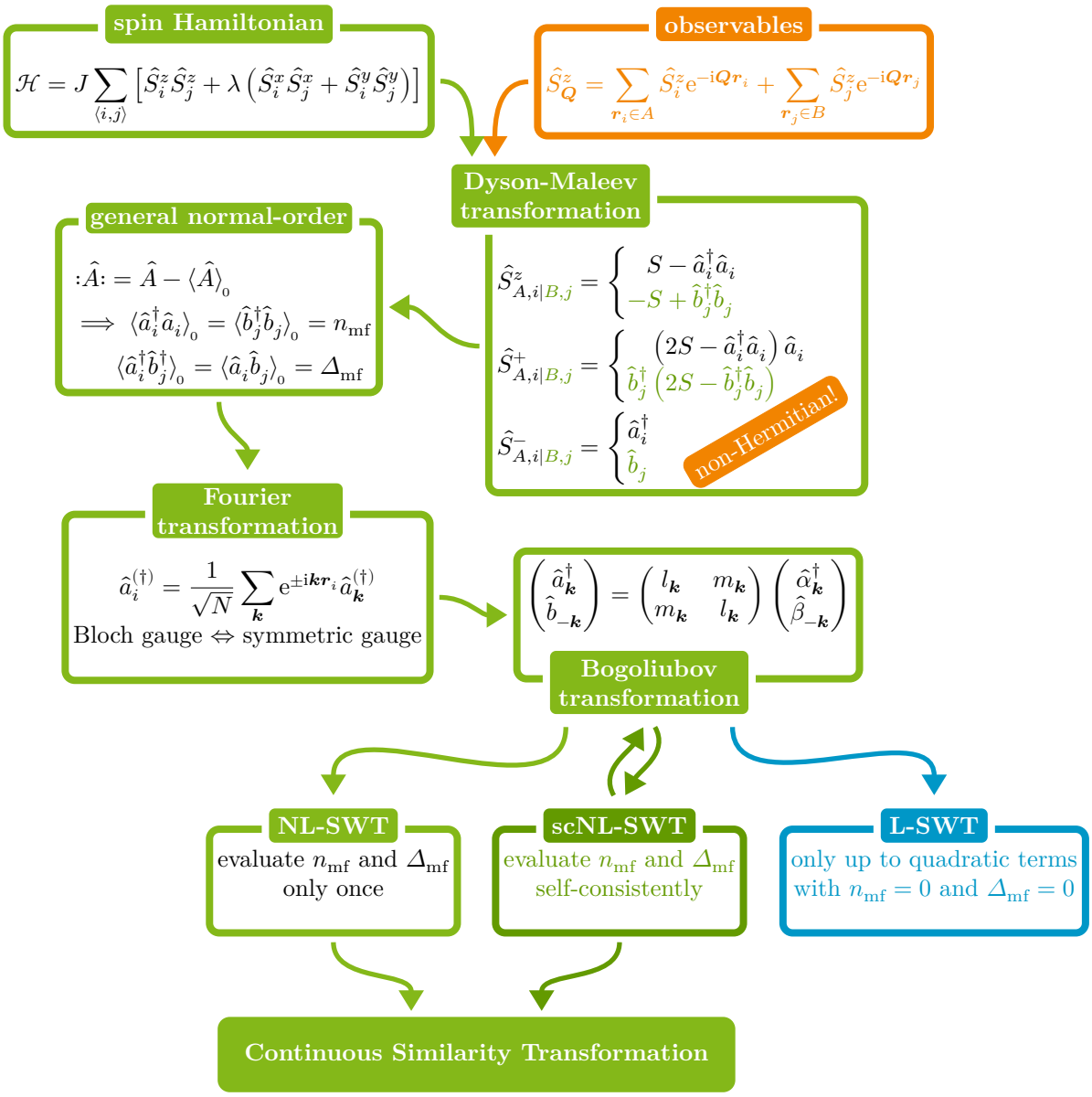

Figure 2.10: A comprehensive visualization of all transformations is displayed, starting from the initial Hamiltonian of the spin-$\frac{1}{2}$ antiferromagnetic easy-axis XXZ model on a square lattice together with observables. First, the Dyson-Maleev representation is inserted, followed by general normal-ordering, which introduces the expectation values as mean-field parameters. Afterwards, a Fourier transformation to momentum space is performed, considering two gauges. Subsequently, a Bogoliubov transformation is carried out to diagonalize the quadratic part of the Hamiltonian. With the solution of the Bogoliubov transformation, the mean-field parameters are determined. Whether these parameters are calculated self-consistently or not leads to the scNL-SWT or NL-SWT, respectively. Finally, the resulting Hamiltonian is transformed with the continuous similarity transformation.

3 | Continuous Similarity Transformation

This chapter introduces the method of continuous similarity transformation and discusses it in detail, as it serves as the backbone of this work. In particular, the method provides a framework for deriving effective models from the previously discussed class of spin Hamiltonians, extending beyond the treatments already considered in Chapter 2. The method of CST, however, represents only a subset within a broader field of research centered on the so-called flow equations approach. Therefore, the chapter begins with a concise introduction to the approach in general. A discussion of basis changes in the context of physics lays the foundation for the subsequent presentation of the underlying principles of the flow equation approach. Next, the chapter provides a brief overview of its various manifestations. This is followed by an in-depth presentation of the specific manifestation used in this work, namely the so-called continuous similarity transformation in momentum space with a truncation scheme based on scaling dimension. In this context, different generator and truncation schemes that play a significant role in the flow equation approach are examined.

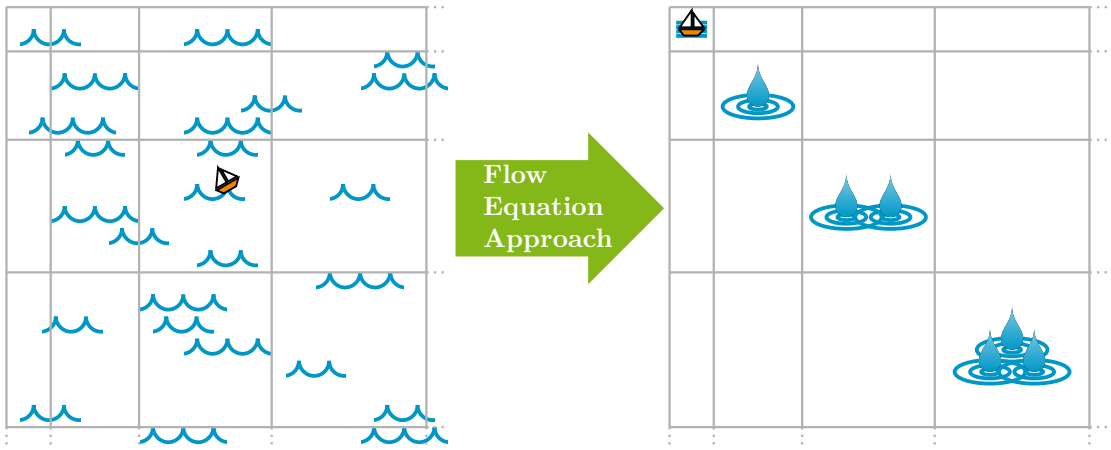

Figure 3.1: Metaphorical depiction illustrating the effect of the flow equation approach on the Hamiltonian of a many-body system. On the left-hand side of the image, a rough sea is shown symbolizing the inherent complexity of many-body problems, which is explored by a sailing boat. On the right-hand side, the sea is shown after applying the flow equation approach. A green arrow represents the transformation induced by the flow equation approach. The right-hand side is characterized by the classification of the sea into distinct regions after the flow equation approach. These regions are defined by the number of drops (quasiparticles), allowing a systematic and controlled exploration of the sea of the many-body problem by the sailing boat.

To provide an intuitive understanding of the effects of the flow equation approach as used in this

thesis, a metaphorical illustration is shown in Fig. 3.1. On the left-hand side of the image, a rough sea is depicted, symbolizing various complex many-body problems. A small sailing boat is shown exploring this sea. It represents a physicist attempting to understand effects occurring within such systems. Amidst so many waves, the sailing boat is at the mercy of the turbulent sea and lacks control over its direction. Using the flow equation approach, illustrated by a green arrow, it is possible to continuously transform the rough sea to a new arranged version. After this transformation the sea is divided into distinct regions. First, there is a calm sea where the sailing boat can safely moor in the harbor, representing the model's ground state. From this starting point, various regions of the sea can now be explored. In each region, the waves stem only from varying numbers of water drops added to the sea. In this newly transformed, effective sea, each wave can be traced back to its composition derived from a specific number of drops. By selectively including or excluding specific drops, the physicist can systematically explore the "sea" of the complex many-body problem in a more controlled manner, thereby identifying the origins of various phenomena.

3.1 Basis Transformations — General

In physics, the concept of basis transformations is a frequently used tool. Physics does not depend on the chosen basis; however, there are symmetries or conservation laws that become more apparent in a specific basis. Thus, a wide variety of different transformations exists, enabling the disentanglement of complex problems and enabling deeper insights into the underlying physical phenomena. Specifically within the domain of quantum mechanics, the range of available transformations is substantial. Already in the previous Chapter 2, the concept of a basis transformation was utilized in the form of a Fourier transformation along with a Bogoliubov transformation to diagonalize the Hamiltonian of the Heisenberg model. Nevertheless, to introduce and motivate the method of flow equations presented in the next section, it is necessary to first revisit the fundamental concepts of basis transformations in quantum mechanics. These concepts are widely covered in various textbooks [Gri17; Von96; Sch02] and are repeated here for the sake of completeness.

From a mathematical perspective, a basis transformation is defined as a linear transformation that changes the basis of a vector space. In the context of quantum mechanics, the vector spaces of interest are the Hilbert spaces. These spaces are characterized by an inner product $\langle \cdot, \cdot \rangle$ which serves to define a norm as well as distances and angles between different states. Within these Hilbert spaces, orthonormal bases $|\nu_i\rangle$ are defined and used to represent the physical states of the system. Quantum-mechanical observables are described by operators that act on these states; in finite-dimensional Hilbert spaces, they can be expressed as matrices. In the Copenhagen interpretation, the eigenvalues of these matrices define all possible measurement outcomes when the wave function collapses into the corresponding eigenstate. Thus, they are invariant under basis transformations. Observables are represented by Hermitian operators, which guarantees a real eigenvalue spectrum. Nevertheless, different basis transformations can simplify the representation of the operators and provide deeper insights into the underlying physics. For operators represented in their diagonalonalized form, the eigenvalues can be easily identified. Thus, it becomes important to determine a linear transformation denoted by the matrix $\underline{\boldsymbol{U}}$, via the eigendecomposition of an operator

$$\underline{\boldsymbol{O}} = \underline{\boldsymbol{U}}^{-1} \underline{\boldsymbol{O}}_D \underline{\boldsymbol{U}} \tag{3.1}$$

in an arbitrary basis. Here, $\underline{\boldsymbol{O_D}}$ represents a diagonal matrix containing the eigenvalues, while $\underline{\boldsymbol{U}}^{-1}$ contains column-wise the corresponding eigenvectors expressed in terms of the original basis.

The linear transformation to the new basis is given by

$$\underline{\boldsymbol{O}}_D = \underline{\boldsymbol{U}}\underline{\boldsymbol{O}}\underline{\boldsymbol{U}}^{-1} \ , \tag{3.2}$$

and allows calculations of the operator's measurement to be carried out in a more suitable basis. In quantum mechanics, unitary basis transformations are fundamental because they preserve the orthonormality of the states and the eigenvalues of the operators. For a transformation such as in Eq. (3.2) to be unitary, the inverse matrix $\underline{\boldsymbol{U}}^{-1}$ needs to correspond directly to its adjoint matrix $\underline{\boldsymbol{U}}^{\dagger}$. Moving beyond the matrix representation, an arbitrary unitary transformation in the operator notation is defined as

$$\hat{\mathcal{H}}' = \hat{U}\hat{\mathcal{H}}\hat{U}^{\dagger} \tag{3.3}$$

which transforms the Hamiltonian $\hat{\mathcal{H}}$ of the system to a new basis. Additionally, the basis vectors are mapped to their corresponding representation in the new basis $|\nu_i\rangle \to \hat{U}\,|\nu_i\rangle$ via application of the unitary operator $\hat{U}$.

Although transforming the Hamiltonian may initially seem a straightforward task, in general, the Hilbert spaces, in which the physical operators act, are of high dimensionality or even infinite, particularly in quantum many-body systems. Consequently, directly determining the transformation into the Hamiltonian's eigenbasis at once is nearly intractable. Nevertheless, general approaches such as the Fourier or Bogoliubov transformations can provide solutions in certain instances, as already demonstrated in Chapter 2. In general, however, these approaches do not necessarily lead to a complete solution of the problem.

Nevertheless, a variety of alternative methods exist to address the remaining challenges. Most of these methods rely on simplifications, approximations, and truncations. The following section presents a systematic approach to derive a more tractable Hamiltonian. The key insight lies in abandoning the attempts to diagonalize the Hamiltonian by a single unitary transformation. Instead, infinitesimal continuous unitary transformations are applied iteratively, ultimately resulting in a disentangled Hamiltonian.

3.2 Continuous Basis Transformations — Flow Equations

Generally, continuous unitary transformations in quantum mechanics are no novel concept. For example, translations in time, rotations, and spatial translations can be described as continuous unitary transformations with the corresponding continuous parameter being time t, rotation angle ϕ, or displacement $\boldsymbol{x}$. In the context of time evolution, the operator responsible for the transformation can be determined from the Schrödinger equation and is given by

$$\hat{U}(t, t_0) = \mathcal{T}\mathrm{e}^{-\frac{\mathrm{i}}{\hbar}\int_{t_0}^{t}\mathrm{d}t'\hat{\mathcal{H}}(t')} \tag{3.4}$$

with the time-ordering operator $\mathcal{T}$ and a time-dependent Hamiltonian $\hat{\mathcal{H}}(t)$. Accordingly, for a time-dependent operator, the time evolution is given by

$$\frac{\mathrm{d}}{\mathrm{d}t}\hat{O}_H(t) = \frac{\mathrm{i}}{\hbar}\left[\hat{\mathcal{H}}_H(t), \hat{O}_H(t)\right] + \partial_t\hat{O}_S \ , \tag{3.5}$$

which is the Heisenberg equation of motion, where the subscripts H and S refer to the Heisenberg and Schrödinger picture, respectively. For a non-explicit time-dependent operator, the last term vanishes[1].

[1] Note that the resulting definition for the time evolution is exactly reversed, reading $\hat{O}_H(t) = \hat{U}^{\dagger}\hat{O}_S\hat{U}$.

These continuous unitary transformations are generally associated with an anti-Hermitian generator $\hat{\eta}$. In the case of time evolution, the generator for translation in time contains the Hamiltonian itself $\hat{\eta} = \frac{\mathrm{i}}{\hbar}\hat{\mathcal{H}}$. In contrast, for spatial translations or rotations, the generator is proportional to either the linear momentum operator $\mathrm{i}\hat{p}$ or the angular momentum operator $\mathrm{i}\hat{L}$ [Sch02]

More generally, a continuous unitary transformation involving an arbitrary continuous parameter ℓ, applied infinitesimally by $\mathrm{d}\ell$, can be expressed as

$$\hat{O}(\ell + \mathrm{d}\ell) = \hat{U}(\ell + \mathrm{d}\ell, \ell)\hat{O}(\ell)\ \hat{U}(\ell + \mathrm{d}\ell, \ell)^\dagger \tag{3.6a}$$

$$= \mathrm{e}^{\hat{\eta}(\ell)\ \mathrm{d}\ell}\hat{O}(\ell)\mathrm{e}^{-\hat{\eta}(\ell)\mathrm{d}\ell} \quad \text{with} \quad \hat{\eta}^\dagger(\ell) = -\hat{\eta}(\ell)\ . \tag{3.6b}$$

The expansion of the exponential functions using Taylor's series

$$\hat{O}(\ell + \mathrm{d}\ell) = (1 + \hat{\eta}(\ell)\mathrm{d}\ell + \dots)\,\hat{O}(\ell)\,(1 - \hat{\eta}(\ell)\mathrm{d}\ell + \dots) \tag{3.6c}$$

$$= \hat{O}(\ell) + \left[\hat{\eta}(\ell), \hat{O}(\ell)\right]\mathrm{d}\ell + \mathcal{O}\left(\mathrm{d}\ell^2\right) \tag{3.6d}$$

leads to the derivation of the so-called flow equation

$$\partial_\ell \hat{O}(\ell) = \left[\hat{\eta}(\ell), \hat{O}(\ell)\right]\ , \tag{3.7}$$

which has a form similar to the Heisenberg equation of motion. This equation determines the continuous unitary transformation induced by the generator $\hat{\eta}$.

To summarize, the primary objective is to transform the Hamiltonian of a given system into a basis that provides deeper insight into the physical processes within the system. Since finding an appropriate transformation in a single step is nearly impossible, the concept of a continuous transformation was introduced. At this point, however, the flow equation merely describes an arbitrary continuous unitary transformation for any operator $\hat{O}$. It does not yet offer a clear way to identify a basis that makes the system's underlying physics more comprehensible. The key to fully utilizing the continuous approach lies in selecting an appropriate generator $\hat{\eta}$, which defines a continuous transformation of the initial Hamiltonian $\hat{\mathcal{H}}(\ell = 0)$ associated with the system of interest, with the property

$$\hat{\mathcal{H}}(\ell) = \hat{U}(\ell)\hat{\mathcal{H}}(\ell = 0)\hat{U}^\dagger(\ell) \quad \text{for} \quad \ell \to \infty \quad \hat{\mathcal{H}}(\ell = \infty) = \hat{\mathcal{H}}_{\text{eff}}\ . \tag{3.8}$$

Here, $\hat{\mathcal{H}}_{\text{eff}}$ describes an effective Hamiltonian that is diagonal or significantly simpler than the original Hamiltonian. In this context, the term flow will be used interchangeably with transformation. The following section will explore the history of the flow equation approach, highlighting challenges related to identifying a suitable generator and further emerging challenges.

3.2.1 Continuous Unitary Transformation

The development of the continuous unitary transformation (CUT) approach began in 1993/1994 and was initially established independently in the field of physics by Wegner [Weg94] as well as Głazek and Wilson [GW93; GW94]. Similar concepts had already been developed by mathematicians specializing in control theory [CD90; Bro91]. However, Wegner, Głazek, and Wilson were unaware of these mathematical developments at the time [Weg06]. For an in-depth introduction to the flow equation approach, the textbook by Kehrein [Keh06] can also be consulted. To identify a suitable generator Wegner's solution was to choose a generator defined as

$$\hat{\eta}(\ell) = \left[\hat{\mathcal{H}}_{\text{diag}}(\ell), \hat{\mathcal{H}}(\ell)\right]\ , \tag{3.9}$$

which is given by the commutator between the diagonal part of the Hamiltonian $\hat{\mathcal{H}}_{\mathrm{diag}}(\ell)$ and the full Hamiltonian $\hat{\mathcal{H}}(\ell)$. If the generator becomes zero, the derivative in the flow equation of Eq. (3.7) vanishes, consequently describing a fixed point of the flow equation. Regarding the Wegner generator, the diagonal Hamiltonian represents such a fixed point, since in this case the commutator defined by Eq. (3.9) obviously vanishes. Determining whether a fixed point in this sense is attracting or repelling within the framework of the flow equation approach is not always possible. In the case of the Wegner generator, however, it can be demonstrated that a diagonal effective Hamiltonian is achieved under certain conditions. This topic is discussed in greater detail in Section 3.3. Furthermore, in Section 3.3, other generators such as the Mielke generator, particle-conserving generator, and particle-block-separating generator are introduced.

Regardless of the explicit form of the generator, three critical caveats should always be considered when applying the flow equation approach. First and foremost, an analytical solution to the emerging flow equations is feasible only in a limited number of simple cases and toy models. In most instances, solving the resulting flow equations requires numerical integration schemes. Since integrating ℓ numerically to infinity is impractical, termination schemes must be established to define an endpoint for integration.

Secondly, evaluating the commutator in the flow equation approach yields a closed set of differential equations only when using a closed basis, such as in a matrix representation of a finite-dimensional Hilbert space. However, in most problems in many-particle physics, this is not the case. As the Hilbert spaces become infinitely large, problems are typically formulated using second quantization, where commutators are evaluated with the help of a corresponding set of elementary commutators, and evaluating such commutators generically results in a non-closed basis.

The following section examines how the flow equation approach is represented in second quantization. To provide some context upfront, evaluating commutators involving terms beyond quadratic order generates new terms of even higher order than initially present. In most cases, this process causes the operator basis to expand infinitely, as newly generated terms must also be considered recursively in subsequent commutators. Consequently, it becomes necessary to define a scheme that determines which operators should be retained and which ones can be neglected. Henceforth, this scheme is referred to as the truncation scheme. There are several established truncation schemes, which are discussed in Section 3.4.

The final consideration combines aspects of the two previous points. In the most challenging scenario, i.e., a non-feasible analytical solution and an infinite operator basis necessitating a truncation scheme, the flow equation approach becomes prone to errors. These arise from truncation errors that accumulate with each rotation step. Hence, it is advisable to perform only small rotations in each step, as well as not attempting to achieve a fully diagonal Hamiltonian. Striving for complete diagonalization increases the required rotations, thereby amplifying the truncation error. To mitigate these issues, one can instead selectively decouple particular sectors of the Hamiltonian, for example, by transforming it into a block-diagonal form. Subsequently, complementary methods can be used to extract the relevant physical quantities. While truncation errors remain unavoidable, they are significantly reduced under such circumstances. To utilize these advantages, the transformations require generators other than Wegner's generator. This topic will be explored further in Section 3.3.

The selection of different generator schemes, combined with sophisticated truncation schemes, has led to various realizations of the CUT approach. In the following, a list of the most common methods of CUT realizations is provided below based on Refs. [Dre14; Sch22]. Additionally, an overview of distinct applications of the CUT approach up to 2006 can be found in Refs. [Keh06; Weg06].

The self-similar CUT (sCUT) uses a finite basis of operators in second quantization, allowing for a distinction of involved quasiparticles in the interaction. Typically, a truncation scheme is required and applied to maintain a finite operator basis. A suitable truncation scheme can be based either on the real-space range of the interaction [RMU04; FDU10] or a small perturbation parameter [Keh06; Mie97]. The flow equations are integrated numerically, yielding a non-perturbative, renormalized effective Hamiltonian.

The perturbative CUT (pCUT) was introduced by Knetter and Uhrig [KU00; UN98; KSU03a]. This implementation of the flow equation approach facilitates the calculation of perturbative expansions up to very high orders. For its application, the unperturbed Hamiltonian must possess a ladder spectrum, i.e., an equidistant energy spectrum. Then it generates model-independent flow equations that can be integrated analytically. The analytical solution is subsequently employed to compute matrix elements of the effective Hamiltonian in various orders of perturbation theory.

The enhanced perturbative CUT (epCUT) can be regarded as a combination of pCUT and sCUT approaches. By combining second quantization and explicit numerical integration from sCUT, in conjunction with the perturbative expansion of pCUT, the epCUT [KDU12] enables the derivation of effective Hamiltonians for a broader range of models compared to pCUT, as the prerequisite of a ladder spectrum is dropped. The coefficient monomials associated with an operator are expanded perturbatively, and the flow equations are solved numerically for each order separately.

The directly evaluated enhanced perturbative CUT (deepCUT) can be considered the non-perturbative counterpart of the epCUT. Similar to epCUT, the deepCUT approach [KDU12; Sch+22] utilizes perturbative expansion to identify relevant contributions for the coefficient monomial. However, unlike in epCUT, the integration is carried out for the entire monomial coefficient rather than for each order individually. This leads to a more efficient and accurate approach that produces a non-perturbative effective Hamiltonian.

The graph-theory based CUT (gCUT) can be interpreted as a modification of CUT based on the exact linked-cluster expansion [IH84], developed by Yang and Schmidt [YS11]. The Hamiltonian's action is decomposed into finite graphs, and the flow equations are solved numerically at the matrix level for each graph. Subsequently, irreducible contributions from each graph are then combined to yield a non-perturbative effective Hamiltonian. The accuracy of this method is determined by the maximum graph size considered. Due to a model-independent effective pCUT Hamiltonian, so-called white graphs can be used to significantly reduce the number of graphs that need to be considered, thereby enabling the treatment of higher perturbation orders [CS15].

In this thesis, however, the focus is on the CST approach, which extends the CUT approach by employing similarity transformations rather than unitary transformations. Why is this extension necessary? Due to the non-Hermitian nature of the final Hamiltonian of Section 6.6, as a consequence of the Dyson-Maleev representation (DM), the use of unitary transformations is not suitable for the problem at hand. Nevertheless, the procedure of the CST closely resembles the sCUT representation. In its representation, the CST approach also utilizes the second quantization. Thus, after a brief examination of the second quantization representation within the flow equation approach, the specifics of the CST approach are explored in detail in Section 3.2.3.

3.2.2 Continuous Unitary Transformation in second quantization

The numerical integration of flow equation for an operator in its matrix representation becomes infeasible for large many-body systems, since the number of matrix elements $h_{nj}(\ell) = \langle n|\widehat{\mathcal{H}}(\ell)|j\rangle$ that need to be tracked throughout the flow grows exponentially with the system size. In this

context, formulating the flow equation approach in second quantization provides a means to mitigate the challenges posed by many-body systems [Weg94]. Instead of relying on the matrix form of the operators, operators such as the Hamiltonian or the generator are expressed as

$$\hat{\mathcal{H}}(\ell) = \sum_i h_i(\ell)\hat{A}_i \quad \text{and} \quad \hat{\eta}(\ell) = \sum_i \eta_i(\ell)\hat{A}_i \ . \tag{3.10}$$

Here, the $\hat{A}_i$ denotes normal-ordered operator monomials in second quantization, which are elements of the operator basis $\mathfrak{H} \coloneqq \{\hat{A}_i\}$. The dependency on ℓ is shifted in the coefficients η_i and h_i, while the operator basis remains constant throughout the flow. As a consequence, the number of coefficients that must be tracked during the flow depends only on the size of the operator basis. In fact, for certain generators the coefficient $\eta_i(\ell)$ is proportional to $h_i(\ell)$ and can therefore be expressed as $\eta_i(\ell) = \eta_i h_i(\ell)$ with $\eta_i \in \{\pm 1\}$. This further reduces the number of coefficients that need to be tracked. One key advantage of the representation in second quantization is that each monomial $\hat{A}_i$ contributes to multiple matrix elements $h_{nj}(\ell) = \langle n|\hat{\mathcal{H}}(\ell)|j\rangle$. By tracking only a few operator monomials, it becomes possible to access a substantial portion of possible processes.

Nevertheless, it is crucial to recognize that truncating the operator basis may result in incomplete matrix elements. For instance, a matrix element describing a two-particle process consists of two irreducible operator contributions, i.e., a single-particle and a two-particle contribution. If the genuine two-particle contribution is truncated, the corresponding matrix element will not be accurately represented. The number of operator monomials grows rapidly if all contributions to matrix elements describing multi-particle interactions are to be captured correctly. It is necessary to find a trade-off between the accuracy of the result and its numerical feasibility. Consequently, it is crucial to define a truncation scheme that does not significantly reduce the accuracy of the results while ensuring manageable computational effort.

A direct comparison between matrix representation and different truncations in second quantization with respect to the number of tracked coefficients is presented for the one-dimensional chain of N localized spin-$\frac{1}{2}$-particles in Chapter 2.2 of Ref. [Sch22]. The comparison highlights the advantages of second quantization by emphasizing that low-energy processes, i.e., processes involving 2 to 3 particles, are typically the primary focus. For such processes, the number of operator monomials required in second quantization is substantially smaller than the coefficients to be tracked in a matrix representation. Moreover, given the necessity of a description of the thermodynamic limit $N \to \infty$, it is highly beneficial to use second quantization over the matrix representation. For instance, it allows translation symmetry to be implemented easily.

With the advantages of second quantization established, the adaptations to the flow equation approach can now be described in greater detail following [KDU12]. By inserting Eq. (3.10) into the flow equation Eq. (3.7) the expression

$$\partial_\ell \left(\sum_i h_i(\ell)\hat{A}_i \right) = \sum_{j,k} \eta_j(\ell) h_k(\ell) \left[\hat{A}_j, \hat{A}_k\right] \tag{3.11}$$

is obtained, which determines the flow of the Hamiltonian. The commutator between $\hat{A}_j$ and $\hat{A}_k$ can be rewritten as

$$\left[\hat{A}_j, \hat{A}_k\right] = \sum_i D_{ijk}\hat{A}_i \ , \tag{3.12}$$

where the tensor D_{ijk} quantifies the occurrence of $\hat{A}_i$ in the result of the commutator $\left[\hat{A}_j, \hat{A}_k\right]$, because the commutator itself generates again normal-ordered monomials $\hat{A}_i$. Those monomials are not necessarily part of the operator basis $\mathfrak{H}$. Consequently, the operator basis needs to be

expanded to include newly generated operator monomials. Even though for $\ell = 0$ the coefficients of these generated monomials are initially zero, their values can become non-zero during the flow $\ell > 0$. This necessitates calculating the commutators for the newly added monomials as well. In most cases, this recursive process leads to an operator basis that proliferates indefinitely. To address this issue, as mentioned above, a truncation scheme must be implemented to ensure a finite base and thereby a closed set of differential equations for each monomial coefficient.

Given a closed monomial basis $\mathfrak{H}$, a flow equation can be derived for each coefficient by comparing the coefficient of each monomial $\hat{A}_i$ on both sides of Eq. (3.11), which yields

$$\partial_\ell h_i(\ell) = \sum_{jk} D_{ijk}\eta_j(\ell)h_k(\ell) \ . \tag{3.13}$$

Similarly, it is possible to determine the form of the operators describing observables within the effective system. In second quantization an arbitrary observable $\hat{O}$ can be expressed as

$$\hat{O} = \sum_i o_i(\ell)\hat{B}_i \ , \tag{3.14}$$

where the operator monomials $\hat{B}_i$ belong to a basis $\mathfrak{O} \coloneqq \{\hat{B}_i\}$. It is neither guaranteed nor required that the basis $\mathfrak{O}$ coincides with the basis $\mathfrak{H}$. Nevertheless, the basis $\mathfrak{O}$ is constructed similarly to $\mathfrak{H}$ and the flow equation for the coefficient $o_i(\ell)$ of an observable is given by

$$\partial_\ell o_i(\ell) = \sum_{jk} \tilde{D}_{ijk}\eta_j(\ell)o_k(\ell) \ . \tag{3.15}$$

The tilde over the tensor accounts for cases in which the observable and the generator use different operator bases. Despite a possible different basis for the observable, the generator is represented in $\mathfrak{H}$. In such cases, the commutator in the flow equation is decomposed in the form

$$\left[\hat{A}_j, \hat{B}_k\right] = \sum_i \tilde{D}_{ijk}\hat{B}_i \ . \tag{3.16}$$

It is important to note that the flow of an observable must be evaluated simultaneously to the flow of the Hamiltonian, since in each step the generator $\eta_j(\ell)$ depends implicitly on the coefficient of the Hamiltonian $h_i(\ell)$ itself.

3.2.3 Continuous Similarity Transformation

In the preceding sections, the flow equation approach was examined in the context of unitary transformations. Interestingly, Wegner restricted his work to unitary transformations [Weg94], whereas Głazek and Wilson did not explicitly impose this restriction, but only applied unitary transformations in their work [GW93]. Nevertheless, the derivation of the flow equation presented in Section 3.2 can also be extended to similarity transformations. Unitary transformations represent a particular subclass of similarity transformations. Consequently, a CUT constitutes merely a special case within the broader framework of CSTs. The key difference is that the generator $\eta(\ell)$ is not necessarily anti-Hermitian for a CST. Despite this fact, the form of the flow equation for the similarity transformation

$$\partial_\ell \hat{\mathcal{H}}(\ell) = \left[\hat{\eta}(\ell), \hat{\mathcal{H}}(\ell)\right] \tag{3.17}$$

remains the same, since the transformation of the Hamiltonian is expressed as

$$\hat{\mathcal{H}}(\ell + \mathrm{d}\ell) = \hat{S}(\ell + \mathrm{d}\ell, \ell)\hat{\mathcal{H}}(\ell)\hat{S}^{-1}(\ell + \mathrm{d}\ell, \ell) \tag{3.18a}$$

$$= \mathrm{e}^{\hat{\eta}(\ell)\ \mathrm{d}\ell}\hat{\mathcal{H}}(\ell)\mathrm{e}^{-\hat{\eta}(\ell)\mathrm{d}\ell} \quad \text{with} \quad \hat{\eta}^\dagger(\ell) \neq -\hat{\eta}(\ell) \tag{3.18b}$$

and for

$$\ell \to \infty \quad \hat{\mathcal{H}}(\ell = \infty) = \hat{\mathcal{H}}_{\text{eff}} \ . \tag{3.19}$$

In contrast to continuous unitary transformation, however, the conditions that ensure convergence of the flow equation do not necessarily hold in the non-unitary similarity transformations [Pow17]. The implications of an anti-Hermitian generator will be discussed in detail in Section 3.3.

Although the extension to similarity transformations may seem superfluous given the Hermitian nature of quantum-mechanical operators, it becomes essential in specific scenarios where non-Hermitian representations provide meaningful physical insights.

One notable exception arises in the context of open quantum systems [Rot09; Vac24] For instance, the dynamics of open quantum systems can be described by the Lindblad-master equations [BP07]

$$\frac{\mathrm{d}}{\mathrm{d}t}\rho(t) \ = \hat{\mathcal{L}}\left[\rho(t)\right] \ . \tag{3.20}$$

This equation describes the time evolution of a density matrix $\rho(t)$ which is governed by the Lindbladian superoperator $\hat{\mathcal{L}}$. Within this framework, the Lindbladian is a non-Hermitian operator. Unlike Hermitian operators, the eigenvalues of the Lindbladian can be complex. The real parts correspond to energies that characterize oscillations within the system, while the imaginary parts account for dissipation and relaxation processes.

Furthermore, another exception arises in models that exhibit $\mathcal{PT}$-symmetry. In such models, the appearance of non-Hermitian operators is also possible. Remarkably, non-Hermitian operators with $\mathcal{PT}$-symmetry possess a real eigenvalue spectrum, similar to Hermitian operators, as shown by Bender and Boettcher in 1998 [BB98]. This has led to the emergence of an entire field of research driven by these intriguing properties [Ben07; El-+18]. Furthermore, non-Hermitian Hamiltonians have emerged as a subject of research within the broader context of topology. The Ref. [BBK21] provides a thorough review of the existing research on this topic.

Aside from the aforementioned examples, a non-Hermitian representation is also encountered in this work in the context of bosonic representations of spin operators. Hermitian spin operators can be mapped to bosonic operators in the DM [Dys56b; Mal58b]. For details regarding the DM, please refer to Section 2.4. Following the representation, the resulting Hamiltonian becomes non-Hermitian. In contrast to the other examples mentioned above, the system's initial representation is Hermitian. Here, a non-Hermitian bosonic DM is preferred over a Hermitian bosonic Holstein-Primakoff representation (HP) to circumvent the square-root expansion in the HP [HP40], as introduced in Section 2.3. Nevertheless, the DM is a similarity mapping and thus conserves the real spectrum of the original Hermitian Hamiltonian and is a valid representation of the physical problem at hand. However, the resulting Hamiltonian and bosonic operators are self-adjoint with respect to two different inner products [Jon13]. The Hamiltonian is not self-adjoint with respect to the usual scalar product. Instead, one has to apply the appropriate adjoint operation defined by the inner product of the original spin system and translated to the DM.

Treating observables and states in a non-Hermitian representation can be challenging. While similarity transformations preserve the spectrum, they do not guarantee that the states remain orthonormal after the transformation. As a result, extracting physical understanding from a non-Hermitian representation is less straightforward than in the Hermitian case. The detailed implications of working with a non-Hermitian representation are thoroughly examined in Section 4.4.

In summary, extending the flow equation approach to non-Hermitian Hamiltonians via CSTs is not merely a mathematical exercise; rather, it enables a range of applications across different fields

of physics, particularly condensed matter physics. For dissipative systems, extensions to the flow equation approach already exist that explore various types of generators when Lindbladians are involved [Ros+20; SU22]. Regarding the application of non-unitary flow equations after the non-Hermitian DM, advancements had already been made prior to this work. Concretely, the isotropic spin-$\frac{1}{2}$ antiferromagnetic Heisenberg model (afHM) on a square lattice, along with its associated spin observables, was successfully analyzed using a non-unitary flow equation approach [PUS15; Pow17; PSU18]. This thesis builds on these achievements. As noted earlier, the CST resembles a sCUT approach. The CST approach is applied in second quantization in momentum space, with its truncation scheme relying on arguments based on the scaling dimensions of operators. Furthermore, a different generator scheme is applied that does not aim for a complete diagonalization but instead focuses on separating distinct blocks of quasiparticle numbers. This generator scheme, along with alternative schemes, is presented and discussed in the following section. Subsequently, various truncation schemes are examined, including those based on scaling dimension arguments.

3.3 Generator Schemes

This section provides a comprehensive overview of various generator schemes employed in the flow equation approach. The structure and properties of the resulting effective model depend strongly on the specific choice of generator. Therefore, selecting an appropriate generator scheme is important and depends on the specific physical problem to be solved. The resulting effective model can be viewed as a fixed point of the flow equation associated with the selected generator scheme. For the flow equation to converge successfully, an attractive fixed point in parameter space must exist. The convergence behavior can be analyzed systematically for various generator schemes to decide which generator scheme is most suitable for addressing a given physical problem.

The overview begins with the previously mentioned Wegner generator, followed by an introduction to the Mielke generator. Since neither is applied in this thesis, both are examined solely within the context of continuous unitary transformations. These two generators illustrate the advantages and disadvantages associated with different generator schemes. Subsequently, two key generator schemes employed in this thesis are introduced: the first is the so-called particle-conserving generator, and the second is the particle-block-separating generator. Both are also discussed in the context of a non-Hermitian representation, leading to CST.

Readers seeking a more detailed discussion or alternative applications of these generators may consult the references that serve as a foundation for this section [Keh06; Dre14; Pow17; Sch22].

3.3.1 Wegner Generator

The generator scheme was suggested by Wegner in Ref. [Weg94]. A notable example of successful application of this generator scheme is the sine-Gordon model [Keh01; Keh99]. The generator in this scheme has the form

$$\hat{\eta}(\ell) = \left[\hat{\mathcal{H}}_{\mathrm{diag}}(\ell), \hat{\mathcal{H}}(\ell)\right] = \left[\hat{\mathcal{H}}_{\mathrm{diag}}(\ell), \hat{\mathcal{H}}_{\mathrm{off-diag}}(\ell)\right] \ , \tag{3.21}$$

where the Hamiltonian divided into a diagonal part $\hat{\mathcal{H}}_{\mathrm{diag}}(\ell)$ and an off-diagonal part $\hat{\mathcal{H}}_{\mathrm{off-diag}}(\ell)$, so that $\hat{\mathcal{H}}(\ell) = \hat{\mathcal{H}}_{\mathrm{diag}}(\ell) + \hat{\mathcal{H}}_{\mathrm{off-diag}}(\ell)$ holds. Contrary to their nomenclature, "diagonal" and "off-diagonal" components should not be interpreted as too strictly limited categories. Within the context of generators for flow equations, "diagonal" and "off-diagonal" are better understood as a

classification of what terms should be kept ("diagonal") and which should vanish ("off-diagonal") in the course of the flow.

The Wegner generator can alternatively be formulated in a matrix representation as

$$\eta^{\text{Wegner}}_{n,j}(\ell) = \big(h_{nn}(\ell) - h_{jj}(\ell)\big)\, h_{nj}(\ell) \ , \tag{3.22}$$

where n, j denote the row and column indices, respectively, of the matrix representation of the Hamiltonian. Then, the flow equations associated with the Wegner generator read

$$\begin{aligned} \partial_\ell h_{nj}(\ell) =& \sum_k \big((h_{nn}(\ell) - h_{kk}(\ell))\, h_{nk}(\ell) h_{kj}(\ell) \\ & - \big(h_{kk}(\ell) - h_{jj}(\ell)\big)\, h_{nk}(\ell) h_{kj}(\ell)\big) \end{aligned} \tag{3.23a}$$

$$\begin{aligned} =& -\big(h_{nn}(\ell) - h_{jj}(\ell)\big)^2 h_{nj}(\ell) \\ & + \sum_{k \notin \{n,j\}} \big(h_{nn}(\ell) + h_{jj}(\ell) - 2h_{kk}(\ell)\big)\, h_{nk}(\ell) h_{kj}(\ell) \ , \end{aligned} \tag{3.23b}$$

where h_{nj} represents an arbitrary matrix element of $\hat{\mathcal{H}}$. Focusing on the diagonal elements simplifies the flow equation to

$$\partial_\ell h_{nn}(\ell) = \sum_{k \neq n} 2\, (h_{nn}(\ell) - h_{kk}(\ell))\, |h_{nk}(\ell)|^2 \ . \tag{3.24}$$

This formulation enables making statements regarding convergence to a fixed point of the flow equation. By examining the sum of the change in the squared diagonal elements of the Hamiltonian

$$\sum_n \partial_\ell \left(h_{nn}(\ell)^2\right) = 2 \sum_{nj} \big(h_{nn}(\ell) - h_{jj}(\ell)\big)^2 |h_{nj}(\ell)|^2 \geq 0 \ , \tag{3.25}$$

it becomes evident that convergence must occur, as the norm of the diagonal part increases throughout the flow but is bounded from above. As a consequence, fixed points of the effective $\hat{\mathcal{H}}$ take the form

$$h_{nj}(\ell = \infty) = 0 \quad \forall n \neq j : h_{nn}(\ell = \infty) \neq h_{jj}(\ell = \infty) \ . \tag{3.26}$$

In cases where $h_{nn}(\ell = \infty) = h_{jj}(\ell = \infty)$, i.e., degenerate states, the Wegner generator does not ensure that off-diagonal elements $h_{nj}(\ell = \infty)$ vanish. Even though a diagonal form is achieved in non-degenerate cases, the convergence of the off-diagonal matrix elements h_{nj} near the diagonal form depends on the energy differences between diagonal matrix elements as

$$h_{nj} \propto \exp\Big(-\big(h_{nn}(\ell = \infty) - h_{jj}(\ell = \infty)\big)^2 \ell\Big) =: \exp\left(-|\Delta E_{nj}|^2 \ell\right) \ . \tag{3.27}$$

Consequently, convergence becomes slow if energy differences are small.

Another issue is that the Wegner generator does not guarantee a block-band-diagonal structure throughout the flow. This means that if the initial Hamiltonian is block-band-diagonal, i.e., $h_{nj} = 0 \ \forall \ |j - n| > \Delta$ with the bandwidth Δ, the flow may generate finite matrix elements h_{nj} for $|j - n| > \Delta$. While this might not initially appear to be a drawback, it can lead to both increased computational effort and greater truncation errors than other generators presented in the following sections. To provide an impression of the behavior of the flow induced by the Wegner generator, Fig. 3.2 illustrates the flow at different stages. The initial form $\hat{\mathcal{H}}(\ell = 0)$, an intermediate form $\hat{\mathcal{H}}(\ell > 0)$ and final from $\hat{\mathcal{H}}(\ell \to \infty)$ are shown for an arbitrary matrix. Thus far, as noted in the

original publication [Weg94], the convergence is only proven for finite matrices. However, it is also possible to prove this even for infinite systems [DU04].

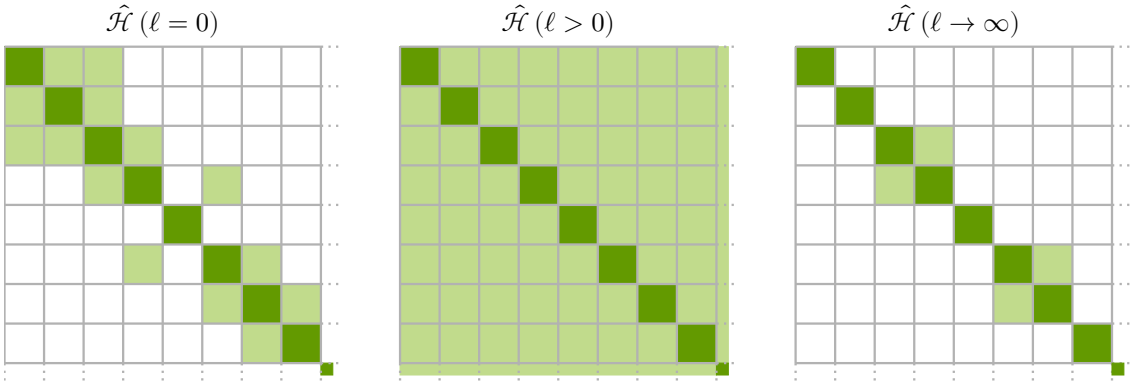

Figure 3.2: Illustration of the effect of the flow on a matrix induced by the Wegner generator. From left to right, the matrix is shown for different ℓ, at $\ell = 0$, during $\ell \geq 0$, and after the flow $\ell \to \infty$. Dark green squares stand for finite matrix elements that belong to $\hat{\mathcal{H}}_{\text{diag}}$, while light green squares indicate elements belonging to $\hat{\mathcal{H}}_{\text{off-diag}}$. During the flow $\ell \geq 0$, previously nonexistent elements may become finite due to lack of preserved band-diagonality. After the flow, the matrix becomes diagonalized except for blocks with degeneracy.

3.3.2 Mielke Generator

An alternative generator scheme is the Mielke generator [Mie98], defined as

$$\hat{\eta}^{\text{Mielke}}(\ell) = \hat{\mathcal{H}}^{(+)}(\ell) - \hat{\mathcal{H}}^{(-)}(\ell)\ , \tag{3.28}$$

where $\hat{\mathcal{H}}^{(+)}$ represents the upper and $\hat{\mathcal{H}}^{(-)}$ the lower triangular part of the Hamiltonian in matrix representation. To analyze its convergence, the matrix representation of the Mielke generator

$$\eta^{\text{Mielke}}_{nj}(\ell) = \text{sign}(n-j)h_{nj}(\ell) \tag{3.29}$$

is considered, where the sign explicitly depends on row and column indices n, j. The primary effect of the Mielke generator is to diagonalize the matrix while simultaneously sorting the diagonal elements in ascending order during the flow. In contrast to the Wegner generator, the flow induced by the Mielke generator only vanishes when all non-diagonal matrix elements are zero, even in the cases of degenerate eigenvalues. The flow equation for an arbitrary matrix element under the Mielke generator scheme is expressed as

$$\partial_\ell h_{nj}(\ell) = \sum_k \big(\text{sign}(n-k)h_{nk}(\ell)h_{kj}(\ell) - \text{sign}(k-j)h_{nk}(\ell)h_{kj}(\ell)\big) \tag{3.30a}$$

$$\begin{aligned} = \quad & -\text{sign}(n-j)\left(h_{nn}(\ell) - h_{jj}(\ell)\right)\ h_{nj}(\ell) \\ & + \sum_{k\notin\{n,j\}} \left(\text{sign}(n-k) - \text{sign}(k-j)\right) h_{nk}(\ell)h_{kj}(\ell)\ . \end{aligned} \tag{3.30b}$$

The convergence behavior of the Mielke generator can be examined by analyzing the diagonal elements of the Hamiltonian [Mie98]. For a diagonal element, the flow equation from Eq. (3.30b)

reduces to

$$\partial_\ell h_{nn}(\ell) = 2 \sum_{k \neq n} \operatorname{sign}(n-k) \, |h_{nk}(\ell)|^2 \ . \tag{3.31}$$

When considering the sum of the r lowest diagonal elements

$$\partial_\ell \left(\sum_{n=1}^{r} h_{nn} \right) = \sum_{n=1}^{r} \sum_{k>r} -2|h_{nk}|^2 \leq 0 \ , \tag{3.32}$$

it becomes evident that this sum can only decrease. If the Hamiltonian is bounded from below, the sum has a lower limit. Namely, the sum cannot be smaller than the sum of the r lowest eigenvalues

$$\sum_{n=1}^{r} h_{nn} \geq \sum_{n=1}^{r} \lambda_n \ . \tag{3.33}$$

Consequently, the derivative of Eq. (3.31) must vanish as $\ell \to \infty$. The flow equation converges to a fixed point where all off-diagonal elements vanish. Whether this fixed point is attractive is determined by

$$\operatorname{sign}(n-j) = \operatorname{sign}(h_{nn}(\ell=\infty) - h_{jj}(\ell=\infty)) \ , \tag{3.34}$$

as the sign of the derivative in Eq. (3.30b), near the fixed point, is determined by the leading order behavior. Thus, the energies are sorted in ascending order within the final Hamiltonian. Additionally, the off-diagonal elements converge like

$$h_{nj}(\ell=\infty) \propto \exp\left(-|h_{nn}(\ell=\infty) - h_{jj}(\ell=\infty)|\ell\right) =: \exp\left(-|\Delta E_{nj}|\ell\right) \ , \tag{3.35}$$

as the matrix approaches a diagonal form. As before, the energy difference ΔE_{nj} determines the convergence speed. Compared to the convergence of the Wegner generator, the energy difference for the Mielke generator is linear rather than quadratic. This is advantageous for convergence when minor energy differences are present. Additionally, the Mielke generator ensures that if the initial matrix is band-diagonal, i.e., $h_{nj} = 0 \ \forall \ |j-n| > \Delta$, the Hamiltonian remains band-diagonal with the same bandwidth Δ throughout the flow [Mie98]. This results in reduced computational effort compared to the Wegner generator, because initial elements outside the bandwidth cannot emerge and therefore do not need to be truncated. However, it should be noted that reordering processes occur if diagonal elements of the matrix are not sorted at the beginning of the flow. These processes can lead to an increase in off-diagonal elements and thus enhance truncation errors [DU04]. An illustration of the flow induced by the Mielke generator scheme is shown in Fig. 3.3.

3.3.3 Particle-Conserving Generator

It is possible to generalize the Mielke generator to the so-called particle-conserving generator or quasiparticle-conserving generator (pc generator). This adaptation differs from the original Mielke generator scheme by selectively including only certain off-diagonal elements into the generator, which are intended to vanish in the effective model. Initially, this approach was formulated by Knetter and Uhrig [KU00] to decouple subspaces associated with different particle numbers. This modification to the generator can be denoted generally in the matrix representation as

$$\eta^{\mathrm{pc}}_{nj}(\ell) = \operatorname{sign}(q_{nn} - q_{jj}) h_{nj}(\ell) \ , \tag{3.36}$$

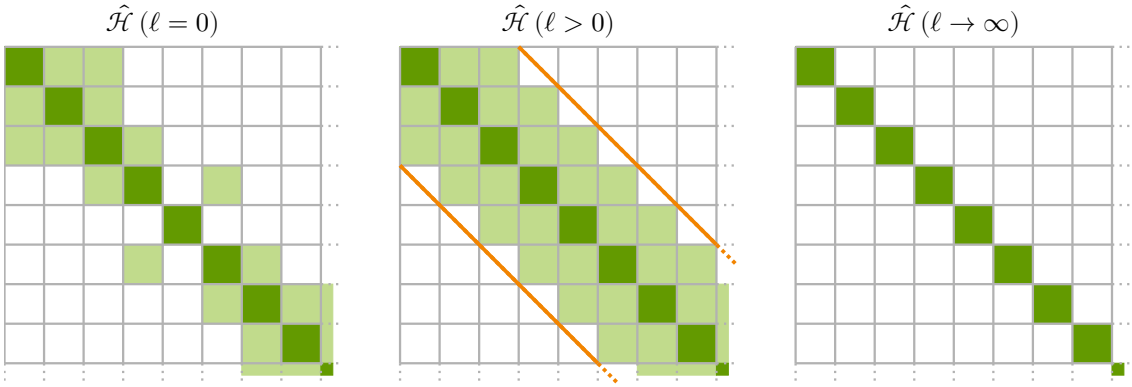

Figure 3.3: Illustration of the effect of the flow on a matrix induced by the Mielke generator. From left to right, the matrix is shown for different ℓ, at $\ell = 0$, during $\ell \geq 0$, and after the flow $\ell \to \infty$. Dark green squares stand for finite diagonal matrix elements, while light green squares indicate off-diagonal matrix elements. During the flow $\ell \geq 0$, the two diagonal orange lines illustrate the conservation of the band-diagonality as no new elements can become finite beyond the orange lines. After the flow, the matrix is diagonalized, and the eigenvalues are ordered according to energy.

where the matrix indices n, j from the Mielke generator are replaced by diagonal elements q_{nn}, q_{jj} of an arbitrary operator $\hat{Q}$. In the original articles [KU00; KSU03b], the operator $\hat{Q}$ counts the number of quasiparticles in the system. The operator $\hat{Q}$ remains unchanged throughout the flow, ensuring that its labeling with q_{nn}, q_{jj} also remains fixed. For a successful convergence of the flow equations, the operator $\hat{Q}$ will become a conserved quantity and thus $[\hat{\mathcal{H}}(\ell = \infty), \hat{Q}] = 0$ holds. Given the aforementioned fact, the name particle-conserving generator is appropriate. In conclusion, the effective Hamiltonian $\hat{\mathcal{H}}_{\text{eff}}$ resulting from the pc generator is only block-diagonal, in contrast to the diagonal form achieved by the Mielke or Wegner generator. Each block corresponds to a constant value of q_{nn} connected to the operator $\hat{Q}$. Henceforth, the operator $\hat{Q}$, associated with the pc generator used in this work, is the quasiparticle counting operator. Specifically, the operator $\hat{Q}$ counts the number of magnons in the system in this thesis.

As established in Section 3.2.2, using second quantization rather than a matrix representation can be advantageous for expressing flow equations. The pc generator is expressed in second quantization as

$$\hat{\eta}^{\text{pc}}(\ell) = \hat{\mathcal{H}}^{+}(\ell) - \hat{\mathcal{H}}^{-}(\ell) \ , \tag{3.37}$$

where the $(+)$ denotes terms that increase the number of particles, while $(-)$ terms correspond to terms that decrease the number of particles. Similar to how the Mielke generator preserves the band diagonality, the pc generator conserves the block-band-diagonal structure of the Hamiltonian, i.e., if the initial Hamiltonian contains no terms that increase or decrease the number of quasiparticles by n or more, such terms will not emerge in the flow. This property reduces computational effort for the pc generator. A schematic representation of a possible flow induced by the pc generator is presented in Fig. 3.4.

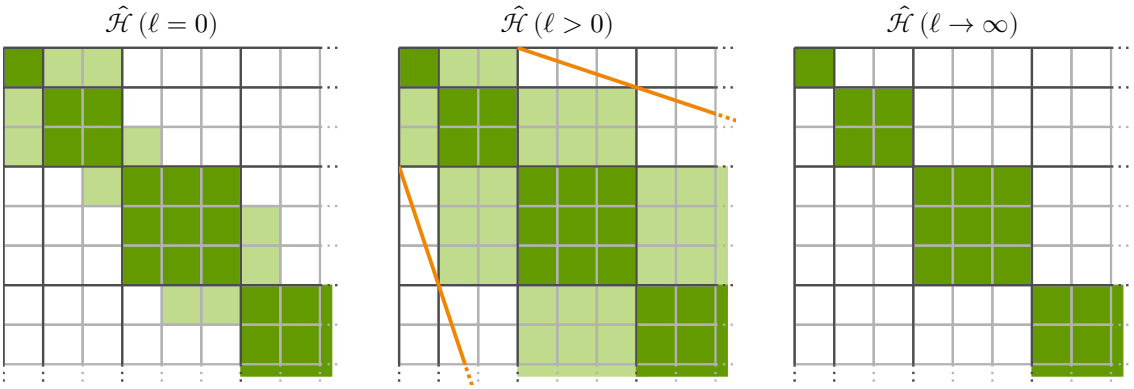

Figure 3.4: Effect of the flow on a matrix induced by the pc generator. From left to right, the matrix is shown for different ℓ, at $\ell = 0$, during $\ell \geq 0$, and after the flow $\ell \to \infty$. Dark green squares stand for finite matrix elements that do not alter the quasiparticle number, whereas light green squares do. Dark gray lines separate blocks corresponding to different effects on the quasiparticle number. During the flow $\ell \geq 0$, the two diagonal orange lines illustrate the conservation of the block-band-diagonality as no new elements can become finite beyond the orange lines. After the flow, the matrix is block-diagonal.

Analogous to the Mielke generator, the convergence of the pc generator is guaranteed provided that the spectrum of the Hamiltonian is bounded from below [KU00]. However, approximations introduced into the flow equations through various truncation schemes can negatively impact convergence, potentially leading to a non-converging flow despite the criterion being satisfied [DU04; Rei06]. Further, the pc generator produces an energy ordering that closely resembles that of the Mielke generator. The key difference lies in how the pc generator orders the energies h_{nn}. It sorts them according to the eigenvalues of the operator $\hat{Q}$

$$\operatorname{sign}(q_{nn} - q_{jj}) = \operatorname{sign}(h_{nn}(\ell = \infty) - h_{jj}(\ell = \infty)) \; . \tag{3.38}$$

Consequently, after convergence of the flow, subspaces with higher eigenvalues correspond to higher energies. Nevertheless, this condition does not hold in every case. Violations of this condition can occur either initially or during the flow, e.g., one-particle dispersion decays into the two-particle continuum at a specific momentum value. The Fig. 3.5 illustrates such a scenario where on the right-hand side, the one-particle dispersion overlaps with the two-particle continuum. As a consequence, the flow induced by the pc generator must rearrange the matrix elements. This process leads to an increase in off-diagonal elements, which can pose numerical problems, especially in conjunction with truncation, and ultimately lead to a divergent flow.

Thus far, only the Hermitian case for the pc generator has been considered. An application of the pc generator is also possible in the non-Hermitian case, which is relevant for this work. Even if $\hat{\mathcal{H}}^+ \neq (\hat{\mathcal{H}}^-)^\dagger$, it remains possible to assign the individual operators to either $\hat{\mathcal{H}}^+$ or $\hat{\mathcal{H}}^-$ respectively, thereby setting up the corresponding flow equations that lead to a continuous similarity transformation. However, conclusions about convergence cannot be drawn in the same way as in the Hermitian case. In Ref. [Pow17], the convergence for the non-Hermitian case of the pc generator is similarly analyzed as in Section 3.3.2 for the Mielke generator. By decomposing a non-Hermitian Hamiltonian into its Hermitian and anti-Hermitian components, it becomes evident that arguments supporting convergence of the flow cannot be applied in the same way as they are

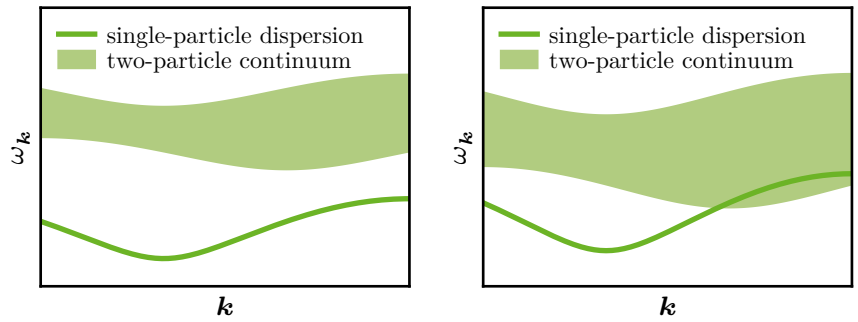

Figure 3.5: Schematic examples of a well-separated one-particle dispersion and two-particle continuum on the left-hand side, and an overlapping one-particle dispersion with the two-particle continuum on the right-hand side.

in the Hermitian case. The issue arises because the diagonal elements of a non-Hermitian matrix are not bounded by its lowest and highest eigenvalues. Hence, it is not possible to make general statements about the convergence of the pc generator in non-Hermitian cases due to the absence of universal theorems providing *a priori* information to support such statements [Pow17]. However, for non-Hermitian matrices with real eigenvalues, it is possible to derive convergence criteria similar to those in the Hermitian case [Sch22]. It should be emphasized that the absence of a rigorous proof for convergence does not rule out the existence of attractive fixed points in non-unitary flow equations. In the non-Hermitian cases, convergent fixed points for the pc generator also possess a block-diagonal structure.

To summarize, while the application of the pc generator is indeed possible in the non-Hermitian cases, it does not guarantee that an effective model will be obtained. This issue is further compounded by the fact that truncations can negatively affect the flow's success, as in Hermitian cases. For completeness, it is worth mentioning that the pc generator with specific adjustments can also be applied to open quantum systems. For this extension, the generator scheme is expanded to the generalized particle-conserving generator (gpc generator) where the sign function in Eq. (3.36) is generalized and replaced by a complex phase factor [SU22; Sch22]. This modification enables the gpc generator to address dissipative quantum systems described by Lindbladians [LSS23]. However, a detailed explanation is beyond the scope of this thesis.

3.3.4 Particle-Block-Separating Generator

For systems where the pc generator is not applicable, i.e., systems in which certain subspaces of $\hat{Q}$ overlap energetically and thus cause a divergent flow, it is possible to adopt a less ambitious approach. Specifically, the goal is to decouple only those subspaces where this issue does not arise. This is achievable using the so-called particle-block-separating generator (pbs generator) scheme proposed by Fischer, Duffe, and Uhrig [FDU10]. The pbs generator scheme imposes additional constraints compared to the pc generator, specifying which terms should be included in the generator and consequently vanish in the effective Hamiltonian. When the operator $\hat{Q}$ is again a particle counting operator, the pbs generator can be expressed in second quantization as

$$\hat{\eta}^{\mathrm{ps}}_{k:n}(\ell) = \sum_{j\leq k}\sum_{i>j}\left[\hat{\mathcal{H}}_{j\to i}(\ell) - \hat{\mathcal{H}}_{i\to j}(\ell)\right], \tag{3.39}$$

where the generator decouples and sorts the k lowest subspaces according to the particle number [DU11; FDU10]. This is accomplished by including only those terms that couple the k lowest

particle subspaces to the higher ones, such as terms like $\hat{\mathcal{H}}_{j\to i}$, which couple the j-th subspace to the i-th subspace. In contrast to the pc generator, the pbs generator does not necessarily preserve a block-band-diagonal structure of the Hamiltonian during the flow, and new elements can arise during the flow [Fis12]. Nevertheless, due to the reduced number of operators in the pbs generator compared to the pc generator, fewer commutators need to be evaluated. A schematic matrix representation illustrating a potential flow induced by the pc generator is shown in Fig. 3.4.

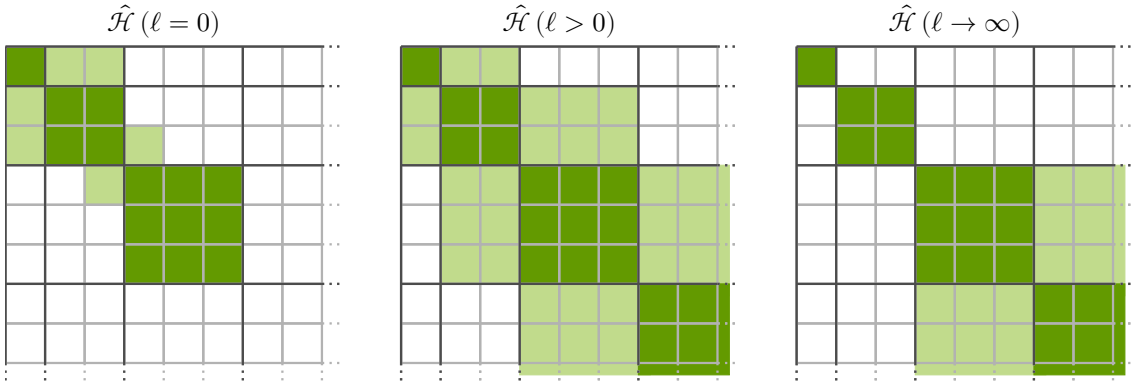

Figure 3.6: Effect of the flow on a matrix induced by the pbs generator for $k = 1$ decoupling the ground state and a single excitation from the remainder of the Hilbert space. From left to right, the matrix is shown for different ℓ, at $\ell = 0$, during $\ell \geq 0$, and after the flow $\ell \to \infty$. Dark green squares stand for finite diagonal matrix elements, while light green squares indicate off-diagonal matrix elements. Blocks for different effects on the quasiparticle number are divided by dark gray lines. During the flow $\ell \geq 0$, new elements may become finite. After the flow, the matrix is block-diagonal up to the number of quasiparticles selected in the pbs generator.

If the application of the pc generator scheme fails to yield a converging flow because of energetic overlaps between subspaces, the pbs generator can be used to determine a lower bound for subspaces where such overlaps are absent. This procedure can be achieved by incrementally increasing k until a non-converging flow equation is observed. For $k = 0$, the pbs generator tries to decouple the ground state from all excited states. If the flow fails to converge at this stage, it may indicate that the presumed phase becomes unstable or breaks down, and that the assumed ground state is evidently not the lowest-energy configuration. Instead, certain excitations within the particle representation exhibit lower energies than the presumed ground state. This indicator can even be used to analyze quantum phase transitions. Similar to the pc generator, it is also not possible to make statements about the convergence of the pbs generator in non-Hermitian cases.

In the context of the pbs generator, it is worth noting that alternative approaches exist to decouple the ground state from the excited states, one of which is formulated in matrix representation [DEO08]. However, since the present work employs the CST in second quantization, this approach is not further discussed.

In this work, the pbs generator is used only for $k = 0$ to decouple the ground state from higher particle subspaces. Consequently, rather than referring to it as the particle-block-separating generator with $k = 0$, it will henceforth be denoted simply as the $0n$ generator.

With the pc generator and pbs generator at hand, it is possible to set up flow equations for a plethora of models in second quantization and derive their effective Hamiltonians. Nevertheless,

as noted in Section 3.2.1, evaluating commutators in the flow equation, e.g., in Eq. (3.11), can lead to an operator basis that proliferates indefinitely. This issue can be mitigated by employing a truncation scheme, which is discussed in detail in the next section.

3.4 Truncation Schemes

The next necessary step is to examine truncation schemes in the context of the flow equation approach. Truncation schemes are crucial to obtain a closed set of differential equations. Even if a closed operator basis and thus a closed set of differential equations exists, the evaluation of these equations in the form of numerical integration can still become computationally too demanding. Thus, implementing a truncation scheme is also essential in such a case. Hence, both numerical and analytical considerations underscore the significance of employing a truncation scheme.

Selecting an appropriate truncation scheme is non-trivial as it significantly impacts the resulting effective model. For small systems, the impact of a truncation scheme can be analyzed explicitly, as demonstrated in one of the earliest applications of the method [KM94]. In that work, only terms present in the initial Hamiltonian were considered first. New terms were subsequently added, and the effective models, with and without them, were compared. If neglecting specific terms did not influence the effective model, the resulting truncation scheme was deemed justified. However, for larger systems, this manual approach becomes impractical. Instead, the truncation scheme should be physically justified *a priori*. Thus, the truncation scheme must be specifically tailored to the system and its physics under consideration.

Accordingly, truncation schemes are closely linked to the different realizations of the flow equation approach, as previously discussed in Section 3.2.1. A key distinction can be drawn between perturbative and non-perturbative realizations. In perturbative truncations, errors are tied to the order of the perturbation parameter, whereas in non-perturbative truncations, the errors stem solely from the truncation scheme. Although the estimation of truncation errors in non-perturbative approaches can sometimes be achieved analytically, this is often highly non-trivial [DFU11]. In most cases, however, comparing resulting effective models obtained under varying degrees of strictness in the truncation scheme provides valuable insights into possible truncation errors [Dre14].

The following section introduces three commonly used truncation schemes based on different approaches: the perturbative expansion, the spatial extension, and the scaling dimensions in momentum space. Since the first two schemes are not utilized in this thesis, they are only briefly described here. For further details, the reader is referred to the literature [Dre14; Sch22].

3.4.1 Perturbative Expansion

To apply a truncation scheme based on a perturbative expansion, the initial Hamiltonian must be expandable in order of a small perturbation parameter x. Realizations of the flow equation approach that utilize this type of truncation scheme to varying degrees, include the pCUT, the epCUT, and the deepCUT. In all these approaches, matrix elements or operators are tracked according to their dependence on the perturbation parameter x. Consequently, their contributions to the flow equations can be traced back to specific orders of the perturbation parameter. Given this premise, the flow equations are truncated at a specified order of the perturbation parameter x, with all higher-order terms being neglected. Of course, there are subtle differences among the different realizations pCUT, epCUT, and deepCUT in how the flow evaluations are set up and evaluated. However, these differences will not be explored in this context. The emphasis should

instead be on the fact that, in specific systems, the perturbation parameter x can serve as an appropriate choice for a truncation criterion.

In the context of perturbative truncation, discrete lattice systems provide a natural transition to another type of truncation scheme, the spatial extension, which will be discussed in the next section. This connection arises because operators connecting different sites are often proportional to the perturbation parameter x. Indeed, for models featuring only nearest-neighbor hopping terms, higher orders generally incorporate larger and larger spatial extensions, which can also be used to study critical behavior quantitatively [SWS24]. In such systems, the perturbative truncation is often similar to a truncation scheme based on the spatial extension of the operators.

3.4.2 Real-Space Extension

In gapped quantum systems on discrete lattices, the energy gap Δ is related to the correlation length ξ of the ground state of the system. Near the critical point, this relation takes the form

$$\Delta \propto \xi^{-z} \ , \tag{3.40}$$

where z is the dynamical critical exponent [Sac11]. The correlation length ξ characterizes the length scales over which physical correlations and processes extend within the system. As the energy gap closes, the correlation length diverges. Away from this critical point, the correlation length becomes finite; therefore, the range over which physical correlations and processes are relevant is also finite. This observation provides a basis for justifying a truncation scheme based on the spatial extent of the operators. Thus, operators should be represented in real space, as this allows their spatial extension to be measured. Moreover, for systems with translation invariance, the absolute position of an operator is irrelevant; instead, only its relative position to other operators matters. In this context, the maximal taxi-cab distance d between local creation or annihilation operators becomes a suitable measure to define the spatial extension of operator monomials [RMU04]. Based on their spatial extension, operators are either retained or truncated in the flow equations. It is important to note that the truncation via real-space extension must be used with caution in systems where the correlation length ξ is large. In such cases, the truncation scheme takes into account a minimal spatial extension $d_{\min}$. To ensure that all relevant processes are captured,

$$d_{\min} \overset{!}{\gtrsim} \xi \tag{3.41}$$

should hold when applying the truncation scheme. Therefore, this truncation scheme is only applicable to systems with a finite correlation length. The condition of Eq. (3.41) must be verified when scanning different parameters. In systems where the energy gap closes, the correlation length diverges, rendering this truncation scheme inappropriate. This limitation leads to the next truncation scheme, the truncation according to scaling dimensions.

3.4.3 Scaling Dimensions

Contrary to the previous truncation scheme, which is applied in real space, the scaling dimension truncation scheme is applied in momentum space. Early applications of this truncation scheme were within the context of the sine-Gordon model [Keh99; Keh01]. However, the specific realization of this truncation scheme, as presented below, has been successfully applied to spin-waves in the two-dimensional spin-$\frac{1}{2}$ antiferromagnetic Heisenberg model [PUS15; Pow17; PSU18]. The core concept behind this truncation scheme is to classify the relevance of operator monomials by their scaling behavior relative to an energy scale. The concept of scaling dimensions is not exclusive to

the flow equation approach. It also finds application in renormalization-group approaches [Car96] and in conformal field theories [FQS84]. Generally speaking, the scaling dimension answers the question of how important a contribution of a particular operator monomial is when zooming in on increasingly smaller energies.

The physical reasoning justifying the utilization of scaling dimension as a suitable indicator for assessing operator relevance in the flow equation approach for gapless systems unfolds as follows. In a gapless system, multi-particle continua are positioned directly adjacent to the dispersion connected to single particle excitations. For simplicity, in the following considerations, the energy gap is assumed to close at $\boldsymbol{k} = 0$. Therefore, multi-particle states in the vicinity of the lower band edges with a momentum $\boldsymbol{q}$ consist of a single particle with $\omega(\boldsymbol{q})$, combined with other particles with low-energy $\omega(\delta\boldsymbol{k}_i \approx 0)$ and correspondingly long wavelengths. This holds for all momenta $\omega(\boldsymbol{q})$, also for high momenta, as shown in the schematic in Fig. 3.7.

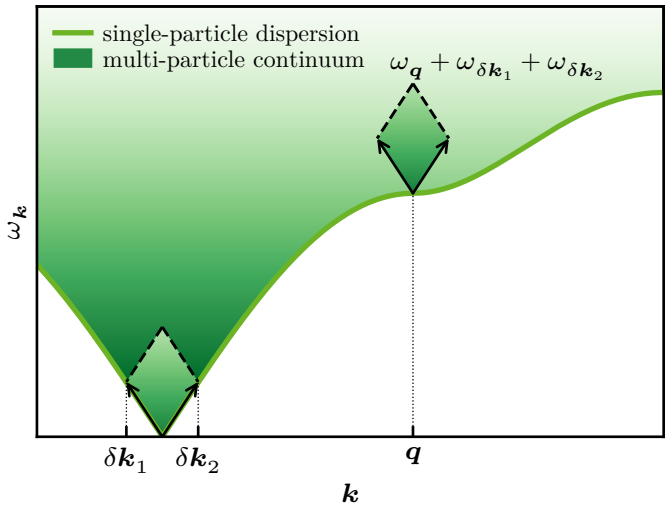

Figure 3.7: Schematic of a gapless single-particle dispersion with adjacent multi-particle continuum. Multi-particle states with momentum $\boldsymbol{q}$ close to the single-particle dispersion consist of a single particle with momentum $\boldsymbol{q}$ together with other particles with low-energy $\omega(\delta\boldsymbol{k}_i \approx 0)$. They are shown for three particles, but this also applies to an arbitrary number of particles.

Accordingly, renormalizations occurring during the flow are significantly influenced by processes associated with long wavelengths, even in regions where high energies and thus short wavelengths occur. Hence, accurately capturing the physics close to $\boldsymbol{k} \approx 0$ is essential. The use of scaling dimensions allows for the classification of an operator monomial's relevance when zooming in on smaller momenta and, consequently, smaller energies. Thus, a truncation based on the scaling dimension ensures that the most important contributions in the critical region near $\boldsymbol{k} = 0$ and, thus, the relevant multi-particle processes close to the entire dispersion are captured correctly.

Since this specific truncation scheme is employed in the course of this work, a thorough derivation to determine the scaling dimension of operator monomials in second quantization is provided below. This derivation is adopted from the aforementioned works [PUS15; Pow17; PSU18].

The rescaling properties of a single bosonic creation and annihilation operator in momentum space serve as a starting point. In a D-dimensional system, if the momentum is rescaled as

$$\boldsymbol{k} \to \lambda\boldsymbol{k} \quad \text{with} \quad \lambda < 1 \,, \tag{3.42}$$

the corresponding bosonic operator scales as follows

$$\hat{a}^\dagger_{\lambda \boldsymbol{k}} = \lambda^{-\frac{D}{2}} \hat{\tilde{a}}^\dagger_{\boldsymbol{k}} \ . \tag{3.43}$$

This scaling property can be derived from the commutator since it must remain invariant under momentum rescaling. Thus, the scaling property in Eq. (3.43) ensures that

$$\left[\hat{\tilde{a}}_{\boldsymbol{k}}, \hat{\tilde{a}}^\dagger_{\boldsymbol{k}'}\right] \stackrel{!}{=} \left[\hat{a}_{\boldsymbol{k}}, \hat{a}^\dagger_{\boldsymbol{k}'}\right] = \delta(\boldsymbol{k} - \boldsymbol{k}') \tag{3.44}$$

is satisfied. Upon establishing the scaling property of a single bosonic operator, the following step involves deriving the scaling property for a generic operator term

$$\mathcal{T} = \int_{\boldsymbol{k}_1,\ldots,\boldsymbol{k}_n \in \mathrm{BZ}} \delta\left(\pm \boldsymbol{k}_1 \pm \cdots \pm \boldsymbol{k}_2\right) C\left(\boldsymbol{k}_1, \ldots, \boldsymbol{k}_n\right) \mathcal{O}\left(\boldsymbol{k}_1, \ldots, \boldsymbol{k}_n\right) \mathrm{d}^D \boldsymbol{k}_1 \ldots \mathrm{d}^D \boldsymbol{k}_n \tag{3.45}$$

that occurs in the flow equations. In this context, $C\left(\boldsymbol{k}_1, \ldots, \boldsymbol{k}_n\right)$ represents a generic coefficient function. Furthermore, $\mathcal{O}\left(\boldsymbol{k}_1, \ldots, \boldsymbol{k}_n\right)$ denotes an operator monomial composed of n bosonic operators. The specific types of operators determine the signs in the delta function, conserving total momentum: a positive sign for momenta of a creation operator and a negative sign for momenta of an annihilation operator. All momenta $\boldsymbol{k}_i$ are integrated over the first Brillouin zone (BZ)(magnetic Brillouin zone (MBZ)).

The next step is to rescale all momenta. This is accomplished by zooming onto the low-energy region, scaling down the integration area with $\mathrm{BZ} \to \lambda\mathrm{BZ}$ where $\lambda < 1$. Thus, the infinitesimal elements in the integral change to

$$\begin{aligned} D\boldsymbol{k} &= \mathrm{d}^D \boldsymbol{k}_1 \ldots \mathrm{d}^D \boldsymbol{k}_n & (3.46)\\ &= \lambda^{nD} \mathrm{d}^D \tilde{\boldsymbol{k}}_1 \ldots \mathrm{d}^D \tilde{\boldsymbol{k}}_n \ , & (3.47) \end{aligned}$$

where each momentum is rescaled as $\boldsymbol{k}_i \to \lambda \tilde{\boldsymbol{k}}_i$, corresponding to the adaptation of the integration area. The full scaling behavior of $\mathcal{T}$ is revealed by analyzing the effects of rescaling in each factor of the integral in Eq. (3.45). Beginning with the delta function, it shows the following scaling behavior

$$\delta\left(\pm\lambda\tilde{\boldsymbol{k}}_1 \pm \cdots \pm \lambda\tilde{\boldsymbol{k}}_n\right) = \lambda^{-D} \delta\left(\pm\tilde{\boldsymbol{k}}_1 \pm \cdots \pm \tilde{\boldsymbol{k}}_n\right) \ . \tag{3.48}$$

For the operator monomial, the scaling property from Eq. (3.43) is applied, yielding

$$\mathcal{O}\left(\lambda\tilde{\boldsymbol{k}}_1, \ldots, \lambda\tilde{\boldsymbol{k}}_n\right) = \prod_{i=1}^{n} \lambda^{-\frac{D}{2}} \mathcal{O}\left(\tilde{\boldsymbol{k}}_i\right) = \lambda^{-\frac{nD}{2}} \mathcal{O}\left(\tilde{\boldsymbol{k}}_1, \ldots, \tilde{\boldsymbol{k}}_n\right) \ . \tag{3.49}$$

Lastly, the general scaling behavior of the coefficient function $C\left(\boldsymbol{k}_1, \ldots, \boldsymbol{k}_n\right)$ is not explicitly known. A reasonable approach is to expand it in a Taylor series in λ, centered around $\tilde{\boldsymbol{k}}_i = 0$, which gives

$$C\left(\lambda\tilde{\boldsymbol{k}}_1, \ldots, \lambda\tilde{\boldsymbol{k}}_n\right) = \sum_m c_m \left(\lambda\tilde{\boldsymbol{k}}_1, \ldots, \lambda\tilde{\boldsymbol{k}}_n\right) \lambda^m \ . \tag{3.50}$$

The leading order term in m determines the dominant contribution to the scaling behavior and is therefore used as the scaling dimension c of the coefficient function, yielding

$$C\left(\lambda\tilde{\boldsymbol{k}}_1, \ldots, \lambda\tilde{\boldsymbol{k}}_n\right) \approx \lambda^c C\left(\tilde{\boldsymbol{k}}_1, \ldots, \tilde{\boldsymbol{k}}_n\right) \ . \tag{3.51}$$

By combining these results, the overall scaling behavior of the generic operator term in Eq. (3.45) can be expressed as

$$\mathcal{T}(\lambda) = \lambda^{nD}\lambda^{-D}\lambda^{-\frac{nD}{2}}\lambda^{c}\mathcal{T}(1) = \lambda^{D(\frac{n}{2}-1)+c}\mathcal{T}(1) \ , \tag{3.52}$$

where the scaling dimension d of a general term $\mathcal{T}$ is defined by the exponent

$$d(D, n, c) \coloneqq D\left(\frac{n}{2} - 1\right) + c \ . \tag{3.53}$$

Using this expression, terms appearing in the flow equation can be classified. Terms with higher scaling dimensions are less significant for describing the system's low-energy physics. Therefore, terms with a scaling dimension d exceeding a specified threshold $d_{\max}$ are truncated while still preserving an accurate description of the relevant low-energy physics. The number of bosonic operators n within the operator monomial plays a crucial role in determining its relevance. For an increasing number of bosonic operators in the monomial, the relevance of the monomial diminishes. This diminishing relevance becomes even more pronounced as the system's dimensionality D increases. Terms involving a larger number of bosonic operators represent a multitude of fluctuations and interactions. However, in higher dimensions, these processes are suppressed or may even vanish entirely for $D \to \infty$. Similar effects are observed in mean-field calculations, where results become exact in the infinite-dimensional limit due to the disappearance of spatial quantum fluctuations [Geo+96; Vol12].

Concerning the influence of the coefficient function on the scaling behavior through the factor c, this factor increases the scaling dimension if the coefficient function is assumed not to diverge, i.e., $c \geq 0$. Consequently, a lower bound for the scaling dimension of a term can be defined as

$$d_{\min}(D, n) = D\left(\frac{n}{2} - 1\right) \ . \tag{3.54}$$

At the start of the flow, $\ell = 0$, the assumptions regarding the coefficient function can be verified analytically; however, as the flow progresses, the analytical form is lost, and this verification becomes impossible. Assuming that the coefficient function undergoes renormalization without divergence throughout the flow, the leading contribution and thus the scaling dimension of a term can only increase. As a result, the lower bound specified in Eq. (3.54) remains valid for all values of ℓ.

In previous works [PUS15; Pow17; PSU18], the truncation based on scaling dimension was applied in two dimensions, with a maximal scaling dimension set to $d_{\max} = 2$. Accordingly, all terms consisting of more than four bosonic operators were neglected, assuming $c \geq 0$. The truncation scheme in this work is applied similarly. Section 4.1 provides detailed information on which terms remain after applying the truncation scheme.

3.5 Termination Scheme — Residual-Off-Diagonality

In the evaluation of the flow equation of Eq. (3.17), integration up to $\ell \to \infty$ can be divided into two cases, one where an analytical evaluation is possible and another where falling back to a numerical evaluation becomes necessary. In the analytical case, integration up to the limit $\ell \to \infty$ is not an issue, for instance, in pCUT [KU00]. However, in the numerical case, this limit is not achievable, requiring termination of the integration at some finite ℓ.

One well-established termination criterion is the residual-off-diagonality (ROD) [RMU04; SU06; FDU10] which can be defined as

$$\mathrm{ROD}[H(\ell)] = \sqrt{\sum_{i,j;i\neq j} |h_{ij}(\ell)|^2} \tag{3.55}$$

in the matrix representation. The ROD for a matrix H describing a D-dimensional system measures the Euclidean norm of all off-diagonal terms h_{ij}, where $i \neq j$. An optional scaling factor $\frac{1}{D}$ can be included in its definition to facilitate comparison across matrices of varying dimensions [Sch22]. Moreover, in earlier definitions, the square root was omitted [RMU04]. However, when the flow equations do not require all off-diagonal elements to be rotated away, defining the ROD based on the corresponding generator is more appropriate.

In second quantization, the ROD for an arbitrary generator can be defined as

$$\mathrm{ROD}[\hat{\mathcal{H}}(\ell)] = \sqrt{\sum_i |\eta_i(\ell)|^2} \ , \tag{3.56}$$

where $\eta_i(\ell)$ represents a prefactor of an operator monomial in the generator $\hat{\eta}$. While exact definitions may vary, in this thesis, the ROD is defined precisely as in Eq. (3.56), without any normalization. Consequently, comparisons between flows of different system sizes are not feasible. Instead, the ROD serves as a worst-case estimate for the absolute numerical error in each flow.

Notably, regardless of its exact definition, a vanishing ROD corresponds to a convergent flow. Thus, if the ROD undercuts a specified threshold $\mathrm{ROD}[H(\ell)] < \mathrm{ROD}_{\mathrm{thres}}$, numerical integration is terminated and an effective model is obtained. However, in cases where a convergence of the flow does not occur, a divergent ROD indicates that obtaining an effective model is impossible. The reasons for such divergence were discussed in Section 3.3.

4 | Methodical Details

This chapter provides an overview of applying the flow equation approach to the antiferromagnetic spin-$\frac{1}{2}$ easy-axis XXZ model on a square lattice. As outlined in the final part of Chapter 2, linear spin-wave theory (L-SWT) and mean-field spin-wave theory (MF-SWT) reach their limits in accurately describing the high-energy physics of the model. The objective is now to apply a continuous similarity transformation (CST), since the final Hamiltonian is non-Hermitian due to the Dyson-Maleev representation (DM), as described in Section 2.5.

Throughout this chapter, the necessary methods for applying the CST and obtaining an effective model that describes emerging physical properties are presented. The primary emphasis will be on techniques for solving the emerging flow equations efficiently and elegantly. That entails exploring various discretization schemes, identifying applicable symmetries, and analyzing their implications for the flow equation. Furthermore, as effective models remain non-Hermitian, challenges associated with their non-Hermitian representation are addressed to enable the extraction of physical observables.

4.1 Implementation — Example of a Flow Equation

Beginning with the final Hamiltonian from Chapter 2, the objective is to perform a CST using the particle-conserving generator (pc generator) $\hat{\eta}^{\mathrm{pc}}$ alongside a truncation scheme based on the scaling dimension threshold of $d_{\max} = 2$, in order to derive an effective model. Additionally, adaptations are discussed for cases where the particle-block-separating generator with $k = 0$ ($0n$ generator) $\hat{\eta}^{\mathrm{pbs}}_{0:n}$ is used instead of the pc generator. The first step is to identify terms in the Hamiltonian that contribute to forming the generator η. For this purpose, the Hamiltonian of Eq. (2.93) is rewritten, with terms highlighted in colors classifying the number of magnons involved in a term

$$
\begin{aligned}
\hat{\mathcal{H}} = \; & C^{0} && \text{(4.1a)}\\
& + \sum_{\boldsymbol{k}_1,\boldsymbol{k}_2} \Big[C^{\hat{\alpha}^\dagger\hat{\alpha}}_{\boldsymbol{k}_1,\boldsymbol{k}_2} \hat{\alpha}^\dagger_{\boldsymbol{k}_1}\hat{\alpha}_{\boldsymbol{k}_2} + C^{\hat{\beta}^\dagger\hat{\beta}}_{\boldsymbol{k}_1,\boldsymbol{k}_2} \hat{\beta}^\dagger_{\boldsymbol{k}_1}\hat{\beta}_{\boldsymbol{k}_2} \\
& \qquad + C^{\hat{\alpha}^\dagger\hat{\beta}^\dagger}_{\boldsymbol{k}_1,\boldsymbol{k}_2} \hat{\alpha}^\dagger_{\boldsymbol{k}_1}\hat{\beta}^\dagger_{\boldsymbol{k}_2} + \underline{C^{\hat{\alpha}\hat{\beta}}_{\boldsymbol{k}_1,\boldsymbol{k}_2} \hat{\alpha}_{\boldsymbol{k}_1}\hat{\beta}_{\boldsymbol{k}_2}} \Big] && \text{(4.1b)}\\
& + \sum_{\boldsymbol{k}_1,\boldsymbol{k}_2,\boldsymbol{k}_3,\boldsymbol{k}_4} \Big[C^{\hat{\alpha}^\dagger\hat{\alpha}^\dagger\hat{\beta}^\dagger\hat{\beta}^\dagger}_{\boldsymbol{k}_1,\boldsymbol{k}_2,\boldsymbol{k}_3,\boldsymbol{k}_4} \hat{\alpha}^\dagger_{\boldsymbol{k}_1}\hat{\alpha}^\dagger_{\boldsymbol{k}_2}\hat{\beta}^\dagger_{\boldsymbol{k}_3}\hat{\beta}^\dagger_{\boldsymbol{k}_4} + \underline{C^{\hat{\alpha}\hat{\alpha}\hat{\beta}\hat{\beta}}_{\boldsymbol{k}_1,\boldsymbol{k}_2,\boldsymbol{k}_3,\boldsymbol{k}_4} \hat{\alpha}_{\boldsymbol{k}_1}\hat{\alpha}_{\boldsymbol{k}_2}\hat{\beta}_{\boldsymbol{k}_3}\hat{\beta}_{\boldsymbol{k}_4}} \\
& \qquad + C^{\hat{\alpha}^\dagger\hat{\alpha}^\dagger\hat{\alpha}\hat{\beta}^\dagger}_{\boldsymbol{k}_1,\boldsymbol{k}_2,\boldsymbol{k}_3,\boldsymbol{k}_4} \hat{\alpha}^\dagger_{\boldsymbol{k}_1}\hat{\alpha}^\dagger_{\boldsymbol{k}_2}\hat{\alpha}_{\boldsymbol{k}_3}\hat{\beta}^\dagger_{\boldsymbol{k}_4} + \underline{C^{\hat{\alpha}\hat{\beta}^\dagger\hat{\beta}\hat{\beta}}_{\boldsymbol{k}_1,\boldsymbol{k}_2,\boldsymbol{k}_3,\boldsymbol{k}_4} \hat{\alpha}_{\boldsymbol{k}_1}\hat{\beta}^\dagger_{\boldsymbol{k}_2}\hat{\beta}_{\boldsymbol{k}_3}\hat{\beta}_{\boldsymbol{k}_4}} \\
& \qquad + C^{\hat{\alpha}^\dagger\hat{\beta}^\dagger\hat{\beta}^\dagger\hat{\beta}}_{\boldsymbol{k}_1,\boldsymbol{k}_2,\boldsymbol{k}_3,\boldsymbol{k}_4} \hat{\alpha}^\dagger_{\boldsymbol{k}_1}\hat{\beta}^\dagger_{\boldsymbol{k}_2}\hat{\beta}^\dagger_{\boldsymbol{k}_3}\hat{\beta}_{\boldsymbol{k}_4} + \underline{C^{\hat{\alpha}^\dagger\hat{\alpha}\hat{\alpha}\hat{\beta}}_{\boldsymbol{k}_1,\boldsymbol{k}_2,\boldsymbol{k}_3,\boldsymbol{k}_4} \hat{\alpha}^\dagger_{\boldsymbol{k}_1}\hat{\alpha}_{\boldsymbol{k}_2}\hat{\alpha}_{\boldsymbol{k}_3}\hat{\beta}_{\boldsymbol{k}_4}} \\
& \qquad + C^{\hat{\alpha}^\dagger\hat{\alpha}^\dagger\hat{\alpha}\hat{\alpha}}_{\boldsymbol{k}_1,\boldsymbol{k}_2,\boldsymbol{k}_3,\boldsymbol{k}_4} \hat{\alpha}^\dagger_{\boldsymbol{k}_1}\hat{\alpha}^\dagger_{\boldsymbol{k}_2}\hat{\alpha}_{\boldsymbol{k}_3}\hat{\alpha}_{\boldsymbol{k}_4} + C^{\hat{\beta}^\dagger\hat{\beta}^\dagger\hat{\beta}\hat{\beta}}_{\boldsymbol{k}_1,\boldsymbol{k}_2,\boldsymbol{k}_3,\boldsymbol{k}_4} \hat{\beta}^\dagger_{\boldsymbol{k}_1}\hat{\beta}^\dagger_{\boldsymbol{k}_2}\hat{\beta}_{\boldsymbol{k}_3}\hat{\beta}_{\boldsymbol{k}_4} \\
& \qquad + C^{\hat{\alpha}^\dagger\hat{\alpha}\hat{\beta}^\dagger\hat{\beta}}_{\boldsymbol{k}_1,\boldsymbol{k}_2,\boldsymbol{k}_3,\boldsymbol{k}_4} \hat{\alpha}^\dagger_{\boldsymbol{k}_1}\hat{\alpha}_{\boldsymbol{k}_2}\hat{\beta}^\dagger_{\boldsymbol{k}_3}\hat{\beta}_{\boldsymbol{k}_4} \Big] . && \text{(4.1c)}
\end{aligned}
$$

For the application of both pc generator and $0n$ generator, it is crucial to classify further whether terms result in a net creation or annihilation of particles. Terms that annihilate more particles than they create are additionally highlighted by underlining. Focusing solely on the effects of the operators, the Hamiltonian can be symbolically abbreviated to

$$\hat{\mathcal{H}} = E + \Gamma_{1\to1} + \Gamma_{0\to2} + \underline{\Gamma_{2\to0}} + \mathcal{V}_{0\to4} + \underline{\mathcal{V}_{4\to0}} + \mathcal{V}_{1\to3} + \underline{\mathcal{V}_{3\to1}} + \mathcal{V}_{2\to2} \ . \tag{4.2}$$

Here, E, $\Gamma_{a\to c}$, $\mathcal{V}_{a\to c}$ represent the ground-state term, quadratic terms, and quartic terms, respectively. The subscripts $a \to c$ denote the numbers of annihilation and creation operators of magnons present in the labeled terms. Consequently, the pc generator $\hat{\eta}^{\mathrm{pc}}$ can be expressed in this representation as

$$\hat{\eta}^{\mathrm{pc}} = \Gamma_{0\to2} - \underline{\Gamma_{2\to0}} + \mathcal{V}_{0\to4} - \underline{\mathcal{V}_{4\to0}} + \mathcal{V}_{1\to3} - \underline{\mathcal{V}_{3\to1}} \ , \tag{4.3}$$

where the underlined terms acquire an additional minus sign, as outlined in Section 3.3.3. Similarly, the $0n$ generator $\hat{\eta}^{\mathrm{pbs}}_{0:n}$ decoupling solely the ground state can be extracted and yields

$$\hat{\eta}^{\mathrm{pbs}}_{0:n} = \Gamma_{0\to2} - \underline{\Gamma_{2\to0}} + \mathcal{V}_{0\to4} - \underline{\mathcal{V}_{4\to0}} \ . \tag{4.4}$$

Here, terms that couple to particle subspaces higher than $k > 0$ are omitted. To be precise, the particle-block-separating generator (pbs generator) $\hat{\eta}^{\mathrm{ps}}_{k:n}$ with $k > 0$ is identical to the pc generator within the given truncation scheme, and thus it is not further discussed. With the generators established, the next step involves determining the flow equation

$$\partial_\ell \hat{\mathcal{H}}(\ell) = \left[\hat{\eta}^{\mathrm{pc}}(\ell), \hat{\mathcal{H}}(\ell)\right] \quad \text{or} \quad \partial_\ell \hat{\mathcal{H}}(\ell) = \left[\hat{\eta}^{\mathrm{pbs}}_{0:n}(\ell), \hat{\mathcal{H}}(\ell)\right] \tag{4.5}$$

in second quantization as described in Section 3.2.2. The initial step is to determine an operator basis $\mathfrak{H} := \{A_i\}$ that complies with the truncation scheme. As previously discussed in Section 3.4.3, the truncation scheme employed is based on the scaling dimension of the operators. For a maximum scaling dimension of $d_{\max} = 2$, all operator monomials containing more than four bosonic operators are truncated. In the initial Hamiltonian Eq. (4.1) only quartic terms or lower are present. Hence, all operators from the initial Hamiltonian are included in the operator basis. Additional operators may emerge during the evaluation of the commutator in the flow equation Eq. (4.5). However, any newly emerging operators must comply with the truncation scheme. Since the Hamiltonian already contains all possible spin-conserving permutations up to quartic order of monomials, as outlined in Section 2.5.4, no new operators with a scaling dimension less than or equal to $d = 2$ can arise in this specific case. As a result, the operator basis consists solely of the initial operator monomials of Eq. (4.1). It is important to note that, with a truncation scheme allowing a higher scaling dimension $d > 2$, additional terms would be added to the operator basis and, consequently, to the generator. In such cases, the pc generator $\hat{\eta}^{\mathrm{pc}}$ and pbs generator $\hat{\eta}^{\mathrm{ps}}_{k:n}$ with $k > 0$ would no longer be identical *a priori*. With all relevant terms identified, it becomes possible to illustrate the effects of the two distinct flow equations in a similar manner previously depicted for the general cases in Figs. 3.4 and 3.6. In Fig. 4.1, the different occurring terms are displayed according to their actions within different particle subspaces.

In second quantization, the operator monomials remain constant during the flow, while only their prefactors exhibit ℓ-dependence. Thus, in what follows, the flow equations for the coefficients are derived by evaluating the commutator and matching corresponding coefficients. Rather than showing all relevant flow equations for each coefficient, only an example is provided here. The remaining flow equations are listed in Appendix B. The distinction between pc generator $\hat{\eta}^{\mathrm{pc}}$ and $0n$ generator $\hat{\eta}^{\mathrm{pbs}}_{0:n}$ lies solely in the absence of the $\mathcal{V}_{1\leftrightarrow3}$ terms. Therefore, to keep it concise, terms that exist in both flow equations are not colored, but terms only present in the $0n$ generator flow equations are highlighted in blue, while terms only present in pc generator flow equations are

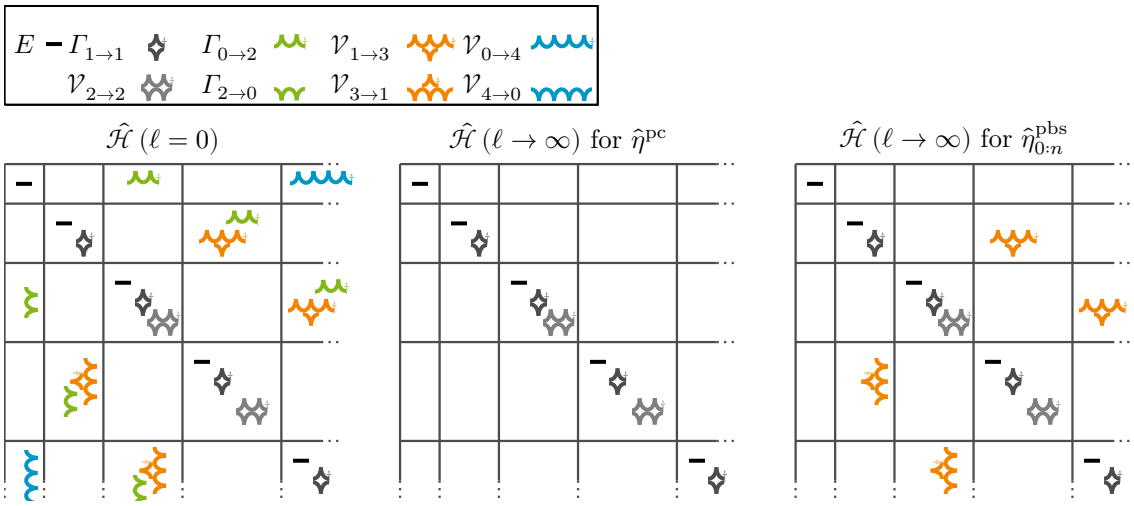

Figure 4.1: The image consists of three matrix representations of different stages of a Hamiltonian, each showing all terms acting within a different particle subspace. The number of creation operators in a term is represented by waves annotated with †, while the other waves without annotation indicate annihilation operators. On the left panel, the initial Hamiltonian is displayed, showing all present operators. In the middle panel, the effective Hamiltonian after applying the flow with the pc generator is depicted. At this stage, only particle-conserving terms remain. Finally, in the right panel, the effective Hamiltonian resulting from the flow with the $0n$ generator $\hat{\eta}^{\mathrm{pbs}}_{0:n}$ is depicted, with only the ground state decoupled.

highlighted in orange. Furthermore, there also exist terms that differ only by a prefactor between the two flow equations. These terms are indicated by the notation $\{x|y\}$, which means that the first value in blue x is used in the $0n$ generator flow equations and the second value in orange y in the pc generator flow equations. By evaluating the commutator with respect to the coefficient functions, one part of the resulting expression may take the following form

$$
\begin{aligned}
\left[\left\{\hat{\eta}^{\mathrm{pbs}}_{0:n}(\ell)|\hat{\eta}^{\mathrm{pc}}(\ell)\right\}, \hat{\mathcal{H}}(\ell)\right] = \ldots \quad & \Bigg(-2C^{\hat{\alpha}\hat{\beta}}_{\boldsymbol{k}_2,-\boldsymbol{k}_2}(\ell) C^{\hat{\alpha}^\dagger\hat{\beta}^\dagger}_{\boldsymbol{k}_1,-\boldsymbol{k}_2}(\ell) \\
& \sum_{\boldsymbol{k}_3} \Big[-\{2|4\}\, C^{\hat{\alpha}\hat{\beta}}_{\boldsymbol{k}_3,-\boldsymbol{k}_3}(\ell) C^{\hat{\alpha}^\dagger\hat{\alpha}^\dagger\hat{\alpha}\hat{\beta}^\dagger}_{\boldsymbol{k}_1,\boldsymbol{k}_3,\boldsymbol{k}_2,-\boldsymbol{k}_3}(\ell) \\
& \qquad -\{2|4\}\, C^{\hat{\alpha}^\dagger\hat{\beta}^\dagger}_{\boldsymbol{k}_3,-\boldsymbol{k}_3}(\ell) C^{\hat{\alpha}^\dagger\hat{\alpha}\hat{\alpha}\hat{\beta}}_{\boldsymbol{k}_1,\boldsymbol{k}_2,\boldsymbol{k}_3,-\boldsymbol{k}_3}(\ell) \Big] \\
& \sum_{\boldsymbol{k}_3,\boldsymbol{k}_4} \Big[-4C^{\hat{\alpha}^\dagger\hat{\alpha}\hat{\alpha}\hat{\beta}}_{\boldsymbol{k}_1,\boldsymbol{k}_3,\boldsymbol{k}_4,\boldsymbol{k}_2-\boldsymbol{k}_3-\boldsymbol{k}_4}(\ell) C^{\hat{\alpha}^\dagger\hat{\alpha}^\dagger\hat{\alpha}\hat{\beta}^\dagger}_{\boldsymbol{k}_3,\boldsymbol{k}_4,\boldsymbol{k}_2,\boldsymbol{k}_2-\boldsymbol{k}_3-\boldsymbol{k}_4}(\ell) \\
& \qquad -16C^{\hat{\alpha}\hat{\alpha}\hat{\beta}\hat{\beta}}_{\boldsymbol{k}_2,\boldsymbol{k}_3,\boldsymbol{k}_4,-\boldsymbol{k}_2-\boldsymbol{k}_3-\boldsymbol{k}_4}(\ell) C^{\hat{\alpha}^\dagger\hat{\alpha}^\dagger\hat{\beta}^\dagger\hat{\beta}^\dagger}_{\boldsymbol{k}_1,\boldsymbol{k}_3,\boldsymbol{k}_4,-\boldsymbol{k}_2-\boldsymbol{k}_3-\boldsymbol{k}_4}(\ell) \Big] \Bigg) \\
& \delta(\boldsymbol{k}_1-\boldsymbol{k}_2)\, \hat{\alpha}^\dagger_{\boldsymbol{k}_1}\hat{\alpha}_{\boldsymbol{k}_2} \ldots \ .
\end{aligned}
\tag{4.6}
$$

For illustration purposes, only the contributions proportional to $\hat{\alpha}^\dagger_{\boldsymbol{k}_1}\hat{\alpha}_{\boldsymbol{k}_2}$ are displayed here. Comparing the coefficient proportional to $\hat{\alpha}^\dagger_{\boldsymbol{k}_1}\hat{\alpha}_{\boldsymbol{k}_2}$ on both sides of Eq. (4.5), the flow equation for

the coefficient function $C^{\hat{\alpha}^\dagger\hat{\alpha}}_{\boldsymbol{k}_1,\boldsymbol{k}_2}$, as defined in the end of Section 2.5.4, is obtained and reads

$$\begin{aligned}\partial_\ell C^{\hat{\alpha}^\dagger\hat{\alpha}}_{\boldsymbol{k}_1,\boldsymbol{k}_2} =& -2C^{\hat{\alpha}\hat{\beta}}_{\boldsymbol{k}_2,-\boldsymbol{k}_2} C^{\hat{\alpha}^\dagger\hat{\beta}^\dagger}_{\boldsymbol{k}_1,-\boldsymbol{k}_2} \\ &- \{2|4\}\, C^{\hat{\alpha}\hat{\beta}}_{\boldsymbol{k}_3,-\boldsymbol{k}_3} C^{\hat{\alpha}^\dagger\hat{\alpha}^\dagger\hat{\alpha}\hat{\beta}^\dagger}_{\boldsymbol{k}_1,\boldsymbol{k}_3,\boldsymbol{k}_2,-\boldsymbol{k}_3} \\ &- \{2|4\}\, C^{\hat{\alpha}^\dagger\hat{\beta}^\dagger}_{\boldsymbol{k}_3,-\boldsymbol{k}_3} C^{\hat{\alpha}^\dagger\hat{\alpha}\hat{\alpha}\hat{\beta}}_{\boldsymbol{k}_1,\boldsymbol{k}_2,\boldsymbol{k}_3,-\boldsymbol{k}_3} \\ &-4C^{\hat{\alpha}^\dagger\hat{\alpha}\hat{\alpha}\hat{\beta}}_{\boldsymbol{k}_1,\boldsymbol{k}_3,\boldsymbol{k}_4,\boldsymbol{k}_2-\boldsymbol{k}_3-\boldsymbol{k}_4} C^{\hat{\alpha}^\dagger\hat{\alpha}^\dagger\hat{\alpha}\hat{\beta}^\dagger}_{\boldsymbol{k}_3,\boldsymbol{k}_4,\boldsymbol{k}_2,\boldsymbol{k}_2-\boldsymbol{k}_3-\boldsymbol{k}_4} \\ &- 16C^{\hat{\alpha}\hat{\alpha}\hat{\beta}\hat{\beta}}_{\boldsymbol{k}_2,\boldsymbol{k}_3,\boldsymbol{k}_4,-\boldsymbol{k}_2-\boldsymbol{k}_3-\boldsymbol{k}_4} C^{\hat{\alpha}^\dagger\hat{\alpha}^\dagger\hat{\beta}^\dagger\hat{\beta}^\dagger}_{\boldsymbol{k}_1,\boldsymbol{k}_3,\boldsymbol{k}_4,-\boldsymbol{k}_2-\boldsymbol{k}_3-\boldsymbol{k}_4}\,. \end{aligned} \tag{4.7}$$

For the sake of simplicity and enhanced readability, some aspects in the equation above have been deliberately omitted. First, the ℓ-dependency is now represented implicitly within the coefficients. Second, all explicit sums over momenta $\boldsymbol{k}_i$ are omitted. Instead, any momentum not explicitly appearing on the left-hand side is implicitly summed over. As before, all momenta are restricted to the first Brillouin zone (BZ) or magnetic Brillouin zone (MBZ) depending on the model. The flow equation for the pc generator $\hat{\eta}^{\mathrm{pc}}$ includes all terms, whereas in the flow equation for the $0n$ generator $\hat{\eta}^{\mathrm{pbs}}_{0:n}$, the colored term must be neglected.

At this point, a remark is necessary regarding the last momentum of each coefficient in the right-hand side of the flow equations. The sum of different momenta stems from the combination of commutations and evaluating delta functions during the setup of the flow equations. In contrast to the other momenta, this last momentum is not guaranteed to fall within the first BZ(MBZ). Before shifting this last momentum back into the first BZ(MBZ), it must be considered that, as already discussed in Section 2.5.2, the periodicity of the coefficients can be altered by different choices of gauges in the Fourier transformation. Thus, this shifting may introduce an additional phase factor to the coefficient when the last momentum is shifted back into the first BZ(MBZ). In the following, applying different symmetries can lead to subtle differences in the flow equations, and if not handled properly, can even cause a divergent flow. In the following Section 4.3, this issue is addressed in more detail.

Once all flow equations for the coefficients are determined, see Appendix B, along with their initial values, see Appendix A, it becomes possible to carry out the CST for both the XXZ model on a square lattice using either pc generator or $0n$ generator. However, one critical aspect remains unaddressed up to this point. The flow equations include sums over momentum within the first BZ(MBZ). Since the flow equations are solved numerically, it is important to examine different discretization schemes for the first BZ(MBZ). The following section discusses in detail the different discretization schemes for both BZ and MBZ, depending on the model.

4.2 Discretization Schemes

This section provides detailed insights into the discretization schemes of the momentum space employed throughout this thesis. The primary aim is to discretize either the first BZ or the first MBZ, depending on the model under investigation. The necessity of these discretization schemes arises from the fact that the flow equations are numerically solved in the momentum space.

Generally, the objective is to derive results that correspond to the thermodynamic limit. To reach this limit, the flow equations need to be considered in the continuum limit, wherein all momentum sums are converted into integrals. Under these conditions, however, the flow equations are non-linear integrable differential equations, for which obtaining an analytical solution is unattainable.

Instead, discretizing the BZ(MBZ) is required to enable a numerical treatment of the corresponding system of differential equations. To recover results in the thermodynamic limit from such discrete calculations, it is necessary to perform a finite-size extrapolation of all relevant parameters.

Furthermore, it is important to note that subtle differences exist among various implementations of discretization schemes, as discussed in the following. Nevertheless, all discretization schemes share the property of ensuring the conservation of momentum as required by all delta functions within any coefficient function. As a consequence, only discretization schemes with equidistant spacing between discretization points are applicable.

4.2.1 Boundary Conditions — One-Dimensional Discretization

The applied discretization schemes can be divided into two categories based on the system's boundary conditions: periodic and antiperiodic. To better understand the two discretization schemes, it is helpful to first consider a 1D chain with L sites, where the lattice constant is set to unity. For periodic boundary conditions, shifting the system by L sites leaves it unchanged. Thus, a bosonic operator $\hat{a}_{i+L} = \hat{a}_i$ maps directly onto itself. This behavior corresponds to the Fourier transformation of a discretized system with the momenta $\boldsymbol{k} = 2\pi\frac{n}{L}$, where n only assumes *integer* values. However, for antiperiodic boundary conditions, shifting the system by L sites induces a phase factor in the form of a minus sign. Consequently, for a shifted bosonic operator $\hat{a}_{i+L} = -\hat{a}_i$ applies, while for a shift of $2L$, it maps onto itself. In terms of the discretized Fourier transformation, this corresponds to momenta $\boldsymbol{k} = 2\pi\frac{n}{L}$ where n can only assume *half-integer* values. From here onward, discretizations with periodic and antiperiodic boundary conditions will be denoted as N_p and N_ap, respectively.

To achieve discretization of the first BZ(MBZ), the discretized k_i-points must satisfy $k_i \in 2\pi m$ for $m \in [-0.5, 0.5)$. In this interval, the lower edge is included, and the upper edge is excluded to ensure unambiguous assignment. The discretization of m for an L-sized system can be expressed for the two different cases as

$$m_{N_\mathrm{p}}(l) = -\frac{L - (L \bmod 2)}{2L} + \frac{2l}{2L} \qquad \text{for} \quad l \in \{0, 1, 2, \dots, L-1\} \tag{4.8a}$$

$$m_{N_\mathrm{ap}}(l) = -\frac{L - (1 - (L \bmod 2))}{2L} + \frac{2l}{2L} \qquad \text{for} \quad l \in \{0, 1, 2, \dots, L-1\}\ . \tag{4.8b}$$

Furthermore, each of these cases is further subdivided based on whether the system size L is even or odd. Altogether, this results in four different cases, as illustrated in Fig. 4.2. The key distinction between the two boundary conditions is that, for both N_p cases $m = 0$ is included, and consequently $k = 0$ is as well. In contrast, for the N_ap cases, $m = 0$ is excluded, along with $k = 0$. Among the same boundary conditions, the distinction between even and odd system size lies in whether the lower edge $m = -0.5$ is included. As illustrated in Fig. 4.2, only N_p with even L, and N_ap with odd L, include the lower edge. Finally, the discretization points for two different system sizes, $L = 4$ and $L = 5$, are explicitly calculated to illustrate the discretization points for each of the four cases. In a system size of $L = 4$ the N_p and N_ap discretization points are given by

$$m_{N_\mathrm{p}}^{L=4}(l) \in \{-0.5, -0.25, 0, 0.25\} \qquad \text{and} \qquad m_{N_\mathrm{ap}}^{L=4}(l) \in \{-0.375, -0.125, 0.125, 0.375\} \tag{4.9a}$$

and for $L = 5$ the discretization points for both boundary conditions are

$$m_{N_\mathrm{p}}^{L=5}(l) \in \{-0.4, -0.2, 0, 0.2, 0.4\} \qquad \text{and} \qquad m_{N_\mathrm{ap}}^{L=5}(l) \in \{-0.5, -0.3, -0.1, 0.1, 0.3\} \tag{4.9b}$$

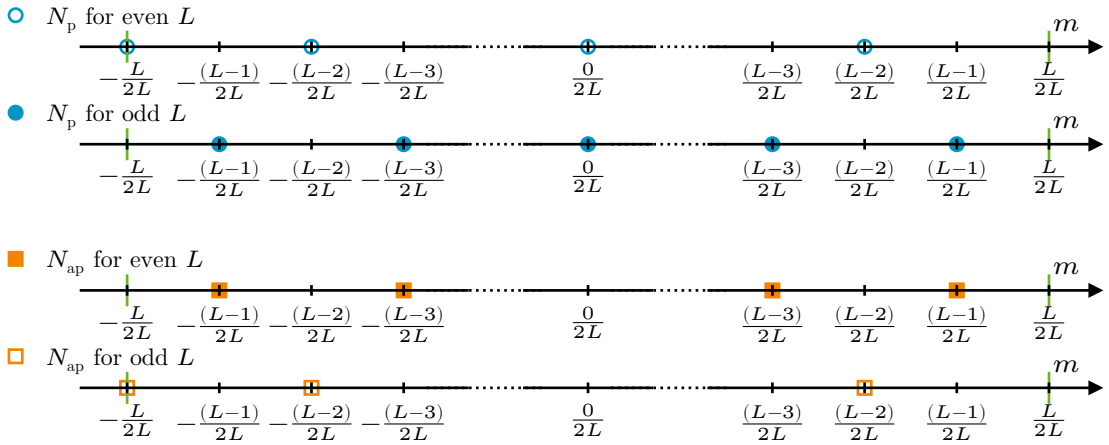

Figure 4.2: Sketch of the four different discretization schemes for m in one dimension. Circular markers represent periodic boundary conditions, whereas square markers indicate antiperiodic boundary conditions. Unfilled markers denote that the discretization scheme includes the lower edge of the BZ. Green vertical lines indicate the boundaries of the first BZ.

4.2.2 Boundary Conditions — Two-Dimensional Discretization

Having discussed the one-dimensional discretization scheme, the next step is to extend it to two dimensions. In a two-dimensional system, momentum within the first BZ(MBZ) can be expressed as

$$\boldsymbol{k} = m_1 \boldsymbol{b}_1 + m_2 \boldsymbol{b}_2 \quad \text{with} \quad m_i \in [-0.5, 0.5) \ , \tag{4.10}$$

where $\boldsymbol{b}_i$ are reciprocal lattice vectors. Since both m_i lie in the same range as before, the same discretization schemes used for the one-dimensional case can be employed to discretize the values of m_i. It is possible to apply distinct boundary conditions or varying discretization sizes L for each m_i separately. However, due to system symmetries, it is advantageous to use identical boundary conditions and discretization sizes for both m_i. Figure 4.3 depicts the four different discretization schemes in two dimensions, showing examples for even $L = 4$ and odd $L = 5$. Additionally, the lower panels of Fig. 4.3 display the resulting discretization of a true first BZ(MBZ) for various lattices, when the discretization scheme is translated via Eq. (4.10) into real momentum coordinates. Manifestly, in two dimensions, a linear discretization size of L yields L^2 discretization points within the first BZ(MBZ). However, in the following, references to system size exclusively pertain to the linear size L.

Why is it necessary to distinguish between the different discretization schemes? Firstly, in certain models, specific points such as the center of the BZ(MBZ), denoted by $\boldsymbol{k} = (0, 0)$ and commonly referred to as the Γ-point, exhibit divergent behavior in the analytical solution of specific coefficients. In an analytical integration within the thermodynamic limit, this divergence does not pose a problem since it is integrable. Ultimately, however, analytical integration of the flow equations is not possible, and they are solved numerically. Nevertheless, numerical algorithms exist to address singularities, e.g., the Tanh-sinh quadrature [TM73], by adapting the distance between interpolation points. However, these methods are not applicable to the flow equations because maintaining equidistant spacing between discretization points is mandatory to ensure momentum conservation. Therefore, the solution to circumvent singularities is to either set all points with singularities to zero or employ a discretization scheme that does not contain points with singularities. Here,

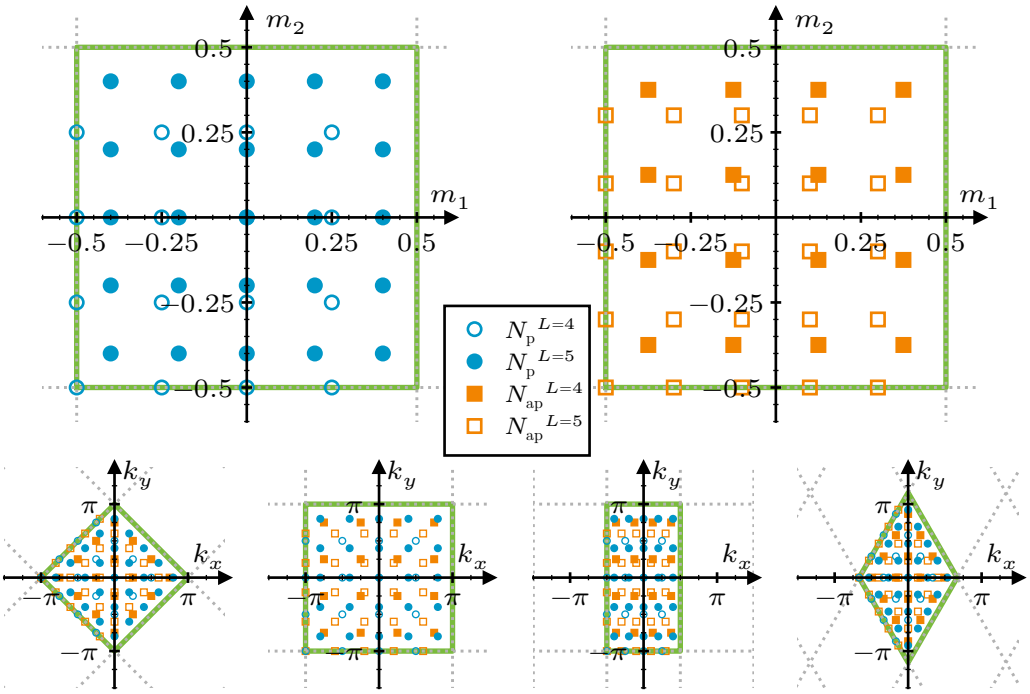

Figure 4.3: Sketch of the four distinct discretization schemes in two dimensions. Two discretization sizes L are considered, one even $L = 4$ and one odd $L = 5$. The upper panels depict the discretizations of m_1 and m_2. The lower panels illustrate possible resulting discretizations of $\boldsymbol{k}$, derived using the relation of Eq. (4.10). Circular markers indicate periodic boundary conditions N_p, whereas square markers represent antiperiodic boundary conditions N_ap. Unfilled markers are used for discretization schemes that include the lower edges of the BZ(MBZ). Green lines mark the boundaries of the first BZ(MBZ).

both options are applicable. For an antiperiodic N_{ap} discretization the Γ-point is simply excluded, whereas for periodic N_{p} discretization, coefficient containing the Γ-point are set to zero.

Additionally, other momenta in the BZ(MBZ), e.g., along specific high-symmetry paths, can be included or excluded based on the chosen discretization scheme. For instance, this applies to the edges of the BZ(MBZ) that contain high-symmetry points, such as the center of an edge or the corner points of the BZ(MBZ). In the case of the square lattice as it will be discussed in Chapter 5, only even N_{p} and odd N_{ap} discretization schemes include the R-point, the corner of the BZ(MBZ). Meanwhile, solely even N_{p} sample the M-point, a center of an edge.

Depending on the points of interest, the discretization scheme must be chosen accordingly to avoid the necessity of interpolation. Furthermore, in a finite-size analysis, all subtle differences among the discretization schemes must be accounted for, as they may lead to varying finite-size effects. In summary, comparing different discretization schemes helps minimize biases introduced by a single discretization scheme, which may negatively influence the results. It is also possible to trace back occurring effects related to the inclusion or exclusion of specific points in the BZ(MBZ).

Another important aspect to consider when using different discretization schemes is the behavior of momentum addition. When adding two momenta from a chosen discretization scheme for a given system size, the resulting momentum is not guaranteed to belong to the same discretized set. In the case of adding two momenta from a N_{p} discretization, the resulting momentum also belongs to the N_{p} discretization. Therefore, periodic boundary conditions N_{p} do not impose any restrictions on momentum addition for either the Hamiltonian or additional observables. Conversely, when adding two momenta from a N_{ap} discretization, the resulting momentum belongs to a N_{p} discretization. Consequently, when working with antiperiodic boundary conditions N_{ap}, all momentum additions in the flow equations need to be an uneven number of momenta from the N_{ap} set. This ensures that the resulting momentum remains within the N_{ap} discretization, as the addition of a N_{ap} momentum with a N_{p} momentum always yields a N_{ap} momentum. In the previously discussed Hamiltonian, only sums involving an odd number of momenta are present. As a consequence, all momenta connected to bosonic operators must be chosen from N_{ap} discretization scheme to ensure momentum conservation. However, the situation changes for additional observables that include an overall momentum $\boldsymbol{Q}$. In this case, using N_{ap} momenta for all bosonic operators is only feasible if the momentum $\boldsymbol{Q}$ is chosen from a N_{p} discretization when the total number of bosonic operators is even, and from a N_{ap} discretization when the total number of bosonic operators is odd.

With the discretization schemes now established, attention can be refocused on evaluating the flow equations. Any momentum sums in the flow equations can now be evaluated using the chosen discretization scheme. To establish an understanding of the complexity of the set of differential equations, the scaling of the number of parameters to track with the linear system size L is first discussed. For instance, the quadratic coefficient $C^{\hat{\alpha}^\dagger\hat{\alpha}}_{\boldsymbol{k}_1,\boldsymbol{k}_2}$ from Eq. (4.7) contains L^2 distinct entries, as the last momentum is determined via conservation of momentum. Given the intrinsic periodicity of all coefficients, it is sufficient to consider only a single representative of each coefficient. Thus, the last momentum is always chosen to be within the first BZ(MBZ) in accordance with the discretization of Eq. (4.10), to reach a unambiguous representation of a coefficient. Therefore, whether it is negative or expressed as a sum in practice, it is always folded back into the first BZ(MBZ), in accordance with the delta function associated with the coefficient. Nevertheless, the parameters to be tracked in a quartic term remain significantly larger even with momentum conservation. For an exemplary coefficient $C^{\hat{\alpha}^\dagger\hat{\alpha}\hat{\beta}^\dagger\hat{\beta}}_{\boldsymbol{k}_1,\boldsymbol{k}_2,\boldsymbol{k}_3,\boldsymbol{k}_4}$, L^6 distinct entries have to be considered. In total, there are 14 different coefficients to track. Of these 14 coefficients, nine are quartic, four are quadratic, and one is a constant representing the ground-state energy C^0. Thus, the total size

of the coefficient vector can be directly calculated, yielding

$$\#\text{elements} = 9L^6 + 4L^2 + 1 \tag{4.11}$$

depending on the linear system size L. Further, it is important to note that each coefficient is governed by its own flow equation, and possible additional coefficients of observables are not taken into consideration in this calculation. As a result, managing the system of flow equations, along with all its coefficients, becomes numerically demanding even for coarse discretizations. System sizes around $L = 12$ already push the limits of current personal computers. High-performance computing clusters become necessary to handle larger system sizes up to $L = 20$, without delving into the specifics of their configurations. As computational effort drastically increases with increasing system size, it is crucial to employ all available simplifications to minimize computational demands. As is often the case in physics, intrinsic symmetries provide also in this case remedy. The next section introduces different symmetries that are employed to reduce the computational effort required for solving the flow equations.

4.3 Symmetries

This section explores various symmetries that can be leveraged to reduce computational effort and enhance numerical stability when solving the flow equations. Two specific categories of symmetries are discussed below. The first category arises from the $\mathcal{PT}$-symmetry of the non-Hermitian Hamiltonian emerging from the utilization of the DM. In this context, $\mathcal{P}$ denotes parity-inversion symmetry, while $\mathcal{T}$ corresponds to time-reversal symmetry. The second category considers intrinsic symmetries within individual coefficient functions arising from the model's underlying lattice.

4.3.1 Symmetries — Hamiltonian

The Ref. [Wal24] provides an in-depth discussion of the $\mathcal{PT}$-symmetry of the non-Hermitian Hamiltonian derived from the spin-wave theory (SWT) combined with the DM. Here, only the key aspects are summarized.

The initial antiferromagnetic Heisenberg model (afHM) of Eq. (2.26) is inherently $\mathcal{T}$-symmetric. Since $\mathcal{T}$-symmetry inverts the direction of time, momentum, and angular momentum, the spin operators transform as

$$\hat{S}^z \xrightarrow{\mathcal{T}} -\hat{S}^z \quad \text{and} \quad \hat{S}^{\mp} \xrightarrow{\mathcal{T}} -\hat{S}^{\pm} \tag{4.12}$$

leaving the Heisenberg Hamiltonian invariant, as they only occur in products of even numbers of spins. However, the classical Néel state is not invariant under time-reversal $\mathcal{T}$-symmetry. In the employed nonlinear spin-wave theory (NL-SWT) or self-consistent nonlinear spin-wave theory (scNL-SWT) based on the DM, the Néel state serves as the reference state around which bosonic excitations are described. Consequently, the resulting Hamiltonian inherits this property of the Néel state and is likewise not invariant under $\mathcal{T}$-symmetry. Similarly, $\mathcal{P}$-symmetry applied to the Hamiltonian alone does not leave it invariant. Nevertheless, the combination of both symmetries, $\mathcal{P}$ and $\mathcal{T}$, leaves both the Hamiltonian and the ground state invariant. For the Néel state, it can be visualized as follows. The $\mathcal{T}$-symmetry flips the spins to the opposite direction, while $\mathcal{P}$-symmetry further inverts the position of the spins around the center of a bond, effectively mapping them back to their original configuration in the initial Néel state.

This leads to a non-Hermitian Hamiltonian exhibiting $\mathcal{PT}$-symmetry, which connects $\hat{a}^{(\dagger)}$ and $\hat{b}^{(\dagger)}$ to each other. Following the Fourier transformation and the Bogoliubov transformation, the $\mathcal{PT}$-symmetry remains valid, now connecting $\hat{\alpha}^{(\dagger)}$ and $\hat{\beta}^{(\dagger)}$. This symmetry can be utilized to establish relationships between different coefficients C_i, thereby eliminating the need for explicit calculation of all coefficients, which significantly reduces computational cost. In general, a coefficient $C^{\hat{x}}$ can be related to another coefficient $C^{\hat{y}}$, allowing only $C^{\hat{x}}$ to be calculated explicitly. This relationship is possible if the operator $\hat{x}$ can be transformed into $\hat{y}$ by reversing the order of operators and converting them, such that $\hat{\alpha}^\dagger \rightleftarrows \hat{\beta}$ and $\hat{\alpha} \rightleftarrows \hat{\beta}^\dagger$. Lastly, the order of momenta in the coefficient must also be reversed, resulting in $C^{\hat{y}}_{\boldsymbol{k}_1 \dots \boldsymbol{k}_n} = C^{\hat{x}}_{\boldsymbol{k}_n \dots \boldsymbol{k}_1}$. The application of this symmetry requires establishing a rule for determining whether the operator is explicitly calculated or derived from the symmetry relation. In this work, the rule is defined as follows: If there are two symmetry-equivalent coefficients, the one with the highest number of $\hat{\alpha}^{(\dagger)}_{\boldsymbol{k}}$ in the related operator is chosen to be explicitly calculated. If both coefficients contain the same number of $\hat{\alpha}^{(\dagger)}_{\boldsymbol{k}}$ in the operator, the coefficient with more $\hat{\alpha}^\dagger_{\boldsymbol{k}}$ is chosen. The application of this rule leads to the following relations

$$
\begin{aligned}
C^{\hat{\beta}^\dagger\hat{\beta}}_{\boldsymbol{k}_1,\boldsymbol{k}_2} &= C^{\hat{\alpha}^\dagger\hat{\alpha}}_{\boldsymbol{k}_2,\boldsymbol{k}_1} \ , & C^{\hat{\alpha}\hat{\beta}}_{\boldsymbol{k}_1,\boldsymbol{k}_2} &= C^{\hat{\alpha}^\dagger\hat{\beta}^\dagger}_{\boldsymbol{k}_2,\boldsymbol{k}_1} \ , \\
C^{\hat{\beta}^\dagger\hat{\beta}^\dagger\hat{\beta}\hat{\beta}}_{\boldsymbol{k}_1,\boldsymbol{k}_2,\boldsymbol{k}_3,\boldsymbol{k}_4} &= C^{\hat{\alpha}^\dagger\hat{\alpha}^\dagger\hat{\alpha}\hat{\alpha}}_{\boldsymbol{k}_4,\boldsymbol{k}_3,\boldsymbol{k}_2,\boldsymbol{k}_1} \ , & C^{\hat{\alpha}\hat{\alpha}\hat{\beta}\hat{\beta}}_{\boldsymbol{k}_1,\boldsymbol{k}_2,\boldsymbol{k}_3,\boldsymbol{k}_4} &= C^{\hat{\alpha}^\dagger\hat{\alpha}^\dagger\hat{\beta}^\dagger\hat{\beta}^\dagger}_{\boldsymbol{k}_4,\boldsymbol{k}_3,\boldsymbol{k}_2,\boldsymbol{k}_1} \ , \\
C^{\hat{\alpha}^\dagger\hat{\beta}^\dagger\hat{\beta}^\dagger\hat{\beta}}_{\boldsymbol{k}_1,\boldsymbol{k}_2,\boldsymbol{k}_3,\boldsymbol{k}_4} &= C^{\hat{\alpha}^\dagger\hat{\alpha}\hat{\alpha}\hat{\beta}}_{\boldsymbol{k}_4,\boldsymbol{k}_3,\boldsymbol{k}_2,\boldsymbol{k}_1} \ , & C^{\hat{\alpha}\hat{\beta}^\dagger\hat{\beta}\hat{\beta}}_{\boldsymbol{k}_1,\boldsymbol{k}_2,\boldsymbol{k}_3,\boldsymbol{k}_4} &= C^{\hat{\alpha}^\dagger\hat{\alpha}^\dagger\hat{\alpha}\hat{\beta}^\dagger}_{\boldsymbol{k}_4,\boldsymbol{k}_3,\boldsymbol{k}_2,\boldsymbol{k}_1} \ ,
\end{aligned}
\tag{4.13}
$$

where the operators on the left-hand sides of the equal signs are implicitly calculated through their symmetry-equivalent counterparts.

At this point, it is necessary to revisit the different gauges used in the Fourier transformation, as discussed in Section 2.5.2. The reason is that the relations above hold only in the Bloch gauge for all momenta. In the symmetric gauge, switching between $\hat{\alpha}^{(\dagger)}$ and $\hat{\beta}^{(\dagger)}$ bosons becomes non-trivial because $\hat{\beta}^{(\dagger)}$ may acquire a phase relative to the $\hat{\alpha}^{(\dagger)}$ if there are Umklapp processes involved. Therefore, if the symmetric gauge is used instead, additional phase factors may arise in the aforementioned relations. The rise of such a phase factor stems from the fact that, to ensure a unique representation of each coefficient, as suggested in Section 4.2, all momenta are restricted to the first BZ(MBZ), and thus Umklapp processes usually occur in the last momentum of the coefficient. Due to these non-trivial Umklapp processes, the relations of Eq. (4.13) change in the case of the symmetric gauge to

$$
\begin{aligned}
C^{\hat{\beta}^\dagger\hat{\beta}}_{\boldsymbol{k}_1,\boldsymbol{k}_2} &= \gamma_\mathrm{S}\left(\boldsymbol{k}_1{-}\boldsymbol{k}_2\right) C^{\hat{\alpha}^\dagger\hat{\alpha}}_{\boldsymbol{k}_2,\boldsymbol{k}_1} \ , \\
C^{\hat{\alpha}\hat{\beta}}_{\boldsymbol{k}_1,\boldsymbol{k}_2} &= \gamma_\mathrm{S}\left(-\boldsymbol{k}_1{-}\boldsymbol{k}_2\right) C^{\hat{\alpha}^\dagger\hat{\beta}^\dagger}_{\boldsymbol{k}_2,\boldsymbol{k}_1} \ , \\
C^{\hat{\beta}^\dagger\hat{\beta}^\dagger\hat{\beta}\hat{\beta}}_{\boldsymbol{k}_1,\boldsymbol{k}_2,\boldsymbol{k}_3,\boldsymbol{k}_4} &= \gamma_\mathrm{S}\left(\boldsymbol{k}_1{+}\boldsymbol{k}_2{-}\boldsymbol{k}_3{-}\boldsymbol{k}_4\right) C^{\hat{\alpha}^\dagger\hat{\alpha}^\dagger\hat{\alpha}\hat{\alpha}}_{\boldsymbol{k}_4,\boldsymbol{k}_3,\boldsymbol{k}_2,\boldsymbol{k}_1} \ , \\
C^{\hat{\alpha}\hat{\alpha}\hat{\beta}\hat{\beta}}_{\boldsymbol{k}_1,\boldsymbol{k}_2,\boldsymbol{k}_3,\boldsymbol{k}_4} &= \gamma_\mathrm{S}\left(-\boldsymbol{k}_1{-}\boldsymbol{k}_2{-}\boldsymbol{k}_3{-}\boldsymbol{k}_4\right) C^{\hat{\alpha}^\dagger\hat{\alpha}^\dagger\hat{\beta}^\dagger\hat{\beta}^\dagger}_{\boldsymbol{k}_4,\boldsymbol{k}_3,\boldsymbol{k}_2,\boldsymbol{k}_1} \ , \\
C^{\hat{\alpha}^\dagger\hat{\beta}^\dagger\hat{\beta}^\dagger\hat{\beta}}_{\boldsymbol{k}_1,\boldsymbol{k}_2,\boldsymbol{k}_3,\boldsymbol{k}_4} &= \gamma_\mathrm{S}\left(\boldsymbol{k}_1{+}\boldsymbol{k}_2{+}\boldsymbol{k}_3{-}\boldsymbol{k}_4\right) C^{\hat{\alpha}^\dagger\hat{\alpha}\hat{\alpha}\hat{\beta}}_{\boldsymbol{k}_4,\boldsymbol{k}_3,\boldsymbol{k}_2,\boldsymbol{k}_1} \ , \\
C^{\hat{\alpha}\hat{\beta}^\dagger\hat{\beta}\hat{\beta}}_{\boldsymbol{k}_1,\boldsymbol{k}_2,\boldsymbol{k}_3,\boldsymbol{k}_4} &= \gamma_\mathrm{S}\left(-\boldsymbol{k}_1{+}\boldsymbol{k}_2{-}\boldsymbol{k}_3{-}\boldsymbol{k}_4\right) C^{\hat{\alpha}^\dagger\hat{\alpha}^\dagger\hat{\alpha}\hat{\beta}^\dagger}_{\boldsymbol{k}_4,\boldsymbol{k}_3,\boldsymbol{k}_2,\boldsymbol{k}_1} \ .
\end{aligned}
\tag{4.14}
$$

To gain a clearer understanding of the phase factor $\gamma_\mathrm{S}(\boldsymbol{G})$, the relation between coefficients $C^{\hat{\alpha}^\dagger\hat{\beta}^\dagger\hat{\beta}^\dagger\hat{\beta}}_{\boldsymbol{k}_1,\boldsymbol{k}_2,\boldsymbol{k}_3,\boldsymbol{k}_4}$ and $C^{\hat{\alpha}^\dagger\hat{\alpha}\hat{\alpha}\hat{\beta}}_{\boldsymbol{k}_4,\boldsymbol{k}_3,\boldsymbol{k}_2,\boldsymbol{k}_1}$ is analyzed as an example. First, the coefficient

$$
C^{\hat{\alpha}^\dagger\hat{\alpha}\hat{\alpha}\hat{\beta}}_{\boldsymbol{k}_4+\boldsymbol{G}_4,\boldsymbol{k}_3+\boldsymbol{G}_3,\boldsymbol{k}_2+\boldsymbol{G}_2,\boldsymbol{k}_1+\boldsymbol{G}_1}
\tag{4.15}
$$

is considered, where each momentum is split into a momentum within the first MBZ $\boldsymbol{k}_i \in$MBZ and a reciprocal lattice vector $\boldsymbol{G}_i$. Next, the coefficient is brought back into the form of Eq. (4.14) by considering Umklapp processes. In the symmetric gauge, the relation

$$C^{\hat{\alpha}^\dagger\hat{\alpha}\hat{\alpha}\hat{\beta}}_{\boldsymbol{k}_4+\boldsymbol{G}_4,\boldsymbol{k}_3+\boldsymbol{G}_3,\boldsymbol{k}_2+\boldsymbol{G}_2,\boldsymbol{k}_1+\boldsymbol{G}_1} = C^{\hat{\alpha}^\dagger\hat{\alpha}\hat{\alpha}\hat{\beta}}_{\boldsymbol{k}_4,\boldsymbol{k}_3,\boldsymbol{k}_2,\boldsymbol{k}_1+\boldsymbol{G}_1} = \gamma_\mathrm{S}\left(-\boldsymbol{G}_1\right) C^{\hat{\alpha}^\dagger\hat{\alpha}\hat{\alpha}\hat{\beta}}_{\boldsymbol{k}_4,\boldsymbol{k}_3,\boldsymbol{k}_2,\boldsymbol{k}_1} \tag{4.16}$$

holds as the $\hat{a}^{(\dagger)}$ bosons are unaffected by Umklapp process, whereas $\hat{b}^{(\dagger)}$ bosons gain an additional phase. Using the corresponding momentum-conserving δ-function, the relation

$$\boldsymbol{G}_1 = \boldsymbol{k}_4 - \boldsymbol{k}_3 - \boldsymbol{k}_2 - \boldsymbol{k}_1 \tag{4.17}$$

is obtained. Inserting this relation into the previous equation while also applying the symmetry of Eq. (4.14) leads to

$$\begin{aligned}\gamma_\mathrm{S}\left(-\boldsymbol{G}_1\right) C^{\hat{\alpha}^\dagger\hat{\alpha}\hat{\alpha}\hat{\beta}}_{\boldsymbol{k}_4,\boldsymbol{k}_3,\boldsymbol{k}_2,\boldsymbol{k}_1} &= \gamma_\mathrm{S}\left(-\boldsymbol{k}_4+\boldsymbol{k}_3+\boldsymbol{k}_2+\boldsymbol{k}_1\right)\gamma_\mathrm{S}\left(-\boldsymbol{k}_1-\boldsymbol{k}_2-\boldsymbol{k}_3+\boldsymbol{k}_4\right) C^{\hat{\alpha}^\dagger\hat{\beta}^\dagger\hat{\beta}^\dagger\hat{\beta}}_{\boldsymbol{k}_1,\boldsymbol{k}_2,\boldsymbol{k}_3,\boldsymbol{k}_4} \\ &= C^{\hat{\alpha}^\dagger\hat{\beta}^\dagger\hat{\beta}^\dagger\hat{\beta}}_{\boldsymbol{k}_1,\boldsymbol{k}_2,\boldsymbol{k}_3,\boldsymbol{k}_4} \ .\end{aligned} \tag{4.18}$$

Consequently, the additional phases on the right-hand side in Eq. (4.14) undo the possible obtained phase of the $\hat{\beta}^{(\dagger)}$.

Regardless of the chosen gauge, exploiting the $\mathcal{PT}$-symmetry in the Hamiltonian is an effective method to reduce the total number of coefficients to be tracked during the flow. Specifically, the number of elements in the coefficient vectors is reduced as follows:

$$\#\text{elements} = 9L^6 + 4L^2 + 1 \overset{\mathcal{PT}\text{-symmetry}}{\longrightarrow} \#\text{elements} = 5L^6 + 2L^2 + 1 \ , \tag{4.19}$$

which nearly corresponds to halving the total number of elements. In summary, employing the $\mathcal{PT}$-symmetry of the coefficients not only minimizes the computational costs associated with solving the flow equation but also substantially lowers memory requirements. These quantities are both limiting factors when studying larger system sizes, which emphasizes the importance of utilizing the $\mathcal{PT}$-symmetry.

4.3.2 Symmetries — Coefficients

The $\mathcal{PT}$-symmetry is not the only symmetry that can be exploited when solving the flow equations. In addition, each coefficient possesses its own set of symmetries. One of these addresses the permutation of momenta in a coefficient corresponding to the same boson operators, e.g., the relation for the coefficient

$$C^{\hat{\alpha}^\dagger\hat{\alpha}^\dagger\hat{\alpha}\hat{\alpha}}_{\boldsymbol{k}_1,\boldsymbol{k}_2,\boldsymbol{k}_3,\boldsymbol{k}_4} = C^{\hat{\alpha}^\dagger\hat{\alpha}^\dagger\hat{\alpha}\hat{\alpha}}_{\boldsymbol{k}_2,\boldsymbol{k}_1,\boldsymbol{k}_3,\boldsymbol{k}_4} = C^{\hat{\alpha}^\dagger\hat{\alpha}^\dagger\hat{\alpha}\hat{\alpha}}_{\boldsymbol{k}_1,\boldsymbol{k}_2,\boldsymbol{k}_4,\boldsymbol{k}_3} = C^{\hat{\alpha}^\dagger\hat{\alpha}^\dagger\hat{\alpha}\hat{\alpha}}_{\boldsymbol{k}_2,\boldsymbol{k}_1,\boldsymbol{k}_4,\boldsymbol{k}_3} \tag{4.20}$$

should remain valid throughout the flow, as $\boldsymbol{k}_1$ and $\boldsymbol{k}_2$, along with $\boldsymbol{k}_3$ and $\boldsymbol{k}_4$ correspond to the same boson operators $\hat{a}^{(\dagger)}$. Before the flow, this symmetrization was applied for each coefficient by calculating its respective superposition, as previously discussed in Section 2.5.4. Naturally, the flow must preserve this symmetrization. Therefore, it is sufficient to calculate a single representation of the coefficient and assign its symmetric counterparts accordingly. The impact of this symmetry on computational effort varies since only coefficients involving identical boson types benefit from it. Nevertheless, this symmetry also enhances the flow's robustness.

Another applicable symmetry within a coefficient relates to potential point-group symmetries associated with the momenta. In all coefficients, the momentum dependence is encapsulated

in functions arising during the Fourier transformation. For the nearest-neighbor interaction, the momentum dependence is exclusively contained within the function $\gamma(\boldsymbol{k})$, as introduced in Section 2.5.2. The specific form and properties of this function are determined by both the lattice symmetry and the choice of the Fourier gauge, as detailed in Section 2.5.2. In general, for an arbitrary function $\gamma(\boldsymbol{k})$ there exists a set of symmetry transformations Θ such that the following relation holds:

$$\gamma(\boldsymbol{k}) = \gamma(\theta(\boldsymbol{k})) \quad \text{with} \quad \theta \in \Theta \, . \tag{4.21a}$$

Depending on the specific symmetry, a complex conjugation may occur. It can be alternatively expressed as

$$\gamma(\boldsymbol{k}) = \gamma^*(\theta(\boldsymbol{k})) = \gamma(-\theta(\boldsymbol{k})) \quad \text{with} \quad \theta \in \Theta \tag{4.21b}$$

with an additional minus sign instead of the complex conjugation due to the specific form of $\gamma(\boldsymbol{k})$. In the initial values of the coefficient, sums of different momenta appear within the $\gamma(\boldsymbol{k})$ functions. Using its distributive property, the point-group symmetry can be applied to each momentum separately, yielding

$$\gamma\left(\boldsymbol{k}_x + \boldsymbol{k}_y\right) = \gamma^{(*)}\left(\theta\left(\boldsymbol{k}_x\right) + \theta\left(\boldsymbol{k}_y\right)\right) \, . \tag{4.22}$$

Overall, this leads to the following symmetry relation for an arbitrary coefficient

$$C^{\hat{x}}_{\boldsymbol{k}_1,\ldots,\boldsymbol{k}_n} = \left(C^{\hat{x}}_{\theta(\boldsymbol{k}_1),\ldots,\theta(\boldsymbol{k}_n)}\right)^{(*)} \, . \tag{4.23}$$

At first glance, the application of this symmetry appears straightforward. However, the seemingly simple form of Eq. (4.23) is misleading because a small yet significant detail is omitted. Namely, with regards to the flow equations, only coefficients containing momenta exclusively within the first BZ(MBZ) are selected as representations of a coefficient. On the contrary, the symmetry transformation described in Eq. (4.23) does not account for this restriction. While $C^{\hat{x}}_{\boldsymbol{k}_1,\ldots,\boldsymbol{k}_n}$ satisfies $\boldsymbol{k}_i \in$BZ(MBZ), this condition may not hold for its symmetry-transformed counterpart $C^{\hat{x}}_{\theta(\boldsymbol{k}_1),\ldots,\theta(\boldsymbol{k}_n)}$. Thus, to utilize this symmetry for the coefficient within the flow equations, additional considerations and adaptations to Eq. (4.23) are required. Moreover, restricting momenta exclusively to the first BZ(MBZ) introduces another caveat: When evaluating the momentum conservation, i.e., the corresponding δ-function of the coefficient, the total momentum can, in that case, be a reciprocal lattice vector $\boldsymbol{G}$. If the symmetry is applied to such a coefficient, the reciprocal lattice vector is similarly transformed according to $\theta(\boldsymbol{G}) \neq \boldsymbol{0}$. Since $\gamma(\theta(\boldsymbol{G}))$ can introduce an additional phase, it is sensible to only apply the symmetry transformation to coefficients with an overall total momentum of $\boldsymbol{G} = \boldsymbol{0}$. Thereby, $\gamma(\boldsymbol{0}) = 1$ always holds and no additional phase is introduced. Naturally, issues with additional arising phases do not occur in the Bloch gauge, as Umklapp processes introduce no phase differences in this gauge. Consequently, Eq. (4.23) can be utilized by simply shifting back momenta that fall outside the defined discretization of the first BZ(MBZ). The next paragraphs address challenges associated with using a symmetric gauge, and each potential phase is carefully broken down.

First, the coefficient is transformed to a representation in which the total momentum is zero. Eventually, this may yield a coefficient containing a momentum $\boldsymbol{k}_i$ outside the BZ(MBZ). In this process, the discussed properties of the gauge play an important role. To gain a clearer understanding, the transformation is demonstrated using an actual coefficient $C^{\hat{\alpha}^\dagger \hat{\alpha} \hat{\beta}^\dagger \hat{\beta}}_{\boldsymbol{k}_1,\boldsymbol{k}_2,\boldsymbol{k}_3,\boldsymbol{k}_4}$ in the symmetric gauge. The total momentum is first determined using the δ-function resulting in

$$\boldsymbol{G} = \boldsymbol{k}_1 - \boldsymbol{k}_2 + \boldsymbol{k}_3 - \boldsymbol{k}_4 \, . \tag{4.24}$$

If the total momentum of the coefficient is not already zero, the last momentum can be used to shift the total momentum to zero. This shift can be realized by writing the last momentum as

$$\boldsymbol{k}_4 = \boldsymbol{k}'_4 - \boldsymbol{G} \tag{4.25}$$

where here and in the following, momenta potentially lying outside the BZ(MBZ) are labeled with a prime as $\boldsymbol{k}'$. Additionally, a phase shift is obtained as a result, since $\boldsymbol{k}_4$ is connected to a $\hat{\beta}$ boson. The overall transformation to a coefficient with total momentum zero can be obtained via

$$C^{\hat{\alpha}^\dagger\hat{\alpha}\hat{\beta}^\dagger\hat{\beta}}_{\boldsymbol{k}_1,\boldsymbol{k}_2,\boldsymbol{k}_3,\boldsymbol{k}_4} = C^{\hat{\alpha}^\dagger\hat{\alpha}\hat{\beta}^\dagger\hat{\beta}}_{\boldsymbol{k}_1,\boldsymbol{k}_2,\boldsymbol{k}_3,\boldsymbol{k}'_4-\boldsymbol{G}} = \gamma_\mathrm{S}(\boldsymbol{G}) C^{\hat{\alpha}^\dagger\hat{\alpha}\hat{\beta}^\dagger\hat{\beta}}_{\boldsymbol{k}_1,\boldsymbol{k}_2,\boldsymbol{k}_3,\boldsymbol{k}'_4} \quad \Big| \cdot \gamma_\mathrm{S}(-\boldsymbol{G}) \tag{4.26a}$$

$$\Leftrightarrow \qquad C^{\hat{\alpha}^\dagger\hat{\alpha}\hat{\beta}^\dagger\hat{\beta}}_{\boldsymbol{k}_1,\boldsymbol{k}_2,\boldsymbol{k}_3,\boldsymbol{k}'_4} = \gamma_\mathrm{S}(-\boldsymbol{G}) C^{\hat{\alpha}^\dagger\hat{\alpha}\hat{\beta}^\dagger\hat{\beta}}_{\boldsymbol{k}_1,\boldsymbol{k}_2,\boldsymbol{k}_3,\boldsymbol{k}_4} \,. \tag{4.26b}$$

It is important to note that the final occurring $\gamma_\mathrm{S}(-\boldsymbol{G})$ function is unaffected by the nature of the last operator, whether it is a creator or an annihilator. In the case of a creator, the definition in Eq. (4.25) would instead read $\boldsymbol{k}_4 = \boldsymbol{k}'_4 + \boldsymbol{G}$, which cancels with the additional phase of the creation operator. Therefore, the sole criterion of relevance is that the last operator must correspond to a $\hat{\beta}^{(\dagger)}$ boson.

Second, with the coefficient's total momentum set to zero, the symmetry outlined in Eq. (4.23) can be applied. Additionally, the notation $\theta(\boldsymbol{k}_i) = \tilde{\boldsymbol{k}}_i$ is introduced, resulting in

$$C^{\hat{\alpha}^\dagger\hat{\alpha}\hat{\beta}^\dagger\hat{\beta}}_{\tilde{\boldsymbol{k}}'_1,\tilde{\boldsymbol{k}}'_2,\tilde{\boldsymbol{k}}'_3,\tilde{\boldsymbol{k}}'_4} = C^{\hat{\alpha}^\dagger\hat{\alpha}\hat{\beta}^\dagger\hat{\beta}}_{\theta(\boldsymbol{k}_1),\theta(\boldsymbol{k}_2),\theta(\boldsymbol{k}_3),\theta(\boldsymbol{k}'_4)} = \left(C^{\hat{\alpha}^\dagger\hat{\alpha}\hat{\beta}^\dagger\hat{\beta}}_{\boldsymbol{k}_1,\boldsymbol{k}_2,\boldsymbol{k}_3,\boldsymbol{k}'_4}\right)^{(*)} \,. \tag{4.27}$$

Third, the resulting momenta must be folded back into the first BZ(MBZ). Accordingly, the momenta are written as

$$\tilde{\boldsymbol{k}}'_i = \tilde{\boldsymbol{k}}_i + \tilde{\boldsymbol{G}}_i \tag{4.28}$$

with a possible reciprocal lattice vector $\tilde{\boldsymbol{G}}_i$ and a momentum $\tilde{\boldsymbol{k}}_i$ in the BZ(MBZ), yielding

$$C^{\hat{\alpha}^\dagger\hat{\alpha}\hat{\beta}^\dagger\hat{\beta}}_{\tilde{\boldsymbol{k}}'_1,\tilde{\boldsymbol{k}}'_2,\tilde{\boldsymbol{k}}'_3,\tilde{\boldsymbol{k}}'_4} = C^{\hat{\alpha}^\dagger\hat{\alpha}\hat{\beta}^\dagger\hat{\beta}}_{\tilde{\boldsymbol{k}}_1+\tilde{\boldsymbol{G}}_1,\tilde{\boldsymbol{k}}_2+\tilde{\boldsymbol{G}}_2,\tilde{\boldsymbol{k}}_3+\tilde{\boldsymbol{G}}_3,\tilde{\boldsymbol{k}}_4+\tilde{\boldsymbol{G}}_4} \,. \tag{4.29}$$

In the next step, all momenta $\tilde{\boldsymbol{G}}_i$ are shifted to the last coefficient while ensuring that the total momentum remains zero. This adjustment can be achieved by adding $-\tilde{\boldsymbol{G}}_i$ to each operator, except the last one. Of course, the additional momenta must be compensated in the last operator. However, introducing this shift to a $\hat{b}^{(\dagger)}$ results in an additional phase. Regarding the example, this can be written as

$$\begin{aligned}
C^{\hat{\alpha}^\dagger\hat{\alpha}\hat{\beta}^\dagger\hat{\beta}}_{\tilde{\boldsymbol{k}}'_1,\tilde{\boldsymbol{k}}'_2,\tilde{\boldsymbol{k}}'_3,\tilde{\boldsymbol{k}}'_4} &= C^{\hat{\alpha}^\dagger\hat{\alpha}\hat{\beta}^\dagger\hat{\beta}}_{\tilde{\boldsymbol{k}}_1+\tilde{\boldsymbol{G}}_1,\tilde{\boldsymbol{k}}_2+\tilde{\boldsymbol{G}}_2,\tilde{\boldsymbol{k}}_3+\tilde{\boldsymbol{G}}_3,\tilde{\boldsymbol{k}}_4+\tilde{\boldsymbol{G}}_4} && \text{(4.30a)}\\
&= \gamma_\mathrm{S}\left(-\tilde{\boldsymbol{G}}_3\right)\gamma_\mathrm{S}\left(\tilde{\boldsymbol{G}}_1\right)\gamma_\mathrm{S}\left(-\tilde{\boldsymbol{G}}_2\right)\gamma_\mathrm{S}\left(\tilde{\boldsymbol{G}}_3\right) && \\
&\qquad C^{\hat{\alpha}^\dagger\hat{\alpha}\hat{\beta}^\dagger\hat{\beta}}_{\tilde{\boldsymbol{k}}_1+\tilde{\boldsymbol{G}}_1-\tilde{\boldsymbol{G}}_1,\tilde{\boldsymbol{k}}_2+\tilde{\boldsymbol{G}}_2-\tilde{\boldsymbol{G}}_2,\tilde{\boldsymbol{k}}_3+\tilde{\boldsymbol{G}}_3-\tilde{\boldsymbol{G}}_3,\tilde{\boldsymbol{k}}_4+\tilde{\boldsymbol{G}}_4-\tilde{\boldsymbol{G}}_1+\tilde{\boldsymbol{G}}_2-\tilde{\boldsymbol{G}}_3} && \text{(4.30b)}\\
&= \gamma_\mathrm{S}\left(\tilde{\boldsymbol{G}}_1\right)\gamma_\mathrm{S}\left(-\tilde{\boldsymbol{G}}_2\right) C^{\hat{\alpha}^\dagger\hat{\alpha}\hat{\beta}^\dagger\hat{\beta}}_{\tilde{\boldsymbol{k}}_1,\tilde{\boldsymbol{k}}_2,\tilde{\boldsymbol{k}}_3,\tilde{\boldsymbol{k}}_4+\underbrace{\tilde{\boldsymbol{G}}_4-\tilde{\boldsymbol{G}}_1+\tilde{\boldsymbol{G}}_2-\tilde{\boldsymbol{G}}_3}_{=\tilde{\boldsymbol{G}}}} \,. && \text{(4.30c)}
\end{aligned}$$

Interestingly, in these equations, the phases of the $\hat{\beta}^{(\dagger)}$ cancel out, leaving only the phases resulting from the momentum shift of $\hat{\alpha}^{(\dagger)}$ bosons in the final expression. The signs of each resulting phase

is determined whether it was a $\hat{\alpha}^\dagger$ operator, contributing a phase factor $\gamma_\mathrm{S}\left(\tilde{\boldsymbol{G}}_i\right)$, or a $\hat{\alpha}$ operator, contributing a phase factor $\gamma_\mathrm{S}\left(-\tilde{\boldsymbol{G}}_i\right)$. As the equation is rearranged to

$$C^{\hat{\alpha}^\dagger\hat{\alpha}\hat{\beta}^\dagger\hat{\beta}}_{\tilde{\boldsymbol{k}}_1,\tilde{\boldsymbol{k}}_2,\tilde{\boldsymbol{k}}_3,\tilde{\boldsymbol{k}}_4+\tilde{\boldsymbol{G}}} = \gamma_\mathrm{S}\left(-\tilde{\boldsymbol{G}}_1\right)\gamma_\mathrm{S}\left(\tilde{\boldsymbol{G}}_2\right) C^{\hat{\alpha}^\dagger\hat{\alpha}\hat{\beta}^\dagger\hat{\beta}}_{\tilde{\boldsymbol{k}}'_1,\tilde{\boldsymbol{k}}'_2,\tilde{\boldsymbol{k}}'_3,\tilde{\boldsymbol{k}}'_4} \,, \tag{4.31}$$

the signs in the phases are exactly reversed.

Lastly, the coefficient can be transformed in the same manner as in Eq. (4.26), yielding

$$C^{\hat{\alpha}^\dagger\hat{\alpha}\hat{\beta}^\dagger\hat{\beta}}_{\tilde{\boldsymbol{k}}_1,\tilde{\boldsymbol{k}}_2,\tilde{\boldsymbol{k}}_3,\tilde{\boldsymbol{k}}_4} = \gamma_\mathrm{S}\left(\tilde{\boldsymbol{G}}\right) C^{\hat{\alpha}^\dagger\hat{\alpha}\hat{\beta}^\dagger\hat{\beta}}_{\tilde{\boldsymbol{k}}_1,\tilde{\boldsymbol{k}}_2,\tilde{\boldsymbol{k}}_3,\tilde{\boldsymbol{k}}'_4} \quad \text{with} \quad \tilde{\boldsymbol{G}} = \tilde{\boldsymbol{k}}_1 - \tilde{\boldsymbol{k}}_2 + \tilde{\boldsymbol{k}}_3 - \tilde{\boldsymbol{k}}_4 \,. \tag{4.32}$$

Finally, all equations leading to $C^{\hat{\alpha}^\dagger\hat{\alpha}\hat{\beta}^\dagger\hat{\beta}}_{\tilde{\boldsymbol{k}}_1,\tilde{\boldsymbol{k}}_2,\tilde{\boldsymbol{k}}_3,\tilde{\boldsymbol{k}}_4}$ can be put together in reversed order resulting in

$$C^{\hat{\alpha}^\dagger\hat{\alpha}\hat{\beta}^\dagger\hat{\beta}}_{\tilde{\boldsymbol{k}}_1,\tilde{\boldsymbol{k}}_2,\tilde{\boldsymbol{k}}_3,\tilde{\boldsymbol{k}}_4} = \gamma_\mathrm{S}\left(\tilde{\boldsymbol{G}}\right)\gamma_\mathrm{S}\left(-\tilde{\boldsymbol{G}}_1\right)\gamma_\mathrm{S}\left(\tilde{\boldsymbol{G}}_2\right)\left(\gamma_\mathrm{S}(-\boldsymbol{G}) C^{\hat{\alpha}^\dagger\hat{\alpha}\hat{\beta}^\dagger\hat{\beta}}_{\boldsymbol{k}_1,\boldsymbol{k}_2,\boldsymbol{k}_3,\boldsymbol{k}_4}\right)^{(*)} \,. \tag{4.33}$$

Now, it is possible to calculate only a single element of a group of the coefficient $C^{\hat{\alpha}^\dagger\hat{\alpha}\hat{\beta}^\dagger\hat{\beta}}_{\boldsymbol{k}_1,\boldsymbol{k}_2,\boldsymbol{k}_3,\boldsymbol{k}_4}$ connected via different symmetry transformation $\theta \in \Theta$ and assign others with this expression.

After all, the goal is to utilize the symmetry in all coefficients. Consequently, by generalizing the concepts derived from the given example, it is possible to write a general formula as

$$C^{\hat{x}}_{\tilde{\boldsymbol{k}}_1,\ldots,\tilde{\boldsymbol{k}}_n} = \gamma_\mathrm{S}\left(\tilde{\boldsymbol{G}}\right)\left[\prod_{i \mid \hat{\alpha}^\dagger_{\tilde{\boldsymbol{k}}_i} \in \hat{x}} \gamma_\mathrm{S}\left(-\tilde{\boldsymbol{G}}_i\right)\right]\left[\prod_{j \mid \hat{\alpha}_{\tilde{\boldsymbol{k}}_j} \in \hat{x}} \gamma_\mathrm{S}\left(\tilde{\boldsymbol{G}}_j\right)\right]\left(\gamma_\mathrm{S}\left(\boldsymbol{G}\right) C^{\hat{x}}_{\boldsymbol{k}_1,\ldots,\boldsymbol{k}_n}\right)^{(*\text{ optional})} \tag{4.34}$$

with

$$\boldsymbol{G} = \sum_{i=1}^{n} \sigma_i \boldsymbol{k}_i \,, \quad \tilde{\boldsymbol{G}} = \sum_{i=1}^{n} \sigma_i \tilde{\boldsymbol{k}}_i \,, \quad \sigma_i = \begin{cases} +1 & \text{if } \hat{\alpha}^\dagger_{\boldsymbol{k}_i}/\hat{\beta}^\dagger_{\boldsymbol{k}_i} \in \hat{x} \\ -1 & \text{if } \hat{\alpha}_{\boldsymbol{k}_i}/\hat{\beta}_{\boldsymbol{k}_i} \in \hat{x} \end{cases} \,. \tag{4.35}$$

Where the notation $i \mid \hat{\alpha}^\dagger_{\tilde{\boldsymbol{k}}_i} \in \hat{x}$ indicates that the product runs over all indices i where the operator $\hat{x}$ contains $\hat{\alpha}^\dagger_{\tilde{\boldsymbol{k}}_i}$ bosons, and similarly for $j \mid \hat{\alpha}_{\tilde{\boldsymbol{k}}_j} \in \hat{x}$. As a reminder, $\tilde{\boldsymbol{k}}_i = \tilde{\boldsymbol{k}}'_i + \tilde{\boldsymbol{G}}_i$ is the symmetry equivalent vector corresponding to $\boldsymbol{k}_i$ with $\tilde{\boldsymbol{k}}'_i = \theta(\boldsymbol{k}_i)$ folded back by $\tilde{\boldsymbol{G}}_i$ in the discretization of the BZ(MBZ). The vectors $\boldsymbol{G}$ and $\tilde{\boldsymbol{G}}$ represent the total momentum of the original and symmetry-transformed coefficients, respectively. The final complex conjugation is only applied if the symmetry transformation θ requires it. Together with the relation introduced between the different coefficients, utilizing the coefficients' intrinsic symmetries further reduces both computational effort and, consequently, the flow's runtime. Because the impact of symmetries on different coefficients varies, precisely quantifying the savings in computational resources is difficult. Additionally, depending on the choice of gauge in the Fourier transformation, the computational effort required to apply the symmetries varies.

Though in general the application of point-group symmetries is beneficial, strictly enforcing them can lead to numerical issues. Namely, it was observed that an otherwise converged flow became divergent when point-group symmetries of the coefficients were strictly enforced after each step of the flow. This issue only arose when using the symmetric gauge in the Fourier transformation. In contrast, when using the Bloch gauge, the flow remained stable even with symmetries enforced.

In the case where $\gamma_S(\boldsymbol{G})$ takes only values of 1 and -1, the instability could be traced back to processes where the symmetry maps a coefficient onto itself with an additional minus sign, e.g.,

$$C^{\hat{\alpha}^\dagger\hat{\beta}^\dagger}_{\tilde{\boldsymbol{k}}_1,\tilde{\boldsymbol{k}}_2} = -C^{\hat{\alpha}^\dagger\hat{\beta}^\dagger}_{\boldsymbol{k}_1,\boldsymbol{k}_2} = -C^{\hat{\alpha}^\dagger\hat{\beta}^\dagger}_{\tilde{\boldsymbol{k}}_1,\tilde{\boldsymbol{k}}_2} \stackrel{!}{=} 0 \ . \tag{4.36}$$

By explicitly setting those coefficients to zero, the instability was resolved. As a possible explanation, numerical inaccuracies may lead to slight deviations from zero. In the non-symmetry-enforced case, these numerical noises are evenly distributed between positive and negative values. However, when symmetry is strictly enforced, a single representation of this noise is chosen and applied to all other symmetry-equivalent coefficients, leading to a directional bias. This bias, which is then amplified during the flow, ultimately leads to divergence of the flow. However, there are also cases where $\gamma_S(\boldsymbol{G})$ can take complex values, e.g., in the case of the honeycomb lattice as discussed in Chapter 6. In this case, Eq. (4.36) cannot occur as $\gamma_S(\boldsymbol{G})$ does not take the value -1. Unfortunately, in these cases, the instability persists for some symmetries, and the exact cause remains unclear. Nevertheless, the Bloch gauge can be used to avoid these issues entirely in the first place, at the cost of not being able to utilize all the system's intrinsic symmetries.

With all methodical detail and subtleties regarding efficient application of the flow equation established, the following section focuses on the challenges that arise after a successful flow, when the resulting effective Hamiltonian is to be analyzed. Explicitly, the non-Hermitian nature of the Hamiltonian, which is still present after the flow, and how to extract physical observables from it.

4.4 Challenges with Non-Hermitian Representations

As mentioned in Section 3.2.3, in particular physical contexts, it is beneficial, or even necessary, to abandon the strictly Hermitian representation that is customary in quantum mechanics. In this work, the use of the DM leads to a transformation of the initial Hermitian Hamiltonian into a non-Hermitian one. This non-Hermitian nature is conserved throughout the application of the CST. This persistent non-Hermitian representation necessitates becoming accustomed to the ramifications of a non-Hermitian Hamiltonian, which are discussed in this section. The first subsection is a summary of the discussion in Chapter 2.6.1 of Ref. [Pow17]. So, for a more detailed discussion of this topic, the reader is referred to this reference. Afterwards, the implications of the non-Hermitian representation in the context of a Lanczos tridiagonalization used to calculate spectral density or extreme eigenvalues are discussed.

4.4.1 Biorthonormal Basis for Non-Hermitian Hamiltonians

Generally, quantum mechanical systems are described by states $|\psi\rangle$ which are elements of a Hilbert space, and observables are represented as Hermitian operators $\hat{O}$ acting on these states. For a given operator $\hat{O}$, it is possible to find a complete orthonormal basis of eigenstates $|n\rangle$ with real eigenvalues o_n fulfilling the eigenvalue equations

$$\hat{O}\,|n\rangle = o_n\,|n\rangle \quad \text{and} \quad \langle m|\,\hat{O} = \langle m|\,o_m \quad \text{with} \qquad \langle m|n\rangle = \delta_{m,n} \ . \tag{4.37}$$

The eigenvalues o_n represent the possible outcomes of a single measurement of the observable $\hat{O}$. If the system is prepared in a state $|\psi\rangle$, the expectation values of a measurement of the observable

$\hat{O}$ is given by

$$\langle\psi|\,\hat{O}\,|\psi\rangle = \sum_n o_n \underbrace{|\langle n|\psi\rangle|^2}_{P(o_n)} , \tag{4.38}$$

where $P(o_n)$ is the probability to measure the eigenvalue o_n.

Now, instead of a Hermitian operator $\hat{O}$, a non-Hermitian operator $\hat{\tilde{O}}$ is considered. However, it is assumed to be similar to the Hermitian operator $\hat{O}$ via a similarity transformation $\hat{S}$ so that

$$\hat{\tilde{O}} = \hat{S}\hat{O}\hat{S}^{-1} . \tag{4.39}$$

As the similarity transformation conserves the spectrum of the operator, the eigenvalues of $\hat{\tilde{O}}$ are still real, and the eigenvalue equations are modified by a multiplication either with $\hat{S}$ or $\hat{S}^{-1}$ to

$$\hat{S}\hat{O}\,|n\rangle = \overbrace{\hat{S}\hat{O}\hat{S}^{-1}}^{\hat{\tilde{O}}}\,\overbrace{\hat{S}\,|n\rangle}^{|R_n\rangle} \quad = \quad \hat{\tilde{O}}\,|R_n\rangle = o_n\,|R_n\rangle \tag{4.40a}$$

$$\langle m|\,\hat{O}\hat{S}^{-1} = \underbrace{\langle m|\,\hat{S}^{-1}}_{\langle L_m|}\,\underbrace{\hat{S}\hat{O}\hat{S}^{-1}}_{\hat{\tilde{O}}} \quad = \quad \langle L_m|\,\hat{\tilde{O}} = \langle L_m|\,o_m . \tag{4.40b}$$

Compared to the Hermitian case, there are now two distinct sets of eigenstates, the left and right eigenstates with $\langle L_m| = \langle m|\,\hat{S}^{-1}$ and $|R_n\rangle = \hat{S}\,|n\rangle$. By themselves, both sets are not an orthonormal basis with respect to the usual scalar product on $\mathbb{C}$

$$\langle L_m\,|\,L_n\rangle \neq \delta_{m,n} \quad \text{and} \quad \langle R_m\,|\,R_n\rangle \neq \delta_{m,n} . \tag{4.41}$$

Instead, together they form a biorthonormal basis fulfilling

$$\langle L_m\,|\,R_n\rangle = \delta_{m,n} . \tag{4.42}$$

Compared to the Hermitian case, where a simple adjoint connects bra and ket states, here the connection between left and right eigenstates is more intricate. They are connected via

$$\langle L_n| = \langle n|\,\hat{S}^{-1} = \left(\left(\hat{S}^{-1}\right)^\dagger |n\rangle\right)^\dagger = \left(\left(\hat{S}^{-1}\right)^\dagger \hat{S}^{-1}\,\underbrace{\hat{S}\,|n\rangle}_{|R_n\rangle}\right)^\dagger \tag{4.43a}$$

$$= \left(\left(\hat{S}^{-1}\right)^\dagger \hat{S}^{-1}\,|R_n\rangle\right)^\dagger = \langle R_n|\,\underbrace{\left(\hat{S}^{-1}\right)^\dagger \hat{S}^{-1}}_{\hat{K}} \tag{4.43b}$$

effectively mapping the eigenvector with the help of the operator $\hat{K} = \left(\hat{S}^{-1}\right)^\dagger \hat{S}^{-1}$ to the opposite part of the biorthonormal basis. With the Hermitian operator, it is possible to define a new scalar product for which the right eigenstates $|R_n\rangle$ alone form an orthonormal basis with

$$(R_m, R_n)_{\hat{K}} = \langle R_m|\,\hat{K}\,|R_n\rangle = \langle L_m\,|\,R_n\rangle = \langle m\,|\,n\rangle = \delta_{m,n} . \tag{4.44}$$

Regarding this new scalar product, the operator $\hat{\tilde{O}}$ is again Hermitian.

As expectation values of an observable are preserved under a similarity transformation

$$\langle\psi|\,\hat{O}\,|\psi\rangle = \langle\psi|\,\hat{S}^{-1}\hat{S}\hat{O}\hat{S}^{-1}\hat{S}\,|\psi\rangle = \langle\psi_L|\,\hat{\tilde{O}}\,|\psi_R\rangle , \tag{4.45}$$

in the non-Hermitian representation, expectation values can be evaluated similarly by

$$\langle \psi_L | \, \hat{\tilde{O}} \, | \psi_R \rangle = \sum_n o_n \, \langle L_n \, | \, \psi_R \rangle \, \langle \psi_L \, | \, R_n \rangle \ . \tag{4.46}$$

Where $\langle L_n \, | \, \psi_R \rangle \, \langle \psi_L \, | \, R_n \rangle$ gives now the probability of measuring o_n in the non-Hermitian representation which is identical to $P(o_n)$ of the Hermitian case.

Overall, the main difference between a Hermitian and a non-Hermitian representation of a quantum mechanical system lies in the treatment of the basis states. In the non-Hermitian case, information of the system is encoded in two distinct sets of basis states, the left and right eigenstates, which together form a biorthonormal basis. Despite this fundamental difference in representation, expectation values and single-measurement results associated with an observable remain invariant. In the context of this work, this implies that although the non-Hermitian representation which arises from the DM contradicts the conventional Hermitian framework of quantum mechanics, it is nevertheless possible to extract the same physical information from it as from a Hermitian representation. However, it should be noted that the non-Hermitian representation is more susceptible to numerical inaccuracies than the Hermitian representation. Especially, in the application of the CST after the DM, where numerical inaccuracies or truncation errors can lead, for example, to unphysical eigenvalues with non-vanishing imaginary parts or small negative spectral weights. Nevertheless, these drawbacks do not outweigh the advantages, particularly in the context of this work where the non-Hermitian DM allows the treatment of the spin-$\frac{1}{2}$ afHM Hamiltonian without the usual $1/S$ expansion as already discussed in Section 2.4.

4.4.2 Non-Symmetric Lanczos Tridiagonalization

After a successful flow, whether with the pc generator or $0n$ generator, different particle sectors are decoupled from each other. Considering first the effective Hamiltonian of a flow with the pc generator, physical properties like the ground-state energy or single-particle dispersion can be straightforwardly extracted from the corresponding coefficients. The situation already differs if, for example, two-particle properties are of interest. This difference stems from the fact that the flow equations are solved in second quantization.

Thus, although the pc generator decouples the different particle sectors, matrix elements in the two-particle space are not solely determined by the two-particle interaction coefficients. Instead, to determine the correct two-particle matrix elements, contributions from one-particle coefficients must also be considered. Similarly, one- and two-particle contributions must be taken into account for the three-particle space even though true three-particle interactions are excluded, in agreement with the truncation scheme used in this thesis. On the contrary, considering the ground-state energy is not necessary for each particle sector, as it solely introduces a constant shift in each diagonal matrix element.

To extract the relevant eigenenergies of these subspaces, the subspaces must be diagonalized. Since numerical exact diagonalization is extremely computationally expensive, it is important to reduce the size of the subspace by identifying additional blocks that can be diagonalized separately. Therefore, as the Hamiltonian is momentum conserving, it is advisable to separate blocks of total momenta $\boldsymbol{Q}$. Despite these considerations, exact diagonalization remains infeasible for large system subspaces, like in the three-particle space.

For example, in the case of a converging flow with the $0n$ generator, which decouples only the ground state, extracting an estimate for the single-particle dispersion requires diagonalizing the one- and three-particle spaces, which remain connected via decay processes. It is important to

note that determining the single-particle dispersion in such a way is only an approximation, as the three-particle space also couples via the same decay processes to higher particle spaces that are neglected. This approximation is necessary to keep the matrix size finite, as the coupling to higher particle spaces would otherwise lead to an infinite-dimensional problem. On the other hand, the necessity of this approximation for the $0n$ generator underlines the strength of the pc generator as it decouples all particle spaces from each other, allowing for an exact calculation of the single-particle dispersion within the considered truncation scheme.

As the interest solely lies in the lowest eigenvalues, a full diagonalization of the space with the size $1 + L^4$ requires an unnecessary amount of computational effort. Instead, it is more efficient to resort to algorithms such as the Lanczos method [Lan50], which can efficiently determine extreme eigenvalues and corresponding eigenvectors. As the Hamiltonian is non-Hermitian, the non-symmetric Lanczos algorithm is employed [Che+] to solve the non-Hermitian eigenvalue problem

$$\hat{\mathcal{H}} \left|R_i\right\rangle = E_i \left|R_i\right\rangle \quad \text{and} \quad \left\langle L_i\right| \hat{\mathcal{H}} = \left\langle L_i\right| E_i \ . \tag{4.47}$$

Compared to the symmetric Lanczos algorithm, the biorthonormal algorithm starts with two start vectors $|\bar{v}_0\rangle$ and $|\bar{w}_0\rangle$ which are biorthonormalized to $\langle w_0|v_0\rangle = 1$. It builds a biorthonormal basis of the two Krylov sequences

$$\{v_0, \mathcal{H} v_0, \mathcal{H}^2 v_0, \dots\} \quad \text{and} \quad \{w_0, \mathcal{H}^* w_0, (\mathcal{H}^*)^2 v_0, \dots\} \tag{4.48}$$

resulting in the biorthonormal basis

$$\mathcal{V}_{N-1} = \{|v_0\rangle, |v_1\rangle, \dots, |v_{N-1}\rangle\} \quad \text{and} \quad \mathcal{W}_{N-1} = \{|w_0\rangle, |w_1\rangle, \dots, |w_{N-1}\rangle\} . \tag{4.49}$$

Thus, the corresponding matrices

$$V_{N-1} = \begin{pmatrix} | & | & & | \\ |v_0\rangle & |v_1\rangle & \cdots & |v_{N-1}\rangle \\ | & | & & | \end{pmatrix} \qquad W_{N-1} = \begin{pmatrix} | & | & & | \\ |w_0\rangle & |w_1\rangle & \cdots & |w_{N-1}\rangle \\ | & | & & | \end{pmatrix} \tag{4.50}$$

fulfill $W^\dagger V = \mathbb{1}$ and tridiagonalize the Hamiltonian with the transformation

$$W^\dagger \mathcal{H} V = \mathcal{H}_{\text{tri}}^{(N-1)} = \begin{pmatrix} \alpha_0 & \gamma_1 & 0 & \cdots & 0 \\ \beta_1 & \alpha_1 & \gamma_2 & \ddots & \vdots \\ 0 & \beta_2 & \alpha_2 & \ddots & 0 \\ \vdots & \ddots & \ddots & \ddots & \gamma_{N-1} \\ 0 & \cdots & 0 & \beta_{N-1} & \alpha_{N-1} \end{pmatrix} . \tag{4.51}$$

A diagonalization of the tridiagonal matrix $\mathcal{H}_{\text{tri}}^{(N-1)}$ yields eigenvalues $\tilde{E}_i^{(N-1)}$ which give approximations for the extreme eigenvalues of $\mathcal{H}$. Additionally, the corresponding left and right eigenvectors $|\tilde{R}_i^{(N-1)}\rangle$ and $\langle \tilde{L}_i^{(N-1)}|$ of $\mathcal{H}_{\text{tri}}$ can be transformed back to the original space via

$$\left|R_i^{(N-1)}\right\rangle = V_{N-1} \left|\tilde{R}_i^{(N-1)}\right\rangle \quad \text{and} \qquad \left\langle L_i^{(N-1)}\right| = \left\langle \tilde{L}_i^{(N-1)}\right| W_{N-1}^\dagger \ . \tag{4.52}$$

The quality of the approximation can be checked via the residuals

$$\left|r_i^{(N-1)}\right\rangle = \mathcal{H} \left|R_i^{(N-1)}\right\rangle - \tilde{E}_i^{(N-1)} \left|R_i^{(N-1)}\right\rangle \tag{4.53a}$$

and

$$\left\langle l_i^{(N-1)}\right| = \left\langle L_i^{(N-1)}\right| \mathcal{H} - \tilde{E}_i^{(N-1)} \left\langle L_i^{(N-1)}\right| \ . \tag{4.53b}$$

As the calculation of the residuals as in Eq. (4.53) requires the application of the full Hamiltonian $\mathcal{H}$, which is numerically expensive, it is more efficient to calculate them via

$$|r_i^{(N-1)}\rangle = \beta_N |v_N\rangle \langle e_{N-1}|\tilde{R}_i^{(N-1)}\rangle \quad \text{and} \qquad \langle l_i^{(N-1)}| = \gamma_N \langle w_N| \langle \tilde{L}_i^{(N-1)}|e_{N-1}\rangle \ , \tag{4.54}$$

where $|e_{N-1}\rangle$ is simply a unit vector [Che+]. The squared absolute values of the residuals $|r_i^{(N-1)}|^2$ and $|l_i^{(N-1)}|^2$ can be used as a convergence criterion for the approximation of the eigenvalues and eigenvectors. Another termination criterion can also be a fixed step size N or that the values of $\beta_{j+1}, \gamma_{j+1} \approx 0$. The non-symmetric Lanczos algorithm is summarized as follows. Here, the step 4ii) is not mandatory and can lead to a computational bottleneck; however, it improves the numerical stability of the algorithm significantly, as the biorthogonality deteriorates over iterations due to finite precision arithmetic [Che+].

Non-Symmetric Lanczos algorithm:

1. Calculate $\beta_0 = \sqrt{|\langle \bar{w}_0|\bar{v}_0\rangle|}$ and $\gamma_0 = \frac{\langle \bar{w}_0|\bar{v}_0\rangle}{\beta_0}$ from unnormalized start vectors $\bar{v}_0$, $\bar{w}_0$
2. Normalize start vectors

$$|v_0\rangle = \frac{|\bar{v}_0\rangle}{\beta_0}, \quad \langle w_0| = \frac{\langle \bar{w}_0|}{\gamma_0} \tag{4.55}$$

3. Calculate first diagonal matrix entry

$$\alpha_0 = \langle w_0|\mathcal{H}|v_0\rangle \tag{4.56}$$

4. Loop for $j = 0, 1, \ldots, N-1$ | until convergence

   i)

$$|\bar{v}_{j+1}\rangle = \mathcal{H}\,|v_j\rangle - \alpha_j\,|v_j\rangle - \gamma_j\,|v_{j-1}\rangle \tag{4.57a}$$
$$\langle \bar{w}_{j+1}| = \langle w_j|\,\mathcal{H} - \alpha_j\,\langle w_j| - \beta_j\,\langle w_{j-1}| \tag{4.57b}$$

   where $|v_{-1}\rangle = 0$ and $\langle w_{-1}| = 0$

   ii) Re-biorthogonalization:

$$|\bar{v}_{j+1}\rangle = |\bar{v}_{j+1}\rangle - \sum_{i\leq j} |v_i\rangle \langle w_i|\bar{v}_{j+1}\rangle \tag{4.58a}$$
$$\langle \bar{w}_{j+1}| = \langle \bar{w}_{j+1}| - \sum_{i\leq j} \langle \bar{w}_{j+1}|v_i\rangle \langle w_i| \tag{4.58b}$$

   iii)

$$\beta_{j+1} = \sqrt{|\langle \bar{w}_{j+1}|\bar{v}_{j+1}\rangle|} \quad \text{and} \quad \gamma_{j+1} = \frac{\langle \bar{w}_{j+1}|\bar{v}_{j+1}\rangle}{\beta_{j+1}} \tag{4.59}$$

   iv)

$$|v_{j+1}\rangle = \frac{1}{\beta_{j+1}}\,|\bar{v}_{j+1}\rangle \quad \text{and} \quad \langle w_{j+1}| = \frac{1}{\gamma_{j+1}}\,\langle \bar{w}_{j+1}| \tag{4.60}$$

v) Calculate next diagonal matrix entry

$$\alpha_{j+1} = \langle w_{j+1}|\mathcal{H}|v_{j+1}\rangle \tag{4.61}$$

vi) Determine eigenvalues $\tilde{E}_i^{(j)}$ and left and right eigenvectors $|\tilde{R}_i^{(j)}\rangle$, $\langle\tilde{L}_i^{(j)}|$ of $\mathcal{H}_{\text{tri}}^{(j)}$

vii) Calculate squared residuals $|r_i^{(j)}|^2$ and $|l_i^{(j)}|^2$ of interest to check for convergence

Evaluation of spectral densities

Moreover, the Lanczos algorithm provides an option for evaluating spectral densities. As this work does not focus on special densities, only a summary is given, and the reader is referred to Ref. [Pow17] for a more detailed discussion.

Generally, spectral densities are calculated from the resolvents in the form

$$R(\omega) = \langle v| \frac{1}{\omega - \hat{\mathcal{H}}} |v\rangle \ . \tag{4.62}$$

In the Hermitian representation where $\hat{\mathcal{H}} = \hat{\mathcal{H}}^\dagger$, the function $R(\omega)$ is determined with the continued fraction

$$R(\omega) = \cfrac{\langle v \,|\, v\rangle}{\omega - a_0 - \cfrac{b_1^2}{\omega - a_1 - \cfrac{b_2^2}{\ddots}}} \tag{4.63}$$

whereby the coefficient a_i and b_i can be determined by the Hermitian Lanczos algorithm [VM94].

In the non-Hermitian case, the resolvent is modified to

$$R(\omega) = \langle v_L| \frac{1}{\omega - \hat{\mathcal{H}}} |v_R\rangle \tag{4.64}$$

with $\hat{\mathcal{H}} \neq \hat{\mathcal{H}}^\dagger$ and $|v_L\rangle \neq |v_R\rangle$. It is possible to show that the non-symmetric Lanczos algorithm with the starting vectors $|\bar{v}_0\rangle = |v_R\rangle$ and $\langle\bar{w}_0| = \langle v_L|$ results in the necessary coefficients to write the resolvent as a continued fraction [Pow17]

$$R(\omega) = \cfrac{\langle v_L \,|\, v_R\rangle}{\omega - \alpha_0 - \cfrac{\beta_1\gamma_1}{\omega - \alpha_1 - \cfrac{\beta_2\gamma_2}{\ddots}}} = \cfrac{\beta_0\gamma_0}{\omega - \alpha_0 - \cfrac{\beta_1\gamma_1}{\omega - \alpha_1 - \cfrac{\beta_2\gamma_2}{\ddots}}} \ . \tag{4.65}$$

Finally, the resolvent is connected to the spectral density via

$$I(\omega) = -\frac{1}{\pi}\text{Im}R(\omega) = \sum_{i=0}^{N} W_i \delta(\omega - E_i) \ . \tag{4.66}$$

For a finite number of Lanczos iterations N, the spectral density consists of N delta peaks at the eigenvalues E_i with the corresponding weights W_i. The weights W_i can be obtained with the corresponding eigenvectors $|R_i\rangle$ and $\langle L_i|$ of $\hat{\mathcal{H}}$, namely by

$$W_i = \langle v_L \,|\, R_i\rangle \, \langle L_i \,|\, v_R\rangle \ . \tag{4.67}$$

As the Hamiltonian is only determined for a finite system, the spectral density consists of discrete delta peaks. To obtain a smooth spectral density, the delta peaks can be broadened with a Gaussian or the last coefficient in the continued fraction can be modified to introduce an artificial imaginary part, resulting in a Lorentzian broadening. It is also possible to use more sophisticated methods to terminate the continued fraction, like the square-root terminator [VM94].

4.5 Numerical Methods and Used Software

The implementation of the CST applied in this work relies heavily on numerical methods and open-source software. This section addresses the specific methods and software used to produce the results presented in the following chapters of this work. In this work, all results were obtained using a specially developed program [MHS] based on the CST method, which implements all the steps previously described in Chapters 2 to 4. The program is written in C++, relying on C++20, and is available upon reasonable request.

Within this program, solving the flow equations requires two types of numerical integrations. The first integration occurs in the context of the evaluation of the general normal-ordering occurring in the Hamiltonian to either determine the NL-SWT or scNL-SWT Hamiltonian, which serves as the starting point for the flow. All mean-field parameters, as introduced in Section 2.5.4, are evaluated in the thermodynamic limit as integrals over the first BZ(MBZ). On the computational side, this is achieved by a standard Gauss-Kronrod integration method [Lau97] implemented by the *boost* C++ libraries [Boo]. For each calculated integral, 601 evaluation points were used in each dimension. With $l(\boldsymbol{k})$ and $m(\boldsymbol{k})$ possessing divergences at the $\boldsymbol{k} = (0,0)^T$, a small area with $|\boldsymbol{k}| < 10^{-8}$ was as excluded from the integration to ensure numerical stability. If the mean-field parameters are calculated self-consistently, the integration is performed iteratively until the change in each parameter is smaller than 10^{-10}.

After the initial Hamiltonian is set up, the flow equations are integrated numerically until the residual-off-diagonality (ROD), as defined in Section 3.5, undercuts a predefined threshold of 10^{-6} or shows divergent behavior. The numerical integration method of choice is a standard Dormand-Prince Runge-Kutta method of order 5(4) with adaptive step-size control [DP80]. The implementation is used from the *odeint* C++ library [AM11] within the *boost* C++ libraries [Boo]. The error tolerance for the adaptive step-size control is set to 10^{-10} for the absolute error and to 10^{-6} for the relative error.

Subsequent numerical matrix operations, such as numerical matrix eigendecompositions, are carried out with the help of the *Eigen* C++ library [Eig]. Additionally, the calculation of spectral densities or energies, using a non-symmetric Lanczos tridiagonalization as discussed in Section 4.4.2, is custom implemented with the help of the *Eigen* C++ library [Eig].

Results obtained after the flow equations are stored as *JSON* files using the *nlohmann/json* C++ library [Loh25]. Further data analysis and visualization are performed using Python. Precisely, the libraries *numpy* [Har+20], *matplotlib* [Hun07; Mat24], *scipy* [Vir+20], *pandas* [Pan25] are utilized.

The overview of numerical methods and software used is hereby completed, and the next chapter presents the results obtained with the methods and implementations discussed so far. To conclude the theoretical and methodological part of this work, Fig. 4.4 provides a comprehensive visualization of all transformations, starting from the initial Hamiltonian of the spin-$\frac{1}{2}$ antiferromagnetic easy-axis XXZ model on a square lattice together with optional observables. The figure resembles the extension of Fig. 2.10 with the focus on the key aspects of the CST instead of the transformations before the CST.

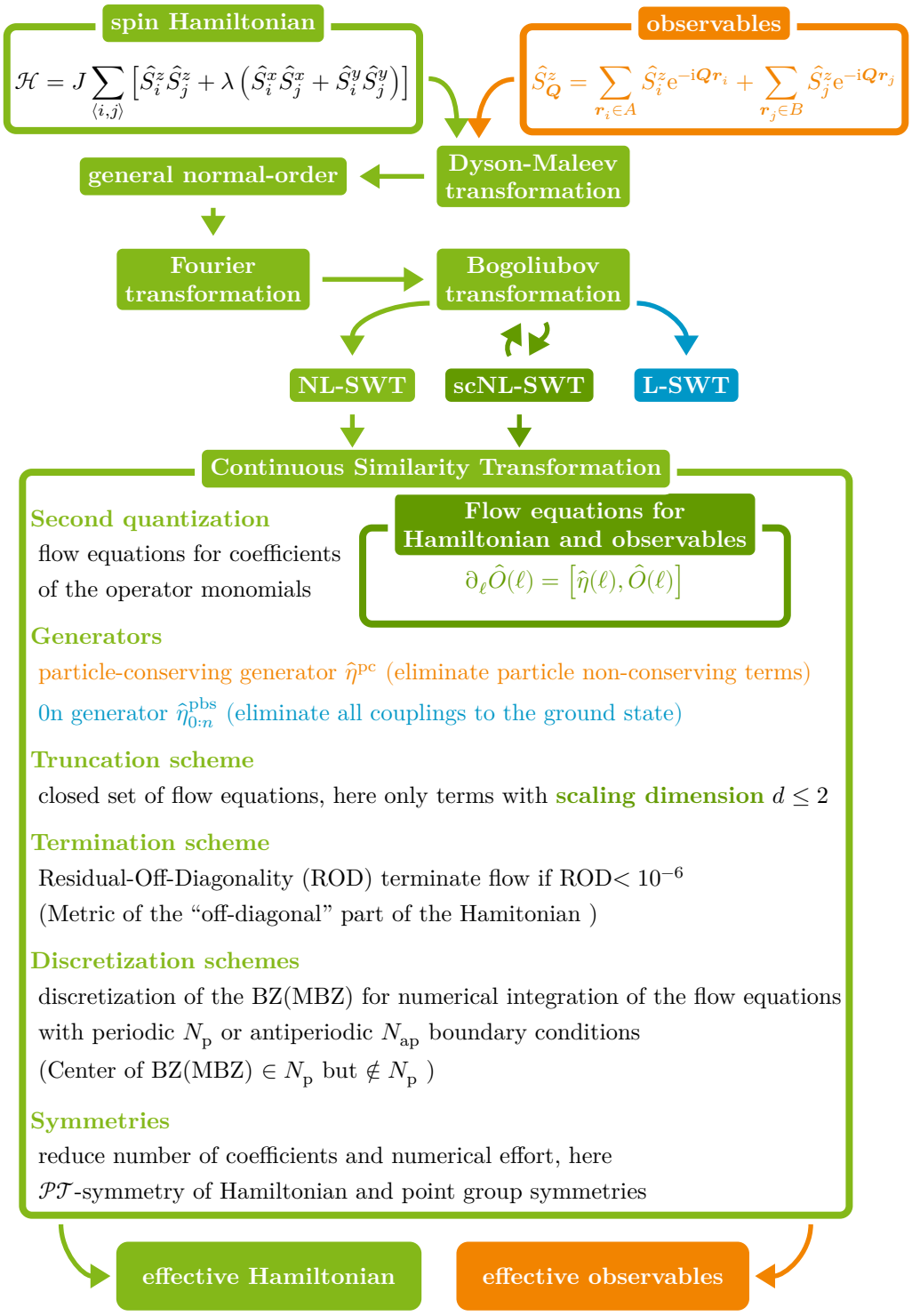

Figure 4.4: A comprehensive visualization of all transformations is displayed, starting from the initial Hamiltonian of the spin-$\frac{1}{2}$ antiferromagnetic easy-axis XXZ model on a square lattice, along with observables. All transformations before the CST are depicted with their different results of either a NL-SWT or scNL-SWT. Both can be inserted in the CST to obtain the final effective Hamiltonian or observable. The CST panel contains all its key aspects. Finally, an effective Hamiltonian and observable are obtained, which can be used to extract physical properties of the system.

5 | XXZ Model on a Square Lattice

In the antiferromagnetic Heisenberg model (afHM) on a square lattice, achieving a quantitative description of the magnon excitation spectrum requires a proper treatment of the magnon-magnon interaction, which could be successfully accomplished using the continuous similarity transformation (CST) [PUS15; Pow17; PSU18]. A natural next step is to ask whether CST can still be applied when the model is modified away from the gapless Heisenberg point. The easy-axis antiferromagnetic XXZ model on a square lattice is one such modification, as it can be continuously tuned from the isotropic afHM to the classical Ising model, with local, gapped magnon excitations. It has the advantage that the magnon excitation spectrum of the easy-axis XXZ model has already been investigated by several methods, making it a suitable candidate for assessing the performance and applicability, as well as possible limitations, of the CST method in describing gapped phases. In particular, the easy-axis XXZ model on a square lattice was already analyzed for example with high-order series expansion [WOH91; ZOH05; Dus+10; Dus+10], diagrammatic spin wave theory [HZA92; Ham09], coupled cluster method [Bis+17], density matrix renormalization group [Ver18; Kad+24], and quantum Monte Carlo simulations [San97; SS01].

In this and in the following chapter, the CST method as described in Chapter 3 is applied to the antiferromagnetic spin-$\frac{1}{2}$ easy-axis XXZ model. This chapter focuses on a square lattice, whereas in the subsequent Chapter 6, the same model is analyzed on a honeycomb lattice. The lattice-independent Hamiltonian of the easy-axis XXZ model is given by

$$\begin{aligned}\hat{\mathcal{H}} =& J \sum_{\langle i,j \rangle} \hat{S}_i^z \hat{S}_j^z + \lambda \left(\hat{S}_i^x \hat{S}_j^x + \hat{S}_i^y \hat{S}_j^y \right) \\ =& J \sum_{\langle i,j \rangle} \hat{S}_i^z \hat{S}_j^z + \frac{\lambda}{2} \left(\hat{S}_i^- \hat{S}_j^+ + \hat{S}_i^+ \hat{S}_j^- \right),\end{aligned} \tag{5.1}$$

where $J > 0$ is the exchange coupling between spins on neighboring sites. The sum over $\langle i, j \rangle$ represents the sum over pairs of nearest neighbors on the lattice, where each bond is counted once. A spin anisotropy is introduced by $\lambda \in [0, 1]$ with the z-axis being the easy axis. All necessary steps to transform this Hamiltonian in the case of the square lattice to a form suitable for the application of the CST were already outlined in Section 2.5. The application of the CST itself was discussed already in Chapter 3. For an overview of all transformations, the reader is referred to Figs. 2.10 and 4.4, which visualize all transformations applied to the initial spin Hamiltonian along with the observables before the CST and also list the key aspects of the CST.

Regarding the CST implementation, all flow equations are set up in momentum space and use either the particle-conserving generator (pc generator) $\hat{\eta}^{\mathrm{pc}}$ of Section 3.3.3 or the particle-block-separating generator with $k = 0$ ($0n$ generator) $\hat{\eta}^{\mathrm{pbs}}_{0:n}$ of Section 3.3.4. Resulting flow equations are truncated according to the scaling dimension as introduced in Section 3.4.3, so that operators in the flow equations under consideration are limited to a maximum scaling dimension of $d = 2$. Section 4.1 gives an example for this explicit implementation on how the flow equations are determined in the context of the XXZ model.

The objectives of this chapter are twofold. First, it demonstrates that the CST method is generally also applicable away from the afHM. The antiferromagnetic easy-axis XXZ model on a square lattice serves this purpose perfectly as it also contains the afHM as a limiting case. Second, given

a converging flow, it should determine whether the results obtained with the CST can provide a quantitative description of relevant physical quantities. Furthermore, this analysis enables a detailed evaluation of the validity of the employed truncation scheme beyond gapless systems, based on scaling dimensions.

Almost all results presented in this chapter have already been published in Refs. [Wal+23; Cac+24], and significant portions of this chapter are adopted from these collaborative works. The corresponding initial values of the coefficient of the flow equations, together with the flow equations for each coefficient itself, are given in Appendix A.

The chapter is structured as follows. First, in Section 5.1, the convergence behavior of the different generators is analyzed. Then, in Section 5.2, the relevant physical quantities are introduced and classified according to the particle sectors in which they are found. In Section 5.3, the finite-size effects stemming from the discretization schemes introduced in Section 4.2 are discussed, and an extrapolation scheme to the thermodynamic limit is presented.

5.1 Convergence of the Generators

Prior to discussing relevant physical quantities, the convergence of the two generators, pc generator and $0n$ generator, for the XXZ model on a square lattice must be examined. The presence or the absence of convergence for each generator has substantial implications for the model at hand. Thus, important insights for Sections 3.3.3 and 3.3.4 are reiterated.

A divergent flow with the pc generator $\hat{\eta}^{\mathrm{pc}}$ indicates that different quasiparticle sectors energetically overlap, i.e., level crossings occur between modes with a different number of quasiparticles. Contrary to this, the convergence of the flow indicates that the underlying quasiparticle picture is valid and that there are no inter-block level crossings in the chosen truncation scheme.

A divergent flow with the particle-block-separating generator (pbs generator) $\hat{\eta}^{\mathrm{ps}}_{(0:N)}$ indicates that the chosen quasiparticle picture breaks down and is inadequate to describe the underlying physics correctly. Specifically, level crossings of excited states with the ground state, such as those induced by a second-order phase transition, render the quasiparticle ground state insufficient. Accordingly, parameter regions may exist where the pc generator flow diverges while the $0n$ generator flow remains convergent. Hence, the description in terms of the chosen quasiparticles accurately reflects the underlying physics.

The convergence analysis entails evaluating the behavior of the flow equations across the entire parameter range $0 \leq \lambda \leq 1$. Furthermore, the system size and the choice of discretization scheme, as described in Section 4.2, influence convergence behavior.

For the XXZ model on a square lattice, convergence analysis reveals that the flow using the pc generator converges for all values of λ with a specific restriction. As already addressed in Section 4.2, the $\boldsymbol{k} = (0, 0)$ point may introduce numerical artifacts. For $\lambda \approx 1$, these artifacts result in divergence when using the N_{p} discretization scheme. Because the antiperiodic discretization scheme N_{ap} excludes the $\boldsymbol{k} = (0, 0)$ point, convergence is maintained for all values of λ and system sizes. As the $0n$ generator holds the same restriction as the pc generator and no parameter range exists where the pc generator diverges while the $0n$ generator converges, all results are obtained with the pc generator. The pc generator is to be preferred over the $0n$ generator, because it yields a fully block-diagonal effective Hamiltonian, as discussed in Section 3.3.

In the analysis of the afHM $\lambda = 1$, the coefficients associated with $\boldsymbol{k} = (0, 0)$ are set to zero, thereby eliminating their contributions in the flow equations. This approach yields a convergent

flow for the N_p discretization for all values of λ. If this modification is not applied, a convergent flow for the N_p discretization is observed only for $\lambda \lesssim 0.99925$. However, this threshold exhibits dependence on the system size. The impact of the numerical artifacts at $\boldsymbol{k} = (0, 0)$ for $\lambda \approx 1$ is attenuated for higher system sizes, and the threshold moves closer to $\lambda = 1$. Here, a linear system size of $L = 18$ determines the threshold above.

5.2 Overview of Physical Quantities

With the flow of the pc generator showing convergence across the full parameter range, this section sets the stage for analyzing the physical quantities of the XXZ model in the framework of the CST and comparing them to other methods in the following sections. The effective model obtained from the CST with the pc generator gives direct access to different particle sectors, as the flow with the pc generator eliminates all couplings between different sectors. Restricting the analysis to the zero-, single-, and two-particle sectors is sufficient, as the focus here is on low-energy excitations in the XXZ model. In the following, the physical quantities of interest are introduced, together with established results from the literature. Further, they are classified according to the particle sector in which they are encountered.

Zero-Particle Sector

The ground-state energy per site e_0 of the model is found in the zero-particle sector and serves as a first testbed for our approach. For the XXZ model, the ground state in the Ising limit ($\lambda = 0$) is precisely the Néel state with a ground-state energy per site $e_0 = -J/2$ that spontaneously breaks the discrete $\mathbb{Z}_2$ symmetry. In the other limiting case $\lambda = 1$, the ground state is that of the isotropic afHM. In the thermodynamic limit, it spontaneously breaks the SU(2) symmetry. The ground-state energy per site obtained from QMC takes the value ${e_0}^{\mathrm{QMC}} = -0.669444(2)J$ [Cac+24]. Between these two limits, also QMC results are available [Cac+24].

The staggered magnetization per site m_z, also referred to as sublattice magnetization, serves also as an important quantity of the ground state. It measures the degree of antiferromagnetic order in the system and serves as the order parameter for the magnetic symmetry-broken phase. In the Ising limit, for the Néel state, the staggered magnetization per site takes its maximal value of $m_z = \frac{1}{2}$. As quantum fluctuations increase with λ, the staggered magnetization decreases continuously. At the isotropic Heisenberg point, QMC simulations yield a value of $m_z = 0.3074(2)$ [Cac+24]. The staggered magnetization can be determined with the CST as a response of the ground-state energy to a small staggered magnetic field or by introducing the observable $\hat{S}^z(\boldsymbol{Q})$.

Single-Particle Sector

The transversal correlation length ξ^x characterizes the spatial decay of transversal spin correlations in the ground state. Close to the isotropic Heisenberg point, ξ^x diverges as the system approaches the point where the symmetry of the Hamiltonian is enhanced, and the continuous SU(2) symmetry is restored. The transversal correlation length is related to the single-particle dispersion [Oku+01; Cac+24], which is used to determine ξ^x here. Therefore, even though the transversal correlation length is a ground-state property, thus a zero-particle quantity, it will be discussed in the context of the single-particle sector.

The single-particle dispersion $\omega(\boldsymbol{k})$ is found in the single-particle sector of the effective Hamiltonian. For $\lambda = 0$, the dispersion is completely flat $\omega(\boldsymbol{k}) = 2J$ because the elementary excitations, spin flips, are completely immobile. For $\lambda > 0$, more and more features emerge. In the magnetic Brillouin zone (MBZ), the dispersion displays a minimum at $\boldsymbol{k} = (0, 0)$ which defines the spin gap $\Delta \coloneqq \omega(\boldsymbol{k} = \boldsymbol{0})$. It closes at the isotropic Heisenberg point $\lambda = 1$ according to Goldstone's theorem. The closure of the spin gap is expected to follow a square root power law as in spin wave theory [WOH91], due to singularities stemming from Goldstone modes and not critical fluctuations [Sin89]. Results of SE [ZOH05] and QMC simulations [Cac+24] are consistent with this. Additionally, the dispersion along the line from $\boldsymbol{k} = (\pi, 0)$ to $\boldsymbol{k} = (\frac{\pi}{2}, \frac{\pi}{2})$ in the Brillouin zone develops a distinct local minimum at $\boldsymbol{k} = (\pi, 0)$, called the roton minimum, and the global maximum at $\boldsymbol{k} = (\frac{\pi}{2}, \frac{\pi}{2})$. The roton minimum occurs only in third-order spin wave theory [Syr10]. It is understood to be due to magnon-magnon interactions [PUS15; PSU18] and due to a peculiar cancellation for motion along the diagonals [Ver18]. In summary, spin gap Δ, roton minimum, and dispersion maximum are all physical quantities of interest contained in the one-particle block of the effective Hamiltonian. The goal is to analyze with the CST their behavior as a function of the anisotropy $\lambda \in [0, 1]$ with a special focus on the critical behavior of Δ for $\lambda \to 1$.

Two-Particle Sector

Two-magnon bound states can occur in the two-particle sector of the effective Hamiltonian. Generally, eigenstates that are built from two elementary excitations, i.e., two magnons, are particularly interesting because they reflect the degree of magnon-magnon interaction. For strong interaction relative to the kinetic energy of the magnons, bound states occur in the gapped phase. The two-particle spectrum of the Ising model features degenerate bound states at $3J$ stemming from adjacent pairs of spin flips. All other states of two magnons have energy $4J$ and are thus highly degenerate. For finite λ, these states evolve into energy continua of scattering states. The four bound states also exist for finite λ, but merge with the continuum for values λ close to but smaller than one [OI73; Ham09; Dus+10] consistent with quantum Monte Carlo simulations of coupled XXZ spin ladders [YSW19]. No bound states are known at the isotropic point, but the attractive interaction between magnons leads to a considerable shift of spectral weight to lower energies [PUS15; PSU18]. These bound states are tracked for all λ and determine at which values of λ the bound states vanish in the two-magnon continuum by analyzing the locality of bound states with the help of the inverse partition ratio (IPR) [KM93; MU19].

5.3 Extrapolation in the Linear System Size L

Even though the initial conditions are determined in the thermodynamic limit by evaluating the mean-field parameters accordingly, the solution of the flow equations is performed on a finite lattice with linear system size L, as discussed in Section 4.2. To get a grasp of the resulting physical quantities in the thermodynamic limit $L \to \infty$, finite-size effects must be carefully analyzed. Consequently, an extrapolation in $1/L \to 0$ is performed for all results shown in the following sections. For small values of λ up to $\lambda \approx 0.8$, the computed values do not show any relevant finite-size effects. Furthermore, in this area, periodic N_p or antiperiodic N_ap boundary conditions show no discernible difference in the results. Hence, all extrapolating schemes yield essentially the same result, see panel (a) in Fig. 5.1. For $\lambda > 0.8$, two trends emerge for increasing L, see panels (b) and (c) in Fig. 5.1. First, the values for N_p discretization decrease monotonically while those for N_ap discretization increase monotonically. Second, the values from the N_ap discretization show

an almost linear relation as function of $1/L$ for $\lambda \lesssim 1$. Values provided in the following sections are the estimates of the extrapolation using monotonic quadratic fits

$$x(1/L) = a + b(1/L + c)^2 \tag{5.2}$$

for the N_{ap} discretization with $c \geq 0$, evaluated at $1/L = 0$.

The error estimate results from the difference between the highest values from the discretizations N_{ap} and N_{p}, see Fig. 5.1. For the transversal correlation length ξ^x a linear extrapolation in $1/L$ was used; the error estimate remains the same. Note that at the time of the analysis, only even values of L for N_{p} and odd values of L for N_{ap} were considered. On the one hand, this choice is reasonable, as in both cases the edge of the MBZ is sampled; on the other hand, the program used at that time was not able to handle both boundary conditions for all values of L.

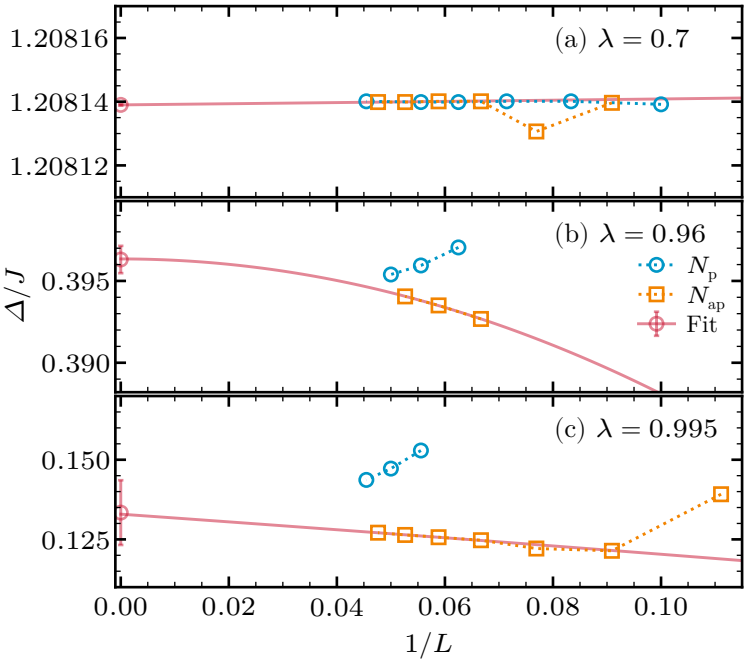

Figure 5.1: Generic extrapolations in $1/L$ for $\lambda = 0.7$, $\lambda = 0.96$, and $\lambda = 0.995$. For small λ, calculations on the discretizations N_{ap}, and N_{p} converge, see panel (a). At higher values of λ, see panels (b) and (c), values from N_{ap} are monotonically increasing while values from N_{p} are monotonically decreasing. For the whole range, a monotonic quadratic fit for the N_{ap} data is used to determine the values for $L \to \infty$. The error estimate depicted as a red bar results from the difference between the values from N_{ap} and N_{p} for the highest reached value of L

5.4 Zero-Particle Sector

The zero-particle sector contains only the coefficient C^0 of the effective Hamiltonian after applying the CST. It corresponds to the system's ground-state energy. Regardless of the convergent flow, whether the pc generator or the $0n$ generator is used, the ground state is fully separated from all excited states. Nevertheless, the ground state energy is not the only relevant physical quantity in the zero-particle sector. Additionally, the staggered ground state magnetization per site m_z and the transversal correlation length ξ^x of the ground state are relevant. In the following, the

ground-state energy per site e_0 and the staggered magnetization per site m_z are analyzed. The transversal correlation length ξ^x, however, is only discussed in the context of the single-particle sector, since it is determined from the single-particle dispersion.

5.4.1 Ground-state energy

The first quantity inspected is the ground-state energy per site $e_0(\lambda) = E_0(\lambda)/(2L^2)$ of the XXZ model. Where $E_0(\lambda)$ is the ground-state energy obtained from the zero-particle sector, with the coefficient $C^0(\lambda) = E_0(\lambda)$ of the effective Hamiltonian after applying the CST with the pc generator. The ground-state energy per site $e_0(\lambda)$ is shown in Fig. 5.2 as computed by CST, SE up to order 14 in λ [ZOH05], and QMC calculations [Cac+24]. Starting from the classical

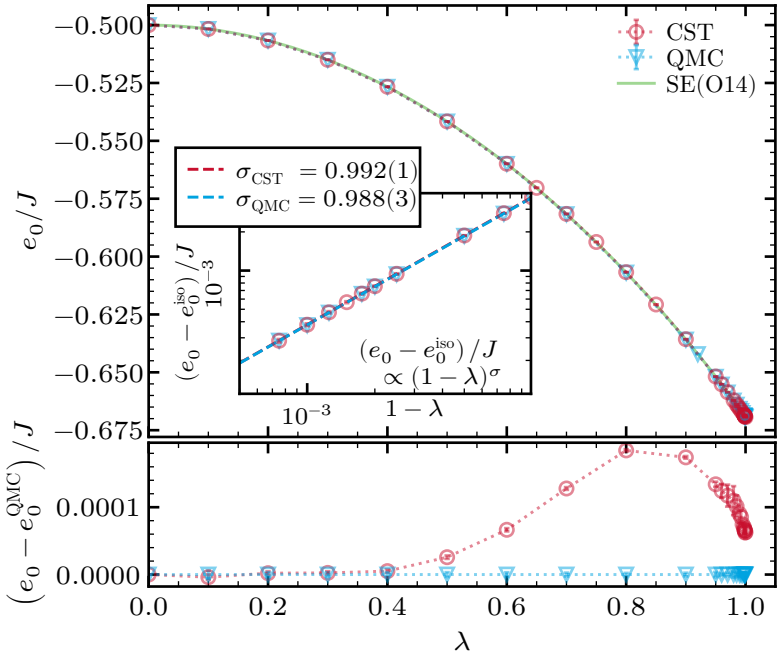

Figure 5.2: The upper panel shows the ground-state energy per site e_0 as a function of λ. The CST data is compared to results of QMC calculations [Cac+24] and SE results [ZOH05]. As expected from second-order perturbation theory, the ground-state energy displays a monotonically decreasing behavior with negative curvature. The inset of the upper panel shows the difference of the ground-state energy per site e_0 to the ground-state energy per site of the isotropic afHM e_0^{iso} in a double logarithmic plot close to the Heisenberg point. The dashed lines indicate the corresponding power-law fits. The lower panel shows the absolute difference of the ground-state energy per site e_0^{QMC} for both QMC and CST data as a function of λ. Trivially, the difference for QMC is zero, with the emphasis being more on the uncertainty of the QMC data.

Néel state in the Ising limit, increasing λ induces increasing quantum fluctuations, leading to a ground-state energy that continuously decreases. The results of the CST are identical to the SE results within line width for the whole λ range. For $\lambda = 1$, the CST result ($e_0 = -0.669\,38(1)\,J$) agrees well with QMC calculations ($e_0^{\mathrm{QMC}} = -0.669444(2)J$), and the extrapolated SE results ($e_0^{\mathrm{SE}} = 0.6693(1)\,J$). However, it should be noted that the self-consistent spin-wave theory at $\lambda = 1$ already yields $e_0 = -0.670\,421\,J$, which is relatively close to the above values despite its mean-field character. This shows that the ground-state energy is a very robust quantity, accessible

by many approaches. Furthermore, the inset of the upper panel of Fig. 5.2 shows the difference of the ground-state energy per site e_0 to the ground-state energy per site of the isotropic afHM e_0^{iso} in a double logarithmic plot close to the Heisenberg point. The resulting power-law fit with $e_0 - e_0^{\mathrm{iso}} \propto (1-\lambda)^{\sigma}$ yields an exponent of $\sigma_{\mathrm{CST}} = 0.992(1)$ for the CST data consistent with QMC data $\sigma_{\mathrm{QMC}} = 0.988(3)$. Both values are close the connected mean-field exponent of $\sigma = 1$.

The lower panel of Fig. 5.2 shows the absolute differences between the QMC and CST data across the whole λ range. The relative errors of the QMC data are of order $O(10^{-6})$ and systematic error of the finite-size extrapolation is negligible, i.e., much smaller than the statistical errors [Cac+24]. The error in the CST data is systematic, as no stochastic factors are involved. Two primary error sources can be identified: (i) the truncation of the flowing Hamiltonian to quartic order and (ii) the finite-size effect. The finite-size effect can be assessed by varying the extrapolations and the boundary conditions, and is estimated to be $O(10^{-5})$. The effect of truncation cannot be estimated intrinsically; it can only be assessed by comparing results with those from other methods. For the comparison of the CST data with the QMC data, it is found that above $\lambda \approx 0.4$, the CST data start to deviate from the QMC data. This deviation is systematic, since it does not change in sign and evolves smoothly. The deviation becomes maximum around $\lambda \approx 0.9$, where it is of order $O(2 \times 10^{-4})$. Still, the agreement is very good.

5.4.2 Staggered Magnetization

Because the total magnetization of an antiferromagnet is zero, the staggered magnetization M_z, also called sublattice magnetization, is an important quantity for characterizing the magnetic order of the ground state. Within the CST framework, M_z can be computed in two distinct ways. First, by introducing a staggered magnetic field in accordance with the magnetic order of the Néel state to the Hamiltonian, resulting in the additional terms

$$\hat{\mathcal{H}}(h_{\mathrm{alt}}) = \hat{\mathcal{H}}_{XXZ} - h_{\mathrm{alt}} \sum_{\boldsymbol{r}_i \in \Gamma_A} S^z_{A,i} + h_{\mathrm{alt}} \sum_{\boldsymbol{r}_j \in \Gamma_B} S^z_{B,j} \tag{5.3}$$

with the alternating magnetic field strength h_{alt}. Where the first sum runs over the sublattice Γ_A and the second sum runs over the sublattice Γ_B. Nevertheless, the modified Hamiltonian is treated in the same way as described before. The additional staggered magnetic field, however, enables the calculation of the staggered magnetization M_z as the response of the ground-state energy to this field

$$|M_z| = \left| \frac{d}{dh_{\mathrm{alt}}} E_0 \Big|_{h_{\mathrm{alt}}=0} \right| = \left| \left\langle \frac{\partial \hat{\mathcal{H}}(h_{\mathrm{alt}})}{\partial h_{\mathrm{alt}}} \right\rangle_0 \right| = \left| \left\langle \sum_{\boldsymbol{r}_i \in \Gamma_A} S^z_{A,i} - \sum_{\boldsymbol{r}_j \in \Gamma_B} S^z_{B,j} \right\rangle_0 \right|, \tag{5.4}$$

according to the Hellmann-Feynman theorem. In practice, the derivative is computed by the ratio

$$|M_z| = \left| \frac{d}{dh_{\mathrm{alt}}} E_0 \Big|_{h_{\mathrm{alt}}=0} \right| \approx \left| \frac{(E_0(h_{\mathrm{alt}}) - E_0(0))}{h_{\mathrm{alt}}} \right| \tag{5.5}$$

cite for small $h_{\mathrm{alt}} \approx 10^{-7} J$.

An alternative way to compute the staggered magnetization M_z is to evaluate the observable of the longitudinal dynamic structure factor

$$\hat{S}^z(\boldsymbol{Q}) = \sum_{\boldsymbol{r}_i \in \Gamma_A} \mathrm{e}^{-\mathrm{i}(\boldsymbol{Q}\boldsymbol{r}_i)} S^z_{A,i} + \sum_{\boldsymbol{r}_j \in \Gamma_B} \mathrm{e}^{-\mathrm{i}(\boldsymbol{Q}\boldsymbol{r}_j)} S^z_{B,j} \,. \tag{5.6}$$

For the square lattice, M_z is obtained if the observable is evaluated at the wave vector $\boldsymbol{Q} = (\pi, \pi)$, yielding

$$|M_z| = \left| \left\langle \sum_{i \in \Gamma_A} S^z_{A,i} - \sum_{j \in \Gamma_B} S^z_{B,j} \right\rangle_0 \right| . \tag{5.7}$$

Comparing the two approaches to compute the staggered magnetization, of course, in an ideal case, both should yield the same result. However, both are in their own way susceptible to systematic and numerical errors. Additionally, both approaches require different adaptations in the implementation. The first approach requires, besides the modification of the Hamiltonian, at least two separate solutions of the flow equations for different values of h_{alt} to compute the derivative numerically. So, evaluating the staggered magnetization at least doubles the computational effort. Additionally, the choice of h_{alt} is also not trivial to minimize numerical errors.

The second approach requires implementing the flow equations for the observable. As a result, additional coefficients must be tracked during the flow, increasing computational effort. Even though the observable introduces no additional tunable parameter h_{alt}, in the setup of the flow equations of the observable, a truncation scheme is applied. So both truncation errors of the Hamiltonian and of the observable may influence the final result.

Figure 5.3 shows the staggered magnetization per site $m_z = M_z/(2L^2)$ obtained with the two different approaches discussed above as a function of the anisotropy λ. Additionally, in Fig. 5.3 the CST data is compared to results of QMC calculations [Cac+24], SE calculation up to an order of $O(10)$ [HZA92] and DMRG calculations [Kad+24]. In the upper panel of Fig. 5.3, across the entire range of λ, the CST shows a good agreement with the QMC, SE, and DMRG results for both approaches. Only close to the isotropic Heisenberg point $\lambda = 1$, the SE results deviate, indicating limitations of the bare series expansion in this regime.

In the inset of the upper panel, the difference of the staggered magnetization per site m_z to the staggered magnetization of the isotropic afHM m_z^{iso} is shown in a double logarithmic plot close to the Heisenberg point. The critical behavior of the staggered magnetization is expected to follow a power law $m_z - m_z^{\text{iso}} \propto (1 - \lambda)^\sigma$. The QMC exponent $\sigma_{\text{QMC}} = 0.50(5)$ confirm again the mean-field behavior, which is $\sigma = 0.5$ for the staggered magnetization. However, both CST approaches deviate slightly and underestimate the magnetization close to $\lambda \approx 1$, as a result, the exponent determined by CST is higher with $\sigma_{\text{CST}} \approx 0.7$. Interestingly, both CST approaches yield very similar results, even though they are obtained in completely different ways, suggesting that a systematic error in the CST may be induced by the truncation scheme rather than by an error in the calculation approach.

In the following discussion, only the results obtained via the response to a staggered magnetic field are considered, as they are due to historical reasons[1] calculated for higher systems sizes ($L \leq 22$). In the lower panel of Fig. 5.3, the difference between CST and QMC shows the same behavior as for the ground-state energy per site. The statistical errors in the QMC calculations are of order $O(10^{-4})$. In terms of the CST, the error of the finite-size effect and the effect of approximating a derivative by a ratio in the CST data is estimated as $O(10^{-3})$ The deviation between the data from CST and QMC becomes maximal around $\lambda \approx 0.9$ as well and is of the order of $O(5 \times 10^{-3})$. Compared to the behavior of the deviation in the ground-state energy, it is not as smooth. This fact may be a result of the additional calculation of the derivative, along with the finite-size effects. However, this is also observed for the observable, where additional errors may be introduced by

[1] The calculation via the observable was at the point of publication of Ref. [Cac+24], not implemented and thus not calculated with the highest feasible system sizes, as here it only serves as a comparison.

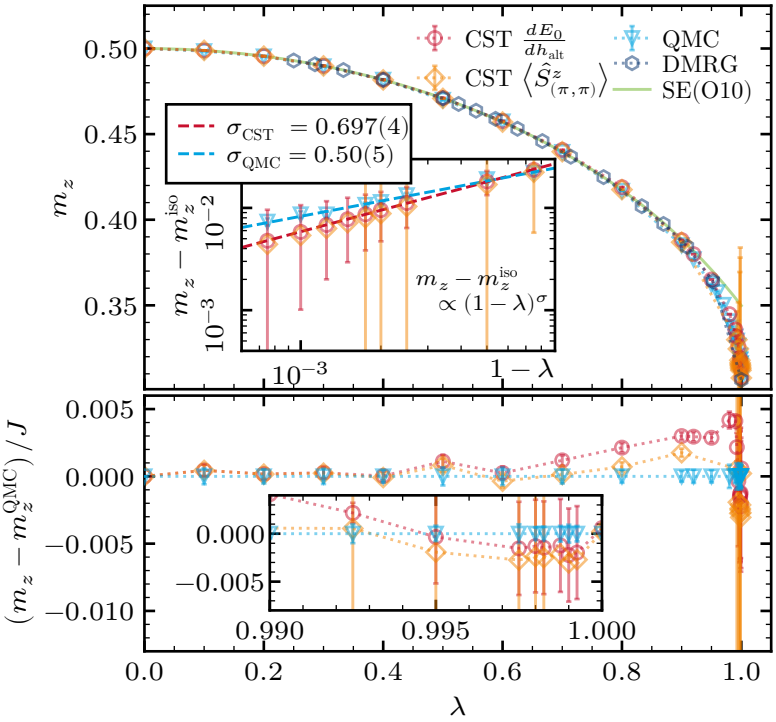

Figure 5.3: The upper panel shows the staggered magnetization per site m_z as a function of λ. The CST data is calculated via the response to a staggered magnetic field h_{alt}, and CST data calculated via the flow of the observable are depicted. Both are compared to results of QMC [Cac+24], SE [HZA92] and DMRG [Kad+24]. The inset of the upper panel shows the difference of the staggered magnetization per site m_z to the staggered magnetization of the isotropic afHM m_z^{iso} in a double logarithmic plot close to the Heisenberg point. The dashed lines indicate the corresponding power-law fits. The lower panel shows the absolute difference of the staggered magnetization per site m_z^{QMC} for both QMC and CST data as a function of λ. Trivially, the difference for QMC is zero, with the emphasis being more on the uncertainty of the QMC data. Note, higher uncertainties for the calculation via the observable with the CST for $\lambda \approx 1$ stem from the fact that smaller system sizes ($L \leq 18$) were considered compared to the calculation via the response ($L \leq 22$), which leads also to higher uncertainties.

the truncation scheme used for the observable. Compared to the Hamiltonian, only terms up to quadratic order are considered. For details on the observables, please refer to Appendix A.2. Nevertheless, the comparison again showed a very good agreement between these two approaches and also the QMC results.

5.5 Single-Particle Sector

In the single-particle sector of the effective Hamiltonian after applying the CST with the pc generator, the single-particle dispersion $\omega(\boldsymbol{k})$ is obtained from the coefficients $C^{\hat{\alpha}^\dagger\hat{\alpha}}(\boldsymbol{k}) = C^{\hat{\beta}^\dagger\hat{\beta}}(\boldsymbol{k})$ directly as the dispersion in the XXZ model is degenerated. The Fig. 5.4 shows the results of the CST for the dispersion along a high-symmetry path through the MBZ for various λ and a linear system size of $L = 16$ with periodic boundary conditions. Additionally, linear spin-wave theory (L-SWT) results together with self-consistent mean-field spin-wave theory (scMF-SWT)

results based on the considerations in Section 2.5 are also shown to illustrate the effect of the CST. At $\lambda = 0$, the XXZ model is reduced to the antiferromagnetic Ising model with a completely flat dispersion $\omega(\boldsymbol{k}) = 2J$. For $\lambda = 1$, the XXZ model coincides with the afHM, which was already studied using the CST method in Refs. [PUS15; PSU18]. At this isotropic point, the dispersion features gapless Goldstone bosons and a distinct minimum at $\boldsymbol{k} = (\pi, 0)$, called the roton minimum. For $0 < \lambda < 1$, a continuous evolution between these two limits takes place. It also becomes evident that the CST produces stronger renormalization for higher λ compared to the mean-field spin-wave theory (MF-SWT) results, especially for momenta connected to higher energies. In the following, both the spin gap and the roton minimum are discussed in more detail.

However, first, another aspect has to be mentioned. Compared to the ground-state energy or the staggered magnetization, given different discretization schemes, as introduced in Section 4.2, it is possible that certain combinations of boundary conditions and linear system sizes exclude specific momenta of interest in their discretization. For example, the gap at $\boldsymbol{k} = (0, 0)$ is excluded in all discretizations with antiperiodic boundary conditions N_{ap}. To this end, the fit

$$\omega(\boldsymbol{k})^2 = \sum_{m=0}^{M} A_m \cos(m\boldsymbol{k}) \tag{5.8}$$

is used, adapted from one dimension [Oku+01] to arbitrary dimensions [Cac+24], to interpolate the dispersion along a given linear path and so determine missing momenta. A very fast convergence of these coefficients is found for increasing M so that the dispersion is interpolated very reliably in the whole MBZ for both boundary conditions. Note that in Eq. (5.8) the square of the dispersion is fitted, as L-SWT predicts a $\omega(\boldsymbol{k})$ containing a square root. This modification ensures a smooth function and thus the capture of the correct dispersion behavior, even at the Heisenberg point.

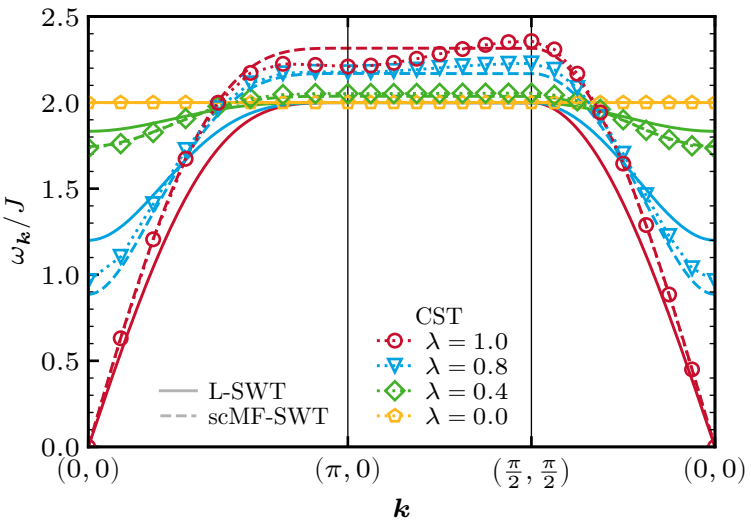

Figure 5.4: CST result of the dispersion $\omega(\boldsymbol{k})$ for $L = 16$ with periodic boundary conditions N_{p} for various λ. For $\lambda = 0$, the XXZ model is the Ising model with a flat dispersion. At the same time, it is the afHM for $\lambda = 1$ with a gapless spectrum and a distinct roton minimum at $\boldsymbol{k} = (\pi, 0)$ [PUS15; Ver18]. For $0 < \lambda < 1$ the CST results interpolate smoothly between these two limits. Additionally, L-SWT and scMF-SWT results are shown for each λ.

5.5.1 Spin Gap

The first quantity of interest for a detailed study in the single-particle dispersion is the spin gap $\Delta := \omega(\boldsymbol{k} = \boldsymbol{0})$. Here, the aim is to track the evolution of the spin gap Δ as a function of the anisotropy λ from the Ising limit at $\lambda = 0$ to the isotropic Heisenberg point at $\lambda = 1$, where the gap closes according to Goldstone's theorem. Figure 5.5 shows the extrapolated CST results for the single-magnon gap Δ compared to other methods. For small λ, it can be compared to high-order SE calculation [ZOH05; Dus+10] and to data obtained by the CCM [Bis+17]. For large $\lambda \lesssim 1$, the asymptotic power law in the critical region derived from SE results [ZOH05] and spin-wave theory (SWT) [HZA92] are presented. The CST results interpolate smoothly between these two limits, capturing both limits quantitatively. The findings are further in agreement with CCM results [Bis+17] and very recent DMRG studies [Kad+24]. Additionally, for comparison, across the whole range of λ, unbiased QMC results [Cac+24] are shown.

The last available data point with the CST is at $\lambda = 0.9995$. The reason is that, for even higher values of λ, no convergence of the flow equations was achieved at the highest system size $L = 22$ with periodic boundary conditions N_p, as required for the error estimate. This is attributed to the fact that for values of λ even closer to the isotropic point, the cluster size L is not large enough to capture the relevant physics. In Section 5.5.2, this observation is further linked to the transversal correlation length ξ^x.

In Fig. 5.5, the agreement between all approaches is perfect for almost all values of λ. For smaller values of λ, the various approaches agree excellently. Only near the vanishing of the gap do the CCM data deviate from the other results, which is likely linked to the attainable cluster sizes. Especially, in the double-logarithmic plot in the inset of the upper panel in Fig. 5.5, the agreement between the extrapolated SE, QMC and the CST results is remarkable since the latter are obtained on a finite lattice of moderate size $L \approx 20$ and extrapolated to the thermodynamic limit without imposing a specific power law.

Both data sets support the conclusion that the spin gap vanishes in a square root fashion $\propto (1-\lambda)^\sigma$ with $\sigma = 0.5$, as reported in Refs. [HZA92; ZOH05]. In the lower panel of Fig. 5.5, the absolute difference between the CST and QMC data is shown. The relative statistical errors of the QMC data are of order $O(10^{-3})$ and near the isotropic Heisenberg point of order $O(10^{-2})$. The relative error estimate for the CST data yields $O(10^{-4})$ and lower for $\lambda < 0.9$ and rises to 0.66% close to the isotropic point. While there is a slight systematic deviation of the CST data, both approaches agree very well. Remarkably, the absolute deviation between CST and QMC data, again, as for the other quantities of Figs. 5.2 and 5.3, shows a decrease upon approaching the isotropic point. This can be interpreted as a justification of the truncation based on the scaling dimension, which allows finding the relevant effective model close to the isotropic point almost quantitatively. This finding corroborates the applicability of CST in momentum space to describe phase transitions with closing gaps.

However, the error estimate also grows for larger values of λ, as the physical quantities develop a stronger finite-size scaling, as also seen in Fig. 5.1, implying larger correlation lengths in the vicinity of the isotropic point.

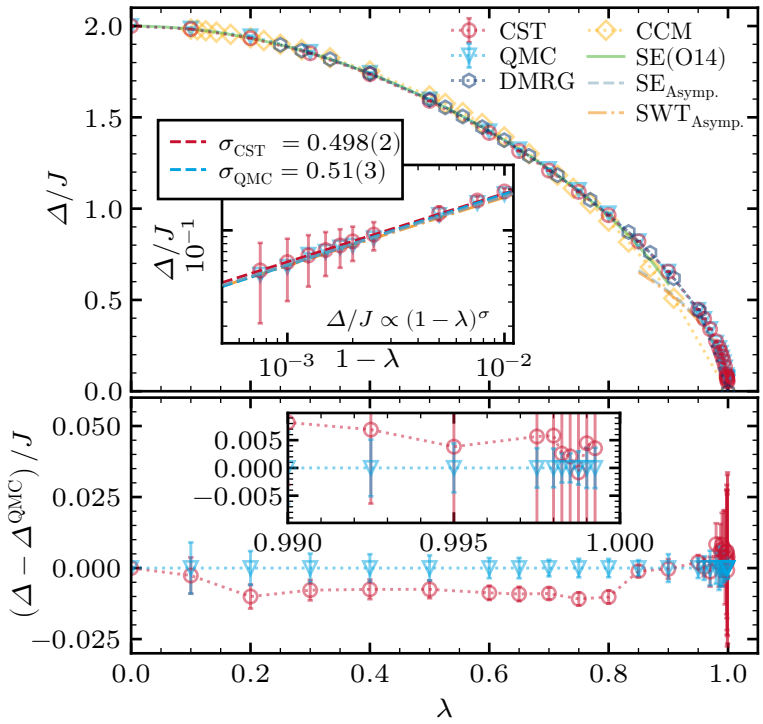

Figure 5.5: The upper panel shows CST results for the one-magnon gap $\Delta = \omega(\boldsymbol{k} = 0)$ of the XXZ model for $0 \leq \lambda \leq 1$. They are compared to QMC data [Cac+24], third order SWT [HZA92; Syr10], CCM data [Bis+17], DMRG data [Kad+24], results from SE about the Ising limit [ZOH05; Dus+10], and the critical power law extracted from SE [ZOH05]. A quantitative comparison of the critical behavior is shown in the inset, underlining excellent agreement. The lower panel shows the absolute difference of the single particle gap Δ^{QMC} for both QMC and CST data as a function of λ. Trivially, the difference for QMC is zero, with the emphasis being more on the uncertainty of the QMC data.

5.5.2 Transversal Correlation Length

As mentioned in Section 2.5.4, the self-consistent nonlinear spin-wave theory (scNL-SWT) to determine the initial conditions is performed in the thermodynamic limit. Nevertheless, the flow equations are solved for a discretized lattice as discussed in Section 4.2. Hence, the CST results combine elements of calculations in the thermodynamic limit with calculations on a finite lattice. In order to judge if the discretization in the MBZ induces finite-size effects, the ground-state transversal correlation length ξ^x is calculated. Whenever it is significantly larger than the system's linear length scale, finite-size effects are likely to occur. The transversal correlation length ξ^x is expected to be the same in all directions for $\xi^x \gg a$ where a is the lattice constant. For $\lambda \to 1$, ξ^x diverges. Thus, it is sufficient to perform the same one-dimensional fit for a single direction as in Eq. (5.8) and calculate ξ^x from the one-magnon dispersion ω via

$$\omega(\mathrm{i}\kappa) = 0 \quad \text{with} \quad \mathrm{Re}(\kappa) = 1/\xi^x \tag{5.9}$$

adapted from Ref. [Oku+01] in 1D to arbitrary dimensions [Cac+24].

Figure 5.6 shows the extrapolated inverse transversal correlation lengths $1/\xi^x$ along the used fit-axes from $\boldsymbol{k} = (0, 0)$ to $\boldsymbol{k} = (\pi, 0)$ for different values λ. Note that $1/a = 1$ is used as units,

since the lattice constant a is set to 1. Additionally, Fig. 5.6 shows a horizontal dashed line for the relevant length scale of the largest used system $L = 22$, namely the shortest occurring wrap-around $\sqrt{2}L$, in this case, in a diagonal direction. In the inset of Fig. 5.6, a zoom to the domain $0.993 < \lambda < 0.9995$ is shown. Figure 5.6 suggest that for $\lambda \leq 0.995$, finite-size effects are not expected. For $\lambda \geq 0.9985$, the finite size of the system might play a noticeable role. The error estimate from $\lambda = 0$ to $\lambda = 0.95$ lies below 0.1 %, below 1 % for $\lambda \leq 0.97$ and below 5 % for $\lambda \leq 0.99$, and it is larger than 10 % for $\lambda \geq 0.995$. However, ξ^x never exceeds these relevant length scales dramatically. Additionally, the extrapolated results for closing of the gap are in agreement with the literature, and the CST results for the afHM in Ref. [PUS15; PSU18] performed for $L = 16$ are consistent with results in the literature. Hence, it appears that the influence of the finite size is not severe in the CST approach.

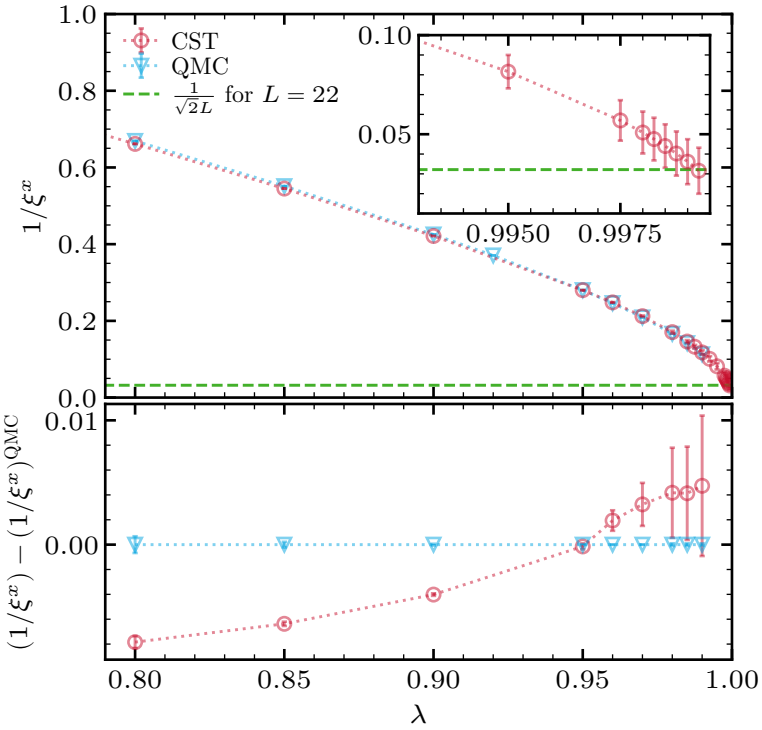

Figure 5.6: The upper panel shows CST results for the inverse ground-state correlation length $1/\xi^x$ for $0.8 \leq \lambda \leq 1$ compared to QMC data [Cac+24]. A comparison of the correlation length with the shortest wrap-around $\sqrt{2}L$ in the largest cluster with $L = 22$ is shown as a dashed line. The lower panel shows the absolute difference of the inverse ground-state correlation length $(1/\xi^x)^{\mathrm{QMC}}$ for both QMC and CST data as a function of λ. Trivially, the difference for QMC is zero, with the emphasis being more on the uncertainty of the QMC data.

Independent of the implications for the other quantities, the transversal correlation length ξ^x determined from Eq. (5.9) can be compared with other methods. Thus, in Fig. 5.6, also results from QMC calculations [Cac+24] are shown. As for the other quantities, the lower panel of Fig. 5.6 shows the absolute difference between the CST and QMC data. Again, as with the other quantities, the agreement is very good. The absolute deviation between the inverse of the correlation lengths between CST and QMC data is of order $O(10^{-3})$. However, the CST data, in contrast to the QMC data, acquire larger errors close to the isotropic point because ξ^x depends inversely proportionally on the spin gap, so that tiny inaccuracies in the latter induce significant

inaccuracies in the correlation length. Nevertheless, the results show that the CST together with the Eq. (5.9) can capture the transversal correlation length ξ^x quantitatively and thus estimate if finite-size effects become relevant.

5.5.3 Roton Minimum

Another prominent feature of the single-particle dispersion in the case of the isotropic afHM is the local minimum at momentum $\boldsymbol{k} = (\pi, 0)$, also called roton minimum or roton dip together with the global maximum of the single-particle dispersion at momentum $\boldsymbol{k} = (\pi/2, \pi/2)$. Here, the development of the roton minimum and dispersion maximum as a function of the anisotropy λ from the Ising limit at $\lambda = 0$ to the isotropic Heisenberg point at $\lambda = 1$ is studied. Figure 5.7 depicts the CST results for both the roton minimum and the dispersion maximum as a function of λ. Additionally, results from high-order SE [ZOH05] and DMRG [Ver18] are shown. Also, QMC data [SS01] are available for the isotropic point. First, the focus lies on the dispersion maximum at $\boldsymbol{k} = (\pi/2, \pi/2)$ which displays a monotonic increase in λ for CST, the SE, and the DMRG data. All data agree very well. At the isotropic point, similar values are obtained: CST (2.369 72(5) J), SE (2.385(1) J), QMC (2.39 J), and DMRG (2.40 J). For the roton minimum, CST, SE, and DMRG

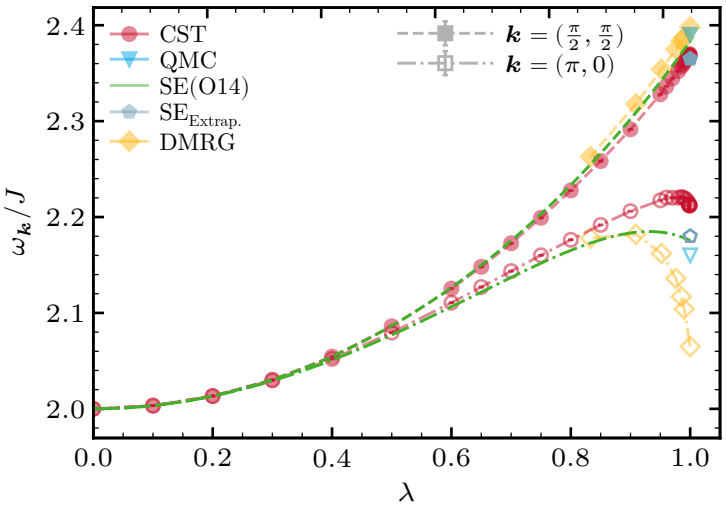

Figure 5.7: CST results for the roton minimum $\boldsymbol{k} = (\pi, 0)$ and the dispersion maximum $\boldsymbol{k} = (\pi/2, \pi/2)$ for $0 \leq \lambda \leq 1$ compared to data from SE [ZOH05], DMRG [Ver18], and QMC [SS01]. All methods agree well, given the maximum dispersion. For the roton minimum, all methods predict an inflection point for $\lambda \gtrsim 0.8$. The values for the depth of the roton minimum differ slightly.

show qualitatively similar results: first, the dispersion increases, and for larger $\lambda \gtrsim 0.8$ an inflection point occurs. This inflection point is consistent with the observation in Ref. [PUS15; PSU18] that the hybridization between the one-magnon state and the three-magnon scattering states causes the dip due to level repulsion. This mechanism becomes increasingly important at higher λ as dispersion and the continuum approach each other. The numerical values for the roton dip for $\lambda = 1$ are 2.211(3) J for the CST, 2.18(1) J for SE, 2.16 J for QMC, and 2.06(1) J for DMRG. Hence, these values are reasonably close but have a wider spread than the maximum values. It can be assumed that the SE and QMC results reflect the actual value best, while the CST result is marginally high due to truncation beyond the quartic monomials. The DMRG data result from a cylindrical geometry with fixed linear extension $L = 10$. A comprehensive finite-size scaling,

therefore, could not be performed. All in all, it can be concluded that a consistent description for the high-energy properties of the dispersion of the XXZ model is reached by CST except for a slight deviation of about 2 % at the roton minimum.

5.6 Two-Particle Sector

This section focuses on the two-particle sector of the effective Hamiltonian obtained by CST. In this sector, all possible two-magnon states are considered. For non-interacting magnons, all possible energies of two-magnon states are straightforwardly given by the sum of the single-particle dispersion of the two individual magnons. In the thermodynamic limit, this leads to a two-magnon continuum, where the lower and upper band edges are determined by the minimum and maximum of the sum of two single-particle dispersions for fixed center-of-mass momentum $\boldsymbol{K} = \boldsymbol{k}_1 + \boldsymbol{k}_2$. Thus, in the non-interacting case, the two-particle sector is entirely determined by the terms of the single-particle sector.

This, however, is not the case for the Hamiltonian under consideration. Instead, the Hamiltonian of the XXZ model indeed features magnon-magnon interactions, which are also considered in the CST approach and thus are renormalized during the flow. These interactions not only can shift the two-magnon continuum relative to the non-interacting case but also can lead to the formation of two-magnon bound states lying below the two-magnon continuum. Provided, of course, that the two-particle continuum is not directly adjacent to the single-particle dispersion, as in the case with a gapless spectrum. Consequently, the gapless afHM at $\lambda = 1$ does not feature two-magnon bound states. However, taking the other extreme, the Ising limit at $\lambda = 0$, it is clear that two-magnon bound states do exist in this limit.

These bound states can be understood in terms of the Ising limit, where two flipped spins generally yield 8 broken bonds with their neighbors. This results in an energy cost of $4J$. However, if the two flipped spins are nearest neighbors as shown in Fig. 5.8a, they only yield a total number of 6 broken bonds, thus having a lower energy of $3J$ compared to other two-particle excitations and forming a bound state. Additionally, these bound states come with 4 different configurations on a square lattice, depending on the orientation of the two flipped spins, as shown in Fig. 5.8b. So altogether, in momentum space, four two-magnon bound states exist in the Ising limit.

In summary, in the Ising limit, there exist bound states below the two-magnon continuum, while in the isotropic Heisenberg limit, no such bound states exist. In the following, the goal is to determine the fate of these bound states as the anisotropy λ increases from 0 to 1, effectively tuning from the Ising model to the isotropic afHM. As the bound states do not exist in the afHM, it is of interest to determine critical values of λ where these bound states cease to exist and merge with the two-particle continuum.

5.6.1 Inverse Participation Ratio

This merging into a continuum generically occurs slowly in the sense that the slope of the lower band edge of the continuum and of the energy of the bound state are the same [US96; US98; Zhi13] Hence, the parameters where the bound state ceases to exist are extremely difficult to determine numerically. Therefore, another criterion is used, namely the locality of the bound state in its relative coordinate. A true bound state is local in the sense that it has a finite extension. If

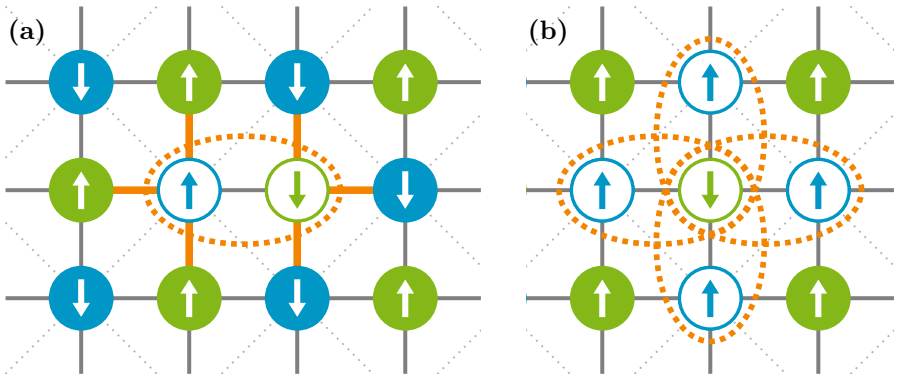

Figure 5.8: Sketches of bound states in the antiferromagnetic Ising model on a square lattice. Figure 5.8a shows a possible realization of a bound state. White-filled circles mark the two flipped spins, and orange lines mark the 6 broken bonds, yielding a total energy of $3J$. Figure 5.8b displays all four possible orientations of the bound states in the antiferromagnetic Ising model on a square lattice. All bound states are marked with dotted orange ellipses.

the extension is determined solely by the system size, no binding occurs. A good measure of the locality of a state is the inverse partition ratio (IPR) [KM93; MU19]

$$I = \sum_{\boldsymbol{r}} |\Psi(r)|^4 = \sum_{\boldsymbol{r}} |\rho(r)|^2. \tag{5.10}$$

with density $\rho(r)$ at site r of the normalized wave function $\Psi(r)$. For an extended state, the IPR I scales proportional to $1/L^2 = 1/N$ if L is the number of sites in one direction in two dimensions. This is easily seen in the limiting case of $\rho(r) = 1/N$ where $I = 1/N$ holds. The other limiting case is an entirely local state with $\rho(0) = 1$ and zero elsewhere, so that $I = 1$ holds. Hence, one has to determine whether the IPR vanishes $\propto 1/N$ for $N \to \infty$ or stays finite in this limit. The locality of bound states is measured by the IPR given in Eq. (5.10). This quantity is extrapolated linearly in $1/N$, which works remarkably well, yielding positive values for bound states and values near zero otherwise.

5.6.2 Bound states and two-magnon continuum

A particular asset of the systematic basis changes by means of CST is that bound states can be directly addressed and computed. The conservation of particle number, here the magnon number, is achieved through a basis change. It allows one to compute the bound states in the two-particle sector for any center-of-mass momentum $\boldsymbol{K} = \boldsymbol{k}_1 + \boldsymbol{k}_2$ in a given discretization. Recently, even three-particle bound states could be addressed in antiferromagnetic spin ladders, which are induced by three-particle irreducible interactions, i.e., by hexatic terms in second quantization [Sch+22]. Here, two-magnon bound states are under consideration as established perturbatively for not too large values of λ [Ham09; Dus+10].

For bound states to be infinitely long-lived, they may not decay into scattering states. Hence, their energy may not overlap with the continuum; it should remain below the continuum's lower boundary. Here, the focus is on the bound states at rest, $\boldsymbol{K} = (0, 0)$, because, generically, the energetically lowest lying bound states occur at a center-of-mass momentum of zero. This is confirmed by series expansions [Ham09; Dus+10]. In addition, the strongest binding occurs for

zero total S^z, i.e., between an α- and a β-magnon living on the A- and B-sublattices, respectively. Again, this is confirmed perturbatively.

It is mandatory to distinguish the four bound states and determine each corresponding wave function correctly, as it is needed to compute the IPR. For degenerate states, a simple numerical diagonalization does not yield the correct eigenstates; instead, arbitrary superpositions of the degenerate states are obtained, which do not lead to the correct IPR. In order to resolve this, the point-group symmetry of rotations $\hat{R}$ by 90° about any site of the lattice is exploited; the effective Hamiltonian is block-diagonal within each eigen subspace of $\hat{R}$. Four eigenvalues of $\hat{R}$ are possible and do occur: ± 1 and $\pm i$.

Since the XXZ model is time-reversal invariant, the imaginary eigenvalues are degenerate, and their complex eigenvectors are complex conjugates. The numerical diagonalization within each eigen subspace of $\hat{R}$ yields the energies of the bound states as depicted in Fig. 5.9, which resolves the degeneracy. Starting in the Ising limit, as expected, four bound states τ_i below the lower edge

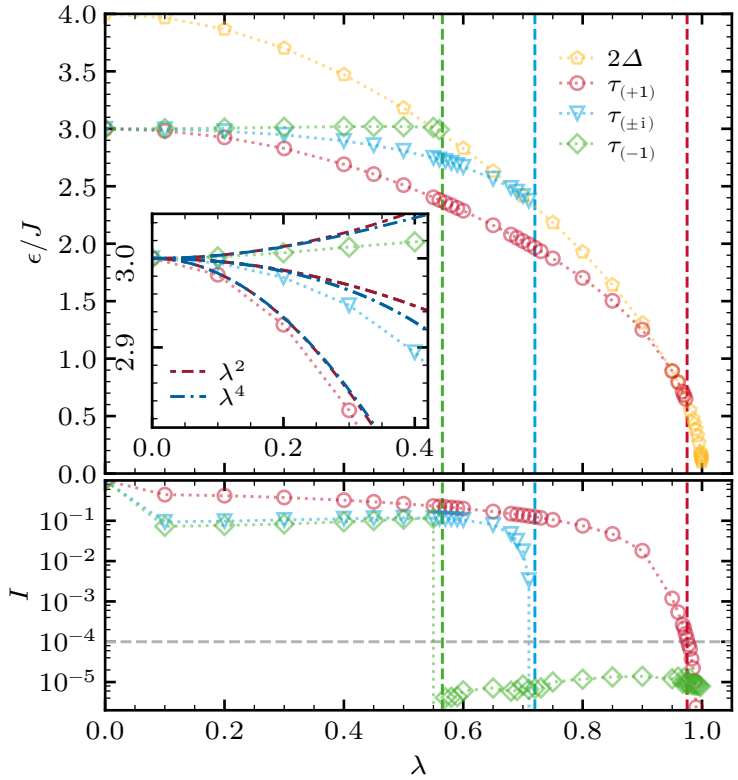

Figure 5.9: The upper panel shows the energies of the four magnon-magnon bound states τ_i calculated by CST as a function of the anisotropy λ and the corresponding lower edge 2Δ of the two-magnon continuum. Triangle symbols depict the two degenerate states with rotation eigenvalue $\pm i$. The inset compares data from truncated CST to data from pCUT up to terms $\propto \lambda^4$ [Dus+10]. One discerns a certain slight deviation in quadratic order. In the lower panel, the inverse participation ratio IPR of the four bound states is plotted; only three curves are shown because the eigen wave functions of the two degenerate bound states are complex conjugates with the same IPR I. The vertical dashed lines mark the decay points for the corresponding bound state determined by a crossing of I with the threshold $I = 10^{-4}$ (horizontal dashed line).

of the two-magnon continuum are found. For increasing λ, they are absorbed in the continuum

one after the other before the isotropic afHM is reached. The decay point where each bound state merges with the continuum is determined by computing and extrapolating its IPR as described in Section 5.6.1 and Section 5.3. Recall that a finite IPR indicates binding while its vanishing indicates delocalization, i.e., the bound state ceases to exist. The results of the extrapolated IPR for the four bound states are displayed in the lower panel of Fig. 5.9.

It is advantageous to determine the merging into the continuum from the vanishing of the IPR because this vanishing occurs as a very rapid drop by many orders of magnitude. In contrast, the crossing of the binding energies with the lower continuum edge is an intersection with a slight, rigorously even vanishing angle. A numerical threshold of 10^{-4} is chosen for the IPR to distinguish between a bound state and a delocalized state in the continuum; i.e., only for IPR $> 10^{-4}$ a binding is deduced. In these calculations, this value is the typical IPR for a generic state well within the continuum, extrapolated to the infinite thermodynamic limit $N \to \infty$. The absorption points are marked as dashed vertical lines.

The bound state $\tau(-1)$ disappears for $\lambda \approx 0.565(5)$ which is a deviation of $\approx 5\,\%$ to $\lambda \approx 0.5401(1)$ from the results determined by a perturbative CUT (pCUT) [Dus+10]. The merging of $\tau(\pm i)$ occurs at $\lambda \approx 0.72(1)$ in CST; no results were given for these bound states in Ref. [Dus+10]. For the curves for $\tau(\pm i)$ in the inset, the hopping amplitudes given in Ref. [Dus+10] were analyzed to calculate the series up to order λ^4. For $\tau(+1)$ a merging point at $\lambda \approx 0.975(5)$ is found with a deviation of only $\approx 0.6\,\%$ to the extrapolated pCUT value of $\lambda \approx 0.97$. It can be concluded that for almost all values $\lambda \in [0, 1]$ at least one bound state exists. But even the lowest bound state $\tau(+1)$ dives into the continuum very close to the isotropic Heisenberg point. Note that this finding is very similar to the decay of bound states in the XXZ model on coupled two-leg ladders. Here QMC simulations reveal the decay of the lowest bound state at $\lambda \approx 0.96$ for different inter-ladder couplings [YSW19].

Comparing the CST result with the results from the perturbative series near the Ising limit (see inset of Fig. 5.9), a sizable deviation in order of λ^2 for all bound states is discernible, in contrast to what is found in the previously studied quantities in the zero- and single-particle sectors. These deviations are a consequence of the truncation scheme neglecting hexatic operators. Indeed, one finds that for a perturbative CST in second order of λ in position space, coefficients for quartic interactions of the type $\hat{a}_i^\dagger \hat{a}_i^\dagger \hat{b}_j^\dagger \hat{b}_j$ are coupled to hexatic terms during the flow. Hence, these contributions are not considered rigorously in the CST as implemented in this thesis. Therefore, the quantitative analysis of properties at intermediate values of the anisotropy should be taken with a grain of salt. Nevertheless, the series expansion and the CST results exhibit very similar behavior. In particular, the results close to the Heisenberg point agree very well. Obviously, the benefits of truncation based on the scaling dimension outweigh the caveat of not precisely capturing all perturbative terms in the Ising limit. This observation holds an attractive promise for the future application of the CST combined with a scaling-based truncation.

5.7 Summary and Outlook — XXZ Model on a Square Lattice

This chapter extended the systematic basis change by a CST as applied to the spin-$\frac{1}{2}$ isotropic afHM on a two-dimensional square lattice in Refs. [PUS15; PSU18] to the two-dimensional easy-axis XXZ model on a square lattice. This model displays the transition from a spontaneously broken discrete symmetry with a finite energy gap to a spontaneously broken continuous symmetry with a vanishing energy gap. The starting point of this calculation was the Hamiltonian in scNL-SWT based on the Dyson-Maleev representation (DM) of the spin operators. The calculation is performed by numerically integrating the flow equations in the prefactors of terms in second

quantization. To this end, the MBZ was discretized in various ways, and it was checked that the results converged within small error bars. In addition, the proliferation of terms was limited by a truncation based on the scaling dimension. All terms of quadratic and quartic form were kept, but hexatic and higher terms that occurred in the flow equations were neglected after normal-ordering them with respect to the self-consistently determined magnon vacuum.

It was verified that this approach can be applied to the paradigmatic transition of the easy-axis XXZ model on a square lattice, including the vanishing of the spin gap. The ground-state energy and the one-magnon dispersion, as well as the two-magnon interaction, were derived and computed. The dispersion displays the expected appearance of the roton minimum and agrees well with all available previous results.

Concerning the power laws upon approaching the isotropic Heisenberg point, the CST yields results close to those from QMC [Cac+24]. Both strongly support the linear behavior of the ground energy and square-root behavior for the staggered magnetization, the spin gap, and the correlation length. The latter two power laws are not independent but are linked by $\xi^x \propto 1/\Delta$. Only for the staggered magnetization determined by the CST, a slight deviation in the exponent is observed. This deviation is attributed to systematic truncation errors, as both distinct approaches that determine the staggered magnetization exhibit it. However, all these power laws agree with the results of spin wave theory [HZA92], which may appear surprising. However, it should be emphasized that approaching the isotropic point does not constitute an actual quantum phase transition, as the system remains in the same long-range-ordered phase. The observed gap closure does not indicate a second-order transition, but rather the restoration of the continuous symmetry of spin rotation, which in turn implies the occurrence of Goldstone bosons. Since no critical quantum fluctuations appear, the exponents remain the same as in mean-field theory.

Additionally, the two-magnon bound states at zero momentum of the center-of-mass in the longitudinal channel, i.e., for vanishing total S^z component, were successfully computed. Four bound states are identified, of which two with complex eigen wave functions are degenerate. Upon approaching the isotropic afHM, they merge successively with the two-magnon continuum. The lowest bound state is rotationally invariant in space, i.e., with respect to rotations by 90°. It vanishes only very close to the isotropic point in nice quantitative agreement with previous perturbative results [Dus+10] within less than 1 %. This agreement is even more remarkable because the energies of the bound states show a larger deviation of the order of 5 % to the perturbative results for intermediate values of λ. This effect is traced back to the truncations beyond the quartic level. The degree of binding and the delocalization upon diving into the continuum are determined reliably by the IPR.

The above sketched achievements hold the promise that the systematic CST with truncation based on the scaling argument can be applied to many more models that have not been studied in great detail to date. Therefore, it is worth emphasizing that with the help of the CST, closing and opening of gaps can be captured as well as the occurrence of binding phenomena. With this successful extension of the CST to the XXZ model, the following chapter addresses the question of how robust the CST approach performs if the underlying lattice is changed. Precisely, the lattice is changed from the square lattice to the honeycomb lattice.

6 | XXZ Model on a Honeycomb Lattice

Following the analysis of the XXZ model on a square lattice, where the continuous similarity transformation (CST) method demonstrated excellent quantitative agreement with complementary theoretical approaches, a natural next step is to investigate its performance under a change of the underlying lattice geometry while maintaining the interaction model. Therefore, this chapter focuses on applying the CST to the XXZ model on a honeycomb lattice.

Compared to the square lattice, the honeycomb lattice possesses a lower coordination number of $Z = 3$ instead of $Z = 4$. Consequently, quantum fluctuations are expected to be more pronounced in systems defined on the honeycomb lattice. In general, the combination of the honeycomb geometry with various types of magnetic interactions gives rise to a wide variety of intriguing physical phenomena. A prominent example is the exactly solvable Kitaev model [Kit06], which features anisotropic bond-dependent spin interactions and realizes a quantum spin-liquid ground state. Hence, materials that exhibit strong spin-orbit coupling combined with significant electron correlation on a honeycomb lattice are intensively investigated in recent years as potential realizations of the Kitaev model [Tak+19]. However, beyond these exotic anisotropic interactions, isotropic Heisenberg-type interactions on the honeycomb lattice are also of considerable interest to describe various materials. In this context, next-nearest-neighbor or even next-next-nearest-neighbor interactions are often included, leading to frustrated magnetic models. Such models exhibit rich phase diagrams featuring multiple magnetically ordered phases alongside quantum spin liquid phases [FSL01; OS11; Li+12; Reh+16; FB20].

Nevertheless, several materials have been identified that realize the spin-$\frac{1}{2}$antiferromagnetic Heisenberg model (afHM) on a honeycomb lattice, such as $YbCl_3$ and $YbBr_3$ [Her+25]. Recent inelastic neutron scattering (INS) experiments on these compounds have revealed magnon-like excitations. [Wes+20; Sal+21; Sal+23; Her+25] However, notable deviations from the predictions of conventional spin-wave theory (SWT), analogous to those found for the afHM on the square lattice, were observed. These discrepancies are most pronounced near the corners of the Brillouin zone (BZ)(K-points). At these points, even the INS intensity measurements reveal evidence of a decay of the one-magnon mode [Wes+20; Her+25]. Consequently, an important question arises as to whether the CST can adequately capture these experimentally observed phenomena on the honeycomb lattice, analogous to its successful application on the square lattice. This issue will be explored in greater detail in Section 6.6.

Before proceeding, certain prerequisites must be established to set up the CST for the honeycomb lattice. First, it is important to note that the honeycomb lattice is still bipartite. Therefore, the magnetic ordering associated with the Néel state naturally suits this lattice. Thus, in the Ising limit $\lambda = 0$ of the XXZ model, the ground state corresponds once again to the classical Néel state, as illustrated in Fig. 6.1. Second, unlike the square lattice, the honeycomb lattice lacks inversion symmetry. The subsequent section provides a detailed discussion of the required adaptations for implementing the CST on the honeycomb lattice, with a special focus on the Fourier transformation.

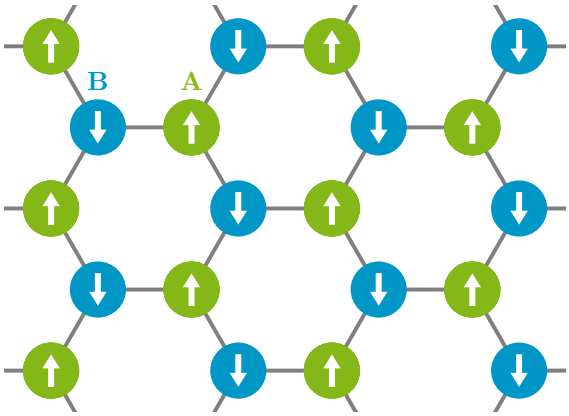

Figure 6.1: Antiferromagnetic order on the honeycomb lattice. The spins on the two sublattices are aligned anti-parallel to each other, resulting in a classical Néel state for the Ising limit $\lambda = 0$.

6.1 Remarks on the Fourier Transformation

In order to set up the CST for the XXZ model on the honeycomb lattice, only a single step discussed in Section 2.5 has to be revisited and adapted to the new lattice structure, namely the Fourier transformation of Section 2.5.2. Before discussing the Fourier transformation, it is helpful to revisit the resulting Hamiltonian after inserting the Dyson-Maleev representation (DM), which reads

$$\begin{aligned}\hat{\mathcal{H}} = &- JN_A S^2 Z + J \sum_{\boldsymbol{r}_i \in \Gamma_A}^{N_A} \sum_{\boldsymbol{d} \in \mathfrak{D}} \Big[S\hat{a}_i^\dagger \hat{a}_i + S\hat{b}_{i+\boldsymbol{d}}^\dagger \hat{b}_{i+\boldsymbol{d}} + \lambda S \hat{a}_i^\dagger \hat{b}_{i+\boldsymbol{d}}^\dagger + \lambda S \hat{a}_i \hat{b}_{i+\boldsymbol{d}} \\ &- \hat{a}_i^\dagger \hat{a}_i \hat{b}_{i+\boldsymbol{d}}^\dagger \hat{b}_{i+\boldsymbol{d}} - \frac{\lambda}{2} \hat{a}_i^\dagger \hat{b}_{i+\boldsymbol{d}}^\dagger \hat{b}_{i+\boldsymbol{d}}^\dagger \hat{b}_{i+\boldsymbol{d}} - \frac{\lambda}{2} \hat{a}_i^\dagger \hat{a}_i \hat{a}_i \hat{b}_{i+\boldsymbol{d}} \Big] \,.\end{aligned} \tag{6.1}$$

with Γ_A being the set of all lattice sites of sublattice A, $N_A = N/2$ the number of sites in sublattice A, and $\mathfrak{D}$ the set of nearest neighbors on the honeycomb lattice. For simplicity, only the Hamiltonian without the generalized normal-ordering is considered here. However, the same steps apply when generalized normal-ordering is applied. Compared to the square lattice Hamiltonian of Eq. (2.32), the main difference is the summation over the nearest neighbors $\mathfrak{D}$ of the honeycomb lattice, which only contains three neighbors instead of four. As for the square lattice, the exact definition of the nearest-neighbor set $\mathfrak{D}$ depends on the chosen gauge for the honeycomb lattice, which is discussed in the following. Furthermore, the distinction between BZ and magnetic Brillouin zone (MBZ) is not necessary for the honeycomb lattice, as the magnetic order fits on the lattice without introducing a magnetic unit cell.

Bloch gauge: With the Bloch gauge, there is no phase difference between the operators $\hat{a}$ and $\hat{b}$ in the Fourier transformation of Eq. (2.33) and therefore only interactions connecting different unit cells obtain a phase factor in the Fourier transformation. In Fig. 6.2, the unit cell of the honeycomb lattice in Bloch gauge is shown, where interactions between neighboring unit cells are marked as transparent orange rhombi. The unit cell is a rhombus with the lattice vectors being $\boldsymbol{a}_1 = (\frac{3}{2}, \frac{\sqrt{3}}{2})^T$ and $\boldsymbol{a}_2 = (\frac{3}{2}, -\frac{\sqrt{3}}{2})^T$, as shown in Fig. 6.2. In this case, the distance between two neighboring sites is set to unity. The corresponding reciprocal lattice vectors are given by $\boldsymbol{b}_1 = (2\pi\frac{1}{3}, 2\pi\frac{1}{\sqrt{3}})^T$ and $\boldsymbol{b}_2 = (2\pi\frac{1}{3}, -2\pi\frac{1}{\sqrt{3}})^T$. Using this gauge, $\mathfrak{D}$ is defined as $\mathfrak{D} = \{0, \boldsymbol{a}_1, \boldsymbol{a}_2\}$

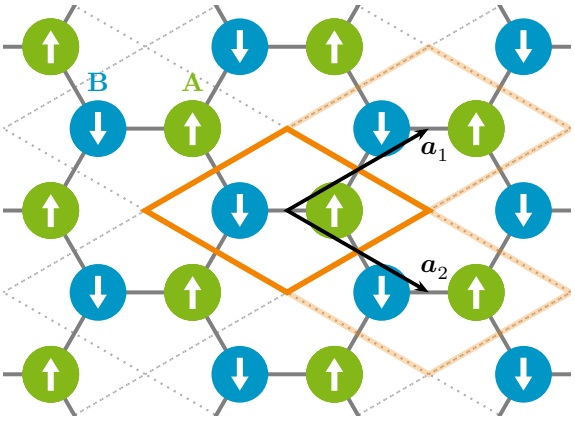

Figure 6.2: The unit cell of Bloch gauge on the honeycomb lattice marked by an orange rhombus. Each atom is clearly assigned to one cell. Neighboring cells that interact are marked as transparent orange rhombi. The lattice vectors $\boldsymbol{a}_1$ and $\boldsymbol{a}_2$ span the lattice marked as grey dotted lines.

and the resulting Fourier transformation function $\gamma_\mathrm{B}(\boldsymbol{k})$ reads

$$\gamma_\mathrm{B}(\boldsymbol{k}) = \frac{1}{Z}\sum_{\boldsymbol{d}\in\mathfrak{D}} \mathrm{e}^{-\mathrm{i}\boldsymbol{k}\boldsymbol{d}} = \frac{1}{3}\left(1 + \mathrm{e}^{-\mathrm{i}\boldsymbol{k}\boldsymbol{a}_1} + \mathrm{e}^{-\mathrm{i}\boldsymbol{k}\boldsymbol{a}_2}\right) . \tag{6.2}$$

The function $\gamma_\mathrm{B}(\boldsymbol{k})$ is visualized in Fig. 6.3. Again as in the square lattice, the expected feature that $\gamma_\mathrm{B}(\boldsymbol{k}) = \gamma_\mathrm{B}(\boldsymbol{k}+\boldsymbol{G})$ holds is clearly visible, where $\boldsymbol{G}$ is any reciprocal lattice vector with $\boldsymbol{G} = g_1\boldsymbol{b}_1 + g_2\boldsymbol{b}_2$ and $g_i \in \mathbb{Z}$. Regarding the symmetry of the function $\gamma_\mathrm{B}(\boldsymbol{k})$, the sixfold rotational symmetry of the honeycomb lattice is not visible in Fig. 6.3 anymore; instead, the symmetries reduce to the same as for the square lattice in the case of the Bloch gauge, which are

$$\gamma_\mathrm{B}(\boldsymbol{k}(m_1,m_2)) = \gamma_\mathrm{B}(\boldsymbol{k}(m_2,m_1)) = \gamma_\mathrm{B}^*(\boldsymbol{k}(-m_1,-m_2)) \;= \gamma_\mathrm{B}^*(\boldsymbol{k}(-m_2,-m_1)) \tag{6.3}$$

with $\boldsymbol{k}(m_1,m_2) = m_1\boldsymbol{b}_1 + m_2\boldsymbol{b}_2$ and $m_{1,2} \in \mathbb{R}$.

Symmetric gauge: As an alternative to the Bloch gauge, the symmetric gauge can also be used for the honeycomb lattice. In this gauge, the operator $\hat{b}$ obtains an additional phase factor in the Fourier transformation as the Fourier transformation is defined as in Eq. (2.43) on each sublattice. In Fig. 6.4, the unit cell of the honeycomb lattice in the symmetric gauge is shown. The lattice points coincide with the sublattice A sites, and the unit cell is again a rhombus spanned by the same lattice vectors $\boldsymbol{a}_1$ and $\boldsymbol{a}_2$ as in the Bloch gauge. By expressing the interaction partners of a single A site relative to the position in the lattice in terms of the lattice vectors, the set $\mathfrak{D}$ is defined as $\mathfrak{D} = \{-\frac{1}{3}(\boldsymbol{a}_1+\boldsymbol{a}_2), \frac{1}{3}(2\boldsymbol{a}_1-\boldsymbol{a}_2), \frac{1}{3}(-\boldsymbol{a}_1+2\boldsymbol{a}_2)\}$. The resulting Fourier transformation function $\gamma_\mathrm{S}(\boldsymbol{k})$ reads

$$\gamma_\mathrm{S}(\boldsymbol{k}) = \frac{1}{Z}\sum_{\boldsymbol{d}\in\mathfrak{D}} \mathrm{e}^{-\mathrm{i}\boldsymbol{k}\boldsymbol{d}} = \frac{1}{3}\left(\mathrm{e}^{\mathrm{i}\frac{\boldsymbol{k}(\boldsymbol{a}_1+\boldsymbol{a}_2)}{3}} + \mathrm{e}^{-\mathrm{i}\frac{2\boldsymbol{k}\boldsymbol{a}_1-\boldsymbol{k}\boldsymbol{a}_2}{3}} + \mathrm{e}^{-\mathrm{i}\frac{-\boldsymbol{k}\boldsymbol{a}_1+2\boldsymbol{k}\boldsymbol{a}_2}{3}}\right) . \tag{6.4}$$

In Fig. 6.5 the function $\gamma_\mathrm{S}(\boldsymbol{k})$ is visualized. Although the symmetric gauge is used, the function is no longer real-valued, compared to the square lattice, similar to the Bloch gauge. However, both the real and imaginary part of $\gamma_\mathrm{S}(\boldsymbol{k})$ show the complete sixfold rotational symmetry of the honeycomb lattice, as expected. The symmetry can be expressed as

$$\gamma_\mathrm{S}(\boldsymbol{k}) = \gamma_\mathrm{S}(\theta_{\frac{\pi}{3}}(\boldsymbol{k}))^* = \gamma_\mathrm{S}(\theta_{\frac{2\pi}{3}}(\boldsymbol{k})) = \gamma_\mathrm{S}(\theta_{\pi}(\boldsymbol{k}))^* = \gamma_\mathrm{S}(\theta_{\frac{4\pi}{3}}(\boldsymbol{k})) = \gamma_\mathrm{S}(\theta_{\frac{5\pi}{3}}(\boldsymbol{k}))^* \tag{6.5}$$

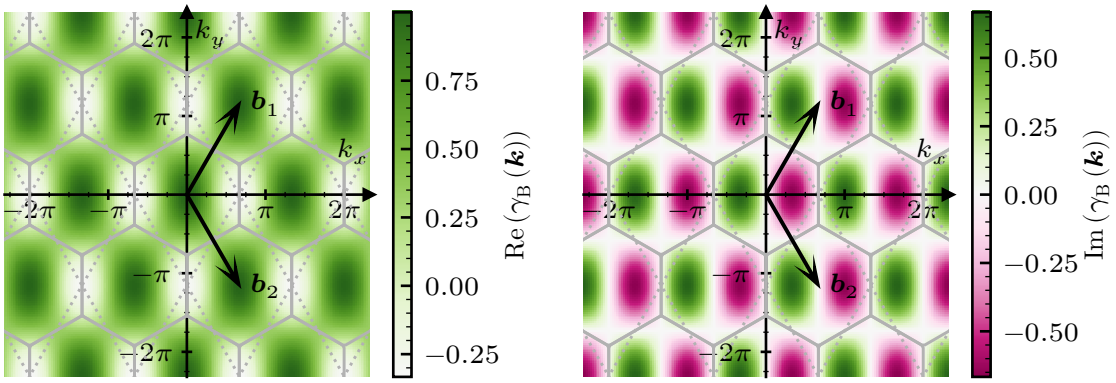

Figure 6.3: The figure depicts $\gamma_\mathrm{B}(\boldsymbol{k})$ in the Bloch gauge of the honeycomb lattice. The real part of $\gamma_\mathrm{B}(\boldsymbol{k})$ is shown on the left-hand side, and the imaginary part of $\gamma_\mathrm{B}(\boldsymbol{k})$ is shown on the right-hand side. In both cases, grey lines mark the first BZ and its extensions, Grey dotted lines indicate the unit cells used for the discretization of the reciprocal space.

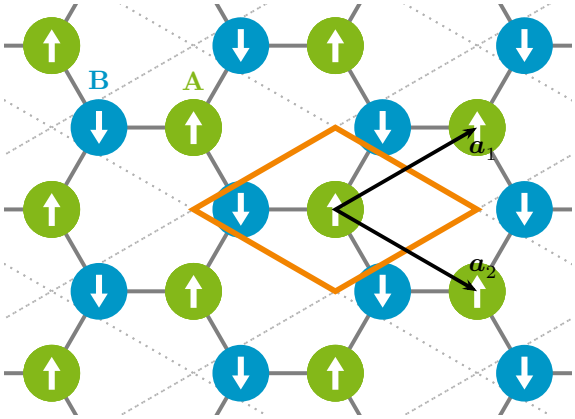

Figure 6.4: Unit cell of symmetric gauge on the honeycomb lattice shown marked by an orange rhombus. The lattice vectors $\boldsymbol{a}_1$ and $\boldsymbol{a}_2$ span the lattice marked as grey dotted lines. Lattice points coincide with the sublattice A sites.

where $\theta_\alpha(\boldsymbol{k})$ denotes the rotation of the vector $\boldsymbol{k}$ by an angle α. By translating the rotational symmetry, e.g., $\alpha = \frac{\pi}{3}$, into the coordinates (m_1, m_2) of the reciprocal lattice vectors

$$\theta_{\frac{\pi}{3}}(\boldsymbol{k}(m_1, m_2)) = \boldsymbol{k}(m_2, \underline{m_2 - m_1}) \ , \tag{6.6}$$

a problem arises with the implementation of these symmetries in the CST. With $m_{1,2}$ are now discretized values depending on the chosen boundary conditions, as discussed in Section 4.2. The underlined part indicates that for an antiperiodic boundary condition, the resulting coordinate $(m_2 - m_1)$ is not connected to any point of the discretization. Thus, only periodic boundary conditions, as implemented in this work, can exploit the complete symmetry of the honeycomb lattice in the symmetric gauge. Furthermore, the symmetric gauge comes with the cost that a shift by a reciprocal lattice Vector $\boldsymbol{G}$ leaves the function $\gamma_\mathrm{S}(\boldsymbol{k})$ not invariant anymore, but introduces an additional phase factor. In this case, the phase factor reads

$$\gamma_\mathrm{S}(\boldsymbol{k} + \boldsymbol{G}) = \gamma_\mathrm{S}(\boldsymbol{G})\gamma_\mathrm{S}(\boldsymbol{k}) \ , \quad \text{where} \quad \gamma_\mathrm{S}(\boldsymbol{G}) = \mathrm{e}^{\mathrm{i}\frac{2\pi}{3}(g_1+g_2)} \tag{6.7}$$

with $\boldsymbol{G} = g_1\boldsymbol{b}_1 + g_2\boldsymbol{b}_2$ and $g_i \in \mathbb{Z}$. Compared to the square lattice where the $\gamma_\mathrm{S}(\boldsymbol{G}) \in \{1, -1\}$, here there exist three different phase factors being $\gamma_\mathrm{S}(\boldsymbol{G}) \in \{1, -0.5 + \frac{\sqrt{3}}{2}\mathrm{i}, -0.5 - \frac{\sqrt{3}}{2}\mathrm{i}\}$, with two of them are irrational complex values.

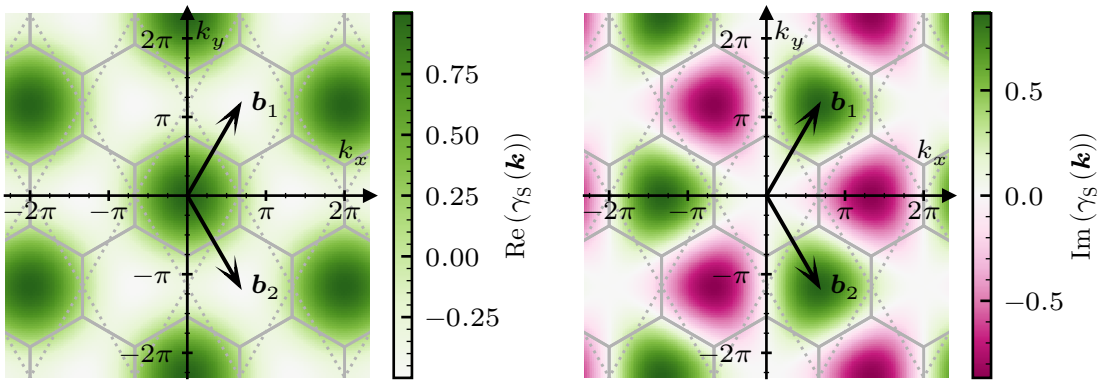

Figure 6.5: The figure depicts $\gamma_\mathrm{S}(\boldsymbol{k})$ in the symmetric gauge of the honeycomb lattice. The real part of $\gamma_\mathrm{S}(\boldsymbol{k})$ is shown on the left-hand side, and the imaginary part of $\gamma_\mathrm{S}(\boldsymbol{k})$ is shown on the right-hand side. In both cases, grey lines mark the first BZ and its extensions, Grey dotted lines indicate the unit cells used for the discretization of the reciprocal space.

In comparison to the square lattice case, where the advantages of the symmetric gauge outweigh the advantages of the Bloch gauge, the situation is less clear for the honeycomb lattice. The symmetric gauge is no longer real-valued, and the additional possible complex phase factors when shifting by reciprocal lattice vectors complicate the implementation of the CST. In particular, the irrational complex phase factors in the symmetric gauge lead to numerical instabilities in the CST implementation when all symmetries of Eq. (6.5) are exploited. Additionally, the complete rotational symmetry can only be exploited for periodic boundary conditions. Conclusively, the Bloch gauge is preferred over the symmetric gauge for the honeycomb lattice in this work.

After the Fourier transformation, the Hamiltonian reads

$$\hat{\mathcal{H}} = -JN_{\mathfrak{T}}S^2Z \tag{6.8a}$$

$$+JSZ\sum_{\boldsymbol{k}}\Big[\delta_{\boldsymbol{G}}\left(\boldsymbol{k}_1-\boldsymbol{k}_2\right)\left(\hat{a}^\dagger_{\boldsymbol{k}_1}\hat{a}_{\boldsymbol{k}_2}+\hat{b}^\dagger_{\boldsymbol{k}_1}\hat{b}_{\boldsymbol{k}_2}\right) + \delta_{\boldsymbol{G}}\left(\boldsymbol{k}_1+\boldsymbol{k}_2\right)\left(\gamma_{\mathrm{B}}(-\boldsymbol{k}_2)\hat{a}_{\boldsymbol{k}_1}\hat{b}_{\boldsymbol{k}_2}+\gamma_{\mathrm{B}}(\boldsymbol{k}_2)\hat{a}^\dagger_{\boldsymbol{k}_1}\hat{b}^\dagger_{\boldsymbol{k}_2}\right)\Big] \tag{6.8b}$$

$$-\frac{JZ}{N_{\mathfrak{T}}}\sum_{\substack{\boldsymbol{k}_1,\boldsymbol{k}_2,\\ \boldsymbol{k}_3,\boldsymbol{k}_4}}\Big[\gamma_{\mathrm{B}}(\boldsymbol{k}_3-\boldsymbol{k}_4)\delta_{\boldsymbol{G}}\left(\boldsymbol{k}_1-\boldsymbol{k}_2+\boldsymbol{k}_3-\boldsymbol{k}_4\right)\hat{a}^\dagger_{\boldsymbol{k}_1}\hat{a}_{\boldsymbol{k}_2}\hat{b}^\dagger_{\boldsymbol{k}_3}\hat{b}_{\boldsymbol{k}_4} + \frac{1}{2}\gamma_{\mathrm{B}}(\boldsymbol{k}_2+\boldsymbol{k}_3-\boldsymbol{k}_4)\delta_{\boldsymbol{G}}\left(\boldsymbol{k}_1+\boldsymbol{k}_2+\boldsymbol{k}_3-\boldsymbol{k}_4\right)\hat{a}^\dagger_{\boldsymbol{k}_1}\hat{b}^\dagger_{\boldsymbol{k}_2}\hat{b}^\dagger_{\boldsymbol{k}_3}\hat{b}_{\boldsymbol{k}_4} + \frac{1}{2}\gamma_{\mathrm{B}}(-\boldsymbol{k}_4)\delta_{\boldsymbol{G}}\left(\boldsymbol{k}_1-\boldsymbol{k}_2-\boldsymbol{k}_3-\boldsymbol{k}_4\right)\hat{a}^\dagger_{\boldsymbol{k}_1}\hat{a}_{\boldsymbol{k}_2}\hat{a}_{\boldsymbol{k}_3}\hat{b}_{\boldsymbol{k}_4}\Big]. \tag{6.8c}$$

This Hamiltonian is similar to the square lattice Hamiltonian of Eq. (2.51), with the difference being that the functions $\gamma_{\mathrm{B}}(\boldsymbol{k})$, respectively $\gamma_{\mathrm{S}}(\boldsymbol{k})$ for the symmetric gauge, are specific to the honeycomb lattice. The coordination number is reduced to $Z = 3$ and the summation is over the true BZ as MBZ and BZ are the same for the honeycomb lattice since the honeycomb can only be realized with a two-atomic unit cell. Further, the delta functions of the quadratic parts are not evaluated to underline that $\gamma_{\mathrm{B}}(\boldsymbol{k})$ respectively $\gamma_{\mathrm{S}}(\boldsymbol{k})$ are not real valued anymore.

Consequently, all following steps to set up the initial values before the CST are identical to the square lattice, including the Bogoliubov transformation (Section 2.5.3) or a possible generalized normal-ordering to obtain a self-consistent nonlinear spin-wave theory (scNL-SWT), see Section 2.5.4. The same holds for the CST itself. All operators are the same, only their prefactors differ, and thus the setup of the flow equation, as described exemplarily in Section 4.1, is identical to the square lattice. To be even more generalized, the flow equations for each coefficient connected to an operator in this magnon picture do not differ as long as the same truncation and generators are used. Only the initial values of the coefficient are model-dependent and therefore have a tremendous influence on the flow. Numerically, the initial values of the coefficients in the honeycomb lattice force a calculation of the CST with complex numbers, doubling the memory consumption as well as the computational cost. Additionally, fewer symmetries can be exploited, further reducing the performance of the CST.

6.2 Nonlinear Spin-Wave Theory

Before discussing the results after the CST, it is beneficial to analyze the model only in the different stages of SWT. Accessible quantities in this case are the ground-state energy, the staggered magnetization, and the single-particle dispersion. At first, the results of the linear spin-wave theory (L-SWT) are determined and compared to more sophisticated approaches such as the mean-field spin-wave theory (MF-SWT) or self-consistent mean-field spin-wave theory (scMF-SWT), as discussed in Section 2.5.4.

In Fig. 6.6 the ground-state energy per site e_0, staggered magnetization per site m_z and spin gap Δ are shown for different anisotropy values λ for all aforementioned approaches. Interestingly, the scMF-SWT on the honeycomb lattice is not able to provide solutions for the full anisotropy range $0 \leq \lambda \leq 1$ in contrast to the square lattice. Instead, beyond the anisotropy value around $\lambda \gtrsim 0.7235(5)$, no self-consistent solution is found anymore, and only at the Heisenberg point $\lambda = 1$ a solution is found again. The explanation why scMF-SWT works again at $\lambda = 1$ lies in the fact that for $\lambda = 1$ the self-consistent parameters cancel each other in the Bogoliubov transformation

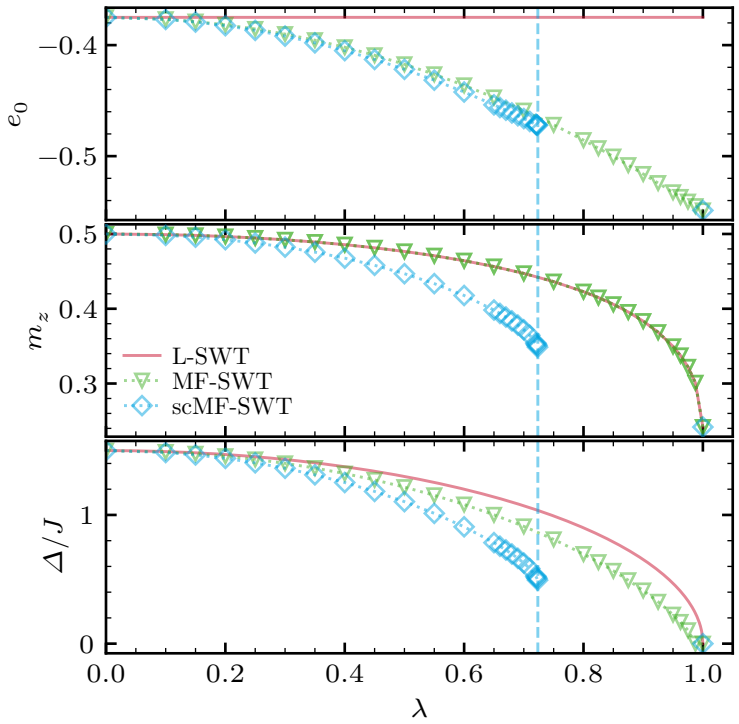

Figure 6.6: Ground-state energy per site e_0, staggered magnetization per site m_z and spin gap Δ for the honeycomb lattice XXZ model using different spin-wave theory approaches. The L-SWT, MF-SWT, and scMF-SWT results are shown. A vertical dashed line indicates the point beyond which the scMF-SWT does not yield a solution anymore. Only at the Heisenberg point $\lambda = 1$ a solution is found again.

and thus only a single evaluation is required. However, a physical interpretation for the behavior in the range $0.7235(5) \lesssim \lambda < 1$ is not yet fully formed. After the critical anisotropy, in the solution of the self-consistency equations, the self-consistent parameters approach values where the radicand of the square root in the Bogoliubov transformation becomes negative, leading to unphysical complex expectation values. Additionally, near the critical anisotropy, the staggered magnetization and the spin gap show unusually strong renormalizations for the scMF-SWT results.

Furthermore, the single-particle dispersion along a high symmetry path in the BZ is shown in Fig. 6.7 for different anisotropy values λ using L-SWT, MF-SWT, and scMF-SWT. All approaches show the expected behavior: as anisotropy λ increases, the spin gap at the Γ-point closes. Furthermore, already for L-SWT the dispersion at the M-point $\boldsymbol{k} = (-\frac{\pi}{3}, \frac{\pi}{\sqrt{3}})^T$ is reduced for increasing anisotropy λ and develops a saddle point. The dispersion for L-SWT at the K-point $\boldsymbol{k} = (\frac{4\pi}{3\sqrt{3}}, 0)^T$ develops a global maximum which remains constant at $1.50J$ for the whole anisotropy range, matching the dispersion value associated with the Ising model. Considering the more sophisticated MF-SWT and scMF-SWT, for both approaches, the dispersion is shifted to higher values between the M- and K- point. Additionally, the maximum at the K-point is no longer constant, but increases with increasing anisotropy λ. Near the Γ-point $\boldsymbol{k} = (0, 0)^T$, the dispersion values are even further reduced compared to L-SWT.

Conclusively, the scMF-SWT on the honeycomb lattice compared to the square lattice is not able to provide solutions for all anisotropy values. Consequently, instead of the scNL-SWT, the

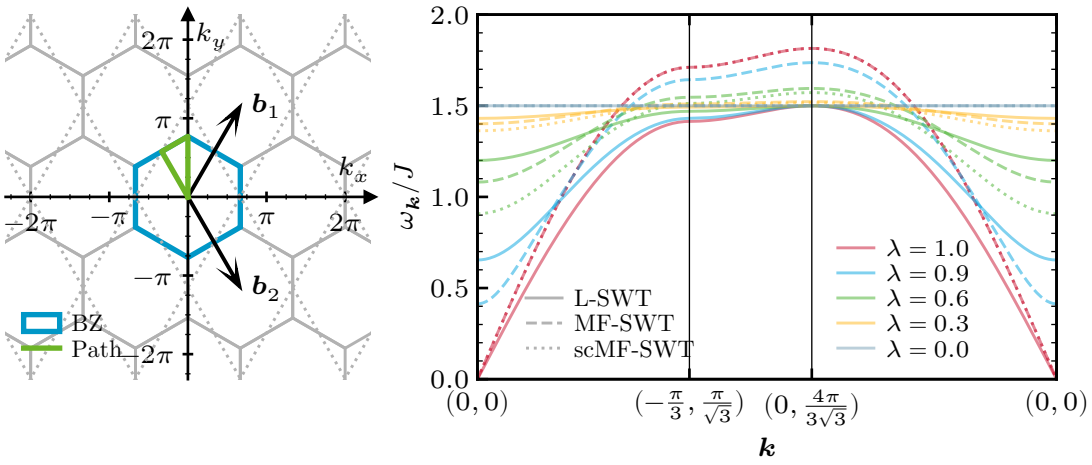

Figure 6.7: Single-particle dispersion using different spin-wave theory approaches along a high symmetry path in the BZ for the honeycomb lattice XXZ model. The path is shown on the left-hand side. On the right-hand side, the dispersion is shown for L-SWT, MF-SWT, and scMF-SWT. Results are shown for different anisotropy values λ.

nonlinear spin-wave theory (NL-SWT) connected to the shown results of the MF-SWT is used as a starting point for the CST in the following.

6.3 Convergence Behavior Continuous Similarity Transformation

Using the non-self-consistent NL-SWT as a starting point, the CST is applied to the XXZ model on the honeycomb lattice. In the evaluation of the results, linear systems of size up to $L = 18$ with both boundary conditions are considered. In the following, special focus is placed on periodic boundary conditions, where the linear system's size satisfies $L \bmod 3 = 0$, as these discretizations sample the edges of the hexagonal-shaped BZ. Further, periodic boundary conditions with $L \bmod 6 = 0$ sample the K-points at the corner of the BZ. Thus, more substantial fluctuations in the physical quantities for different L can be expected in the extrapolation to the thermodynamic limit compared to the square lattice. Focusing only on discretization with $L \bmod 3 = 0$ extenuates possible fluctuations in the extrapolation.

Strikingly, compared to the XXZ model on the square lattice, the particle-conserving generator (pc generator) $\hat{\eta}^{\mathrm{pc}}$ does not lead to an effective model for the whole range of anisotropies $0 \leq \lambda \leq 1$. Instead, similar to the scMF-SWT, only up to a critical anisotropy around $\lambda = 0.575(5)$ a converged effective model is obtained. This point is stable across the considered system sizes and boundary conditions. A divergence of the flow for the pc generator can be interpreted as a smoking gun for an energetic crossing of states with a different number of magnons. Therefore, one goal for the following sections is to analyze the nature of this breakdown of the pc generator in more detail.

However, the pc generator $\hat{\eta}^{\mathrm{pc}}$ is not the only generator that can be applied in the CST framework. As discussed in Section 3.3.4, the particle-block-separating generator (pbs generator) can also be used as a generator for the CST. In contrast to the pc generator, the pbs generator is less ambitious and only decouples the k lowest magnon subspaces from all other subspaces instead

of decoupling all subspaces from each other. Here, the particle-block-separating generator with $k = 0$ ($0n$ generator) $\hat{\eta}^{\mathrm{pbs}}_{0:n}$ is considered, which only decouples the zero-magnon subspace, i.e., the ground state, from all other subspaces. A divergence of the flow for this generator would indicate an energetic crossing of the ground state with an excited state, i.e., a second-order phase transition, rendering the assumed long-range ordered Néel ground state invalid. This criterion was already successfully applied to determine quantum phase transitions out of a long-range ordered phase in the framework of the CST for the J_1-J_2 model on a square lattice and the Heisenberg bilayer [Her+24]. Here, the parameter for which the phase transition occurs is determined with sufficient accuracy; however, extracting the correct critical exponents associated with such quantum phase transitions proved difficult with the CST, as the known exponents for the bilayer could not be reliably reproduced.

In the XXZ model on a honeycomb lattice, using the $0n$ generator $\hat{\eta}^{\mathrm{pbs}}_{0:n}$, no divergence in the flow is observed across the entire range of anisotropy, from $0 \leq \lambda \leq 1$. This finding aligns with existing literature, which indicates that even at the Heisenberg point ($\lambda = 1$), various methods predict a sustained long-range order despite significant quantum fluctuations. Among them are series expansion (SE) [OHZ92], second order spin-wave results [WOH91], exact diagonalization [OB78], coupled cluster method (CCM) [BR98; Bis+15; BL16] and quantum Monte Carlo (QMC) [RRY89; Cas+06]. The latter QMC study determined the remaining staggered magnetization in the afHM as $m_z^{\mathrm{qmc}} = 0.2677(6)$ [Cas+06], in accordance with other QMC studies [Löw09; Jia12]. The reduced magnetization compared to the square lattice, where QMC observed a staggered magnetization of $m_z^{\mathrm{qmc}} = 0.3070(3)$ [San97], demonstrates that quantum fluctuations are more substantial on the honeycomb lattice. Thus, the quasiparticle picture of magnons on top of a long-range ordered Néel state remains valid for the whole anisotropy range $0 \leq \lambda \leq 1$ on the honeycomb lattice, even if strong quantum fluctuations render the pc generator $\hat{\eta}^{\mathrm{pc}}$ inapplicable beyond a critical anisotropy and instead the $0n$ generator $\hat{\eta}^{\mathrm{pbs}}_{0:n}$ is used.

6.4 Comparison of Particle-Conserving Generator and Particle-Sorting Generator

As established in the previous section, the pc generator is not applicable in the whole parameter range of the XXZ model on the honeycomb lattice. In contrast, the $0n$ generator is applicable for all anisotropies $0 \leq \lambda \leq 1$. Compared to the square lattice case, where both generators were applicable over the entire anisotropy range, a slightly different approach is required here. Of course, the pc generator $\hat{\eta}^{\mathrm{pc}}$ is the superior generator, as its effective model is fully particle conserving. Therefore, it is preferable to use pc generator $\hat{\eta}^{\mathrm{pc}}$ over the $0n$ generator $\hat{\eta}^{\mathrm{pbs}}_{0:n}$, whenever possible. Thus far, only results using the pc generator have been presented. The question arises how well the less ambitious $0n$ generator $\hat{\eta}^{\mathrm{pbs}}_{0:n}$ performs compared to the pc generator $\hat{\eta}^{\mathrm{pc}}$. To answer this question, results from the square lattice case are revisited, where both generators are applicable for the whole anisotropy range.

In Fig. 6.8 only the staggered magnetization per site m_z, spin gap Δ, roton minimum, and dispersion maximum are shown for both generators. Concerning the ground state, as it is fully decoupled for both the pc generator and the $0n$ generator, the ground-state energy per site e_0 deviations are close to zero $\approx 10^{-5}$ and thus not further discussed, which is expected as in both cases the ground state is fully decoupled. Since the staggered magnetization can also be derived from the ground-state energy and is therefore assumed to be robust under changes of the generator, here only results obtained via the observable flow are shown for the magnetization.

In the case of the results of the $0n$ generator $\hat{\eta}^{\mathrm{pbs}}_{0:n}$ for the single-magnon dispersion, the single-magnon space is still coupled to the three-magnon space in accordance with the truncation scheme. The three-magnon space itself, with the operator of the effective Hamiltonian, is coupled to the higher five-magnon spaces, and so on. The single-magnon space is therefore indirectly coupled in the effective model of the $0n$ generator $\hat{\eta}^{\mathrm{pbs}}_{0:n}$ to all higher odd magnon spaces. However, in the following, as an additional approximation, only the coupling to the three-particle space is considered. Consequently, to obtain the single-magnon dispersion, the effective Hamiltonian is diagonalized in the coupled single and three-magnon space. This approach differs significantly from the pc generator $\hat{\eta}^{\mathrm{pc}}$, where the single-magnon space is fully decoupled during the CST from all higher magnon spaces in the effective model. This distinction must be kept in mind when discussing the differences in results between the two generators. Independent of this, all results are extrapolated to the thermodynamic limit, and the two different boundary conditions give an error estimate as discussed in Section 5.3 for linear system sizes up to $L = 18$.

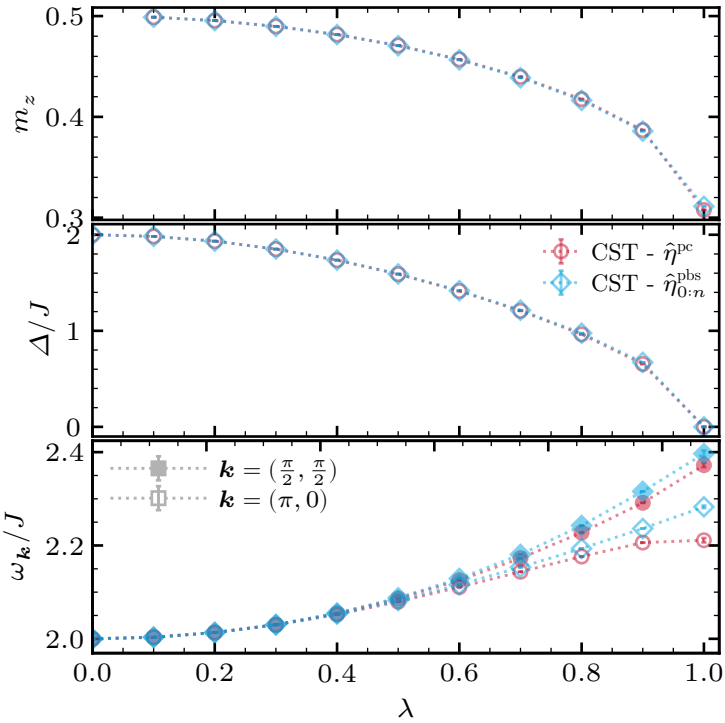

Figure 6.8: Comparison of results for the XXZ model on the square lattice using the pc generator $\hat{\eta}^{\mathrm{pc}}$ and $0n$ generator $\hat{\eta}^{\mathrm{pbs}}_{0:n}$ as generators in the CST. The upper panel shows the staggered magnetization per site m_z obtained via the corresponding observable flow. The middle panel shows the spin gap Δ and the lower panel the roton minimum at $\boldsymbol{k} = (\pi, 0)^T$ and the dispersion maximum at $\boldsymbol{k} = (\frac{\pi}{2}, \frac{\pi}{2})^T$.

Regarding the staggered magnetization per site m_z in the upper panel of Fig. 6.8, both generators yield identical results for the whole anisotropy range $0 \leq \lambda \leq 1$. Astoundingly, the same holds for the spin gap Δ shown in the middle panel of Fig. 6.8. The first differences between both generators occur in the lower panel of Fig. 6.8 where the roton minimum and dispersion maximum are depicted. For lower anisotropies, both generators yield nearly identical results, but as λ increases, deviations become visible. In this higher λ regime close to the Heisenberg point, the $0n$ generator

$\hat{\eta}^{\mathrm{pbs}}_{0:n}$ yields higher values for both quantities compared to the pc generator $\hat{\eta}^{\mathrm{pc}}$. Especially for the roton minimum at $\boldsymbol{k} = (\pi, 0)^T$, the deviations become significant for anisotropies close to the Heisenberg point $\lambda = 1$. This obervation not only shows the limitations of the $0n$ generator $\hat{\eta}^{\mathrm{pbs}}_{0:n}$ with an additional diagonalization of the coupled single and three-magnon space in extracting the correct single-magnon dispersion, in particular, at high energy momenta, but also highlights the superiority of the pc generator $\hat{\eta}^{\mathrm{pc}}$. The pc generator can fully account for all interactions with higher-magnon spaces, which are apparently significant for accurately capturing the roton minimum, stemming from strong magnon-magnon interactions.

However, regarding low-energy properties such as ground-state energy, staggered magnetization, and spin gap, both generators yield almost identical results within the numerical accuracy of the CST. Consequently, for the honeycomb lattice where the pc generator $\hat{\eta}^{\mathrm{pc}}$ is not applicable for the whole anisotropy range, the $0n$ generator $\hat{\eta}^{\mathrm{pbs}}_{0:n}$ can be used as a reliable alternative to extract low-energy properties of the system. Nevertheless, caution is advised when extracting high-energy properties, such as the roton minimum, where significant deviations between the two generators can occur.

6.5 Results of Continuous Similarity Transformation

In this section, the results of the CST using the $0n$ generator $\hat{\eta}^{\mathrm{pbs}}_{0:n}$ as a generator for the XXZ model on the honeycomb lattice are presented. Additionally, results of the pc generator $\hat{\eta}^{\mathrm{pc}}$ are shown for anisotropies up to the critical anisotropy around $\lambda = 0.575(5)$,up to where this generator is still applicable.

It should be noted that compared to the square lattice case, the single-particle dispersion determined by the pc generator or the $0n$ generator shows non-vanishing non-physical imaginary contribution in the order of $10^{-4}J$. Of course, the crucial difference between them is that the square lattice can be calculated without complex numbers, using the symmetric gauge. However, using the Bloch gauge for the square lattice, the resulting imaginary contributions are still significantly lower and only in the order of $10^{-10}J$. The difference in the magnitude of these imaginary contributions is attributed to the more complicated structure of the honeycomb lattice. The associated complex-valued functions $\gamma_{\mathrm{B}}(\boldsymbol{k})$ or $\gamma_{\mathrm{S}}(\boldsymbol{k})$ are more prone to numerical errors, which can accumulate during the integration of the flow equations. Additionally, the approximation due to the re-diagonalization of the coupled single- and three-magnon space is another factor. Nevertheless, the imaginary parts are significantly smaller than the energy scales of interest and are therefore neglected in the following discussions.

In Fig. 6.9 the ground-state energy per site e_0, staggered magnetization per site m_z and spin gap Δ are shown for different anisotropy values λ. To capture the effect of the CST, the data is compared to the MF-SWT results discussed in Section 6.2, which are connected to the NL-SWT used as the starting point for the CST. Furthermore, the results are compared to results from the literature obtained by SE [OHZ92], asymptotic SWT [WOH91], QMC [Löw09], CCM [BR98; Bis+15], and density matrix renormalization group (DMRG) [Kad+24]. In the following, each quantity is discussed in detail.

The ground-state energy per site e_0 is shown in the upper panel of Fig. 6.9. Here, both generators yield identical results across the whole anisotropy range where the pc generator $\hat{\eta}^{\mathrm{pc}}$ is applicable. Regarding the results from the literature, the results from the $0n$ generator $\hat{\eta}^{\mathrm{pbs}}_{0:n}$ are in good agreement with all of them. May it be CCM results [BR98; BL16], SE calculation up to an order of $O(14)$ [OHZ92] and close to the isotropic point asymptotic SWT [WOH91] or at the isotropic point also with available QMC results [Löw09]. For the isotropic point $\lambda = 1$, the CST

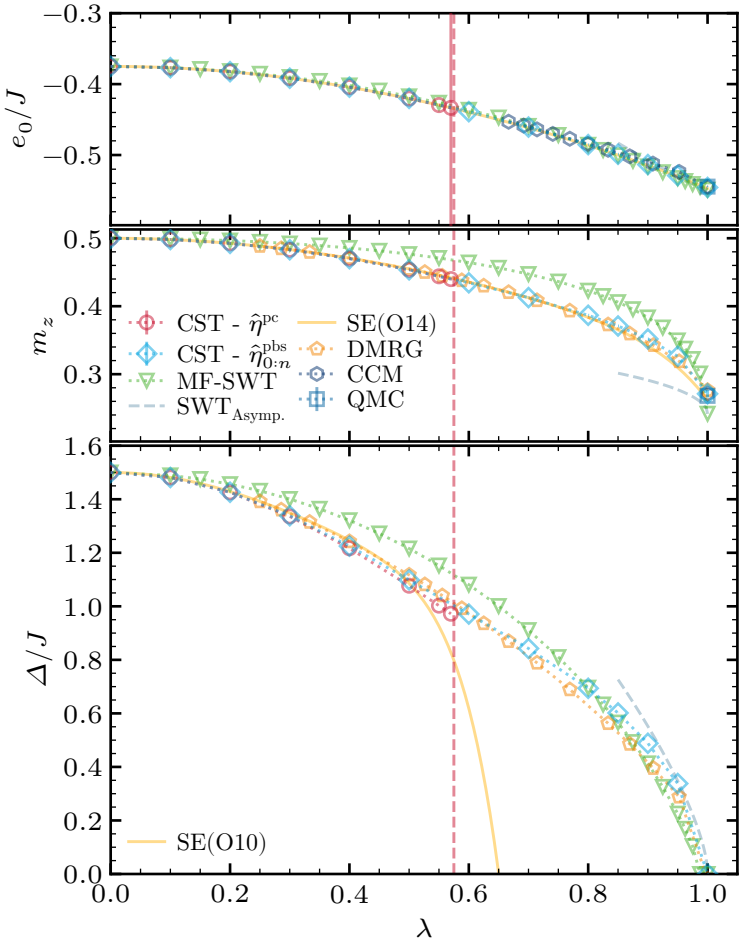

Figure 6.9: Comparison of results for the XXZ model on the honeycomb lattice using the pc generator $\hat{\eta}^{\mathrm{pc}}$ and $0n$ generator $\hat{\eta}^{\mathrm{pbs}}_{0:n}$ as generators in the CST. The upper panel shows the ground-state energy per site e_0. The middle panel shows the staggered magnetization per site m_z obtained via the corresponding observable flow. The lower panel shows the spin gap Δ. If possible results are compared to literature data, i.e., SE [OHZ92], asymptotic SWT [WOH91], QMC [Löw09], CCM [BR98; Bis+15] and DMRG [Kad+24]. The vertical dashed line marks the boundary where the pc generator still converges.

with the $0n$ generator $\hat{\eta}^{\mathrm{pbs}}_{0:n}$ yields a ground-state energy per site of $e_0^{\mathrm{cst}} = -0.545\,736(2)J$, which is in very good agreement with $e_0^{\mathrm{QMC}} = -0.5446(2)J$, $e_0^{\mathrm{CCM}} = -0.544\,66(2)J$, and $e_0^{\mathrm{SE}} = -0.5443(3)J$. However, compared to the MF-SWT starting point, the renormalizations are only moderate, indicating that the MF-SWT already correctly captures a large part of the quantum fluctuations affecting the ground-state energy. It is therefore not surprising that the $0n$ generator also shows accurate results.

The staggered magnetization per site m_z is shown in the middle panel of Fig. 6.9. Nevertheless, before discussing the CST results, it is important to note that the staggered magnetization per site m_z is here only calculated via an observable flow as shown in Section 5.4.2. In the square lattice case, the staggered magnetization could be extracted from the flow of the longitudinal dynamic structure factor evaluated at $\boldsymbol{Q} = (\pi, \pi)^T$ with the ground-state expectation value. However, this is not possible for the honeycomb lattice due to its different geometry. Instead, a separate observable flow for the staggered magnetization is implemented. The new observable reads

$$\hat{M}_z(\boldsymbol{Q}) = \sum_{\boldsymbol{r}_i \in \Gamma_A} \mathrm{e}^{-\mathrm{i}(\boldsymbol{Q}\boldsymbol{r}_i)} S^z_{A,i} - \sum_{\boldsymbol{r}_j \in \Gamma_B} \mathrm{e}^{-\mathrm{i}(\boldsymbol{Q}\boldsymbol{r}_j)} S^z_{B,j} \tag{6.9}$$

and is evaluated after the flow with the ground-state expectation value at $\boldsymbol{Q} = (0, 0)$. The initial values are listed in Appendix A.2.1 and the corresponding flow equations are shown in Appendix B.2.1. Both generators yield identical results up to the divergence of the pc generator $\hat{\eta}^{\mathrm{pc}}$. Interestingly, the MF-SWT captures the ground-state energies well, but the renormalization of the CST to the MF-SWT results are considerably larger for the staggered magnetization. Though, the comparison to literature shows that the CST with the $0n$ generator $\hat{\eta}^{\mathrm{pbs}}_{0:n}$ yields results in good agreement for the whole anisotropy range $0 \leq \lambda \leq 1$ with SE [OHZ92] and DMRG calculations [Kad+24]. Close to the isotropic point, the comparison with asymptotic SWT [WOH91] shows that the second-order asymptotic SWT overestimates the quantum fluctuations, effectively reducing the staggered magnetization too much. Compared to available QMC results [Löw09], CCM data [Bis+15] and DMRG data [Kad+24] at the isotropic point $\lambda = 1$ the CST with $0n$ generator yields a staggered magnetization of $m_z^{\mathrm{cst}} = 0.271(6)$, which is in very good agreement with $m_z^{\mathrm{QMC}} = 0.2681(8)$, $m_z^{\mathrm{CCM}} = 0.271(1)$, and $m_z^{\mathrm{DMRG}} = 0.276\,37$. Concluding, the CST with the $0n$ generator $\hat{\eta}^{\mathrm{pbs}}_{0:n}$ can capture the staggered magnetization per site m_z qualitatively for the whole anisotropy range $0 \leq \lambda \leq 1$ which adequate accuracy.

The spin gap Δ is shown in the lower panel of Fig. 6.9. Comparing the results of both generators, the spin gap is the first quantity where deviations between both generators already become visible before the divergence of the pc generator $\hat{\eta}^{\mathrm{pc}}$. Where the pc generator is still applicable, the spin gap is slightly lower compared to the $0n$ generator. This deviation is increasing with increasing anisotropy λ. Compared to the MF-SWT, the renormalization effect of the CST to lower spin gap values is most significant for anisotropies in the middle around $\lambda \approx 0.5$. Regarding the comparison to literature, the CST results with the $0n$ generator $\hat{\eta}^{\mathrm{pbs}}_{0:n}$ are in good agreement with DMRG [Kad+24] results for the whole anisotropy range $0 \leq \lambda \leq 1$. Confirming the previous findings of Section 6.4, that the $0n$ generator with only an additional diagonalization of the coupled single and three-magnon space can capture low-energy properties of the system with adequate accuracy.

Nevertheless, a comparison with SE results [OHZ92] up to order of $O(10)$ shows that capturing the correct behavior is challenging. For anisotropies greater than $\lambda \approx 0.4$, the SE results deviate significantly from the results obtained using CST and DMRG. This fact suggests that higher-order terms are necessary in the series expansion to achieve accurate results for the spin gap, highlighting the strong influence of quantum fluctuations on this quantity. However, close to the isotropic point, the asymptotic SWT [WOH91] seems to capture the spin gap behavior quite well and overestimates the spin gap only slightly.

A detailed analysis of the high-energy regions of the dispersion, particularly at high-symmetry points like the K-point and the M-point, similar to the roton minimum and dispersion maximum in the case of the square lattice, is omitted here for the full anisotropy range. This omission is partly due to a lack of comparable literature and partly because, for the square lattice, comparing the pc generator and the $0n$ generator results showed that the $0n$ generator fails to capture the high-energy regions of the dispersion accurately. Instead, the focus lies on the isotropic afHM $\lambda = 1$ in the following.

6.6 Antiferromagnetic Heisenberg Model

This section is particularly devoted to the isotropic Heisenberg limit $\lambda = 1$ of the XXZ model, i.e., the afHM, on the honeycomb lattice. The results of this section are already published in Ref. [Krä+25]. The primary motivation of this section is to understand the high-energy features of the single-magnon dispersion of the afHM on the honeycomb lattice, especially at the K-point, where QMC calculations [Krä+25] predict a roton-like local minima but with a vanishing single-particle weight. This behavior is also observed by neutron scattering experiments and matrix product state calculations [Her+25], which is contrary to the behavior predicted by MF-SWT, see Section 6.2, where the global dispersion maximum is located at the K-point.

The goal of this section is to give a possible interpretation of this observation with the help of CST. The absence of a single-particle weight at the K-point indicates that, in contrast to other momenta in the Brillouin zone, there exists no intact single-magnon mode at the lower edge of the spectrum. Instead, the single-magnon mode decays completely into the multi-magnon continuum. As a consequence, the observation of the divergent flow of the pc generator $\hat{\eta}^{\mathrm{pc}}$ at the Heisenberg point $\lambda = 1$ can be understood due to the persistent energetic overlap of the single-magnon mode with the multi-magnon continuum.

As the $0n$ generator $\hat{\eta}^{\mathrm{pbs}}_{0:n}$ converges also for $\lambda = 1$, the same approach used to extract the spin gap is applied here to calculate the full dispersion. Even though previous findings of Section 6.4 suggest that the $0n$ generator with the re-diagonalization of the one and three-magnon space is not able to capture high-energy features of the dispersion entirely correctly, at least for the afHM on a square lattice.

In Fig. 6.10 the single-magnon dispersion along a high-symmetry path in the BZ is shown for the afHM on the honeycomb lattice. For comparison, QMC results ω_{QMC} together with high-order SE ω_{SE} calculated with linked-cluster expansions and a subsequent padé extrapolation, both from Ref. [Krä+25] are shown as well. The QMC results clearly show a roton-like minimum at the K-point; additionally, the high-order SE results are in good agreement with the QMC data along the entire path. However, the determined uncertainties of ω_{SE} are especially close to the K-point and the Γ-point quite significant, indicating that the padé extrapolation of the single-magnon dispersion from the SE is challenging in these momentum regions. This finding matches the observation of the other SE results shown in Fig. 6.9, where the spin gap behavior is not straightforwardly captured for higher anisotropies. Apart from the literature results, the single-particle dispersion calculated with MF-SWT $\omega^{\mathrm{MF}}_{\mathrm{Init}}$ and the re-diagonalized CST dispersion $\tilde{\omega}_{\hat{\eta}^{\mathrm{pbs}}_{0:n}}$, calculated using the $0n$ generator $\hat{\eta}^{\mathrm{pbs}}_{0:n}$ for a linear system size of $L = 18$ with periodic boundary conditions, are shown as well. Note that for $\lambda = 1$ the initial values of scNL-SWT are identical to NL-SWT and thus not further discussed. Unfortunately, the differences between $\omega^{\mathrm{MF}}_{\mathrm{Init}}$ and $\tilde{\omega}_{\hat{\eta}^{\mathrm{pbs}}_{0:n}}$ are marginal compared to the uncertainties of the SE results. Consequently, the CST with the $0n$ generator $\hat{\eta}^{\mathrm{pbs}}_{0:n}$ is not able to capture the roton-like minimum at the K-point, as the resulting dispersion still shows a global maximum at the K-point.

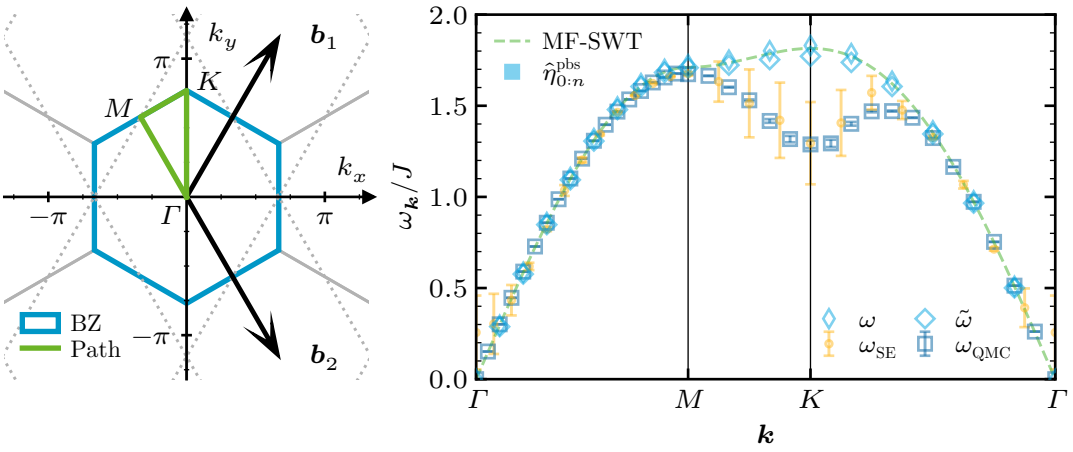

Figure 6.10: The right panel shows the single-particle dispersion along a high symmetry path in the BZ, depicted on the left panel, for the afHM on a honeycomb lattice calculated with different approaches, i.e., the MF-SWT, the CST $N_{\mathrm{p}}, L = 18$ with the $0n$ generator $\hat{\eta}^{\mathrm{pbs}}_{0:n}$, with ($\tilde{\omega}$) and without ($\omega$) a re-diagonalization of the one and three-magnon space, SE [Krä+25], QMC [Krä+25].

Apparently, the concerns that using the $0n$ generator $\hat{\eta}^{\mathrm{pbs}}_{0:n}$ is not sufficient to describe the high-energy properties of the dispersion also prove to be justified for the afHM on the honeycomb lattice. A possible route to improve the description of this high-energy feature within the CST approach is to resort to the pc generator $\hat{\eta}^{\mathrm{pc}}$. However, a convergence of the pc generator for the afHM on the honeycomb lattice due to the persistent energetic overlap of the single-magnon mode with the multi-magnon continuum is not achievable. Instead, a different strategy is required. As the transformation is continuous, it is still possible to stop the flow with the pc generator at any flow parameter ℓ before the divergence occurs. Thus, the idea is to stop the flow of the pc generator $\hat{\eta}^{\mathrm{pc}}$ at a finite flow parameter ℓ^* before an increased divergence is reached, and then to analyze the resulting Hamiltonian $\widehat{\mathcal{H}}(\ell^*)$. At this stage, it is crucial to establish a criterion to determine the termination point ℓ^*. As long as the residual-off-diagonality (ROD), see Section 3.5, is decreasing, the rotation to an effective model is not anticipated to be influenced by diverging non-physical terms. Of course, if the flow is terminated at a specific finite ℓ^*, off-diagonal terms will remain. Nevertheless, the effective Hamiltonian is expected to contain more relevant interactions, stemming from the rotation of the off-diagonal terms compared to the initial Hamiltonian. A logical point to stop the flow may be where the ROD reaches a minimum before it begins to diverge. In Fig. 6.11 the ROD during the flow of the pc generator $\hat{\eta}^{\mathrm{pc}}$ for different system sizes with periodic N_{p} but also antiperiodic N_{ap} boundary conditions is shown. It is possible to subdivide the ROD into subsets connected to each specific type of off-diagonal operator coefficient

$$C^{\hat{x}}_{\mathrm{ROD}}(\ell) \coloneqq \sqrt{\sum_{\boldsymbol{k}_1,\ldots,\boldsymbol{k}_n} \left| C^{\hat{x}}_{\boldsymbol{k}_1,\ldots,\boldsymbol{k}_n}(\ell) \right|^2}, \tag{6.10}$$

with $\hat{x} \in \hat{\eta}^{\mathrm{pc}}$. Here, already the subset $C^{\hat{\alpha}^\dagger\hat{\alpha}^\dagger\hat{\alpha}\hat{\beta}^\dagger}_{\mathrm{ROD}}(\ell)$ shows a minimum around $\ell = 1.0$ before the full ROD does, see Fig. 6.11. Furthermore, all determined minima show almost no finite-size scaling and also no sensitivity to different boundary conditions.

In conclusion, the flow of the pc generator $\hat{\eta}^{\mathrm{pc}}$ is terminated at the determined minimum of $C^{\hat{\alpha}^\dagger\hat{\alpha}^\dagger\hat{\alpha}\hat{\beta}^\dagger}_{\mathrm{ROD}}(\ell)$ around $\ell^* = 1.0$ for all different system sizes and boundary conditions, to ensure no

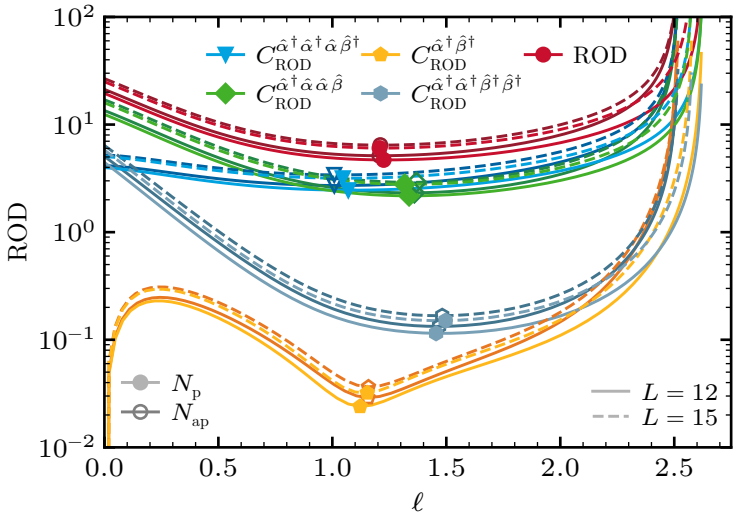

Figure 6.11: The ROD in dependence of the flow parameter ℓ during the CST with the pc generator for the afHM on a honeycomb lattice. Additionally, subsets of ROD only connected to a specific type of off-diagonal operator coefficient $C^{\hat{c}}_{\mathrm{ROD}}$ are shown, where the symmetry between two coefficients is used so that only one of the symmetry equivalent coefficients is considered. The local minima for each subset of ROD before divergence occur are highlighted by a corresponding marker.

influence of the divergence are incorporated during the CST into the effective Hamiltonian. The effective Hamiltonian is then handled in the same manner as for the $0n$ generator $\hat{\eta}^{\mathrm{pbs}}_{0:n}$, i.e., the single-magnon dispersion is extracted by re-diagonalizing the coupled single and three-magnon space. Thereby, it is important to note that also coefficients $C^{\hat{\alpha}^\dagger\hat{\beta}^\dagger}$ and $C^{\hat{\alpha}\hat{\beta}}$ have to be included in the re-diagonalization as they are not fully rotated to zero at the termination point ℓ^*, as seen in Fig. 6.11.

Figure 6.12 shows additionally to the results shown in Fig. 6.10 the resulting bare single-magnon dispersion $\omega_{\hat{\eta}^{\mathrm{pc}}}$ extracted from $C^{\hat{\alpha}^\dagger\hat{\alpha}}$ after terminating the flow of the pc generator $\hat{\eta}^{\mathrm{pc}}$ at $\ell = 1.0$. Furthermore, the re-diagonalized dispersion $\tilde{\omega}_{\hat{\eta}^{\mathrm{pc}}}$ of the coupled single and three-magnon space is shown as well. Strikingly, the re-diagonalized dispersion $\tilde{\omega}_{\hat{\eta}^{\mathrm{pc}}}$ showed a significant renormalization compared to both the bare dispersion $\omega_{\hat{\eta}^{\mathrm{pc}}}$ and also to the $0n$ generator results $\tilde{\omega}_{\hat{\eta}^{\mathrm{pbs}}_{0:n}}$. Namely, in the high energy area, the dispersion $\tilde{\omega}_{\hat{\eta}^{\mathrm{pc}}}$ is broadly lowered to a value close to the minimum of the QMC dispersion ω_{QMC} at the K-point. However, compared to the QMC results ω_{QMC}, the dispersion rather forms a plateau between the M- and the K-point. Consequently, both dispersion ω_{QMC} and $\tilde{\omega}_{\hat{\eta}^{\mathrm{pc}}}$ show a rather significant difference at the M-point.

In order to understand the formation of the plateau in $\tilde{\omega}_{\hat{\eta}^{\mathrm{pc}}}$ significantly below the initial MF-SWT dispersion $\omega^{\mathrm{MF}}_{\mathrm{Init}}$, the two-magnon subspace is also considered. In particular, the subspace with $S^z = 0$ is analyzed, as it comprises the strongest magnon-magnon interactions. Additionally, Fig. 6.12 contains the two lowest eigenvalues $\epsilon_{1,2}$ of this subspace. Evidently, the lowest eigenvalue ϵ_1 is connected to a bound state as it lies well below the bare dispersion $\omega_{\hat{\eta}^{\mathrm{pc}}}$, whereas ϵ_2 matches with $\omega_{\hat{\eta}^{\mathrm{pc}}}$. Interestingly, the dispersion of the bound state coincides almost with the single-magnon dispersion $\tilde{\omega}_{\hat{\eta}^{\mathrm{pc}}}$, which gives a strong evidence that $\tilde{\omega}_{\hat{\eta}^{\mathrm{pc}}}$ in fact in the vicinity of M- and K-point consist of excitations of three magnons instead of a single magnon.

The observation strongly indicates that the single-particle dispersion in this region decays into

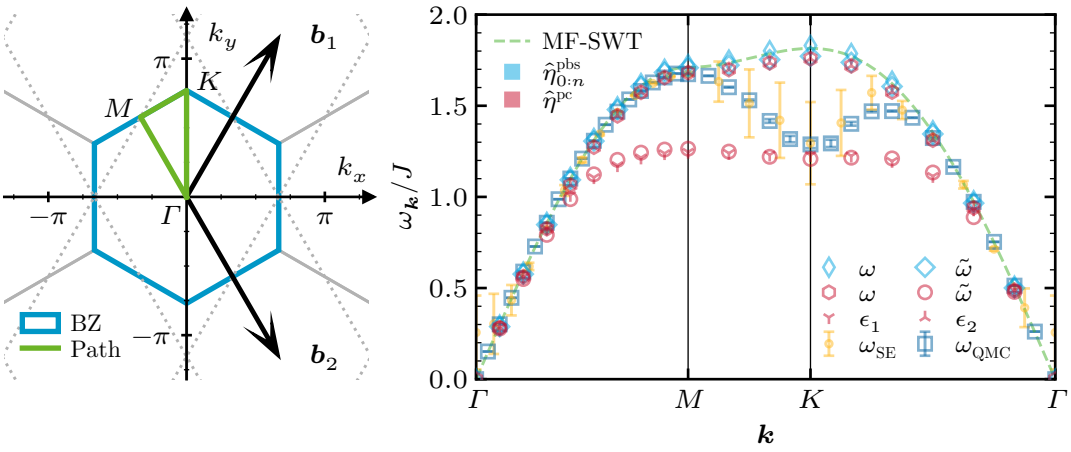

Figure 6.12: The right panel shows the single-particle dispersion along a high symmetry path in the BZ, depicted on the left panel, for the afHM on a honeycomb lattice calculated with different approaches, i.e., the MF-SWT, the CST with the $0n$ generator $\hat{\eta}^{\mathrm{pbs}}_{0:n}$ and the pc generator $\hat{\eta}^{\mathrm{pc}}$, with ($\tilde{\omega}$) and without (ω) a re-diagonalization of the one and three-magnon space, SE [Krä+25], QMC [Krä+25]. The tripod markers show the two lowest eigenvalues $\epsilon_{1,2}$ of the two-magnon subspace with $S^z = 0$ for the same path, calculated after the CST with the pc generator $\hat{\eta}^{\mathrm{pc}}$.

the multi-magnon continuum. This decay stands in contrast to the findings related to the afHM on a square lattice, where the single-particle dispersion remains well-defined for all momenta. Furthermore, this observation is consistent with the divergence of the pc generator, as it is not possible to decouple the energetically overlapping particle subspaces, ultimately leading to a divergent flow. When considering a terminated flow, it is observed that attempts to rotate the non-particle-conserving terms, especially scattering terms with $1 \leftrightarrows 3$ magnons, to zero with the pc generator lead to strong magnon-magnon interactions. If the flow is not terminated, these effects ultimately lead to a divergent pc generator flow. However, these interaction effects are not captured at all when considering a flow with the $0n$ generator and a subsequent re-diagonalization.

Nevertheless, the terminated CST with the pc generator captures the height and the building of the local minima at the K-point with a vanishing single-particle weight at the edge of the continuum quantitatively. The formation of the plateau between the M- and K-points remains indecisive, as QMC predicts a notably higher maximum and a still-present single-particle weight at the edge of the continuum at the M-point. A possible reason for this mismatched, unphysical plateau may be errors stemming from the applied truncation scheme, consisting first of truncation in the CST via the scaling dimension and second of the re-diagonalization of only the coupled single- and three-magnon space by neglecting higher-magnon subspaces.

The plateau might be an artifact of the unachievable endeavor of the pc generator to untangle the different particle spaces fully. Additionally, the behavior of this plateau is analyzed as a function of the termination parameter ℓ^*. The plateau forms already for $\ell^* = 0.5$ and its height decreases overall as ℓ^* increases. It is particularly impressive that the height aligns well with the QMC results at the K-point when the previously defined flow termination condition is used.

All in all, the observation of a vanishing single-particle weight in the QMC results at the K-point perfectly fits the observation made within the CST framework. Thus, a bound state in the two-magnon block may lead to this vanishing weight. It is precisely the correct treatment of

the scattering $1 \leftrightarrows 3$ magnon terms that is responsible for the formation of this bound state, since the bound state is not observable for the $0n$ generator. However, interaction terms might be overestimated within the CST, leading to a bound state throughout the higher-energy sector, i.e., close to the BZ boundaries. In contrast, the results of QMC and SE only see such effects in the vicinity of the K-point. In the following section, as an addition to the Heisenberg point, the behavior of bound states in the two and three-magnon subspace is analyzed for the whole anisotropy range of the XXZ model.

6.7 Bound States and Multi-Magnon Continuum

For the XXZ model on a square lattice, the fate of the bound states in the two-magnon subspace $S^z = 0$ with increasing anisotropy λ is already successfully discussed in Section 5.6.2. In this section, the same analysis is performed for the honeycomb lattice. However, the focus differs from that for the square lattice, where the goal was to determine the critical anisotropy using the inverse partition ratio (IPR) at which the bound states vanish.

Here, the goal is more to understand the behavior of these bound states, especially since a bound state is found for the terminated pc generator flow at the Heisenberg point for high momenta. In addition, this analysis should provide further insights why a divergence flow is observed for the pc generator at higher anisotropies, by also considering the lowest eigenvalue of the untangled three-magnon block with $S^z = 1$ for the pc generator $\hat{\eta}^{\mathrm{pc}}$ or the second-lowest eigenvalue of the one three-magnon block for the $0n$ generator $\hat{\eta}^{\mathrm{pbs}}_{0:n}$, respectively. The starting point, as in the square lattice case, is the Ising model at $\lambda = 0$ where the bound states are well understood. Figure 6.13 shows an exemplary bound state as well as sketches of possible configurations of bound states in the antiferromagnetic Ising model on a honeycomb lattice.

Due to its lower coordination number for a bound state, only four broken bonds exist as shown in Fig. 6.13a. Therefore, the energy of a bound state in the Ising limit on the honeycomb lattice with $2J$ is already closer to the single-particle energy of $1.5J$ compared to the square lattice with $3J$ to $2J$. Compared to the square lattice, only a distinction of three orientations of the bound states exists due to the different geometry of the honeycomb lattice, as shown in Fig. 6.13b.

Considering the continuum for two non-interacting magnons in the Ising limit, it starts at $3J$, where for the square lattice it starts at $4J$. Already in the Ising limit, the two-magnon bound states on the honeycomb lattice are further away from the continuum and closer to the single-magnon energy compared to the square lattice, thus showing more substantial binding effects.

The same analysis is carried out for three-magnon spaces. Occurring energies are $2.5J$ for a three-magnon bound state, $3.5J$ for a two-magnon bound state with an additional non-interacting magnon, and $4.5J$ for three non-interacting magnons. Interestingly, possible three-magnon bound states lie even below the two-magnon continuum. Consequently, already in the Ising limit, the particle spaces overlap energetically, indicating that a divergence of the pc generator seems inevitable. However, as the Hamiltonian conserves the total spin S^z, the two and three-magnon spaces are not directly coupled, and transitions between these spaces are prohibited. As a result, the pc generator still converges even if two- and three-magnon spaces overlap energetically in the Ising limit. Hence, the comparison between the lowest eigenvalue of the three-magnon space with $S^z = 1$ and the single-particle dispersion gives insights into whether the reason for the divergence of the pc generator at higher anisotropies lies in energetic overlaps of these spaces.

In the following, the behavior of the bound states in the two- and three-magnon subspaces is analyzed over the full anisotropy range $0 \leq \lambda \leq 1$ at different high-symmetry points in the BZ.

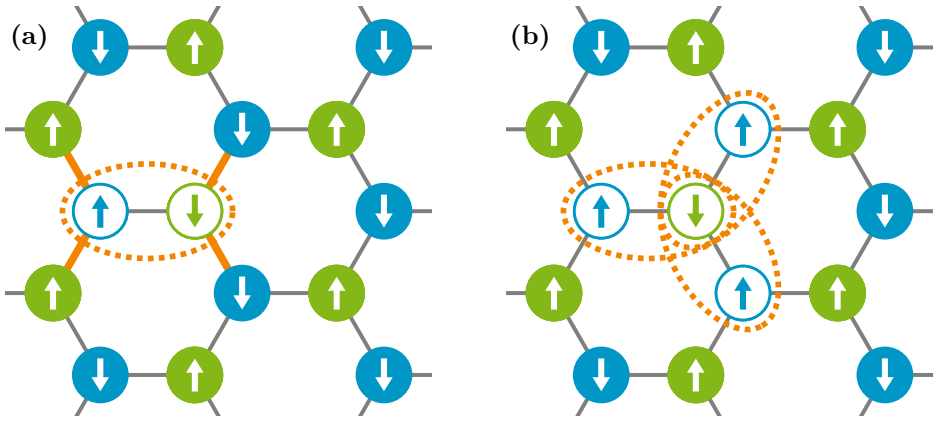

Figure 6.13: Sketches of bound states in the antiferromagnetic Ising model on a honeycomb lattice. The Fig. 6.13a shows a possible realization of a bound state. White-filled circles mark the two flipped spins, and orange lines mark the four broken bonds, yielding a total energy of $2J$. The Fig. 6.13b displays all three possible orientations of the bound states in the antiferromagnetic Ising model on a honeycomb lattice. All bound states are marked with dotted orange ellipses.

Results with the pc generator $\hat{\eta}^{\mathrm{pc}}$ are shown up to the anisotropy where the flow diverges, whereas results with the $0n$ generator $\hat{\eta}^{\mathrm{pbs}}_{0:n}$ are shown for the full anisotropy range. In the two-magnon subspace with $S^z = 0$, three bound states are expected and analyzed here. Where for the three-magnon subspace with $S^z = 1$ the focus lies only on the lowest three-magnon state. Results obtained by the CST with the $0n$ generator $\hat{\eta}^{\mathrm{pbs}}_{0:n}$ include the re-diagonalizing of the coupled one and three-magnon space. The lowest eigenvalue corresponds to the single-particle dispersion, and the second-lowest gives the three-magnon bound state energy, in this case. Figure 6.14 shows the behavior of the single-particle energy together with bound states in the two- and three-magnon subspace at different high-symmetry points in the BZ, i.e., Γ-, K-, and M-point, for both generators. Additionally, the two- and three-magnon continua are shown as shaded areas. Their boundaries are determined by calculating all possible combinations of non-interacting magnon energies that satisfy the conservation of momenta for the given $\boldsymbol{k}$-point. The minima and maxima of these combinations yield the lower and upper boundaries of the respective continuum.

In Fig. 6.14 for the Ising limit at $\lambda = 0$, all energies match the expected values discussed above and show no momentum dependencies as expected for the Ising limit. However, the picture changes with increasing anisotropy λ. The three-fold degeneracy of the two-magnon bound states at the Ising limit is resolved for finite anisotropies, for both generators. To be precise, the degeneracy is only for the M-point fully lifted, whereas at the Γ- and K-point, two bound states remain degenerate, having a slightly higher energy compared to the third. This degeneracy is due to the higher symmetry at these points in the BZ. There, the satisfied three-fold rotational symmetry of the honeycomb lattice leads, similarly to the square lattice (see Section 5.6.2), to energetic degenerate bound states.

When comparing both generators, the results for the single-particle dispersion at all $\boldsymbol{k}$-points show almost no differences. The first differences appear in the bound states of the two-magnon subspace. Here, the pc generator $\hat{\eta}^{\mathrm{pc}}$ yields slightly lower energies, especially for the lowest bound state. The differences increase with increasing anisotropy λ. Interestingly, at the K-point, the lowest two-magnon bound state crosses the single-particle dispersion around $\lambda \approx 0.55$ for the pc generator

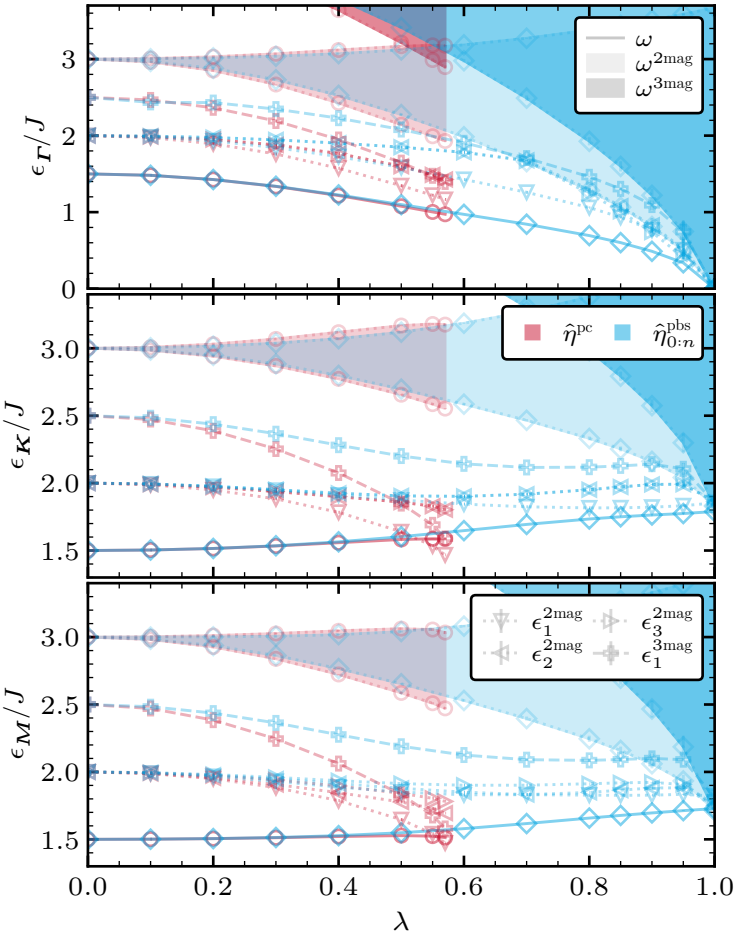

Figure 6.14: Characteristic energies of the different magnon subspaces at high-symmetry points in the BZ for the XXZ model on a honeycomb lattice. They are determined with the CST either with the pc generator $\hat{\eta}^{\mathrm{pc}}$ or the $0n$ generator $\hat{\eta}^{\mathrm{pbs}}_{0:n}$. The upper panel shows the energies at the Γ-point, the middle panel at the K-point, and the lower panel at the M-point. Each panel itself shows the single-particle energy ω, the two-magnon continuum $\omega^{2\mathrm{mag}}$ with $S^z = 0$, and the three-magnon continuum $\omega^{3\mathrm{mag}}$ with $S^z = 1$. Additionally, the bound states in the two-magnon subspace $\epsilon^{2\mathrm{mag}}_{1,2,3}$ and the lowest energy in the three-magnon subspace $\epsilon^{3\mathrm{mag}}_1$ are shown.

$\hat{\eta}^{\mathrm{pc}}$. Contrary to the $0n$ generator $\hat{\eta}^{\mathrm{pbs}}_{0:n}$, no such crossing is observed for the whole anisotropy range. Instead, similar to the square lattice, the bound states in the two-magnon subspace decay into the continuum with increasing anisotropy λ, at all $\boldsymbol{k}$-points. With the $0n$ generator $\hat{\eta}^{\mathrm{pbs}}_{0:n}$, the same behavior is observed for the lowest bound state in the three-magnon subspace. Its energy stays for all considered $\boldsymbol{k}$-points well above the two-magnon bound states until it finally decays into the three-magnon continuum for higher anisotropies.

The picture for the pc generator $\hat{\eta}^{\mathrm{pc}}$ differs significantly. Here, the lowest three-magnon bound state energy crosses the energies of the two higher bound states around $\lambda \approx 0.5$. As the single-magnon space is not connected directly to the two-magnon space, this crossing does not lead to a divergence of the flow. However, at the last available anisotropy before the divergence of the flow, i.e., $\lambda = 0.57$, the lowest three-magnon bound state even crosses the single-particle dispersion at the K-point. This observation is significant as it confirms that the energetic overlap between the single-particle dispersion and the three-magnon space is indeed a reason for the divergence of flow with the pc generator $\hat{\eta}^{\mathrm{pc}}$ at higher anisotropies.

Although the crossing is initially observed only at the K-point, it also seems to occur at the M-point. This is because the lowest three-magnon bound state gets very close to the single-particle dispersion there. So, for slightly higher anisotropies, the crossing might also happen at the M-point.

At the Γ-point, the lowest three-magnon bound state is also close to the single-particle dispersion. However, unlike the other points, here the single-particle dispersion decreases together with the bound-state energy as anisotropy increases, rendering a crossing unlikely.

Both predictions can be assessed by recalling the results of the Heisenberg point in Section 6.6, where the terminated pc generator flow showed that the single-particle dispersion between the M- and K-point decays into the continuum, whereas at close to the Γ-point, the single-particle dispersion remains well-defined. Thus, the predictions made here for higher anisotropies are reasonable. Nevertheless, for the M-point this crossing behavior is unphysical, as no such behavior is observed in QMC calculations for the afHM [Krä+25]. Therefore, the decay of the single-particle dispersion into the continuum at the K-point for anisotropies $\lambda < 1$ is most likely a physical behavior, whereas at the M-point it is rather an artifact of the applied truncation scheme within the CST with the pc generator $\hat{\eta}^{\mathrm{pc}}$.

All in all, the analysis of the bound states in the two- and three-magnon subspace for the XXZ model on a honeycomb lattice confirms the previous assumption that the divergence of the pc generator at higher anisotropies is due to energetic overlaps of the single-particle dispersion with the three-magnon space. Furthermore, it shows that the $0n$ generator is not able to capture these energetic overlaps resulting from magnon-magnon interactions, as no crossing of the single-particle dispersion with the three-magnon bound state is observed for the whole anisotropy range. However, the pc generator seems to overestimate these interaction effects, leading to unphysical crossings even at the M-point instead of only at the K-point for anisotropies below the Heisenberg point. Whether this first crossing at the K-point of the single-particle dispersion with a three-particle bound state precisely occurs close to $\lambda \approx 0.57$, cannot be answered definitely here. Nevertheless, it can give a reasonable estimate for other methods analyzing the same model.

6.8 Summary and Outlook — XXZ Model on the Honeycomb Lattice

Within this chapter, the systematic basis change by a CST as applied in Chapter 5 to the two-dimensional XXZ model on a square lattice was extended to the two-dimensional XXZ model on a honeycomb lattice. Identical to the square lattice, this model on a honeycomb lattice displays the transition from a spontaneously broken discrete symmetry with a finite energy gap to a spontaneously broken continuous symmetry with a vanishing energy gap.

First deviations compared to the procedure applied to the square lattice arise within the choice of the SWT based on the DM of the spin operators. For the square lattice, as a starting point, a scNL-SWT was used, whereas for the honeycomb lattice, it turned out that a scNL-SWT yields no solution for higher anisotropies close to the isotropic point. Therefore, instead of a scNL-SWT, only a NL-SWT without the self-consistency was used as the starting point of the CST.

Not only does the starting point differ compared to the square lattice, but also the behavior of the pc generator $\hat{\eta}^{\mathrm{pc}}$ shows significant differences. For the square lattice, the pc generator converges for all anisotropies, whereas for the honeycomb lattice, a divergence of the flow is observed for anisotropies $\lambda \gtrsim 0.57$. This divergence is traced back to energetic overlaps between the single-particle dispersion and the three-magnon space, as the analysis of bound states in the two- and three-magnon subspaces revealed. In order to analyze the full range of anisotropies, including the isotropic Heisenberg point, the $0n$ generator $\hat{\eta}^{\mathrm{pbs}}_{0:n}$ was used instead. To approximate the single-particle dispersion for the $0n$ generator results, a re-diagonalization of the coupled one and three-magnon space is performed.

A comparison of the single-particle dispersion in the square lattice model, determined via $0n$ generator or via pc generator, showed almost no differences for low-energy properties such as magnetization and spin gap. However, for high-energy properties, such as the single-particle dispersion near the MBZ edges, significant differences were observed. The difference between the roton minimum and dispersion maximum was underestimated by the $0n$ generator compared to the pc generator. This finding Indicates that magnon-magnon interaction effects are not captured sufficiently by the $0n$ generator.

The same analysis was performed for the honeycomb lattice. Of course, here, the comparison can only be carried out up to the anisotropy where the pc generator diverges. Interestingly, the dispersion determined by the $0n$ generator or the pc generator showed non-vanishing non-physical imaginary contribution in the order of $10^{-4}J$. These complex contributions are attributed to numerical inaccuracies during the integration of the flow equations and to approximations arising from the re-diagonalization of the coupled one- and three-magnon spaces. They are significantly smaller than the energy scales of interest and are therefore neglected. Within the considered anisotropy range, the differences between the two generators are marginal for low-energy properties such as the ground-state energy and the spin gap. Additional comparisons with literature results from DMRG, high-order SE calculations, and CCM showed good agreement for these low-energy properties. However, a strict comparison over the full anisotropy range, including also the power law behavior close to the Heisenberg point, as done for the square lattice with QMC results [Cac+24], is still due.

Only for the Heisenberg limit, a comparison of the single-particle dispersion to literature results from QMC and high-order SE calculations was carried out. Especially in the vicinity of the K-point, where a roton-like minimum is reported in the literature, significant differences between the $0n$ generator results and the literature results were observed. In an attempt to capture this roton-like minimum correctly, the pc generator flow was terminated at a finite flow parameter before

the divergence occurs. The resulting effective Hamiltonian was then analyzed by re-diagonalizing the coupled one and three-magnon space, similar to the $0n$ generator approach. The resulting single-particle dispersion showed a significant renormalization and developed a plateau between the M- and K-point energetically close to the roton minimum observed in QMC. This plateau is traced back to a bound state in the two-magnon subspace that crosses the single-particle dispersion for momenta close to the BZ edge. This finding underscores the decay of the single-particle dispersion into the continuum in this area, attributed to strong magnon-magnon interactions captured by the pc generator. However, interaction terms might be overestimated, as the plateau extends throughout the whole higher-energy regime. These deviations are likely due to possible truncation errors and the unattainable goal of untangling the different magnon subspaces. A generator scheme that distinguishes the $1 \leftrightarrow 3$ processes according to momentum suggests itself for further exploration of the plateau with an improved flow. However, this exceeded the scope of this thesis.

Finally, as for the square lattice, the behavior of bound states in the two-magnon subspace with $S^z = 0$ was analyzed for the full anisotropy range. With an observed decay of the single-particle dispersion in the higher-energy sector at the Heisenberg point, the bound states were not only analyzed at the Γ-point but also at the K- and M-point. Furthermore, the lowest bound state in the three-magnon subspace with $S^z = 1$ was considered as well. Three distinct bound states are observed in the two-magnon subspace, where the three-fold degeneracy of the Ising limit is lifted for finite anisotropies. The behavior of these bound states differs significantly between the two generators. The pc generator yields lower bound state energies, especially for the lowest bound state. At the K-point, the lowest two-magnon bound state even crosses the single-particle dispersion for anisotropies around $\lambda \approx 0.55$. On the contrary, the $0n$ generator shows no such crossing for the whole anisotropy range.

Remarkably, the behavior of the lowest bound state in the three-magnon subspace differs even more between the two generators. With the $0n$ generator, the bound state decays into the three-magnon continuum for higher anisotropies at all considered $\boldsymbol{k}$-points. In contrast, the pc generator shows a crossing of the lowest three-magnon bound state with the single-particle dispersion at the K-point for anisotropies close to the divergence point around $\lambda \approx 0.57$. This observation confirms that energetic overlaps of the single-particle dispersion with the three-magnon space are indeed the reason for the divergence of the pc generator at higher anisotropies.

The question whether this crossing at the K-point indeed occurs close to $\lambda \approx 0.57$ cannot be answered definitively here. However, it can provide a reasonable estimate for other methods that analyze the same model. However, the divergence of the pc generator at higher anisotropies can be definitely interpreted as a strong indication that the single-particle dispersion decays already into the continuum at the K-point for anisotropies below the Heisenberg point.

7 | Conclusions

7.1 Summary

This thesis investigates two-dimensional quantum antiferromagnets, with a special focus on the spin-$\frac{1}{2}$ antiferromagnetic easy-axis XXZ model on both the square and the honeycomb lattice. The objective is to correctly capture the excitations and interactions of magnons, the fundamental quasiparticles of such systems. The method of choice for this investigation is the continuous similarity transformation (CST), which allows for a systematic derivation of an effective quasiparticle picture via flow equations.

To this end, the thesis begins with a systematic and consistent derivation of a nonlinear spin-wave theory (NL-SWT) for the antiferromagnetic easy-axis XXZ model on a bipartite lattice, particularly on the square lattice. In this context, two different bosonic representations of the spin operators are discussed, and the non-Hermitian Dyson-Maleev representation (DM) is found to be the most suitable, due to its closed form without the need for an expansion. An in-depth derivation, including several standard analytical techniques such as Fourier and Bogoliubov transformations, is carried out to obtain a NL-SWT Hamiltonian in momentum space. Additionally, a self-consistent nonlinear spin-wave theory (scNL-SWT) is derived, leading to a Hamiltonian diagonal on the mean-field level. Furthermore, two choices of gauge for the Fourier transformation, namely the Bloch and symmetric gauge, are discussed, and their influence on the results is analyzed.

To analyze the full Hamiltonian, including quartic interaction terms that do not conserve particle number, a crucial next step is necessary: a controlled change of basis in a continuous fashion via the flow equation approach. A comprehensive overview of the general method is provided, encompassing its different manifestations. In particular, various generators and truncation schemes, central components of the flow equation approach, are discussed in detail. Ultimately, the CST is identified as the most suitable flow equation scheme for the problem at hand. The reason for this choice is due to the non-Hermitian nature of the DM and the resulting NL-SWT Hamiltonian. The CST is applied in momentum space and second quantization. A truncation scheme based on the scaling dimension d is employed, retaining only operator terms satisfying $d \leq 2$. Moreover, two different generator schemes are employed for the problem at hand, namely the particle-conserving generator (pc generator) and the particle-block-separating generator with $k = 0$ ($0n$ generator). The pc generator leads to an effective Hamiltonian conserving the number of quasiparticles. In contrast, the $0n$ generator leads to an effective Hamiltonian in which the ground state is decoupled from all excited states.

The exact methodical implementation of the CST is outlined. Thereby, an example of a coefficient's flow equation is given for both generators. Additionally, the numerical implementation of the CST is discussed, including two different discretization schemes of the Brillouin zone (BZ) or magnetic Brillouin zone (MBZ). The discretized meshes result from periodic (N_p) and antiperiodic (N_ap) boundary conditions. The main difference between these two schemes is that N_p includes the center, i.e., the Γ-point, of the BZ(MBZ) and N_ap excludes it.

Furthermore, a detailed analysis of possible exploitations of symmetries in the context of the CST is presented. There are two types of distinguishable symmetries. First, there exist symmetries of the

different coefficients of the terms in second quantization to one another, based on $\mathcal{PT}$-symmetry of the non-Hermitian Hamiltonian. Second, there are intrinsic symmetries of a single coefficient, based on the point-group symmetries of the underlying lattice. Applying these symmetries significantly reduces the computational effort required to solve the large set of coupled ordinary differential equations arising in the flow equations of the CST.

Moreover, since the Hamiltonian is non-Hermitian even after the CST, special care must be taken when evaluating physical observables. To this end, a biorthogonal basis of left and right eigenvectors is introduced, which is used to determine physical observables. In this context, the non-symmetric Lanczos algorithm is employed as a suitable numerical tool to compute the low-energy spectrum of the effective Hamiltonian.

The antiferromagnetic easy-axis XXZ model on the square lattice is studied in detail, applying the previously established theoretical and numerical framework. The XXZ model on the square lattice is chosen as it is a straightforward extension of the paradigmatic antiferromagnetic Heisenberg model (afHM), for which the CST has already been successfully applied before [PUS15; Pow17; PSU18]. Compared to the Heisenberg model, the XXZ model introduces an additional anisotropy parameter λ, which allows interpolating between the gapped Ising limit at $\lambda = 0$ and the gapless Heisenberg limit at $\lambda = 1$. A central aspect of this thesis is to analyze how the anisotropy, which induces a gap, influences the results of the CST, especially given that the CST was initially developed for the gapless, isotropic Heisenberg model.

With this objective in mind, effective Hamiltonians are derived by CST for various values of the anisotropy parameter λ. For the whole anisotropy range $0 \leq \lambda \leq 1$, the flow of the pc generator converges successfully, leading to effective Hamiltonians conserving the number of quasiparticles. An application of the $0n$ generator is unnecessary. Different physical properties, including the ground-state, single-magnon, and two-magnon properties, are determined. As these properties depend on the considered system size and discretization scheme, a thorough finite-size analysis is performed to extrapolate all the results to the thermodynamic limit.

First, ground-state properties are analyzed. The ground-state energy is compared to results from quantum Monte Carlo (QMC) simulations [Her+24], showing excellent agreement for the whole anisotropy range. Additionally, two approaches for determining the staggered magnetization are presented. One method uses the response of the ground-state energy to an infinitesimal staggered magnetic field as a measure, while the other calculates the expectation value of the staggered magnetization observable directly in the basis transformation. Both calculations are consistent with each other and with the QMC results, yielding almost perfect agreement over the entire anisotropy range. Slight deviations to QMC occur near the isotropic point, indicating a systematic error that hinders the correct determination of the critical exponent. The transversal correlation length also shows excellent agreement with the QMC results. Through it, the sufficiency of the analyzed system sizes near the divergence is validated.

Second, single-magnon properties are studied in detail. The single-magnon dispersion is analyzed for different anisotropy parameters λ. Increasing anisotropies lead to a closing of the spin gap and the emergence of the roton minimum at the $(\pi, 0)^T$ point as well as a dispersion maximum at $(\frac{\pi}{2}, \frac{\pi}{2})^T$. A detailed analysis of the spin gap Δ shows excellent agreement between various methods, including QMC [Her+24], high-order series expansion (SE) [ZOH05], and density matrix renormalization group (DMRG) [Kad+24]. Close to the isotropic point, the square-root behavior $\Delta \propto \sqrt{1-\lambda}$ is reproduced with very high accuracy. The anisotropy dependence of the roton minimum and dispersion maximum is also analyzed. Both show almost excellent agreement with the other methods, albeit with slight deviations near the roton minimum, due to truncation beyond the quartic monomials.

Third, a special advantage of the CST is that it also enables the analysis of two-magnon properties. In particular, the decay of two-magnon bound states into the two-magnon continuum is studied. Based on their locality of the bound state determined by the inverse partition ratio (IPR) the decay points, i.e., where the bound state vanishes into the continuum, are determined to be $\lambda_{\tau(-1)} \approx 0.565(5)$, $\lambda_{\tau(\pm \mathrm{i})} \approx 0.72(1)$, and $\lambda_{\tau(1)} \approx 0.975(5)$, which agree within a few percent with results from high-order SE [Dus+10]. However, close to the Ising point, slight deviations to SE in the second order of λ are observed, which are attributed to neglecting hexatic terms in the CST.

In summary, almost excellent agreement with other established methods is observed across the entire anisotropy range for all analyzed properties of the different particle sectors. Even quantitative agreement is achieved for the spin gap. These results support that the CST using the pc generator is a robust and reliable method also for gapped systems. Even though the CST with a truncation scheme based on scaling dimension was initially developed for the gapless systems. Only for the two-magnon bound states, the truncation beyond the quartic monomials leads to slight deviations caused by truncation errors for smaller λ close to the Ising point.

With the successful application of the CST to the antiferromagnetic easy-axis XXZ model on the square lattice, a natural next step is to study a bipartite lattice with the same model but with a lower coordination number, leading to stronger quantum fluctuations. This serves as a motivation for applying the CST to the antiferromagnetic easy-axis XXZ model on the honeycomb lattice. In this context, the main differences compared to the square lattice are highlighted, including modifications to the Fourier transformation and different point-group symmetries that affect the symmetries of the coefficients. Due to the inevitable occurrence of complex coefficients caused by the lack of inversion symmetry around sites, the Fourier transformation is performed using the Bloch instead of the symmetric gauge. This choice avoids irrational phase factors in the symmetric gauge when considering Umklapp processes.

Initially, the results are obtained for linear spin-wave theory (L-SWT), mean-field spin-wave theory (MF-SWT), and self-consistent mean-field spin-wave theory (scMF-SWT). Interestingly, the scMF-SWT is not able to produce a self-consistent solution for anisotropies $0.7235(5) \lesssim \lambda < 1$. Furthermore, scMF-SWT shows a strong renormalization close to the interval where no solution could be found. However, it is also possible to start the CST from the NL-SWT, which does not suffer from this issue. In the NL-SWT quadratic off-diagonal terms are not zero due to the non-self-consistent Bogoliubov transformation.

No convergence of the pc generator on the honeycomb lattice is found for larger anisotropies $\lambda \gtrsim 0.575(5)$, where the flow starts to diverge. This observation provides the first indication that energetic crossing between different particle sectors occurs, which is detrimental to the convergence of the pc generator. To circumvent this problem, the $0n$ generator is applied, resulting in converged flows for all analyzed anisotropies $0 \leq \lambda \leq 1$. Consequently, the ground state in the honeycomb lattice is still antiferromagnetically ordered for the whole anisotropy range, but higher anisotropies induce energetic overlaps between higher particle sectors.

To assess the difference in the results from both generators, the square lattice is revisited, and the $0n$ generator is applied there as well. Ground-state properties and single-magnon properties are compared for both generators. To this end, the single-magnon dispersion for the $0n$ generator is obtained by diagonalizing the one- and three-magnon subspace, neglecting the coupling to higher particle sectors. Only for high-energy features of the single-magnon dispersion, slight deviations are observed for higher λ. However, for lower-energy properties or lower λ in general, both generators yield consistent results.

In accordance with this assessment, the low-energy properties of the honeycomb lattice are analyzed. The $0n$ generator is used for the whole anisotropy range and the pc generator for all λ for which it converges. For both generators, good agreement of the ground-state energy, the staggered

magnetization, and the spin gap is observed with the likes of DMRG [Kad+24], coupled cluster method (CCM) [BR98; BL16], and high-order SE [OHZ92]. The only exception is the SE results for the spin gap; here, higher-order terms appear to be necessary to reach agreement also for higher λ compared to the other methods. This characteristic is not observed in the square lattice, which underscores the influence of stronger quantum fluctuations on the honeycomb lattice. A detailed comparison with QMC results, including critical exponents, as done for the square lattice, is not possible due to the lack of available data. Future calculations in combination with QMC results are therefore highly desirable.

For the afHM on the honeycomb lattice, QMC results are available from Ref. [Krä+25]. A comparison with CST results using the $0n$ generator shows that the CST in this configuration is not able to reproduce the high-energy features of the single-magnon dispersion. Especially, a possible decay at the K point, i.e., a corner point of the BZ, is not reproduced. To further investigate this discrepancy, the CST is applied using the pc generator. The flow of the pc generator is terminated to avoid the effects of the divergence that would occur otherwise. Persistent transitions of different particle sectors, e.g., between the single-magnon and three-magnon subspaces, are handled in the same way as for the $0n$ generator after the termination. Within this approach, a two-magnon bound state is identified below the one-magnon dispersion for higher momenta. This bound state serves as a possible explanation for the decay of the single-magnon dispersion, as it can energetically overlap with the single-magnon dispersion and thus lead to a decay of the single-magnon into the three-magnon continuum. Unfortunately, this bound state is observed not only at the corner but also near the edges of the BZ, in contrast to the QMC results, where a decay is observed only in the vicinity of BZ corners. However, it shows that the binding effects between magnons can serve as a possible explanation for the occurring decay, even if the CST with the terminated pc generator flow overestimates the extent of this effect.

Finally, an analysis of the two-magnon and three-magnon spaces on the honeycomb lattice over the entire anisotropy range is presented. Due to the lower coordination number, only three bound states are expected and found in the two-magnon sector. They are analyzed over the full anisotropy range and at three different points of the BZ. Additionally, the lowest three-magnon bound state is also studied. A comparison between pc generator and $0n$ generator reveals that the energy renormalization of these bound states is much stronger for the pc generator. Directly related to this strong renormalization, the divergence point of the pc generator can be linked to the energetic overlap of the single-magnon dispersion with a three-magnon bound state. Compared to the square lattice, such bound states are much closer to the single-magnon dispersion even for lower λ. This stems from the honeycomb lattice's lower coordination number. However, it remains unclear whether the decay of the single-magnon dispersion already occurs at such a low anisotropy $\lambda \approx 0.575(5)$. Additional studies in the spirit of Ref. [Dus+10], which determined SE results for the bound states in the case of the square lattice, specifically targeting this question for the honeycomb lattice, would be highly desirable.

All in all, these findings indicate that for lattices with lower coordination numbers and thus stronger quantum fluctuations, such as the honeycomb lattice, the CST with the pc generator can face limitations due to the increased likelihood of energetic overlaps between different particle sectors. However, low-energy properties are captured sufficiently well in such cases using the CST with the $0n$ generator. Although the resulting high-energy features have to be taken with a grain of salt.

7.2 Conclusion

This thesis demonstrates that the application of the CST as implemented in this work leads to two contrasting results, depending on the underlying lattice structure. For the spin-$\frac{1}{2}$ antiferromagnetic easy-axis XXZ model on the square lattice, the CST produces almost quantitatively correct results for the entire anisotropy range $0 \leq \lambda \leq 1$. Only small deviations are observed for the two-magnon bound states near the Ising point, which can be attributed to truncation errors. However, for the same model on the honeycomb lattice, the CST can only reproduce low-energy properties accurately, while high-energy features are not fully captured. This dichotomy highlights the strengths and limitations of the CST approach. While it excels at providing an effective particle-conserving Hamiltonian when all particle sectors are energetically well separated, it fails to capture certain high-energy phenomena when significant overlaps between different particle sectors persist. These overlaps are more likely to occur in systems where binding effects are stronger than the kinetic energy of the quasiparticles. This is the case with the honeycomb lattice. Due to its lower coordination number compared to the square lattice, quantum fluctuations are enhanced, leading to stronger binding effects. It is important to note that essentially the sole difference between both cases lies in the initial values of the coefficients entering the CST, while the rest of the apparatus, i.e., the truncation scheme and the general structure of the flow equations, remains unchanged. Thus, already at the starting point of the CST, the specific lattice geometry and its interaction parameters crucially influence the method's effectiveness.

7.3 Outlook

Starting from this work, two different further research paths suggest themselves: On the one hand, further investigations of alternative generator schemes or truncation methods in the CST framework can be pursued to better handle systems with strong quantum fluctuations and overlapping particle sectors. Generators that adeptly account for such overlaps, e.g., by rotating only non-critical parts to zero and even considering specific momentum dependencies, might improve the results in such challenging scenarios [FDU10; FDU11]. Advanced truncation schemes that involve specific interactions with higher scaling dimensions could also improve the method's ability to capture high-energy features accurately.

On the other hand, another direction is the extension of the application of the CST to other lattices and models with characteristics similar to those of the square lattice, while being aware of its limitations. To this end, only new initial conditions for the coefficients are necessary, while the rest of the method remains unchanged. It is also possible to calculate additional physical observables, like the dynamic structure factors and spectral densities, as is done in the initial works on the spin-$\frac{1}{2}$ antiferromagnetic Heisenberg model on the square lattice [PUS15; Pow17; PSU18], and compare them to experiment or other numerical calculations.

Especially for resonant inelastic x-ray scattering (RIXS) experiments [Ame+11], the calculation of their corresponding spectral response observables via the CST would be rewarding. This direction has already been initiated in the context of the flow equation approach with a continuous unitary transformation (CUT) by Ref. [Sch+22], calculating RIXS spectra for an antiferromagnetic spin ladder in terms of a triplon language. A first reasonable step in this direction is to calculate RIXS spectra for the afHM on the square lattice [Pal+23] via the CST. Since RIXS measurements focus on cuprates or iridates, an additional step beyond the observables is to extend the model to more realistic Hamiltonians to reproduce experimental results accurately. This entails also including next-nearest-neighbor and the ring-exchange terms [Col+01; MFU12] in the model. Those additional terms can be derived from the $\frac{t}{U}$ expansion of the Hubbard model at half

filling [Tak77]. Of course, this could be done not only for the square lattice but also for the bilayer, in view of recent RIXS measurements on such materials [Kim12; Maz+22; Mor+15].

Already in the course of Ref. [Her+24], the CST with the $0n$ generator was applied to the bilayer afHM on the square lattice and to the J_1-J_2 model on the square lattice in both its Néel and collinear phase. These studies showed that the application is also possible with additional variation compared to the plain square lattice afHM and the XXZ model. Where, however, the focus was on capturing quantum phase transitions, not on physical observables, well within the magnetically ordered phase.

Studying such quantum phase transitions further with the CST also entails exciting future research directions. For example, with the help of the $0n$ generator, the phase boundaries of additional magnetically ordered phases can be determined. The J_1-J_2-J_3 model on the honeycomb lattice with its various ordered phases [FSL01; OS11; Li+12] can be investigated.

Nevertheless, the results of Ref. [Her+24] draw limitations of the CST in capturing the critical behavior close to such quantum phase transitions, regarding the critical exponents. To overcome these limitations, an interesting approach could be to change the underlying spin representation from a DM to a Schwinger boson representation [Aro88; Zha+22], which is capable of describing both the magnetically ordered and unordered phase. Of course, a thorough analysis and comparison to the established CST with DM would be necessary to validate such an approach.

In conclusion, the CST as implemented in this thesis has a promising future ahead. The CST offers a wide scope for further investigation, both in terms of practical applications to various quantum spin systems as well as in terms of methodological advancements.

A | Initial Coefficient before the Continuous Similarity Transformation

In this appendix, the initial coefficients of the continuous similarity transformation (CST) for the XXZ model using the Dyson-Maleev representation (DM) are listed. The initial Hamiltonian in this spin representation is given by

$$\begin{aligned}\hat{\mathcal{H}} =& J\sum_{\langle i,j\rangle}\hat{S}_i^z\hat{S}_j^z + \lambda\left(\hat{S}_i^x\hat{S}_j^x + \hat{S}_i^y\hat{S}_j^y\right) - h_{\mathrm{alt}}\sum_{\boldsymbol{r}_i\in\Gamma_A}S_{A,i}^z + h_{\mathrm{alt}}\sum_{\boldsymbol{r}_j\in\Gamma_B}S_{B,j}^z \\ =& J\sum_{\langle i,j\rangle}\hat{S}_i^z\hat{S}_j^z + \frac{\lambda}{2}\left(\hat{S}_i^-\hat{S}_j^+ + \hat{S}_i^+\hat{S}_j^-\right) - h_{\mathrm{alt}}\sum_{\boldsymbol{r}_i\in\Gamma_A}S_{A,i}^z + h_{\mathrm{alt}}\sum_{\boldsymbol{r}_j\in\Gamma_B}S_{B,j}^z,\end{aligned} \tag{A.1}$$

where $J > 0$ is the antiferromagnetic exchange coupling and λ the anisotropy parameter and $\langle i,j\rangle$ denotes the sum over all nearest neighbor pairs. Additionally, a staggered magnetic field h_{alt} is included to access the staggered magnetization. In this form, the Hamiltonian is not specific to a particular lattice structure. In the following, the initial coefficients should retain a lattice-independent form. To achieve this, it is necessary to introduce certain functions and constants that depend on the lattice structure but are kept general in the coefficient notation. Afterwards, these are specified for the two lattices used in this work: the square and honeycomb lattices.

Even if the lattice structure is not specified in the beginning, it has to fulfill specific prerequisites in order even to be a candidate for the CST treatment as set up in this work. First and foremost, the lattice must be bipartite, as the chosen DM relies on this property. With this asserted, the first variables are the total spin per site, S, and the coordination number, Z, of the lattice. Although in this work only the case of spin $S = \frac{1}{2}$ is treated, the coefficients are kept general in this regard, as the DM also allows for $S > \frac{1}{2}$. The coordination number Z counts the number of nearest neighbors of a lattice site, relevant for evaluating the sum over the nearest neighbors in Eq. (A.1).

Following Section 2.5, the DM is applied and, in the same manner as in Section 2.5.4, the mean-field parameters can be introduced regardless of the lattice structure, by the general normal-ordering. However, the evaluation of these parameters depends on the lattice structure, as they involve momentum-space integrals over the Brillouin zone (BZ) or magnetic Brillouin zone (MBZ), which are specified later. At this stage, the mean-field parameters are denoted as n_{mf} and Δ_{mf}.

In particular, the Fourier transformation and the subsequent Bogoliubov transformation depend on the lattice structure. However, it is possible to keep the coefficient notation general by introducing lattice-dependent functions that arise in these transformations. The first function is $\gamma_{\mathrm{X}}(\boldsymbol{k})$ which appears within the Fourier transformation of the Hamiltonian

$$\gamma_{\mathrm{X}}(\boldsymbol{k}) = \frac{1}{Z}\sum_{\boldsymbol{d}\in\mathfrak{D}}\mathrm{e}^{-\mathrm{i}\boldsymbol{k}\boldsymbol{d}} \tag{A.2}$$

with the set of nearest neighbor vectors $\mathfrak{D}$ and the coordination number $Z = \sum_{\boldsymbol{d}\in\mathfrak{D}} 1$. The set of nearest neighbor vectors $\mathfrak{D}$ contains all vectors that connect a lattice site to its nearest neighbors, where the lattice geometry and the choice of the gauge influence the exact form of $\mathfrak{D}$. Directly

connected to the function $\gamma_{\mathrm{X}}(\boldsymbol{k})$ is the solution of the Bogoliubov transformation. The solution contains the functions $l_{\boldsymbol{k}}$ and $m_{\boldsymbol{k}}$, which are defined in Section 2.5.4 as

$$l(\boldsymbol{k}) = -\frac{\mu_{\boldsymbol{k}}}{\sqrt{|\mu_{\boldsymbol{k}}|^2 - |h_{\boldsymbol{k}}|^2}} \quad \text{and} \quad m(\boldsymbol{k}) = \frac{h_{\boldsymbol{k}}}{\sqrt{|\mu_{\boldsymbol{k}}|^2 - |h_{\boldsymbol{k}}|^2}} \quad \text{and} \quad \mu_{\boldsymbol{k}} = \omega_\alpha(\boldsymbol{k}) + f_{-\boldsymbol{k}} \ . \tag{A.3}$$

Additionally, the following functions are introduced to keep the coefficient notation general

$$\omega_\alpha(\boldsymbol{k}) = \Delta_{\boldsymbol{k}} + \sqrt{R_{\boldsymbol{k}}^2 - |h_{\boldsymbol{k}}|^2} \ , \qquad \omega_\beta(-\boldsymbol{k}) = -\Delta_{\boldsymbol{k}} + \sqrt{R_{\boldsymbol{k}}^2 - |h_{\boldsymbol{k}}|^2} \tag{A.4}$$

with

$$R_{\boldsymbol{k}} = \frac{g_{\boldsymbol{k}} + f_{-\boldsymbol{k}}}{2} \ , \qquad \Delta_{\boldsymbol{k}} = \frac{g_{\boldsymbol{k}} - f_{-\boldsymbol{k}}}{2} \ . \tag{A.5}$$

and

$$f_{\boldsymbol{k}} = g_{\boldsymbol{k}} = JZ\,(S - n_{\mathrm{mf}} - \lambda\Delta_{\mathrm{mf}}) + h_{\mathrm{alt}} \ , \tag{A.6a}$$

$$h_{\boldsymbol{k}} = JZ\,(S - \lambda n_{\mathrm{mf}} - \Delta_{\mathrm{mf}})\,\gamma_{\mathrm{X}}(\boldsymbol{k}) \ . \tag{A.6b}$$

The latter two functions are extracted from the general normal ordered and Fourier transformed Hamiltonian before the Bogoliubov transformation is applied. For more details on the derivation of these functions, please refer to Sections 2.5.2 to 2.5.4. Furthermore, it is assumed that $\gamma_{\mathrm{X}}(\boldsymbol{k})$ can be complex-valued for all $\boldsymbol{k}$ in the BZ or MBZ, respectively. Consequently, the functions $l_{\boldsymbol{k}}$ and $m_{\boldsymbol{k}}$ are complex-valued as well. With these definitions, the mean-field parameters in the initial coefficients of the CST can be expressed in a lattice-independent form

$$n_{\mathrm{mf}} = \frac{1}{N_{\mathfrak{T}}} \sum_{\boldsymbol{k}} |m(\boldsymbol{k})|^2 \ , \tag{A.7a}$$

$$\Delta_{\mathrm{mf}} = \frac{1}{N_{\mathfrak{T}}} \sum_{\boldsymbol{k}} \gamma_{\mathrm{X}}(\boldsymbol{k}) l(\boldsymbol{k}) m^*(\boldsymbol{k}) \ . \tag{A.7b}$$

The specific spin-wave theory (SWT) treatment as described in Section 2.5.4 depends on how these parameters are evaluated before the CST. For nonlinear spin-wave theory (NL-SWT), only one evaluation is performed, while for self-consistent nonlinear spin-wave theory (scNL-SWT) the parameters are calculated self-consistently until convergence is reached. It should be noted that not only do the mean-field parameters change if they are evaluated self-consistently for the scNL-SWT, but also the functions $l_{\boldsymbol{k}}$ and $m_{\boldsymbol{k}}$ depend on them via the functions defined previously. However, the form of the initial coefficients as listed in the next section remains the same in both cases.

In the following section, the initial values can be adjusted by specifying the introduced functions and constants for a given lattice structure and gauge. For the square lattice, they are given by

$$\gamma_{\mathrm{X}}(\boldsymbol{k}) \xrightarrow[\text{Bloch gauge}]{\text{square lattice } Z=4} \quad \gamma_{\mathrm{B}}(\boldsymbol{k}) = \frac{1}{Z}\left(1 + \mathrm{e}^{-\mathrm{i}\boldsymbol{k}\boldsymbol{a}_1} + \mathrm{e}^{-\mathrm{i}\boldsymbol{k}\boldsymbol{a}_2} + \mathrm{e}^{-\mathrm{i}\boldsymbol{k}(\boldsymbol{a}_1+\boldsymbol{a}_2)}\right) \ , \tag{A.8a}$$

$$\gamma_{\mathrm{X}}(\boldsymbol{k}) \xrightarrow[\text{Symmetric gauge}]{\text{square lattice } Z=4} \quad \gamma_{\mathrm{S}}(\boldsymbol{k}) = \frac{1}{Z}\left(\mathrm{e}^{-\frac{\mathrm{i}}{2}\boldsymbol{k}(\boldsymbol{a}_1+\boldsymbol{a}_2)} + \mathrm{e}^{\frac{\mathrm{i}}{2}\boldsymbol{k}(\boldsymbol{a}_1-\boldsymbol{a}_2)} + \mathrm{e}^{-\frac{\mathrm{i}}{2}\boldsymbol{k}(\boldsymbol{a}_1-\boldsymbol{a}_2)} + \mathrm{e}^{\frac{\mathrm{i}}{2}\boldsymbol{k}(\boldsymbol{a}_1+\boldsymbol{a}_2)}\right)$$

$$= \frac{4}{Z}\cos\left(\frac{1}{2}\boldsymbol{k}\boldsymbol{a}_1\right)\cos\left(\frac{1}{2}\boldsymbol{k}\boldsymbol{a}_2\right) \ . \tag{A.8b}$$

For the honeycomb lattice, they are given by

$$\gamma_{\mathrm{X}}(\boldsymbol{k}) \xrightarrow[\text{Bloch gauge}]{\text{honeycomb lattice } Z=3} \quad \gamma_{\mathrm{B}}(\boldsymbol{k}) = \frac{1}{Z}\left(1 + \mathrm{e}^{-\mathrm{i}\boldsymbol{k}\boldsymbol{a}_1} + \mathrm{e}^{-\mathrm{i}\boldsymbol{k}\boldsymbol{a}_2}\right) \ , \tag{A.9a}$$

$$\gamma_{\mathrm{X}}(\boldsymbol{k}) \xrightarrow[\text{Symmetric gauge}]{\text{honeycomb lattice } Z=3} \quad \gamma_{\mathrm{S}}(\boldsymbol{k}) = \frac{1}{Z}\left(\mathrm{e}^{\mathrm{i}\frac{\boldsymbol{k}(\boldsymbol{a}_1+\boldsymbol{a}_2)}{3}} + \mathrm{e}^{-\mathrm{i}\frac{2\boldsymbol{k}\boldsymbol{a}_1-\boldsymbol{k}\boldsymbol{a}_2}{3}} + \mathrm{e}^{-\mathrm{i}\frac{-\boldsymbol{k}\boldsymbol{a}_1+2\boldsymbol{k}\boldsymbol{a}_2}{3}}\right) \ . \tag{A.9b}$$

A.1 Coefficients of the Hamiltonian

After applying all the steps discussed in Section 2.5 to the Hamiltonian in Eq. (A.1), the result can be expressed as

$$
\begin{aligned}
\widehat{\mathcal{H}} = \; & C^0 \\
& + \sum_{\boldsymbol{k}_1,\boldsymbol{k}_2} \Big[\; C^{\hat{\alpha}^\dagger\hat{\alpha}}_{\boldsymbol{k}_1,\boldsymbol{k}_2}\, \hat{\alpha}^\dagger_{\boldsymbol{k}_1}\hat{\alpha}_{\boldsymbol{k}_2} + C^{\hat{\beta}^\dagger\hat{\beta}}_{\boldsymbol{k}_1,\boldsymbol{k}_2}\hat{\beta}^\dagger_{\boldsymbol{k}_1}\hat{\beta}_{\boldsymbol{k}_2} \\
& \qquad + C^{\hat{\alpha}^\dagger\hat{\beta}^\dagger}_{\boldsymbol{k}_1,\boldsymbol{k}_2}\hat{\alpha}^\dagger_{\boldsymbol{k}_1}\hat{\beta}^\dagger_{\boldsymbol{k}_2} + C^{\hat{\alpha}\hat{\beta}}_{\boldsymbol{k}_1,\boldsymbol{k}_2}\hat{\alpha}_{\boldsymbol{k}_1}\hat{\beta}_{\boldsymbol{k}_2} \Big] \\
& + \sum_{\boldsymbol{k}_1,\boldsymbol{k}_2,\boldsymbol{k}_3,\boldsymbol{k}_4} \Big[\; C^{\hat{\alpha}^\dagger\hat{\alpha}^\dagger\hat{\beta}^\dagger\hat{\beta}^\dagger}_{\boldsymbol{k}_1,\boldsymbol{k}_2,\boldsymbol{k}_3,\boldsymbol{k}_4}\hat{\alpha}^\dagger_{\boldsymbol{k}_1}\hat{\alpha}^\dagger_{\boldsymbol{k}_2}\hat{\beta}^\dagger_{\boldsymbol{k}_3}\hat{\beta}^\dagger_{\boldsymbol{k}_4} + C^{\hat{\alpha}\hat{\alpha}\hat{\beta}\hat{\beta}}_{\boldsymbol{k}_1,\boldsymbol{k}_2,\boldsymbol{k}_3,\boldsymbol{k}_4}\hat{\alpha}_{\boldsymbol{k}_1}\hat{\alpha}_{\boldsymbol{k}_2}\hat{\beta}_{\boldsymbol{k}_3}\hat{\beta}_{\boldsymbol{k}_4} \\
& \qquad + C^{\hat{\alpha}^\dagger\hat{\alpha}^\dagger\hat{\alpha}\hat{\beta}^\dagger}_{\boldsymbol{k}_1,\boldsymbol{k}_2,\boldsymbol{k}_3,\boldsymbol{k}_4}\hat{\alpha}^\dagger_{\boldsymbol{k}_1}\hat{\alpha}^\dagger_{\boldsymbol{k}_2}\hat{\alpha}_{\boldsymbol{k}_3}\hat{\beta}^\dagger_{\boldsymbol{k}_4} + C^{\hat{\alpha}\hat{\beta}^\dagger\hat{\beta}\hat{\beta}}_{\boldsymbol{k}_1,\boldsymbol{k}_2,\boldsymbol{k}_3,\boldsymbol{k}_4}\hat{\alpha}_{\boldsymbol{k}_1}\hat{\beta}^\dagger_{\boldsymbol{k}_2}\hat{\beta}^\dagger_{\boldsymbol{k}_3}\hat{\beta}_{\boldsymbol{k}_4} \\
& \qquad + C^{\hat{\alpha}^\dagger\hat{\beta}^\dagger\hat{\beta}^\dagger\hat{\beta}}_{\boldsymbol{k}_1,\boldsymbol{k}_2,\boldsymbol{k}_3,\boldsymbol{k}_4}\hat{\alpha}^\dagger_{\boldsymbol{k}_1}\hat{\beta}^\dagger_{\boldsymbol{k}_2}\hat{\beta}^\dagger_{\boldsymbol{k}_3}\hat{\beta}_{\boldsymbol{k}_4} + C^{\hat{\alpha}^\dagger\hat{\alpha}\hat{\alpha}\hat{\beta}}_{\boldsymbol{k}_1,\boldsymbol{k}_2,\boldsymbol{k}_3,\boldsymbol{k}_4}\hat{\alpha}^\dagger_{\boldsymbol{k}_1}\hat{\alpha}_{\boldsymbol{k}_2}\hat{\alpha}_{\boldsymbol{k}_3}\hat{\beta}_{\boldsymbol{k}_4} \\
& \qquad + C^{\hat{\alpha}^\dagger\hat{\alpha}^\dagger\hat{\alpha}\hat{\alpha}}_{\boldsymbol{k}_1,\boldsymbol{k}_2,\boldsymbol{k}_3,\boldsymbol{k}_4}\hat{\alpha}^\dagger_{\boldsymbol{k}_1}\hat{\alpha}^\dagger_{\boldsymbol{k}_2}\hat{\alpha}_{\boldsymbol{k}_3}\hat{\alpha}_{\boldsymbol{k}_4} + C^{\hat{\beta}^\dagger\hat{\beta}^\dagger\hat{\beta}\hat{\beta}}_{\boldsymbol{k}_1,\boldsymbol{k}_2,\boldsymbol{k}_3,\boldsymbol{k}_4}\hat{\beta}^\dagger_{\boldsymbol{k}_1}\hat{\beta}^\dagger_{\boldsymbol{k}_2}\hat{\beta}_{\boldsymbol{k}_3}\hat{\beta}_{\boldsymbol{k}_4} \\
& \qquad + C^{\hat{\alpha}^\dagger\hat{\alpha}\hat{\beta}^\dagger\hat{\beta}}_{\boldsymbol{k}_1,\boldsymbol{k}_2,\boldsymbol{k}_3,\boldsymbol{k}_4}\hat{\alpha}^\dagger_{\boldsymbol{k}_1}\hat{\alpha}_{\boldsymbol{k}_2}\hat{\beta}^\dagger_{\boldsymbol{k}_3}\hat{\beta}_{\boldsymbol{k}_4} \Big] \, .
\end{aligned}
\tag{A.10}
$$

For readability the subscripts indicating the gauge for $l_{\boldsymbol{k}}$ and $m_{\boldsymbol{k}}$ are neglected in the following. The initial coefficient functions corresponding to $\widehat{\mathcal{H}}$ for $\ell = 0$ are given by

$$
\begin{aligned}
C^0 =& JZN_{\mathfrak{T}}\Big[Sn_{\mathrm{mf}} + \lambda S\Delta_{\mathrm{mf}} - \lambda n_{\mathrm{mf}}\Delta_{\mathrm{mf}} - S^2 - n_{\mathrm{mf}}^2 - \Delta_{\mathrm{mf}}^2\Big] \\
& + 2h_{\mathrm{alt}}N_{\mathfrak{T}}\left(n_{\mathrm{mf}} - S\right) \, ,
\end{aligned}
\tag{A.11a}
$$

$$
\begin{aligned}
C^{\hat{\alpha}^\dagger\hat{\alpha}}_{\boldsymbol{k}_1,\boldsymbol{k}_2} =& \delta\left(\boldsymbol{k}_1 - \boldsymbol{k}_2\right) \Big[\\
& h_{\mathrm{alt}}\left(l_{\boldsymbol{k}_2}l^*_{\boldsymbol{k}_1} + \gamma_{\mathrm{X}}\left(\boldsymbol{k}_1 - \boldsymbol{k}_2\right) m_{\boldsymbol{k}_2}m^*_{\boldsymbol{k}_1}\right) \\
& + JZ\left(S - n_{\mathrm{mf}} - \lambda\Delta_{\mathrm{mf}}\right)\left(l_{\boldsymbol{k}_2}l^*_{\boldsymbol{k}_1} + \gamma_{\mathrm{X}}\left(\boldsymbol{k}_1 - \boldsymbol{k}_2\right) m_{\boldsymbol{k}_2}m^*_{\boldsymbol{k}_1}\right) \\
& + JZ\left(\lambda S - \lambda n_{\mathrm{mf}} - \Delta_{\mathrm{mf}}\right)\left(\gamma_{\mathrm{X}}\left(\boldsymbol{k}_1\right) l_{\boldsymbol{k}_2}m^*_{\boldsymbol{k}_1} + \gamma_{\mathrm{X}}\left(-\boldsymbol{k}_2\right) l^*_{\boldsymbol{k}_1}m_{\boldsymbol{k}_2}\right)\Big] \, ,
\end{aligned}
\tag{A.11b}
$$

$$
\begin{aligned}
C^{\hat{\beta}^\dagger\hat{\beta}}_{\boldsymbol{k}_1,\boldsymbol{k}_2} =& \delta\left(\boldsymbol{k}_1 - \boldsymbol{k}_2\right) \Big[\\
& h_{\mathrm{alt}}\left(\gamma_{\mathrm{X}}\left(\boldsymbol{k}_1 - \boldsymbol{k}_2\right) l_{-\boldsymbol{k}_2}l^*_{-\boldsymbol{k}_1} + m_{-\boldsymbol{k}_2}m^*_{-\boldsymbol{k}_1}\right) \\
& + JZ\left(S - n_{\mathrm{mf}} - \lambda\Delta_{\mathrm{mf}}\right)\left(\gamma_{\mathrm{X}}\left(\boldsymbol{k}_1 - \boldsymbol{k}_2\right) l_{-\boldsymbol{k}_2}l^*_{-\boldsymbol{k}_1} + m_{-\boldsymbol{k}_2}m^*_{-\boldsymbol{k}_1}\right) \\
& + JZ\left(\lambda S - \lambda n_{\mathrm{mf}} - \Delta_{\mathrm{mf}}\right)\left(\gamma_{\mathrm{X}}\left(\boldsymbol{k}_1\right) l^*_{-\boldsymbol{k}_1}m_{-\boldsymbol{k}_2} + \gamma_{\mathrm{X}}\left(-\boldsymbol{k}_2\right) l_{-\boldsymbol{k}_2}m^*_{-\boldsymbol{k}_1}\right)\Big] \, ,
\end{aligned}
\tag{A.11c}
$$

$$
\begin{aligned}
C^{\hat{\alpha}^\dagger\hat{\beta}^\dagger}_{\boldsymbol{k}_1,\boldsymbol{k}_2} =& \delta\left(\boldsymbol{k}_1 + \boldsymbol{k}_2\right) \Big[\\
& h_{\mathrm{alt}}\left(l^*_{\boldsymbol{k}_1}m^*_{-\boldsymbol{k}_2} + \gamma_{\mathrm{X}}\left(\boldsymbol{k}_1 + \boldsymbol{k}_2\right) l^*_{-\boldsymbol{k}_2}m^*_{\boldsymbol{k}_1}\right) \\
& + JZ\delta\left(S - n_{\mathrm{mf}} - \lambda\Delta_{\mathrm{mf}}\right)\left(l^*_{\boldsymbol{k}_1}m^*_{-\boldsymbol{k}_2} + \gamma_{\mathrm{X}}\left(\boldsymbol{k}_1 + \boldsymbol{k}_2\right) l^*_{-\boldsymbol{k}_2}m^*_{\boldsymbol{k}_1}\right) \\
& + JZ\delta\left(\lambda S - \lambda n_{\mathrm{mf}} - \Delta_{\mathrm{mf}}\right)\left(\gamma_{\mathrm{X}}\left(\boldsymbol{k}_2\right) l^*_{\boldsymbol{k}_1}l^*_{-\boldsymbol{k}_2} + \gamma_{\mathrm{X}}\left(\boldsymbol{k}_1\right) m^*_{\boldsymbol{k}_1}m^*_{-\boldsymbol{k}_2}\right)\Big] \, ,
\end{aligned}
\tag{A.11d}
$$

$$
\begin{aligned}
C^{\hat{\alpha}\hat{\beta}}_{\boldsymbol{k}_1,\boldsymbol{k}_2} =& \delta\left(-\boldsymbol{k}_1-\boldsymbol{k}_2\right)\Big[\\
& h_{\mathrm{alt}}\left(\gamma_{\mathrm{X}}\left(-\boldsymbol{k}_1-\boldsymbol{k}_2\right) l_{-\boldsymbol{k}_2} m_{\boldsymbol{k}_1} + l_{\boldsymbol{k}_1} m_{-\boldsymbol{k}_2}\right) \\
& + JZ\left(S - n_{\mathrm{mf}} - \lambda\Delta_{\mathrm{mf}}\right)\left(\gamma_{\mathrm{X}}\left(-\boldsymbol{k}_1-\boldsymbol{k}_2\right) l_{-\boldsymbol{k}_2} m_{\boldsymbol{k}_1} + l_{\boldsymbol{k}_1} m_{-\boldsymbol{k}_2}\right) \\
& + JZ\left(\lambda S - \lambda n_{\mathrm{mf}} - \Delta_{\mathrm{mf}}\right)\left(\gamma_{\mathrm{X}}\left(-\boldsymbol{k}_2\right) l_{\boldsymbol{k}_1} l_{-\boldsymbol{k}_2} + \gamma_{\mathrm{X}}\left(-\boldsymbol{k}_1\right) m_{\boldsymbol{k}_1} m_{-\boldsymbol{k}_2}\right)\Big] ,
\end{aligned} \tag{A.11e}
$$

$$
\begin{aligned}
C^{\hat{\alpha}^\dagger\hat{\alpha}\hat{\beta}^\dagger\hat{\beta}}_{\boldsymbol{k}_1,\boldsymbol{k}_2,\boldsymbol{k}_3,\boldsymbol{k}_4} =& -J\frac{1}{N_{\mathfrak{T}}} Z\delta\left(\boldsymbol{k}_1-\boldsymbol{k}_2+\boldsymbol{k}_3-\boldsymbol{k}_4\right)\Big[\\
& \gamma_{\mathrm{X}}\left(\boldsymbol{k}_1-\boldsymbol{k}_2\right) m_{\boldsymbol{k}_2} m_{-\boldsymbol{k}_4} m^*_{\boldsymbol{k}_1} m^*_{-\boldsymbol{k}_3} + \gamma_{\mathrm{X}}\left(\boldsymbol{k}_3-\boldsymbol{k}_4\right) l_{\boldsymbol{k}_2} l_{-\boldsymbol{k}_4} l^*_{\boldsymbol{k}_1} l^*_{-\boldsymbol{k}_3} \\
& + \gamma_{\mathrm{X}}\left(\boldsymbol{k}_1+\boldsymbol{k}_3\right) l_{\boldsymbol{k}_2} l^*_{-\boldsymbol{k}_3} m_{-\boldsymbol{k}_4} m^*_{\boldsymbol{k}_1} + \gamma_{\mathrm{X}}\left(-\boldsymbol{k}_2-\boldsymbol{k}_4\right) l_{-\boldsymbol{k}_4} l^*_{\boldsymbol{k}_1} m_{\boldsymbol{k}_2} m^*_{-\boldsymbol{k}_3} \\
& + \gamma_{\mathrm{X}}\left(\boldsymbol{k}_1\right) l_{\boldsymbol{k}_2} m_{-\boldsymbol{k}_4} m^*_{\boldsymbol{k}_1} m^*_{-\boldsymbol{k}_3} + \gamma_{\mathrm{X}}\left(-\boldsymbol{k}_2+\boldsymbol{k}_3-\boldsymbol{k}_4\right) l_{-\boldsymbol{k}_4} l^*_{\boldsymbol{k}_1} l^*_{-\boldsymbol{k}_3} m_{\boldsymbol{k}_2} \\
& + \gamma_{\mathrm{X}}\left(-\boldsymbol{k}_4\right) l_{\boldsymbol{k}_2} l_{-\boldsymbol{k}_4} l^*_{\boldsymbol{k}_1} m^*_{-\boldsymbol{k}_3} + \gamma_{\mathrm{X}}\left(\boldsymbol{k}_1-\boldsymbol{k}_2+\boldsymbol{k}_3\right) l^*_{-\boldsymbol{k}_3} m_{\boldsymbol{k}_2} m_{-\boldsymbol{k}_4} m^*_{\boldsymbol{k}_1}\Big] ,
\end{aligned} \tag{A.11f}
$$

$$
\begin{aligned}
C^{\hat{\alpha}^\dagger\hat{\alpha}^\dagger\hat{\alpha}\hat{\beta}^\dagger}_{\boldsymbol{k}_1,\boldsymbol{k}_2,\boldsymbol{k}_3,\boldsymbol{k}_4} =& -\frac{1}{2} J\frac{1}{N_{\mathfrak{T}}} Z\delta\left(\boldsymbol{k}_1+\boldsymbol{k}_2-\boldsymbol{k}_3+\boldsymbol{k}_4\right)\Big[\\
& \gamma_{\mathrm{X}}\left(\boldsymbol{k}_1-\boldsymbol{k}_3\right) l^*_{\boldsymbol{k}_2} m_{\boldsymbol{k}_3} m^*_{\boldsymbol{k}_1} m^*_{-\boldsymbol{k}_4} + \gamma_{\mathrm{X}}\left(\boldsymbol{k}_2+\boldsymbol{k}_4\right) l_{\boldsymbol{k}_3} l^*_{\boldsymbol{k}_1} l^*_{-\boldsymbol{k}_4} m^*_{\boldsymbol{k}_2} \\
& + \gamma_{\mathrm{X}}\left(\boldsymbol{k}_1+\boldsymbol{k}_4\right) l_{\boldsymbol{k}_3} l^*_{\boldsymbol{k}_2} l^*_{-\boldsymbol{k}_4} m^*_{\boldsymbol{k}_1} + \gamma_{\mathrm{X}}\left(\boldsymbol{k}_2-\boldsymbol{k}_3\right) l^*_{\boldsymbol{k}_1} m_{\boldsymbol{k}_3} m^*_{\boldsymbol{k}_2} m^*_{-\boldsymbol{k}_4} \\
& + \lambda\gamma_{\mathrm{X}}\left(\boldsymbol{k}_1\right) l_{\boldsymbol{k}_3} l^*_{\boldsymbol{k}_2} m^*_{\boldsymbol{k}_1} m^*_{-\boldsymbol{k}_4} + \lambda\gamma_{\mathrm{X}}\left(\boldsymbol{k}_2-\boldsymbol{k}_3+\boldsymbol{k}_4\right) l^*_{\boldsymbol{k}_1} l^*_{-\boldsymbol{k}_4} m_{\boldsymbol{k}_3} m^*_{\boldsymbol{k}_2} \\
& + \lambda\gamma_{\mathrm{X}}\left(\boldsymbol{k}_2\right) l_{\boldsymbol{k}_3} l^*_{\boldsymbol{k}_1} m^*_{\boldsymbol{k}_2} m^*_{-\boldsymbol{k}_4} + \lambda\gamma_{\mathrm{X}}\left(\boldsymbol{k}_1-\boldsymbol{k}_3+\boldsymbol{k}_4\right) l^*_{\boldsymbol{k}_2} l^*_{-\boldsymbol{k}_4} m_{\boldsymbol{k}_3} m^*_{\boldsymbol{k}_1}\Big] ,
\end{aligned} \tag{A.11g}
$$

$$
\begin{aligned}
C^{\hat{\alpha}\hat{\beta}^\dagger\hat{\beta}\hat{\beta}}_{\boldsymbol{k}_1,\boldsymbol{k}_2,\boldsymbol{k}_3,\boldsymbol{k}_4} =& -\frac{1}{2} J\frac{1}{N_{\mathfrak{T}}} Z\delta\left(\boldsymbol{k}_1-\boldsymbol{k}_2+\boldsymbol{k}_3+\boldsymbol{k}_4\right)\Big[\\
& \gamma_{\mathrm{X}}\left(-\boldsymbol{k}_1-\boldsymbol{k}_3\right) l_{-\boldsymbol{k}_3} m_{\boldsymbol{k}_1} m_{-\boldsymbol{k}_4} m^*_{-\boldsymbol{k}_2} + \gamma_{\mathrm{X}}\left(\boldsymbol{k}_2-\boldsymbol{k}_4\right) l_{\boldsymbol{k}_1} l_{-\boldsymbol{k}_4} l^*_{-\boldsymbol{k}_2} m_{-\boldsymbol{k}_3} \\
& + \gamma_{\mathrm{X}}\left(\boldsymbol{k}_2-\boldsymbol{k}_3\right) l_{\boldsymbol{k}_1} l_{-\boldsymbol{k}_3} l^*_{-\boldsymbol{k}_2} m_{-\boldsymbol{k}_4} + \gamma_{\mathrm{X}}\left(-\boldsymbol{k}_1-\boldsymbol{k}_4\right) l_{-\boldsymbol{k}_4} m_{\boldsymbol{k}_1} m_{-\boldsymbol{k}_3} m^*_{-\boldsymbol{k}_2} \\
& + \lambda\gamma_{\mathrm{X}}\left(-\boldsymbol{k}_1+\boldsymbol{k}_2-\boldsymbol{k}_3\right) l_{-\boldsymbol{k}_3} l^*_{-\boldsymbol{k}_2} m_{\boldsymbol{k}_1} m_{-\boldsymbol{k}_4} + \lambda\gamma_{\mathrm{X}}\left(-\boldsymbol{k}_4\right) l_{\boldsymbol{k}_1} l_{-\boldsymbol{k}_4} m_{-\boldsymbol{k}_3} m^*_{-\boldsymbol{k}_2} \\
& + \lambda\gamma_{\mathrm{X}}\left(-\boldsymbol{k}_1+\boldsymbol{k}_2-\boldsymbol{k}_4\right) l_{-\boldsymbol{k}_4} l^*_{-\boldsymbol{k}_2} m_{\boldsymbol{k}_1} m_{-\boldsymbol{k}_3} + \lambda\gamma_{\mathrm{X}}\left(-\boldsymbol{k}_3\right) l_{\boldsymbol{k}_1} l_{-\boldsymbol{k}_3} m_{-\boldsymbol{k}_4} m^*_{-\boldsymbol{k}_2}\Big] ,
\end{aligned} \tag{A.11h}
$$

$$
\begin{aligned}
C^{\hat{\alpha}^\dagger\hat{\alpha}^\dagger\hat{\beta}^\dagger\hat{\beta}^\dagger}_{\boldsymbol{k}_1,\boldsymbol{k}_2,\boldsymbol{k}_3,\boldsymbol{k}_4} =& -\frac{1}{4} J\frac{1}{N_{\mathfrak{T}}} Z\delta\left(\boldsymbol{k}_1+\boldsymbol{k}_2+\boldsymbol{k}_3+\boldsymbol{k}_4\right)\Big[\\
& \gamma_{\mathrm{X}}\left(\boldsymbol{k}_1+\boldsymbol{k}_3\right) l^*_{\boldsymbol{k}_2} l^*_{-\boldsymbol{k}_3} m^*_{\boldsymbol{k}_1} m^*_{-\boldsymbol{k}_4} + \gamma_{\mathrm{X}}\left(\boldsymbol{k}_2+\boldsymbol{k}_4\right) l^*_{\boldsymbol{k}_1} l^*_{-\boldsymbol{k}_4} m^*_{\boldsymbol{k}_2} m^*_{-\boldsymbol{k}_3} \\
& + \gamma_{\mathrm{X}}\left(\boldsymbol{k}_1+\boldsymbol{k}_4\right) l^*_{\boldsymbol{k}_2} l^*_{-\boldsymbol{k}_4} m^*_{\boldsymbol{k}_1} m^*_{-\boldsymbol{k}_3} + \gamma_{\mathrm{X}}\left(\boldsymbol{k}_2+\boldsymbol{k}_3\right) l^*_{\boldsymbol{k}_1} l^*_{-\boldsymbol{k}_3} m^*_{\boldsymbol{k}_2} m^*_{-\boldsymbol{k}_4} \\
& + \lambda\gamma_{\mathrm{X}}\left(\boldsymbol{k}_1\right) l^*_{\boldsymbol{k}_2} m^*_{\boldsymbol{k}_1} m^*_{-\boldsymbol{k}_3} m^*_{-\boldsymbol{k}_4} + \lambda\gamma_{\mathrm{X}}\left(\boldsymbol{k}_2+\boldsymbol{k}_3+\boldsymbol{k}_4\right) l^*_{\boldsymbol{k}_1} l^*_{-\boldsymbol{k}_3} l^*_{-\boldsymbol{k}_4} m^*_{\boldsymbol{k}_2} \\
& + \lambda\gamma_{\mathrm{X}}\left(\boldsymbol{k}_2\right) l^*_{\boldsymbol{k}_1} m^*_{\boldsymbol{k}_2} m^*_{-\boldsymbol{k}_3} m^*_{-\boldsymbol{k}_4} + \lambda\gamma_{\mathrm{X}}\left(\boldsymbol{k}_1+\boldsymbol{k}_3+\boldsymbol{k}_4\right) l^*_{\boldsymbol{k}_2} l^*_{-\boldsymbol{k}_3} l^*_{-\boldsymbol{k}_4} m^*_{\boldsymbol{k}_1}\Big] ,
\end{aligned} \tag{A.11i}
$$

$$
\begin{aligned}
C^{\hat{\alpha}^\dagger\hat{\alpha}^\dagger\hat{\beta}^\dagger\hat{\beta}^\dagger}_{\boldsymbol{k}_1,\boldsymbol{k}_2,\boldsymbol{k}_3,\boldsymbol{k}_4} =& -\frac{1}{4} J\frac{1}{N_{\mathfrak{T}}} Z\delta\left(-\boldsymbol{k}_1-\boldsymbol{k}_2-\boldsymbol{k}_3-\boldsymbol{k}_4\right)\Big[\\
& \gamma_{\mathrm{X}}\left(-\boldsymbol{k}_1-\boldsymbol{k}_3\right) l_{\boldsymbol{k}_2} l_{-\boldsymbol{k}_3} m_{\boldsymbol{k}_1} m_{-\boldsymbol{k}_4} + \gamma_{\mathrm{X}}\left(-\boldsymbol{k}_2-\boldsymbol{k}_4\right) l_{\boldsymbol{k}_1} l_{-\boldsymbol{k}_4} m_{\boldsymbol{k}_2} m_{-\boldsymbol{k}_3} \\
& + \gamma_{\mathrm{X}}\left(-\boldsymbol{k}_2-\boldsymbol{k}_3\right) l_{\boldsymbol{k}_1} l_{-\boldsymbol{k}_3} m_{\boldsymbol{k}_2} m_{-\boldsymbol{k}_4} + \gamma_{\mathrm{X}}\left(-\boldsymbol{k}_1-\boldsymbol{k}_4\right) l_{\boldsymbol{k}_2} l_{-\boldsymbol{k}_4} m_{\boldsymbol{k}_1} m_{-\boldsymbol{k}_3} \\
& + \lambda\gamma_{\mathrm{X}}\left(-\boldsymbol{k}_1-\boldsymbol{k}_2-\boldsymbol{k}_3\right) l_{-\boldsymbol{k}_3} m_{\boldsymbol{k}_1} m_{\boldsymbol{k}_2} m_{-\boldsymbol{k}_4} + \lambda\gamma_{\mathrm{X}}\left(-\boldsymbol{k}_4\right) l_{\boldsymbol{k}_1} l_{\boldsymbol{k}_2} l_{-\boldsymbol{k}_4} m_{-\boldsymbol{k}_3} \\
& + \lambda\gamma_{\mathrm{X}}\left(-\boldsymbol{k}_1-\boldsymbol{k}_2-\boldsymbol{k}_4\right) l_{-\boldsymbol{k}_4} m_{\boldsymbol{k}_1} m_{\boldsymbol{k}_2} m_{-\boldsymbol{k}_3} + \lambda\gamma_{\mathrm{X}}\left(-\boldsymbol{k}_3\right) l_{\boldsymbol{k}_1} l_{\boldsymbol{k}_2} l_{-\boldsymbol{k}_3} m_{-\boldsymbol{k}_4}\Big] ,
\end{aligned} \tag{A.11j}
$$

$$
\begin{aligned}
C^{\hat{\alpha}^\dagger\hat{\alpha}^\dagger\hat{\alpha}\hat{\alpha}}_{\boldsymbol{k}_1,\boldsymbol{k}_2,\boldsymbol{k}_3,\boldsymbol{k}_4} = -\frac{1}{4}J\frac{1}{N_{\mathfrak{T}}}Z\delta\left(\boldsymbol{k}_1+\boldsymbol{k}_2-\boldsymbol{k}_3-\boldsymbol{k}_4\right)\Big[& \\
\gamma_{\mathrm{X}}\left(\boldsymbol{k}_1-\boldsymbol{k}_3\right) l_{\boldsymbol{k}_4} l^*_{\boldsymbol{k}_2} m_{\boldsymbol{k}_3} m^*_{\boldsymbol{k}_1} + \gamma_{\mathrm{X}}\left(\boldsymbol{k}_2-\boldsymbol{k}_4\right) l_{\boldsymbol{k}_3} l^*_{\boldsymbol{k}_1} m_{\boldsymbol{k}_4} m^*_{\boldsymbol{k}_2} & \\
+\gamma_{\mathrm{X}}\left(\boldsymbol{k}_1-\boldsymbol{k}_4\right) l_{\boldsymbol{k}_3} l^*_{\boldsymbol{k}_2} m_{\boldsymbol{k}_4} m^*_{\boldsymbol{k}_1} + \gamma_{\mathrm{X}}\left(\boldsymbol{k}_2-\boldsymbol{k}_3\right) l_{\boldsymbol{k}_4} l^*_{\boldsymbol{k}_1} m_{\boldsymbol{k}_3} m^*_{\boldsymbol{k}_2} & \\
+\lambda\gamma_{\mathrm{X}}\left(\boldsymbol{k}_1\right) l_{\boldsymbol{k}_3} l_{\boldsymbol{k}_4} l^*_{\boldsymbol{k}_2} m^*_{\boldsymbol{k}_1} + \lambda\gamma_{\mathrm{X}}\left(\boldsymbol{k}_2-\boldsymbol{k}_3-\boldsymbol{k}_4\right) l^*_{\boldsymbol{k}_1} m_{\boldsymbol{k}_3} m_{\boldsymbol{k}_4} m^*_{\boldsymbol{k}_2} & \\
+\lambda\gamma_{\mathrm{X}}\left(\boldsymbol{k}_2\right) l_{\boldsymbol{k}_3} l_{\boldsymbol{k}_4} l^*_{\boldsymbol{k}_1} m^*_{\boldsymbol{k}_2} + \lambda\gamma_{\mathrm{X}}\left(\boldsymbol{k}_1-\boldsymbol{k}_3-\boldsymbol{k}_4\right) l^*_{\boldsymbol{k}_2} m_{\boldsymbol{k}_3} m_{\boldsymbol{k}_4} m^*_{\boldsymbol{k}_1}\Big] , &
\end{aligned}
\tag{A.11k}
$$

$$
\begin{aligned}
C^{\hat{\beta}^\dagger\hat{\beta}^\dagger\hat{\beta}\hat{\beta}}_{\boldsymbol{k}_1,\boldsymbol{k}_2,\boldsymbol{k}_3,\boldsymbol{k}_4} = -\frac{1}{4}J\frac{1}{N_{\mathfrak{T}}}Z\delta\left(\boldsymbol{k}_1+\boldsymbol{k}_2-\boldsymbol{k}_3-\boldsymbol{k}_4\right)\Big[& \\
\gamma_{\mathrm{X}}\left(\boldsymbol{k}_1-\boldsymbol{k}_3\right) l_{-\boldsymbol{k}_3} l^*_{-\boldsymbol{k}_1} m_{-\boldsymbol{k}_4} m^*_{-\boldsymbol{k}_2} + \gamma_{\mathrm{X}}\left(\boldsymbol{k}_2-\boldsymbol{k}_4\right) l_{-\boldsymbol{k}_4} l^*_{-\boldsymbol{k}_2} m_{-\boldsymbol{k}_3} m^*_{-\boldsymbol{k}_1} & \\
+\gamma_{\mathrm{X}}\left(\boldsymbol{k}_1-\boldsymbol{k}_4\right) l_{-\boldsymbol{k}_4} l^*_{-\boldsymbol{k}_1} m_{-\boldsymbol{k}_3} m^*_{-\boldsymbol{k}_2} + \gamma_{\mathrm{X}}\left(\boldsymbol{k}_2-\boldsymbol{k}_3\right) l_{-\boldsymbol{k}_3} l^*_{-\boldsymbol{k}_2} m_{-\boldsymbol{k}_4} m^*_{-\boldsymbol{k}_1} & \\
+\gamma_{\mathrm{X}}\left(\boldsymbol{k}_1+\boldsymbol{k}_2-\boldsymbol{k}_3\right) l_{-\boldsymbol{k}_3} l^*_{-\boldsymbol{k}_1} l^*_{-\boldsymbol{k}_2} m_{-\boldsymbol{k}_4} + \gamma_{\mathrm{X}}\left(-\boldsymbol{k}_4\right) l_{-\boldsymbol{k}_4} m_{-\boldsymbol{k}_3} m^*_{-\boldsymbol{k}_1} m^*_{-\boldsymbol{k}_2} & \\
+\gamma_{\mathrm{X}}\left(\boldsymbol{k}_1+\boldsymbol{k}_2-\boldsymbol{k}_4\right) l_{-\boldsymbol{k}_4} l^*_{-\boldsymbol{k}_1} l^*_{-\boldsymbol{k}_2} m_{-\boldsymbol{k}_3} + \gamma_{\mathrm{X}}\left(-\boldsymbol{k}_3\right) l_{-\boldsymbol{k}_3} m_{-\boldsymbol{k}_4} m^*_{-\boldsymbol{k}_1} m^*_{-\boldsymbol{k}_2}\Big] , &
\end{aligned}
\tag{A.11l}
$$

$$
\begin{aligned}
C^{\hat{\alpha}^\dagger\hat{\alpha}\hat{\alpha}\hat{\beta}}_{\boldsymbol{k}_1,\boldsymbol{k}_2,\boldsymbol{k}_3,\boldsymbol{k}_4} = -\frac{1}{2}J\frac{1}{N_{\mathfrak{T}}}Z\delta\left(\boldsymbol{k}_1-\boldsymbol{k}_2-\boldsymbol{k}_3-\boldsymbol{k}_4\right)\Big[& \\
\gamma_{\mathrm{X}}\left(\boldsymbol{k}_1-\boldsymbol{k}_2\right) l_{\boldsymbol{k}_3} m_{\boldsymbol{k}_2} m_{-\boldsymbol{k}_4} m^*_{\boldsymbol{k}_1} + \gamma_{\mathrm{X}}\left(-\boldsymbol{k}_3-\boldsymbol{k}_4\right) l_{\boldsymbol{k}_2} l_{-\boldsymbol{k}_4} l^*_{\boldsymbol{k}_1} m_{\boldsymbol{k}_3} & \\
+\gamma_{\mathrm{X}}\left(\boldsymbol{k}_1-\boldsymbol{k}_3\right) l_{\boldsymbol{k}_2} m_{\boldsymbol{k}_3} m_{-\boldsymbol{k}_4} m^*_{\boldsymbol{k}_1} + \gamma_{\mathrm{X}}\left(-\boldsymbol{k}_2-\boldsymbol{k}_4\right) l_{\boldsymbol{k}_3} l_{-\boldsymbol{k}_4} l^*_{\boldsymbol{k}_1} m_{\boldsymbol{k}_2} & \\
+\gamma_{\mathrm{X}}\left(\boldsymbol{k}_1\right) l_{\boldsymbol{k}_2} l_{\boldsymbol{k}_3} m_{-\boldsymbol{k}_4} m^*_{\boldsymbol{k}_1} + \gamma_{\mathrm{X}}\left(-\boldsymbol{k}_2-\boldsymbol{k}_3-\boldsymbol{k}_4\right) l_{-\boldsymbol{k}_4} l^*_{\boldsymbol{k}_1} m_{\boldsymbol{k}_2} m_{\boldsymbol{k}_3} & \\
+\gamma_{\mathrm{X}}\left(-\boldsymbol{k}_4\right) l_{\boldsymbol{k}_2} l_{\boldsymbol{k}_3} l_{-\boldsymbol{k}_4} l^*_{\boldsymbol{k}_1} + \gamma_{\mathrm{X}}\left(\boldsymbol{k}_1-\boldsymbol{k}_2-\boldsymbol{k}_3\right) m_{\boldsymbol{k}_2} m_{\boldsymbol{k}_3} m_{-\boldsymbol{k}_4} m^*_{\boldsymbol{k}_1}\Big] , &
\end{aligned}
\tag{A.11m}
$$

$$
\begin{aligned}
C^{\hat{\alpha}^\dagger\hat{\beta}^\dagger\hat{\beta}^\dagger\hat{\beta}}_{\boldsymbol{k}_1,\boldsymbol{k}_2,\boldsymbol{k}_3,\boldsymbol{k}_4} = -\frac{1}{2}J\frac{1}{N_{\mathfrak{T}}}Z\delta\left(\boldsymbol{k}_1+\boldsymbol{k}_2+\boldsymbol{k}_3-\boldsymbol{k}_4\right)\Big[& \\
\gamma_{\mathrm{X}}\left(\boldsymbol{k}_1+\boldsymbol{k}_2\right) l^*_{-\boldsymbol{k}_2} m_{-\boldsymbol{k}_4} m^*_{\boldsymbol{k}_1} m^*_{-\boldsymbol{k}_3} + \gamma_{\mathrm{X}}\left(\boldsymbol{k}_3-\boldsymbol{k}_4\right) l_{-\boldsymbol{k}_4} l^*_{\boldsymbol{k}_1} l^*_{-\boldsymbol{k}_3} m^*_{-\boldsymbol{k}_2} & \\
+\gamma_{\mathrm{X}}\left(\boldsymbol{k}_1+\boldsymbol{k}_3\right) l^*_{-\boldsymbol{k}_3} m_{-\boldsymbol{k}_4} m^*_{\boldsymbol{k}_1} m^*_{-\boldsymbol{k}_2} + \gamma_{\mathrm{X}}\left(\boldsymbol{k}_2-\boldsymbol{k}_4\right) l_{-\boldsymbol{k}_4} l^*_{\boldsymbol{k}_1} l^*_{-\boldsymbol{k}_2} m^*_{-\boldsymbol{k}_3} & \\
+\gamma_{\mathrm{X}}\left(\boldsymbol{k}_1+\boldsymbol{k}_2+\boldsymbol{k}_3\right) l^*_{-\boldsymbol{k}_2} l^*_{-\boldsymbol{k}_3} m_{-\boldsymbol{k}_4} m^*_{\boldsymbol{k}_1} + \gamma_{\mathrm{X}}\left(-\boldsymbol{k}_4\right) l_{-\boldsymbol{k}_4} l^*_{\boldsymbol{k}_1} m^*_{-\boldsymbol{k}_2} m^*_{-\boldsymbol{k}_3} & \\
+\gamma_{\mathrm{X}}\left(\boldsymbol{k}_2+\boldsymbol{k}_3-\boldsymbol{k}_4\right) l_{-\boldsymbol{k}_4} l^*_{\boldsymbol{k}_1} l^*_{-\boldsymbol{k}_2} l^*_{-\boldsymbol{k}_3} + \gamma_{\mathrm{X}}\left(\boldsymbol{k}_1\right) m_{-\boldsymbol{k}_4} m^*_{\boldsymbol{k}_1} m^*_{-\boldsymbol{k}_2} m^*_{-\boldsymbol{k}_3}\Big] . &
\end{aligned}
\tag{A.11n}
$$

As discussed in Section 4.3.1, the number of coefficient functions can be reduced by exploiting symmetries of the Hamiltonian. However, depending on the chosen gauge, the relations between the coefficient functions differ slightly. In the following, the difference is indicated by $\{\boldsymbol{X}|\boldsymbol{Y}\}$ where the first argument $\boldsymbol{X}$ corresponds to the Bloch gauge marked in green and the second argument $\boldsymbol{Y}$ to the symmetric gauge marked in blue. They can be written as

$$
\begin{aligned}
C^{\hat{\beta}^\dagger\hat{\beta}}_{\boldsymbol{k}_1,\boldsymbol{k}_2} &= \{1|\gamma_{\mathrm{X}}\left(\boldsymbol{k}_1-\boldsymbol{k}_2\right)\}\, C^{\hat{\alpha}^\dagger\hat{\alpha}}_{\boldsymbol{k}_2,\boldsymbol{k}_1} , \\
C^{\hat{\alpha}\hat{\beta}}_{\boldsymbol{k}_1,\boldsymbol{k}_2} &= \{1|\gamma_{\mathrm{X}}\left(-\boldsymbol{k}_1-\boldsymbol{k}_2\right)\}\, C^{\hat{\alpha}^\dagger\hat{\beta}^\dagger}_{\boldsymbol{k}_2,\boldsymbol{k}_1} , \\
C^{\hat{\beta}^\dagger\hat{\beta}^\dagger\hat{\beta}\hat{\beta}}_{\boldsymbol{k}_1,\boldsymbol{k}_2,\boldsymbol{k}_3,\boldsymbol{k}_4} &= \{1|\gamma_{\mathrm{X}}\left(\boldsymbol{k}_1+\boldsymbol{k}_2-\boldsymbol{k}_3-\boldsymbol{k}_4\right)\}\, C^{\hat{\alpha}^\dagger\hat{\alpha}^\dagger\hat{\alpha}\hat{\alpha}}_{\boldsymbol{k}_4,\boldsymbol{k}_3,\boldsymbol{k}_2,\boldsymbol{k}_1} , \\
C^{\hat{\alpha}\hat{\alpha}\hat{\beta}\hat{\beta}}_{\boldsymbol{k}_1,\boldsymbol{k}_2,\boldsymbol{k}_3,\boldsymbol{k}_4} &= \{1|\gamma_{\mathrm{X}}\left(-\boldsymbol{k}_1-\boldsymbol{k}_2-\boldsymbol{k}_3-\boldsymbol{k}_4\right)\}\, C^{\hat{\alpha}^\dagger\hat{\alpha}^\dagger\hat{\beta}^\dagger\hat{\beta}^\dagger}_{\boldsymbol{k}_4,\boldsymbol{k}_3,\boldsymbol{k}_2,\boldsymbol{k}_1} , \\
C^{\hat{\alpha}^\dagger\hat{\beta}^\dagger\hat{\beta}^\dagger\hat{\beta}}_{\boldsymbol{k}_1,\boldsymbol{k}_2,\boldsymbol{k}_3,\boldsymbol{k}_4} &= \{1|\gamma_{\mathrm{X}}\left(\boldsymbol{k}_1+\boldsymbol{k}_2+\boldsymbol{k}_3-\boldsymbol{k}_4\right)\}\, C^{\hat{\alpha}^\dagger\hat{\alpha}\hat{\alpha}\hat{\beta}}_{\boldsymbol{k}_4,\boldsymbol{k}_3,\boldsymbol{k}_2,\boldsymbol{k}_1} , \\
C^{\hat{\alpha}\hat{\beta}^\dagger\hat{\beta}\hat{\beta}}_{\boldsymbol{k}_1,\boldsymbol{k}_2,\boldsymbol{k}_3,\boldsymbol{k}_4} &= \{1|\gamma_{\mathrm{X}}\left(-\boldsymbol{k}_1+\boldsymbol{k}_2-\boldsymbol{k}_3-\boldsymbol{k}_4\right)\}\, C^{\hat{\alpha}^\dagger\hat{\alpha}^\dagger\hat{\alpha}\hat{\beta}^\dagger}_{\boldsymbol{k}_4,\boldsymbol{k}_3,\boldsymbol{k}_2,\boldsymbol{k}_1} .
\end{aligned}
\tag{A.12a}
$$

So that only the coefficient functions on the right-hand side need to be stored and calculated explicitly.

A.2 Coefficients of the Observable

In this section, the initial values of the observable's coefficients are listed. They are derived by transforming the observable in the same way as the Hamiltonian outlined in Section 2.5.4. The main difference is that they are not truncated with respect to the scaling dimension; instead, they are kept up to the terms that couple the ground state to the relevant magnon channels. Here, the relevant magnon channels for evaluating an observable are the single-, two-, and three-magnon channels. Even if, in this work only, the magnetization is considered as an observable, the coefficients for the transversal and longitudinal dynamic structure factors are also listed for completeness, in accordance with Ref. [Pow17]

Before listing the coefficients, a brief note on the influence of the additional phase factor depending on the momentum transfer $\boldsymbol{Q}$ appearing in the observable is given. In the calculations of observable terms like

$$\ldots \sum_{\boldsymbol{r}_j \in \Gamma_A} \mathrm{e}^{-\mathrm{i}(\boldsymbol{Q}\boldsymbol{r}_j)} \hat{S}^{(z|-|+)}_{A,j} + \sum_{\boldsymbol{r}_j \in \Gamma_B} \mathrm{e}^{-\mathrm{i}(\boldsymbol{Q}\boldsymbol{r}_j)} \hat{S}^{(z|-|+)}_{B,j} + \ldots \tag{A.13}$$

occur initially. The steps for dealing with such terms are almost identical to those for the Hamiltonian. At the beginning, the DM is inserted, leading to terms like

$$\ldots \sum_{\boldsymbol{r}_i \in \Gamma_A} \mathrm{e}^{-\mathrm{i}(\boldsymbol{Q}\boldsymbol{r}_i)} \prod_x \hat{a}^{(\dagger)}_{x,i} + \sum_{\boldsymbol{r}_j \in \Gamma_B} \mathrm{e}^{-\mathrm{i}(\boldsymbol{Q}\boldsymbol{r}_j)} \prod_x \hat{b}^{(\dagger)}_{x,j} + \ldots \tag{A.14}$$

Afterwards, a general normal-ordering may be introduced, but the crucial step is the Fourier transformation. Here, an additional phase factor is added to the momentum-conserving delta functions appearing after the Fourier transformation. However, there is an additional subtlety to consider regarding the two different gauges. As in the Bloch gauge the $\hat{b}^{(\dagger)}_{x,j}$ does not obtain an additional phase factor, the function

$$\Gamma_{\mathrm{X}}(\boldsymbol{Q}) = \mathrm{e}^{-\mathrm{i}\boldsymbol{Q}\boldsymbol{d}} \tag{A.15}$$

is introduced before all terms summed over Γ_B according to

$$\sum_{\boldsymbol{r}_j \in \Gamma_B} \mathrm{e}^{-\mathrm{i}\boldsymbol{Q}\boldsymbol{r}_j} \ldots = \sum_{\boldsymbol{r}_i \in \Gamma_A} \mathrm{e}^{-\mathrm{i}\boldsymbol{Q}(\boldsymbol{r}_i+\boldsymbol{d})} \ldots = \mathrm{e}^{-\mathrm{i}\boldsymbol{Q}\boldsymbol{d}} \sum_{\boldsymbol{r}_i \in \Gamma_A} \mathrm{e}^{-\mathrm{i}\boldsymbol{Q}(\boldsymbol{r}_i)} \ldots = \Gamma_{\mathrm{X}}(\boldsymbol{Q}) \sum_{\boldsymbol{r}_i \in \Gamma_A} \mathrm{e}^{-\mathrm{i}\boldsymbol{Q}(\boldsymbol{r}_i)} \ldots \ , \tag{A.16}$$

with $\boldsymbol{d}$ being the vector connecting the two sublattices. On the contrary, in the symmetric gauge, the Fourier transformation of $\hat{b}^{(\dagger)}_{x,j}$ contains a phase factor, so that the momenta of $\hat{b}^{(\dagger)}_{\boldsymbol{k}_i}$ also have the additional phase factor. Thus, in the symmetric gauge, the function Γ_{X} contains the same momentum sum as the corresponding momentum-conserving delta function. In the following, the difference is indicated by $\{\boldsymbol{X}|\boldsymbol{Y}\}$ where the first argument $\boldsymbol{X}$ corresponds to the Bloch gauge marked in green and the second argument $\boldsymbol{Y}$ to the symmetric gauge marked in blue .

Additionally, the initial values can be adjusted by specifying the functions and constants introduced above for a given lattice structure and gauge. For the square lattice, they are given by

$$\Gamma_{\mathrm{X}}(\boldsymbol{k}) \xRightarrow[\text{Bloch gauge}]{\text{square lattice } Z=4} \qquad \Gamma_{\mathrm{B}}(\boldsymbol{k}) = \mathrm{e}^{-\mathrm{i}\frac{1}{2}\boldsymbol{k}(\boldsymbol{a}_1+\boldsymbol{a}_2)} \ , \tag{A.17a}$$

$$\Gamma_{\mathrm{X}}(\boldsymbol{k}) \xRightarrow[\text{Symmetric gauge}]{\text{square lattice } Z=4} \qquad \Gamma_{\mathrm{S}}(\boldsymbol{k}) = \gamma_{\mathrm{S}}(\boldsymbol{k}) \ . \tag{A.17b}$$

For the honeycomb lattice, they are given by

$$\Gamma_{\mathrm{X}}(\boldsymbol{k}) \xrightarrow[\text{Bloch gauge}]{\text{honeycomb lattice } Z=3} \Gamma_{\mathrm{B}}(\boldsymbol{k}) = \mathrm{e}^{-\mathrm{i}\frac{1}{3}\boldsymbol{k}(\boldsymbol{a}_1+\boldsymbol{a}_2)} \,, \tag{A.18a}$$

$$\Gamma_{\mathrm{X}}(\boldsymbol{k}) \xrightarrow[\text{Symmetric gauge}]{\text{honeycomb lattice } Z=3} \Gamma_{\mathrm{S}}(\boldsymbol{k}) = \gamma_{\mathrm{S}}(\boldsymbol{k}) \,. \tag{A.18b}$$

A.2.1 Coefficients — Magnetization

The coefficients for the magnetization observable

$$\hat{S}^{\mathrm{mag}}(\boldsymbol{Q}) = \sum_{\boldsymbol{r}_i \in \Gamma_A} \mathrm{e}^{-\mathrm{i}(\boldsymbol{Q}\boldsymbol{r}_i)} \hat{S}^z_{A,i} - \sum_{\boldsymbol{r}_j \in \Gamma_B} \mathrm{e}^{-\mathrm{i}(\boldsymbol{Q}\boldsymbol{r}_j)} \hat{S}^z_{B,j} \tag{A.19}$$

are determined in the same fashion as for the Hamiltonian, so that the observable can be expressed as

$$\begin{aligned} \hat{S}^{\mathrm{mag}}(\boldsymbol{Q}) = m^0_{\boldsymbol{Q}} + \sum_{\boldsymbol{k}_1,\boldsymbol{k}_2} \Big[& m^{\hat{\alpha}^\dagger\hat{\alpha}}_{\boldsymbol{Q},\boldsymbol{k}_1,\boldsymbol{k}_2} \hat{\alpha}^\dagger_{\boldsymbol{k}_1} \hat{\alpha}_{\boldsymbol{k}_2} + m^{\hat{\beta}^\dagger\hat{\beta}}_{\boldsymbol{Q},\boldsymbol{k}_1,\boldsymbol{k}_2} \hat{\beta}^\dagger_{\boldsymbol{k}_1} \hat{\beta}_{\boldsymbol{k}_2} \\ & + m^{\hat{\alpha}^\dagger\hat{\beta}^\dagger}_{\boldsymbol{Q},\boldsymbol{k}_1,\boldsymbol{k}_2} \hat{\alpha}^\dagger_{\boldsymbol{k}_1} \hat{\beta}^\dagger_{\boldsymbol{k}_2} + m^{\hat{\alpha}\hat{\beta}}_{\boldsymbol{Q},\boldsymbol{k}_1,\boldsymbol{k}_2} \hat{\alpha}_{\boldsymbol{k}_1} \hat{\beta}_{\boldsymbol{k}_2} \Big] \,. \end{aligned} \tag{A.20}$$

The initial values of the coefficient functions corresponding to $\hat{S}^{\mathrm{mag}}(\boldsymbol{Q})$ for $\ell = 0$ are given by

$$m^0_{\boldsymbol{Q}} = N\delta(\boldsymbol{Q})(S - n_{\mathrm{mf}})(1 + \Gamma_{\mathrm{X}}(\boldsymbol{Q})) \,, \tag{A.21a}$$

$$m^{\hat{\alpha}^\dagger\hat{\alpha}}_{\boldsymbol{Q},\boldsymbol{k}_1,\boldsymbol{k}_2} = -\delta(\boldsymbol{Q}+\boldsymbol{k}_1-\boldsymbol{k}_2)\left[l_{\boldsymbol{k}_2} l^*_{\boldsymbol{k}_1} + \Gamma_{\mathrm{X}}(\{\boldsymbol{Q}|\boldsymbol{Q}+\boldsymbol{k}_1-\boldsymbol{k}_2\})\, m_{\boldsymbol{k}_2} m^*_{\boldsymbol{k}_1}\right] \,, \tag{A.21b}$$

$$m^{\hat{\alpha}^\dagger\hat{\beta}^\dagger}_{\boldsymbol{Q},\boldsymbol{k}_1,\boldsymbol{k}_2} = -\delta(\boldsymbol{Q}+\boldsymbol{k}_1+\boldsymbol{k}_2)\left[l^*_{\boldsymbol{k}_1} m^*_{-\boldsymbol{k}_2} + \Gamma_{\mathrm{X}}(\{\boldsymbol{Q}|\boldsymbol{Q}+\boldsymbol{k}_1+\boldsymbol{k}_2\})\, l^*_{-\boldsymbol{k}_2} m^*_{\boldsymbol{k}_1}\right] \,, \tag{A.21c}$$

$$m^{\hat{\alpha}\hat{\beta}}_{\boldsymbol{Q},\boldsymbol{k}_1,\boldsymbol{k}_2} = -\delta(\boldsymbol{Q}-\boldsymbol{k}_1-\boldsymbol{k}_2)\left[l_{\boldsymbol{k}_1} m_{-\boldsymbol{k}_2} + \Gamma_{\mathrm{X}}(\{\boldsymbol{Q}|\boldsymbol{Q}-\boldsymbol{k}_1-\boldsymbol{k}_2\})\, l_{-\boldsymbol{k}_2} m_{\boldsymbol{k}_1}\right] \,, \tag{A.21d}$$

$$m^{\hat{\beta}^\dagger\hat{\beta}}_{\boldsymbol{Q},\boldsymbol{k}_1,\boldsymbol{k}_2} = -\delta(\boldsymbol{Q}+\boldsymbol{k}_1-\boldsymbol{k}_2)\left[m_{-\boldsymbol{k}_2} m^*_{-\boldsymbol{k}_1} + \Gamma_{\mathrm{X}}(\{\boldsymbol{Q}|\boldsymbol{Q}+\boldsymbol{k}_1-\boldsymbol{k}_2\})\, l_{-\boldsymbol{k}_2} l^*_{-\boldsymbol{k}_1}\right] \,. \tag{A.21e}$$

The number of coefficient functions can be reduced by exploiting symmetries of the observable. They can be written as

$$m^{\hat{\beta}^\dagger\hat{\beta}}_{\boldsymbol{Q},\boldsymbol{k}_1,\boldsymbol{k}_2} = m^{\hat{\alpha}^\dagger\hat{\alpha}}_{-\boldsymbol{Q},\boldsymbol{k}_2,\boldsymbol{k}_1} \Gamma_{\mathrm{X}}(\{\boldsymbol{Q}|\boldsymbol{Q}+\boldsymbol{k}_1-\boldsymbol{k}_2\}) \,, \tag{A.22a}$$

$$m^{\hat{\alpha}\hat{\beta}}_{\boldsymbol{Q},\boldsymbol{k}_1,\boldsymbol{k}_2} = m^{\hat{\alpha}^\dagger\hat{\beta}^\dagger}_{-\boldsymbol{Q},\boldsymbol{k}_2,\boldsymbol{k}_1} \Gamma_{\mathrm{X}}(\{\boldsymbol{Q}|\boldsymbol{Q}-\boldsymbol{k}_1-\boldsymbol{k}_2\}) \,. \tag{A.22b}$$

A.2.2 Coefficients — Longitudinal Dynamic Structure Factor

The observable for the longitudinal dynamic structure factor reads

$$\hat{S}^z_{\boldsymbol{Q}} = \sum_{\boldsymbol{r}_i \in \Gamma_A} \mathrm{e}^{-\mathrm{i}(\boldsymbol{Q}\boldsymbol{r}_i)} \hat{S}^z_{A,i} + \sum_{\boldsymbol{r}_j \in \Gamma_B} \mathrm{e}^{-\mathrm{i}(\boldsymbol{Q}\boldsymbol{r}_j)} \hat{S}^z_{B,j} \,. \tag{A.23}$$

With the same procedure as for the magnetization observable, the initial coefficients read

$$\hat{S}^z_{\boldsymbol{Q}} = s^{z0}_{\boldsymbol{Q}} + \sum_{\boldsymbol{k}_1,\boldsymbol{k}_2} \Big[s^{z\hat{\alpha}^\dagger\hat{\alpha}}_{\boldsymbol{Q},\boldsymbol{k}_1,\boldsymbol{k}_2} \hat{\alpha}^\dagger_{\boldsymbol{k}_1}\hat{\alpha}_{\boldsymbol{k}_2} + s^{z\hat{\beta}^\dagger\hat{\beta}}_{\boldsymbol{Q},\boldsymbol{k}_1,\boldsymbol{k}_2} \hat{\beta}^\dagger_{\boldsymbol{k}_1}\hat{\beta}_{\boldsymbol{k}_2} + s^{z\hat{\alpha}^\dagger\hat{\beta}^\dagger}_{\boldsymbol{Q},\boldsymbol{k}_1,\boldsymbol{k}_2} \hat{\alpha}^\dagger_{\boldsymbol{k}_1}\hat{\beta}^\dagger_{\boldsymbol{k}_2} + s^{z\hat{\alpha}\hat{\beta}}_{\boldsymbol{Q},\boldsymbol{k}_1,\boldsymbol{k}_2} \hat{\alpha}_{\boldsymbol{k}_1}\hat{\beta}_{\boldsymbol{k}_2} \Big] \tag{A.24}$$

The initial values of the coefficient functions corresponding to $\hat{S}^z_{\boldsymbol{Q}}$ for $\ell = 0$ are given by

$$s^{z0}_{\boldsymbol{Q}} = N\delta(\boldsymbol{Q})(S - n_{\mathrm{mf}})(1 - \Gamma_{\mathrm{X}}(\boldsymbol{Q})) \ , \tag{A.25a}$$

$$s^{z\hat{\alpha}^\dagger\hat{\alpha}}_{\boldsymbol{Q},\boldsymbol{k}_1,\boldsymbol{k}_2} = -\delta(\boldsymbol{Q}+\boldsymbol{k}_1-\boldsymbol{k}_2)\left[l_{\boldsymbol{k}_2} l^*_{\boldsymbol{k}_1} - \Gamma_{\mathrm{X}}(\{\boldsymbol{Q}|\boldsymbol{Q}+\boldsymbol{k}_1-\boldsymbol{k}_2\})\, m_{\boldsymbol{k}_2} m^*_{\boldsymbol{k}_1}\right] \ , \tag{A.25b}$$

$$s^{z\hat{\alpha}^\dagger\hat{\beta}^\dagger}_{\boldsymbol{Q},\boldsymbol{k}_1,\boldsymbol{k}_2} = -\delta(\boldsymbol{Q}+\boldsymbol{k}_1+\boldsymbol{k}_2)\left[l^*_{\boldsymbol{k}_1} m^*_{-\boldsymbol{k}_2} - \Gamma_{\mathrm{X}}(\{\boldsymbol{Q}|\boldsymbol{Q}+\boldsymbol{k}_1+\boldsymbol{k}_2\})\, l^*_{-\boldsymbol{k}_2} m^*_{\boldsymbol{k}_1}\right] \ , \tag{A.25c}$$

$$s^{z\hat{\alpha}\hat{\beta}}_{\boldsymbol{Q},\boldsymbol{k}_1,\boldsymbol{k}_2} = -\delta(\boldsymbol{Q}-\boldsymbol{k}_1-\boldsymbol{k}_2)\left[l_{\boldsymbol{k}_1} m_{-\boldsymbol{k}_2} - \Gamma_{\mathrm{X}}(\{\boldsymbol{Q}|\boldsymbol{Q}-\boldsymbol{k}_1-\boldsymbol{k}_2\})\, l_{-\boldsymbol{k}_2} m_{\boldsymbol{k}_1}\right] \ , \tag{A.25d}$$

$$s^{z\hat{\beta}^\dagger\hat{\beta}}_{\boldsymbol{Q},\boldsymbol{k}_1,\boldsymbol{k}_2} = -\delta(\boldsymbol{Q}+\boldsymbol{k}_1-\boldsymbol{k}_2)\left[m_{-\boldsymbol{k}_2} m^*_{-\boldsymbol{k}_1} - \Gamma_{\mathrm{X}}(\{\boldsymbol{Q}|\boldsymbol{Q}+\boldsymbol{k}_1-\boldsymbol{k}_2\})\, l_{-\boldsymbol{k}_2} l^*_{-\boldsymbol{k}_1}\right] \ . \tag{A.25e}$$

The number of coefficient functions can be reduced by exploiting symmetries of the observable. They can be written as

$$s^{z\hat{\beta}^\dagger\hat{\beta}}_{\boldsymbol{Q},\boldsymbol{k}_1,\boldsymbol{k}_2} = -s^{z\hat{\alpha}^\dagger\hat{\alpha}}_{-\boldsymbol{Q},\boldsymbol{k}_2,\boldsymbol{k}_1} \Gamma_{\mathrm{X}}(\{\boldsymbol{Q}|\boldsymbol{Q}+\boldsymbol{k}_1-\boldsymbol{k}_2\}) \ , \tag{A.26a}$$

$$s^{z\hat{\alpha}\hat{\beta}}_{\boldsymbol{Q},\boldsymbol{k}_1,\boldsymbol{k}_2} = -s^{z\hat{\alpha}^\dagger\hat{\beta}^\dagger}_{-\boldsymbol{Q},\boldsymbol{k}_2,\boldsymbol{k}_1} \Gamma_{\mathrm{X}}(\{\boldsymbol{Q}|\boldsymbol{Q}-\boldsymbol{k}_1-\boldsymbol{k}_2\}) \ . \tag{A.26b}$$

A.2.3 Coefficients — Transversal Structure Factor

To determine the observable for the transversal structure factor, the operators

$$\hat{S}^+_{\boldsymbol{Q}} = \sum_{\boldsymbol{r}_i \in \Gamma_A} \mathrm{e}^{-\mathrm{i}(\boldsymbol{Q}\boldsymbol{r}_i)} \hat{S}^+_{A,i} + \sum_{\boldsymbol{r}_j \in \Gamma_B} \mathrm{e}^{-\mathrm{i}(\boldsymbol{Q}\boldsymbol{r}_j)} \hat{S}^+_{B,j} \tag{A.27}$$

and

$$\hat{S}^-_{\boldsymbol{Q}} = \sum_{\boldsymbol{r}_i \in \Gamma_A} \mathrm{e}^{-\mathrm{i}(\boldsymbol{Q}\boldsymbol{r}_i)} \hat{S}^-_{A,i} + \sum_{\boldsymbol{r}_j \in \Gamma_B} \mathrm{e}^{-\mathrm{i}(\boldsymbol{Q}\boldsymbol{r}_j)} \hat{S}^-_{B,j} \tag{A.28}$$

need to be considered, and, together with the Hamiltonian, transformed via the same CST. The same steps as for the Hamiltonian are applied to derive the initial coefficients of both operators. After that, the operators can be written as

$$
\begin{aligned}
\hat{S}^{-}_{\boldsymbol{Q}} = \sum_{\boldsymbol{k}_1} \Bigg[& s^{-\hat{\alpha}^\dagger}_{\boldsymbol{Q},\boldsymbol{k}_1} \hat{\alpha}^\dagger_{\boldsymbol{k}_1} + s^{-\hat{\beta}}_{\boldsymbol{Q},\boldsymbol{k}_1} \hat{\beta}_{\boldsymbol{k}_1} \Bigg] \\
& + \sum_{\boldsymbol{k}_1,\boldsymbol{k}_2,\boldsymbol{k}_3} \Big[s^{-\hat{\alpha}^\dagger\hat{\alpha}^\dagger\hat{\alpha}}_{\boldsymbol{Q},\boldsymbol{k}_1,\boldsymbol{k}_2,\boldsymbol{k}_3} \hat{\alpha}^\dagger_{\boldsymbol{k}_1} \hat{\alpha}^\dagger_{\boldsymbol{k}_2} \hat{\alpha}_{\boldsymbol{k}_3} + s^{-\hat{\beta}^\dagger\hat{\beta}\hat{\beta}}_{\boldsymbol{Q},\boldsymbol{k}_1,\boldsymbol{k}_2,\boldsymbol{k}_3} \hat{\beta}^\dagger_{\boldsymbol{k}_1} \hat{\beta}_{\boldsymbol{k}_2} \hat{\beta}_{\boldsymbol{k}_3} \\
& \quad + s^{-\hat{\alpha}^\dagger\hat{\alpha}\hat{\beta}}_{\boldsymbol{Q},\boldsymbol{k}_1,\boldsymbol{k}_2,\boldsymbol{k}_3} \hat{\alpha}^\dagger_{\boldsymbol{k}_1} \hat{\alpha}_{\boldsymbol{k}_2} \hat{\beta}_{\boldsymbol{k}_3} + s^{-\hat{\alpha}^\dagger\hat{\beta}^\dagger\hat{\beta}}_{\boldsymbol{Q},\boldsymbol{k}_1,\boldsymbol{k}_2,\boldsymbol{k}_3} \hat{\alpha}^\dagger_{\boldsymbol{k}_1} \hat{\beta}^\dagger_{\boldsymbol{k}_2} \hat{\beta}_{\boldsymbol{k}_3} \\
& \quad + s^{-\hat{\alpha}^\dagger\hat{\alpha}^\dagger\hat{\beta}^\dagger}_{\boldsymbol{Q},\boldsymbol{k}_1,\boldsymbol{k}_2,\boldsymbol{k}_3} \hat{\alpha}^\dagger_{\boldsymbol{k}_1} \hat{\alpha}^\dagger_{\boldsymbol{k}_2} \hat{\beta}^\dagger_{\boldsymbol{k}_3} + s^{-\hat{\alpha}\hat{\beta}\hat{\beta}}_{\boldsymbol{Q},\boldsymbol{k}_1,\boldsymbol{k}_2,\boldsymbol{k}_3} \hat{\alpha}_{\boldsymbol{k}_1} \hat{\beta}_{\boldsymbol{k}_2} \hat{\beta}_{\boldsymbol{k}_3} \Big] ,
\end{aligned}
\tag{A.29}
$$

$$
\begin{aligned}
\hat{S}^{+}_{\boldsymbol{Q}} = \sum_{\boldsymbol{k}_1} \Bigg[& s^{+\hat{\alpha}}_{\boldsymbol{Q},\boldsymbol{k}_1} \hat{\alpha}_{\boldsymbol{k}_1} + s^{+\hat{\beta}^\dagger}_{\boldsymbol{Q},\boldsymbol{k}_1} \hat{\beta}^\dagger_{\boldsymbol{k}_1} \Bigg] \\
& + \sum_{\boldsymbol{k}_1,\boldsymbol{k}_2,\boldsymbol{k}_3} \Big[s^{+\hat{\alpha}^\dagger\hat{\alpha}\hat{\alpha}}_{\boldsymbol{Q},\boldsymbol{k}_1,\boldsymbol{k}_2,\boldsymbol{k}_3} \hat{\alpha}^\dagger_{\boldsymbol{k}_1} \hat{\alpha}_{\boldsymbol{k}_2} \hat{\alpha}_{\boldsymbol{k}_3} + s^{+\hat{\beta}^\dagger\hat{\beta}^\dagger\hat{\beta}}_{\boldsymbol{Q},\boldsymbol{k}_1,\boldsymbol{k}_2,\boldsymbol{k}_3} \hat{\beta}^\dagger_{\boldsymbol{k}_1} \hat{\beta}^\dagger_{\boldsymbol{k}_2} \hat{\beta}_{\boldsymbol{k}_3} \\
& \quad + s^{+\hat{\alpha}^\dagger\hat{\alpha}\hat{\beta}^\dagger}_{\boldsymbol{Q},\boldsymbol{k}_1,\boldsymbol{k}_2,\boldsymbol{k}_3} \hat{\alpha}^\dagger_{\boldsymbol{k}_1} \hat{\alpha}_{\boldsymbol{k}_2} \hat{\beta}^\dagger_{\boldsymbol{k}_3} + s^{+\hat{\alpha}\hat{\beta}^\dagger\hat{\beta}}_{\boldsymbol{Q},\boldsymbol{k}_1,\boldsymbol{k}_2,\boldsymbol{k}_3} \hat{\alpha}_{\boldsymbol{k}_1} \hat{\beta}^\dagger_{\boldsymbol{k}_2} \hat{\beta}_{\boldsymbol{k}_3} \\
& \quad + s^{+\hat{\alpha}\hat{\alpha}\hat{\beta}}_{\boldsymbol{Q},\boldsymbol{k}_1,\boldsymbol{k}_2,\boldsymbol{k}_3} \hat{\alpha}_{\boldsymbol{k}_1} \hat{\alpha}_{\boldsymbol{k}_2} \hat{\beta}_{\boldsymbol{k}_3} + s^{+\hat{\alpha}^\dagger\hat{\beta}^\dagger\hat{\beta}^\dagger}_{\boldsymbol{Q},\boldsymbol{k}_1,\boldsymbol{k}_2,\boldsymbol{k}_3} \hat{\alpha}^\dagger_{\boldsymbol{k}_1} \hat{\beta}^\dagger_{\boldsymbol{k}_2} \hat{\beta}^\dagger_{\boldsymbol{k}_3} \Big] .
\end{aligned}
\tag{A.30}
$$

The initial values of the coefficient functions corresponding to $\hat{S}^{-}_{\boldsymbol{Q}}$ for $\ell = 0$ are given by

$$
s^{-\hat{\alpha}^\dagger}_{\boldsymbol{Q},\boldsymbol{k}_1} = \sqrt{N_\Sigma}\,\delta(\boldsymbol{Q}+\boldsymbol{k}_1) \left[l^*_{\boldsymbol{k}_1} + \Gamma_{\mathrm{X}}(\{\boldsymbol{Q}|\boldsymbol{Q}+\boldsymbol{k}_1\})\, m^*_{\boldsymbol{k}_1} \right] , \tag{A.31a}
$$

$$
s^{-\hat{\beta}}_{\boldsymbol{Q},\boldsymbol{k}_1} = \sqrt{N_\Sigma}\,\delta(\boldsymbol{Q}-\boldsymbol{k}_1) \left[m_{-\boldsymbol{k}_1} + \Gamma_{\mathrm{X}}(\{\boldsymbol{Q}|\boldsymbol{Q}-\boldsymbol{k}_1\})\, l_{-\boldsymbol{k}_1} \right] , \tag{A.31b}
$$

$$
s^{-\hat{\alpha}^\dagger\hat{\alpha}^\dagger\hat{\alpha}}_{\boldsymbol{Q},\boldsymbol{k}_1,\boldsymbol{k}_2,\boldsymbol{k}_3} = 0 , \tag{A.31c}
$$

$$
s^{-\hat{\alpha}^\dagger\hat{\beta}^\dagger\hat{\beta}}_{\boldsymbol{Q},\boldsymbol{k}_1,\boldsymbol{k}_2,\boldsymbol{k}_3} = 0 , \tag{A.31d}
$$

$$
s^{-\hat{\alpha}^\dagger\hat{\alpha}\hat{\beta}}_{\boldsymbol{Q},\boldsymbol{k}_1,\boldsymbol{k}_2,\boldsymbol{k}_3} = 0 , \tag{A.31e}
$$

$$
s^{-\hat{\alpha}^\dagger\hat{\alpha}^\dagger\hat{\beta}^\dagger}_{\boldsymbol{Q},\boldsymbol{k}_1,\boldsymbol{k}_2,\boldsymbol{k}_3} = 0 , \tag{A.31f}
$$

$$
s^{-\hat{\alpha}\hat{\beta}\hat{\beta}}_{\boldsymbol{Q},\boldsymbol{k}_1,\boldsymbol{k}_2,\boldsymbol{k}_3} = 0 , \tag{A.31g}
$$

$$
s^{-\hat{\beta}^\dagger\hat{\beta}\hat{\beta}}_{\boldsymbol{Q},\boldsymbol{k}_1,\boldsymbol{k}_2,\boldsymbol{k}_3} = 0 . \tag{A.31h}
$$

The corresponding symmetry relations read

$$
s^{-\hat{\beta}}_{\boldsymbol{Q},\boldsymbol{k}_1} = s^{-\hat{\alpha}^\dagger}_{-\boldsymbol{Q},\boldsymbol{k}_1} \Gamma_{\mathrm{X}}(\{\boldsymbol{Q}|\boldsymbol{Q}-\boldsymbol{k}_1\}) , \tag{A.32a}
$$

$$
s^{-\hat{\beta}^\dagger\hat{\beta}\hat{\beta}}_{\boldsymbol{Q},\boldsymbol{k}_1,\boldsymbol{k}_2,\boldsymbol{k}_3} = s^{-\hat{\alpha}^\dagger\hat{\alpha}^\dagger\hat{\alpha}}_{-\boldsymbol{Q},\boldsymbol{k}_3,\boldsymbol{k}_2,\boldsymbol{k}_1} \Gamma_{\mathrm{X}}(\{\boldsymbol{Q}|\boldsymbol{Q}+\boldsymbol{k}_1-\boldsymbol{k}_2-\boldsymbol{k}_3\}) , \tag{A.32b}
$$

$$
s^{-\hat{\alpha}^\dagger\hat{\beta}^\dagger\hat{\beta}}_{\boldsymbol{Q},\boldsymbol{k}_1,\boldsymbol{k}_2,\boldsymbol{k}_3} = s^{-\hat{\alpha}^\dagger\hat{\alpha}\hat{\beta}}_{-\boldsymbol{Q},\boldsymbol{k}_3,\boldsymbol{k}_2,\boldsymbol{k}_1} \Gamma_{\mathrm{X}}(\{\boldsymbol{Q}|\boldsymbol{Q}+\boldsymbol{k}_1+\boldsymbol{k}_2-\boldsymbol{k}_3\}) , \tag{A.32c}
$$

$$
s^{-\hat{\alpha}\hat{\beta}\hat{\beta}}_{\boldsymbol{Q},\boldsymbol{k}_1,\boldsymbol{k}_2,\boldsymbol{k}_3} = s^{-\hat{\alpha}^\dagger\hat{\alpha}^\dagger\hat{\beta}^\dagger}_{-\boldsymbol{Q},\boldsymbol{k}_3,\boldsymbol{k}_2,\boldsymbol{k}_1} \Gamma_{\mathrm{X}}(\{\boldsymbol{Q}|\boldsymbol{Q}-\boldsymbol{k}_1-\boldsymbol{k}_2-\boldsymbol{k}_3\}) . \tag{A.32d}
$$

The initial values of the coefficient functions corresponding to $\hat{S}^{+}_{\boldsymbol{Q}}$ for $\ell = 0$ are given by

$$s^{+\hat{\alpha}}_{\boldsymbol{Q},\boldsymbol{k}_1} = 2\sqrt{N_{\mathfrak{T}}}\delta(\boldsymbol{Q}-\boldsymbol{k}_1)\ (S-n_{\mathrm{mf}})\left(l_{\boldsymbol{k}_1} + \Gamma_{\mathrm{X}}(\{\boldsymbol{Q}|\boldsymbol{Q}-\boldsymbol{k}_1\})\, m_{\boldsymbol{k}_1}\right)\ , \tag{A.33a}$$

$$s^{+\hat{\beta}^\dagger}_{\boldsymbol{Q},\boldsymbol{k}_1} = 2\sqrt{N_{\mathfrak{T}}}\delta(\boldsymbol{Q}+\boldsymbol{k}_1)\,(S-n_{\mathrm{mf}})\left(m^*_{-\boldsymbol{k}_1} + \Gamma_{\mathrm{X}}(\{\boldsymbol{Q}|\boldsymbol{Q}+\boldsymbol{k}_1\})\, l^*_{-\boldsymbol{k}_1}\right)\ , \tag{A.33b}$$

$$\begin{aligned} s^{+\hat{\alpha}^\dagger\hat{\alpha}\hat{\alpha}}_{\boldsymbol{Q},\boldsymbol{k}_1,\boldsymbol{k}_2,\boldsymbol{k}_3} = &-\frac{1}{\sqrt{N_{\mathfrak{T}}}}\delta(\boldsymbol{Q}+\boldsymbol{k}_1-\boldsymbol{k}_2-\boldsymbol{k}_3) \\ &\left[l_{\boldsymbol{k}_2} l_{\boldsymbol{k}_3} l^*_{\boldsymbol{k}_1} + \Gamma_{\mathrm{X}}(\{\boldsymbol{Q}|\boldsymbol{Q}+\boldsymbol{k}_1-\boldsymbol{k}_2-\boldsymbol{k}_3\})\, m_{\boldsymbol{k}_2} m_{\boldsymbol{k}_3} m^*_{\boldsymbol{k}_1}\right]\ , \end{aligned} \tag{A.33c}$$

$$\begin{aligned} s^{+\hat{\alpha}\hat{\beta}^\dagger\hat{\beta}}_{\boldsymbol{Q},\boldsymbol{k}_1,\boldsymbol{k}_2,\boldsymbol{k}_3} = &-\frac{2}{\sqrt{N_{\mathfrak{T}}}}\delta(\boldsymbol{Q}-\boldsymbol{k}_1+\boldsymbol{k}_2-\boldsymbol{k}_3) \\ &\left[l_{\boldsymbol{k}_1} m_{-\boldsymbol{k}_3} m^*_{-\boldsymbol{k}_2} + \Gamma_{\mathrm{X}}(\{\boldsymbol{Q}|\boldsymbol{Q}-\boldsymbol{k}_1+\boldsymbol{k}_2-\boldsymbol{k}_3\})\, l_{-\boldsymbol{k}_3} l^*_{-\boldsymbol{k}_2} m_{\boldsymbol{k}_1}\right]\ , \end{aligned} \tag{A.33d}$$

$$\begin{aligned} s^{+\hat{\alpha}\hat{\alpha}\hat{\beta}}_{\boldsymbol{Q},\boldsymbol{k}_1,\boldsymbol{k}_2,\boldsymbol{k}_3} = &-\frac{1}{\sqrt{N_{\mathfrak{T}}}}\delta(\boldsymbol{Q}-\boldsymbol{k}_1-\boldsymbol{k}_2-\boldsymbol{k}_3) \\ &\left[l_{\boldsymbol{k}_1} l_{\boldsymbol{k}_2} m_{-\boldsymbol{k}_3} + \Gamma_{\mathrm{X}}(\{\boldsymbol{Q}|\boldsymbol{Q}-\boldsymbol{k}_1-\boldsymbol{k}_2-\boldsymbol{k}_3\})\, l_{-\boldsymbol{k}_3} m_{\boldsymbol{k}_1} m_{\boldsymbol{k}_2}\right]\ , \end{aligned} \tag{A.33e}$$

$$\begin{aligned} s^{+\hat{\alpha}^\dagger\hat{\alpha}\hat{\beta}^\dagger}_{\boldsymbol{Q},\boldsymbol{k}_1,\boldsymbol{k}_2,\boldsymbol{k}_3} = &-\frac{2}{\sqrt{N_{\mathfrak{T}}}}\delta(\boldsymbol{Q}+\boldsymbol{k}_1-\boldsymbol{k}_2+\boldsymbol{k}_3) \\ &\left[l_{\boldsymbol{k}_2} l^*_{\boldsymbol{k}_1} m^*_{-\boldsymbol{k}_3} + \Gamma_{\mathrm{X}}(\{\boldsymbol{Q}|\boldsymbol{Q}+\boldsymbol{k}_1-\boldsymbol{k}_2+\boldsymbol{k}_3\})\, l^*_{-\boldsymbol{k}_3} m_{\boldsymbol{k}_2} m^*_{\boldsymbol{k}_1}\right]\ , \end{aligned} \tag{A.33f}$$

$$\begin{aligned} s^{+\hat{\alpha}^\dagger\hat{\beta}^\dagger\hat{\beta}^\dagger}_{\boldsymbol{Q},\boldsymbol{k}_1,\boldsymbol{k}_2,\boldsymbol{k}_3} = &-\frac{1}{\sqrt{N_{\mathfrak{T}}}}\delta(\boldsymbol{Q}+\boldsymbol{k}_1+\boldsymbol{k}_2+\boldsymbol{k}_3) \\ &\left[l^*_{\boldsymbol{k}_1} m^*_{-\boldsymbol{k}_2} m^*_{-\boldsymbol{k}_3} + \Gamma_{\mathrm{X}}(\{\boldsymbol{Q}|\boldsymbol{Q}+\boldsymbol{k}_1+\boldsymbol{k}_2+\boldsymbol{k}_3\})\, l^*_{-\boldsymbol{k}_2} l^*_{-\boldsymbol{k}_3} m^*_{\boldsymbol{k}_1}\right]\ , \end{aligned} \tag{A.33g}$$

$$\begin{aligned} s^{+\hat{\beta}^\dagger\hat{\beta}^\dagger\hat{\beta}}_{\boldsymbol{Q},\boldsymbol{k}_1,\boldsymbol{k}_2,\boldsymbol{k}_3} = &-\frac{1}{\sqrt{N_{\mathfrak{T}}}}\delta(\boldsymbol{Q}+\boldsymbol{k}_1+\boldsymbol{k}_2-\boldsymbol{k}_3) \\ &\left[m_{-\boldsymbol{k}_3} m^*_{-\boldsymbol{k}_1} m^*_{-\boldsymbol{k}_2} + \Gamma_{\mathrm{X}}(\{\boldsymbol{Q}|\boldsymbol{Q}+\boldsymbol{k}_1+\boldsymbol{k}_2-\boldsymbol{k}_3\})\, l_{-\boldsymbol{k}_3} l^*_{-\boldsymbol{k}_1} l^*_{-\boldsymbol{k}_2}\right]\ . \end{aligned} \tag{A.33h}$$

The corresponding symmetry relations read

$$s^{+\hat{\beta}^\dagger}_{\boldsymbol{Q},\boldsymbol{k}_1} = s^{+\hat{\alpha}}_{-\boldsymbol{Q},\boldsymbol{k}_1}\Gamma_{\mathrm{X}}(\{\boldsymbol{Q}|\boldsymbol{Q}+\boldsymbol{k}_1\})\ , \tag{A.34a}$$

$$s^{+\hat{\beta}^\dagger\hat{\beta}^\dagger\hat{\beta}}_{\boldsymbol{Q},\boldsymbol{k}_1,\boldsymbol{k}_2,\boldsymbol{k}_3} = s^{+\hat{\alpha}^\dagger\hat{\alpha}\hat{\alpha}}_{-\boldsymbol{Q},\boldsymbol{k}_3,\boldsymbol{k}_2,\boldsymbol{k}_1}\Gamma_{\mathrm{X}}(\{\boldsymbol{Q}|\boldsymbol{Q}+\boldsymbol{k}_1+\boldsymbol{k}_2-\boldsymbol{k}_3\})\ , \tag{A.34b}$$

$$s^{+\hat{\alpha}\hat{\beta}^\dagger\hat{\beta}}_{\boldsymbol{Q},\boldsymbol{k}_1,\boldsymbol{k}_2,\boldsymbol{k}_3} = s^{+\hat{\alpha}^\dagger\hat{\alpha}\hat{\beta}^\dagger}_{-\boldsymbol{Q},\boldsymbol{k}_3,\boldsymbol{k}_2,\boldsymbol{k}_1}\Gamma_{\mathrm{X}}(\{\boldsymbol{Q}|\boldsymbol{Q}-\boldsymbol{k}_1+\boldsymbol{k}_2-\boldsymbol{k}_3\})\ , \tag{A.34c}$$

$$s^{+\hat{\alpha}^\dagger\hat{\beta}^\dagger\hat{\beta}^\dagger}_{\boldsymbol{Q},\boldsymbol{k}_1,\boldsymbol{k}_2,\boldsymbol{k}_3} = s^{+\hat{\alpha}\hat{\alpha}\hat{\beta}}_{-\boldsymbol{Q},\boldsymbol{k}_3,\boldsymbol{k}_2,\boldsymbol{k}_1}\Gamma_{\mathrm{X}}(\{\boldsymbol{Q}|\boldsymbol{Q}+\boldsymbol{k}_1+\boldsymbol{k}_2+\boldsymbol{k}_3\})\ . \tag{A.34d}$$

B | Flow Equations for the Coefficients

In this appendix, all flow equations for each coefficient discussed above are listed explicitly below. For simplicity and readability, in the following, the ℓ dependence of all coefficients is omitted. Furthermore, the sums over momenta are also omitted. The summation over momentum indices either over the Brillouin zone (BZ) or magnetic Brillouin zone (MBZ), depending on the model, is implied, such that momenta not present on the left-hand side of the equations are summed over. Also, the momentum-conservation delta functions are omitted but can be easily determined from the coefficients on the left-hand side. To distinguish between the flow equations connected to the particle-conserving generator (pc generator) $\hat{\eta}^{\mathrm{pc}}$ or the particle-block-separating generator with $k = 0$ ($0n$ generator) $\hat{\eta}^{\mathrm{pbs}}_{0:n}$, the terms are color-coded. All terms existing in both flows are not colored, but terms only present in the $0n$ generator flow equations are colored in blue, while terms only present in the pc generator flow equations are colored in orange. However, there also exist terms that differ only by a prefactor between the two flows. These terms are indicated by the notation $\{x|y\}$, which means that the first value in blue x is used in the $0n$ generator flow equations and the second value in orange y in the pc generator flow equations. Additionally, the flow equations are further subdivided into flow equations of the Hamiltonian in Appendix B.1 and flow equations of the observables in Appendix B.2. Regarding the flow equations for the observables, only the flow equation for the magnetization is used in this work. Nevertheless, the others are listed for completeness in accordance with Ref. [Pow17].

B.1 Flow Equations of the Hamiltonian

The flow equations produced with the tool set of [MHS] of the Hamiltonian coefficients as listed in Eq. (A.10) read as follows

$$
\begin{aligned}
\partial_\ell C^{0} =& -2C^{\hat{\alpha}\hat{\beta}}_{\boldsymbol{k}_1,-\boldsymbol{k}_1} C^{\hat{\alpha}^\dagger\hat{\beta}^\dagger}_{\boldsymbol{k}_1,-\boldsymbol{k}_1} \\
&- 8C^{\hat{\alpha}\hat{\alpha}\hat{\beta}\hat{\beta}}_{\boldsymbol{k}_1,\boldsymbol{k}_2,\boldsymbol{k}_3,-\boldsymbol{k}_1-\boldsymbol{k}_2-\boldsymbol{k}_3} C^{\hat{\alpha}^\dagger\hat{\alpha}^\dagger\hat{\beta}^\dagger\hat{\beta}^\dagger}_{\boldsymbol{k}_1,\boldsymbol{k}_2,\boldsymbol{k}_3,-\boldsymbol{k}_1-\boldsymbol{k}_2-\boldsymbol{k}_3} \,, \qquad \text{(B.1)} \\
\partial_\ell C^{\hat{\alpha}^\dagger\hat{\alpha}}_{\boldsymbol{k}_1,\boldsymbol{k}_2} =& -2C^{\hat{\alpha}\hat{\beta}}_{\boldsymbol{k}_2,-\boldsymbol{k}_2} C^{\hat{\alpha}^\dagger\hat{\beta}^\dagger}_{\boldsymbol{k}_1,-\boldsymbol{k}_2} \\
&- \{2|4\}\, C^{\hat{\alpha}\hat{\beta}}_{\boldsymbol{k}_3,-\boldsymbol{k}_3} C^{\hat{\alpha}^\dagger\hat{\alpha}^\dagger\hat{\alpha}\hat{\beta}^\dagger}_{\boldsymbol{k}_1,\boldsymbol{k}_3,\boldsymbol{k}_2,-\boldsymbol{k}_3} \\
&- \{2|4\}\, C^{\hat{\alpha}^\dagger\hat{\beta}^\dagger}_{\boldsymbol{k}_3,-\boldsymbol{k}_3} C^{\hat{\alpha}^\dagger\hat{\alpha}\hat{\alpha}\hat{\beta}}_{\boldsymbol{k}_1,\boldsymbol{k}_2,\boldsymbol{k}_3,-\boldsymbol{k}_3} \qquad \text{(B.2)} \\
&-4C^{\hat{\alpha}^\dagger\hat{\alpha}\hat{\alpha}\hat{\beta}}_{\boldsymbol{k}_1,\boldsymbol{k}_3,\boldsymbol{k}_4,\boldsymbol{k}_2-\boldsymbol{k}_3-\boldsymbol{k}_4} C^{\hat{\alpha}^\dagger\hat{\alpha}^\dagger\hat{\alpha}\hat{\beta}^\dagger}_{\boldsymbol{k}_3,\boldsymbol{k}_4,\boldsymbol{k}_2,\boldsymbol{k}_2-\boldsymbol{k}_3-\boldsymbol{k}_4} \\
&- 16C^{\hat{\alpha}\hat{\alpha}\hat{\beta}\hat{\beta}}_{\boldsymbol{k}_2,\boldsymbol{k}_3,\boldsymbol{k}_4,-\boldsymbol{k}_2-\boldsymbol{k}_3-\boldsymbol{k}_4} C^{\hat{\alpha}^\dagger\hat{\alpha}^\dagger\hat{\beta}^\dagger\hat{\beta}^\dagger}_{\boldsymbol{k}_1,\boldsymbol{k}_3,\boldsymbol{k}_4,-\boldsymbol{k}_2-\boldsymbol{k}_3-\boldsymbol{k}_4} \,,
\end{aligned}
$$

$$
\begin{aligned}
\partial_\ell C^{\hat\alpha^\dagger\hat\beta^\dagger}_{\boldsymbol{k}_1,\boldsymbol{k}_2} =& -8C^{\hat\alpha\hat\beta}_{\boldsymbol{k}_3,-\boldsymbol{k}_3} C^{\hat\alpha^\dagger\hat\alpha^\dagger\hat\beta^\dagger\hat\beta^\dagger}_{\boldsymbol{k}_1,\boldsymbol{k}_3,\boldsymbol{k}_2,-\boldsymbol{k}_3} \\
&- C^{\hat\alpha^\dagger\hat\alpha}_{\boldsymbol{k}_1,-\boldsymbol{k}_2} C^{\hat\alpha^\dagger\hat\beta^\dagger}_{-\boldsymbol{k}_2,\boldsymbol{k}_2} \\
&- C^{\hat\alpha^\dagger\hat\beta^\dagger}_{\boldsymbol{k}_1,\boldsymbol{k}_2} C^{\hat\beta^\dagger\hat\beta}_{\boldsymbol{k}_2,\boldsymbol{k}_2} \\
&- C^{\hat\alpha^\dagger\hat\beta^\dagger}_{\boldsymbol{k}_3,-\boldsymbol{k}_3} C^{\hat\alpha^\dagger\hat\alpha\hat\beta^\dagger\hat\beta}_{\boldsymbol{k}_1,\boldsymbol{k}_3,\boldsymbol{k}_2,-\boldsymbol{k}_3} \\
&- \{4|8\}\, C^{\hat\alpha\hat\beta^\dagger\hat\beta\hat\beta}_{\boldsymbol{k}_3,\boldsymbol{k}_2,\boldsymbol{k}_4,\boldsymbol{k}_2-\boldsymbol{k}_3-\boldsymbol{k}_4} C^{\hat\alpha^\dagger\hat\alpha^\dagger\hat\beta^\dagger\hat\beta^\dagger}_{\boldsymbol{k}_1,\boldsymbol{k}_3,\boldsymbol{k}_4,\boldsymbol{k}_2-\boldsymbol{k}_3-\boldsymbol{k}_4} \\
&- \{4|8\}\, C^{\hat\alpha^\dagger\hat\alpha\hat\alpha\hat\beta}_{\boldsymbol{k}_1,\boldsymbol{k}_3,\boldsymbol{k}_4,-\boldsymbol{k}_2-\boldsymbol{k}_3-\boldsymbol{k}_4} C^{\hat\alpha^\dagger\hat\alpha^\dagger\hat\beta^\dagger\hat\beta^\dagger}_{\boldsymbol{k}_3,\boldsymbol{k}_4,\boldsymbol{k}_2,-\boldsymbol{k}_2-\boldsymbol{k}_3-\boldsymbol{k}_4}\,,
\end{aligned}
\tag{B.3}
$$

$$
\begin{aligned}
\partial_\ell C^{\hat\alpha\hat\beta}_{\boldsymbol{k}_1,\boldsymbol{k}_2} =& - C^{\hat\alpha\hat\beta}_{\boldsymbol{k}_1,\boldsymbol{k}_2} C^{\hat\beta^\dagger\hat\beta}_{\boldsymbol{k}_2,\boldsymbol{k}_2} \\
&- C^{\hat\alpha\hat\beta}_{-\boldsymbol{k}_2,\boldsymbol{k}_2} C^{\hat\alpha^\dagger\hat\alpha}_{-\boldsymbol{k}_2,\boldsymbol{k}_1} \\
&- C^{\hat\alpha\hat\beta}_{\boldsymbol{k}_3,-\boldsymbol{k}_3} C^{\hat\alpha^\dagger\hat\alpha\hat\beta^\dagger\hat\beta}_{\boldsymbol{k}_3,\boldsymbol{k}_1,-\boldsymbol{k}_3,\boldsymbol{k}_2} \\
&- 8C^{\hat\alpha^\dagger\hat\beta^\dagger}_{\boldsymbol{k}_3,-\boldsymbol{k}_3} C^{\hat\alpha\hat\alpha\hat\beta\hat\beta}_{\boldsymbol{k}_1,\boldsymbol{k}_3,\boldsymbol{k}_2,-\boldsymbol{k}_3} \\
&- \{4|8\}\, C^{\hat\alpha^\dagger\hat\beta^\dagger\hat\beta^\dagger\hat\beta}_{\boldsymbol{k}_3,\boldsymbol{k}_4,\boldsymbol{k}_2-\boldsymbol{k}_3-\boldsymbol{k}_4,\boldsymbol{k}_2} C^{\hat\alpha\hat\alpha\hat\beta\hat\beta}_{\boldsymbol{k}_1,\boldsymbol{k}_3,\boldsymbol{k}_4,\boldsymbol{k}_2-\boldsymbol{k}_3-\boldsymbol{k}_4} \\
&- \{4|8\}\, C^{\hat\alpha^\dagger\hat\alpha^\dagger\hat\alpha\hat\beta^\dagger}_{\boldsymbol{k}_3,\boldsymbol{k}_4,\boldsymbol{k}_1,-\boldsymbol{k}_2-\boldsymbol{k}_3-\boldsymbol{k}_4} C^{\hat\alpha\hat\alpha\hat\beta\hat\beta}_{\boldsymbol{k}_3,\boldsymbol{k}_4,\boldsymbol{k}_2,-\boldsymbol{k}_2-\boldsymbol{k}_3-\boldsymbol{k}_4}\,,
\end{aligned}
\tag{B.4}
$$

$$
\begin{aligned}
\partial_\ell C^{\hat\beta^\dagger\hat\beta}_{\boldsymbol{k}_1,\boldsymbol{k}_2} =& -2C^{\hat\alpha\hat\beta}_{-\boldsymbol{k}_2,\boldsymbol{k}_2} C^{\hat\alpha^\dagger\hat\beta^\dagger}_{-\boldsymbol{k}_2,\boldsymbol{k}_1} \\
&- \{2|4\}\, C^{\hat\alpha\hat\beta}_{\boldsymbol{k}_3,-\boldsymbol{k}_3} C^{\hat\alpha^\dagger\hat\beta^\dagger\hat\beta^\dagger\hat\beta}_{\boldsymbol{k}_3,\boldsymbol{k}_1,-\boldsymbol{k}_3,\boldsymbol{k}_2} \\
&- \{2|4\}\, C^{\hat\alpha^\dagger\hat\beta^\dagger}_{\boldsymbol{k}_3,-\boldsymbol{k}_3} C^{\hat\alpha\hat\beta^\dagger\hat\beta\hat\beta}_{\boldsymbol{k}_3,\boldsymbol{k}_1,\boldsymbol{k}_2,-\boldsymbol{k}_3} \\
&-4C^{\hat\alpha\hat\beta^\dagger\hat\beta\hat\beta}_{\boldsymbol{k}_3,\boldsymbol{k}_1,\boldsymbol{k}_4,\boldsymbol{k}_2-\boldsymbol{k}_3-\boldsymbol{k}_4} C^{\hat\alpha^\dagger\hat\beta^\dagger\hat\beta^\dagger\hat\beta}_{\boldsymbol{k}_3,\boldsymbol{k}_4,\boldsymbol{k}_2-\boldsymbol{k}_3-\boldsymbol{k}_4,\boldsymbol{k}_2} \\
&- 16C^{\hat\alpha\hat\alpha\hat\beta\hat\beta}_{\boldsymbol{k}_3,\boldsymbol{k}_4,\boldsymbol{k}_2,-\boldsymbol{k}_2-\boldsymbol{k}_3-\boldsymbol{k}_4} C^{\hat\alpha^\dagger\hat\alpha^\dagger\hat\beta^\dagger\hat\beta^\dagger}_{\boldsymbol{k}_3,\boldsymbol{k}_4,\boldsymbol{k}_1,-\boldsymbol{k}_2-\boldsymbol{k}_3-\boldsymbol{k}_4}\,,
\end{aligned}
\tag{B.5}
$$

$$
\begin{aligned}
\partial_\ell C^{\hat\alpha^\dagger\hat\alpha^\dagger\hat\alpha\hat\alpha}_{\boldsymbol{k}_1,\boldsymbol{k}_2,\boldsymbol{k}_3,\boldsymbol{k}_4} = &-\left\{\frac{1}{2}|1\right\} C^{\hat\alpha\hat\beta}_{\boldsymbol{k}_3,-\boldsymbol{k}_3} C^{\hat\alpha^\dagger\hat\alpha^\dagger\hat\alpha\hat\beta^\dagger}_{\boldsymbol{k}_1,\boldsymbol{k}_2,\boldsymbol{k}_4,-\boldsymbol{k}_3} \\
&-\left\{\frac{1}{2}|1\right\} C^{\hat\alpha\hat\beta}_{\boldsymbol{k}_4,-\boldsymbol{k}_4} C^{\hat\alpha^\dagger\hat\alpha^\dagger\hat\alpha\hat\beta^\dagger}_{\boldsymbol{k}_1,\boldsymbol{k}_2,\boldsymbol{k}_3,-\boldsymbol{k}_4} \\
&-\frac{1}{2} C^{\hat\alpha^\dagger\hat\beta^\dagger}_{\boldsymbol{k}_1,-\boldsymbol{k}_1} C^{\hat\alpha^\dagger\hat\alpha\hat\alpha\hat\beta}_{\boldsymbol{k}_2,\boldsymbol{k}_3,\boldsymbol{k}_4,-\boldsymbol{k}_1} \\
&-\frac{1}{2} C^{\hat\alpha^\dagger\hat\beta^\dagger}_{\boldsymbol{k}_1,\boldsymbol{k}_2-\boldsymbol{k}_3-\boldsymbol{k}_4} C^{\hat\alpha^\dagger\hat\alpha\hat\alpha\hat\beta}_{\boldsymbol{k}_2,\boldsymbol{k}_3,\boldsymbol{k}_4,\boldsymbol{k}_2-\boldsymbol{k}_3-\boldsymbol{k}_4} \\
&-\frac{1}{2} C^{\hat\alpha^\dagger\hat\beta^\dagger}_{\boldsymbol{k}_2,\boldsymbol{k}_1-\boldsymbol{k}_3-\boldsymbol{k}_4} C^{\hat\alpha^\dagger\hat\alpha\hat\alpha\hat\beta}_{\boldsymbol{k}_1,\boldsymbol{k}_3,\boldsymbol{k}_4,\boldsymbol{k}_1-\boldsymbol{k}_3-\boldsymbol{k}_4} \\
&-\frac{1}{2} C^{\hat\alpha^\dagger\hat\beta^\dagger}_{\boldsymbol{k}_2,-\boldsymbol{k}_2} C^{\hat\alpha^\dagger\hat\alpha\hat\alpha\hat\beta}_{\boldsymbol{k}_1,\boldsymbol{k}_3,\boldsymbol{k}_4,-\boldsymbol{k}_2} \\
&-C^{\hat\alpha^\dagger\hat\alpha\hat\alpha\hat\beta}_{\boldsymbol{k}_1,\boldsymbol{k}_3,\boldsymbol{k}_5,\boldsymbol{k}_1-\boldsymbol{k}_3-\boldsymbol{k}_5} C^{\hat\alpha^\dagger\hat\alpha^\dagger\hat\alpha\hat\beta^\dagger}_{\boldsymbol{k}_2,\boldsymbol{k}_5,\boldsymbol{k}_4,\boldsymbol{k}_1-\boldsymbol{k}_3-\boldsymbol{k}_5} \\
&-C^{\hat\alpha^\dagger\hat\alpha\hat\alpha\hat\beta}_{\boldsymbol{k}_1,\boldsymbol{k}_3,\boldsymbol{k}_5,-\boldsymbol{k}_2+\boldsymbol{k}_4-\boldsymbol{k}_5} C^{\hat\alpha^\dagger\hat\alpha^\dagger\hat\alpha\hat\beta^\dagger}_{\boldsymbol{k}_2,\boldsymbol{k}_5,\boldsymbol{k}_4,-\boldsymbol{k}_2+\boldsymbol{k}_4-\boldsymbol{k}_5} \\
&-C^{\hat\alpha^\dagger\hat\alpha\hat\alpha\hat\beta}_{\boldsymbol{k}_1,\boldsymbol{k}_4,\boldsymbol{k}_5,\boldsymbol{k}_1-\boldsymbol{k}_4-\boldsymbol{k}_5} C^{\hat\alpha^\dagger\hat\alpha^\dagger\hat\alpha\hat\beta^\dagger}_{\boldsymbol{k}_2,\boldsymbol{k}_5,\boldsymbol{k}_3,\boldsymbol{k}_1-\boldsymbol{k}_4-\boldsymbol{k}_5} \\
&-C^{\hat\alpha^\dagger\hat\alpha\hat\alpha\hat\beta}_{\boldsymbol{k}_1,\boldsymbol{k}_4,\boldsymbol{k}_5,-\boldsymbol{k}_2+\boldsymbol{k}_3-\boldsymbol{k}_5} C^{\hat\alpha^\dagger\hat\alpha^\dagger\hat\alpha\hat\beta^\dagger}_{\boldsymbol{k}_2,\boldsymbol{k}_5,\boldsymbol{k}_3,-\boldsymbol{k}_2+\boldsymbol{k}_3-\boldsymbol{k}_5} \\
&-C^{\hat\alpha^\dagger\hat\alpha\hat\alpha\hat\beta}_{\boldsymbol{k}_2,\boldsymbol{k}_3,\boldsymbol{k}_5,-\boldsymbol{k}_1+\boldsymbol{k}_4-\boldsymbol{k}_5} C^{\hat\alpha^\dagger\hat\alpha^\dagger\hat\alpha\hat\beta^\dagger}_{\boldsymbol{k}_1,\boldsymbol{k}_5,\boldsymbol{k}_4,-\boldsymbol{k}_1+\boldsymbol{k}_4-\boldsymbol{k}_5} \\
&-C^{\hat\alpha^\dagger\hat\alpha\hat\alpha\hat\beta}_{\boldsymbol{k}_2,\boldsymbol{k}_3,\boldsymbol{k}_5,\boldsymbol{k}_2-\boldsymbol{k}_3-\boldsymbol{k}_5} C^{\hat\alpha^\dagger\hat\alpha^\dagger\hat\alpha\hat\beta^\dagger}_{\boldsymbol{k}_1,\boldsymbol{k}_5,\boldsymbol{k}_4,\boldsymbol{k}_2-\boldsymbol{k}_3-\boldsymbol{k}_5} \\
&-C^{\hat\alpha^\dagger\hat\alpha\hat\alpha\hat\beta}_{\boldsymbol{k}_2,\boldsymbol{k}_4,\boldsymbol{k}_5,-\boldsymbol{k}_1+\boldsymbol{k}_3-\boldsymbol{k}_5} C^{\hat\alpha^\dagger\hat\alpha^\dagger\hat\alpha\hat\beta^\dagger}_{\boldsymbol{k}_1,\boldsymbol{k}_5,\boldsymbol{k}_3,-\boldsymbol{k}_1+\boldsymbol{k}_3-\boldsymbol{k}_5} \\
&-C^{\hat\alpha^\dagger\hat\alpha\hat\alpha\hat\beta}_{\boldsymbol{k}_2,\boldsymbol{k}_4,\boldsymbol{k}_5,\boldsymbol{k}_2-\boldsymbol{k}_4-\boldsymbol{k}_5} C^{\hat\alpha^\dagger\hat\alpha^\dagger\hat\alpha\hat\beta^\dagger}_{\boldsymbol{k}_1,\boldsymbol{k}_5,\boldsymbol{k}_3,\boldsymbol{k}_2-\boldsymbol{k}_4-\boldsymbol{k}_5} \\
&-4C^{\hat\alpha\hat\alpha\hat\beta\hat\beta}_{\boldsymbol{k}_3,\boldsymbol{k}_4,\boldsymbol{k}_5,-\boldsymbol{k}_3-\boldsymbol{k}_4-\boldsymbol{k}_5} C^{\hat\alpha^\dagger\hat\alpha^\dagger\hat\beta^\dagger\hat\beta^\dagger}_{\boldsymbol{k}_1,\boldsymbol{k}_2,\boldsymbol{k}_5,-\boldsymbol{k}_3-\boldsymbol{k}_4-\boldsymbol{k}_5} ,
\end{aligned}
\tag{B.6}
$$

$$
\begin{aligned}
\partial_\ell C^{\hat\alpha^\dagger\hat\alpha^\dagger\hat\alpha\hat\beta^\dagger}_{\boldsymbol{k}_1,\boldsymbol{k}_2,\boldsymbol{k}_3,\boldsymbol{k}_4} = &-4C^{\hat\alpha\hat\beta}_{\boldsymbol{k}_3,-\boldsymbol{k}_3} C^{\hat\alpha^\dagger\hat\alpha^\dagger\hat\beta^\dagger\hat\beta^\dagger}_{\boldsymbol{k}_1,\boldsymbol{k}_2,-\boldsymbol{k}_3,\boldsymbol{k}_4} \\
&-C^{\hat\alpha^\dagger\hat\alpha}_{\boldsymbol{k}_1,-\boldsymbol{k}_2+\boldsymbol{k}_3-\boldsymbol{k}_4} C^{\hat\alpha^\dagger\hat\alpha^\dagger\hat\alpha\hat\beta^\dagger}_{\boldsymbol{k}_2,-\boldsymbol{k}_2+\boldsymbol{k}_3-\boldsymbol{k}_4,\boldsymbol{k}_3,\boldsymbol{k}_4} \\
&-C^{\hat\alpha^\dagger\hat\alpha}_{\boldsymbol{k}_2,-\boldsymbol{k}_1+\boldsymbol{k}_3-\boldsymbol{k}_4} C^{\hat\alpha^\dagger\hat\alpha^\dagger\hat\alpha\hat\beta^\dagger}_{\boldsymbol{k}_1,-\boldsymbol{k}_1+\boldsymbol{k}_3-\boldsymbol{k}_4,\boldsymbol{k}_3,\boldsymbol{k}_4} \\
&+C^{\hat\alpha^\dagger\hat\alpha}_{\boldsymbol{k}_3,\boldsymbol{k}_3} C^{\hat\alpha^\dagger\hat\alpha^\dagger\hat\alpha\hat\beta^\dagger}_{\boldsymbol{k}_1,\boldsymbol{k}_2,\boldsymbol{k}_3,\boldsymbol{k}_4} \\
&-\frac{1}{2}C^{\hat\alpha^\dagger\hat\beta^\dagger}_{\boldsymbol{k}_1,-\boldsymbol{k}_1} C^{\hat\alpha^\dagger\hat\alpha\hat\beta^\dagger\hat\beta}_{\boldsymbol{k}_2,\boldsymbol{k}_3,\boldsymbol{k}_4,-\boldsymbol{k}_1} \\
&-\frac{1}{2}C^{\hat\alpha^\dagger\hat\beta^\dagger}_{\boldsymbol{k}_2,-\boldsymbol{k}_2} C^{\hat\alpha^\dagger\hat\alpha\hat\beta^\dagger\hat\beta}_{\boldsymbol{k}_1,\boldsymbol{k}_3,\boldsymbol{k}_4,-\boldsymbol{k}_2} \\
&-2C^{\hat\alpha^\dagger\hat\beta^\dagger}_{-\boldsymbol{k}_4,\boldsymbol{k}_4} C^{\hat\alpha^\dagger\hat\alpha^\dagger\hat\alpha\hat\alpha}_{\boldsymbol{k}_1,\boldsymbol{k}_2,\boldsymbol{k}_3,-\boldsymbol{k}_4} \\
&-C^{\hat\beta^\dagger\hat\beta}_{\boldsymbol{k}_4,\boldsymbol{k}_4} C^{\hat\alpha^\dagger\hat\alpha^\dagger\hat\alpha\hat\beta^\dagger}_{\boldsymbol{k}_1,\boldsymbol{k}_2,\boldsymbol{k}_3,\boldsymbol{k}_4} \\
&-C^{\hat\alpha^\dagger\hat\alpha\hat\beta^\dagger\hat\beta}_{\boldsymbol{k}_1,\boldsymbol{k}_5,\boldsymbol{k}_4,-\boldsymbol{k}_2+\boldsymbol{k}_3-\boldsymbol{k}_5} C^{\hat\alpha^\dagger\hat\alpha^\dagger\hat\alpha\hat\beta^\dagger}_{\boldsymbol{k}_2,\boldsymbol{k}_5,\boldsymbol{k}_3,-\boldsymbol{k}_2+\boldsymbol{k}_3-\boldsymbol{k}_5} \\
&-C^{\hat\alpha^\dagger\hat\alpha\hat\beta^\dagger\hat\beta}_{\boldsymbol{k}_2,\boldsymbol{k}_5,\boldsymbol{k}_4,-\boldsymbol{k}_1+\boldsymbol{k}_3-\boldsymbol{k}_5} C^{\hat\alpha^\dagger\hat\alpha^\dagger\hat\alpha\hat\beta^\dagger}_{\boldsymbol{k}_1,\boldsymbol{k}_5,\boldsymbol{k}_3,-\boldsymbol{k}_1+\boldsymbol{k}_3-\boldsymbol{k}_5} \\
&-\{2|4\}\, C^{\hat\alpha\hat\beta^\dagger\hat\beta\hat\beta}_{\boldsymbol{k}_3,\boldsymbol{k}_4,\boldsymbol{k}_5,-\boldsymbol{k}_3+\boldsymbol{k}_4-\boldsymbol{k}_5} C^{\hat\alpha^\dagger\hat\alpha^\dagger\hat\beta^\dagger\hat\beta^\dagger}_{\boldsymbol{k}_1,\boldsymbol{k}_2,\boldsymbol{k}_5,-\boldsymbol{k}_3+\boldsymbol{k}_4-\boldsymbol{k}_5} \\
&-4C^{\hat\alpha^\dagger\hat\alpha\hat\alpha\hat\beta}_{\boldsymbol{k}_1,\boldsymbol{k}_3,\boldsymbol{k}_5,\boldsymbol{k}_1-\boldsymbol{k}_3-\boldsymbol{k}_5} C^{\hat\alpha^\dagger\hat\alpha^\dagger\hat\beta^\dagger\hat\beta^\dagger}_{\boldsymbol{k}_2,\boldsymbol{k}_5,\boldsymbol{k}_4,\boldsymbol{k}_1-\boldsymbol{k}_3-\boldsymbol{k}_5} \\
&-4C^{\hat\alpha^\dagger\hat\alpha\hat\alpha\hat\beta}_{\boldsymbol{k}_1,\boldsymbol{k}_3,\boldsymbol{k}_5,-\boldsymbol{k}_2-\boldsymbol{k}_4-\boldsymbol{k}_5} C^{\hat\alpha^\dagger\hat\alpha^\dagger\hat\beta^\dagger\hat\beta^\dagger}_{\boldsymbol{k}_2,\boldsymbol{k}_5,\boldsymbol{k}_4,-\boldsymbol{k}_2-\boldsymbol{k}_4-\boldsymbol{k}_5} \\
&-4C^{\hat\alpha^\dagger\hat\alpha\hat\alpha\hat\beta}_{\boldsymbol{k}_2,\boldsymbol{k}_3,\boldsymbol{k}_5,-\boldsymbol{k}_1-\boldsymbol{k}_4-\boldsymbol{k}_5} C^{\hat\alpha^\dagger\hat\alpha^\dagger\hat\beta^\dagger\hat\beta^\dagger}_{\boldsymbol{k}_1,\boldsymbol{k}_5,\boldsymbol{k}_4,-\boldsymbol{k}_1-\boldsymbol{k}_4-\boldsymbol{k}_5} \\
&-4C^{\hat\alpha^\dagger\hat\alpha\hat\alpha\hat\beta}_{\boldsymbol{k}_2,\boldsymbol{k}_3,\boldsymbol{k}_5,\boldsymbol{k}_2-\boldsymbol{k}_3-\boldsymbol{k}_5} C^{\hat\alpha^\dagger\hat\alpha^\dagger\hat\beta^\dagger\hat\beta^\dagger}_{\boldsymbol{k}_1,\boldsymbol{k}_5,\boldsymbol{k}_4,\boldsymbol{k}_2-\boldsymbol{k}_3-\boldsymbol{k}_5} \\
&-2C^{\hat\alpha^\dagger\hat\alpha^\dagger\hat\alpha\hat\beta^\dagger}_{\boldsymbol{k}_5,\boldsymbol{k}_3-\boldsymbol{k}_4-\boldsymbol{k}_5,\boldsymbol{k}_3,\boldsymbol{k}_4} C^{\hat\alpha^\dagger\hat\alpha^\dagger\hat\alpha\hat\alpha}_{\boldsymbol{k}_1,\boldsymbol{k}_2,\boldsymbol{k}_5,\boldsymbol{k}_3-\boldsymbol{k}_4-\boldsymbol{k}_5}\ ,
\end{aligned}
\tag{B.7}
$$

$$
\begin{aligned}
\partial_\ell C^{\hat\alpha^\dagger\hat\alpha^\dagger\hat\beta^\dagger\hat\beta^\dagger}_{\boldsymbol{k}_1,\boldsymbol{k}_2,\boldsymbol{k}_3,\boldsymbol{k}_4} = &- C^{\hat\alpha^\dagger\hat\alpha}_{\boldsymbol{k}_1,-\boldsymbol{k}_2-\boldsymbol{k}_3-\boldsymbol{k}_4} C^{\hat\alpha^\dagger\hat\alpha^\dagger\hat\beta^\dagger\hat\beta^\dagger}_{\boldsymbol{k}_2,-\boldsymbol{k}_2-\boldsymbol{k}_3-\boldsymbol{k}_4,\boldsymbol{k}_3,\boldsymbol{k}_4} \\
&- C^{\hat\alpha^\dagger\hat\alpha}_{\boldsymbol{k}_2,-\boldsymbol{k}_1-\boldsymbol{k}_3-\boldsymbol{k}_4} C^{\hat\alpha^\dagger\hat\alpha^\dagger\hat\beta^\dagger\hat\beta^\dagger}_{\boldsymbol{k}_1,-\boldsymbol{k}_1-\boldsymbol{k}_3-\boldsymbol{k}_4,\boldsymbol{k}_3,\boldsymbol{k}_4} \\
&- \frac{1}{2} C^{\hat\alpha^\dagger\hat\beta^\dagger}_{\boldsymbol{k}_1,-\boldsymbol{k}_1} C^{\hat\alpha^\dagger\hat\beta^\dagger\hat\beta^\dagger\hat\beta}_{\boldsymbol{k}_2,\boldsymbol{k}_3,\boldsymbol{k}_4,-\boldsymbol{k}_1} \\
&- \frac{1}{2} C^{\hat\alpha^\dagger\hat\beta^\dagger}_{\boldsymbol{k}_2,-\boldsymbol{k}_2} C^{\hat\alpha^\dagger\hat\beta^\dagger\hat\beta^\dagger\hat\beta}_{\boldsymbol{k}_1,\boldsymbol{k}_3,\boldsymbol{k}_4,-\boldsymbol{k}_2} \\
&- \frac{1}{2} C^{\hat\alpha^\dagger\hat\beta^\dagger}_{-\boldsymbol{k}_3,\boldsymbol{k}_3} C^{\hat\alpha^\dagger\hat\alpha^\dagger\hat\alpha\hat\beta^\dagger}_{\boldsymbol{k}_1,\boldsymbol{k}_2,-\boldsymbol{k}_3,\boldsymbol{k}_4} \\
&- \frac{1}{2} C^{\hat\alpha^\dagger\hat\beta^\dagger}_{-\boldsymbol{k}_4,\boldsymbol{k}_4} C^{\hat\alpha^\dagger\hat\alpha^\dagger\hat\alpha\hat\beta^\dagger}_{\boldsymbol{k}_1,\boldsymbol{k}_2,-\boldsymbol{k}_4,\boldsymbol{k}_3} \\
&- C^{\hat\beta^\dagger\hat\beta}_{\boldsymbol{k}_3,\boldsymbol{k}_3} C^{\hat\alpha^\dagger\hat\alpha^\dagger\hat\beta^\dagger\hat\beta^\dagger}_{\boldsymbol{k}_1,\boldsymbol{k}_2,\boldsymbol{k}_3,\boldsymbol{k}_4} \\
&- C^{\hat\beta^\dagger\hat\beta}_{\boldsymbol{k}_4,\boldsymbol{k}_4} C^{\hat\alpha^\dagger\hat\alpha^\dagger\hat\beta^\dagger\hat\beta^\dagger}_{\boldsymbol{k}_1,\boldsymbol{k}_2,\boldsymbol{k}_3,\boldsymbol{k}_4} \\
&- C^{\hat\alpha^\dagger\hat\alpha\hat\beta^\dagger\hat\beta}_{\boldsymbol{k}_1,\boldsymbol{k}_5,\boldsymbol{k}_3,-\boldsymbol{k}_2-\boldsymbol{k}_4-\boldsymbol{k}_5} C^{\hat\alpha^\dagger\hat\alpha^\dagger\hat\beta^\dagger\hat\beta^\dagger}_{\boldsymbol{k}_2,\boldsymbol{k}_5,\boldsymbol{k}_4,-\boldsymbol{k}_2-\boldsymbol{k}_4-\boldsymbol{k}_5} \\
&- C^{\hat\alpha^\dagger\hat\alpha\hat\beta^\dagger\hat\beta}_{\boldsymbol{k}_1,\boldsymbol{k}_5,\boldsymbol{k}_4,-\boldsymbol{k}_2-\boldsymbol{k}_3-\boldsymbol{k}_5} C^{\hat\alpha^\dagger\hat\alpha^\dagger\hat\beta^\dagger\hat\beta^\dagger}_{\boldsymbol{k}_2,\boldsymbol{k}_5,\boldsymbol{k}_3,-\boldsymbol{k}_2-\boldsymbol{k}_3-\boldsymbol{k}_5} \\
&- C^{\hat\alpha^\dagger\hat\alpha\hat\beta^\dagger\hat\beta}_{\boldsymbol{k}_2,\boldsymbol{k}_5,\boldsymbol{k}_3,-\boldsymbol{k}_1-\boldsymbol{k}_4-\boldsymbol{k}_5} C^{\hat\alpha^\dagger\hat\alpha^\dagger\hat\beta^\dagger\hat\beta^\dagger}_{\boldsymbol{k}_1,\boldsymbol{k}_5,\boldsymbol{k}_4,-\boldsymbol{k}_1-\boldsymbol{k}_4-\boldsymbol{k}_5} \\
&- C^{\hat\alpha^\dagger\hat\alpha\hat\beta^\dagger\hat\beta}_{\boldsymbol{k}_2,\boldsymbol{k}_5,\boldsymbol{k}_4,-\boldsymbol{k}_1-\boldsymbol{k}_3-\boldsymbol{k}_5} C^{\hat\alpha^\dagger\hat\alpha^\dagger\hat\beta^\dagger\hat\beta^\dagger}_{\boldsymbol{k}_1,\boldsymbol{k}_5,\boldsymbol{k}_3,-\boldsymbol{k}_1-\boldsymbol{k}_3-\boldsymbol{k}_5} \\
&- 2C^{\hat\alpha^\dagger\hat\alpha^\dagger\hat\alpha\hat\alpha}_{\boldsymbol{k}_1,\boldsymbol{k}_2,\boldsymbol{k}_5,-\boldsymbol{k}_3-\boldsymbol{k}_4-\boldsymbol{k}_5} C^{\hat\alpha^\dagger\hat\alpha^\dagger\hat\beta^\dagger\hat\beta^\dagger}_{\boldsymbol{k}_5,-\boldsymbol{k}_3-\boldsymbol{k}_4-\boldsymbol{k}_5,\boldsymbol{k}_3,\boldsymbol{k}_4} \\
&- 2C^{\hat\alpha^\dagger\hat\alpha^\dagger\hat\beta^\dagger\hat\beta^\dagger}_{\boldsymbol{k}_1,\boldsymbol{k}_2,\boldsymbol{k}_5,\boldsymbol{k}_3+\boldsymbol{k}_4-\boldsymbol{k}_5} C^{\hat\beta^\dagger\hat\beta^\dagger\hat\beta\hat\beta}_{\boldsymbol{k}_3,\boldsymbol{k}_4,\boldsymbol{k}_5,\boldsymbol{k}_3+\boldsymbol{k}_4-\boldsymbol{k}_5} ,
\end{aligned}
\tag{B.8}
$$

$$
\begin{aligned}
\partial_\ell C^{\hat\alpha^\dagger\hat\alpha\hat\alpha\hat\beta}_{\boldsymbol{k}_1,\boldsymbol{k}_2,\boldsymbol{k}_3,\boldsymbol{k}_4} = &- \frac{1}{2} C^{\hat\alpha\hat\beta}_{\boldsymbol{k}_2,-\boldsymbol{k}_2} C^{\hat\alpha^\dagger\hat\alpha\hat\beta^\dagger\hat\beta}_{\boldsymbol{k}_1,\boldsymbol{k}_3,-\boldsymbol{k}_2,\boldsymbol{k}_4} \\
&- \frac{1}{2} C^{\hat\alpha\hat\beta}_{\boldsymbol{k}_3,-\boldsymbol{k}_3} C^{\hat\alpha^\dagger\hat\alpha\hat\beta^\dagger\hat\beta}_{\boldsymbol{k}_1,\boldsymbol{k}_2,-\boldsymbol{k}_3,\boldsymbol{k}_4} \\
&- 2C^{\hat\alpha\hat\beta}_{-\boldsymbol{k}_4,\boldsymbol{k}_4} C^{\hat\alpha^\dagger\hat\alpha^\dagger\hat\alpha\hat\alpha}_{\boldsymbol{k}_1,-\boldsymbol{k}_4,\boldsymbol{k}_2,\boldsymbol{k}_3} \\
&+ C^{\hat\alpha^\dagger\hat\alpha}_{\boldsymbol{k}_1,\boldsymbol{k}_2+\boldsymbol{k}_3+\boldsymbol{k}_4} C^{\hat\alpha^\dagger\hat\alpha\hat\alpha\hat\beta}_{\boldsymbol{k}_2+\boldsymbol{k}_3+\boldsymbol{k}_4,\boldsymbol{k}_2,\boldsymbol{k}_3,\boldsymbol{k}_4} \\
&- C^{\hat\alpha^\dagger\hat\alpha}_{\boldsymbol{k}_2,\boldsymbol{k}_2} C^{\hat\alpha^\dagger\hat\alpha\hat\alpha\hat\beta}_{\boldsymbol{k}_1,\boldsymbol{k}_2,\boldsymbol{k}_3,\boldsymbol{k}_4} \\
&- C^{\hat\alpha^\dagger\hat\alpha}_{\boldsymbol{k}_3,\boldsymbol{k}_3} C^{\hat\alpha^\dagger\hat\alpha\hat\alpha\hat\beta}_{\boldsymbol{k}_1,\boldsymbol{k}_2,\boldsymbol{k}_3,\boldsymbol{k}_4} \\
&- 4C^{\hat\alpha^\dagger\hat\beta^\dagger}_{\boldsymbol{k}_1,-\boldsymbol{k}_2-\boldsymbol{k}_3-\boldsymbol{k}_4} C^{\hat\alpha\hat\alpha\hat\beta\hat\beta}_{\boldsymbol{k}_2,\boldsymbol{k}_3,\boldsymbol{k}_4,-\boldsymbol{k}_2-\boldsymbol{k}_3-\boldsymbol{k}_4} \\
&- C^{\hat\beta^\dagger\hat\beta}_{\boldsymbol{k}_4,\boldsymbol{k}_4} C^{\hat\alpha^\dagger\hat\alpha\hat\alpha\hat\beta}_{\boldsymbol{k}_1,\boldsymbol{k}_2,\boldsymbol{k}_3,\boldsymbol{k}_4} \\
&- C^{\hat\alpha^\dagger\hat\alpha\hat\beta^\dagger\hat\beta}_{\boldsymbol{k}_5,\boldsymbol{k}_2,\boldsymbol{k}_2+\boldsymbol{k}_4-\boldsymbol{k}_5,\boldsymbol{k}_4} C^{\hat\alpha^\dagger\hat\alpha\hat\alpha\hat\beta}_{\boldsymbol{k}_1,\boldsymbol{k}_3,\boldsymbol{k}_5,\boldsymbol{k}_2+\boldsymbol{k}_4-\boldsymbol{k}_5} \\
&- C^{\hat\alpha^\dagger\hat\alpha\hat\beta^\dagger\hat\beta}_{\boldsymbol{k}_5,\boldsymbol{k}_3,\boldsymbol{k}_3+\boldsymbol{k}_4-\boldsymbol{k}_5,\boldsymbol{k}_4} C^{\hat\alpha^\dagger\hat\alpha\hat\alpha\hat\beta}_{\boldsymbol{k}_1,\boldsymbol{k}_2,\boldsymbol{k}_5,\boldsymbol{k}_3+\boldsymbol{k}_4-\boldsymbol{k}_5} \\
&- 2C^{\hat\alpha^\dagger\hat\alpha\hat\alpha\hat\beta}_{\boldsymbol{k}_1,\boldsymbol{k}_5,\boldsymbol{k}_2+\boldsymbol{k}_3-\boldsymbol{k}_5,\boldsymbol{k}_4} C^{\hat\alpha^\dagger\hat\alpha^\dagger\hat\alpha\hat\alpha}_{\boldsymbol{k}_5,\boldsymbol{k}_2+\boldsymbol{k}_3-\boldsymbol{k}_5,\boldsymbol{k}_2,\boldsymbol{k}_3} \\
&- \{2|4\}\, C^{\hat\alpha^\dagger\hat\beta^\dagger\hat\beta^\dagger\hat\beta}_{\boldsymbol{k}_1,\boldsymbol{k}_5,-\boldsymbol{k}_2-\boldsymbol{k}_3-\boldsymbol{k}_5,\boldsymbol{k}_4} C^{\hat\alpha\hat\alpha\hat\beta\hat\beta}_{\boldsymbol{k}_2,\boldsymbol{k}_3,\boldsymbol{k}_5,-\boldsymbol{k}_2-\boldsymbol{k}_3-\boldsymbol{k}_5} \\
&- \{4|8\}\, C^{\hat\alpha^\dagger\hat\alpha^\dagger\hat\alpha\hat\beta^\dagger}_{\boldsymbol{k}_1,\boldsymbol{k}_5,\boldsymbol{k}_2,-\boldsymbol{k}_3-\boldsymbol{k}_4-\boldsymbol{k}_5} C^{\hat\alpha\hat\alpha\hat\beta\hat\beta}_{\boldsymbol{k}_3,\boldsymbol{k}_5,\boldsymbol{k}_4,-\boldsymbol{k}_3-\boldsymbol{k}_4-\boldsymbol{k}_5} \\
&- \{4|8\}\, C^{\hat\alpha^\dagger\hat\alpha^\dagger\hat\alpha\hat\beta^\dagger}_{\boldsymbol{k}_1,\boldsymbol{k}_5,\boldsymbol{k}_3,-\boldsymbol{k}_2-\boldsymbol{k}_4-\boldsymbol{k}_5} C^{\hat\alpha\hat\alpha\hat\beta\hat\beta}_{\boldsymbol{k}_2,\boldsymbol{k}_5,\boldsymbol{k}_4,-\boldsymbol{k}_2-\boldsymbol{k}_4-\boldsymbol{k}_5} ,
\end{aligned}
\tag{B.9}
$$

$$
\begin{aligned}
\partial_\ell C^{\hat\alpha^\dagger\hat\alpha\hat\beta^\dagger\hat\beta}_{\boldsymbol{k}_1,\boldsymbol{k}_2,\boldsymbol{k}_3,\boldsymbol{k}_4} = &- \{2|4\}\, C^{\hat\alpha\hat\beta}_{\boldsymbol{k}_2,-\boldsymbol{k}_2} C^{\hat\alpha^\dagger\hat\beta^\dagger\hat\beta^\dagger\hat\beta}_{\boldsymbol{k}_1,-\boldsymbol{k}_2,\boldsymbol{k}_3,\boldsymbol{k}_4} \\
&- \{2|4\}\, C^{\hat\alpha\hat\beta}_{-\boldsymbol{k}_4,\boldsymbol{k}_4} C^{\hat\alpha^\dagger\hat\alpha^\dagger\hat\alpha\hat\beta^\dagger}_{\boldsymbol{k}_1,-\boldsymbol{k}_4,\boldsymbol{k}_2,\boldsymbol{k}_3} \\
&- \{2|4\}\, C^{\hat\alpha^\dagger\hat\beta^\dagger}_{\boldsymbol{k}_1,-\boldsymbol{k}_2+\boldsymbol{k}_3-\boldsymbol{k}_4} C^{\hat\alpha\hat\beta^\dagger\hat\beta\hat\beta}_{\boldsymbol{k}_2,\boldsymbol{k}_3,\boldsymbol{k}_4,-\boldsymbol{k}_2+\boldsymbol{k}_3-\boldsymbol{k}_4} \\
&- \{2|4\}\, C^{\hat\alpha^\dagger\hat\beta^\dagger}_{-\boldsymbol{k}_3,\boldsymbol{k}_3} C^{\hat\alpha^\dagger\hat\alpha\hat\alpha\hat\beta}_{\boldsymbol{k}_1,\boldsymbol{k}_2,-\boldsymbol{k}_3,\boldsymbol{k}_4} \\
&- 4C^{\hat\alpha\hat\beta^\dagger\hat\beta\hat\beta}_{\boldsymbol{k}_2,\boldsymbol{k}_3,\boldsymbol{k}_5,-\boldsymbol{k}_2+\boldsymbol{k}_3-\boldsymbol{k}_5} C^{\hat\alpha^\dagger\hat\beta^\dagger\hat\beta^\dagger\hat\beta}_{\boldsymbol{k}_1,\boldsymbol{k}_5,-\boldsymbol{k}_2+\boldsymbol{k}_3-\boldsymbol{k}_5,\boldsymbol{k}_4} \\
&- 8C^{\hat\alpha\hat\beta^\dagger\hat\beta\hat\beta}_{\boldsymbol{k}_5,\boldsymbol{k}_3,\boldsymbol{k}_4,\boldsymbol{k}_3-\boldsymbol{k}_4-\boldsymbol{k}_5} C^{\hat\alpha^\dagger\hat\alpha^\dagger\hat\alpha\hat\beta^\dagger}_{\boldsymbol{k}_1,\boldsymbol{k}_5,\boldsymbol{k}_2,\boldsymbol{k}_3-\boldsymbol{k}_4-\boldsymbol{k}_5} \\
&- 8C^{\hat\alpha^\dagger\hat\alpha\hat\alpha\hat\beta}_{\boldsymbol{k}_1,\boldsymbol{k}_2,\boldsymbol{k}_5,-\boldsymbol{k}_3+\boldsymbol{k}_4-\boldsymbol{k}_5} C^{\hat\alpha^\dagger\hat\beta^\dagger\hat\beta^\dagger\hat\beta}_{\boldsymbol{k}_5,\boldsymbol{k}_3,-\boldsymbol{k}_3+\boldsymbol{k}_4-\boldsymbol{k}_5,\boldsymbol{k}_4} \\
&- 4C^{\hat\alpha^\dagger\hat\alpha\hat\alpha\hat\beta}_{\boldsymbol{k}_1,\boldsymbol{k}_5,\boldsymbol{k}_2-\boldsymbol{k}_3-\boldsymbol{k}_5,\boldsymbol{k}_4} C^{\hat\alpha^\dagger\hat\alpha^\dagger\hat\alpha\hat\beta^\dagger}_{\boldsymbol{k}_5,\boldsymbol{k}_2-\boldsymbol{k}_3-\boldsymbol{k}_5,\boldsymbol{k}_2,\boldsymbol{k}_3} \\
&- 32C^{\hat\alpha\hat\alpha\hat\beta\hat\beta\hat\beta}_{\boldsymbol{k}_2,\boldsymbol{k}_5,\boldsymbol{k}_4,-\boldsymbol{k}_2-\boldsymbol{k}_4-\boldsymbol{k}_5} C^{\hat\alpha^\dagger\hat\alpha^\dagger\hat\beta^\dagger\hat\beta^\dagger}_{\boldsymbol{k}_1,\boldsymbol{k}_5,\boldsymbol{k}_3,-\boldsymbol{k}_2-\boldsymbol{k}_4-\boldsymbol{k}_5}\,, \\
\partial_\ell C^{\hat\alpha^\dagger\hat\beta^\dagger\hat\beta^\dagger\hat\beta}_{\boldsymbol{k}_1,\boldsymbol{k}_2,\boldsymbol{k}_3,\boldsymbol{k}_4} = &- 4C^{\hat\alpha\hat\beta}_{-\boldsymbol{k}_4,\boldsymbol{k}_4} C^{\hat\alpha^\dagger\hat\alpha^\dagger\hat\beta^\dagger\hat\beta^\dagger}_{\boldsymbol{k}_1,-\boldsymbol{k}_4,\boldsymbol{k}_2,\boldsymbol{k}_3} \\
&- C^{\hat\alpha^\dagger\hat\alpha}_{\boldsymbol{k}_1,-\boldsymbol{k}_2-\boldsymbol{k}_3+\boldsymbol{k}_4} C^{\hat\alpha^\dagger\hat\beta^\dagger\hat\beta^\dagger\hat\beta}_{-\boldsymbol{k}_2-\boldsymbol{k}_3+\boldsymbol{k}_4,\boldsymbol{k}_2,\boldsymbol{k}_3,\boldsymbol{k}_4} \\
&- 2C^{\hat\alpha^\dagger\hat\beta^\dagger}_{\boldsymbol{k}_1,\boldsymbol{k}_2+\boldsymbol{k}_3-\boldsymbol{k}_4} C^{\hat\beta^\dagger\hat\beta^\dagger\hat\beta\hat\beta}_{\boldsymbol{k}_2,\boldsymbol{k}_3,\boldsymbol{k}_4,\boldsymbol{k}_2+\boldsymbol{k}_3-\boldsymbol{k}_4} \\
&- \frac{1}{2} C^{\hat\alpha^\dagger\hat\beta^\dagger}_{-\boldsymbol{k}_2,\boldsymbol{k}_2} C^{\hat\alpha^\dagger\hat\alpha\hat\beta^\dagger\hat\beta}_{\boldsymbol{k}_1,-\boldsymbol{k}_2,\boldsymbol{k}_3,\boldsymbol{k}_4} \\
&- \frac{1}{2} C^{\hat\alpha^\dagger\hat\beta^\dagger}_{-\boldsymbol{k}_3,\boldsymbol{k}_3} C^{\hat\alpha^\dagger\hat\alpha\hat\beta^\dagger\hat\beta}_{\boldsymbol{k}_1,-\boldsymbol{k}_3,\boldsymbol{k}_2,\boldsymbol{k}_4} \\
&- C^{\hat\beta^\dagger\hat\beta}_{\boldsymbol{k}_2,\boldsymbol{k}_2} C^{\hat\alpha^\dagger\hat\beta^\dagger\hat\beta^\dagger\hat\beta}_{\boldsymbol{k}_1,\boldsymbol{k}_2,\boldsymbol{k}_3,\boldsymbol{k}_4} \\
&- C^{\hat\beta^\dagger\hat\beta}_{\boldsymbol{k}_3,\boldsymbol{k}_3} C^{\hat\alpha^\dagger\hat\beta^\dagger\hat\beta^\dagger\hat\beta}_{\boldsymbol{k}_1,\boldsymbol{k}_2,\boldsymbol{k}_3,\boldsymbol{k}_4} \\
&+ C^{\hat\beta^\dagger\hat\beta}_{\boldsymbol{k}_4,\boldsymbol{k}_4} C^{\hat\alpha^\dagger\hat\beta^\dagger\hat\beta^\dagger\hat\beta}_{\boldsymbol{k}_1,\boldsymbol{k}_2,\boldsymbol{k}_3,\boldsymbol{k}_4} \\
&- C^{\hat\alpha^\dagger\hat\alpha\hat\beta^\dagger\hat\beta}_{\boldsymbol{k}_1,\boldsymbol{k}_5,\boldsymbol{k}_2,-\boldsymbol{k}_3+\boldsymbol{k}_4-\boldsymbol{k}_5} C^{\hat\alpha^\dagger\hat\beta^\dagger\hat\beta^\dagger\hat\beta}_{\boldsymbol{k}_5,\boldsymbol{k}_3,-\boldsymbol{k}_3+\boldsymbol{k}_4-\boldsymbol{k}_5,\boldsymbol{k}_4} \\
&- C^{\hat\alpha^\dagger\hat\alpha\hat\beta^\dagger\hat\beta}_{\boldsymbol{k}_1,\boldsymbol{k}_5,\boldsymbol{k}_3,-\boldsymbol{k}_2+\boldsymbol{k}_4-\boldsymbol{k}_5} C^{\hat\alpha^\dagger\hat\beta^\dagger\hat\beta^\dagger\hat\beta}_{\boldsymbol{k}_5,\boldsymbol{k}_2,-\boldsymbol{k}_2+\boldsymbol{k}_4-\boldsymbol{k}_5,\boldsymbol{k}_4} \\
&- \{4|8\}\, C^{\hat\alpha\hat\beta^\dagger\hat\beta\hat\beta}_{\boldsymbol{k}_5,\boldsymbol{k}_2,\boldsymbol{k}_4,\boldsymbol{k}_2-\boldsymbol{k}_4-\boldsymbol{k}_5} C^{\hat\alpha^\dagger\hat\alpha^\dagger\hat\beta^\dagger\hat\beta^\dagger}_{\boldsymbol{k}_1,\boldsymbol{k}_5,\boldsymbol{k}_3,\boldsymbol{k}_2-\boldsymbol{k}_4-\boldsymbol{k}_5} \\
&- \{4|8\}\, C^{\hat\alpha\hat\beta^\dagger\hat\beta\hat\beta}_{\boldsymbol{k}_5,\boldsymbol{k}_3,\boldsymbol{k}_4,\boldsymbol{k}_3-\boldsymbol{k}_4-\boldsymbol{k}_5} C^{\hat\alpha^\dagger\hat\alpha^\dagger\hat\beta^\dagger\hat\beta^\dagger}_{\boldsymbol{k}_1,\boldsymbol{k}_5,\boldsymbol{k}_2,\boldsymbol{k}_3-\boldsymbol{k}_4-\boldsymbol{k}_5} \\
&- \{2|4\}\, C^{\hat\alpha^\dagger\hat\alpha\hat\alpha\hat\beta}_{\boldsymbol{k}_1,\boldsymbol{k}_5,-\boldsymbol{k}_2-\boldsymbol{k}_3-\boldsymbol{k}_5,\boldsymbol{k}_4} C^{\hat\alpha^\dagger\hat\alpha^\dagger\hat\beta^\dagger\hat\beta^\dagger}_{\boldsymbol{k}_5,-\boldsymbol{k}_2-\boldsymbol{k}_3-\boldsymbol{k}_5,\boldsymbol{k}_2,\boldsymbol{k}_3} \\
&- 2C^{\hat\alpha^\dagger\hat\beta^\dagger\hat\beta^\dagger\hat\beta}_{\boldsymbol{k}_1,\boldsymbol{k}_5,\boldsymbol{k}_2+\boldsymbol{k}_3-\boldsymbol{k}_5,\boldsymbol{k}_4} C^{\hat\beta^\dagger\hat\beta^\dagger\hat\beta\hat\beta}_{\boldsymbol{k}_2,\boldsymbol{k}_3,\boldsymbol{k}_5,\boldsymbol{k}_2+\boldsymbol{k}_3-\boldsymbol{k}_5}\,,
\end{aligned}
\tag{B.10}
\tag{B.11}
$$

$$
\begin{aligned}
\partial_\ell C^{\hat\alpha\hat\alpha\hat\beta\hat\beta}_{\boldsymbol{k}_1,\boldsymbol{k}_2,\boldsymbol{k}_3,\boldsymbol{k}_4} =& -\frac{1}{2} C^{\hat\alpha\hat\beta}_{\boldsymbol{k}_1,-\boldsymbol{k}_1} C^{\hat\alpha\hat\beta^\dagger\hat\beta\hat\beta}_{\boldsymbol{k}_2,-\boldsymbol{k}_1,\boldsymbol{k}_3,\boldsymbol{k}_4} \\
& -\frac{1}{2} C^{\hat\alpha\hat\beta}_{\boldsymbol{k}_2,-\boldsymbol{k}_2} C^{\hat\alpha\hat\beta^\dagger\hat\beta\hat\beta}_{\boldsymbol{k}_1,-\boldsymbol{k}_2,\boldsymbol{k}_3,\boldsymbol{k}_4} \\
& -\frac{1}{2} C^{\hat\alpha\hat\beta}_{-\boldsymbol{k}_3,\boldsymbol{k}_3} C^{\hat\alpha^\dagger\hat\alpha\hat\alpha\hat\beta}_{-\boldsymbol{k}_3,\boldsymbol{k}_1,\boldsymbol{k}_2,\boldsymbol{k}_4} \\
& -\frac{1}{2} C^{\hat\alpha\hat\beta}_{-\boldsymbol{k}_4,\boldsymbol{k}_4} C^{\hat\alpha^\dagger\hat\alpha\hat\alpha\hat\beta}_{-\boldsymbol{k}_4,\boldsymbol{k}_1,\boldsymbol{k}_2,\boldsymbol{k}_3} \\
& - C^{\hat\alpha^\dagger\hat\alpha}_{-\boldsymbol{k}_1-\boldsymbol{k}_3-\boldsymbol{k}_4,\boldsymbol{k}_2} C^{\hat\alpha\hat\alpha\hat\beta\hat\beta}_{\boldsymbol{k}_1,-\boldsymbol{k}_1-\boldsymbol{k}_3-\boldsymbol{k}_4,\boldsymbol{k}_3,\boldsymbol{k}_4} \\
& - C^{\hat\alpha^\dagger\hat\alpha}_{-\boldsymbol{k}_2-\boldsymbol{k}_3-\boldsymbol{k}_4,\boldsymbol{k}_1} C^{\hat\alpha\hat\alpha\hat\beta\hat\beta}_{\boldsymbol{k}_2,-\boldsymbol{k}_2-\boldsymbol{k}_3-\boldsymbol{k}_4,\boldsymbol{k}_3,\boldsymbol{k}_4} \\
& - C^{\hat\beta^\dagger\hat\beta}_{\boldsymbol{k}_3,\boldsymbol{k}_3} C^{\hat\alpha\hat\alpha\hat\beta\hat\beta}_{\boldsymbol{k}_1,\boldsymbol{k}_2,\boldsymbol{k}_3,\boldsymbol{k}_4} - C^{\hat\beta^\dagger\hat\beta}_{\boldsymbol{k}_4,\boldsymbol{k}_4} C^{\hat\alpha\hat\alpha\hat\beta\hat\beta}_{\boldsymbol{k}_1,\boldsymbol{k}_2,\boldsymbol{k}_3,\boldsymbol{k}_4} \\
& - C^{\hat\alpha^\dagger\hat\alpha\hat\beta^\dagger\hat\beta}_{\boldsymbol{k}_5,\boldsymbol{k}_1,-\boldsymbol{k}_2-\boldsymbol{k}_3-\boldsymbol{k}_5,\boldsymbol{k}_4} C^{\hat\alpha\hat\alpha\hat\beta\hat\beta}_{\boldsymbol{k}_2,\boldsymbol{k}_5,\boldsymbol{k}_3,-\boldsymbol{k}_2-\boldsymbol{k}_3-\boldsymbol{k}_5} \\
& - C^{\hat\alpha^\dagger\hat\alpha\hat\beta^\dagger\hat\beta}_{\boldsymbol{k}_5,\boldsymbol{k}_1,-\boldsymbol{k}_2-\boldsymbol{k}_4-\boldsymbol{k}_5,\boldsymbol{k}_3} C^{\hat\alpha\hat\alpha\hat\beta\hat\beta}_{\boldsymbol{k}_2,\boldsymbol{k}_5,\boldsymbol{k}_4,-\boldsymbol{k}_2-\boldsymbol{k}_4-\boldsymbol{k}_5} \\
& - C^{\hat\alpha^\dagger\hat\alpha\hat\beta^\dagger\hat\beta}_{\boldsymbol{k}_5,\boldsymbol{k}_2,-\boldsymbol{k}_1-\boldsymbol{k}_3-\boldsymbol{k}_5,\boldsymbol{k}_4} C^{\hat\alpha\hat\alpha\hat\beta\hat\beta}_{\boldsymbol{k}_1,\boldsymbol{k}_5,\boldsymbol{k}_3,-\boldsymbol{k}_1-\boldsymbol{k}_3-\boldsymbol{k}_5} \\
& - C^{\hat\alpha^\dagger\hat\alpha\hat\beta^\dagger\hat\beta}_{\boldsymbol{k}_5,\boldsymbol{k}_2,-\boldsymbol{k}_1-\boldsymbol{k}_4-\boldsymbol{k}_5,\boldsymbol{k}_3} C^{\hat\alpha\hat\alpha\hat\beta\hat\beta}_{\boldsymbol{k}_1,\boldsymbol{k}_5,\boldsymbol{k}_4,-\boldsymbol{k}_1-\boldsymbol{k}_4-\boldsymbol{k}_5} \\
& - 2C^{\hat\alpha\hat\alpha\hat\beta\hat\beta}_{\boldsymbol{k}_1,\boldsymbol{k}_2,\boldsymbol{k}_5,\boldsymbol{k}_3+\boldsymbol{k}_4-\boldsymbol{k}_5} C^{\hat\beta^\dagger\hat\beta^\dagger\hat\beta\hat\beta}_{\boldsymbol{k}_5,\boldsymbol{k}_3+\boldsymbol{k}_4-\boldsymbol{k}_5,\boldsymbol{k}_3,\boldsymbol{k}_4} \\
& - 2C^{\hat\alpha\hat\alpha\hat\beta\hat\beta}_{\boldsymbol{k}_5,-\boldsymbol{k}_3-\boldsymbol{k}_4-\boldsymbol{k}_5,\boldsymbol{k}_3,\boldsymbol{k}_4} C^{\hat\alpha^\dagger\hat\alpha^\dagger\hat\alpha\hat\alpha}_{\boldsymbol{k}_5,-\boldsymbol{k}_3-\boldsymbol{k}_4-\boldsymbol{k}_5,\boldsymbol{k}_1,\boldsymbol{k}_2} \,,
\end{aligned}
\tag{B.12}
$$

$$
\begin{aligned}
\partial_\ell C^{\hat\alpha\hat\beta^\dagger\hat\beta\hat\beta}_{\boldsymbol{k}_1,\boldsymbol{k}_2,\boldsymbol{k}_3,\boldsymbol{k}_4} =& - 2C^{\hat\alpha\hat\beta}_{\boldsymbol{k}_1,-\boldsymbol{k}_2+\boldsymbol{k}_3+\boldsymbol{k}_4} C^{\hat\beta^\dagger\hat\beta^\dagger\hat\beta\hat\beta}_{\boldsymbol{k}_2,-\boldsymbol{k}_2+\boldsymbol{k}_3+\boldsymbol{k}_4,\boldsymbol{k}_3,\boldsymbol{k}_4} \\
& - \frac{1}{2} C^{\hat\alpha\hat\beta}_{-\boldsymbol{k}_3,\boldsymbol{k}_3} C^{\hat\alpha^\dagger\hat\alpha\hat\beta^\dagger\hat\beta}_{-\boldsymbol{k}_3,\boldsymbol{k}_1,\boldsymbol{k}_2,\boldsymbol{k}_4} \\
& - \frac{1}{2} C^{\hat\alpha\hat\beta}_{-\boldsymbol{k}_4,\boldsymbol{k}_4} C^{\hat\alpha^\dagger\hat\alpha\hat\beta^\dagger\hat\beta}_{-\boldsymbol{k}_4,\boldsymbol{k}_1,\boldsymbol{k}_2,\boldsymbol{k}_3} \\
& - C^{\hat\alpha^\dagger\hat\alpha}_{\boldsymbol{k}_2-\boldsymbol{k}_3-\boldsymbol{k}_4,\boldsymbol{k}_1} C^{\hat\alpha\hat\beta^\dagger\hat\beta\hat\beta}_{\boldsymbol{k}_2-\boldsymbol{k}_3-\boldsymbol{k}_4,\boldsymbol{k}_2,\boldsymbol{k}_3,\boldsymbol{k}_4} \\
& - 4C^{\hat\alpha^\dagger\hat\beta^\dagger}_{-\boldsymbol{k}_2,\boldsymbol{k}_2} C^{\hat\alpha\hat\alpha\hat\beta\hat\beta}_{\boldsymbol{k}_1,-\boldsymbol{k}_2,\boldsymbol{k}_3,\boldsymbol{k}_4} \\
& + C^{\hat\beta^\dagger\hat\beta}_{\boldsymbol{k}_2,\boldsymbol{k}_2} C^{\hat\alpha\hat\beta^\dagger\hat\beta\hat\beta}_{\boldsymbol{k}_1,\boldsymbol{k}_2,\boldsymbol{k}_3,\boldsymbol{k}_4} \\
& - C^{\hat\beta^\dagger\hat\beta}_{\boldsymbol{k}_3,\boldsymbol{k}_3} C^{\hat\alpha\hat\beta^\dagger\hat\beta\hat\beta}_{\boldsymbol{k}_1,\boldsymbol{k}_2,\boldsymbol{k}_3,\boldsymbol{k}_4} \\
& - C^{\hat\beta^\dagger\hat\beta}_{\boldsymbol{k}_4,\boldsymbol{k}_4} C^{\hat\alpha\hat\beta^\dagger\hat\beta\hat\beta}_{\boldsymbol{k}_1,\boldsymbol{k}_2,\boldsymbol{k}_3,\boldsymbol{k}_4} \\
& - C^{\hat\alpha^\dagger\hat\alpha\hat\beta^\dagger\hat\beta}_{\boldsymbol{k}_5,\boldsymbol{k}_1,\boldsymbol{k}_2-\boldsymbol{k}_3-\boldsymbol{k}_5,\boldsymbol{k}_4} C^{\hat\alpha\hat\beta^\dagger\hat\beta\hat\beta}_{\boldsymbol{k}_5,\boldsymbol{k}_2,\boldsymbol{k}_3,\boldsymbol{k}_2-\boldsymbol{k}_3-\boldsymbol{k}_5} \\
& - C^{\hat\alpha^\dagger\hat\alpha\hat\beta^\dagger\hat\beta}_{\boldsymbol{k}_5,\boldsymbol{k}_1,\boldsymbol{k}_2-\boldsymbol{k}_4-\boldsymbol{k}_5,\boldsymbol{k}_3} C^{\hat\alpha\hat\beta^\dagger\hat\beta\hat\beta}_{\boldsymbol{k}_5,\boldsymbol{k}_2,\boldsymbol{k}_4,\boldsymbol{k}_2-\boldsymbol{k}_4-\boldsymbol{k}_5} \\
& - 2C^{\hat\alpha\hat\beta^\dagger\hat\beta\hat\beta}_{\boldsymbol{k}_1,\boldsymbol{k}_2,\boldsymbol{k}_5,\boldsymbol{k}_3+\boldsymbol{k}_4-\boldsymbol{k}_5} C^{\hat\beta^\dagger\hat\beta^\dagger\hat\beta\hat\beta}_{\boldsymbol{k}_5,\boldsymbol{k}_3+\boldsymbol{k}_4-\boldsymbol{k}_5,\boldsymbol{k}_3,\boldsymbol{k}_4} \\
& - \{4|8\}\, C^{\hat\alpha^\dagger\hat\beta^\dagger\hat\beta^\dagger\hat\beta}_{\boldsymbol{k}_5,\boldsymbol{k}_2,-\boldsymbol{k}_2+\boldsymbol{k}_3-\boldsymbol{k}_5,\boldsymbol{k}_3} C^{\hat\alpha\hat\alpha\hat\beta\hat\beta}_{\boldsymbol{k}_1,\boldsymbol{k}_5,\boldsymbol{k}_4,-\boldsymbol{k}_2+\boldsymbol{k}_3-\boldsymbol{k}_5} \\
& - \{4|8\}\, C^{\hat\alpha^\dagger\hat\beta^\dagger\hat\beta^\dagger\hat\beta}_{\boldsymbol{k}_5,\boldsymbol{k}_2,-\boldsymbol{k}_2+\boldsymbol{k}_4-\boldsymbol{k}_5,\boldsymbol{k}_4} C^{\hat\alpha\hat\alpha\hat\beta\hat\beta}_{\boldsymbol{k}_1,\boldsymbol{k}_5,\boldsymbol{k}_3,-\boldsymbol{k}_2+\boldsymbol{k}_4-\boldsymbol{k}_5} \\
& - \{2|4\}\, C^{\hat\alpha^\dagger\hat\alpha^\dagger\hat\alpha\hat\beta^\dagger}_{\boldsymbol{k}_5,-\boldsymbol{k}_3-\boldsymbol{k}_4-\boldsymbol{k}_5,\boldsymbol{k}_1,\boldsymbol{k}_2} C^{\hat\alpha\hat\alpha\hat\beta\hat\beta}_{\boldsymbol{k}_5,-\boldsymbol{k}_3-\boldsymbol{k}_4-\boldsymbol{k}_5,\boldsymbol{k}_3,\boldsymbol{k}_4} \,,
\end{aligned}
\tag{B.13}
$$

$$
\begin{aligned}
\partial_\ell C^{\hat\beta^\dagger\hat\beta^\dagger\hat\beta\hat\beta}_{\boldsymbol{k}_1,\boldsymbol{k}_2,\boldsymbol{k}_3,\boldsymbol{k}_4} = &-\left\{\frac{1}{2}|1\right\} C^{\hat\alpha\hat\beta}_{-\boldsymbol{k}_3,\boldsymbol{k}_3} C^{\hat\alpha^\dagger\hat\beta^\dagger\hat\beta^\dagger\hat\beta}_{-\boldsymbol{k}_3,\boldsymbol{k}_1,\boldsymbol{k}_2,\boldsymbol{k}_4} \\
&-\left\{\frac{1}{2}|1\right\} C^{\hat\alpha\hat\beta}_{-\boldsymbol{k}_4,\boldsymbol{k}_4} C^{\hat\alpha^\dagger\hat\beta^\dagger\hat\beta^\dagger\hat\beta}_{-\boldsymbol{k}_4,\boldsymbol{k}_1,\boldsymbol{k}_2,\boldsymbol{k}_3} \\
&-\left\{\frac{1}{2}|1\right\} C^{\hat\alpha^\dagger\hat\beta^\dagger}_{-\boldsymbol{k}_1,\boldsymbol{k}_1} C^{\hat\alpha\hat\beta^\dagger\hat\beta\hat\beta}_{-\boldsymbol{k}_1,\boldsymbol{k}_2,\boldsymbol{k}_3,\boldsymbol{k}_4} \\
&-\left\{\frac{1}{2}|1\right\} C^{\hat\alpha^\dagger\hat\beta^\dagger}_{-\boldsymbol{k}_2,\boldsymbol{k}_2} C^{\hat\alpha\hat\beta^\dagger\hat\beta\hat\beta}_{-\boldsymbol{k}_2,\boldsymbol{k}_1,\boldsymbol{k}_3,\boldsymbol{k}_4} \\
&- C^{\hat\alpha\hat\beta^\dagger\hat\beta\hat\beta}_{\boldsymbol{k}_5,\boldsymbol{k}_1,\boldsymbol{k}_3,\boldsymbol{k}_1-\boldsymbol{k}_3-\boldsymbol{k}_5} C^{\hat\alpha^\dagger\hat\beta^\dagger\hat\beta^\dagger\hat\beta}_{\boldsymbol{k}_5,\boldsymbol{k}_2,\boldsymbol{k}_1-\boldsymbol{k}_3-\boldsymbol{k}_5,\boldsymbol{k}_4} \\
&- C^{\hat\alpha\hat\beta^\dagger\hat\beta\hat\beta}_{\boldsymbol{k}_5,\boldsymbol{k}_1,\boldsymbol{k}_3,-\boldsymbol{k}_2+\boldsymbol{k}_4-\boldsymbol{k}_5} C^{\hat\alpha^\dagger\hat\beta^\dagger\hat\beta^\dagger\hat\beta}_{\boldsymbol{k}_5,\boldsymbol{k}_2,-\boldsymbol{k}_2+\boldsymbol{k}_4-\boldsymbol{k}_5,\boldsymbol{k}_4} \\
&- C^{\hat\alpha\hat\beta^\dagger\hat\beta\hat\beta}_{\boldsymbol{k}_5,\boldsymbol{k}_1,\boldsymbol{k}_4,\boldsymbol{k}_1-\boldsymbol{k}_4-\boldsymbol{k}_5} C^{\hat\alpha^\dagger\hat\beta^\dagger\hat\beta^\dagger\hat\beta}_{\boldsymbol{k}_5,\boldsymbol{k}_2,\boldsymbol{k}_1-\boldsymbol{k}_4-\boldsymbol{k}_5,\boldsymbol{k}_3} \\
&- C^{\hat\alpha\hat\beta^\dagger\hat\beta\hat\beta}_{\boldsymbol{k}_5,\boldsymbol{k}_1,\boldsymbol{k}_4,-\boldsymbol{k}_2+\boldsymbol{k}_3-\boldsymbol{k}_5} C^{\hat\alpha^\dagger\hat\beta^\dagger\hat\beta^\dagger\hat\beta}_{\boldsymbol{k}_5,\boldsymbol{k}_2,-\boldsymbol{k}_2+\boldsymbol{k}_3-\boldsymbol{k}_5,\boldsymbol{k}_3} \\
&- C^{\hat\alpha\hat\beta^\dagger\hat\beta\hat\beta}_{\boldsymbol{k}_5,\boldsymbol{k}_2,\boldsymbol{k}_3,-\boldsymbol{k}_1+\boldsymbol{k}_4-\boldsymbol{k}_5} C^{\hat\alpha^\dagger\hat\beta^\dagger\hat\beta^\dagger\hat\beta}_{\boldsymbol{k}_5,\boldsymbol{k}_1,-\boldsymbol{k}_1+\boldsymbol{k}_4-\boldsymbol{k}_5,\boldsymbol{k}_4} \\
&- C^{\hat\alpha\hat\beta^\dagger\hat\beta\hat\beta}_{\boldsymbol{k}_5,\boldsymbol{k}_2,\boldsymbol{k}_3,\boldsymbol{k}_2-\boldsymbol{k}_3-\boldsymbol{k}_5} C^{\hat\alpha^\dagger\hat\beta^\dagger\hat\beta^\dagger\hat\beta}_{\boldsymbol{k}_5,\boldsymbol{k}_1,\boldsymbol{k}_2-\boldsymbol{k}_3-\boldsymbol{k}_5,\boldsymbol{k}_4} \\
&- C^{\hat\alpha\hat\beta^\dagger\hat\beta\hat\beta}_{\boldsymbol{k}_5,\boldsymbol{k}_2,\boldsymbol{k}_4,-\boldsymbol{k}_1+\boldsymbol{k}_3-\boldsymbol{k}_5} C^{\hat\alpha^\dagger\hat\beta^\dagger\hat\beta^\dagger\hat\beta}_{\boldsymbol{k}_5,\boldsymbol{k}_1,-\boldsymbol{k}_1+\boldsymbol{k}_3-\boldsymbol{k}_5,\boldsymbol{k}_3} \\
&- C^{\hat\alpha\hat\beta^\dagger\hat\beta\hat\beta}_{\boldsymbol{k}_5,\boldsymbol{k}_2,\boldsymbol{k}_4,\boldsymbol{k}_2-\boldsymbol{k}_4-\boldsymbol{k}_5} C^{\hat\alpha^\dagger\hat\beta^\dagger\hat\beta^\dagger\hat\beta}_{\boldsymbol{k}_5,\boldsymbol{k}_1,\boldsymbol{k}_2-\boldsymbol{k}_4-\boldsymbol{k}_5,\boldsymbol{k}_3} \\
&- 4C^{\hat\alpha\hat\alpha\hat\beta\hat\beta}_{\boldsymbol{k}_5,-\boldsymbol{k}_3-\boldsymbol{k}_4-\boldsymbol{k}_5,\boldsymbol{k}_3,\boldsymbol{k}_4} C^{\hat\alpha^\dagger\hat\alpha^\dagger\hat\beta^\dagger\hat\beta^\dagger}_{\boldsymbol{k}_5,-\boldsymbol{k}_3-\boldsymbol{k}_4-\boldsymbol{k}_5,\boldsymbol{k}_1,\boldsymbol{k}_2} \,.
\end{aligned}
\tag{B.14}
$$

B.2 Flow Equations of the Observables

The flow equations of the different observable coefficients produced with the tool set of [MHS] are listed here.

B.2.1 Flow Equations — Magnetization

The flow equations of the coefficients connected to the operators of Eq. (A.20) read as follows

$$\begin{aligned}\partial_\ell m^0_{\boldsymbol{Q}} =& - C^{\hat{\alpha}\hat{\beta}}_{\boldsymbol{k}_1,-\boldsymbol{k}_1} m^{\hat{\alpha}^\dagger\hat{\beta}^\dagger}_{\boldsymbol{Q},\boldsymbol{k}_1,-\boldsymbol{k}_1} \\ & - C^{\hat{\alpha}^\dagger\hat{\beta}^\dagger}_{\boldsymbol{k}_1,-\boldsymbol{k}_1} m^{\hat{\alpha}\hat{\beta}}_{\boldsymbol{Q},\boldsymbol{k}_1,-\boldsymbol{k}_1} \,,\end{aligned} \tag{B.15}$$

$$\begin{aligned}\partial_\ell m^{\hat{\alpha}^\dagger\hat{\alpha}}_{\boldsymbol{Q},\boldsymbol{k}_1,\boldsymbol{k}_2} =& - C^{\hat{\alpha}\hat{\beta}}_{\boldsymbol{k}_2,-\boldsymbol{k}_2} m^{\hat{\alpha}^\dagger\hat{\beta}^\dagger}_{\boldsymbol{Q},\boldsymbol{k}_1,-\boldsymbol{k}_2} \\ & - C^{\hat{\alpha}^\dagger\hat{\beta}^\dagger}_{\boldsymbol{k}_1,-\boldsymbol{k}_1} m^{\hat{\alpha}\hat{\beta}}_{\boldsymbol{Q},\boldsymbol{k}_2,-\boldsymbol{k}_1} \\ & -2m^{\hat{\alpha}\hat{\beta}}_{\boldsymbol{Q},\boldsymbol{k}_3,-\boldsymbol{k}_1+\boldsymbol{k}_2-\boldsymbol{k}_3} C^{\hat{\alpha}^\dagger\hat{\alpha}^\dagger\hat{\alpha}\hat{\beta}^\dagger}_{\boldsymbol{k}_1,\boldsymbol{k}_3,\boldsymbol{k}_2,-\boldsymbol{k}_1+\boldsymbol{k}_2-\boldsymbol{k}_3} \\ & -2m^{\hat{\alpha}^\dagger\hat{\beta}^\dagger}_{\boldsymbol{Q},\boldsymbol{k}_3,\boldsymbol{k}_1-\boldsymbol{k}_2-\boldsymbol{k}_3} C^{\hat{\alpha}^\dagger\hat{\alpha}\hat{\alpha}\hat{\beta}}_{\boldsymbol{k}_1,\boldsymbol{k}_2,\boldsymbol{k}_3,\boldsymbol{k}_1-\boldsymbol{k}_2-\boldsymbol{k}_3} \,,\end{aligned} \tag{B.16}$$

$$\begin{aligned}\partial_\ell m^{\hat{\alpha}^\dagger\hat{\beta}^\dagger}_{\boldsymbol{Q},\boldsymbol{k}_1,\boldsymbol{k}_2} =& - C^{\hat{\alpha}^\dagger\hat{\beta}^\dagger}_{\boldsymbol{k}_1,-\boldsymbol{k}_1} m^{\hat{\beta}^\dagger\hat{\beta}}_{\boldsymbol{Q},\boldsymbol{k}_2,-\boldsymbol{k}_1} \\ & - C^{\hat{\alpha}^\dagger\hat{\beta}^\dagger}_{-\boldsymbol{k}_2,\boldsymbol{k}_2} m^{\hat{\alpha}^\dagger\hat{\alpha}}_{\boldsymbol{Q},\boldsymbol{k}_1,-\boldsymbol{k}_2} \\ & - 4m^{\hat{\alpha}\hat{\beta}}_{\boldsymbol{Q},\boldsymbol{k}_3,-\boldsymbol{k}_1-\boldsymbol{k}_2-\boldsymbol{k}_3} C^{\hat{\alpha}^\dagger\hat{\alpha}^\dagger\hat{\beta}^\dagger\hat{\beta}^\dagger}_{\boldsymbol{k}_1,\boldsymbol{k}_3,\boldsymbol{k}_2,-\boldsymbol{k}_1-\boldsymbol{k}_2-\boldsymbol{k}_3} \,,\end{aligned} \tag{B.17}$$

$$\begin{aligned}\partial_\ell m^{\hat{\alpha}\hat{\beta}}_{\boldsymbol{Q},\boldsymbol{k}_1,\boldsymbol{k}_2} =& - C^{\hat{\alpha}\hat{\beta}}_{\boldsymbol{k}_1,-\boldsymbol{k}_1} m^{\hat{\beta}^\dagger\hat{\beta}}_{\boldsymbol{Q},-\boldsymbol{k}_1,\boldsymbol{k}_2} \\ & - C^{\hat{\alpha}\hat{\beta}}_{-\boldsymbol{k}_2,\boldsymbol{k}_2} m^{\hat{\alpha}^\dagger\hat{\alpha}}_{\boldsymbol{Q},-\boldsymbol{k}_2,\boldsymbol{k}_1} \\ & - 4m^{\hat{\alpha}^\dagger\hat{\beta}^\dagger}_{\boldsymbol{Q},\boldsymbol{k}_3,-\boldsymbol{k}_1-\boldsymbol{k}_2-\boldsymbol{k}_3} C^{\hat{\alpha}\hat{\alpha}\hat{\beta}\hat{\beta}}_{\boldsymbol{k}_1,\boldsymbol{k}_3,\boldsymbol{k}_2,-\boldsymbol{k}_1-\boldsymbol{k}_2-\boldsymbol{k}_3} \,,\end{aligned} \tag{B.18}$$

$$\begin{aligned}\partial_\ell m^{\hat{\beta}^\dagger\hat{\beta}}_{\boldsymbol{Q},\boldsymbol{k}_1,\boldsymbol{k}_2} =& - C^{\hat{\alpha}\hat{\beta}}_{-\boldsymbol{k}_2,\boldsymbol{k}_2} m^{\hat{\alpha}^\dagger\hat{\beta}^\dagger}_{\boldsymbol{Q},-\boldsymbol{k}_2,\boldsymbol{k}_1} \\ & - C^{\hat{\alpha}^\dagger\hat{\beta}^\dagger}_{-\boldsymbol{k}_1,\boldsymbol{k}_1} m^{\hat{\alpha}\hat{\beta}}_{\boldsymbol{Q},-\boldsymbol{k}_1,\boldsymbol{k}_2} \\ & -2m^{\hat{\alpha}\hat{\beta}}_{\boldsymbol{Q},\boldsymbol{k}_3,-\boldsymbol{k}_1+\boldsymbol{k}_2-\boldsymbol{k}_3} C^{\hat{\alpha}^\dagger\hat{\beta}^\dagger\hat{\beta}^\dagger\hat{\beta}}_{\boldsymbol{k}_3,\boldsymbol{k}_1,-\boldsymbol{k}_1+\boldsymbol{k}_2-\boldsymbol{k}_3,\boldsymbol{k}_2} \\ & -2m^{\hat{\alpha}^\dagger\hat{\beta}^\dagger}_{\boldsymbol{Q},\boldsymbol{k}_3,\boldsymbol{k}_1-\boldsymbol{k}_2-\boldsymbol{k}_3} C^{\hat{\alpha}\hat{\beta}^\dagger\hat{\beta}\hat{\beta}}_{\boldsymbol{k}_3,\boldsymbol{k}_1,\boldsymbol{k}_2,\boldsymbol{k}_1-\boldsymbol{k}_2-\boldsymbol{k}_3} \,.\end{aligned} \tag{B.19}$$

B.2.2 Flow Equations — Longitudinal Dynamical Structure Factor

The flow equations of the coefficients connected to the operator of the longitudinal dynamical structure factor in Eq. (A.24) read as follows

$$\begin{aligned}\partial_\ell s^{z\,0}_{\boldsymbol{Q}} =& - C^{\hat{\alpha}\hat{\beta}}_{\boldsymbol{k}_1,-\boldsymbol{k}_1} s^{z\,\hat{\alpha}^\dagger\hat{\beta}^\dagger}_{\boldsymbol{Q},\boldsymbol{k}_1,-\boldsymbol{k}_1} \\ & - C^{\hat{\alpha}^\dagger\hat{\beta}^\dagger}_{\boldsymbol{k}_1,-\boldsymbol{k}_1} s^{z\,\hat{\alpha}\hat{\beta}}_{\boldsymbol{Q},\boldsymbol{k}_1,-\boldsymbol{k}_1} \,,\end{aligned} \tag{B.20}$$

$$
\begin{aligned}
\partial_\ell s^{z\hat{\alpha}^\dagger\hat{\alpha}}_{\boldsymbol{Q},\boldsymbol{k}_1,\boldsymbol{k}_2} =& - C^{\hat{\alpha}\hat{\beta}}_{\boldsymbol{k}_2,-\boldsymbol{k}_2} s^{z\hat{\alpha}^\dagger\hat{\beta}^\dagger}_{\boldsymbol{Q},\boldsymbol{k}_1,-\boldsymbol{k}_2} \\
& - C^{\hat{\alpha}^\dagger\hat{\beta}^\dagger}_{\boldsymbol{k}_1,-\boldsymbol{k}_1} s^{z\hat{\alpha}\hat{\beta}}_{\boldsymbol{Q},\boldsymbol{k}_2,-\boldsymbol{k}_1} \\
& -2 s^{z\hat{\alpha}\hat{\beta}}_{\boldsymbol{Q},\boldsymbol{k}_3,-\boldsymbol{k}_1+\boldsymbol{k}_2-\boldsymbol{k}_3} C^{\hat{\alpha}^\dagger\hat{\alpha}^\dagger\hat{\alpha}\hat{\beta}^\dagger}_{\boldsymbol{k}_1,\boldsymbol{k}_3,\boldsymbol{k}_2,-\boldsymbol{k}_1+\boldsymbol{k}_2-\boldsymbol{k}_3} \\
& -2 s^{z\hat{\alpha}^\dagger\hat{\beta}^\dagger}_{\boldsymbol{Q},\boldsymbol{k}_3,\boldsymbol{k}_1-\boldsymbol{k}_2-\boldsymbol{k}_3} C^{\hat{\alpha}^\dagger\hat{\alpha}\hat{\alpha}\hat{\beta}}_{\boldsymbol{k}_1,\boldsymbol{k}_2,\boldsymbol{k}_3,\boldsymbol{k}_1-\boldsymbol{k}_2-\boldsymbol{k}_3} \,,
\end{aligned} \tag{B.21}
$$

$$
\begin{aligned}
\partial_\ell s^{z\hat{\alpha}^\dagger\hat{\beta}^\dagger}_{\boldsymbol{Q},\boldsymbol{k}_1,\boldsymbol{k}_2} =& - C^{\hat{\alpha}^\dagger\hat{\beta}^\dagger}_{\boldsymbol{k}_1,-\boldsymbol{k}_1} s^{z\hat{\beta}^\dagger\hat{\beta}}_{\boldsymbol{Q},\boldsymbol{k}_2,-\boldsymbol{k}_1} \\
& - C^{\hat{\alpha}^\dagger\hat{\beta}^\dagger}_{-\boldsymbol{k}_2,\boldsymbol{k}_2} s^{z\hat{\alpha}^\dagger\hat{\alpha}}_{\boldsymbol{Q},\boldsymbol{k}_1,-\boldsymbol{k}_2} \\
& - 4 s^{z\hat{\alpha}\hat{\beta}}_{\boldsymbol{Q},\boldsymbol{k}_3,-\boldsymbol{k}_1-\boldsymbol{k}_2-\boldsymbol{k}_3} C^{\hat{\alpha}^\dagger\hat{\alpha}^\dagger\hat{\beta}^\dagger\hat{\beta}^\dagger}_{\boldsymbol{k}_1,\boldsymbol{k}_3,\boldsymbol{k}_2,-\boldsymbol{k}_1-\boldsymbol{k}_2-\boldsymbol{k}_3} \,,
\end{aligned} \tag{B.22}
$$

$$
\begin{aligned}
\partial_\ell s^{z\hat{\alpha}\hat{\beta}}_{\boldsymbol{Q},\boldsymbol{k}_1,\boldsymbol{k}_2} =& - C^{\hat{\alpha}\hat{\beta}}_{\boldsymbol{k}_1,-\boldsymbol{k}_1} s^{z\hat{\beta}^\dagger\hat{\beta}}_{\boldsymbol{Q},-\boldsymbol{k}_1,\boldsymbol{k}_2} \\
& - C^{\hat{\alpha}\hat{\beta}}_{-\boldsymbol{k}_2,\boldsymbol{k}_2} s^{z\hat{\alpha}^\dagger\hat{\alpha}}_{\boldsymbol{Q},-\boldsymbol{k}_2,\boldsymbol{k}_1} \\
& - 4 s^{z\hat{\alpha}^\dagger\hat{\beta}^\dagger}_{\boldsymbol{Q},\boldsymbol{k}_3,-\boldsymbol{k}_1-\boldsymbol{k}_2-\boldsymbol{k}_3} C^{\hat{\alpha}\hat{\alpha}\hat{\beta}\hat{\beta}}_{\boldsymbol{k}_1,\boldsymbol{k}_3,\boldsymbol{k}_2,-\boldsymbol{k}_1-\boldsymbol{k}_2-\boldsymbol{k}_3} \,,
\end{aligned} \tag{B.23}
$$

$$
\begin{aligned}
\partial_\ell s^{z\hat{\beta}^\dagger\hat{\beta}}_{\boldsymbol{Q},\boldsymbol{k}_1,\boldsymbol{k}_2} =& - C^{\hat{\alpha}\hat{\beta}}_{-\boldsymbol{k}_2,\boldsymbol{k}_2} s^{z\hat{\alpha}^\dagger\hat{\beta}^\dagger}_{\boldsymbol{Q},-\boldsymbol{k}_2,\boldsymbol{k}_1} \\
& - C^{\hat{\alpha}^\dagger\hat{\beta}^\dagger}_{-\boldsymbol{k}_1,\boldsymbol{k}_1} s^{z\hat{\alpha}\hat{\beta}}_{\boldsymbol{Q},-\boldsymbol{k}_1,\boldsymbol{k}_2} \\
& -2 s^{z\hat{\alpha}\hat{\beta}}_{\boldsymbol{Q},\boldsymbol{k}_3,-\boldsymbol{k}_1+\boldsymbol{k}_2-\boldsymbol{k}_3} C^{\hat{\alpha}^\dagger\hat{\beta}^\dagger\hat{\beta}^\dagger\hat{\beta}}_{\boldsymbol{k}_3,\boldsymbol{k}_1,-\boldsymbol{k}_1+\boldsymbol{k}_2-\boldsymbol{k}_3,\boldsymbol{k}_2} \\
& -2 s^{z\hat{\alpha}^\dagger\hat{\beta}^\dagger}_{\boldsymbol{Q},\boldsymbol{k}_3,\boldsymbol{k}_1-\boldsymbol{k}_2-\boldsymbol{k}_3} C^{\hat{\alpha}\hat{\beta}^\dagger\hat{\beta}\hat{\beta}}_{\boldsymbol{k}_3,\boldsymbol{k}_1,\boldsymbol{k}_2,\boldsymbol{k}_1-\boldsymbol{k}_2-\boldsymbol{k}_3} \,.
\end{aligned} \tag{B.24}
$$

B.2.3 Flow Equations — Transversal Dynamical Structure Factor

The flow equations of the coefficients connected to the operator of the transversal dynamical structure factor in Eqs. (A.29) and (A.30) read as follows. First for the coefficients of the $\hat{S}^{-}_{\boldsymbol{Q}}$ operator:

$$
\begin{aligned}
\partial_\ell s^{-\hat{\alpha}^\dagger}_{\boldsymbol{Q},\boldsymbol{k}_1} =& - 2 C^{\hat{\alpha}\hat{\beta}}_{\boldsymbol{k}_2,-\boldsymbol{k}_2} s^{-\hat{\alpha}^\dagger\hat{\alpha}^\dagger\hat{\beta}^\dagger}_{\boldsymbol{Q},\boldsymbol{k}_1,\boldsymbol{k}_2,-\boldsymbol{k}_2} \\
& - C^{\hat{\alpha}^\dagger\hat{\beta}^\dagger}_{\boldsymbol{k}_1,-\boldsymbol{k}_1} s^{-\hat{\beta}}_{\boldsymbol{Q},-\boldsymbol{k}_1} \\
& - C^{\hat{\alpha}^\dagger\hat{\beta}^\dagger}_{\boldsymbol{k}_2,-\boldsymbol{k}_2} s^{-\hat{\alpha}^\dagger\hat{\alpha}\hat{\beta}}_{\boldsymbol{Q},\boldsymbol{k}_1,\boldsymbol{k}_2,-\boldsymbol{k}_2} \\
& - 4 s^{-\hat{\alpha}\hat{\beta}\hat{\beta}}_{\boldsymbol{Q},\boldsymbol{k}_2,\boldsymbol{k}_3,-\boldsymbol{k}_1-\boldsymbol{k}_2-\boldsymbol{k}_3} C^{\hat{\alpha}^\dagger\hat{\alpha}^\dagger\hat{\beta}^\dagger\hat{\beta}^\dagger}_{\boldsymbol{k}_1,\boldsymbol{k}_2,\boldsymbol{k}_3,-\boldsymbol{k}_1-\boldsymbol{k}_2-\boldsymbol{k}_3} \\
& -2 C^{\hat{\alpha}^\dagger\hat{\alpha}\hat{\alpha}\hat{\beta}}_{\boldsymbol{k}_1,\boldsymbol{k}_2,\boldsymbol{k}_3,\boldsymbol{k}_1-\boldsymbol{k}_2-\boldsymbol{k}_3} s^{-\hat{\alpha}^\dagger\hat{\alpha}^\dagger\hat{\beta}^\dagger}_{\boldsymbol{Q},\boldsymbol{k}_2,\boldsymbol{k}_3,\boldsymbol{k}_1-\boldsymbol{k}_2-\boldsymbol{k}_3} \,,
\end{aligned} \tag{B.25}
$$

$$
\begin{aligned}
\partial_\ell s^{-\hat{\beta}}_{\boldsymbol{Q},\boldsymbol{k}_1} =& - C^{\hat{\alpha}\hat{\beta}}_{-\boldsymbol{k}_1,\boldsymbol{k}_1} s^{-\hat{\alpha}^\dagger}_{\boldsymbol{Q},-\boldsymbol{k}_1} \\
& - C^{\hat{\alpha}\hat{\beta}}_{\boldsymbol{k}_2,-\boldsymbol{k}_2} s^{-\hat{\alpha}^\dagger\hat{\beta}^\dagger\hat{\beta}}_{\boldsymbol{Q},\boldsymbol{k}_2,-\boldsymbol{k}_2,\boldsymbol{k}_1} \\
& - 2 C^{\hat{\alpha}^\dagger\hat{\beta}^\dagger}_{\boldsymbol{k}_2,-\boldsymbol{k}_2} s^{-\hat{\alpha}\hat{\beta}\hat{\beta}}_{\boldsymbol{Q},\boldsymbol{k}_2,\boldsymbol{k}_1,-\boldsymbol{k}_2} \\
& -2 s^{-\hat{\alpha}\hat{\beta}\hat{\beta}}_{\boldsymbol{Q},\boldsymbol{k}_2,\boldsymbol{k}_3,\boldsymbol{k}_1-\boldsymbol{k}_2-\boldsymbol{k}_3} C^{\hat{\alpha}^\dagger\hat{\beta}^\dagger\hat{\beta}^\dagger\hat{\beta}}_{\boldsymbol{k}_2,\boldsymbol{k}_3,\boldsymbol{k}_1-\boldsymbol{k}_2-\boldsymbol{k}_3,\boldsymbol{k}_1} \\
& - 4 s^{-\hat{\alpha}^\dagger\hat{\alpha}^\dagger\hat{\beta}^\dagger}_{\boldsymbol{Q},\boldsymbol{k}_2,\boldsymbol{k}_3,-\boldsymbol{k}_1-\boldsymbol{k}_2-\boldsymbol{k}_3} C^{\hat{\alpha}\hat{\alpha}\hat{\beta}\hat{\beta}}_{\boldsymbol{k}_2,\boldsymbol{k}_3,\boldsymbol{k}_1,-\boldsymbol{k}_1-\boldsymbol{k}_2-\boldsymbol{k}_3} \,,
\end{aligned} \tag{B.26}
$$

$$
\begin{aligned}
\partial_\ell s^{-\hat{\alpha}^\dagger\hat{\alpha}^\dagger\hat{\alpha}}_{\boldsymbol{Q},\boldsymbol{k}_1,\boldsymbol{k}_2,\boldsymbol{k}_3} = &- C^{\hat{\alpha}\hat{\beta}}_{\boldsymbol{k}_3,-\boldsymbol{k}_3} s^{-\hat{\alpha}^\dagger\hat{\alpha}^\dagger\hat{\beta}^\dagger}_{\boldsymbol{Q},\boldsymbol{k}_1,\boldsymbol{k}_2,-\boldsymbol{k}_3} \\
&- \frac{1}{2} C^{\hat{\alpha}^\dagger\hat{\beta}^\dagger}_{\boldsymbol{k}_1,-\boldsymbol{k}_1} s^{-\hat{\alpha}^\dagger\hat{\alpha}\hat{\beta}}_{\boldsymbol{Q},\boldsymbol{k}_2,\boldsymbol{k}_3,-\boldsymbol{k}_1} \\
&- \frac{1}{2} C^{\hat{\alpha}^\dagger\hat{\beta}^\dagger}_{\boldsymbol{k}_2,-\boldsymbol{k}_2} s^{-\hat{\alpha}^\dagger\hat{\alpha}\hat{\beta}}_{\boldsymbol{Q},\boldsymbol{k}_1,\boldsymbol{k}_3,-\boldsymbol{k}_2} \\
&- s^{-\hat{\beta}}_{\boldsymbol{Q},-\boldsymbol{k}_1-\boldsymbol{k}_2+\boldsymbol{k}_3} C^{\hat{\alpha}^\dagger\hat{\alpha}^\dagger\hat{\alpha}\hat{\beta}^\dagger}_{\boldsymbol{k}_1,\boldsymbol{k}_2,\boldsymbol{k}_3,-\boldsymbol{k}_1-\boldsymbol{k}_2+\boldsymbol{k}_3} \\
&- s^{-\hat{\alpha}^\dagger\hat{\alpha}\hat{\beta}}_{\boldsymbol{Q},\boldsymbol{k}_1,\boldsymbol{k}_4,-\boldsymbol{k}_2+\boldsymbol{k}_3-\boldsymbol{k}_4} C^{\hat{\alpha}^\dagger\hat{\alpha}^\dagger\hat{\alpha}\hat{\beta}^\dagger}_{\boldsymbol{k}_2,\boldsymbol{k}_4,\boldsymbol{k}_3,-\boldsymbol{k}_2+\boldsymbol{k}_3-\boldsymbol{k}_4} \\
&- s^{-\hat{\alpha}^\dagger\hat{\alpha}\hat{\beta}}_{\boldsymbol{Q},\boldsymbol{k}_2,\boldsymbol{k}_4,-\boldsymbol{k}_1+\boldsymbol{k}_3-\boldsymbol{k}_4} C^{\hat{\alpha}^\dagger\hat{\alpha}^\dagger\hat{\alpha}\hat{\beta}^\dagger}_{\boldsymbol{k}_1,\boldsymbol{k}_4,\boldsymbol{k}_3,-\boldsymbol{k}_1+\boldsymbol{k}_3-\boldsymbol{k}_4} \\
&- 2s^{-\hat{\alpha}\hat{\beta}\hat{\beta}}_{\boldsymbol{Q},\boldsymbol{k}_3,\boldsymbol{k}_4,-\boldsymbol{k}_1-\boldsymbol{k}_2-\boldsymbol{k}_4} C^{\hat{\alpha}^\dagger\hat{\alpha}^\dagger\hat{\beta}^\dagger\hat{\beta}^\dagger}_{\boldsymbol{k}_1,\boldsymbol{k}_2,\boldsymbol{k}_4,-\boldsymbol{k}_1-\boldsymbol{k}_2-\boldsymbol{k}_4} \\
&- 2C^{\hat{\alpha}^\dagger\hat{\alpha}\hat{\alpha}\hat{\beta}}_{\boldsymbol{k}_1,\boldsymbol{k}_3,\boldsymbol{k}_4,\boldsymbol{k}_1-\boldsymbol{k}_3-\boldsymbol{k}_4} s^{-\hat{\alpha}^\dagger\hat{\alpha}^\dagger\hat{\beta}^\dagger}_{\boldsymbol{Q},\boldsymbol{k}_2,\boldsymbol{k}_4,\boldsymbol{k}_1-\boldsymbol{k}_3-\boldsymbol{k}_4} \\
&- 2C^{\hat{\alpha}^\dagger\hat{\alpha}\hat{\alpha}\hat{\beta}}_{\boldsymbol{k}_2,\boldsymbol{k}_3,\boldsymbol{k}_4,\boldsymbol{k}_2-\boldsymbol{k}_3-\boldsymbol{k}_4} s^{-\hat{\alpha}^\dagger\hat{\alpha}^\dagger\hat{\beta}^\dagger}_{\boldsymbol{Q},\boldsymbol{k}_1,\boldsymbol{k}_4,\boldsymbol{k}_2-\boldsymbol{k}_3-\boldsymbol{k}_4} ,
\end{aligned}
\tag{B.27}
$$

$$
\begin{aligned}
\partial_\ell s^{-\hat{\alpha}^\dagger\hat{\alpha}^\dagger\hat{\beta}^\dagger}_{\boldsymbol{Q},\boldsymbol{k}_1,\boldsymbol{k}_2,\boldsymbol{k}_3} = &- \frac{1}{2} C^{\hat{\alpha}^\dagger\hat{\beta}^\dagger}_{\boldsymbol{k}_1,-\boldsymbol{k}_1} s^{-\hat{\alpha}^\dagger\hat{\beta}^\dagger\hat{\beta}}_{\boldsymbol{Q},\boldsymbol{k}_2,\boldsymbol{k}_3,-\boldsymbol{k}_1} \\
&- \frac{1}{2} C^{\hat{\alpha}^\dagger\hat{\beta}^\dagger}_{\boldsymbol{k}_2,-\boldsymbol{k}_2} s^{-\hat{\alpha}^\dagger\hat{\beta}^\dagger\hat{\beta}}_{\boldsymbol{Q},\boldsymbol{k}_1,\boldsymbol{k}_3,-\boldsymbol{k}_2} \\
&- C^{\hat{\alpha}^\dagger\hat{\beta}^\dagger}_{-\boldsymbol{k}_3,\boldsymbol{k}_3} s^{-\hat{\alpha}^\dagger\hat{\alpha}^\dagger\hat{\alpha}}_{\boldsymbol{Q},\boldsymbol{k}_1,\boldsymbol{k}_2,-\boldsymbol{k}_3} \\
&+ s^{-\hat{\alpha}^\dagger}_{\boldsymbol{Q},\boldsymbol{k}_1+\boldsymbol{k}_2+\boldsymbol{k}_3} C^{\hat{\alpha}^\dagger\hat{\alpha}^\dagger\hat{\alpha}\hat{\beta}^\dagger}_{\boldsymbol{k}_1,\boldsymbol{k}_2,\boldsymbol{k}_1+\boldsymbol{k}_2+\boldsymbol{k}_3,\boldsymbol{k}_3} \\
&- 2s^{-\hat{\beta}}_{\boldsymbol{Q},-\boldsymbol{k}_1-\boldsymbol{k}_2-\boldsymbol{k}_3} C^{\hat{\alpha}^\dagger\hat{\alpha}^\dagger\hat{\beta}^\dagger\hat{\beta}^\dagger}_{\boldsymbol{k}_1,\boldsymbol{k}_2,\boldsymbol{k}_3,-\boldsymbol{k}_1-\boldsymbol{k}_2-\boldsymbol{k}_3} \\
&- 2s^{-\hat{\alpha}^\dagger\hat{\alpha}\hat{\beta}}_{\boldsymbol{Q},\boldsymbol{k}_1,\boldsymbol{k}_4,-\boldsymbol{k}_2-\boldsymbol{k}_3-\boldsymbol{k}_4} C^{\hat{\alpha}^\dagger\hat{\alpha}^\dagger\hat{\beta}^\dagger\hat{\beta}^\dagger}_{\boldsymbol{k}_2,\boldsymbol{k}_4,\boldsymbol{k}_3,-\boldsymbol{k}_2-\boldsymbol{k}_3-\boldsymbol{k}_4} \\
&- 2s^{-\hat{\alpha}^\dagger\hat{\alpha}\hat{\beta}}_{\boldsymbol{Q},\boldsymbol{k}_2,\boldsymbol{k}_4,-\boldsymbol{k}_1-\boldsymbol{k}_3-\boldsymbol{k}_4} C^{\hat{\alpha}^\dagger\hat{\alpha}^\dagger\hat{\beta}^\dagger\hat{\beta}^\dagger}_{\boldsymbol{k}_1,\boldsymbol{k}_4,\boldsymbol{k}_3,-\boldsymbol{k}_1-\boldsymbol{k}_3-\boldsymbol{k}_4} \\
&- 2s^{-\hat{\beta}^\dagger\hat{\beta}\hat{\beta}}_{\boldsymbol{Q},\boldsymbol{k}_3,\boldsymbol{k}_4,-\boldsymbol{k}_1-\boldsymbol{k}_2-\boldsymbol{k}_4} C^{\hat{\alpha}^\dagger\hat{\alpha}^\dagger\hat{\beta}^\dagger\hat{\beta}^\dagger}_{\boldsymbol{k}_1,\boldsymbol{k}_2,\boldsymbol{k}_4,-\boldsymbol{k}_1-\boldsymbol{k}_2-\boldsymbol{k}_4} ,
\end{aligned}
\tag{B.28}
$$

$$
\begin{aligned}
\partial_\ell s^{-\hat{\alpha}^\dagger\hat{\alpha}^\dagger\hat{\beta}^\dagger}_{\boldsymbol{Q},\boldsymbol{k}_1,\boldsymbol{k}_2,\boldsymbol{k}_3} = &- C^{\hat{\alpha}\hat{\beta}}_{\boldsymbol{k}_2,-\boldsymbol{k}_2} s^{-\hat{\alpha}^\dagger\hat{\beta}^\dagger\hat{\beta}}_{\boldsymbol{Q},\boldsymbol{k}_1,-\boldsymbol{k}_2,\boldsymbol{k}_3} \\
&- 2C^{\hat{\alpha}\hat{\beta}}_{-\boldsymbol{k}_3,\boldsymbol{k}_3} s^{-\hat{\alpha}^\dagger\hat{\alpha}^\dagger\hat{\alpha}}_{\boldsymbol{Q},\boldsymbol{k}_1,-\boldsymbol{k}_3,\boldsymbol{k}_2} \\
&- 2C^{\hat{\alpha}^\dagger\hat{\beta}^\dagger}_{\boldsymbol{k}_1,-\boldsymbol{k}_1} s^{-\hat{\alpha}\hat{\beta}\hat{\beta}}_{\boldsymbol{Q},\boldsymbol{k}_2,-\boldsymbol{k}_1,\boldsymbol{k}_3} \\
&- 2s^{-\hat{\alpha}^\dagger}_{\boldsymbol{Q},\boldsymbol{k}_1-\boldsymbol{k}_2-\boldsymbol{k}_3} C^{\hat{\alpha}^\dagger\hat{\alpha}\hat{\alpha}\hat{\beta}}_{\boldsymbol{k}_1,\boldsymbol{k}_2,\boldsymbol{k}_1-\boldsymbol{k}_2-\boldsymbol{k}_3,\boldsymbol{k}_3} \\
&- 2s^{-\hat{\alpha}^\dagger\hat{\beta}^\dagger\hat{\beta}}_{\boldsymbol{Q},\boldsymbol{k}_4,\boldsymbol{k}_1-\boldsymbol{k}_2-\boldsymbol{k}_4,\boldsymbol{k}_3} C^{\hat{\alpha}^\dagger\hat{\alpha}\hat{\alpha}\hat{\beta}}_{\boldsymbol{k}_1,\boldsymbol{k}_2,\boldsymbol{k}_4,\boldsymbol{k}_1-\boldsymbol{k}_2-\boldsymbol{k}_4} \\
&- 2s^{-\hat{\alpha}\hat{\beta}\hat{\beta}}_{\boldsymbol{Q},\boldsymbol{k}_2,\boldsymbol{k}_4,-\boldsymbol{k}_1+\boldsymbol{k}_3-\boldsymbol{k}_4} C^{\hat{\alpha}^\dagger\hat{\beta}^\dagger\hat{\beta}^\dagger\hat{\beta}}_{\boldsymbol{k}_1,\boldsymbol{k}_4,-\boldsymbol{k}_1+\boldsymbol{k}_3-\boldsymbol{k}_4,\boldsymbol{k}_3} \\
&- 4s^{-\hat{\alpha}\hat{\beta}\hat{\beta}}_{\boldsymbol{Q},\boldsymbol{k}_4,\boldsymbol{k}_3,-\boldsymbol{k}_1+\boldsymbol{k}_2-\boldsymbol{k}_4} C^{\hat{\alpha}^\dagger\hat{\alpha}^\dagger\hat{\alpha}\hat{\beta}^\dagger}_{\boldsymbol{k}_1,\boldsymbol{k}_4,\boldsymbol{k}_2,-\boldsymbol{k}_1+\boldsymbol{k}_2-\boldsymbol{k}_4} \\
&- 2C^{\hat{\alpha}^\dagger\hat{\alpha}\hat{\alpha}\hat{\beta}}_{\boldsymbol{k}_1,\boldsymbol{k}_4,\boldsymbol{k}_1-\boldsymbol{k}_3-\boldsymbol{k}_4,\boldsymbol{k}_3} s^{-\hat{\alpha}^\dagger\hat{\alpha}^\dagger\hat{\alpha}}_{\boldsymbol{Q},\boldsymbol{k}_4,\boldsymbol{k}_1-\boldsymbol{k}_3-\boldsymbol{k}_4,\boldsymbol{k}_2} \\
&- 8s^{-\hat{\alpha}^\dagger\hat{\alpha}^\dagger\hat{\beta}^\dagger}_{\boldsymbol{Q},\boldsymbol{k}_1,\boldsymbol{k}_4,-\boldsymbol{k}_2-\boldsymbol{k}_3-\boldsymbol{k}_4} C^{\hat{\alpha}\hat{\alpha}\hat{\beta}\hat{\beta}}_{\boldsymbol{k}_2,\boldsymbol{k}_4,\boldsymbol{k}_3,-\boldsymbol{k}_2-\boldsymbol{k}_3-\boldsymbol{k}_4} ,
\end{aligned}
\tag{B.29}
$$

$$
\begin{aligned}
\partial_\ell s^{-\hat{\alpha}^\dagger\hat{\beta}^\dagger\hat{\beta}}_{\boldsymbol{Q},\boldsymbol{k}_1,\boldsymbol{k}_2,\boldsymbol{k}_3} = &-2C^{\hat{\alpha}\hat{\beta}}_{-\boldsymbol{k}_3,\boldsymbol{k}_3} s^{-\hat{\alpha}^\dagger\hat{\alpha}^\dagger\hat{\beta}^\dagger}_{\boldsymbol{Q},\boldsymbol{k}_1,-\boldsymbol{k}_3,\boldsymbol{k}_2} \\
&-2C^{\hat{\alpha}^\dagger\hat{\beta}^\dagger}_{\boldsymbol{k}_1,-\boldsymbol{k}_1} s^{-\hat{\beta}^\dagger\hat{\beta}\hat{\beta}}_{\boldsymbol{Q},\boldsymbol{k}_2,-\boldsymbol{k}_1,\boldsymbol{k}_3} \\
&-C^{\hat{\alpha}^\dagger\hat{\beta}^\dagger}_{-\boldsymbol{k}_2,\boldsymbol{k}_2} s^{-\hat{\alpha}^\dagger\hat{\alpha}\hat{\beta}}_{\boldsymbol{Q},\boldsymbol{k}_1,-\boldsymbol{k}_2,\boldsymbol{k}_3} \\
&-2s^{-\hat{\beta}}_{\boldsymbol{Q},-\boldsymbol{k}_1-\boldsymbol{k}_2+\boldsymbol{k}_3} C^{\hat{\alpha}^\dagger\hat{\beta}^\dagger\hat{\beta}^\dagger\hat{\beta}}_{\boldsymbol{k}_1,\boldsymbol{k}_2,-\boldsymbol{k}_1-\boldsymbol{k}_2+\boldsymbol{k}_3,\boldsymbol{k}_3} \\
&-2s^{-\hat{\alpha}^\dagger\hat{\alpha}\hat{\beta}}_{\boldsymbol{Q},\boldsymbol{k}_1,\boldsymbol{k}_4,-\boldsymbol{k}_2+\boldsymbol{k}_3-\boldsymbol{k}_4} C^{\hat{\alpha}^\dagger\hat{\beta}^\dagger\hat{\beta}^\dagger\hat{\beta}}_{\boldsymbol{k}_4,\boldsymbol{k}_2,-\boldsymbol{k}_2+\boldsymbol{k}_3-\boldsymbol{k}_4,\boldsymbol{k}_3} \\
&-4C^{\hat{\alpha}\hat{\beta}^\dagger\hat{\beta}\hat{\beta}}_{\boldsymbol{k}_4,\boldsymbol{k}_2,\boldsymbol{k}_3,\boldsymbol{k}_2-\boldsymbol{k}_3-\boldsymbol{k}_4} s^{-\hat{\alpha}^\dagger\hat{\alpha}^\dagger\hat{\beta}^\dagger}_{\boldsymbol{Q},\boldsymbol{k}_1,\boldsymbol{k}_4,\boldsymbol{k}_2-\boldsymbol{k}_3-\boldsymbol{k}_4} \\
&-8s^{-\hat{\alpha}\hat{\beta}\hat{\beta}}_{\boldsymbol{Q},\boldsymbol{k}_4,\boldsymbol{k}_3,-\boldsymbol{k}_1-\boldsymbol{k}_2-\boldsymbol{k}_4} C^{\hat{\alpha}^\dagger\hat{\alpha}^\dagger\hat{\beta}^\dagger\hat{\beta}^\dagger}_{\boldsymbol{k}_1,\boldsymbol{k}_4,\boldsymbol{k}_2,-\boldsymbol{k}_1-\boldsymbol{k}_2-\boldsymbol{k}_4} \\
&-2s^{-\hat{\beta}^\dagger\hat{\beta}\hat{\beta}}_{\boldsymbol{Q},\boldsymbol{k}_2,\boldsymbol{k}_4,-\boldsymbol{k}_1+\boldsymbol{k}_3-\boldsymbol{k}_4} C^{\hat{\alpha}^\dagger\hat{\beta}^\dagger\hat{\beta}^\dagger\hat{\beta}}_{\boldsymbol{k}_1,\boldsymbol{k}_4,-\boldsymbol{k}_1+\boldsymbol{k}_3-\boldsymbol{k}_4,\boldsymbol{k}_3} \\
&-2C^{\hat{\alpha}^\dagger\hat{\alpha}\hat{\alpha}\hat{\beta}}_{\boldsymbol{k}_1,\boldsymbol{k}_4,\boldsymbol{k}_1-\boldsymbol{k}_3-\boldsymbol{k}_4,\boldsymbol{k}_3} s^{-\hat{\alpha}^\dagger\hat{\alpha}^\dagger\hat{\beta}^\dagger}_{\boldsymbol{Q},\boldsymbol{k}_4,\boldsymbol{k}_1-\boldsymbol{k}_3-\boldsymbol{k}_4,\boldsymbol{k}_2} \,,
\end{aligned}
\tag{B.30}
$$

$$
\begin{aligned}
\partial_\ell s^{-\hat{\alpha}\hat{\beta}\hat{\beta}}_{\boldsymbol{Q},\boldsymbol{k}_1,\boldsymbol{k}_2,\boldsymbol{k}_3} = &-C^{\hat{\alpha}\hat{\beta}}_{\boldsymbol{k}_1,-\boldsymbol{k}_1} s^{-\hat{\beta}^\dagger\hat{\beta}\hat{\beta}}_{\boldsymbol{Q},-\boldsymbol{k}_1,\boldsymbol{k}_2,\boldsymbol{k}_3} \\
&-\frac{1}{2}C^{\hat{\alpha}\hat{\beta}}_{-\boldsymbol{k}_2,\boldsymbol{k}_2} s^{-\hat{\alpha}^\dagger\hat{\alpha}\hat{\beta}}_{\boldsymbol{Q},-\boldsymbol{k}_2,\boldsymbol{k}_1,\boldsymbol{k}_3} \\
&-\frac{1}{2}C^{\hat{\alpha}\hat{\beta}}_{-\boldsymbol{k}_3,\boldsymbol{k}_3} s^{-\hat{\alpha}^\dagger\hat{\alpha}\hat{\beta}}_{\boldsymbol{Q},-\boldsymbol{k}_3,\boldsymbol{k}_1,\boldsymbol{k}_2} \\
&-2s^{-\hat{\alpha}^\dagger}_{\boldsymbol{Q},-\boldsymbol{k}_1-\boldsymbol{k}_2-\boldsymbol{k}_3} C^{\hat{\alpha}\hat{\alpha}\hat{\beta}\hat{\beta}}_{\boldsymbol{k}_1,-\boldsymbol{k}_1-\boldsymbol{k}_2-\boldsymbol{k}_3,\boldsymbol{k}_2,\boldsymbol{k}_3} \\
&+s^{-\hat{\beta}}_{\boldsymbol{Q},\boldsymbol{k}_1+\boldsymbol{k}_2+\boldsymbol{k}_3} C^{\hat{\alpha}\hat{\beta}^\dagger\hat{\beta}\hat{\beta}}_{\boldsymbol{k}_1,\boldsymbol{k}_1+\boldsymbol{k}_2+\boldsymbol{k}_3,\boldsymbol{k}_2,\boldsymbol{k}_3} \\
&-2s^{-\hat{\alpha}^\dagger\hat{\beta}^\dagger\hat{\beta}}_{\boldsymbol{Q},\boldsymbol{k}_4,-\boldsymbol{k}_1-\boldsymbol{k}_2-\boldsymbol{k}_4,\boldsymbol{k}_3} C^{\hat{\alpha}\hat{\alpha}\hat{\beta}\hat{\beta}}_{\boldsymbol{k}_1,\boldsymbol{k}_4,\boldsymbol{k}_2,-\boldsymbol{k}_1-\boldsymbol{k}_2-\boldsymbol{k}_4} \\
&-2s^{-\hat{\alpha}^\dagger\hat{\beta}^\dagger\hat{\beta}}_{\boldsymbol{Q},\boldsymbol{k}_4,-\boldsymbol{k}_1-\boldsymbol{k}_3-\boldsymbol{k}_4,\boldsymbol{k}_2} C^{\hat{\alpha}\hat{\alpha}\hat{\beta}\hat{\beta}}_{\boldsymbol{k}_1,\boldsymbol{k}_4,\boldsymbol{k}_3,-\boldsymbol{k}_1-\boldsymbol{k}_3-\boldsymbol{k}_4} \\
&-2s^{-\hat{\alpha}^\dagger\hat{\alpha}^\dagger\hat{\alpha}}_{\boldsymbol{Q},\boldsymbol{k}_4,-\boldsymbol{k}_2-\boldsymbol{k}_3-\boldsymbol{k}_4,\boldsymbol{k}_1} C^{\hat{\alpha}\hat{\alpha}\hat{\beta}\hat{\beta}}_{\boldsymbol{k}_4,-\boldsymbol{k}_2-\boldsymbol{k}_3-\boldsymbol{k}_4,\boldsymbol{k}_2,\boldsymbol{k}_3} \,,
\end{aligned}
\tag{B.31}
$$

$$
\begin{aligned}
\partial_\ell s^{-\hat{\beta}^\dagger\hat{\beta}\hat{\beta}}_{\boldsymbol{Q},\boldsymbol{k}_1,\boldsymbol{k}_2,\boldsymbol{k}_3} = &-\frac{1}{2}C^{\hat{\alpha}\hat{\beta}}_{-\boldsymbol{k}_2,\boldsymbol{k}_2} s^{-\hat{\alpha}^\dagger\hat{\beta}^\dagger\hat{\beta}}_{\boldsymbol{Q},-\boldsymbol{k}_2,\boldsymbol{k}_1,\boldsymbol{k}_3} \\
&-\frac{1}{2}C^{\hat{\alpha}\hat{\beta}}_{-\boldsymbol{k}_3,\boldsymbol{k}_3} s^{-\hat{\alpha}^\dagger\hat{\beta}^\dagger\hat{\beta}}_{\boldsymbol{Q},-\boldsymbol{k}_3,\boldsymbol{k}_1,\boldsymbol{k}_2} \\
&-C^{\hat{\alpha}^\dagger\hat{\beta}^\dagger}_{-\boldsymbol{k}_1,\boldsymbol{k}_1} s^{-\hat{\alpha}\hat{\beta}\hat{\beta}}_{\boldsymbol{Q},-\boldsymbol{k}_1,\boldsymbol{k}_2,\boldsymbol{k}_3} \\
&-s^{-\hat{\alpha}^\dagger}_{\boldsymbol{Q},\boldsymbol{k}_1-\boldsymbol{k}_2-\boldsymbol{k}_3} C^{\hat{\alpha}\hat{\beta}^\dagger\hat{\beta}\hat{\beta}}_{\boldsymbol{k}_1-\boldsymbol{k}_2-\boldsymbol{k}_3,\boldsymbol{k}_1,\boldsymbol{k}_2,\boldsymbol{k}_3} \\
&-s^{-\hat{\alpha}^\dagger\hat{\beta}^\dagger\hat{\beta}}_{\boldsymbol{Q},\boldsymbol{k}_4,\boldsymbol{k}_1-\boldsymbol{k}_2-\boldsymbol{k}_4,\boldsymbol{k}_3} C^{\hat{\alpha}\hat{\beta}^\dagger\hat{\beta}\hat{\beta}}_{\boldsymbol{k}_4,\boldsymbol{k}_1,\boldsymbol{k}_2,\boldsymbol{k}_1-\boldsymbol{k}_2-\boldsymbol{k}_4} \\
&-s^{-\hat{\alpha}^\dagger\hat{\beta}^\dagger\hat{\beta}}_{\boldsymbol{Q},\boldsymbol{k}_4,\boldsymbol{k}_1-\boldsymbol{k}_3-\boldsymbol{k}_4,\boldsymbol{k}_2} C^{\hat{\alpha}\hat{\beta}^\dagger\hat{\beta}\hat{\beta}}_{\boldsymbol{k}_4,\boldsymbol{k}_1,\boldsymbol{k}_3,\boldsymbol{k}_1-\boldsymbol{k}_3-\boldsymbol{k}_4} \\
&-2s^{-\hat{\alpha}\hat{\beta}\hat{\beta}}_{\boldsymbol{Q},\boldsymbol{k}_4,\boldsymbol{k}_2,-\boldsymbol{k}_1+\boldsymbol{k}_3-\boldsymbol{k}_4} C^{\hat{\alpha}^\dagger\hat{\beta}^\dagger\hat{\beta}^\dagger\hat{\beta}}_{\boldsymbol{k}_4,\boldsymbol{k}_1,-\boldsymbol{k}_1+\boldsymbol{k}_3-\boldsymbol{k}_4,\boldsymbol{k}_3} \\
&-2s^{-\hat{\alpha}\hat{\beta}\hat{\beta}}_{\boldsymbol{Q},\boldsymbol{k}_4,\boldsymbol{k}_3,-\boldsymbol{k}_1+\boldsymbol{k}_2-\boldsymbol{k}_4} C^{\hat{\alpha}^\dagger\hat{\beta}^\dagger\hat{\beta}^\dagger\hat{\beta}}_{\boldsymbol{k}_4,\boldsymbol{k}_1,-\boldsymbol{k}_1+\boldsymbol{k}_2-\boldsymbol{k}_4,\boldsymbol{k}_2} \\
&-2s^{-\hat{\alpha}^\dagger\hat{\alpha}^\dagger\hat{\beta}^\dagger}_{\boldsymbol{Q},\boldsymbol{k}_4,-\boldsymbol{k}_2-\boldsymbol{k}_3-\boldsymbol{k}_4,\boldsymbol{k}_1} C^{\hat{\alpha}\hat{\alpha}\hat{\beta}\hat{\beta}}_{\boldsymbol{k}_4,-\boldsymbol{k}_2-\boldsymbol{k}_3-\boldsymbol{k}_4,\boldsymbol{k}_2,\boldsymbol{k}_3} \,.
\end{aligned}
\tag{B.32}
$$

$$
\begin{aligned}
\partial_\ell s^{+\hat{\alpha}}_{\boldsymbol{Q},\boldsymbol{k}_1} =& -C^{\hat{\alpha}\hat{\beta}}_{\boldsymbol{k}_1,-\boldsymbol{k}_1} s^{+\hat{\beta}^\dagger}_{\boldsymbol{Q},-\boldsymbol{k}_1} \\
&- C^{\hat{\alpha}\hat{\beta}}_{\boldsymbol{k}_2,-\boldsymbol{k}_2} s^{+\hat{\alpha}^\dagger\hat{\alpha}\hat{\beta}^\dagger}_{\boldsymbol{Q},\boldsymbol{k}_2,\boldsymbol{k}_1,-\boldsymbol{k}_2} \\
&- 2C^{\hat{\alpha}^\dagger\hat{\beta}^\dagger}_{\boldsymbol{k}_2,-\boldsymbol{k}_2} s^{+\hat{\alpha}\hat{\alpha}\hat{\beta}}_{\boldsymbol{Q},\boldsymbol{k}_1,\boldsymbol{k}_2,-\boldsymbol{k}_2} \\
&- 4s^{+\hat{\alpha}^\dagger\hat{\beta}^\dagger\hat{\beta}^\dagger}_{\boldsymbol{Q},\boldsymbol{k}_2,\boldsymbol{k}_3,-\boldsymbol{k}_1-\boldsymbol{k}_2-\boldsymbol{k}_3} C^{\hat{\alpha}\hat{\alpha}\hat{\beta}\hat{\beta}}_{\boldsymbol{k}_1,\boldsymbol{k}_2,\boldsymbol{k}_3,-\boldsymbol{k}_1-\boldsymbol{k}_2-\boldsymbol{k}_3} \\
&-2s^{+\hat{\alpha}\hat{\alpha}\hat{\beta}}_{\boldsymbol{Q},\boldsymbol{k}_2,\boldsymbol{k}_3,\boldsymbol{k}_1-\boldsymbol{k}_2-\boldsymbol{k}_3} C^{\hat{\alpha}^\dagger\hat{\alpha}^\dagger\hat{\alpha}\hat{\beta}^\dagger}_{\boldsymbol{k}_2,\boldsymbol{k}_3,\boldsymbol{k}_1,\boldsymbol{k}_1-\boldsymbol{k}_2-\boldsymbol{k}_3} ,
\end{aligned}
\tag{B.33}
$$

$$
\begin{aligned}
\partial_\ell s^{+\hat{\beta}^\dagger}_{\boldsymbol{Q},\boldsymbol{k}_1} =& -2C^{\hat{\alpha}\hat{\beta}}_{\boldsymbol{k}_2,-\boldsymbol{k}_2} s^{+\hat{\alpha}^\dagger\hat{\beta}^\dagger\hat{\beta}^\dagger}_{\boldsymbol{Q},\boldsymbol{k}_2,\boldsymbol{k}_1,-\boldsymbol{k}_2} \\
&- C^{\hat{\alpha}^\dagger\hat{\beta}^\dagger}_{-\boldsymbol{k}_1,\boldsymbol{k}_1} s^{+\hat{\alpha}}_{\boldsymbol{Q},-\boldsymbol{k}_1} \\
&- C^{\hat{\alpha}^\dagger\hat{\beta}^\dagger}_{\boldsymbol{k}_2,-\boldsymbol{k}_2} s^{+\hat{\alpha}\hat{\beta}^\dagger\hat{\beta}}_{\boldsymbol{Q},\boldsymbol{k}_2,\boldsymbol{k}_1,-\boldsymbol{k}_2} \\
&-2C^{\hat{\alpha}\hat{\beta}^\dagger\hat{\beta}\hat{\beta}}_{\boldsymbol{k}_2,\boldsymbol{k}_1,\boldsymbol{k}_3,\boldsymbol{k}_1-\boldsymbol{k}_2-\boldsymbol{k}_3} s^{+\hat{\alpha}^\dagger\hat{\beta}^\dagger\hat{\beta}^\dagger}_{\boldsymbol{Q},\boldsymbol{k}_2,\boldsymbol{k}_3,\boldsymbol{k}_1-\boldsymbol{k}_2-\boldsymbol{k}_3} \\
&- 4s^{+\hat{\alpha}\hat{\alpha}\hat{\beta}}_{\boldsymbol{Q},\boldsymbol{k}_2,\boldsymbol{k}_3,-\boldsymbol{k}_1-\boldsymbol{k}_2-\boldsymbol{k}_3} C^{\hat{\alpha}^\dagger\hat{\alpha}^\dagger\hat{\beta}^\dagger\hat{\beta}^\dagger}_{\boldsymbol{k}_2,\boldsymbol{k}_3,\boldsymbol{k}_1,-\boldsymbol{k}_1-\boldsymbol{k}_2-\boldsymbol{k}_3} ,
\end{aligned}
\tag{B.34}
$$

$$
\begin{aligned}
\partial_\ell s^{+\hat{\alpha}^\dagger\hat{\alpha}\hat{\alpha}}_{\boldsymbol{Q},\boldsymbol{k}_1,\boldsymbol{k}_2,\boldsymbol{k}_3} =& -\frac{1}{2} C^{\hat{\alpha}\hat{\beta}}_{\boldsymbol{k}_2,-\boldsymbol{k}_2} s^{+\hat{\alpha}^\dagger\hat{\alpha}\hat{\beta}^\dagger}_{\boldsymbol{Q},\boldsymbol{k}_1,\boldsymbol{k}_3,-\boldsymbol{k}_2} \\
&- \frac{1}{2} C^{\hat{\alpha}\hat{\beta}}_{\boldsymbol{k}_3,-\boldsymbol{k}_3} s^{+\hat{\alpha}^\dagger\hat{\alpha}\hat{\beta}^\dagger}_{\boldsymbol{Q},\boldsymbol{k}_1,\boldsymbol{k}_2,-\boldsymbol{k}_3} \\
&- C^{\hat{\alpha}^\dagger\hat{\beta}^\dagger}_{\boldsymbol{k}_1,-\boldsymbol{k}_1} s^{+\hat{\alpha}\hat{\alpha}\hat{\beta}}_{\boldsymbol{Q},\boldsymbol{k}_2,\boldsymbol{k}_3,-\boldsymbol{k}_1} \\
&-s^{+\hat{\beta}^\dagger}_{\boldsymbol{Q},\boldsymbol{k}_1-\boldsymbol{k}_2-\boldsymbol{k}_3} C^{\hat{\alpha}^\dagger\hat{\alpha}\hat{\alpha}\hat{\beta}}_{\boldsymbol{k}_1,\boldsymbol{k}_2,\boldsymbol{k}_3,\boldsymbol{k}_1-\boldsymbol{k}_2-\boldsymbol{k}_3} \\
&-s^{+\hat{\alpha}^\dagger\hat{\alpha}\hat{\beta}^\dagger}_{\boldsymbol{Q},\boldsymbol{k}_4,\boldsymbol{k}_2,\boldsymbol{k}_1-\boldsymbol{k}_3-\boldsymbol{k}_4} C^{\hat{\alpha}^\dagger\hat{\alpha}\hat{\alpha}\hat{\beta}}_{\boldsymbol{k}_1,\boldsymbol{k}_3,\boldsymbol{k}_4,\boldsymbol{k}_1-\boldsymbol{k}_3-\boldsymbol{k}_4} \\
&-s^{+\hat{\alpha}^\dagger\hat{\alpha}\hat{\beta}^\dagger}_{\boldsymbol{Q},\boldsymbol{k}_4,\boldsymbol{k}_3,\boldsymbol{k}_1-\boldsymbol{k}_2-\boldsymbol{k}_4} C^{\hat{\alpha}^\dagger\hat{\alpha}\hat{\alpha}\hat{\beta}}_{\boldsymbol{k}_1,\boldsymbol{k}_2,\boldsymbol{k}_4,\boldsymbol{k}_1-\boldsymbol{k}_2-\boldsymbol{k}_4} \\
&- 2s^{+\hat{\alpha}^\dagger\hat{\beta}^\dagger\hat{\beta}^\dagger}_{\boldsymbol{Q},\boldsymbol{k}_1,\boldsymbol{k}_4,-\boldsymbol{k}_2-\boldsymbol{k}_3-\boldsymbol{k}_4} C^{\hat{\alpha}\hat{\alpha}\hat{\beta}\hat{\beta}}_{\boldsymbol{k}_2,\boldsymbol{k}_3,\boldsymbol{k}_4,-\boldsymbol{k}_2-\boldsymbol{k}_3-\boldsymbol{k}_4} \\
&-2s^{+\hat{\alpha}\hat{\alpha}\hat{\beta}}_{\boldsymbol{Q},\boldsymbol{k}_2,\boldsymbol{k}_4,-\boldsymbol{k}_1+\boldsymbol{k}_3-\boldsymbol{k}_4} C^{\hat{\alpha}^\dagger\hat{\alpha}^\dagger\hat{\alpha}\hat{\beta}^\dagger}_{\boldsymbol{k}_1,\boldsymbol{k}_4,\boldsymbol{k}_3,-\boldsymbol{k}_1+\boldsymbol{k}_3-\boldsymbol{k}_4} \\
&-2s^{+\hat{\alpha}\hat{\alpha}\hat{\beta}}_{\boldsymbol{Q},\boldsymbol{k}_3,\boldsymbol{k}_4,-\boldsymbol{k}_1+\boldsymbol{k}_2-\boldsymbol{k}_4} C^{\hat{\alpha}^\dagger\hat{\alpha}^\dagger\hat{\alpha}\hat{\beta}^\dagger}_{\boldsymbol{k}_1,\boldsymbol{k}_4,\boldsymbol{k}_2,-\boldsymbol{k}_1+\boldsymbol{k}_2-\boldsymbol{k}_4} ,
\end{aligned}
\tag{B.35}
$$

$$
\begin{aligned}
\partial_\ell s^{+\hat{\alpha}^\dagger\hat{\alpha}\hat{\beta}^\dagger}_{\boldsymbol{Q},\boldsymbol{k}_1,\boldsymbol{k}_2,\boldsymbol{k}_3} =& -2C^{\hat{\alpha}\hat{\beta}}_{\boldsymbol{k}_2,-\boldsymbol{k}_2} s^{+\hat{\alpha}^\dagger\hat{\beta}^\dagger\hat{\beta}^\dagger}_{\boldsymbol{Q},\boldsymbol{k}_1,-\boldsymbol{k}_2,\boldsymbol{k}_3} \\
&- C^{\hat{\alpha}^\dagger\hat{\beta}^\dagger}_{\boldsymbol{k}_1,-\boldsymbol{k}_1} s^{+\hat{\alpha}\hat{\beta}^\dagger\hat{\beta}}_{\boldsymbol{Q},\boldsymbol{k}_2,\boldsymbol{k}_3,-\boldsymbol{k}_1} \\
&- 2C^{\hat{\alpha}^\dagger\hat{\beta}^\dagger}_{-\boldsymbol{k}_3,\boldsymbol{k}_3} s^{+\hat{\alpha}^\dagger\hat{\alpha}\hat{\alpha}}_{\boldsymbol{Q},\boldsymbol{k}_1,\boldsymbol{k}_2,-\boldsymbol{k}_3} \\
&-2s^{+\hat{\alpha}}_{\boldsymbol{Q},-\boldsymbol{k}_1+\boldsymbol{k}_2-\boldsymbol{k}_3} C^{\hat{\alpha}^\dagger\hat{\alpha}^\dagger\hat{\alpha}\hat{\beta}^\dagger}_{\boldsymbol{k}_1,-\boldsymbol{k}_1+\boldsymbol{k}_2-\boldsymbol{k}_3,\boldsymbol{k}_2,\boldsymbol{k}_3} \\
&-2s^{+\hat{\alpha}\hat{\beta}^\dagger\hat{\beta}}_{\boldsymbol{Q},\boldsymbol{k}_4,\boldsymbol{k}_3,-\boldsymbol{k}_1+\boldsymbol{k}_2-\boldsymbol{k}_4} C^{\hat{\alpha}^\dagger\hat{\alpha}^\dagger\hat{\alpha}\hat{\beta}^\dagger}_{\boldsymbol{k}_1,\boldsymbol{k}_4,\boldsymbol{k}_2,-\boldsymbol{k}_1+\boldsymbol{k}_2-\boldsymbol{k}_4} \\
&-2C^{\hat{\alpha}\hat{\beta}^\dagger\hat{\beta}\hat{\beta}}_{\boldsymbol{k}_2,\boldsymbol{k}_3,\boldsymbol{k}_4,-\boldsymbol{k}_2+\boldsymbol{k}_3-\boldsymbol{k}_4} s^{+\hat{\alpha}^\dagger\hat{\beta}^\dagger\hat{\beta}^\dagger}_{\boldsymbol{Q},\boldsymbol{k}_1,\boldsymbol{k}_4,-\boldsymbol{k}_2+\boldsymbol{k}_3-\boldsymbol{k}_4} \\
&-2s^{+\hat{\alpha}^\dagger\hat{\alpha}\hat{\alpha}}_{\boldsymbol{Q},\boldsymbol{k}_1,\boldsymbol{k}_4,\boldsymbol{k}_2-\boldsymbol{k}_3-\boldsymbol{k}_4} C^{\hat{\alpha}^\dagger\hat{\alpha}^\dagger\hat{\alpha}\hat{\beta}^\dagger}_{\boldsymbol{k}_4,\boldsymbol{k}_2-\boldsymbol{k}_3-\boldsymbol{k}_4,\boldsymbol{k}_2,\boldsymbol{k}_3} \\
&-4s^{+\hat{\alpha}^\dagger\hat{\beta}^\dagger\hat{\beta}^\dagger}_{\boldsymbol{Q},\boldsymbol{k}_4,\boldsymbol{k}_3,\boldsymbol{k}_1-\boldsymbol{k}_2-\boldsymbol{k}_4} C^{\hat{\alpha}^\dagger\hat{\alpha}\hat{\alpha}\hat{\beta}}_{\boldsymbol{k}_1,\boldsymbol{k}_2,\boldsymbol{k}_4,\boldsymbol{k}_1-\boldsymbol{k}_2-\boldsymbol{k}_4} \\
&- 8s^{+\hat{\alpha}\hat{\alpha}\hat{\beta}}_{\boldsymbol{Q},\boldsymbol{k}_2,\boldsymbol{k}_4,-\boldsymbol{k}_1-\boldsymbol{k}_3-\boldsymbol{k}_4} C^{\hat{\alpha}^\dagger\hat{\alpha}^\dagger\hat{\beta}^\dagger\hat{\beta}^\dagger}_{\boldsymbol{k}_1,\boldsymbol{k}_4,\boldsymbol{k}_3,-\boldsymbol{k}_1-\boldsymbol{k}_3-\boldsymbol{k}_4} ,
\end{aligned}
\tag{B.36}
$$

$$
\begin{aligned}
\partial_\ell s^{+\hat{\alpha}^\dagger\hat{\beta}^\dagger\hat{\beta}^\dagger}_{\boldsymbol{Q},\boldsymbol{k}_1,\boldsymbol{k}_2,\boldsymbol{k}_3} = &- C^{\hat{\alpha}^\dagger\hat{\beta}^\dagger}_{\boldsymbol{k}_1,-\boldsymbol{k}_1} s^{+\hat{\beta}^\dagger\hat{\beta}^\dagger\hat{\beta}}_{\boldsymbol{Q},\boldsymbol{k}_2,\boldsymbol{k}_3,-\boldsymbol{k}_1} \\
&- \frac{1}{2} C^{\hat{\alpha}^\dagger\hat{\beta}^\dagger}_{-\boldsymbol{k}_2,\boldsymbol{k}_2} s^{+\hat{\alpha}^\dagger\hat{\alpha}\hat{\beta}^\dagger}_{\boldsymbol{Q},\boldsymbol{k}_1,-\boldsymbol{k}_2,\boldsymbol{k}_3} \\
&- \frac{1}{2} C^{\hat{\alpha}^\dagger\hat{\beta}^\dagger}_{-\boldsymbol{k}_3,\boldsymbol{k}_3} s^{+\hat{\alpha}^\dagger\hat{\alpha}\hat{\beta}^\dagger}_{\boldsymbol{Q},\boldsymbol{k}_1,-\boldsymbol{k}_3,\boldsymbol{k}_2} \\
&- 2 s^{+\hat{\alpha}}_{\boldsymbol{Q},-\boldsymbol{k}_1-\boldsymbol{k}_2-\boldsymbol{k}_3} C^{\hat{\alpha}^\dagger\hat{\alpha}^\dagger\hat{\beta}^\dagger\hat{\beta}^\dagger}_{\boldsymbol{k}_1,-\boldsymbol{k}_1-\boldsymbol{k}_2-\boldsymbol{k}_3,\boldsymbol{k}_2,\boldsymbol{k}_3} \\
&+ s^{+\hat{\beta}^\dagger}_{\boldsymbol{Q},\boldsymbol{k}_1+\boldsymbol{k}_2+\boldsymbol{k}_3} C^{\hat{\alpha}^\dagger\hat{\beta}^\dagger\hat{\beta}^\dagger\hat{\beta}}_{\boldsymbol{k}_1,\boldsymbol{k}_2,\boldsymbol{k}_3,\boldsymbol{k}_1+\boldsymbol{k}_2+\boldsymbol{k}_3} \\
&- 2 s^{+\hat{\alpha}\hat{\beta}^\dagger\hat{\beta}}_{\boldsymbol{Q},\boldsymbol{k}_4,\boldsymbol{k}_2,-\boldsymbol{k}_1-\boldsymbol{k}_3-\boldsymbol{k}_4} C^{\hat{\alpha}^\dagger\hat{\alpha}^\dagger\hat{\beta}^\dagger\hat{\beta}^\dagger}_{\boldsymbol{k}_1,\boldsymbol{k}_4,\boldsymbol{k}_3,-\boldsymbol{k}_1-\boldsymbol{k}_3-\boldsymbol{k}_4} \\
&- 2 s^{+\hat{\alpha}\hat{\beta}^\dagger\hat{\beta}}_{\boldsymbol{Q},\boldsymbol{k}_4,\boldsymbol{k}_3,-\boldsymbol{k}_1-\boldsymbol{k}_2-\boldsymbol{k}_4} C^{\hat{\alpha}^\dagger\hat{\alpha}^\dagger\hat{\beta}^\dagger\hat{\beta}^\dagger}_{\boldsymbol{k}_1,\boldsymbol{k}_4,\boldsymbol{k}_2,-\boldsymbol{k}_1-\boldsymbol{k}_2-\boldsymbol{k}_4} \\
&- 2 s^{+\hat{\alpha}^\dagger\hat{\alpha}\hat{\alpha}}_{\boldsymbol{Q},\boldsymbol{k}_1,\boldsymbol{k}_4,-\boldsymbol{k}_2-\boldsymbol{k}_3-\boldsymbol{k}_4} C^{\hat{\alpha}^\dagger\hat{\alpha}^\dagger\hat{\beta}^\dagger\hat{\beta}^\dagger}_{\boldsymbol{k}_4,-\boldsymbol{k}_2-\boldsymbol{k}_3-\boldsymbol{k}_4,\boldsymbol{k}_2,\boldsymbol{k}_3} \,,
\end{aligned}
\tag{B.37}
$$

$$
\begin{aligned}
\partial_\ell s^{+\hat{\alpha}\hat{\alpha}\hat{\beta}}_{\boldsymbol{Q},\boldsymbol{k}_1,\boldsymbol{k}_2,\boldsymbol{k}_3} = &- \frac{1}{2} C^{\hat{\alpha}\hat{\beta}}_{\boldsymbol{k}_1,-\boldsymbol{k}_1} s^{+\hat{\alpha}\hat{\beta}^\dagger\hat{\beta}}_{\boldsymbol{Q},\boldsymbol{k}_2,-\boldsymbol{k}_1,\boldsymbol{k}_3} \\
&- \frac{1}{2} C^{\hat{\alpha}\hat{\beta}}_{\boldsymbol{k}_2,-\boldsymbol{k}_2} s^{+\hat{\alpha}\hat{\beta}^\dagger\hat{\beta}}_{\boldsymbol{Q},\boldsymbol{k}_1,-\boldsymbol{k}_2,\boldsymbol{k}_3} \\
&- C^{\hat{\alpha}\hat{\beta}}_{-\boldsymbol{k}_3,\boldsymbol{k}_3} s^{+\hat{\alpha}^\dagger\hat{\alpha}\hat{\alpha}}_{\boldsymbol{Q},-\boldsymbol{k}_3,\boldsymbol{k}_1,\boldsymbol{k}_2} \\
&+ s^{+\hat{\alpha}}_{\boldsymbol{Q},\boldsymbol{k}_1+\boldsymbol{k}_2+\boldsymbol{k}_3} C^{\hat{\alpha}^\dagger\hat{\alpha}\hat{\alpha}\hat{\beta}}_{\boldsymbol{k}_1+\boldsymbol{k}_2+\boldsymbol{k}_3,\boldsymbol{k}_1,\boldsymbol{k}_2,\boldsymbol{k}_3} \\
&- 2 s^{+\hat{\beta}^\dagger}_{\boldsymbol{Q},-\boldsymbol{k}_1-\boldsymbol{k}_2-\boldsymbol{k}_3} C^{\hat{\alpha}\hat{\alpha}\hat{\beta}\hat{\beta}}_{\boldsymbol{k}_1,\boldsymbol{k}_2,\boldsymbol{k}_3,-\boldsymbol{k}_1-\boldsymbol{k}_2-\boldsymbol{k}_3} \\
&- 2 s^{+\hat{\alpha}^\dagger\hat{\alpha}\hat{\beta}^\dagger}_{\boldsymbol{Q},\boldsymbol{k}_4,\boldsymbol{k}_1,-\boldsymbol{k}_2-\boldsymbol{k}_3-\boldsymbol{k}_4} C^{\hat{\alpha}\hat{\alpha}\hat{\beta}\hat{\beta}}_{\boldsymbol{k}_2,\boldsymbol{k}_4,\boldsymbol{k}_3,-\boldsymbol{k}_2-\boldsymbol{k}_3-\boldsymbol{k}_4} \\
&- 2 s^{+\hat{\alpha}^\dagger\hat{\alpha}\hat{\beta}^\dagger}_{\boldsymbol{Q},\boldsymbol{k}_4,\boldsymbol{k}_2,-\boldsymbol{k}_1-\boldsymbol{k}_3-\boldsymbol{k}_4} C^{\hat{\alpha}\hat{\alpha}\hat{\beta}\hat{\beta}}_{\boldsymbol{k}_1,\boldsymbol{k}_4,\boldsymbol{k}_3,-\boldsymbol{k}_1-\boldsymbol{k}_3-\boldsymbol{k}_4} \\
&- 2 s^{+\hat{\beta}^\dagger\hat{\beta}^\dagger\hat{\beta}}_{\boldsymbol{Q},\boldsymbol{k}_4,-\boldsymbol{k}_1-\boldsymbol{k}_2-\boldsymbol{k}_4,\boldsymbol{k}_3} C^{\hat{\alpha}\hat{\alpha}\hat{\beta}\hat{\beta}}_{\boldsymbol{k}_1,\boldsymbol{k}_2,\boldsymbol{k}_4,-\boldsymbol{k}_1-\boldsymbol{k}_2-\boldsymbol{k}_4} \,,
\end{aligned}
\tag{B.38}
$$

$$
\begin{aligned}
\partial_\ell s^{+\hat{\alpha}\hat{\beta}^\dagger\hat{\beta}}_{\boldsymbol{Q},\boldsymbol{k}_1,\boldsymbol{k}_2,\boldsymbol{k}_3} = &- 2 C^{\hat{\alpha}\hat{\beta}}_{\boldsymbol{k}_1,-\boldsymbol{k}_1} s^{+\hat{\beta}^\dagger\hat{\beta}^\dagger\hat{\beta}}_{\boldsymbol{Q},-\boldsymbol{k}_1,\boldsymbol{k}_2,\boldsymbol{k}_3} \\
&- C^{\hat{\alpha}\hat{\beta}}_{-\boldsymbol{k}_3,\boldsymbol{k}_3} s^{+\hat{\alpha}^\dagger\hat{\alpha}\hat{\beta}^\dagger}_{\boldsymbol{Q},-\boldsymbol{k}_3,\boldsymbol{k}_1,\boldsymbol{k}_2} \\
&- 2 C^{\hat{\alpha}^\dagger\hat{\beta}^\dagger}_{-\boldsymbol{k}_2,\boldsymbol{k}_2} s^{+\hat{\alpha}\hat{\alpha}\hat{\beta}}_{\boldsymbol{Q},\boldsymbol{k}_1,-\boldsymbol{k}_2,\boldsymbol{k}_3} \\
&- 2 s^{+\hat{\beta}^\dagger}_{\boldsymbol{Q},-\boldsymbol{k}_1+\boldsymbol{k}_2-\boldsymbol{k}_3} C^{\hat{\alpha}\hat{\beta}^\dagger\hat{\beta}\hat{\beta}}_{\boldsymbol{k}_1,\boldsymbol{k}_2,\boldsymbol{k}_3,-\boldsymbol{k}_1+\boldsymbol{k}_2-\boldsymbol{k}_3} \\
&- 2 s^{+\hat{\alpha}^\dagger\hat{\alpha}\hat{\beta}^\dagger}_{\boldsymbol{Q},\boldsymbol{k}_4,\boldsymbol{k}_1,\boldsymbol{k}_2-\boldsymbol{k}_3-\boldsymbol{k}_4} C^{\hat{\alpha}\hat{\beta}^\dagger\hat{\beta}\hat{\beta}}_{\boldsymbol{k}_4,\boldsymbol{k}_2,\boldsymbol{k}_3,\boldsymbol{k}_2-\boldsymbol{k}_3-\boldsymbol{k}_4} \\
&- 2 C^{\hat{\alpha}\hat{\beta}^\dagger\hat{\beta}\hat{\beta}}_{\boldsymbol{k}_1,\boldsymbol{k}_2,\boldsymbol{k}_4,-\boldsymbol{k}_1+\boldsymbol{k}_2-\boldsymbol{k}_4} s^{+\hat{\beta}^\dagger\hat{\beta}^\dagger\hat{\beta}}_{\boldsymbol{Q},\boldsymbol{k}_4,-\boldsymbol{k}_1+\boldsymbol{k}_2-\boldsymbol{k}_4,\boldsymbol{k}_3} \\
&- 8 s^{+\hat{\alpha}^\dagger\hat{\beta}^\dagger\hat{\beta}^\dagger}_{\boldsymbol{Q},\boldsymbol{k}_4,\boldsymbol{k}_2,-\boldsymbol{k}_1-\boldsymbol{k}_3-\boldsymbol{k}_4} C^{\hat{\alpha}\hat{\alpha}\hat{\beta}\hat{\beta}}_{\boldsymbol{k}_1,\boldsymbol{k}_4,\boldsymbol{k}_3,-\boldsymbol{k}_1-\boldsymbol{k}_3-\boldsymbol{k}_4} \\
&- 4 C^{\hat{\alpha}^\dagger\hat{\beta}^\dagger\hat{\beta}^\dagger\hat{\beta}}_{\boldsymbol{k}_4,\boldsymbol{k}_2,-\boldsymbol{k}_2+\boldsymbol{k}_3-\boldsymbol{k}_4,\boldsymbol{k}_3} s^{+\hat{\alpha}\hat{\alpha}\hat{\beta}}_{\boldsymbol{Q},\boldsymbol{k}_1,\boldsymbol{k}_4,-\boldsymbol{k}_2+\boldsymbol{k}_3-\boldsymbol{k}_4} \\
&- 2 s^{+\hat{\alpha}\hat{\alpha}\hat{\beta}}_{\boldsymbol{Q},\boldsymbol{k}_4,\boldsymbol{k}_1-\boldsymbol{k}_2-\boldsymbol{k}_4,\boldsymbol{k}_3} C^{\hat{\alpha}^\dagger\hat{\alpha}^\dagger\hat{\alpha}\hat{\beta}^\dagger}_{\boldsymbol{k}_4,\boldsymbol{k}_1-\boldsymbol{k}_2-\boldsymbol{k}_4,\boldsymbol{k}_1,\boldsymbol{k}_2} \,,
\end{aligned}
\tag{B.39}
$$

$$
\begin{aligned}
\partial_\ell s^{+\hat{\beta}^\dagger\hat{\beta}^\dagger\hat{\beta}}_{\boldsymbol{Q},\boldsymbol{k}_1,\boldsymbol{k}_2,\boldsymbol{k}_3} = &- C^{\hat{\alpha}\hat{\beta}}_{-\boldsymbol{k}_3,\boldsymbol{k}_3} s^{+\hat{\alpha}^\dagger\hat{\beta}^\dagger\hat{\beta}^\dagger}_{\boldsymbol{Q},-\boldsymbol{k}_3,\boldsymbol{k}_1,\boldsymbol{k}_2} \\
&- \frac{1}{2} C^{\hat{\alpha}^\dagger\hat{\beta}^\dagger}_{-\boldsymbol{k}_1,\boldsymbol{k}_1} s^{+\hat{\alpha}\hat{\beta}^\dagger\hat{\beta}}_{\boldsymbol{Q},-\boldsymbol{k}_1,\boldsymbol{k}_2,\boldsymbol{k}_3} \\
&- \frac{1}{2} C^{\hat{\alpha}^\dagger\hat{\beta}^\dagger}_{-\boldsymbol{k}_2,\boldsymbol{k}_2} s^{+\hat{\alpha}\hat{\beta}^\dagger\hat{\beta}}_{\boldsymbol{Q},-\boldsymbol{k}_2,\boldsymbol{k}_1,\boldsymbol{k}_3} \\
&- s^{+\hat{\alpha}}_{\boldsymbol{Q},-\boldsymbol{k}_1-\boldsymbol{k}_2+\boldsymbol{k}_3} C^{\hat{\alpha}^\dagger\hat{\beta}^\dagger\hat{\beta}^\dagger\hat{\beta}}_{-\boldsymbol{k}_1-\boldsymbol{k}_2+\boldsymbol{k}_3,\boldsymbol{k}_1,\boldsymbol{k}_2,\boldsymbol{k}_3} \\
&- s^{+\hat{\alpha}\hat{\beta}^\dagger\hat{\beta}}_{\boldsymbol{Q},\boldsymbol{k}_4,\boldsymbol{k}_1,-\boldsymbol{k}_2+\boldsymbol{k}_3-\boldsymbol{k}_4} C^{\hat{\alpha}^\dagger\hat{\beta}^\dagger\hat{\beta}^\dagger\hat{\beta}}_{\boldsymbol{k}_4,\boldsymbol{k}_2,-\boldsymbol{k}_2+\boldsymbol{k}_3-\boldsymbol{k}_4,\boldsymbol{k}_3} \\
&- s^{+\hat{\alpha}\hat{\beta}^\dagger\hat{\beta}}_{\boldsymbol{Q},\boldsymbol{k}_4,\boldsymbol{k}_2,-\boldsymbol{k}_1+\boldsymbol{k}_3-\boldsymbol{k}_4} C^{\hat{\alpha}^\dagger\hat{\beta}^\dagger\hat{\beta}^\dagger\hat{\beta}}_{\boldsymbol{k}_4,\boldsymbol{k}_1,-\boldsymbol{k}_1+\boldsymbol{k}_3-\boldsymbol{k}_4,\boldsymbol{k}_3} \\
&- 2C^{\hat{\alpha}\hat{\beta}^\dagger\hat{\beta}\hat{\beta}}_{\boldsymbol{k}_4,\boldsymbol{k}_1,\boldsymbol{k}_3,\boldsymbol{k}_1-\boldsymbol{k}_3-\boldsymbol{k}_4} s^{+\hat{\alpha}^\dagger\hat{\beta}^\dagger\hat{\beta}^\dagger}_{\boldsymbol{Q},\boldsymbol{k}_4,\boldsymbol{k}_2,\boldsymbol{k}_1-\boldsymbol{k}_3-\boldsymbol{k}_4} \\
&- 2C^{\hat{\alpha}\hat{\beta}^\dagger\hat{\beta}\hat{\beta}}_{\boldsymbol{k}_4,\boldsymbol{k}_2,\boldsymbol{k}_3,\boldsymbol{k}_2-\boldsymbol{k}_3-\boldsymbol{k}_4} s^{+\hat{\alpha}^\dagger\hat{\beta}^\dagger\hat{\beta}^\dagger}_{\boldsymbol{Q},\boldsymbol{k}_4,\boldsymbol{k}_1,\boldsymbol{k}_2-\boldsymbol{k}_3-\boldsymbol{k}_4} \\
&- 2s^{+\hat{\alpha}\hat{\alpha}\hat{\beta}}_{\boldsymbol{Q},\boldsymbol{k}_4,-\boldsymbol{k}_1-\boldsymbol{k}_2-\boldsymbol{k}_4,\boldsymbol{k}_3} C^{\hat{\alpha}^\dagger\hat{\alpha}^\dagger\hat{\beta}^\dagger\hat{\beta}^\dagger}_{\boldsymbol{k}_4,-\boldsymbol{k}_1-\boldsymbol{k}_2-\boldsymbol{k}_4,\boldsymbol{k}_1,\boldsymbol{k}_2} \,.
\end{aligned}
\tag{B.40}
$$

Bibliography

[AM11] Karsten Ahnert and Mario Mulansky. "Odeint – Solving Ordinary Differential Equations in C++." *AIP Conference Proceedings* **1389**,1, 2011, pages 1586–1589.
DOI: 10.1063/1.3637934.

[Ame+11] Luuk J. P. Ament et al. "Resonant Inelastic X-Ray Scattering Studies of Elementary Excitations." *Reviews of Modern Physics* **83**,2, 2011, pages 705–767.
DOI: 10.1103/RevModPhys.83.705.

[And51] P. W. Anderson. "Limits on the Energy of the Antiferromagnetic Ground State." *Physical Review* **83**,6, 1951, pages 1260–1260.
DOI: 10.1103/PhysRev.83.1260.

[And72] P. W. Anderson. "More Is Different." *Science* **177**,4047, 1972, pages 393–396.
DOI: 10.1126/science.177.4047.393.

[Aro88] Daniel P. Arovas. "Functional Integral Theories of Low-Dimensional Quantum Heisenberg Models." *Physical Review B* **38**,1, 1988, pages 316–332.
DOI: 10.1103/PhysRevB.38.316.

[AS23] Alexander Altland and Ben Simons. *Condensed Matter Field Theory*. 3rd ed. Cambridge University Press, Cambridge, 2023.
DOI: 10.1017/9781108781244.

[Aue94] Assa Auerbach. *Interacting Electrons and Quantum Magnetism*. Red. by Joseph L. Birman et al. Graduate Texts in Contemporary Physics. Springer, New York, NY, 1994.
DOI: 10.1007/978-1-4612-0869-3.

[Bal+18] V. Baltz et al. "Antiferromagnetic Spintronics." *Reviews of Modern Physics* **90**,1, 2018, page 015005.
DOI: 10.1103/RevModPhys.90.015005.

[Bar+21] Anjan Barman et al. "The 2021 Magnonics Roadmap." *Journal of Physics: Condensed Matter* **33**,41, 2021, page 413001.
DOI: 10.1088/1361-648X/abec1a.

[BB98] Carl M. Bender and Stefan Boettcher. "Real Spectra in Non-Hermitian Hamiltonians Having PT Symmetry." *Physical Review Letters* **80**,24, 1998, pages 5243–5246.
DOI: 10.1103/PhysRevLett.80.5243.

[BBK21] Emil J. Bergholtz, Jan Carl Budich, and Flore K. Kunst. "Exceptional Topology of Non-Hermitian Systems." *Reviews of Modern Physics* **93**,1, 2021, page 015005.
DOI: 10.1103/RevModPhys.93.015005.

[BCS57] J. Bardeen, L. N. Cooper, and J. R. Schrieffer. "Theory of Superconductivity." *Physical Review* **108**,5, 1957, pages 1175–1204.
DOI: 10.1103/PhysRev.108.1175.

[BDN12] Immanuel Bloch, Jean Dalibard, and Sylvain Nascimbène. "Quantum Simulations with Ultracold Quantum Gases." *Nature Physics* **8**,4, 2012, pages 267–276.
DOI: 10.1038/nphys2259.

[Ben07] Carl M Bender. "Making Sense of Non-Hermitian Hamiltonians." *Reports on Progress in Physics* **70**,6, 2007, page 947.
DOI: 10.1088/0034-4885/70/6/R03.

[BHU22] Philip Bleicker, Dag-Björn Hering, and Götz S. Uhrig. "Charge Dynamics in Magnetically Disordered Mott Insulators." *Physical Review B* **105**,8, 2022, page 085121.
DOI: 10.1103/PhysRevB.105.085121.

[Bis+15] R. F. Bishop et al. "Frustrated Heisenberg Antiferromagnet on the Honeycomb Lattice: Spin Gap and Low-Energy Parameters." *Physical Review B* **92**,22, 2015, page 224434.
DOI: 10.1103/PhysRevB.92.224434.

[Bis+17] R. F. Bishop et al. "The Spin-Half *XXZ* Antiferromagnet on the Square Lattice Revisited: A High-Order Coupled Cluster Treatment." *Journal of Magnetism and Magnetic Materials* **428**, 2017, pages 178–188.
DOI: 10.1016/j.jmmm.2016.11.043.

[BKU23] Katrin Bolsmann, Asliddin Khudoyberdiev, and Götz S. Uhrig. "Switching the Magnetization in Quantum Antiferromagnets." *PRX Quantum* **4**,3, 2023, page 030332.
DOI: 10.1103/PRXQuantum.4.030332.

[BL16] R. F. Bishop and P. H. Y. Li. "Large-s Expansions for the Low-Energy Parameters of the Honeycomb-Lattice Heisenberg Antiferromagnet with Spin Quantum Number s." *Journal of Magnetism and Magnetic Materials* **407**, 2016, pages 348–357.
DOI: 10.1016/j.jmmm.2016.01.101.

[Blo30] F. Bloch. "Zur Theorie des Ferromagnetismus." *Zeitschrift für Physik* **61**,3, 1930, pages 206–219.
DOI: 10.1007/BF01339661.

[BM09] Cristina Bena and Gilles Montambaux. "Remarks on the Tight-Binding Model of Graphene." *New Journal of Physics* **11**,9, 2009, page 095003.
DOI: 10.1088/1367-2630/11/9/095003.

[BMP18] Kenneth S. Burch, David Mandrus, and Je-Geun Park. "Magnetism in Two-Dimensional van Der Waals Materials." *Nature* **563**,7729, 2018, pages 47–52.
DOI: 10.1038/s41586-018-0631-z.

[Bog47] N. Bogoliubov. "On the Theory of Superfluidity." *J. Phys* **11**,1, 1947, page 23.

[Bog58] N. N. Bogoljubov. "On a New Method in the Theory of Superconductivity." *Il Nuovo Cimento (1955-1965)* **7**,6, 1958, pages 794–805.
DOI: 10.1007/BF02745585.

[Boo] Boost Development Team. *Boost Libraries*. Version 1.78.0.

[BP07] Heinz-Peter Breuer and Francesco Petruccione. *The Theory of Open Quantum Systems*. Oxford University Press, 2007.
DOI: 10.1093/acprof:oso/9780199213900.001.0001.

[BR98] R. F. Bishop and J. Rosenfeld. "The Coupled Cluster Method Applied to the Spin-Half XXZ Model on the Honeycomb Lattice." *International Journal of Modern Physics B* **12**,23, 1998, pages 2371–2383.
DOI: 10.1142/S0217979298001381.

[Bro91] R. W. Brockett. "Dynamical Systems That Sort Lists, Diagonalize Matrices, and Solve Linear Programming Problems." *Linear Algebra and its Applications* **146**, 1991, pages 79–91.
DOI: 10.1016/0024-3795(91)90021-N.

[Cac+24] Nils Caci et al. "Quantitative Description of Long-Range Order in the spin−$\frac{1}{2}$ XXZ Antiferromagnet on the Square Lattice." *Physical Review B* **110**,5, 2024, page 054411. DOI: 10.1103/PhysRevB.110.054411.

[Car96] John Cardy. *Scaling and Renormalization in Statistical Physics*. Cambridge Lecture Notes in Physics. Cambridge University Press, Cambridge, 1996. DOI: 10.1017/CBO9781316036440.

[Cas+06] Eduardo V. Castro et al. "Site Dilution of Quantum Spins in the Honeycomb Lattice." *Physical Review B* **73**,5, 2006, page 054422. DOI: 10.1103/PhysRevB.73.054422.

[CD90] Moody T. Chu and Kenneth R. Driessel. "The Projected Gradient Method for Least Squares Matrix Approximations with Spectral Constraints." *SIAM Journal on Numerical Analysis* **27**,4, 1990, pages 1050–1060. DOI: 10.1137/0727062.

[Che+] T. Chen et al. "7. Non-hermitian Eigenvalue Problems." In: *Templates for the Solution of Algebraic Eigenvalue Problems*, pages 149–231. DOI: 10.1137/1.9780898719581.ch7. eprint: https://epubs.siam.org/doi/pdf/10.1137/1.9780898719581.ch7.

[Che+24] Qijin Chen et al. "When Superconductivity Crosses over: From BCS to BEC." *Reviews of Modern Physics* **96**,2, 2024, page 025002. DOI: 10.1103/RevModPhys.96.025002.

[Chr+04] N. B. Christensen et al. "Deviations from Linear Spin Wave Theory in the 2D, $S = \frac{1}{2}$ Heisenberg Antiferromagnet CFTD." *Journal of Magnetism and Magnetic Materials*. Proceedings of the International Conference on Magnetism (ICM 2003) **272–276**, 2004, pages 896–897. DOI: 10.1016/j.jmmm.2004.01.056.

[Chr+07] N. B. Christensen et al. "Quantum Dynamics and Entanglement of Spins on a Square Lattice." *Proceedings of the National Academy of Sciences* **104**,39, 2007, pages 15264–15269. DOI: 10.1073/pnas.0703293104.

[Chu+15] A. V. Chumak et al. "Magnon Spintronics." *Nature Physics* **11**,6, 2015, pages 453–461. DOI: 10.1038/nphys3347.

[Col+01] R. Coldea et al. "Spin Waves and Electronic Interactions in La_2CuO_4." *Physical Review Letters* **86**,23, 2001, pages 5377–5380. DOI: 10.1103/PhysRevLett.86.5377.

[Col78] J. H. P. Colpa. "Diagonalization of the Quadratic Boson Hamiltonian." *Physica A: Statistical Mechanics and its Applications* **93**,3–4, 1978, pages 327–353.

[CS15] K. Coester and K. P. Schmidt. "Optimizing Linked-Cluster Expansions by White Graphs." *Physical Review E* **92**,2, 2015, page 022118. DOI: 10.1103/PhysRevE.92.022118.

[Dal+15] B. Dalla Piazza et al. "Fractional Excitations in the Square-Lattice Quantum Antiferromagnet." *Nature Physics* **11**,1, 2015, pages 62–68. DOI: 10.1038/nphys3172.

[DDM15] E. Dobardžić, M. Dimitrijević, and M. V. Milovanović. "Generalized Bloch Theorem and Topological Characterization." *Physical Review B* **91**,12, 2015, page 125424. DOI: 10.1103/PhysRevB.91.125424.

[DEO08] C. M. Dawson, J. Eisert, and T. J. Osborne. "Unifying Variational Methods for Simulating Quantum Many-Body Systems." *Physical Review Letters* **100**,13, 2008, page 130501.
DOI: 10.1103/PhysRevLett.100.130501.

[DFU11] N. A. Drescher, T. Fischer, and G. S. Uhrig. "Truncation Errors in Self-Similar Continuous Unitary Transformations." *The European Physical Journal B* **79**,2, 2011, pages 225–240.
DOI: 10.1140/epjb/e2010-10723-6.

[Dir28] Paul Adrien Maurice Dirac. "The Quantum Theory of the Electron." *Proceedings of the Royal Society of London. Series A, Containing Papers of a Mathematical and Physical Character* **117**,778, 1928, pages 610–624.
DOI: 10.1098/rspa.1928.0023.

[DP80] J. R. Dormand and P. J. Prince. "A Family of Embedded Runge-Kutta Formulae." *Journal of Computational and Applied Mathematics* **6**,1, 1980, pages 19–26.
DOI: 10.1016/0771-050X(80)90013-3.

[Dre14] Nils Alexander Drescher. "Variational and Perturbative Extensions of Continuous Unitary Transformations for Low-Dimensional Spin Systems." PhD thesis. Technischen Universität Dortmund, 2014. HDL: 2003/33917.

[DU04] Sébastien Dusuel and Götz S Uhrig. "The Quartic Oscillator: A Non-Perturbative Study by Continuous Unitary Transformations." *Journal of Physics A: Mathematical and General* **37**,39, 2004, pages 9275–9294.
DOI: 10.1088/0305-4470/37/39/014.

[DU11] S. Duffe and G. S. Uhrig. "Hole Dispersions for Antiferromagnetic Spin-$\frac{1}{2}$ Two-Leg Ladders by Self-Similar Continuous Unitary Transformations." *The European Physical Journal B* **84**,3, 2011, pages 475–490.
DOI: 10.1140/epjb/e2011-20150-x.

[Dus+10] Sébastien Dusuel et al. "Bound States in Two-Dimensional Spin Systems near the Ising Limit: A Quantum Finite-Lattice Study." *Physical Review B* **81**,6, 2010, page 064412.
DOI: 10.1103/PhysRevB.81.064412.

[Dys56a] Freeman J. Dyson. "General Theory of Spin-Wave Interactions." *Physical Review* **102**,5, 1956, pages 1217–1230.
DOI: 10.1103/PhysRev.102.1217.

[Dys56b] Freeman J. Dyson. "Thermodynamic Behavior of an Ideal Ferromagnet." *Physical Review* **102**,5, 1956, pages 1230–1244.
DOI: 10.1103/PhysRev.102.1230.

[Eck19] Gerhard Ecker. *Particles, Fields, Quanta: From Quantum Mechanics to the Standard Model of Particle Physics*. Undergraduate Lecture Notes in Physics. Springer International Publishing, Cham, 2019.
DOI: 10.1007/978-3-030-14479-1.

[Eig] Eigen Development Team. *Eigen*. Version 3.4.0.

[El-+18] Ramy El-Ganainy et al. "Non-Hermitian Physics and PT Symmetry." *Nature Physics* **14**,1, 2018, pages 11–19.
DOI: 10.1038/nphys4323.

[Fal15] Brigitte Falkenburg. "How Do Quasi-Particles Exist?" In: *Why More Is Different: Philosophical Issues in Condensed Matter Physics and Complex Systems*. Ed. by Brigitte Falkenburg and Margaret Morrison. Springer, Berlin, Heidelberg, 2015, pages 227–250.
DOI: 10.1007/978-3-662-43911-1_12.

[Faz99] Patrick Fazekas. *Lecture Notes on Electron Correlation and Magnetism*. WORLD SCIENTIFIC, 1999.
DOI: 10.1142/2945. eprint: https://www.worldscientific.com/doi/pdf/10.1142/2945.

[FB20] Francesco Ferrari and Federico Becca. "Dynamical Properties of Néel and Valence-Bond Phases in the J1–J2 Model on the Honeycomb Lattice." *Journal of Physics: Condensed Matter* **32**,27, 2020, page 274003.
DOI: 10.1088/1361-648X/ab7f6e.

[FDU10] Tim Fischer, Sebastian Duffe, and Götz S Uhrig. "Adapted Continuous Unitary Transformation to Treat Systems with Quasi-Particles of Finite Lifetime." *New Journal of Physics* **12**,3, 2010, page 033048.
DOI: 10.1088/1367-2630/12/3/033048.

[FDU11] T. Fischer, S. Duffe, and G. S. Uhrig. "Microscopic Model for Bose-Einstein Condensation and Quasiparticle Decay." *Europhysics Letters* **96**,4, 2011, page 47001.
DOI: 10.1209/0295-5075/96/47001.

[Fis12] Tim Fischer. "Description of Quasiparticle Decay by Continuous Unitary Transformations." PhD thesis. Technischen Universität Dortmund, 2012. HDL: 2003/29513.

[Fle+24] Benedetta Flebus et al. "The 2024 Magnonics Roadmap." *Journal of Physics: Condensed Matter* **36**,36, 2024, page 363501.
DOI: 10.1088/1361-648X/ad399c.

[FQS84] Daniel Friedan, Zongan Qiu, and Stephen Shenker. "Conformal Invariance, Unitarity, and Critical Exponents in Two Dimensions." *Physical Review Letters* **52**,18, 1984, pages 1575–1578.
DOI: 10.1103/PhysRevLett.52.1575.

[FSL01] J.B. Fouet, P. Sindzingre, and C. Lhuillier. "An Investigation of the Quantum J_1-J_2-J_3 Model on the Honeycomb Lattice." *The European Physical Journal B - Condensed Matter and Complex Systems* **20**,2, 2001, pages 241–254.
DOI: 10.1007/s100510170273.

[GB17] Christian Gross and Immanuel Bloch. "Quantum Simulations with Ultracold Atoms in Optical Lattices." *Science* **357**,6355, 2017, pages 995–1001.
DOI: 10.1126/science.aal3837.

[Geo+96] Antoine Georges et al. "Dynamical Mean-Field Theory of Strongly Correlated Fermion Systems and the Limit of Infinite Dimensions." *Reviews of Modern Physics* **68**,1, 1996, pages 13–125.
DOI: 10.1103/RevModPhys.68.13.

[Gol61] J. Goldstone. "Field Theories with «Superconductor» Solutions." *Il Nuovo Cimento (1955-1965)* **19**,1, 1961, pages 154–164.
DOI: 10.1007/BF02812722.

[Grä+21] Timo Gräßer et al. "Dynamic Mean-Field Theory for Dense Spin Systems at Infinite Temperature." *Physical Review Research* **3**,4, 2021, page 043168.
DOI: 10.1103/PhysRevResearch.3.043168.

[Gri17] David J. Griffiths. *Introduction to Quantum Mechanics*. Cambridge University Press, 2017. 481 pp. ISBN: 978-1-107-17986-8.

[GSW62] Jeffrey Goldstone, Abdus Salam, and Steven Weinberg. "Broken Symmetries." *Physical Review* **127**,3, 1962, pages 965–970.
DOI: 10.1103/PhysRev.127.965.

[Gut63] Martin C. Gutzwiller. "Effect of Correlation on the Ferromagnetism of Transition Metals." *Physical Review Letters* **10**,5, 1963, pages 159–162.
DOI: 10.1103/PhysRevLett.10.159.

[GW93] Stanisław D. Głazek and Kenneth G. Wilson. "Renormalization of Hamiltonians." *Physical Review D* **48**,12, 1993, pages 5863–5872.
DOI: 10.1103/PhysRevD.48.5863.

[GW94] Stanislaw D. Głazek and Kenneth G. Wilson. "Perturbative Renormalization Group for Hamiltonians." *Physical Review D* **49**,8, 1994, pages 4214–4218.
DOI: 10.1103/PhysRevD.49.4214.

[Ham09] C. J. Hamer. "Energy Spectrum of the Two-Magnon Bound States in the Heisenberg-Ising Antiferromagnet on the Square Lattice." *Physical Review B* **79**,21, 2009, page 212413.
DOI: 10.1103/PhysRevB.79.212413.

[Har+20] Charles R. Harris et al. "Array Programming with NumPy." *Nature* **585**,7825, 2020, pages 357–362.
DOI: 10.1038/s41586-020-2649-2.

[Hei28] W. Heisenberg. "Zur Theorie des Ferromagnetismus." *Zeitschrift für Physik* **49**,9, 1928, pages 619–636.
DOI: 10.1007/BF01328601.

[Her+24] Dag-Björn Hering et al. "Quantum Melting of Long-Range Ordered Quantum Antiferromagnets Investigated by Momentum-Space Continuous Similarity Transformations." *Physical Review B* **110**,8, 2024, page 085115.
DOI: 10.1103/PhysRevB.110.085115.

[Her+25] J. A. Hernández et al. "Field-Induced Magnon Decay, Magnon Shadows, and Rotonlike Excitations in the Honeycomb Antiferromagnet $YbBr_3$." *Physical Review Letters* **135**,14, 2025, page 146701.
DOI: 10.1103/q29r-8x1m.

[Her26] Dag-Björn Hering. *Spin Wave Excitations and Their Interactions in Two-Dimensional Antiferromagnets*. Version V1. TUDOdata, 2026.
DOI: 10.17877/TUDODATA-2026-MP10K2XT.

[Hop58] J. J. Hopfield. "Theory of the Contribution of Excitons to the Complex Dielectric Constant of Crystals." *Physical Review* **112**,5, 1958, pages 1555–1567.
DOI: 10.1103/PhysRev.112.1555.

[HP40] T. Holstein and H. Primakoff. "Field Dependence of the Intrinsic Domain Magnetization of a Ferromagnet." *Physical Review* **58**,12, 1940, pages 1098–1113.
DOI: 10.1103/PhysRev.58.1098.

[Hub63] J. Hubbard. "Electron Correlations in Narrow Energy Bands." *Proceedings of the Royal Society of London. A. Mathematical and Physical Sciences* **276**,1365, 1963, pages 238–257.
DOI: 10.1098/rspa.1963.0204.

[Hun07] John D. Hunter. "Matplotlib: A 2D Graphics Environment." *Computing in Science & Engineering* **9**,3, 2007, pages 90–95.
DOI: 10.1109/MCSE.2007.55.

[HZA92] C. J. Hamer, Zheng Weihong, and Peter Arndt. "Third-Order Spin-Wave Theory for the Heisenberg Antiferromagnet." *Physical Review B* **46**,10, 1992, pages 6276–6292.
DOI: 10.1103/PhysRevB.46.6276.

[IH84] A. C. Irving and C. J. Hamer. "Methods in Hamiltonian Lattice Field Theory (II). Linked-cluster Expansions." *Nuclear Physics B* **230**,3, 1984, pages 361–384.
DOI: 10.1016/0550-3213(84)90218-9.

[Jia12] F.J. Jiang. "High Precision Determination of the Low-Energy Constants for the Two-Dimensional Quantum Heisenberg Model on the Honeycomb Lattice." *The European Physical Journal B* **85**,12, 2012, page 402.
DOI: 10.1140/epjb/e2012-30784-7.

[Jon13] Katherine Jones-Smith. "A 'Dysonization' Scheme for Identifying Quasi-Particles Using Non-Hermitian Quantum Mechanics." *Philosophical Transactions of the Royal Society A: Mathematical, Physical and Engineering Sciences* **371**,1989, 2013, page 20120056.
DOI: 10.1098/rsta.2012.0056.

[Jun+16] T. Jungwirth et al. "Antiferromagnetic Spintronics." *Nature Nanotechnology* **11**,3, 2016, pages 231–241.
DOI: 10.1038/nnano.2016.18.

[Kad+24] Masahiro Kadosawa et al. "Comparing Quantum Fluctuations in the Spin-$\frac{1}{2}$ and Spin-1 XXZ Heisenberg Models on the Square and Honeycomb Lattices." *Physical Review B* **110**,13, 2024, page 134418.
DOI: 10.1103/PhysRevB.110.134418.

[KDU12] H. Krull, N. A. Drescher, and G. S. Uhrig. "Enhanced Perturbative Continuous Unitary Transformations." *Physical Review B* **86**,12, 2012, page 125113.
DOI: 10.1103/PhysRevB.86.125113.

[Keh01] Stefan Kehrein. "Flow Equation Approach to the Sine-Gordon Model." *Nuclear Physics B* **592**,3, 2001, pages 512–562.
DOI: 10.1016/S0550-3213(00)00507-1.

[Keh06] Stefan Kehrein. *The Flow Equation Approach to Many-Particle Systems*. Red. by G. Höhler et al. Vol. 217. Springer Tracts in Modern Physics. Springer, Berlin, Heidelberg, 2006.
DOI: 10.1007/3-540-34068-8.

[Keh99] Stefan Kehrein. "Flow Equation Solution for the Weak- to Strong-Coupling Crossover in the Sine-Gordon Model." *Physical Review Letters* **83**,24, 1999, pages 4914–4917.
DOI: 10.1103/PhysRevLett.83.4914.

[Kim12] Jungho Kim. "Large Spin-Wave Energy Gap in the Bilayer Iridate $Sr_3Ir_2O_7$: Evidence for Enhanced Dipolar Interactions Near the Mott Metal-Insulator Transition." *Physical Review Letters* **109**,15, 2012.
DOI: 10.1103/PhysRevLett.109.157402.

[Kit06] Alexei Kitaev. "Anyons in an Exactly Solved Model and Beyond." *Annals of Physics*. January Special Issue **321**,1, 2006, pages 2–111.
DOI: 10.1016/j.aop.2005.10.005.

[KLS88] Tom Kennedy, Elliott H. Lieb, and B. Sriram Shastry. "Existence of Néel Order in Some Spin-1/2 Heisenberg Antiferromagnets." *Journal of Statistical Physics* **53**,5, 1988, pages 1019–1030.
DOI: 10.1007/BF01023854.

[KM17] B. Keimer and J. E. Moore. "The Physics of Quantum Materials." *Nature Physics* **13**,11, 2017, pages 1045–1055.
DOI: 10.1038/nphys4302.

[KM93] B. Kramer and A. MacKinnon. "Localization: Theory and Experiment." *Reports on Progress in Physics* **56**,12, 1993, page 1469.
DOI: 10.1088/0034-4885/56/12/001.

[KM94] S. K. Kehrein and A. Mielke. "Flow Equations for the Anderson Hamiltonian." *Journal of Physics A: Mathematical and General* **27**,12, 1994, page 4259.
DOI: 10.1088/0305-4470/27/12/030.

[Krä+25] Calvin Krämer et al. *Quantum Decay of Magnons in the Unfrustrated Honeycomb Heisenberg Model*. 2025.
DOI: 10.48550/arXiv.2512.19162. ARXIV: 2512.19162. Preprint.

[KSU03a] C. Knetter, K. P. Schmidt, and G. S. Uhrig. "High Order Perturbation Theory for Spectral Densities of Multi-Particle Excitations: $\mathsf{S} = \frac{1}{2}$ Two-Leg Heisenberg Ladder." *The European Physical Journal B - Condensed Matter and Complex Systems* **36**,4, 2003, pages 525–544.
DOI: 10.1140/epjb/e2004-00008-2.

[KSU03b] Christian Knetter, Kai P. Schmidt, and Götz S. Uhrig. "The Structure of Operators in Effective Particle-Conserving Models." *Journal of Physics A: Mathematical and General* **36**,29, 2003, page 7889.
DOI: 10.1088/0305-4470/36/29/302.

[KU00] C. Knetter and G.S. Uhrig. "Perturbation Theory by Flow Equations: Dimerized and Frustrated S = 1/2 Chain." *The European Physical Journal B - Condensed Matter and Complex Systems* **13**,2, 2000, pages 209–225.
DOI: 10.1007/s100510050026.

[Kub52] Ryogo Kubo. "The Spin-Wave Theory of Antiferromagnetics." *Physical Review* **87**,4, 1952, pages 568–580.
DOI: 10.1103/PhysRev.87.568.

[Lan50] C. Lanczos. "An Iteration Method for the Solution of the Eigenvalue Problem of Linear Differential and Integral Operators." *Journal of Research of the National Bureau of Standards* **45**,4, 1950, page 255.
DOI: 10.6028/jres.045.026.

[Lan66] Robert V. Lange. "Nonrelativistic Theorem Analogous to the Goldstone Theorem." *Physical Review* **146**,1, 1966, pages 301–303.
DOI: 10.1103/PhysRev.146.301.

[Lau97] Dirk Laurie. "Calculation of Gauss-Kronrod Quadrature Rules." *Mathematics of Computation* **66**,219, 1997, pages 1133–1145.
DOI: 10.1090/S0025-5718-97-00861-2.

[Lau99] R. B. Laughlin. "Nobel Lecture: Fractional Quantization." *Reviews of Modern Physics* **71**,4, 1999, pages 863–874.
DOI: 10.1103/RevModPhys.71.863.

[Li+12] P. H. Y. Li et al. "Phase Diagram of a Frustrated Heisenberg Antiferromagnet on the Honeycomb Lattice: The J_1-J_2-J_3 Model." *Physical Review B* **86**,14, 2012, page 144404.
DOI: 10.1103/PhysRevB.86.144404.

[LM89] Zhiping Liu and Efstratios Manousakis. "Variational Calculations for the Square-Lattice Quantum Antiferromagnet." *Physical Review B* **40**,16, 1989, pages 11437–11440.
DOI: 10.1103/PhysRevB.40.11437.

[Loh25] Niels Lohmann. *JSON for Modern C++*. Version 3.12.0. 2025.

[Löw09] Löw. "Properties of the Two-Dimensional Spin-1/2 Heisenberg Model on a Honeycomb Lattice with Interlayer Coupling." *Condensed Matter Physics* **12**,3, 2009, pages 497–506.
DOI: 10.5488/CMP.12.3.497.

[LSS23] Lea Lenke, Andreas Schellenberger, and Kai Phillip Schmidt. "Series Expansions in Closed and Open Quantum Many-Body Systems with Multiple Quasiparticle Types." *Physical Review A* **108**,1, 2023, page 013323.
DOI: 10.1103/PhysRevA.108.013323.

[Mal58a] S. V. Maleev. "Multimagnon Processes in the Scattering of Slow Neutrons in Ferro-Magnets." *Soviet Physics JETP* **34**,7, 1958.

[Mal58b] S. V. Maleev. "Scattering of Slow Neutrons in Ferromagnets." *Sov. Phys. JETP* **6**,4, 1958, page 776.

[Man91] Efstratios Manousakis. "The Spin-½ Heisenberg Antiferromagnet on a Square Lattice and Its Application to the Cuprous Oxides." *Reviews of Modern Physics* **63**,1, 1991, pages 1–62.
DOI: 10.1103/RevModPhys.63.1.

[Mat24] Matplotlib Development Team. *Matplotlib: Visualization with Python*. Version 3.9.2. Zenodo, 2024.
DOI: 10.5281/zenodo.13308876.

[Mat81] Daniel C. Mattis. *The Theory of Magnetism I: Statics and Dynamics*. Red. by Manuel Cardona et al. Vol. 17. Springer Series in Solid-State Sciences. Springer, Berlin, Heidelberg, 1981.
DOI: 10.1007/978-3-642-83238-3.

[Maz+22] D. G. Mazzone et al. "Antiferromagnetic Excitonic Insulator State in Sr3Ir2O7." *Nature Communications* **13**,1, 2022, page 913.
DOI: 10.1038/s41467-022-28207-w.

[MFU12] Kingshuk Majumdar, Douglas Furton, and Götz S. Uhrig. "Effects of Ring Exchange Interaction on the Néel Phase of Two-Dimensional, Spatially Anisotropic, Frustrated Heisenberg Quantum Antiferromagnet." *Physical Review B* **85**,14, 2012, page 144420.
DOI: 10.1103/PhysRevB.85.144420.

[MHS] Matthias Walther, Dag-Björn Hering, and Vanessa Sulaiman. *CST Pipeline*. Version not published, available upon request.

[Mie97] Andreas Mielke. "Similarity Renormalization of the Electron-Phonon Coupling." *Annalen der Physik* **509**,3, 1997, pages 215–233.
DOI: 10.1002/andp.19975090305.

[Mie98] A. Mielke. "Flow Equations for Band-Matrices." *The European Physical Journal B - Condensed Matter and Complex Systems* **5**,3, 1998, pages 605–611.
DOI: 10.1007/s100510050485.

[Mor+15] M. Moretti Sala et al. "Evidence of Quantum Dimer Excitations in $Sr_3Ir_2O_7$." *Physical Review B* **92**,2, 2015, page 024405.
DOI: 10.1103/PhysRevB.92.024405.

[MU19] M. Malki and G. S. Uhrig. "Delocalization of Edge States in Topological Phases." *Europhysics Letters* **127**,2, 2019, page 27001.
DOI: 10.1209/0295-5075/127/27001.

[MW66] N. D. Mermin and H. Wagner. "Absence of Ferromagnetism or Antiferromagnetism in One- or Two-Dimensional Isotropic Heisenberg Models." *Physical Review Letters* **17**,22, 1966, pages 1133–1136.
DOI: 10.1103/PhysRevLett.17.1133.

[Née32] L. Néel. "Influence des fluctuations du champ moléculaire sur les propriétés magnétiques des corps." *Annales de Physique* **10**,18, 1932, pages 5–105.
DOI: 10.1051/anphys/193210180005.

[Née71] Louis Néel. "Magnetism and Local Molecular Field." *Science* **174**,4013, 1971, pages 985–992.
DOI: 10.1126/science.174.4013.985.

[Nol15] Wolfgang Nolting. *Grundkurs Theoretische Physik 7: Viel-Teilchen-Theorie*. Springer-Lehrbuch. Springer, Berlin, Heidelberg, 2015.
DOI: 10.1007/978-3-642-25808-4.

[Nov+04] K. S. Novoselov et al. "Electric Field Effect in Atomically Thin Carbon Films." *Science* **306**,5696, 2004, pages 666–669.
DOI: 10.1126/science.1102896.

[Nov+16] K. S. Novoselov et al. "2D Materials and van Der Waals Heterostructures." *Science* **353**,6298, 2016, aac9439.
DOI: 10.1126/science.aac9439.

[OB78] J. Oitmaa and DD Betts. "The Ground State of Two Quantum Models of Magnetism." *Canadian Journal of Physics* **56**,7, 1978, pages 897–901.
DOI: 10.1139/p78-120.

[Ogu60] Takehiko Oguchi. "Theory of Spin-Wave Interactions in Ferro- and Antiferromagnetism." *Physical Review* **117**,1, 1960, pages 117–123.
DOI: 10.1103/PhysRev.117.117.

[OHZ92] J. Oitmaa, C. J. Hamer, and Zheng Weihong. "Quantum Magnets on the Honeycomb and Triangular Lattices at T =0." *Physical Review B* **45**,17, 1992, pages 9834–9841.
DOI: 10.1103/PhysRevB.45.9834.

[OI73] Takehiko Oguchi and Takuma Ishikawa. "Theory of Two-Magnon Bound States in a Two-Dimensional Antiferromagnet." *Journal of the Physical Society of Japan* **34**,6, 1973, pages 1486–1490.
DOI: 10.1143/JPSJ.34.1486.

[Oku+01] K. Okunishi et al. "Universal Relation between the Dispersion Curve and the Ground-State Correlation Length in One-Dimensional Antiferromagnetic Quantum Spin Systems." *Physical Review B* **64**,10, 2001, page 104432.
DOI: 10.1103/PhysRevB.64.104432.

[OS11] J. Oitmaa and R. R. P. Singh. "Phase Diagram of the $J_1 - J_2 - J_3$ Heisenberg Model on the Honeycomb Lattice: A Series Expansion Study." *Physical Review B* **84**,9, 2011, page 094424.
DOI: 10.1103/PhysRevB.84.094424.

[Pal+23] Subhajyoti Pal et al. "Theoretical Analysis of Multimagnon Excitations in Resonant Inelastic X-Ray Scattering Spectra of Two-Dimensional Antiferromagnets." *Physical Review B* **108**,21, 2023, page 214405.
DOI: 10.1103/PhysRevB.108.214405.

[Pan25] Pandas Development Team. *Pandas-Dev/Pandas: Pandas*. Version 2.2.2. Zenodo, 2025.
DOI: 10.5281/zenodo.17992932.

[Pir21] Antonio Sergio Teixeira Pires. *Theoretical Tools for Spin Models in Magnetic Systems*. IOP Publishing, 2021. ISBN: 978-0-7503-3879-0.

[Pow17] Michael Powalski. "Dynamics and Interaction of Magnons in the Two Dimensional Heisenberg Antiferromagnet." PhD thesis. Technischen Universität Dortmund, 2017. HDL: 2003/36028.

[PSU18] Michael Powalski, Kai Phillip Schmidt, and Götz S. Uhrig. "Mutually Attracting Spin Waves in the Square-Lattice Quantum Antiferromagnet." *SciPost Physics* **4**,1, 2018, page 001.
DOI: 10.21468/SciPostPhys.4.1.001.

[PUS15] M. Powalski, G. S. Uhrig, and K. P. Schmidt. "Roton Minimum as a Fingerprint of Magnon-Higgs Scattering in Ordered Quantum Antiferromagnets." *Physical Review Letters* **115**,20, 2015, page 207202.
DOI: 10.1103/PhysRevLett.115.207202.

[Reh+16] J. Rehn et al. "Classical Spin Liquid on the Maximally Frustrated Honeycomb Lattice." *Physical Review Letters* **117**,16, 2016, page 167201.
DOI: 10.1103/PhysRevLett.117.167201.

[Rei06] Alexander Antonius Reischl. "Derivation of Effective Models Using Self-Similar Continuous Unitary Transformations in Real Space." PhD thesis. Universität zu Köln, 2006.

[Rez20] Sergio M. Rezende. *Fundamentals of Magnonics*. Vol. 969. Lecture Notes in Physics. Springer International Publishing, Cham, 2020.
DOI: 10.1007/978-3-030-41317-0.

[RMU04] Alexander Reischl, Erwin Müller-Hartmann, and Götz S. Uhrig. "Systematic Mapping of the Hubbard Model to the Generalized $t-J$ Model." *Physical Review B* **70**,24, 2004, page 245124.
DOI: 10.1103/PhysRevB.70.245124.

[Ros+20] Lorenzo Rosso et al. "Dissipative Flow Equations." *SciPost Physics* **9**,6, 2020, page 091.
DOI: 10.21468/SciPostPhys.9.6.091.

[Rot09] Ingrid Rotter. "A Non-Hermitian Hamilton Operator and the Physics of Open Quantum Systems." *Journal of Physics A: Mathematical and Theoretical* **42**,15, 2009, page 153001.
DOI: 10.1088/1751-8113/42/15/153001.

[RRY89] J. D. Reger, J. A. Riera, and A. P. Young. "Monte Carlo Simulations of the Spin-1/2 Heisenberg Antiferromagnet in Two Dimensions." *Journal of Physics: Condensed Matter* **1**,10, 1989, page 1855.
DOI: 10.1088/0953-8984/1/10/007.

[Sac11] Subir Sachdev. *Quantum Phase Transitions*. 2nd ed. Cambridge University Press, Cambridge, 2011.
DOI: 10.1017/CBO9780511973765.

[Sal+21] G. Sala et al. "Van Hove Singularity in the Magnon Spectrum of the Antiferromagnetic Quantum Honeycomb Lattice." *Nature Communications* **12**,1, 2021, page 171.
DOI: 10.1038/s41467-020-20335-5.

[Sal+23] Gabriele Sala et al. "Field-Tuned Quantum Renormalization of Spin Dynamics in the Honeycomb Lattice Heisenberg Antiferromagnet YbCl3." *Communications Physics* **6**,1, 2023, pages 1–7.
DOI: 10.1038/s42005-023-01333-7.

[San+17] D Sander et al. "The 2017 Magnetism Roadmap." *Journal of Physics D: Applied Physics* **50**,36, 2017, page 363001.
DOI: 10.1088/1361-6463/aa81a1.

[San97] Anders W. Sandvik. "Finite-Size Scaling of the Ground-State Parameters of the Two-Dimensional Heisenberg Model." *Physical Review B* **56**,18, 1997, pages 11678–11690.
DOI: 10.1103/PhysRevB.56.11678.

[Sch+22] Gary Schmiedinghoff et al. "Three-Body Bound States in Antiferromagnetic Spin Ladders." *Communications Physics* **5**,1, 2022, pages 1–8.
DOI: 10.1038/s42005-022-00986-0.

[Sch02] Franz Schwabl. *Quantum Mechanics*. Springer, Berlin, Heidelberg, 2002.
DOI: 10.1007/978-3-662-04840-5.

[Sch22] Gary Schmiedinghoff. "Applications and Extensions of Flow Equations to Closed and Open Quantum Systems." PhD thesis. Technischen Universität Dortmund, 2022. HDL: 2003/41108.

[Sch26] E. Schrödinger. "An Undulatory Theory of the Mechanics of Atoms and Molecules." *Physical Review* **28**,6, 1926, pages 1049–1070.
DOI: 10.1103/PhysRev.28.1049.

[Sin89] Rajiv R. P. Singh. "Thermodynamic Parameters of the $T=0$, Spin-1/2 Square-Lattice Heisenberg Antiferromagnet." *Physical Review B* **39**,13, 1989, pages 9760–9763.
DOI: 10.1103/PhysRevB.39.9760.

[SK16] Daniele Sanvitto and Stephane Kena-Cohen. "The Road towards Polaritonic Devices." *Nature Materials* **15**,10, 2016, pages 1061–1073.
DOI: 10.1038/NMAT4668.

[SS01] Anders W. Sandvik and Rajiv R. P. Singh. "High-Energy Magnon Dispersion and Multimagnon Continuum in the Two-Dimensional Heisenberg Antiferromagnet." *Physical Review Letters* **86**,3, 2001, pages 528–531.
DOI: 10.1103/PhysRevLett.86.528.

[Sta+14] Robert L Stamps et al. "The 2014 Magnetism Roadmap." *Journal of Physics D: Applied Physics* **47**,33, 2014, page 333001.
DOI: 10.1088/0022-3727/47/33/333001.

[Str+18] Giancarlo Calvanese Strinati et al. "The BCS-BEC Crossover: From Ultra-Cold Fermi Gases to Nuclear Systems." *Physics Reports-Review Section of Physics Letters* **738**, 2018, pages 1–76.
DOI: 10.1016/j.physrep.2018.02.004.

[SU06] K. P. Schmidt and G. S. Uhrig. "Hard-Core Magnons in the $S = 1 / 2$ Heisenberg Model on the Square Lattice." *Physical Review B* **73**,17, 2006, page 172407.
DOI: 10.1103/PhysRevB.73.172407.

[SU22] Gary Schmiedinghoff and Götz S. Uhrig. "Efficient Flow Equations for Dissipative Systems." *SciPost Physics* **13**,6, 2022, page 122.
DOI: 10.21468/SciPostPhys.13.6.122.

[SWS24] L. Schamriß, M. R. Walther, and Kai Phillip Schmidt. "Extracting Quantum-Critical Properties from Directly Evaluated Enhanced Perturbative Continuous Unitary Transformations." *SciPost Physics* **17**,3, 2024, page 094.
DOI: 10.21468/SciPostPhys.17.3.094.

[Syr10] A V Syromyatnikov. "Spectrum of Short-Wavelength Magnons in a Two-Dimensional Quantum Heisenberg Antiferromagnet on a Square Lattice: Third-Order Expansion in 1/S." *Journal of Physics: Condensed Matter* **22**,21, 2010, page 216003.
DOI: 10.1088/0953-8984/22/21/216003.

[Tak+19] Hidenori Takagi et al. "Concept and Realization of Kitaev Quantum Spin Liquids." *Nature Reviews Physics* **1**,4, 2019, pages 264–280.
DOI: 10.1038/s42254-019-0038-2.

[Tak77] M. Takahashi. "Half-Filled Hubbard Model at Low Temperature." *Journal of Physics C: Solid State Physics* **10**,8, 1977, page 1289.
DOI: 10.1088/0022-3719/10/8/031.

[TM73] Hidetosi Takahasi and Masatake Mori. "Double Exponential Formulas for Numerical Integration." *Publications of the Research Institute for Mathematical Sciences* **9**,3, 1973, pages 721–741.
DOI: 10.2977/prims/1195192451.

[UM13] Götz S. Uhrig and Kingshuk Majumdar. "Varied Perturbation Theory for the Dispersion Dip in the Two-Dimensional Heisenberg Quantum Antiferromagnet." *The European Physical Journal B* **86**,6, 2013, page 282.
DOI: 10.1140/epjb/e2013-40159-3.

[UN98] G. S. Uhrig and B. Normand. "Magnetic Properties of $(VO)_2P_2O_7$ from Frustrated Interchain Coupling." *Physical Review B* **58**,22, 1998, R14705–R14708.
DOI: 10.1103/PhysRevB.58.R14705.

[US96] Götz S. Uhrig and H. J. Schulz. "Magnetic Excitation Spectrum of Dimerized Antiferromagnetic Chains." *Physical Review B* **54**,14, 1996, R9624–R9627.
DOI: 10.1103/PhysRevB.54.R9624.

[US98] Götz S. Uhrig and H. J. Schulz. "Erratum: Magnetic Excitation Spectrum of Dimerized Antiferromagnetic Chains [Phys. Rev. B 54, R9624 (1996)]." *Physical Review B* **58**,5, 1998, pages 2900–2900.
DOI: 10.1103/PhysRevB.58.2900.

[Vac24] Bassano Vacchini. *Open Quantum Systems: Foundations and Theory*. Graduate Texts in Physics. Springer Nature Switzerland, Cham, 2024.
DOI: 10.1007/978-3-031-58218-9.

[Val58] J. G. Valatin. "Comments on the Theory of Superconductivity." *Il Nuovo Cimento* **7**,6, 1958, pages 843–857.
DOI: 10.1007/BF02745589.

[Ved+20] E Y Vedmedenko et al. "The 2020 Magnetism Roadmap." *Journal of Physics D: Applied Physics* **53**,45, 2020, page 453001.
DOI: 10.1088/1361-6463/ab9d98.

[Ven+16] Liesbeth Venema et al. "The Quasiparticle Zoo." *Nature Physics* **12**,12, 2016, pages 1085–1089.
DOI: 10.1038/nphys3977.

[Ver18] Ruben Verresen. "Quantum Dynamics of the Square-Lattice Heisenberg Model." *Physical Review B* **98**,15, 2018.
DOI: 10.1103/PhysRevB.98.155102.

[Vir+20] Pauli Virtanen et al. "SciPy 1.0: Fundamental Algorithms for Scientific Computing in Python." *Nature Methods* **17**,3, 2020, pages 261–272.
DOI: 10.1038/s41592-019-0686-2.

[VM94] V. S. Viswanath and Gerhard Müller. *The Recursion Method: Application to Many-Body Dynamics*. Red. by H. Araki et al. Vol. 23. Lecture Notes in Physics Monographs. Springer, Berlin, Heidelberg, 1994.
DOI: 10.1007/978-3-540-48651-0.

[Vol12] D. Vollhardt. "Dynamical Mean-Field Theory for Correlated Electrons." *Annalen der Physik* **524**,1, 2012, pages 1–19.
DOI: 10.1002/andp.201100250.

[Von96] John Von Neumann. *Mathematische Grundlagen der Quantenmechanik*. Springer, Berlin, Heidelberg, 1996.
DOI: 10.1007/978-3-642-61409-5.

[Wal+23] Matthias R. Walther et al. "Continuous Similarity Transformation for Critical Phenomena: Easy-axis Antiferromagnetic XXZ Model." *Physical Review Research* **5**,1, 2023, page 013132.
DOI: 10.1103/PhysRevResearch.5.013132.

[Wal24] Matthias Walther. "Effective Models for Interacting Spin Waves in Two-Dimensional Quantum Antiferromagnets." PhD thesis. Friedrich-Alexander-Universität Erlangen-Nürnberg, 2024.
DOI: 10.25593/open-fau-1456.

[Wan+25] Chao Wang et al. "Swarm Intelligence: A Survey of Model Classification and Applications." *Chinese Journal of Aeronautics* **38**,3, 2025, page 102982.
DOI: 10.1016/j.cja.2024.03.019.

[Weg06] Franz Wegner. "Flow Equations and Normal Ordering: A Survey." *Journal of Physics A: Mathematical and General* **39**,25, 2006, page 8221.
DOI: 10.1088/0305-4470/39/25/S29.

[Weg94] Franz Wegner. "Flow-Equations for Hamiltonians." *Annalen der Physik* **506**,2, 1994, pages 77–91.
DOI: 10.1002/andp.19945060203.

[Wei+20] Songrui Wei et al. "Emerging Intrinsic Magnetism in Two-Dimensional Materials: Theory and Applications." *2D Materials* **8**,1, 2020, page 012005.
DOI: 10.1088/2053-1583/abc8cb.

[Wes+20] Christian Wessler et al. "Observation of Plaquette Fluctuations in the Spin-1/2 Honeycomb Lattice." *npj Quantum Materials* **5**,1, 2020, page 85.
DOI: 10.1038/s41535-020-00287-1.

[Wic50] G. C. Wick. "The Evaluation of the Collision Matrix." *Physical Review* **80**,2, 1950, pages 268–272.
DOI: 10.1103/PhysRev.80.268.

[Wie+25] Raymond Wiedmann et al. *Quantum Effects in the Magnon Spectrum of 2D Altermagnets via Continuous Similarity Transformations*. 2025.
DOI: 10.48550/arXiv.2511.03528. ARXIV: 2511.03528. Preprint.

[WOH91] Zheng Weihong, J. Oitmaa, and C. J. Hamer. "Second-Order Spin-Wave Results for the Quantum XXZ and XY Models with Anisotropy." *Physical Review B* **44**,21, 1991, pages 11869–11881.
DOI: 10.1103/PhysRevB.44.11869.

[YS11] H. Y. Yang and K. P. Schmidt. "Effective Models for Gapped Phases of Strongly Correlated Quantum Lattice Models." *Europhysics Letters* **94**,1, 2011, page 17004.
DOI: 10.1209/0295-5075/94/17004.

[YSW19] T. Ying, K. P. Schmidt, and S. Wessel. "Higgs Mode of Planar Coupled Spin Ladders and Its Observation in $C_9H_{18}N_2CuBr_4$." *Physical Review Letters* **122**,12, 2019, page 127201.
DOI: 10.1103/PhysRevLett.122.127201.

[Zha+22] Shang-Shun Zhang et al. "Schwinger Boson Theory of Ordered Magnets." *Physical Review B* **105**,22, 2022, page 224404.
DOI: 10.1103/PhysRevB.105.224404.

[Zhi13] M. E. Zhitomirsky. "*Colloquium*: Spontaneous Magnon Decays." *Reviews of Modern Physics* **85**,1, 2013, pages 219–242.
DOI: 10.1103/RevModPhys.85.219.

[ZOH05] Weihong Zheng, J. Oitmaa, and C. J. Hamer. "Series Studies of the Spin-$\frac{1}{2}$ Heisenberg Antiferromagnet at $T = 0$: Magnon Dispersion and Structure Factors." *Physical Review B* **71**,18, 2005, page 184440.
DOI: 10.1103/PhysRevB.71.184440.

List of Figures

List of Tables

Danksagung

Mein erster Dank gilt Götz Uhrig, der mir die Möglichkeit gegeben hat, in seiner Arbeitsgruppe nicht nur zu promovieren, sondern mich bereits während meiner Bachelor- und Masterarbeit bei allen auftretenden Problemen stets mit Rat und Lösungen unterstützt hat. Ebenso danke ich Kai Phillip Schmidt von der Friedrich-Alexander-Universität Erlangen-Nürnberg für seine Unterstützung bei fachlichen Fragen und Diskussionen sowie für seine stets offene und konstruktive Art. Ich möchte euch beiden ausdrücklich dafür danken, dass ihr gemeinsam diese wissenschaftliche Zusammenarbeit ins Leben gerufen habt, aus der schließlich dieses Projekt hervorging und bei dem ihr mich während der gesamten Zeit stets unterstützt habt.

Dieses Projekt war von Anfang an als eine Zusammenarbeit zwischen den beiden Universitäten und damit auch zwischen zwei Doktoranden ausgelegt. Was mich zu Matthias Walther bringt, der von Anfang an mein Mitstreiter in diesem Projekt war. Auch wenn unsere Zusammenarbeit aufgrund der globalen Lage zunächst ausschließlich digital stattfinden konnte, war sie doch von Beginn an sehr intensiv und hat mir große Freude bereitet. Von langen Codingsessions, um noch mehr aus dem Programm herauszuholen, bis hin zu Diskussionen über die Physik hinter den Ergebnissen mit unseren Betreuern Götz und Kai wurde alles digital bewerkstelligt. So entstand aus dieser intensiven Kollaboration auch eine enge Freundschaft, die sicherlich auch über die Promotion hinaus Bestand haben wird. Danke Matthias für die tolle Zeit und Zusammenarbeit in den letzten Jahren! In diesem Zusammenhang möchte ich mich ebenfalls herzlich bei den Mitgliedern der KPS-Gruppe bedanken, die mich stets herzlich aufgenommen haben, wann immer ich zu Besuch in Erlangen war.

Ein weiterer herzlicher Dank gilt Vanessa Sulaiman, die Matthias und mich seit Mitte 2024 tatkräftig bei dem Projekt unterstützt. Dank deiner engagierten Mitarbeit fiel mir die Zeit nach Abschluss von Matthias' Promotion deutlich leichter, und gemeinsam konnten wir das Projekt erfolgreich weiterführen – vielen Dank dafür! Ebenso möchte ich allen bisher nicht namentlich erwähnten Co-Autor*innen meiner Veröffentlichungen danken; es hat mir viel Freude bereitet, mit euch zusammenzuarbeiten.

Mein ausdrücklicher Dank gilt zudem Timo Gräßer, Joshua Althüser, Sinja Behrensmeier, Benedikt Sanders sowie Matthias und Vanessa, die das Lektorat meiner Arbeit übernommen haben. Euer wertvolles Feedback hat maßgeblich dazu beigetragen, die Qualität dieser Arbeit zu verbessern. Darüber hinaus möchte ich mich auch bei allen aktuellen und ehemaligen Mitgliedern der Uhrig-Gruppe bedanken, die mich während meiner Promotion in den vergangenen Jahren stets begleitet und unterstützt haben.

Meinen Freunden außerhalb der Universität danke ich herzlich dafür, dass sie mich stets motiviert und wann immer es notwendig war, auch mal von der Arbeit abgelenkt haben.

Natürlich möchte ich mich auch bei meiner Familie bedanken. Auch wenn ihr vielleicht nicht jedes Detail dessen nachvollziehen konntet, was ich euch über Quantenphysik erzählt habe, wart ihr jederzeit bereit zuzuhören und habt mir in allen – auch den nicht immer einfachen – Lebenslagen während meines Studiums und meiner Promotion Rückhalt und Unterstützung gegeben.

Zum Schluss gebührt mein besonderer Dank Anika Schulte. Danke, dass du stets für mich da bist und mich in jeder Hinsicht unterstützt. Ich bin gespannt darauf, was die kommenden Jahre bringen werden, und freue mich sehr darauf, sie gemeinsam mit dir zu erleben!